FIRE PERFORMANCE OF FRP-STRENGTHENED CONCRETE FLEXURAL MEMBERS

By

Pratik Prashant Bhatt

A DISSERTATION

Submitted to
Michigan State University
in partial fulfillment of the requirements
for the degree of

Civil Engineering - Doctor of Philosophy

2021

ABSTRACT

FIRE PERFORMANCE OF FRP-STRENGTHENED CONCRETE FLEXURAL MEMBERS

By

Pratik Prashant Bhatt

Over the last three decades, fiber reinforced polymer (FRP) materials have emerged as a promising solution for strengthening and retrofitting of concrete structural members owing to its high strength and durability properties. However, FRP undergoes rapid degradation in strength, modulus, and bond properties due to softening of polymer matrix and bonding adhesive even at moderately elevated temperatures. Therefore, an FRP-strengthened concrete member experiences rapid loss in capacity and stiffness resulting in lower fire resistance than an un-strengthened concrete member. The fire response of FRP-strengthened concrete structural members is influenced by several factors, and thus fire resistance evaluation requires advanced analysis. While several studies are available on fire resistance evaluation of FRP-strengthened reinforced concrete (RC) beams, limited information available on fire performance of FRP-strengthened concrete slabs. Moreover, the available studies on beams do not fully account for all the important factors influencing fire response of strengthened structural members. To address some of the knowledge gaps and to develop a fundamental understanding on the fire resistance of FPR-strengthened RC flexural members, experimental and numerical studies were carried out.

As part of experimental studies, a series of tests were conducted at both material level and structural level. For material property characterization, uniaxial tensile tests and double lap shear tests were conducted at elevated temperatures to evaluate high temperature tensile strength of FRP and bond strength of FRP-concrete interface, respectively. For structural fire resistance characterization, tests were conducted on five FRP-strengthened concrete T-beams and two FRP-

strengthened concrete slabs, wherein effect of strengthening level, reinforcement ratio, load levels, as well as insulation thickness and configuration was evaluated.

As part of numerical studies, a macroscopic finite element based model, originally developed for strengthened RC beams, was further enhanced for evaluating thermo-mechanical response of strengthened RC slabs under fire conditions. The model accounts for temperature dependent material properties, as well as geometric and material nonlinearity. The novelty of model lies in consideration of temperature induced bond degradation through use of different temperature dependent bond-slip relations and in conducting a member level structural analysis rather than analyzing a single critical section. The model was validated using the above generated test data by comparing various response parameters and was applied to quantify the effect of critical factors influencing the fire resistance of FRP-strengthened concrete beams and slabs, through a set of parametric studies. Results from these studies indicate that the fire resistance of FRP-strengthened RC flexural members is significantly influenced by insulation geometry, fire scenario, and load levels, and is moderately influenced by strengthening level or reinforcement ratio.

The generated test data as well as those reported in literature were utilized to develop machine learning (ML) based approach for predicting fire resistance of FRP-strengthened concrete beams. Three different ML algorithms, namely support vector regression, random forest regression, and deep neural networks, were successfully trained over the compiled dataset to develop fire resistance prediction models for strengthened RC beams. The accuracy of the trained models was determined by comparing the predictions from the model for an un-seen dataset Results indicate that ML based approaches can be effectively utilized for developing simplified tools for predicting fire resistance of strengthened concrete beams with different geometrical configuration, load levels, reinforcement ratio, and strengthening level.

I dedicate my humble efforts to
My father,
Shree Prashant H Bhatt (1960-2021),
A man who taught me everything that matters specially the virtues of discipline, dedication, determination, and excellence
&
My Mother,
Smt. Anamika Bhatt (1961 ~)
A lady who filled my heart with love and dreams and encouraged me to take on every adventure especially this one

ACKNOWLEDGMENTS

PhD research is often perceived as a formidable, colossal, and solitary expedition, but the reality couldn't be far from the truth. In fact, my PhD was an interesting, insightful, and sometimes painful but enjoyable journey accompanied by many of the greatest souls I have ever come across. At the outset of this wonderful accomplishment, I would like to acknowledge these folks.

First and foremost, I would like to express my sincerest and deepest gratitude to my advisor, Dr. Venkatesh Kodur, for his endless patience, tremendous support, invaluable guidance, and encouragement during the entire PhD journey. His continuous motivation and perseverance convincingly instilled in me a spirit of adventure towards research and kept me riveted to my main objective. I feel immensely fortunate to have had opportunity to work with Prof. Kodur and couldn't have imagined having a better advisor and mentor for my PhD thesis.

I would like to thank the members of my committee Dr. Nizar Lajnef, Dr. Mahmoodul Haq, and Dr. Thomas Pence who invested their valuable time to read my reports and thesis and provided insightful remarks and constructive comments which helped me shape this thesis in a better manner. Apart from the committee members, my dear friend Dr. Mohannad Naser deserves a special mention, with whom I had countless thoughtful discussions for long hours which helped me address some of the complexities and intricacies of the research problem with relative ease.

I would like to thank my peers and friends; Esam Aziz, Derek Hibner, Saleh Mohammad Alogla, Roya Solhmirzaei, Anuj Shakya, Srishti Banerji, Svetha Venkatachari, Puneet Kumar, and Augusto Masiero Gil for their help in lab work. I would like to express my appreciation to the manager of civil infrastructure laboratory, Mr. Siavosh Ravanbakhsh and Mr. Charles Meddaugh (Chuck) for their support and help during the experimental program in this research. Additionally, I would like to thank Laura Taylor, Laura Post, Margaret Conner, and Bailey Weber for all the administrative assistance they provided. I am thankful for the support from the Department of Civil and Environmental Engineering and College of Engineering for providing several resources during my graduate studies through fellowships, travel grants, and workshops. In addition, I would also like to acknowledge the funding from Qatar National Research Fund (QNRF) and Structural Technologies LLC for experimental studies.

I would like to specially thank my dear wife, *Nidhi*, for her never-ending love and unconditional support. Her encouraging words of wisdom helped me keep focus on the bigger picture. I would also like to express my sincere gratitude to brother (*Utsav*) and sis-in-law (*Rutu*) who motivated me and supported me by taking great care of our parents and graciously fulfilled all my responsibilities of an elder child towards the family, so I can focus on my work. Last but not the least, I would like to thank my loving *grandparents*, whos' everlasting love and fondness for me as well as incessant pride in me helped me keep faith and believe in myself. I would like to thank my *in-laws* who showed their faith in me by allowing me to marry their daughter during my PhD.

Lastly, I would like to acknowledge my parents without whom I wouldn't be here. No words can remotely express the love and gratitude I have for them. In the end, I would like to thank Bhagwan Ganesh, Bhagwan Hanuman, and Maa Gayatri for bestowing upon me this opportunity and helping me in various forms through different people at every stage of my PhD journey and blessing me with such great parents and mentor.

TABLE OF CONTENTS

LIST OF TABLES

LIST OF FIGURES

KEY TO SYMBOLS AND ABBREVIATIONS

» Abbreviations

AFRP	:	Aramid fiber reinforced polymer
AI	:	Artificial intelligence
ANN	:	Artificial neural network
API	:	Application programing interface
CART	:	Classification and regression trees model
CFRP	:	Carbon fiber reinforced polymer
CTE	:	Co-efficient of thermal expansion
DLd	:	Dead load
DNN	:	Deep neural network
DT	:	Decision trees
EB	:	Externally bonded
EF	:	Environmental factor for properties of FRP
ELU	:	Exponential linear units
FR	:	Fire resistance time
FRP	:	Fiber reinforced polymer
FRPSL	:	FRP strengthening level
FRR	:	Fire resistance rating
FS	:	Fire scenario
GFRP	:	Glass fiber reinforced polymer
GP	:	Genetic programming

HL	:	Hidden layers
HSC	:	High strength concrete
LL	:	Load level
LLd	:	Live load
MAE	:	Mean absolute error
MAPE	:	Mean absolute percentage error
ML	:	Machine learning
MLP	:	Multi-layered perceptron
MPa	:	Mega Pascal
MSE	:	Mean squared error
NN	:	Neural network
NRCC	:	National research council Canada
NSC	:	Normal strength concrete
NSM	:	Near surface mounted
OOB	:	Out-of-bag
RBF	:	Radial basis function
RC	:	Reinforced concrete
ReLu	:	Rectified linear unit
RF	:	Random Forest
RFR	:	Random Forest regressor
RMSE	:	Root mean squared error
SELU	:	Scaled exponential linear units
SFRM	:	Spray applied fire resistive material

SG#	:	Strain gauge number
SVR	:	Support vector regression
TC#	:	Thermocouple number
XGB	:	Extreme gradient boosting

» **Greek symbols**

β_1	:	Force resultants
β_w	:	FRP-to-concrete width ratio factor
δ	:	Interfacial slip between FRP and concrete (mm)
δ_v	:	Vertical deflection at mid-span of beam or slab due to transverse loading (mm)
Δ	:	Axial expansion in the length of the flexural member
ε_{bi}	:	Initial strain at the soffit of the strengthened member
ε_c	:	Assumed strain at the topmost fiber in concrete
ε_{cr}	:	Creep strain
ε_f	:	Emissivity of fire
ε_{mec}	:	Mechanical strain
ε_s	:	Emissivity of the exposed surface of the structural member
ε_{slip}	:	Strain resulting from relative slip
ε_t	:	Total strain
ε_{th}	:	Thermal strain
ε_{tr}	:	Transient strain (exclusive to concrete)
ε_u	:	Rupture strain of CFRP (%)
ε_y	:	Yield strain in steel rebars (%)

ϕ	:	Diameter of steel rebars/ concrete cylinder/ semicircular plate (mm)
ϕ_c	:	Diameter of compressive (top) steel rebars in beam (mm)
ϕ_s	:	Diameter of stirrups and temperature rebar (mm)
ϕ_t	:	Diameter of tensile (bottom) steel rebars in beam or slab (mm)
$\in$	:	User specified error tolerance (width of the insensitive zone)
φ	:	Strength reduction factor
φ_j	:	Nonlinear mapping (kernel) function
κ	:	Assumed curvature
μ	:	Mean of the original values of input parameter x
∇	:	Differential operator:
θ	:	Constant parameter
ρ	:	Density (kg/m^3)
ρ_{ins}	:	Density of insulation (kg/m^3)
ρ_s	:	Steel reinforcement ratio ($A_{s\,t}/bd$)
σ	:	Stefan-Boltzmann constant 5.67×10^{-8} (W/m^2 K^4)
σ_e	:	Stress at the center of element in cross-section
σ_{std}	:	Standard deviation of the original values of the input parameter
$\tau_{f,T}$	:	shear bond stress at temperature T (N/mm^2)
τ_i	:	Average shear stress
Ψ	:	FRP strength reduction factor
ξ_j, ξ_j^*	:	Non-negative slack variables

» **Lettered symbols**

a	:	Depth of stress block (mm)
A_c	:	Area of concrete (mm^2)
A_e	:	Area of each element in the cross-section (mm^2)
A_f	:	Area of FRP (mm^2)
anc_t_{ins}	:	Thickness of insulation in anchorages (mm)
A_s	:	Area of steel (mm^2)
B_0	:	Interfacial brittleness index at ambient temperature (1/mm)
b_c	:	Width of concrete in web of T-beam or in c/s of rectangular beam /slab (mm)
b_f	:	Width of flange (mm)
b_{frp}	:	Width of FRP (mm)
b_{ins}	:	Width of insulation at the bottom of slab cross-section(mm)
b_p	:	Width of FRP concrete interface (mm)
b_s	:	Width of slab (mm)
b_t	:	Bias term
B_T	:	Interfacial brittleness index at elevated temperature (1/mm)
C	:	Regularization parameter
c	:	Specific heat (J/kg°C)
c_a	:	Actual depth of neutral axis
C_c	:	Concrete cover to the rebars(mm)
c_{ins}	:	Specific heat of insulation (J/kg°C)
D	:	Deflection limit state
d	:	Effective depth of the structural member (mm)
d_c	:	Total depth of concrete in beam or slab cross-section (mm)

d_f	:	Effective depth of FRP (up to mid height of FRP, mm)
d_t	:	Maximum depth of tree
ec	:	effective cover in tension zone
E_c	:	Elastic modulus of concrete (GPa)
E_f	:	Elastic modulus of CFRP (GPa)
EI_0	:	Initial rigidity (Nmm^2)
E_s	:	Elastic modulus of steel rebars (GPa)
f_c'	:	Compressive strength of concrete (MPa)
f_t	:	Tensile strength of concrete (MPa)
f_u	:	Ultimate tensile strength of FRP (MPa)
$f_{u,T}$	:	Ultimate tensile strength of FRP at elevated temperature T (MPa)
f_y	:	Yield strength of steel rebars (MPa)
$G_{f,T}$	:	Interfacial fracture energy at elevated temperature (N/mm)
G_{f0}	:	Interfacial fracture energy at ambient temperature (N/mm)
h	:	Depth of web below the flange (mm)
h_a	:	Heat transfer coefficient of the unexposed side (W/ m^2 K^4)
h_c	:	Convective heat transfer coefficient (W /m^2 K^4)
h_f	:	Heat transfer coefficient of the fire exposed side (W /m^2 K^4)
h_i	:	Depth of insulation on the sides up to bottom of concrete (mm)
h_r	:	Radiative heat transfer coefficient (W /m^2 K^4)
i_1, i_2	:	End nodes of the segment (i)
K	:	Sub-dataset
k	:	Thermal conductivity (W/m°C)

k_{ins}	:	Thermal conductivity of insulation (W/m°C)
kp	:	Number of data points (#)
ks	:	Spring stiffness (kN/mm)
L	:	Clear span of the beam or slab specimen (mm)
l_1	:	Distance of concentrated load from nearest end support (mm)
l_2	:	Distance between two concentrated loads (mm)
Ld	:	Total load applied on beams (kN)
L_i	:	Length of segment (i)
l_i	:	Projected length of the deformed segment (i)
lr	:	Applied load ratio (%)
m	:	Number of input features (#)
M	:	Section moment capacity (kNm)
M_a	:	Secondary moment (kNm)
M_n	:	Nominal moment capacity of un-strengthened member (kNm)
M_{n_PB}	:	Nominal un-strengthened capacity of the beam used for parametric study (kNm)
M_{n_PS}	:	Nominal un-strengthened capacity of the slab used for parametric study (kNm)
M_{n_upg}	:	Nominal moment capacity of strengthened member (kNm)
M_{nf}	:	Nominal moment capacity due to FRP (kNm)
M_{ns}	:	Nominal moment capacity due to steel (kNm)
M_{nupg_PB}	:	Nominal strengthened capacity of the beam used for parametric study (kNm)
M_{nupg_PS}	:	Nominal un-strengthened capacity of the slab used for parametric study (kNm)
m_{try}	:	Maximum number of input features for splitting a node (#)
M_u	:	Design moment capacity (kNm)

$\hat{n}$	:	outward surface normal
n_d	:	Bootstrap datasets
$N_{frp(i)}$	:	Force in FRP reinforcement for segment (*i*)
n_s	:	Minimum samples for splitting at a node (#)
n_{tree}	:	Number of decision tress (#)
ncs	:	Number of compressive rebars (#)
nts	:	Number of tensile rebars (#)
O_f	:	Width of overhang (mm)
P_{ai}	:	Axial force in each segment (*i*)
P_n	:	Nominal load capacity (kN)
P_u	:	Ultimate design load capacity (kN)
Q	:	Internal heat source (W/m^3)
q_c	:	Heat absorbed by the exposed surface of structure due to convection
q_f	:	Heat generated from fire
q_L	:	Heat loss to the surrounding environment
q_r	:	Heat absorbed by the exposed surface of structure due to radiation
r_1	:	Ratio 1 for minimum shear check
r_2	:	Ratio 2 for minimum shear check
rf_{bond}	:	Reduction factor for bond strength of CFRP
$rf_{tensile}$	:	Reduction factor for tensile strength of CFRP
r_{s}	:	Shear reinforcement ratio
S	:	Strength limit state
s_i	:	Length of the deformed segment (*i*)

T	:	Temperature (°C)
T_0	:	Initial temperature (°C)
T_a	:	Unexposed side temperatures (°C)
T_E	:	Temperature of surrounding enviornment (°C)
T_f	:	Temperature of fire (°C)
T_f	:	Fire exposed side temperatures (°C)
T_f	:	Temperature of the fire (°C)
t_f	:	Thickness of flange (mm)
t_{frp}	:	Thickness of FRP (mm)
T_g	:	Glass transition temperature of adhesive (°C)
t_h	:	Time (hours)
t_{ins}	:	Thickness of insulation at on sides and bottom of the cross-section (mm)
T_n	:	Temperatures at the beginning and end of time step (°C)
T_{n+1}	:	Temperatures at the beginning and end of time step (°C)
ts	:	time step
T_α	:	Surrounding boundary temperature (°C)
v	:	Vertical deflection at the end nodes of segment (i_1, i_2)
V_c	:	Shear capacity due to concrete (kN)
V_n	:	Nominal shear capacity (kN)
V_s	:	Shear capacity due to stirrups (kN)
V_u	:	Design shear capacity
W	:	Applied transverse loading on structural member (kN)
W_{rc}	:	Applied transverse loading on RC beams or slabs (kN)

x_{norm} : New value of input variable x

y : Distance from uppermost fiber in concrete to the center of the element (mm)

» <u>**Matrices and vectors**</u>

$[K_e]$: Stiffness matrix

$[K_g]$: Global stiffness matrix

$[K_{geo}]$: Geometric stiffness matrix

$[M]$: Global mass (capacitance) matrix

$[M_e]$: Mass matrix

$[X]$: Input matrix consisting of N input features

$\{\delta_v\}$: Vector of nodal deflections

$\{F\}$: Equivalent nodal heat flux due to the natural boundary conditions

$\{F_e\}$: Equivalent nodal heat flux vector

$\{N\}$: Vector of shape functions

$\{P\}$: Equivalent nodal load vector

$\{P_f\}$: Equivalent nodal load vector due to applied loading

$\{P_s\}$: Equivalent nodal load vector due to axial restraint

$\{\dot{T}\}$: Vector corresponding to first order derivative of temperature with respect to time

$\{w\}$: Weight vector

$\{x\}$: Input variables vector

$\{Y\}$: Target output vector

CHAPTER 1

INTRODUCTION

1.1 Background

Concrete is widely used as primary material in construction industry due to several advantages including, ease of fabrication, economic efficiency, flexibility in application, as well as superior fire resistance and durability. During their service life, concrete structures experience deterioration due to poor maintenance, degradation of concrete quality due to aging, and degradation of steel rebars resulting from corrosion and/or chloride exposure, as shown in Figure 1.1. Moreover, in some instances, concrete structures need enhancement in load carrying capacity due to changes in occupancy type or functionality, or to comply with new building code requirements, or to improve performance against extreme loading events such as blast or earthquakes. These factors necessitate the need for retrofitting and strengthening of structural members in built infrastructure.

Majority of the infrastructure in United States (US) was constructed during early to mid-19th century, and is therefore, either deteriorating or approaching end of the service life. The American Society of Civil Engineers (ASCE, 2020), in their recent "Report Card for America's infrastructure condition", provides a D+ rating, indicating that the infrastructure is in very poor condition and needs immediate fixing or replacement. The report further states that a daunting investment worth more than $3.6 trillion over the next ten years is required for repairing the nation's infrastructure. Moreover, repair and retrofitting costs of seismically deficient structures, deteriorating civil and military infrastructure may run into additional billions of dollars annually. Considering these statistics, there is a need for feasible strengthening or retrofitting techniques that can efficiently strengthen/repair the concrete structures with minimal alterations to dimensions of structures as well as with reasonable maintenance cost and longer service life.

Till 1990's, strengthening of concrete structures was carried out by attaching the steel plates or concrete and steel jackets to the outer surface of the structure, as shown in Figure 1.2 or by applying external post-tensioned steel tendons. These techniques increased the stiffness and load bearing capacity of the structures at a reasonable cost through use of steel reinforcement plates. However, techniques change the aesthetics of structures, increase the weight and geometrical dimensions of the structural members, and require specialized equipment's and bulky formwork for implementation. Further, steel plates are heavy, difficult to handle, susceptible to corrosion, and have poor fire resistance. Owing to these disadvantages, in recent years, the construction industry has moved towards the use of fiber reinforced polymer (FRP) for strengthening of concrete structures.

FRP is a composite which is made of high-strength fibers and a matrix for binding these fibers into structural shapes. Initially developed for aerospace and automotive applications, FRP has emerged as an attractive and promising alternative to the steel plates for strengthening of infrastructure. Use of FRP offers several advantages such as, high strength-to-weight ratio, corrosion resistance, ease of application, and inherent tailor ability over steel plates [1]. Thus, use of FRP can overcome many shortcomings of traditional materials based strengthening techniques described above.

Strengthening of concrete structures using FRP is essentially carried out by two techniques namely, externally bonded reinforcing (EBR) technique and near surface mounted (NSM) technique, as shown in Figure 1.3 and Figure 1.4, respectively. In EBR, FRP sheets saturated with resin or precured FRP laminates is applied (bonded/wrapped) to exterior of the concrete structure using a bonding adhesive (Figure 1.3 (b-c)), whereas in NSM precured FRP strips/ rods are inserted in precut grooves in the concrete cover and are then filled with resin (Figure 1.4 (b-c)). The EBR FRP strengthening is used for flexural and shear strengthening of beams or seismic confinement of columns, while NSM FRP strengthening is primarily used for flexural strengthening of concrete beams and slabs. Several research studies [2–4] and practical applications have shown that both these strengthening techniques are effective for enhancing the capacity of the concrete structures. Therefore, FRP is increasingly being used for retrofitting and strengthening of a wide range of civil infrastructures, such as reinforced concrete (RC) and unreinforced masonry walls, bridges, columns, girder as well as flexural concrete members such as beams and slabs in buildings.

Structural members when used in buildings are required to satisfy the fire resistance rating (FRR) requirements as prescribed in building codes and standards, to ensure the safety of occupants and fire fighters, control spread of fire, and minimize property damage during a fire incident. For instance, in an event of fire in a building, beams are required transfer the load to columns while supporting the ceiling, roof, and floor assembly, while slabs are required to provide compartmentation to contain the flame and smoke while sustaining the service loads during fire exposure duration. FRR is the minimum duration that is required for a structural member to exhibit resistance to fire and is often rounded off to a nearest hour or half-hour. Typically, FRR is prescribed in 0.5, 1, 1.5, 2, 3, 4 hours duration, and it depends on the type of structural member, occupancy, building height and compartment area. Fire resistance of a structural member is defined as the duration for which the structural member sustains the applied loading under fire exposure, without breaching the insulation, integrity and stability failure criteria [5] and is influenced by type of construction materials, applied loading, fire severity, and geometric properties [6]. Thus, the properties of concrete and FRP play a major role in determining the fire resistance of a strengthened concrete member.

Concrete has excellent fire resistance properties, whereas FRP has poor fire resistance characteristics. In fact, there is clear evidence that the strength, modulus, and bond properties of FRP degrade significantly even at modest temperatures (less than 200°C) due to transitioning of polymer matrix and resulting loss of bond [7]. Owing to the poor properties of FRP at elevated temperatures, fire resistance of FRP-strengthened member is a major concern in building applications. Currently there is limited understanding on the performance of FRP-strengthened concrete flexural members, i.e., beams and slab under structural loading and fire conditions, which hinders widespread use of FRP in building applications. Therefore, in this dissertation an attempt is made to develop a fundamental understanding of fire response of FRP-strengthened concrete flexural members through experimental and numerical studies.

1.2 Behavior of FRP Composites at Elevated Temperatures

The behavior of FRP at elevated temperatures is significantly different from that of concrete and steel. FRP essentially comprises of continuous fibers embedded in a resin, wherein fibers form the main load bearing component while the resin forms load distributing and binding component. Hence, the material behavior of FRP is influenced by the properties of fibers and resin material. Generally thermosetting polymer materials such as, polyester, vinyl ester, and epoxy are the most used as a resin material in the construction industry, due to their easy and relatively inexpensive manufacturing process as well as better adhesion characteristics [8, 9]. On the other hand, three different types of fibers namely, carbon, glass, and aramid fibers are usually used as reinforcement in polymers. The combination of polymer matrices with fibers is collectively known as carbon fiber reinforced polymer (CFRP), glass fiber reinforced polymer (GFRP), and aramid fiber reinforced polymer (AFRP), respectively. Of these, CFRP is known to have high tensile-strength-to-weight and high tensile-modulus-to- weight ratios as well as superior durability properties and is widely used for strengthening of RC structural members such as, beams, slabs, and columns. Therefore, discussion in this study is limited to carbon fiber reinforced thermosetting polymer strengthening materials.

Carbon fibers are thermally stable, non-flammable, and have very high melting temperatures (> 3500°C). Therefore, carbon fibers have high resistance to flaming and are also capable of retaining strength at elevated temperatures [10]. However, polymer resins, being a thermosetting material, are highly susceptible to high temperature exposure. At ambient conditions, the covalent molecular bonds of thermosetting polymers are intact, and this state is known as glassy state. However, when these polymers are heated to moderately elevated temperatures (about 80-150°C), the molecular bonds in them weakens. As a result, the polymer undergoes phase change and reaches a leathery state. The range between glassy and leathery state is known as glass transition zone, and the corresponding temperature at which the transition starts is known as glass transition temperature (T_g) [11].

When the temperature in FRP exceeds T_g, the strength and modulus properties of FRP start decreasing. As the temperature increases above 300-400°C, the polymer resin starts to decompose as the molecular bond damaged severely. This thermal decomposition of polymer releases heat, smoke, soot, and combustible volatiles in the environment [12] and induces creep and distortion in FRP material. The emission of smoke, soot, and combustible volatiles, creates a smoggy, toxic environment, with increased flame spread, which in turn increases the severity of fire, reduces the visibility, and hinders the evacuation activity. While the creep and distortion of FRP material causes significant reduction in strength and stiffness properties.

The emission of combustible volatiles, soot, and smoke is measured in terms of flammability, flame spread index (FSI) and smoke density index (SDI) as per the procedure described in ASTM E162, ASTM E84, and NFPA 255, respectively. These characteristics are important from the health and environment safety point of view. Since the volume of FRP used in strengthening applications is very small compared to the total mass of concrete structural members, the health and safety related concerns are negligible. Moreover, FRP manufacturers list their products for smoke generation and flame spread classifications in directories after getting specified tests from specialized testing facilities (laboratories). Thus, for this research, it is assumed that FRP's have met the relevant flame spread and smoke generation rating specified in building codes and standards.

The mechanical properties, i.e., tensile strength, elastic modulus, and bond strength of FRP together with mechanical properties of concrete and reinforcing steel determine the fire resistance of FRP-strengthened RC member. Like other construction materials, at elevated temperatures FRP loses its strength and modulus properties. However, the degradation in FRP properties is faster as compared to concrete or steel since properties of FRP matrix start to deteriorate even at a modest temperature rise. Figure 1.5 shows comparative variation in temperature dependent compressive strength of concrete, yield strength of steel rebars, tensile strength of wood, and tensile strength of CFRP, GFRP, and AFRP. It can be seen from the figure that tensile strength of all the FRPs degrade at a faster rate as compared to steel and concrete [13]. The loss of FRP strength with temperature is negligible up to 100°C, and thereafter, strength degradation is faster, resulting in 50% strength loss around 350°C.

Apart from the above-mentioned mechanical properties, another important property that needs consideration, in case of FRP-strengthened concrete members, is the bond strength between FRP and concrete. Typically, bonding adhesive used for applying FRP to concrete surface is same as the polymer used for matrix of FRP, and is therefore, a thermosetting material, which is highly susceptible to rise in temperature. Figure 1.6 shows the temperature induced degradation in bond strength of FRP. It can be seen from the figure that the bond strength of FRP decreases at a much faster rate than the strength and modulus properties of FRP. The bond strength starts decreasing as soon as temperature approaches T_g and then continues decrease rapidly with increase in temperature [14]. The bond strength diminishes completely in the temperature range of 120°C to 150°C, indicating complete loss of composite action between FRP and concrete. The above discussion clearly indicates that FRP is highly vulnerable when exposed to fire, which in turn can affect the fire performance of strengthened concrete member as discussed below.

1.3 Fire Resistance of FRP-Strengthened RC Flexural Members

Flexural strengthening of RC flexural members (beams and slabs) is usually achieved by applying thin layers of FRP sheets on tension face (i.e., soffit of beams and slabs) using a bonding adhesive, which provides a path for transfer of stresses from concrete to FRP [15]. Fire resistance of a FRP-strengthened RC member is primarily governed by high temperature properties of constituent materials, i.e., concrete, steel reinforcement, and FRP, as well as applied loading and temperature exposure level [6] (Kodur 1999). Additionally, FRP-strengthening being a bond-critical application, the degradation of bond at FRP-concrete interface is another critical factor which affects the fire resistance of an FRP-strengthened structural member.

Generally, concrete structural member exhibits good fire resistance, and in most cases, required fire resistance can be achieved without any external fire insulation. However, FRP-strengthened concrete structural member exhibits poor fire resistance and, in most cases, do not achieve satisfactory fire resistance without external fire protection, due to the reasons explained below.

Figure 1.7 shows the comparison of moment capacity degradation as function of fire exposure time for these beams. While Figure 1.8 shows a schematic illustration of bending moment due to applied loading and change in moment capacity at different time interval for a simply supported conventional RC beam and a FRP-strengthened RC strengthened beam. The beams are loaded to 50% of their respective ultimate capacity at room temperature. Since the ultimate capacity of the strengthened beam is much higher than the un-strengthened RC beam, the applied loading and hence, the bending moment is significantly higher on the strengthened beam. The beams are considered to have failed when the capacity falls below the bending moment due to applied loading. It can be seen from Figure 1.7 that the capacity of un-strengthened RC beam remains constant in the initial stages of fire exposure and then starts decreasing gradually. This is attributed to the low thermal conductivity and high thermal capacity of concrete, as well as to slower degradation of strength and modulus properties of concrete and steel rebars. Thus, RC structural member fails after a significantly longer (almost after 210 minutes) fire exposure duration.

In case of FRP-strengthened beam, capacity starts decreasing rapidly from the start of fire exposure, as can be seen from Figure 1.7. This is attributed to the fact that when a strengthened concrete member is directly exposed to fire, FRP experiences rapid loss of strength and modulus properties under elevated temperature exposure (as illustrated Figure 1.5) due to softening of polymer matrix in FRP. Apart from temperature induced loss of strength, the temperature induced degradation of bond at FRP-concrete interface affects the fire resistance of an FRP-strengthened structural member. Since the binding adhesive is a polymeric material, it turns viscous at moderately elevated temperature, and as a result the bond between FRP and concrete deteriorates rapidly with increase in temperature (*cf*. Figure 1.6). The degradation of bond causes a relative slip between FRP and concrete, which in turn reduces the stress transfer from concrete to FRP. Thus, the rapid degradation of bond properties reduces the FRP-concrete composite action at a faster rate. Since strengthened concrete members are subjected to higher load level than that of an un-strengthened concrete member, the rapid reduction in load carrying capacity of the strengthened member, results in earlier failure, as shown in Figure 1.7 and Figure 1.8. As a result, a strengthened concrete member has lower fire resistance as compared to un-strengthened concrete member.

To prevent the rapid degradation in strength and bond properties of FRP, and to increase the fire resistance of an FRP-strengthened structural member, various researchers (Blontrock et al. 2000; Williams et al. 2008; Ahmed and V. Kodur 2011) have recommended applying a layer of external fire insulation. Provision of such fire insulation slows down temperature rise within the FRP-strengthened RC structural member during a fire event, and as a result, mechanical and bond properties of FRP decrease at a much slower pace. Indeed, it is difficult to maintain the FRP-concrete interface temperature below T_g during fire, even with significantly thicker fire insulation. Hence, the effectiveness of FRP is eventually lost, and as a result, the FRP-strengthened RC member eventually behaves as an un-strengthened RC structural member after certain fire exposure time and has to sustain the service loads applied during the fire, as shown in Figure 1.7. Therefore, suitable insulation configuration and thickness should be designed to improve fire resistance of FRP-strengthened concrete structural members. As a thin insulation layer may not yield reasonable enhancement of fire resistance and too thick layer could lead to delamination of insulation from concrete surface due to self-weight, thereby leaving the strengthened structure unprotected.

At present, there is limited information regarding the optimum thickness and configuration of insulation layer required to achieve the necessary fire resistance. Further, the type of insulation, and its associated thermal properties dictates the level of fire resistance in a FRP-strengthened RC member. Therefore, there are concerns whether the insulated FRP-strengthened would achieve necessary fire rating even after applying insulation. Hence, it is necessary to evaluate the fire resistance of insulated FRP-strengthened RC structural members.

1.4 Approaches for Evaluating Fire Resistance

Fire resistance of an FRP-strengthened RC structural member is generally evaluated through standard fire test as per ASTM E119 [5] or ISO 834 [16] test methods. However, these tests have numerous limitations, including the test equipment, loading facilities, size of specimens, and availability of sensors for measuring different response parameters at elevated temperature. Additionally, the fire resistance tests are very costly, laborious, and time consuming. Therefore, it would be impractical to evaluate the fire resistance of FRP-strengthened concrete flexural members with different insulation thickness and configuration, applied loading levels, loading through fire resistance tests.

Design standards for FRP-strengthened RC structures [17–19] contain strength equations for evaluating the capacity of FRP-strengthened concrete member at ambient temperature. However, these standards do not provide any specific equations or methods for determining the fire resistance of the strengthened members. Rather these standards recommend neglecting the contribution of FRP under fire conditions and suggest taking fire resistance of un-strengthened RC member, determined using the prescriptive design provisions in ACI 216.1-14 [20], as the fire resistance of strengthened member. These prescriptive design provision in ACI 216.1-14 [20] are derived based on data from standard fire tests and prescribe tabulated fire resistance ratings linked to concrete cover thickness, type of aggregate, and restraint conditions. These prescriptive methods do not account for actual design variables, such as FRP-concrete interfacial bond and realistic failure modes, and thus might not yield realistic fire resistance of FRP-strengthened concrete members.

Recently, Kodur and Yu [21] and Gao et al. [22] proposed rational approaches for fire resistant design of FRP-strengthened beams. These approaches use oversimplified assumptions and do not account for all the important factors affecting fire resistance of strengthened beams.

To overcome these limitations, a rational approach, involving advanced analysis procedure and numerical model, accounting for all the necessary parameters affecting the fire resistance of FRP-strengthened members must be developed. Undertaking fire resistance analysis through a rational approach involves several steps namely, assessing multiple fire scenarios, evaluating sectional temperature, determining structural response, and then applying failure criteria for evaluating failure state. For implementing rational design approach to evaluate fire resistance, a validated computer model to perform thermo-structural analysis is required. The model must be able to account for the temperature dependent properties of the material, including bond degradation, and applicable failure limit states.

1.5 Need for Current Research

At present, the available information on high temperature strength, elastic modulus, and bond properties of FRP is based on the limited material property tests available in the literature. These tests are carried out on specific FRP materials with different type and volume fraction of fibers and polymers, which significantly influence the high temperature properties. Moreover, at present there are no standardized test methods for evaluating the properties of FRP at elevated temperatures. Thus, previous researchers have adopted different parameters such as, type of specimen, heating rate, and load levels during the tests on FRP. Additionally, majority of these tests are carried out on precured FRP strips, rods, or plates which has a higher T_g then the FRP sheets. Owing to the dissimilar FRP materials and testing conditions, there exists a wide variation in the available data on the high temperature properties of FRP. Therefore, there is a need for evaluating the temperature dependent strength and bond properties of FRP sheets.

A review of literature indicates that there are limited experimental studies evaluating fire resistance of FRP-strengthened RC beams, however, there are very few studies evaluating the fire resistance of FRP-strengthened RC slabs. The available studies are on specific type of FRP-strengthening with small to mid-scale strengthened slabs, with limited variation in critical factors. Thus, there is serious lack of test data on fire response of full scale FRP-strengthened RC beams and slabs under different loading, strengthening level, and insulation configuration. Therefore, it is necessary to evaluate the fire resistance of FRP-strengthened RC members.

In terms of numerical studies, currently limited numerical studies are available to evaluate the fire performance of FRP-strengthened RC beams and no numerical studies for evaluating thermal-structural response of FRP-strengthened RC slabs. The available numerical models either assume a perfect bond condition or adopt indirect approaches, such as deformation of glue, to account for FRP-concrete bond behavior. Consequently, these numerical models did not provide insights on the fire resistance of FRP-strengthened concrete beams due to the bond degradation. Only a limited number of numerical models have simulated the FRP-concrete bond behavior using the temperature dependent nonlinear or bilinear bond-slip relations. These numerical studies were able to predict better fire response of FRP-strengthened behavior, indicating the critical role of bond-slip relations in predicting the fire performance of FRP-strengthened concrete beams. However, these numerical models involve use of complex cohesive zone models demanding high computational effort. Further, these numerical models often face the challenge of convergence and needs to be calibrated for each structural member separately and do not provide important outputs such as, degradation of moment capacity with fire exposure time. Therefore, a numerical model which can account for necessary factors affecting the fire resistance of FRP-strengthened structural members and provide detailed outputs which can aid in understanding the fire performance of strengthened members needs to be developed.

The use of numerical models for detailed fire resistance evaluation, although serves as a great alternative to the fire tests, their use for regular design is impractical, as design engineers are only interested in fire resistance of the structural member. Moreover, the use of these models requires specific training for conducting the advanced analysis and interpreting the generated outputs. However, there are very few simplified design procedures for fire design of FRP-strengthened concrete structural members for use in design offices. Moreover, these procedures involve significant programming and are based on several assumptions, which do not account for all the parameters governing the fire response of FRP-strengthened structural member. Therefore, there is a need to develop a coherent ready to use tool for predicting fire resistance of FRP-strengthened concrete members which encompasses the effect of all the important factors influencing the performance of strengthened structural members under fire conditions.

1.6 Objectives

From the above discussion, it is evident that there is need for developing comprehensive understanding of the behavior of FRP at material level and at structural level. To achieve this objective, experimental and numerical studies are proposed to examine relevant high temperature material properties of FRP as well as to evaluate fire response behavior of FRP-strengthened RC beams and slabs under fire conditions. The specific research objectives of proposed study are as follows:

- Carry out a detailed state-of-the-art review to identify knowledge gaps on the material properties of FRP such as, strength, stiffness, and bond properties at elevated temperatures as well as on the fire performance of FRP-strengthened RC flexural members.
- Conduct numerical studies to propose suitable material property relations for FRP and insulation for use in fire resistance modeling of FRP-strengthened concrete flexural members.
- Carry out material property test on precured FRP sheets at elevated temperature to quantify the effect of high temperature exposure properties of FRP, namely tensile strength, stiffness, and bond strength.
- Conduct full scale fire resistance tests on FRP-strengthened concrete flexural members to evaluate their behavior under different load level, strengthening level, insulation thickness and configuration.
- Develop a macroscopic finite element based numerical model to trace the response of FRP-strengthened RC flexural members under fire conditions. The model will account for material nonlinearities as well as temperature dependent properties of constituent material, including FRP-concrete bond degradation. Use data generated from the fire resistance tests to validate the numerical model.
- Conduct parametric studies to quantify the influence of various factors on the fire resistance of FRP-strengthened concrete beams and slabs.
- Develop a systematic ready to use tool for fire resistance prediction of FRP-strengthened concrete beams through use of machine learning (ML) algorithms, which can be used in design offices.

1.7 Outline

The research undertaken to accomplish the aforementioned objectives is organized in seven chapters. Chapter 1 provides a general background information on the behavior of FRP at elevated temperatures, and layouts the objectives of the study. Chapter 2 summarizes a detailed state-of-the-art review on the performance of FRP at elevated temperatures at material level and as a component of a structural member. A brief summary of the experimental and numerical studies evaluating the performance of FRP-strengthened RC beams and slabs, reported thus far. The chapter concludes by outlining the major knowledge gaps available in the literature.

Chapter 3 describes the fire resistance tests on five FRP-strengthened RC beams and two FRP-strengthened RC slabs. The data from the tests is used to examine the comparative performance of FRP-strengthened RC beams and slabs under different conditions. Chapter 4 presents the development of the numerical model to trace the response of FRP-strengthened RC beams and slabs from preloading stage to failure under fire condition. The validation of thermal and structural model is also presented by comparing the predicted response of beams and slabs with the response measured in the tests.

Chapter 5 presents results from a parametric study on the influence of critical factors affecting the response of FRP-strengthened RC beams and slabs subjected to simultaneous fire and structural loading. A detailed discussion on the trends generated from the parametric studies is presented. Chapter 6 provides ML based artificial intelligence (AI) models for predicting fire resistance of FRP-strengthened concrete beams. Finally, chapter 7 summarizes the main findings from current study and lay out recommendation for future research.

(a) **(b)**

Figure 1.1: Examples of deterioration in concrete structural members: (a) degradation of concrete quality due to chemical attack; (b) corrosion in steel reinforcement

(a) **(b)**

Figure 1.2: Strengthening of concrete structures using traditional materials: (a) concrete jacketing; (b) steel plates bonding

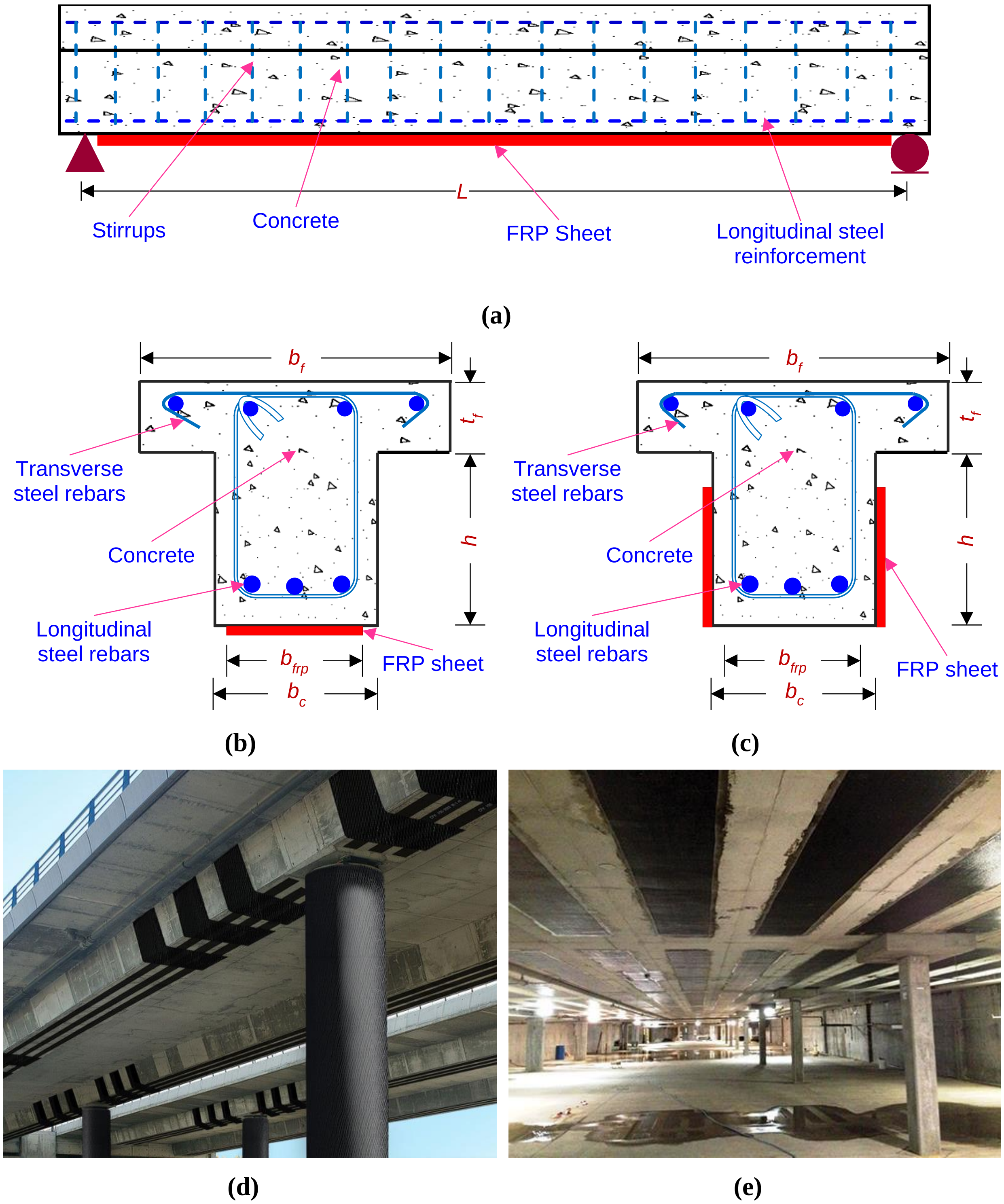

Figure 1.3: EBR FRP-strengthening of concrete structures: (a) schematic elevation; (b) schematic flexural strengthening of beam cross-section; (c) schematic shear strengthening of beam cross-section; (d-e) FRP-strengthened beams, columns, and slabs

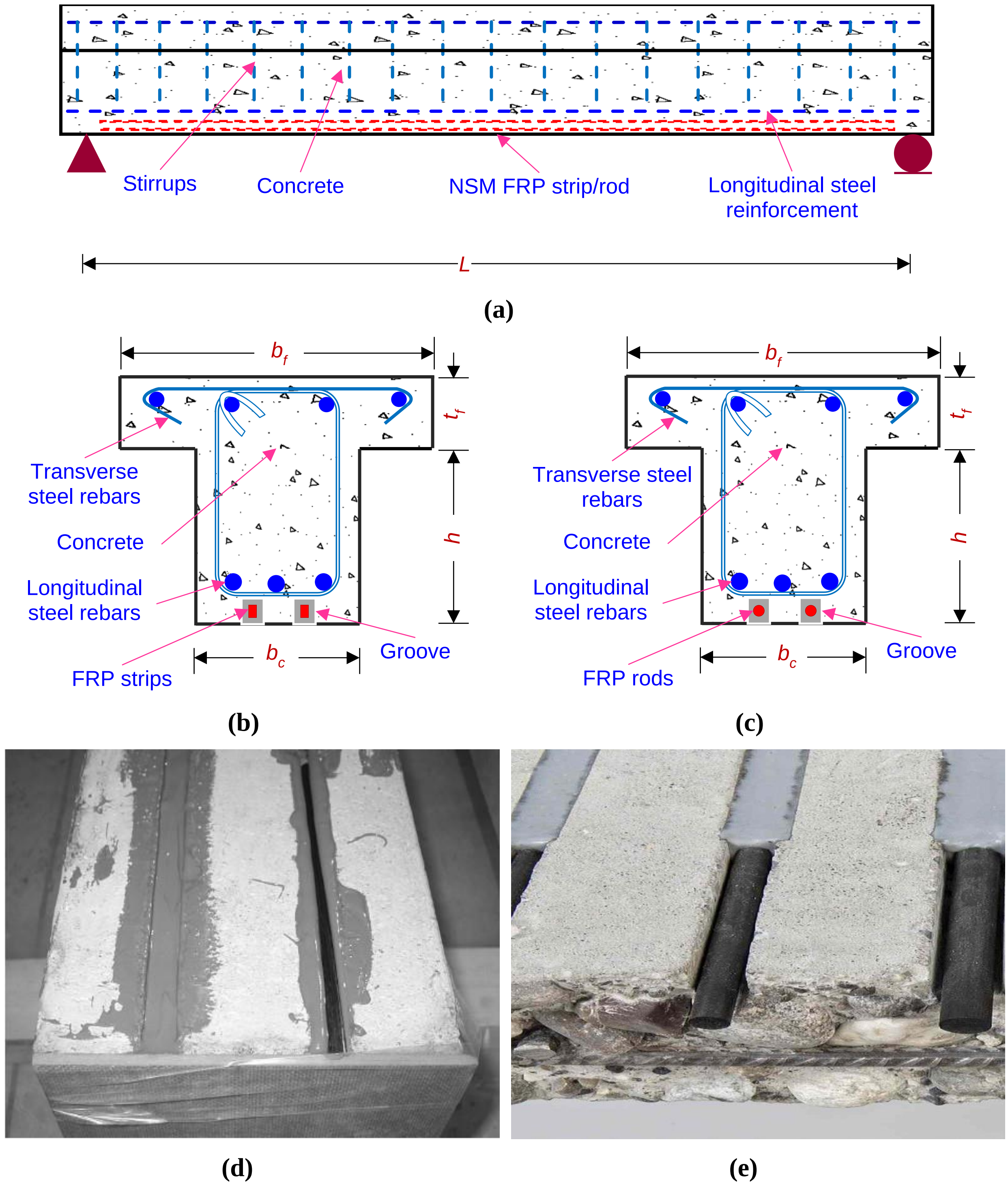

Figure 1.4: NSM FRP-strengthening of concrete structures: (a) schematic elevation; (b) schematic cross-section strengthening with FRP strips; (c) schematic cross-section strengthening with FRP rods; (d) beam strengthened with NSM FRP strips; (e) beam strengthened NSM FRP rods

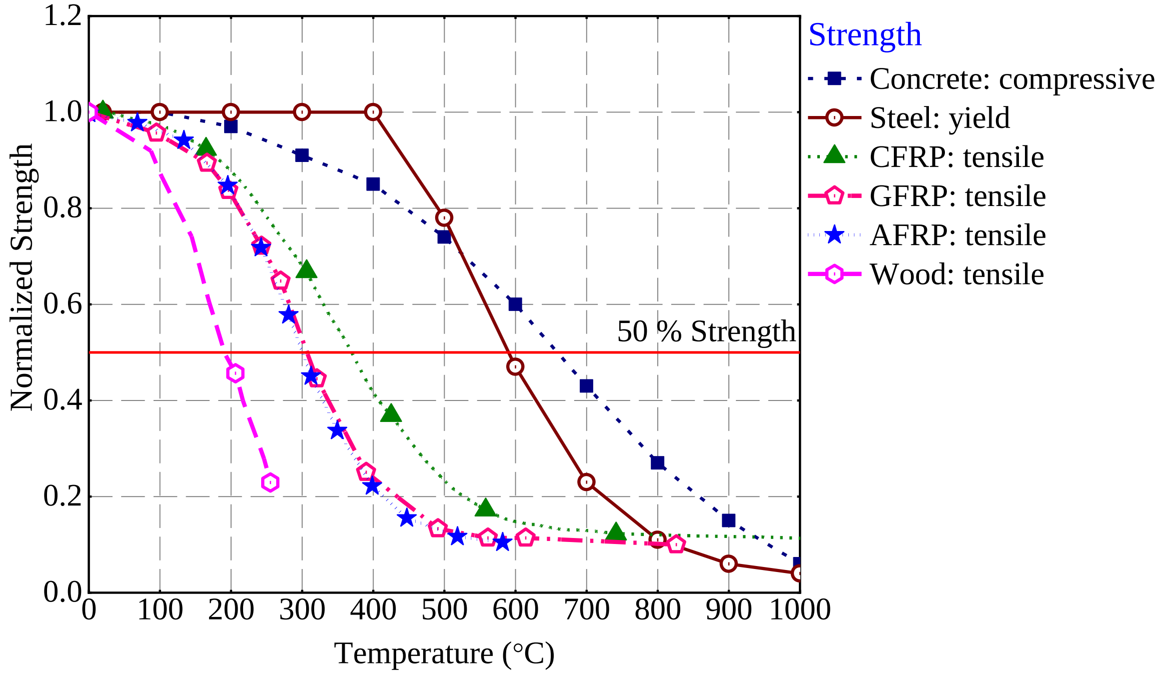

Figure 1.5: Comparison of degradation in strength of different materials at elevated temperature

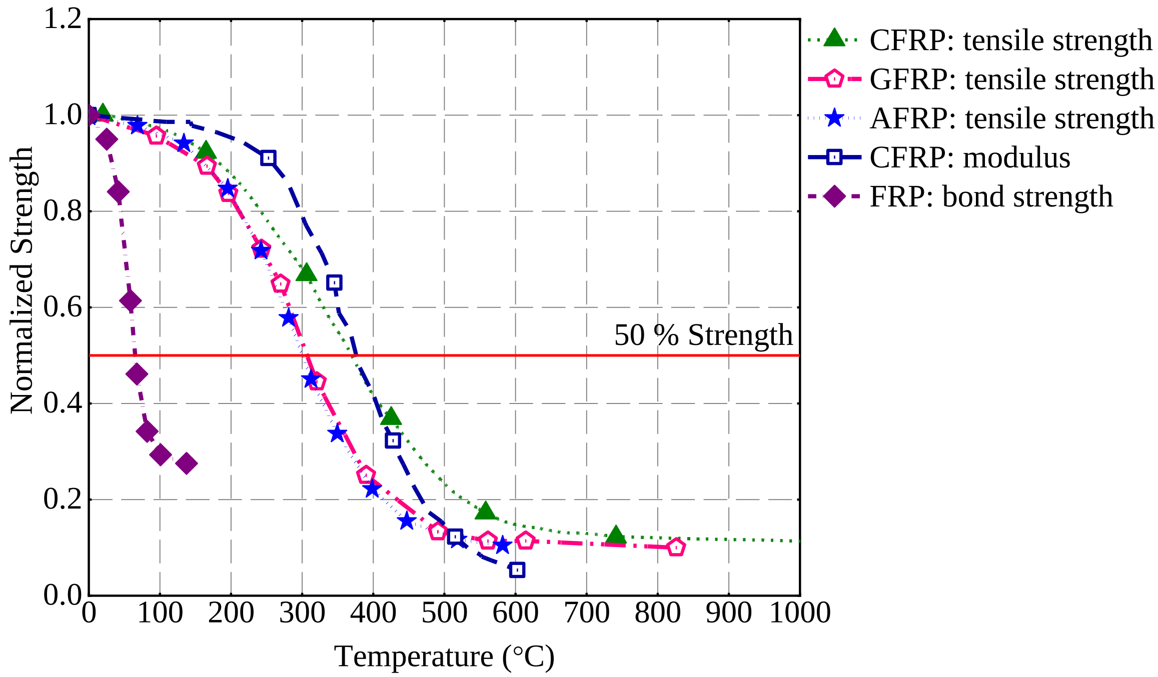

Figure 1.6: Comparison of degradation in tensile and bond strength of FRP at elevated temperature

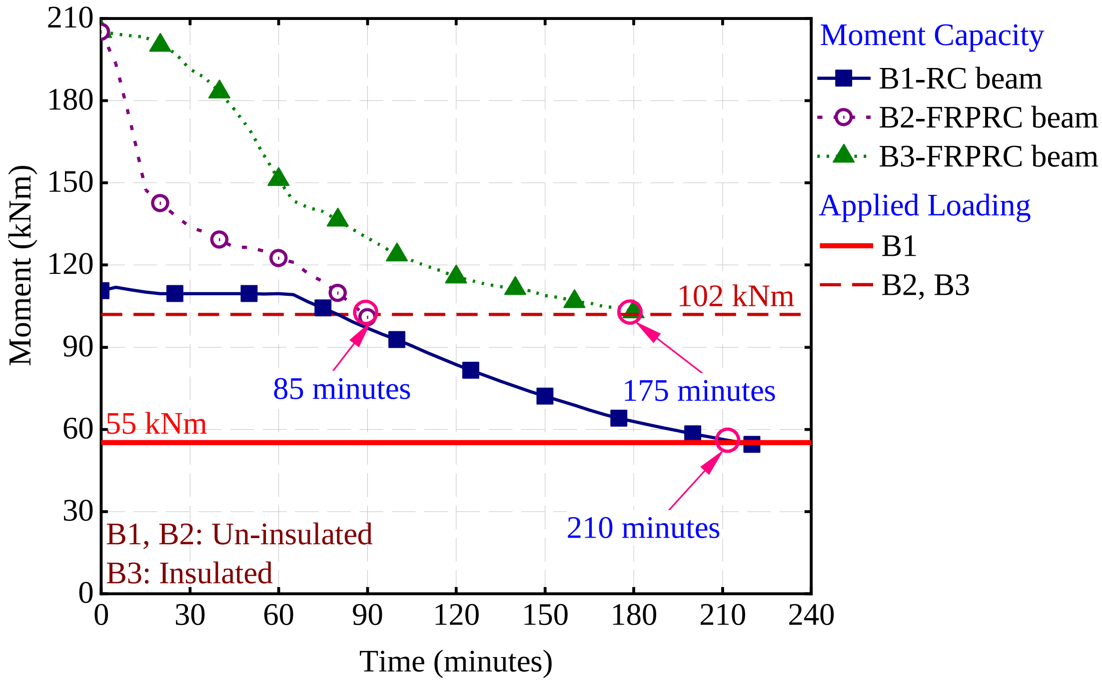

Figure 1.7: Degradation in moment capacity of un-strengthened and FRP-strengthened RC beams as a function of fire exposure time

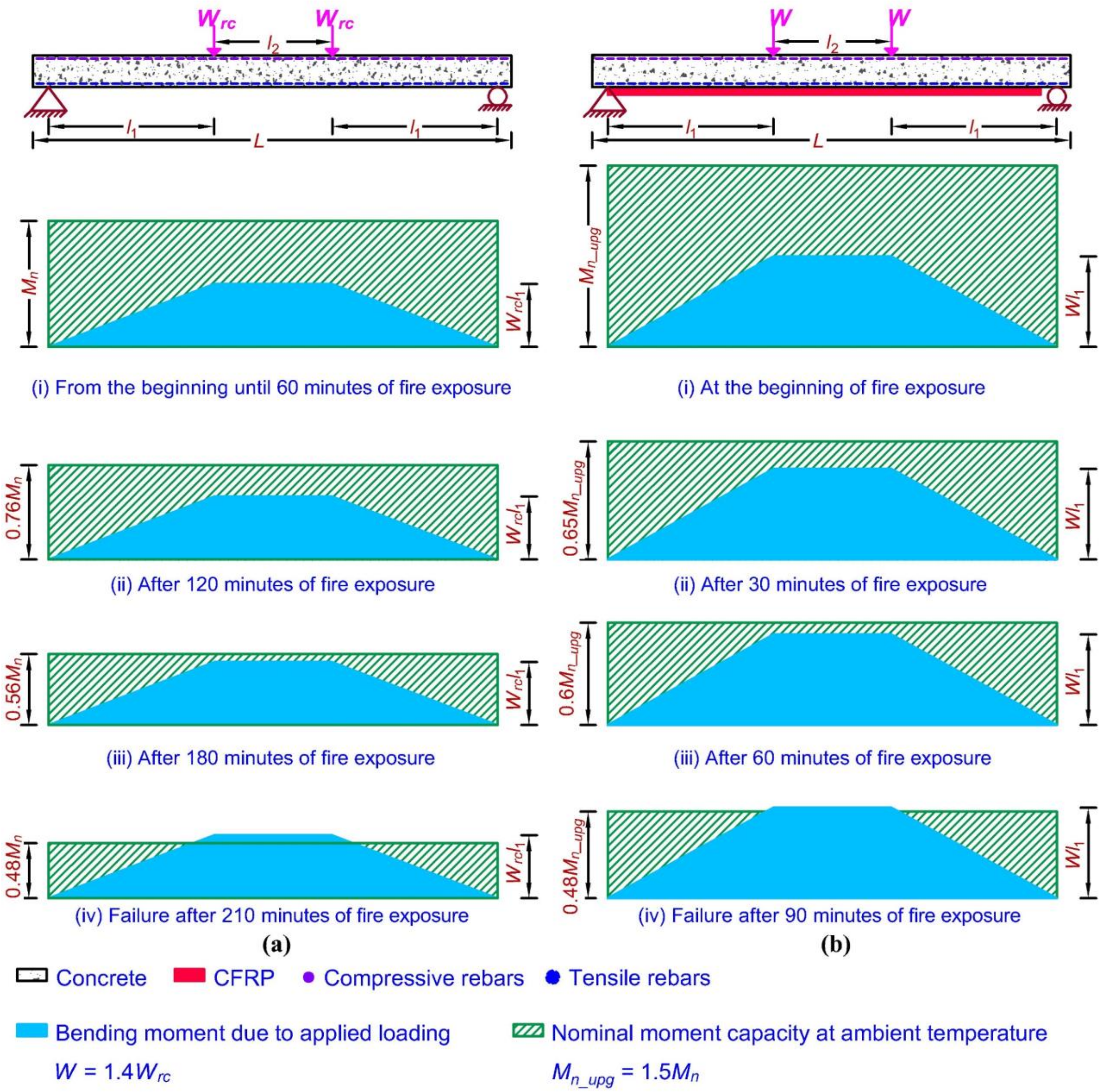

Figure 1.8: Bending moment diagram superimposed over flexural capacity of beams at different intervals of fire exposure for: (a) un-strengthened RC beam; (b) FRP-strengthened RC beam

CHAPTER 2

STATE-OF-THE-ART REVIEW

2.1 General

In the second half of the 20th century, the aviation and defense industries developed a new class of material with enhanced properties by embedding high strength fibers in organic polymer known as fiber reinforced polymer (FRP) composites. The composite material was costly but had high strength, and low weight and was therefore, used in wide range of applications such as, parts for aircrafts, ships, automotive, and military hardware. With the advancement of technology towards the end of 20th century, the prices of FRP started decreasing, and hence, the use of FRP was extended towards civil infrastructure applications for strengthening of bridge girders and RC columns. Due to more recent improvements in properties of FRP such as corrosion resistance characteristics, environmental durability, and tailorability, as well as the ease of installation, FRP composites are increasingly being used for strengthening and retrofitting of building structural members such as, beams, slabs, columns, and shear walls

Over the past few decades, several studies have been conducted evaluating material and structural characteristics of FRP under fire conditions. These research studies as well as several field applications have demonstrated that FRP exhibits poor performance under fire conditions. The poor fire resistance characteristics of FRP is a major factor limiting the widespread acceptance of FRP in buildings or other places where structural fire resistance is a primary requirement. This chapter presents a detailed state-of-the-art review on the currently available studies pertaining to material and structural behavior of FRP at elevated temperatures. The review starts with an overview of type of FRP products and application techniques followed by the behavior FRP-strengthened flexural members under ambient conditions. Following this a review of temperature dependent material properties of constituent materials of FRP-strengthened concrete flexural members, i.e., concrete, steel rebars, FRP, and insulation is provided. Then the main findings from the previous experimental and numerical studies evaluating fire response of strengthened concrete flexural members as well as the design provisions in current codes and standards for strengthened concrete members are reviewed and discussed. Finally, the knowledge gaps in the current literature are summarized at the end of chapter.

2.2 FRP Composites - An Overview

FRP composites comprise of high strength continuous reinforcing fibers, a polymer matrix, and some additives such as, fillers or coupling agents. The composites have superior properties compared to its parent materials, provide several advantages, such as light weight, high strength, stiffness, durability etc. and are available in numerous forms. Depending on the type of fiber and polymer matrix, the behavior of FRP composites can vary significantly, especially with regard to their mechanical properties. A brief overview of commonly used fibers, polymers, and types of FRP composite products is discussed here.

2.2.1 Fibers

The fibers in a FRP composites carry major portion of the applied loading. Therefore, the type, orientation, and volume fraction of fibers influence the properties and behavior of FRP composites. Typically, fibers occupy 40 – 65% of volume fraction in a FRP composite and can be oriented in any direction. However, to utilize the high strength and modulus properties of FRP composite, the fibers must be oriented along the loading direction.

Three types of fibers, namely carbon (ultra-high modulus, high modulus, and high-strength), E-, S-, and Z-glass, and aramid (aromatic polyamides, Kevlar 49) are commonly used for different applications. A complete review of fiber types and properties is avoided here as this information is available in most composite materials textbooks such as [12, 23, 24], however a qualitative comparison of different characteristics of these three fibers with respect to each other is summarized in Table 2.1. It can be seen from the table that among the three fibers carbon fibers have highest strength, modulus, and strength to weight ratio whereas, glass fibers have the lowest strength, modulus, and strength to weight ratio. Additionally, carbon fibers have excellent resistance to fatigue, heat, chemicals, and moisture absorption compared to glass and aramid fibers. The strength and modulus of aramid fibers lie between carbon and glass fibers; however, aramid fibers have lowest resistance to moisture absorption as well as lowest adhesion to resin materials. Further, it can be seen from the table that carbon and glass fibers have moderate to low cost, respectively, whereas aramid fibers have the highest cost. Therefore, aramid fibers are the least commonly used amongst the three high performing fibers, whereas carbon fibers are extensively used for structural strengthening applications.

2.2.2 Resin Material

Resin, also known as matrix, binds the reinforced fibers together, protects them against harsh environment or mechanical abrasion and provides a medium for transfer of load to-and-between the fibers. The matrix also provides lateral support for fibers against buckling under compression or a combination of forces. A major selection criterion for resin materials is that they should have a low density (considerably less than fibers), so that overall weight of the composite is minimized. Additionally, resin materials should be thermally compatible with the fibers as much as possible to reduce differential thermal expansion, therefore, the choice of resin is also governed by type of reinforcing fiber.

Typically, in majority of composite materials, polymer is used as resin material. Polymers are organic compounds made up of long chains of carbon and hydrogen molecules. Depending on the type of connection within the chains, the polymers are broadly classified as thermosetting polymers and thermoplastics polymers [25]. Thermosetting polymers have cross-linked chains of the molecule connected by strong covalent bonded atoms. Since they are formed under the influence of heat, they cannot be reheated to soften and reformed into different shapes. However, these polymers have better thermal stability as well as better impregnation and adhesion properties. Whereas thermoplastic polymers consist of molecular chains held together by weak van der Waals forces. These polymers are thermally unstable, have high creep effect, low chemical resistance and require difficult and expensive manufacturing process as compared to thermosetting polymers [26].

Generally, thermoplastics polymers such as, polyethylene, polyvinyl chloride, polypropylene, polyurethane, etc. are used for automotive, marine, and aerospace applications. Whereas thermosetting polymers such as, vinyl esters, epoxies, polyesters, etc., are used for structural engineering applications [8]. Again, a complete review of polymer types and properties is avoided here, however, advantages and disadvantages of the commonly used polymer types are summarized in Table 2.2. It can be seen from the table that polyesters and vinyl esters have poor bonding capability and require specific surface preparations, whereas epoxy resins have excellent bonding capability as well as high resistant to wear and tear. Additionally, epoxy resins are compatible with all the three fiber types, whereas polyester and vinyl esters are more suitable for glass fibers only. Therefore, polyester and vinyl ester resins are used for temporary fixes with low strength requirement, or chemically aggressive environment (vinyl ester only), whereas epoxy resins can be used for majority of the structural application. However, as mentioned in Chapter 1, all these thermosetting polymer materials are highly susceptible to temperature rise resulting in poor fire resistance characteristics.

To address some of these concerns of organic polymers, inorganic matrix materials have been developed in recent years [27–29]. Among the many types of inorganic matrices, a new class of material called geopolymers has shown potential to replace organic polymers [30–32] attention in the past decades. Geopolymers represent a new class of high-performance inorganic materials characterized by a three dimensional, CaO-free, aluminosilicates based chemical structure. They are synthesized by mixing strong alkaline solutions such as sodium silicate, potassium silicates, NaOH, KOH with reactive aluminosilicate materials such as, metakaolin, fly ash, or industrial and natural waste products [33–37]. Several studies have been reported in literature evaluating the mechanical properties geopolymer materials at ambient and elevated temperatures [29, 31, 38–43]. Similarly, studies evaluating structural behavior of RC beams strengthened with fiber sheet bonded using geopolymer matrix have also been reported in literature. These studies indicate that geopolymer is a promising viable alternative to organic polymers. However, very few studies (only one study reported thus far by Zhang et al. [44], described later) is reported in literature, evaluating the structural behavior of RC members strengthened with fiber sheet geopolymer system). Therefore, use of geopolymer is currently limited to certain research-based applications only.

2.2.3 Types of FRP Composite Products

Depending on the type of fibers and polymeric resin materials different types of FRP composite products are available in market. Some of the commonly available FRP composites include, CFRP, GFRP, AFRP composite materials. Recently, some newly developed FRP composite materials such as, basalt FRP (BFRP), polythylene naphthalate (PEN) and polyethylene terephthalate (PET) composites are also being considered for application in construction industry [9]. All these composites have a linear elastic stress-strain response, as illustrated in Figure 2.1. The stress-strain response ends in brittle failure due to rupture of fibers or cracking of resin.

One of the main advantages of FRP composites is that they can be tailored in any shape and size, depending on the intended use. FRP composites used in structural engineering applications are primarily developed using two manufacturing methods, namely pultrusion and hand lay-up. The former method involves automated industrialized process, wherein FRP composites are manufactured in a factory and transported to construction site for installation. Whereas, the latter method, also known as wet lay-up, is a manual method, wherein FRP composite is manufactured on the construction site typically minutes before installation. Figure 2.2 shows the FRP composites products developed using pultrusion or hand lay-up method.

Pultrusion process is used to manufacture prefabricated FRP composites such as, plates, bars, sheets, anchorages, tendons, and stay-in-place FRP formwork for reinforced concrete members, Prefabricated FRP elements are typically stiff and are difficult to bend or use as internal reinforcement (stirrups). The prefabricated rods, tendons, and bars typically are used as an internal reinforcement in new structural members such as, beams, and slabs. Whereas plates and sheets are used for strengthening/retrofitting of deteriorated old structural members. For strengthening applications these composites are applied concrete surface using an external bonding adhesive. In recent years, the premanufactured rods or strip are also applied directly inserted in the tension zones of beams and slabs by cutting grooves at the surface of the concrete member, which are then filled with adhesive. This method of strengthening using FRP rods and sheets is known as near surface mounting (NSM)

Hand lay-up is used to manufacture and install dry fiber sheets-based composites on the structural member. FRP fabrics are available in continuous uni-or bi-directional sheets supplied that can be easily tailored to fit any geometry and wrapped around complex profiles. Therefore, the fabric sheets are used as an external reinforcement for strengthening of concrete structural members. In this method, the polymer resin acts as FRP matrix as well as the binding material (adhesive) between FRP composite and the substrate, and hence, no other bonding adhesive is required to attach these sheets to concrete surface. For instance, FRP fabrics after saturating with relevant polymer resin material, can be adhered to the tension side of concrete flexural members to provide additional tension reinforcement to increase flexural strength, wrapped around the webs of joists and beams to increase their shear strength, and wrapped around columns to increase their shear and axial strength and improve ductility and energy dissipation characteristics.

2.3 FRP-Strengthened Concrete Flexural Members

In recent years, FRP-strengthening has emerged as a reliable solution to address the ever-growing age-related concerns in infrastructure and is hailed by design engineers and researchers alike. Some of the major advantages of FRP-strengthening over traditional materials include, high strength and stiffness, easier and faster installation, high corrosion resistance, high durability, better customization to specific requirements, and minimum maintenance. FRP-strengthening is categorized as bond-critical application and contact critical application carried out using different types of FRP products. The former is used for flexure/shear strengthening of concrete flexural members, while latter is used for lateral confinement of column. The discussion in this thesis is limited to the bond-critical application of FRP-strengthening used for strengthening of concrete flexural members.

Extensive experimental and numerical studies [45, 46, 55–64, 47, 65–67, 48–54], have been conducted across the world evaluating the overall performance of FRP-strengthened RC flexural members under different types of loading conditions. These studies have demonstrated the benefits of FRP-strengthening at ambient conditions and have aided the development of formal design guidelines and standards such as, FiB-14 [17], ISIS [18], and ACI 440.2R-17 [19]. Based on the review of these studies, the behavior FRP-strengthened flexural member at ambient conditions including the governing failure modes is briefly discussed below.

The flexural capacity of plain and reinforced concrete (RC) elements can be enhanced up to 160% through attaching externally bonded FRP plates, strips, or fabrics at the soffit of simply supported beams or slabs. Several failure modes were experimentally observed of RC beams and slabs when externally strengthened with FRP laminates. The potential failure modes of externally strengthened RC flexural members with FRP laminates are shown in Figure 2.3. According to ACI 440.2R-17 [19] design guidelines, steel yielding followed by rupture of FRP laminates, FRP debonding from adjacent concrete surface, and concrete cover separation (cover delamination) are common failure modes of strengthened RC members in flexure with FRP laminates. Rupture of the externally bonded FRP laminate will occur if the strain in the FRP reaches its ultimate strain, before the concrete in the top compression fiber reaches its crushing strain.

FRP debonding or cover delamination usually occurs if the axial force in the flexural FRP reinforcement cannot be sustained by the concrete substrate. Debonding of FRP can occur at the end of FRP sheet/laminate or at the mid-span of the beam/slab. The former is known as plate end debonding, while the latter is known as intermediate crack induced debonding, as shown in Figure 2.3 (b). Debonding of FRP laminates is usually initiated by flexural and/or flexural-shear cracks in the vicinity of maximum moment region of strengthened member and then progress along the length of FRP through the bonding agent. Such cracks open and widen under loading and will thus develop high levels of shear stress at the interface between the FRP sheets/plate and concrete substrate, causing FRP debonding.

Concrete cover delamination, as shown in Figure 2.3 (c) is another type of the debonding brittle failure mode that is usually initiated by the formation of a crack at the high stress concentration point close to the end of FRP laminate. The crack will then propagate to and along the level of flexural steel reinforcement, causing the separation of concrete cover. Failure of the concrete cover is initiated by the formation of a crack near the plate end. The crack propagates to and then along the level of the steel tension reinforcement, resulting in the separation of the concrete cover layer from the rest of RC beam or slab.

2.4 High Temperature Material Properties

Fire response of FRP-strengthened concrete structural members is governed by thermal, mechanical, and deformation properties of constituent materials as well as by the level of bond developed at FRP-concrete interface. The thermal properties, namely thermal conductivity (*k*) and specific heat (*c*), and density (ρ) govern the temperature rise and associated thermal gradients that develop within the section. Whereas mechanical properties, namely strength () and elastic modulus (E_c, E_s, E_f) determine the extent of fire induced degradation in capacity and stiffness of the structural member. Deformation properties, namely thermal expansion, creep, etc., control the extent of deformation in concrete members incorporating FRP, while the bond properties determine the level of stress transfer from concrete to FRP. All these properties vary significantly with increase in temperature. A re $f_c^{'}, f_y, f_{frp}$ view of the information available on temperature variation of these properties for concrete, steel rebars, FRP, and insulation is presented in following sections.

2.4.1 Concrete

Concrete is a non-combustible, heterogeneous material comprising of cement, coarse aggregate, sand, and water, along with some additives, such as plasticizers. Each of these components behave differently at elevated temperatures. Moreover, concrete upon heating experiences distinct physiochemical changes depending on the components in concrete mixture, giving rise to distinct variation in properties at elevated temperatures. The temperature variation of thermal, mechanical, and deformation properties of concrete has been extensively studied in the literature [68–77]. Additionally, empirical relations defining the temperature dependence of these properties are also reported in various documents, such as ASCE manual [78] and Eurocode 2 [79]. These relations are primarily categorized either on the basis of type of aggregate (siliceous/carbonaceous/lightweight) or strength of concrete (NSC/HSC). For instance, relations provided in ASCE manual [78] are applicable for NSC ($f_c^{'}$ < 50 MPa) only, whereas relations provided in Eurocode 2 [79] are applicable on both NSC and HSC ($f_c^{'}$ > 70 MPa). Since FRP-strengthening is typically applied to NSC structural members, the literature review herein mainly focuses on the properties of NSC with both siliceous and carbonaceous aggregates, at elevated temperatures.

(i) <u>Thermal Properties</u>

Thermal properties of concrete, namely thermal conductivity and specific heat influence the temperature rise within the cross-section of the concrete flexural member. Over the past few decades, various researchers [75, 77, 80–85] have evaluated thermal properties of concrete through different experimental procedures. There is a considerable variation in these tests data due to differences in test procedure and measuring techniques [86]. Nevertheless, these studies indicate that the thermal properties of concrete are primarily influenced by the type of coarse aggregates, i.e., carbonaceous, siliceous, or lightweight aggregates used in batch mix of concrete, and up to a certain extent on the strength of concrete, and moisture content.

Based on the data generated from above-mentioned studies empirical relations defining the variation of the thermal properties of concrete with temperature are specified in Eurocode 2 [79], and ASCE manual [78]. The ASCE constitutive model was developed for NSC only, whereas the Eurocode constitutive model was developed for both NSC and HSC. The empirical relations for thermal properties of NSC are presented in Appendix A.

Figure 2.4 (a) shows the temperature variation of thermal conductivity of concrete, as specified in Eurocode 2 and in ASCE manual. It can be seen from the figures that there is significant difference in the relations defined in both these documents. Due to the considerable difference in the reported test data, Eurocode 2 conservatively defines two limits (upper and lower) for the thermal conductivity of concrete but does not account for strength or type of aggregates. Whereas ASCE manual provides different relations for NSC based on three different types of aggregates. Further, it can be seen from the figure, that siliceous aggregate based concrete has larger initial value of thermal conductivity which decreases rapidly with increase in temperature. Whereas the carbonate aggregate based concrete has smaller initial value which decreases at a relatively slower rate with increase in temperature. Moreover, the thermal conductivity of lightweight aggregate concrete remains almost constant over a wide range of temperature.

Like thermal conductivity, the relations for temperature variation of specific heat of concrete defined in Eurocode 2 and ASCE manual are significantly different (see Figure 2.4 (b)). For instance, Eurocode 2 defines same relation for temperature variation of specific heat for both siliceous and carbonate aggregate concrete, which is very conservative. Whereas ASCE manual provides three different relations for different types of aggregate and accounts for the significant increase in specific heat in the temperature range 600-800˚C, due to decomposition of dolomite (an endothermic reaction). Additionally, the Eurocode 2 relations explicitly accounts for moisture content in concrete, which is completely ignored by ASCE manual. Further, it can be seen from the figure that the specific heat values of three types of aggregates are close, except around 700°C.

Based on the above review, it can be inferred that carbonate aggregate concrete possess a higher specific heat and lower thermal conductivity, as compared to siliceous concrete. Thus, carbonate concrete is usually preferred over siliceous aggregate when a superior high temperature behavior is required in structural members [86].

(ii) Mechanical Properties

The temperature variation of mechanical properties of concrete, namely compressive strength, tensile strength, elastic modulus, and stress-strain relations significantly influence the fire resistance of FRP-strengthened concrete flexural members. The temperature variation of mechanical properties of concrete has been studied extensively as compared to that of thermal properties. Therefore, significant amount of test data is available for temperature dependent mechanical properties of NSC fabricated using different types of aggregates. This test data defining the variation in compressive strength of NSC with temperature is shown in Figure 2.5 (a). It can be seen from the figure that there is significant variation in the compiled test data, which may be attributed to use of different heating and loading rates, testing procedure, as well as age, curing, and moisture content of specimen at the time of testing.

Various researchers have proposed constitutive relations for degradation of compressive strength of NSC with temperature based on their respective test data. However, the constitutive relations specified in ASCE manual [78] and Eurocode 2 [79] are the most widely used constitutive models and are shown in Figure 2.5 (a). These relations do not account for any variations in other parameters, such as material composition, heating and loading rate. It can be seen from the figure that there is negligible degradation in strength of all types of concrete until 300°C temperature. Beyond 400°C, concrete strength decreases quickly, due to changes developed in the internal concrete structures. Further, it can be seen from the figure that there is a significant difference in degradation of strength with temperature as per the relations specified in ASCE manual and Eurocode 2. A major reason for this difference is the ASCE manual does not specifically account for the effect of aggregate types on compressive strength of concrete at elevated temperatures. Moreover, it can be inferred from the figure that ASCE model defines the upper bound of test data, while Eurocode 2 model defines the lower bound of test data. Based on the results of recent numerical studies [86], both ASCE manual and Eurocode give conservative predictions on fire resistance of columns made of carbonate concrete. However, ASCE constitutive model provides better predictions in the simulations as compared to Eurocode constitutive model.

Tensile strength of concrete also degrades with increase in temperatures. While there are relatively fewer studies on tensile behavior of concrete at elevated temperature, as compared to compressive strength, it is generally accepted that rate of degradation in tensile strength is significantly more rapid as compared to compressive strength, especially for temperatures less than 400°C. Only Eurocode 2 provides relation for degradation in tensile strength of concrete at elevated temperature, as shown in Figure 2.5 (a). It can be seen from the figure that tensile strength decreases linearly for temperatures exceeding 100°C.

Elastic modulus of different aggregates-based concrete also experiences deterioration with increase in temperature, as shown in Figure 2.5 (b) [87]. It can be seen that unlike compressive strength, the elastic modulus of concrete starts decreasing immediately with increase in temperature above room temperature. The elastic modulus degrades by about 50-60% of its room temperature value for both siliceous and carbonate concrete. However, the degradation in carbonate aggregate based concrete is slightly lower than that of siliceous concrete, and this can result from better temperature resistance of carbonate aggregate. Lightweight concrete has relatively slower degradation on modulus of elasticity, and this is probably attributed to less aggregate and less voids inside of concrete.

(iii) Deformation Properties

Thermal expansion, creep strain, and transient strain of concrete are the primary deformation properties affecting the fire resistance of FRP-strengthened concrete flexural members. These properties depend on the type of aggregate used, and chemical and physical reactions occurring in cement paste [87]. Thermal expansion is quantified using the coefficient of thermal expansion (CTE), which is defined as the change in a unit length of a material caused by a unit (degree) increase in temperature, i.e., thermal strain per unit increase temperature. CTE quantifies structural movement and thermal stresses resulting from temperature changes [88], particularly during monotonic heating.

Figure 2.6 (a) shows the variation of thermal strain at elevated temperatures as defined in ASCE manual and Eurocode 2, and published test data. It can be seen from the figure that the temperature variation of thermal strain is significantly influenced by the type of coarse aggregates, as these aggregates makes up to 70-80% of total solid concrete volume. Typically, thermal expansion of concrete with siliceous aggregate is more significant as compared to concrete with carbonate aggregate. However, if concrete is subjected to stress levels larger than 35% of its ultimate strength, thermal expansion is essentially eliminated, as it is counteracted by the applied stress [89].

Creep strain is time-dependent plastic strain under constant stress level. Creep strain is primarily associated to moisture movement in concrete and therefore, varies significantly with temperature. Apart from moisture movement, creep is also influenced by stress level, temperature level, time, and batch mix of concrete [90]. There are very limited studies evaluating the effect of these factors on creep strain in concrete. These limited studies indicate that creep strains and the rate of deformations resulting from creep increases rapidly at elevated temperature, resulting in significant deflections in concrete members. Moreover, creep strain increases rapidly with increasing stress level, and are irreversible in nature. Creep strains also affect the stress redistribution within the concrete cross-section, and hence play an important role in deflection progression during both heating, and cooling phases of fire exposure.

In addition to movement of moisture, the chemical composition of the cement paste and moisture content of concrete also changes with increase in temperature. Moreover, internal stresses and micro-cracking develop in concrete due to a mismatch in thermal expansion between the cement paste and the aggregate [87]. These changes and the micro-cracking induce transient strain concrete, which develops in concrete only during the first heating cycle under loading, but not upon subsequent heating, and is independent of time [91]. These transient strains are irreversible and do not recover during cooling phase and remain constant after cooldown (residual conditions) [91]. Thus, creep and transient strains must be accounted for accurate assessment of fire resistance of FRP-strengthened concrete members. Therefore, high temperature stress-strain relations for concrete specified in

At present there are only two constitutive models explicitly defining variation of creep and transient strain in concrete at elevated temperature [92]. These models are proposed by Anderberg and Thelandersson [93] (1976) and Harmathy [94] for creep and transient strain, respectively. These models generally produce reasonable estimates for creep and transient strains in concrete under fire conditions when used in conjunction with high temperature stress-strain relations provided in ASCE manual [86, 95] and summarized in Appendix A. However, when relations specified in Eurocode 2 are used for defining the high temperature stress-strain response of concrete, these models can be ignored as Eurocode 2 implicitly accounts for transient strains experienced during fire exposure.

Apart from thermal, creep, and transient strain, another important deformation property that needs consideration is fire induced spalling in concrete. When the pore pressure resulting from moisture evaporation in the concrete member, in the initial stages of fire exposure, exceeds tensile strength of concrete, chunks of concrete fall off from the member. This falling off of chunks of concrete is termed as spalling, which is often accompanied with loud noise. Spalling can reduce the cross-section area of concrete, accelerate the strength loss, which in turn can reduce the fire resistance of the concrete member. The extent of spalling in concrete depends on many factors, such as, moisture content, concrete permeability, concrete strength, fire scenario, and compressive stress level [96–98]. These studies also indicate that HSC are more prone to spalling than NSC. Since, FRP-strengthened concrete members are typically made of NSC, spalling is not a primary concern in this study.

2.4.2 Steel rebars

The cross-sectional area of steel rebars is significantly smaller compared to the overall cross-section area of concrete, therefore, the high temperature thermal properties of steel have a little influence on the temperature rise in structural member [99]. However, the high temperature mechanical properties of steel rebars have significant influence on the fire resistance of concrete flexural members. The behavior of reinforcing steel rebars has been extensively studied by various researchers around the world. A brief review of some of the notable studies evaluating the thermal and mechanical properties of steel rebars at elevated temperatures is presented here.

(i) Thermal Properties

At room temperature the thermal properties of steel rebars, i.e., thermal conductivity and specific heat are governed by the composition/type of steel [100], while at elevated temperature these properties are governed by temperature level reached in steel rebar [92]. Since steel is a good conductor of heat, the conductivity of steel is very high at room temperature compared to that of concrete. Therefore, heat gets distributed rapidly along the length of steel rebars. Figure 2.7 shows the variation in thermal conductivity and specific heat of steel rebars based on the relations provided in ASCE manual. It can be seen from the figure that the thermal conductivity decreases linearly until about 900°C and then remain constant until 1000°C [78]. On the contrary, specific heat of steel increases linearly with increase in temperature, with a large spike between 700°C and 800°C, as can be seen in Figure 2.7. The spike occurring around 750°C is attributed to the phase transformation of steel material. After overcoming the rapid spike and drop, the specific heat of steel rebars remains almost constant until 1000°C. Despite these changes in thermal properties of steel rebar, the temperature rise in concrete is not affected due to the smaller cross-section area of steel rebar, and therefore, these properties are not very important for heat transfer analysis.

(ii) Mechanical Properties

Steel rebars are the primary component resisting the tensile stresses in a concrete flexural member. Therefore, degradation in mechanical properties of steel rebars significantly influence the response of RC flexural members. The mechanical properties of steel rebar that influence fire response are yield strength, elastic modulus, and ultimate strength. These properties are generally represented by stress-strain relationship. A review of literature indicates that there is considerable variation in degradation of yield and ultimate strength of steel rebars. The variation is attributed to the composition of steel as well as the definition of yield strength [101].

Figure 2.8 shows the temperature dependent degradation in yield strength of steel rebars as per the relations specified in ASCE manual [78] and Eurocode 2 [79]. It can be seen from the figure that there is significant difference in the above-mentioned relations. For instance, according to ASCE manual the yield strength starts degrading gradually with increase in temperature, whereas according to Eurocode 2 (2004), the yield strength remains constant until 400°C. Additionally, ASCE manual provides a separate relation for degradation in yield strength and ultimate strength with degradation in ultimate strength lower than that in yield strength (see Figure 2.8). Whereas Eurocode 2 considers that both yield strength and ultimate strength degrade at the same rate. Thus, ASCE manual accounts for strain hardening effects in steel, whereas Eurocode 2 considers steel to be elasto-plastic material, i.e., no strain hardening after yielding. The detailed constitutive relations for stress-stress response and other mechanical properties of reinforcing steel as defined in ASCE manual and Eurocode 2, are summarized in the Appendix A.

(iii) Deformation Properties

Thermal strain and creep strain are the primary deformation properties of steel rebars which influence the fire response of strengthened RC member. Thermal strain is used to determine the coefficient of thermal expansion (CTE), which is defined as strain induced per degree of change in temperature. The CTE is used to quantify the expansion/elongation of steel rebars due to temperature rise. Figure 2.9 shows the variation of thermal strain as a function of temperature as specified in ASCE Manual and Eurocode 2. It can be seen from the figure that there is negligible difference between the two models for thermal strain of steel up to 700°C. However, ASCE model assumes a continuously increasing thermal strain in the temperature range of 700-850°C the, whereas the Eurocode model shows a constant strain from 750 to 850°C to account for the phase change that occurs in steel in this temperature range. After that the thermal strain in steel increases linearly up to 1,000°C.

Creep is defined as the time-dependent plastic strain under constant stress and temperature. At room temperature and under service load levels, creep deformations of steel are insignificant, however, at elevated temperatures; creep deformations accelerate and may affect the global response of structures. Generally, creep deformations in steel become noticeable at temperatures above 400°C. However, it was found experimentally that when the stress level is high, the effect of creep becomes significant in steel members even at temperatures of 300°C (Huang et al., 2006; Huang and Tan 2003). A review of literature indicates that very little information is available on the effect of high temperature creep on the structural response. At present, most fire resistance analyzes are carried out using Harmathy's [88] high-temperature creep model which is mainly based on Dorn's theory. This creep model for reinforcing steel is summarized in Appendix A.

2.4.3 FRP

Currently, a wide range of FRP products are available in the market and any small change in the composition of FRP (polymer or fiber) can influence their high temperature properties significantly. Thus, it is difficult to quantify the property variation of each FRP product used in various applications (aerospace and marine infrastructure). Therefore, the review is limited to the elevated temperature material properties of some of the primary CFRP products used in structural strengthening applications.

(i) Thermal Properties of FRP

The thermal properties required for evaluating temperature rise in a fire exposed FRP-strengthened RC member include thermal conductivity, specific heat and density of concrete, steel reinforcement, FRP, and insulation. There is limited test data on thermal conductivity and specific heat of FRP. This is attributed to lack of research and specific instrumentation required to handle the complex nature of chemical reactions taking place in FRP at high temperatures. Moreover, there are no empirical relations currently available describing thermal properties of FRP as a function of temperature. Figure 2.10 (a) and (b) shows thermal conductivity and specific heat of FRP as a function of temperature, compiled using limited published data from the tests carried out on FRP used in aerospace and automobile applications [102–105].

It can be seen from the Figure 2.10 (a) and (b) that both thermal conductivity and specific heat of FRP varies almost linearly with increase in temperature and there exists a wide variation in the available test data. A closer examination of Figure 2.10 (a) shows that the temperature variation of thermal conductivity as reported by Griffis et al. [102] is contradictory to trends reported by other researchers. The variation in the reported test data is attributed to different polymer matrix, as well as different type, orientation, and volume fraction of fibers in the FRP systems used in tests. On the contrary, the similar trends are reported for specific heat of FRP at elevated temperature. The sharp increase followed by a plateau between 350-510°C is attributed to the consumption of additional heat due to thermal degradation (decomposition) of polymer matrix. Additionally, it can be seen from Figure 2.10 (a) and (b) that except for Griffis et al. [102], most of the test data is available only up to a small temperature range (less than 200°C). This is because the tests were terminated once the polymer matrix started burning due to thermal decomposition. Therefore, there is lack of data on variation of thermal properties of FRP at temperature above the decomposition temperature of polymer matrix.

(ii) Mechanical Properties of FRP

Mechanical properties required for fire resistance of FRP-strengthened RC structural member include tensile strength and elastic modulus of FRP as well as strength of FRP-concrete interfacial bond. A review of literature indicates that high-temperature strength properties of FRP have been studied more widely than the thermal properties of FRP. In these studies, the strength properties were measured either during exposure to a specific constant temperature level or after exposure to elevated temperature level and then cooling down the to room temperature.

› Strength and Elastic modulus

Figure 2.11 (a) and Figure 2.11 (b) shows the reported test data on the tensile strength and elastic modulus of FRP composites, respectively, as a function of temperature. The test data is shown for CFRP and GFRP. The figure is compiled using the limited test data available on strength tests of CFRP and GFRP at elevated temperature, reported by, [8, 67, 114–118, 106–113]. For clear comparison, the tensile strength and elastic modulus values of FRP composites at different temperatures are normalized to that at ambient temperature.

It is evident from the figure that there is a significant variation in the test data available on the high-temperature strength properties of FRP. These variations can be attributed to factors, such as, test procedures, heating rates as well as specific polymer type, orientation, and volume fraction of fibers. Therefore, the plotted data cannot be directly compared/ extrapolated to other FRP materials. However, the plotted data is a representative of the mechanical behavior of typical FRP systems used in strengthening of RC structural members.

It can be seen from Figure 2.11 (a), the strength properties of FRP deteriorate significantly with increasing temperature. In general, the strength and elastic modulus of FRP experience a steep reduction at temperature close to glass transition temperature (T_g) of the polymer matrix, followed by a gradual reduction during the decomposition of polymer. Even after glass transition and decomposition of polymer matrix FRP are able to retain a considerable fraction of their ambient temperature tensile properties as fibers (i.e., carbon or glass) are able to retain much of their strength at high temperature. However, with increase in temperature beyond 500°C, the strength and elastic modulus of FRP once again experience a steep reduction due to oxidation of fibers and is more intense in the temperature range of 600-800°C. Additionally, it can be seen that FRP loses nearly 50% of its strength in the temperature range of 250°-350°C, which is much more rapid as compared to loss in strength of steel rebars.

Apart from the test data, relations defining the variation of strength and elastic modulus of CFRP and GFRP, with temperature are available in literature and are shown in Figure 2.11 (b) and Figure 2.11 (c), respectively. These relations are proposed by [108, 111, 112, 114, 115, 119–121] for FRP. Majority of these relations define the temperature dependent variation in strength properties of CFRP, while relatively few relations define the variation in strength properties of GFRP. Additionally, most of these relations are in form of semi-empirical equations and express the variation of strength and stiffness of FRP up to 800°C, whereas some relations are in the form of reduction factors providing percentage degradation in ambient temperature strength and stiffness of FRP at different temperature level.

Saafi [119] proposed linear/ bilinear relations for expressing degradation of strength and stiffness of CFRP and GFRP at elevated temperature. These relations are based on the tests carried out on CFRP and GFRP rebars reported by Blontrock et al. [8]. The strength and stiffness degradation relation for CFRP are given as:

$$\frac{f_T}{f_{20°\text{C}}} = \begin{cases} 1; & 0 \le T \le 100 \\ 1.267 - 0.00267T; & 100 \le T \le 475 \\ 0; & 475 < T \end{cases}$$
$$\frac{E_T}{E_{20°\text{C}}} = \begin{cases} 1; & 0 \le T \le 100 \\ 1.175 - 0.00175T; & 100 \le T \le 300 \\ 1.625 - 0.00325T; & 300 \le T \le 500 \\ 0; & 500 < T \end{cases} \tag{2.1}$$

where, f and E denotes the strength and stiffness of CFRP.

Bisby et al. [120] compiled the test data available until then on the high temperature strength properties and proposed a sigmoid function to define the variation in strength and stiffness of CFRP and GFRP. This function is given as:

$$\frac{f_T}{f_0} = \left(\frac{1-a}{2}\right)\tanh\left(-b\left(T-c\right)\right) + \left(\frac{1+a}{2}\right) \tag{2.2}$$

where, f_T is the strength property in question (strength or elastic modulus) at temperature T; f_0 is the value of the strength property at ambient temperature; a, b, and c are the constants derived from least-squares regression analysis, and their values depends on the type of fiber (i.e., carbon or glass). The constant a describes the residual value for the strength property in question, whereas b and c describe severity of property degradation and central temperature. The sigmoid function i.e., Eq. [2.2] does not consider the effect of T_g of the polymer, which significantly Most of the test data compiled by the authors was from the tensile strength tests on prefabricated FRP rebars, which has slightly higher T_g than the FRP sheets. The sigmoid function Eq. [2.2] was further modified by Dai et al. [121] to account for T_g of the polymer matrix and is given as:

$$\frac{f_T}{f_0} = \left(\frac{1-a}{2}\right)\tanh\left(-b\left(\frac{T}{T_g}-c\right)\right) + \left(\frac{1+a}{2}\right) \tag{2.3}$$

Wang et al. [111] proposed a relation for defining degradation in strength of CFRP with temperature, by fitting the strength test data of CFRP to the [122] model proposed for structural steel and is given as:

$$\frac{F_{u,T}}{F_{u,normal}} = A - \frac{\left(T - B\right)^{n}}{C} \tag{2.4}$$

where, A, B, C, and n are constants the values for which varies with temperature. Yu and Kodur [112] proposed a semi-empirical relation for expressing the variation of strength and stiffness of CFRP strips and rods with temperature by fitting the test data to the hyperbolic function proposed by Gibson et al. [123]. The relations proposed by for strength and stiffness of CFRP strips at elevated temperatures are given as:

$$\begin{aligned}
f_{\mathrm{strip}}\left(T\right) &= 0.56 - 0.44\tanh\left(0.0052\left(T - 305\right)\right) \\
E_{\mathrm{strip}}\left(T\right) &= 0.51 - 0.49\tanh\left(0.0035\left(T - 340\right)\right) \\
f_{\mathrm{rod}}\left(T\right) &= 0.54 - 0.46\tanh\left(0.0064\left(T - 330\right)\right) \\
E_{\mathrm{rod}}\left(T\right) &= 0.51 - 0.49\tanh\left(0.0033\left(T - 320\right)\right)
\end{aligned} \tag{2.5}$$

Nguyen et al. [115] calibrated a three-degree polynomial function to illustrate the strength reduction of CFRP. The function was calibrated using the test data generated by the authors from the elevated temperature tests on wet lay-up CFRP coupons and is given as:

$$\frac{\sigma_{u,T}}{\sigma_{u,20°\mathrm{C}}} = K_0 - K_1\left(\frac{T - T_m}{T_{\max,10\%}}\right)^3 - K_2\left(\frac{T - T_m}{T_{\max,10\%}}\right) \tag{2.6}$$

where, T_{m} is the mechanical glass transition temperature, $T_{\max,10\%}$ is failure temperature at 10% of the stress ratio, K_0 is the coefficient (ranging from 0.4 to 0.6), K_1 and K_2 are calibrated coefficients.

As is the case with test data, there also exists a significant variation in the empirical relations for strength properties of both CFRP and GFRP. These variations are due to the large variation in the test data used to compile the respective relations. The variations are also due to the different parameters (such as, T_g of adhesive, stress ratio, failure load etc.) considered and technique used for deriving the respective relations. In some cases, the strength degradation relations are nearly same, but the stiffness degradation relations are significantly different. For instance, the strength degradation in CFRP, as predicted by the generalized sigmoid function proposed by Bisby et al. [120], is nearly same as that predicted by the specific relations for CFRP strips and CFRP rods proposed by Yu and Kodur [112]. However, the degradation of stiffness with temperature is significantly different during the entire temperature range up to 600°C, in these two studies.

The property relations proposed by Wang et al. [111] and Dai et al. [121] describe rapid reduction (up to 60%) in the strength and elastic modulus of FRP at temperatures below 200°C, whereas the relations proposed by [112, 115, 119, 120] (only for strength in ref. 119) consider a gradual reduction. Furthermore, the relation proposed by Dai et al. considers the strength and elastic modulus to be constant beyond T_g of polymer matrix used in FRP, whereas the other models predict continuous reduction in strength and elastic modulus until 600-700°C. This is attributed to the fact that the relations derived by Dai et al. assumes that the FRP-concrete interface would lose the bond-capacity beyond 200°C completely and therefore the contribution of FRP would be completely lost.

Another difference in the available relations, is the behavior of elastic modulus predicted by Nguyen et al. [114] and Nguyen et al. [115] relations, which shows an increase in the elastic modulus with increase in temperature (Figure 2.11 (c)). This behavior contradicts the behavior predicted using other relations and is attributed to the method used for preparing CFRP coupons (wet lay-up), the test method and the resulting test data used for the deriving the relation.

› FRP-concrete interfacial bond

The reported test data available on bond strength of the FRP-concrete interface is plotted as function of temperature in Figure 2.12 (a). Majority of these tests [8, 14, 124–127] are carried out on concrete specimens strengthened with FRP using EB technique. Whereas relatively little test data [128–130] is available on the elevated temperature bond behavior of concrete strengthened with FRP using NSM technique. It can be seen from the figure that a large variation exists in the available test data on bond strength of FRP-concrete interface. Further, it can be seen that the bond strength decreases rapidly with rise in temperature and diminishes after about 120-150°C.

The bond between FRP and concrete is critical for stress transfer from concrete to FRP, and therefore, influences the response of FRP-strengthened RC structures under fire exposure. Hence, the temperature induced degradation in interfacial bond must be duly accounted for evaluating fire resistance of FRP-strengthened RC structures. In many previous studies, researchers adopted a perfect bonding between FRP and concrete, as it is simplest approach to account for bond behavior. However, this approach leads to stiffer response and thus, higher fire resistance prediction which is unrealistic Ahmed and Kodur [131]. Alternatively, others adopted a crude approach in which the FRP-concrete interfacial bond was assumed to be completely lost once temperature at the interface exceeded the T_g of adhesive. This approach, on the other hand provides too conservative response [132] and again unrealistic.

A better approach to account for realistic (actual) bond behavior is through temperature dependent bond stress-slip relation, which can be expressed as a bilinear curve or as a single exponential curve. While several bond stress-slip relations are available in literature for modeling FRP-concrete interfacial bond at ambient temperature, very few relations are available for modeling bond behavior at elevated temperature. Due to the lack of information on bond stress-slip relations at elevated temperature, several researchers have used ambient temperature bond stress-slip relations, together with bond strength degradation, for fire resistance analysis of FRP-strengthened RC beams.

At present, the widely accepted bond stress-slip relations available in the literature are in the form of bilinear model proposed by Arruda et al. [133] and exponential curve model proposed by Dai et al. [134] and are shown in Figure 2.12 (b). The bilinear bond-slip relations are defined using three different parameters namely, stiffness of the interface (K), maximum shear strength (τ_{LM}), and ultimate slip (s_{L0}). The values of these parameters were calibrated by the authors based on the experimental and numerical studies on a specific type of carbon FRP (CFRP) laminates. The bond-slip relations proposed by Dai et al. [134] are based on temperature variation of two parameters, namely, interfacial fracture energy (G_f) and the interfacial brittleness index (B). These bond-slip relations are shown in Figure 2.12 (b). For clear comparison, the bond strength at elevated temperatures is normalized by the peak strength at ambient temperature.

It can be seen from the figure that the bond strength decreases significantly with increase in temperature and vanishes completely at about 120°C. Further, it can be seen from the figure that there exists a significant difference in the behavior described by different bond stress-slip relations, specifically in the ascending branch of the curve before peak bond-strength is reached. The difference can be attributed to the test data and the parameters considered in deriving the relations. A closer examination of the figure indicates that at room temperature conditions, the stiffness of both the relations is nearly the same, however at elevated temperatures the nonlinear bond-slip relations predict a stiffer response compared to the bilinear relations. Further, the bilinear bond-slip relation reaches a bond stress value of zero at the ultimate slip value indicating complete loss of bond between FRP-concrete interface. Whereas the nonlinear relations by Dai et al. (2013)

being an exponential curve do not lead to zero bond stress indicating that the bond is never completely lost.

(iii) *Deformation Properties of FRP*

Deformation properties such as thermal expansion and creep strain determine the extent of deformation in concrete members incorporating FRP. The thermal strain in FRP is determined using the coefficient of thermal expansion (CTE) values for FRP which depends on type of polymer, type of fiber and volume fraction of fibers. Like thermal and mechanical properties, the CTE of FRP in longitudinal direction is dominated by fibers, while the transverse direction CTE depends on the polymer matrix [135]. The CTE of polymer matrix is considerably higher than the CTE of fibers and increases significantly with the increase in temperature. Therefore, CTE of FRP in transverse direction is higher than the CTE in longitudinal direction.

Limited information is available on the variation of CTE of FRP at elevated temperatures. In the temperature range of 20-200°C, the CTE of carbon FRP (CFRP) is quite small and fluctuates around zero, while the CTE of glass FRP (GFRP) reaches around 15×10^{-6} /K. This is attributed to the fact that glass fibers experience much higher expansion as compared to that of carbon fibers. There is a lack of test data on CTE of FRP in the temperature range of 200-800°C, as the polymer matrix starts melting beyond 200°C and it is difficult to measure the CTE of FRP as one whole piece. Based on the theoretical studies by Nomura and Ball [136], CTE values of CFRP and GFRP in the temperature range of 20-1000°C can be assumed to be 5×10^{-6} /K and 15×10^{-6} /K, respectively.

Creep is defined as the time-dependent plastic strain under constant stress and temperature. At room temperature and under service loads, creep deformations of FRP are insignificant. However, at elevated temperatures, creep deformations accelerate and may affect the global response of structures. In general, creep stain in FRP increases with increase in temperature and is largely governed by the type of polymer used in FRP. For instance, FRPs incorporating thermoset polymers, which have high T_g due to heavy cross-linking, exhibit less creep than FRPs incorporating thermoplastic polymeric materials [137]. Creep strain in FRP also depends on the type and orientation of fibers. For instance, when fibers are in the loading direction the creep in fibers govern the creep in composite. However, it has been observed that commercially available fibers (except aramid fibers) do not creep significantly. Therefore, thermally accelerated creep at elevated temperature can be neglected for unidirectional FRP sheets and laminates used in strengthening applications [138].

Owing to the softening and melting of polymer at elevated temperatures, it is extremely difficult to measure creep strain of FRP at high temperatures. Therefore, very limited information is available on high temperature creep strain of FRP. The only available information is based on the tests carried out by [139] on CFRP sheets at various stress levels in temperature range of 20-150°C. The study showed that at the same stress levels, CFRP composite experienced twice the creep effect at 150°C as that at room temperature. Based on the test data, the authors also proposed a relation to predict creep strain of FRP at elevated temperatures, given as:

$$\begin{aligned} &\varepsilon_{frp}^{cr} = \int_0^t B\sigma^{0.01} e^{H/kT} \sinh\left(\frac{\sigma}{kT}\right) dt \\ &B = 2.03\times 10^{-4} T^{1.55} t^{0.25} \end{aligned} \qquad (2.7)$$

where, ε_{frp}^{cr} is creep strain of FRP; T is FRP temperature (°K); σ is the stress; t is fire exposure time (s), and k is Boltzmann's constant; H is the activation energy which depends on experimental data.

The above review clearly indicates that limited test data is available on high temperature strength, stiffness and bond properties of FRP. Similarly, only few analytical relations are available describing the variation in material properties of FRP. Further, there exists a wide variation in the available test data as well as analytical relations on the high temperature material properties of FRP. Since use of different property relations may result in varying fire resistance prediction, it is important to critically examine and arrive at the most suitable high temperature material properties of FRP for fire resistance evaluation.

2.4.4 Thermal Properties of Fire Insulation

Thermal properties of fire insulation required for fire resistance evaluation of FRP-strengthened RC members include thermal conductivity and heat capacity. These thermal properties depend on the type and composition of the insulation material used such as, calcium silicate board, gypsum wall board, Rockwool, or spray applied fire resistive materials (SFRM). Even a small variation in the composition of fire insulation can lead to significant changes in the thermal properties.

Limited test data is available on temperature dependent thermal properties of insulation material. Moreover, in most cases these thermal properties are evaluated in the temperature range of 20-400°C. Figure 2.13 (a-b) show the plots of available data on thermal conductivity and heat capacity of different types of fire insulation, as a function of fire exposure time. The fire insulation materials considered for compiling the figure include insulation boards (Promatect H, Promatect L 500, Promasil), and cementitious SFRMs (CAFCO 300, Carboline Type 5-MD, Tyfo WR-AFP, TB tunnel fire proofing). The insulation boards comprise of different proportions of calcium silicate, gypsum and vermiculite as main components, whereas the cementitious materials consist of different proportions of cellulose, Portland cement, gypsum, and vermiculite as main components. The properties of insulation boards are based on the test and analytical studies reported by [140–142]. Whereas the properties of cementitious materials are based on the tests carried out by Kodur and Shakya [143] on different SFRMs. Bai et al. [140] and Kodur and Shakya

[143] also proposed relations for defining the variation of thermal properties of insulation material with temperature. However, these relations are specific to the type of insulation material with specific composition and hence, cannot be used as a general relation for all fire insulation materials.

It can be seen from the figure that the thermal properties of all the insulation materials vary significantly with increase in temperature. Further, it can be seen that even for similar type of insulation material i.e., board or cementitious material, the variation in thermal properties with temperature is significantly different. Initially, the thermal conductivity of cementitious insulation materials decreases in the temperature range of 100-200°C due to the evaporation of free moisture present in them. However, with increase in temperature the thermal conductivity of these cementitious material increases significantly. This can be attributed to the crystallinity of gypsum at elevated temperature. In case of insulation boards, the thermal conductivity increases continuously with increase in temperature at a constant rate, however, the increase is very small and, in some cases, (Promatect L 500) negligible.

Like thermal conductivity, the heat capacity of the cementitious materials varies significantly with temperature as compared to insulation boards. Initially the heat capacity of the cementitious materials increases with increase in temperature. This is attributed to the evaporation of free moisture present in the insulation. The heat capacity remains almost constant or decreases at a very slow rate until 400°C and then start increasing at gradually. The increase in heat capacity beyond 500°C is to be due to the release of chemically bound water present in the ingredients of the cementitious material. In case of insulation boards, the heat capacity increases at a faster rate until 100°C after which the change in heat capacity of the insulation boards is negligible. The increase in the heat capacity until 100°C is attribute to evaporation of moisture present in the boards. These temperature dependent variations in thermal properties of fire insulation are to be duly accounted for in analysis for realistic fire resistance predictions in FRP-strengthened RC members.

2.5 Structural Behavior of FRP-Strengthened RC Members under Fire Exposure

2.5.1 Experimental Studies

The response of FRP-strengthened concrete flexural members under fire conditions is typically evaluated through fire resistance tests. A number of fire resistance tests have been conducted for evaluating the fire response of FRP-strengthened concrete beams and slab. Some of the notable experimental studies are discussed below briefly.

(i) Fire Tests on FRP-Strengthened RC Beams

Deuring [144] was one of the earliest researchers who conducted first ever fire tests on RC beams strengthened with CFRP strips and steel plates. The test program comprised of standard fire test on six RC beams, wherein four beams were strengthened with CFRP strip, one beam was strengthened with adhesively bonded steel plate, and remaining one beam was un-strengthened. All the beams were exposed to ISO 834 standard fire exposure and were loaded to approximately 55% of their ultimate capacity at room temperature. Of the four CFRP-strengthened beams, two beams were protected with calcium silicate fire insulation boards of different thickness. In the fire tests, the loss of interaction between FRP and concrete was observed (based on sudden increase in deflection) after 20 minutes and 60 minutes of fire exposure in unprotected and protected beams, respectively. The unprotected beams achieved a fire resistance of 81 minutes, whereas the protected beams achieved a fire resistance of 146 minutes. The study concluded that the CFRP-strengthened beams can achieve the required fire resistance if they are provided with proper external thermal protection.

Blontrock et al. [145] tested two un-strengthened RC beams and six CFRP-strengthened RC beams by exposing them to ISO 834 standard fire exposure under service load level. The CFRP-strengthened RC beams were provided with Promatect H and Promatect 100 fire insulation material in varying thickness and configuration. The test results indicated that compared to flat insulation system (insulation only at the soffit), the U-shaped insulation system was more effective in maintaining the FRP-concrete for a longer duration as well as in increasing the fire resistance of the strengthened beams. Additionally, the test results also indicated that providing the insulation only in the anchorage zones can maintain the structural effectiveness of CFRP for a longer duration and hence, increase the fire resistance of the strengthened beams.

Williams et al. [146] tested two RC T-beams strengthened with CFRP sheets and protected on the sides and at the soffit with cementitious fire insulation material of 25 mm and 38 mm thickness. The beams were subjected to service load levels (approximately 48% of ultimate room temperature capacity) and were exposed to ASTM E119 standard fire exposure. During the tests, the temperature of the FRP-concrete interface reached the adhesive T_g within 60 to 90 minutes of fire exposure, however, it was not possible to identify the loss of CFRP-concrete bond. Although the interface temperature exceeded the adhesive T_g quite early in fire exposure, the beams did not fail and achieved a fire resistance rating of 4 hour based on ASTM E119 failure criteria. The authors also developed a numerical model to predict the temperature rise in the beams.

Ahmed and Kodur [147] tested four CFRP-strengthened RC beams under combined effect of fire and structural loading. The beams were provided with two different types of 25 mm thick cementitious fire insulation material at the bottom extending on the sides up to 100 mm. The insulation layer was further coated with intumescent spray to increase the stability of the cementitious insulation. During the fire tests, the beams were loaded up to 50% of their ambient temperature strengthened capacity and were exposed to ASTM E119 standard fire or design fire conditions. The effect of providing cooler anchorages, as well as different restraint conditions on fire resistance of the strengthened beams was evaluated in this study. Based on the temperature level reached at the CFRP-concrete interface and the sudden increase in deflection, the authors deduced the CFRP-concrete debonding time between 20-25 minutes of start of fire exposure. However, the beams were able to sustain the applied loading for 3 hours under standard (ASTM E119) and non-standard (design) fire conditions. The results from the tests demonstrated that the unbonded fibers in the fire exposed zone of the beam can contribute to the stiffness of the beam through cable action and can reduce the deformation of the beam, provided cooler anchorage zones are available. It was also observed that the fire-induced axial restraint force can significantly increase the fire resistance.

Firmo et al. [148] conducted fire tests on one un-strengthened and five CFRP-strengthened RC beams, by exposing them to ISO 834 standard fire exposure. The beams were tested under four-point loading system, wherein structural loading equivalent to 50% of ambient temperature ultimate capacity was applied on the beams. During the fire test, the soffit of four CFRP-strengthened beams was protected using calcium silicate boards or vermiculite perlite mortar fire insulation in varying thickness (25 mm to 40 mm), and the remaining one beam was tested without any thermal protection. Additionally, the extremities of CFRP strengthening system, i.e., anchorage zones, approximately 200 mm on either side were thermally insulated by the furnace walls and were not directly exposed to thermal loading due to ISO 834 fire conditions. Fire test results indicated that if the strengthening system were left unprotected, CFRP laminate de-bonded after 23 minutes into fire exposure. However, if the fire insulation was applied, the debonding time was significantly delayed (60-89 minutes for 25 mm fire insulation, 137-167 minutes for 40 mm fire insulation). The results also confirmed that the presence of cooler anchorages allowed for the use of unbonded CFRP through cable action and the debonding in the anchorage zones leads to failure of strengthening system as opposed to debonding of CFRP in fire exposed zone.

Firmo and Correia [149] conducted fire resistance tests on nine RC beams strengthened with CFRP strips and one un-strengthened RC beam in a small scale furnace, as shown in Figure 2.14. The beams were subjected to structural loading equivalent to 70% of their ambient temperature capacity and were exposed to ISO 834 standard fire conditions in a setup similar to that of (Firmo et al. 2012). However, in these tests the entire strengthened portion of the beams, i.e., including the anchorage zones was exposed to fire. Effect of different insulation thickness and configuration, epoxy type, and anchorage schemes were evaluated in the tests. For instance, seven CFRP-strengthened beams were protected at bottom surface with Promatect-L500 fire insulation boards with different thickness in the anchorage zones and central zone of the CFRP strips. Whereas the remaining two strengthened beams were tested without any fire insulation, however in one of the uninsulated beams, the CFRP strip was provided with mechanical anchorages in form of bolted with steel plates at the ends.

The authors reported that the strengthening system de-bonded within few minutes of fire exposure, with severe discoloration and decomposition of CFRP. Moreover, the debonding of CFRP initiated at one end and extended until the center. Whereas, in case of uninsulated beam with mechanical anchorages, the strengthening system de-bonded at the mid-span and then failed at one of anchorage through slip. Similarly, in the beam with insulation only in anchorages, CFRP sheet de-bonded only at the mid-span while the end anchorages were intact. These failure modes of the of the strengthening system at the end of the test in the two uninsulated beams and one beam with insulation only in the anchorages, as reported by authors [149], are shown in Figure 2.15.

Based on these the authors concluded that securing the anchorage zones or ensuring lower temperatures in the anchorage zone can extend the beneficial effects of CFRP-strengthening through cable action and can significantly improve the fire performance of the strengthened beams. The results also demonstrated that using an adhesive with higher T_g value or providing mechanical anchorages delays the debonding of CFRP and improves the fire performance significantly. The authors also reported that the strengthening system fails when the CFRP-concrete interface temperature in anchorage zones exceeds $1.2 \times T_g$ to $1.5 \times T_g$.

Dong et al. [150] tested four CFRP-strengthened RC beams L1, L2, L3, and L4, under combined effects of structural loading and ISO834 standard fire exposure. The effect of three different insulation types, two different insulation schemes, as well as effect of cooler and fire exposed anchorage zones was evaluated in this study. The geometrical details of the beams are shown in Figure 2.16. Beams L1, L2 were 4.7 m long, and were insulated with 50 mm thick coating of cementitious material. Beams L3, L4 were 5.2 m long, wherein beam L3 was protected with 40 mm thick calcium silicate board system, and beam L4 was protected with an ultrathin (1.5 mm) fireproof coating (SB60-2). Additionally, beams L1, L3, and L4 were completely protected at the bottom and on the sides for entire depth throughout the span length. Whereas beam L2 completely protected in the anchorages and partially in the mid-span region, as shown in Figure 2.16 (e). Additionally, a 400 mm wide U-shaped CFRP sheet was wrapped in the anchorage zones of all the beams. These anchorage zones were exposed to fire in case of beams L3, L4.

All the beams sustained the applied loading for two hours, however, the level of deflection in each of these beams was significantly different, as shown in Figure 2.17. For instance, beam L1 experienced lowest deflection (less than 50 mm), whereas in case of beams L2 and L3, deflections exceeded 150 mm. However, beam L4 experienced most rapid increase in deflection which exceeded 250 mm at the end of 2 hours. Thus, the test results revealed that satisfactory fire endurance for CFRP-strengthened concrete beams can be obtained with the protection of the three insulation systems. In addition, it was indicated that cooler anchorages reduce the deflection in beam, while the fire exposed anchorages (L3, L4) lead to earlier debonding and rapid increase in deflection. Similar test program was conducted by Gao et al. [151]; however, the reported results are in Chinese language and are therefore not reviewed here. The authors also developed a numerical model, which is discussed later.

Zhang et al. [44] tested eight RC beams by exposing them to ISO 834 standard fire exposure under sustained structural loading. Of the eight beams, one beam was strengthened with basalt fiber mixed epoxy, one beam was strengthened with CFRP, and five beams were strengthened with carbon fiber reinforced geo-polymer (CFRG). Remaining one beam was tested without any strengthening to serve as a control beam. All the strengthened beams were protected with 10 mm thick SFRM fire insulation. Additionally, two of the CFRG-strengthened beams were provided with a layer of insulation primer between the SFRM and CFRG material. The results from the tests indicated that the CFRG-strengthened beams (without insulation primer) did not perform better than the CFRP-strengthened beams due to the falling off of the insulation. However, the two CFRG-strengthened beams with insulation primer performed much better than CFRP-strengthened beam and achieved three-hour fire resistance. Based on the tests, the authors concluded that the CFRG-strengthened beams provided with fire insulation and insulation primer can achieve satisfactory fire resistance.

(ii) <u>Fire Tests on FRP-Strengthened Slabs</u>

Blontrock et al. [152] tested two RC slabs, and five CFRP-strengthened RC slabs under ISO 834 [16] standard fire conditions. The strengthened slabs were protected with different insulation systems comprising of gypsum boards, with or without Rockwool insulation. Results from the test indicated that interaction between CFRP and concrete was lost between 24 to 55 minutes, and observed CFRP temperature, at the time of loss of interaction, varied from 47°C to 68°C. Moreover, fire resistance of the strengthened slabs was between 75 minutes to 90 minutes, which was close to the fire resistance (85 minutes) of the un-strengthened unprotected RC slabs. The authors concluded that thermal insulation system is required to maintain the composite action between CFRP and concrete as well as to achieve sufficient fire resistance.

Williams et al. [153] conducted fire tests on four "intermediate-scale" RC slabs strengthened with different types of externally bonded CFRP sheets and protected by different types of spray applied fire resistive material (SFRM) of varying thickness (19 mm to 38 mm). The test furnace and the two slabs are shown in Figure 2.18. During each test, the slab was exposed to ASTM E119 (2002) standard fire conditions under their self-weight, but without any external loading. The main purpose of these tests was to evaluate thermal performance of fire insulation. Therefore, the failure of the slabs was evaluated based on the limiting temperatures in the rebar and unexposed (top) surface of the slab, as specified in ASTM E119 [5]. Since the slabs were not loaded, the tests did not provide a realistic assessment of the structural response of the slabs under fire conditions. In all four slabs, the temperature at the CFRP-concrete interface exceeded the adhesive T_g (84°C) in the early stages (about 42-104 minutes), but this did not lead to thermal failure of slabs. The slabs achieved a fire resistance rating of more than 4 hours, according to ASTM E119 thermal criteria. The authors concluded that sufficiently thick thermal insulation is required for CFRP-strengthened RC slabs to achieve satisfactory performance under fire exposure. Further, these authors also developed a numerical model based on finite difference method to predict the temperature progression in slabs. However, this model does not assess structural response of the strengthened slab under fire conditions. Similar research was carried out by Adelzadeh et al. [154], wherein, unloaded FRP-strengthened slabs insulated with a cement-based mortar were exposed to ASTM E119 fire conditions. The test results showed that the temperature at the CFRP-concrete interface exceeded the adhesive T_g within 30 minutes. However, the slabs achieved a fire resistance rating of 4 hours as per thermal criteria. The authors also developed a numerical model to predict the temperature rise in the slabs.

Stratford et al. [155] investigated the performance of RC slab strengthened with CFRP strips and bars applied as EB and NSM reinforcement, respectively, in a real compartment fire (Dalmarnock fire tests). The slab was subjected only to their self-weight and was exposed to a fire load of 32 kg/m^2 over the floor area. The slab was provided with thermal protection using gypsum boards and intumescent coating. In the test, the temperature at the CFRP-concrete interface exceeded the adhesive T_g within 6 minutes of fire initiation, and the CFRP strips started de-bonding after 10 minutes. The test results indicated that CFRP is extremely vulnerable under real fire exposure even with the presence of insulation. The authors concluded that NSM CFRP bars have better performance as compared to the EBR strips, as the bond between NSM bars and concrete remained intact for a longer duration as compared to the bond between EBR strips and concrete. Since the slab was subjected to self-weight only no inferences on structural response of the CFRP strengthening system were drawn.

López et al. [141] tested one RC slab, and five CFRP-strengthened RC slab strips in an intermediate scale oven, as shown in Figure 2.14, by exposing them to ISO 834 fire conditions and loading at service load levels. Four of the five strengthened slabs were protected with external fire insulation using calcium silicate boards or vermiculite/perlite cement-based mortar. Data from the tests indicated that provision of fire insulation in anchorage zones increases the effectiveness of

CFRP strengthening system for a relatively longer duration of fire. The FRP debonding observed in one of the slabs is shown in Figure 2.19.

The above review clearly illustrate that limited tests have been conducted to evaluate the fire performance of FRP-strengthened RC beams and slabs. In particular the tests carried out on strengthened slabs are far less than that on strengthened beams. All the above experimental studies unanimously reported that strength and stiffness of FRP-strengthened RC flexural members deteriorates significantly, under fire exposure, due to rapid degradation in tensile and bond strength properties of FRP laminates. Further, these studies have identified temperature induced bond degradation as a primary reason for early failure of FRP-strengthened beams under fire conditions. Additionally, these studies demonstrated that the bond between FRP and concrete can be maintained for a longer duration and satisfactory fire resistance can be achieved by providing a layer of fire insulation over the strengthening system. However, in majority of these studies, it was not possible to identify and ascertain the degradation mechanism of FRP-concrete interface, and therefore, these studies did not provide any understanding of the interface bond behavior and its effect on fire performance of the strengthened beams. Moreover, these experimental studies used a specific type of FRP material and insulation material and provided limited response parameters. Additionally, the properties of the FRP and insulation material were not available in most cases, which in turn reduces the applicability of the generated test data. Thus, there is a need to generate comprehensive test data with detailed output parameters.

2.5.2 Numerical Studies

Fire resistance tests are expensive and time consuming and thus, limit the number of parameters that can be studied. Hence, numerical simulations can serve as a powerful alternative to fire tests at a fraction of the cost and time. A number of numerical studies evaluating fire performance of FRP-strengthened concrete flexural members have been reported in literature. Macroscopic or microscopic finite element-based model were utilized in these numerical models. Some the of the notable studies are presented here.

Williams et al. [153] developed a 2-D heat transfer model, wherein explicit finite difference formulation was used to solve the heat transfer equations and determine temperature at each time step. The model was validated against the experimental data generated from the fire tests carried out on T-beams and slabs carried out at National Research Council, Canada (NRCC). The model was capable of predicting temperature distribution in FRP-strengthened rectangular and T-shaped beams as well as slabs exposed to standard fire scenarios, with reasonable accuracy. However, the model under predicts temperature at the interface of FRP and insulation for entire fire exposure duration. Moreover, the model was not capable of tracing structural response of the slabs under fire conditions.

Hawileh et al. [156] developed a three-dimensional finite element model to evaluate the thermal and structural response of FRP-strengthened RC T-beams exposed to fire, using commercially available software ANSYS®. The model accounted for temperature dependent properties of concrete, steel rebar, FRP, and insulation material. However, the model did not account for bond-slip at the FRP-concrete interface and used the element killing approach to simulate the failure of the strengthening system The model was validated against the test data generated from the fire tests carried out by Williams et al. (2008) on FRP-strengthened T-beams at NRCC. The predictions from the model agree reasonably well with the measured thermal and structural response, however, the model was not able to accurately simulate the effect of temperature induced bond degradation at the FRP-concrete interface.

Kodur and Ahmed [95] developed a macroscopic finite element based numerical model to trace the response of FRP-strengthened RC beams under combined effects of structural loading and fire conditions. The model uses secant stiffness, computed from temperature dependent sectional moment-curvature relations, to compute the strength and deflection in the beams. The model accounts for high temperature material properties, different fire scenarios, and different failure limit states. However, the model doesn't incorporate the effect of temperature induced bond degradation. The predictions from the model were in reasonable agreement with the response measured in fire tests. This model was further modified by Ahmed and Kodur [131], to incorporate the effect of bond-slip at the FRP-concrete interface. In this model, the FRP-concrete bond degradation was attributed to the reduction in shear modulus of adhesive with temperature. The relative slip between FRP and concrete was computed using shear deformation of the bonding adhesive. Moreover, the relative slip was evaluated only at the critical section and was assumed uniform throughout the beam length. Although the predicted response was fairly close to the experimentally measured response, the simplified approach was not able to capture the highly nonlinear bond-slip behavior of the FRP-concrete interface. Additionally, the assumption of uniform slip throughout the beam the predicted abrupt loss of FRP-concrete composite action, which is unrealistic.

López et al. [141] developed a finite element based numerical model using commercial package ABAQUS to predict the temperature rise in the full-scale insulated FRP-strengthened RC slabs and evaluated the effects of different insulation geometry and thickness in central and anchorage zones. Based on the analyses, the authors concluded that adequate insulation in the central zone and thicker insulation in the anchorage zones is needed to achieve satisfactory fire resistance in FRP-strengthened RC slabs. However, predicted optimum insulation thickness required on fire exposed strengthened slabs were based on a predefined limiting FRP-concrete interface temperature, without any consideration to the structural aspects.

Dai et al. [121] developed a three-dimensional finite element in ABAQUS to evaluate the fire performance of FRP-strengthened RC beams. This numerical model was the first model to explicitly account for temperature-dependent nonlinear bond-slip relations for FRP-concrete interface as well as steel rebar-concrete interface, through zero thickness cohesive zone elements and spring elements, respectively. The model also accounted for temperature dependent material properties of constituent materials and was validated by comparing the model predictions with test data reported by Blontrock et al. [145] and Williams et al. [146]. Figure 2.20 (a) the elevation and cross-section details of a beam tested by Blontrock et al. (2000). While Figure 2.20 (b-c) compares the thermal and structural response as predicted by the finite element model proposed by Dai et al. [121] for this beam with those measured in test. It can be seen from the figure that the thermal and deflection response predicted by the model were in close agreement with the measured value for entire fire exposure duration. The authors (Dai et al.) also analyzed a case for this beam with perfect bonding, the results for which are plotted in Figure 2.20 (c). It can be seen that the perfect bond assumption provides a much stiffer response as compared to that measured in the test. Thus the importance of considering the effect of temperature induced bond-degradation of FRP-concrete interface is clearly illustrated in this study. However, the authors did not apply the model to evaluate the effect of different parameters as well as different insulation configuration, affecting the fire resistance of FRP-strengthened beams.

Firmo et al. [142, 157] developed two-dimensional and three dimensional (*cf.* Figure 2.21) finite element based numerical model, respectively, using ABAQUS software package, to simulate the fire response of FRP-strengthened RC beams. The model accounted for high temperature material properties of the constituent materials. The effect of temperature induced bond degradation was accounted using simplified bilinear temperature dependent bond-slip relations, applied using complex cohesive zone model option available in ABAQUS. The relations were developed for the specific CFRP and concrete type through experimental tests and optimization of the test data. The model was validated by comparing the predicted response parameters with the response parameters measured in the fire tests carried out by authors. Figure 2.22 shows the comparison of the measured and predicted deflection for the beams, as reported by Firmo et al. [157]. It can be seen from the figure that although the numerical results follow trends similar to that measured in the tests, the predicted values and debonding times are significantly different than the experimentally measured results. This was due to the use of temperature dependent simplified bilinear bond-slip relations to account for highly nonlinear bond degradation process. The authors also reported the stress level in steel rebars and CFRP laminate during the fire exposure time, as shown in Figure 2.23. The tensile stresses were normalized with respect to the respective strength at ambient temperature. In the initial stages the stresses in steel rebars and CFRP are nearly similarly however, after few minutes, when the CFRP starts to debond the stresses in steel rebars increases rapidly and remains much higher than the CFRP until the end of fire exposure duration. The authors applied the model to evaluate the effect of different insulation configuration on the fire performance of strengthened beam. Results from the analysis confirmed that the providing thicker insulation in the anchorage zones can prolong the structural effectiveness of the FRP strengthening system through cable action.

Dong et al. [150] developed a finite element based numerical model using ANSYS® software. The model was first validated using the generated from the fire tests conducted by the authors (described earlier). The model accounted for high temperature thermal and mechanical properties of the materials, however, they considered perfect bonding between CFRP and concrete. The bond degradation, was implicitly accounted by evaluating the temperature degradation in strength of CFRP as:

$$f_{u,T} = f_u \times rf_{tensile} \times rf_{bond} \tag{2.8}$$

where, $rf_{tensile}$ is reduction factor for tensile strength of CFRP; rf_{bond} is reduction factor for bond strength of CFRP; F_u is strength of CFRP at room temperature; $F_{u,T}$ is the strength of CFRP at elevated temperature. The thermal response predicted by the model was in good agreement with the measured response. However, the predicted structural response followed trends similar to that of measured values but was not in good agreement with the measured values due to the unconventional method of accounting for bond degradation. The authors also applied the model to conduct a parametric study, wherein the effect of insulation thickness, thermal properties of insulation, as well as strengthening and load ratio were quantified. The analysis indicated that insulation thickness, insulation thermal conductivity, strengthening and load ratio had significant effects on the fire resistance of insulated CFRP-strengthened RC beams, whereas the density and specific heat of insulation had very minimal effect on fire resistance.

The above discussed review clearly indicates that limited numerical studies were conducted to evaluate the fire performance of FRP-strengthened RC flexural members. In particular there are almost no numerical studies evaluating the thermal and structural response of FRP-strengthened RC slabs exposed to fire. Moreover, majority of the available studies either assumed a perfect bond condition at the FRP-concrete interface or used a simplified approach to account for temperature induced bond degradation. The studies that did explicitly account for bond degradation, involve use of complex cohesive zone model which require use of commercially available FE software. These softwares require use of skills for interpreting and analyzing results. Therefore, a robust and simplified computer model capable of incorporating critical parameters and failure modes needs to be developed.

2.6 Codal Provisions for Fire Design

In recent years, a significant research effort has been carried out to quantify the behavior of the FRP-strengthened RC structural members (beams, slabs, and columns) as well as to quantify the factors influencing the performance of these structural members at ambient temperature. As a result, guidelines for design of FRP-strengthened RC structural members at ambient temperature conditions are available in various standards [17–19] and design documents. However, relatively little guidance is available on fire resistant design of FRP-strengthened RC structural members. For instance, ACI 440.2R-17 [19] requires that FRP-strengthened members should meet all building and fire code guidelines spelled out for RC structures. Further, ACI 440.2R-17 [19]also requires that the nominal capacity ($M_{n\_upg,T}$) of the FRP-strengthened RC member at elevated temperature must be capable of withstanding the combined effect of 1.0 times dead load (DLd) and 1.0 times live load (LLd), to prevent collapse that might arise from failure of FRP under fire exposure. However, $M_{n\_upg,T}$ should not account for the contribution of FRP systems unless it can be demonstrated the temperature level in FRP would remain below a critical temperature value. Thus, the un-strengthened concrete member should be capable of resisting service dead and live loads under fire conditions.

FIB Bulletin-14 [17] recommends computing the fire resistance using “refined calculation method” involving thermal analysis followed by a mechanical analysis and incorporating temperature-dependent material properties. It further recommends that the insulation layer should be designed such that the temperature in the adhesive remain below a certain “temperature limit” ranging from 50°C and 100°C. However, no guidance is provided regarding the determination of the temperature limit, nor on the temperature-dependent properties of the materials, for any specific FRP system.

A limited number of research documents are available providing guidance for fire resistant design of FRP-strengthened RC structural members. For instance, Kodur et al. [158] provided preliminary prescriptive guidelines for design of FRP-strengthened structural members under fire conditions. These guidelines are rather prescriptive and provide recommendations on the allowable maximum strengthening levels as well as the load ratio to be considered during fire scenarios. Further, these guidelines recommend that the strength of FRP can be utilized for fire resistance computation provided the temperature of FRP is kept below some critical temperature and suggest using T_g of the adhesive and 300°C as lower and upper bound for the critical temperature limit, respectively. However, these guidelines do not provide any equations for determining the fire resistance of the strengthened structural members.

Kodur and Yu [21] proposed the first rational approach for evaluating fire resistance of FRP-strengthened concrete beams. In this method, the moment capacity of the strengthened member is evaluated as a function of fire exposure time, as per the flowchart shown in Figure 2.24. At each time increment, the following four steps are executed:

- Temperature level within the beam cross-section is determined using a set of simplified equations.
- Degradation in strength properties of the materials is computed based on the temperature level in the material.
- Moment capacity is computed using the degraded strength values and applying strain compatibility and force equilibrium principles.

- Compare the capacity with the bending moment due to applied loading and determine fire resistance.

Each of the above-mentioned four steps involve several sub-steps with rigorous calculations. For instance, equivalent concrete layer, as shown in Figure 2.25, must be determined to evaluate the temperatures within the insulated FRP-strengthened beams. Similarly average equivalent concrete width needs to be interpolated using the several predefined section sizes analyzed by Kodur and Yu [21]. This average section width of concrete is then used to determine the contribution of concrete in compression to the capacity of the strengthened beam. Moreover, the neutral axis needs to be determined at each time steps through several iterations for satisfying the force equilibrium and strain compatibility conditions.

The approach provides reasonable estimate of fire resistance of insulated and uninsulated FRP-strengthened member, but it suffers from several drawbacks. First and foremost, this approach is that it does not account for temperature induced bond degradation at the FRP-concrete interface and therefore, provide a slightly higher estimate of fire resistance of FRP-strengthened RC beams. Another major drawback of the approach is that it is applicable only for standard fire exposures (ASTM E119 or ISO 834) and for FRP-strengthened beams protected with limited insulation types. Moreover, this approach involves significant amount of long and tedious calculations which are not suitable for a design office.

Recently Gao et al. [22] proposed a three tier (level) approach for fire resistance design of FRP-strengthened members. Figure 2.26 shows a pictorial representation of the framework of the design procedure. The proposed procedure primarily determines amount/thickness of insulation that must be provided to the strengthened structural member to achieve a specific predefined level of fire resistance. The procedure defines three distinct levels of fire resistance (Level I, Level II, and Level III) for determining the amount of fire insulation required to satisfy the specified fire resistance rating.

Level I is concerned with situations where bare minimum fire resistance is required which can be achieved without any external fire protection. In this level, it is assumed that FRP doesn't contribute to the capacity of the beam and the fire resistance is determined using the simplified equations for fire resistance calculations of RC beams proposed by Gao et al. (2016) and are given as:

$$M_d = \left(\gamma_{RC}, c, \frac{l}{h}, \rho_s, \frac{A_{sc}}{A_{st}}, b\right) = \varphi\left(\gamma_{RC}\right)\cdot\omega\left(c\right)\cdot\psi\left(\frac{l}{h},\rho_s\right)\cdot\xi\left(\frac{A_{sc}}{A_{st}}\right)\cdot\varnothing\left(b\right) \tag{2.9}$$

where, M_d is fire resistance period (min); $\varphi\left(\gamma_{RC}\right), \omega\left(c\right), \psi\left(\frac{l}{h},\rho_s\right), \xi\left(\frac{A_{sc}}{A_{st}}\right)$, and $\varnothing\left(b\right)$ are effects of load ratio, concrete cover depth (mm), span-to-depth ratio (for a given tensile reinforcement ratio), distribution ratio of tension rebars, and beam width (in mm), respectively; A_{sc} and A_{st} are total area of corner tension rebars and total area of tension rebars, respectively. For the unprotected FRP-strengthened RC beam, the load ratio, γ_{RC}, is equal to the new service load divided by the nominal load-bearing capacity of the equivalent RC beam at room temperature.

At the other extreme is Level-III design, in which the FRP system and the original RC beam need to be so insulated that they both remain effective during the required fire resistance period. To realize the design in level III, the authors propose to use a finite element based numerical model accounting for all the necessary temperature variations in the material properties as well as account for temperature induced bond degradation through complex cohesive zone model as per Dai et al. (2015).

Thus, level I recommends considering the FRP-strengthened beam to be a un-strengthened uninsulated RC beam subjected to higher load level, for which fire resistance must be computed using simplified method based on simplified assumptions. Whereas level III suggests using a commercial finite element-based software involving complex computations and requires specific training and computational expertise. Between these two extremities is Level II which involves design of insulated FRP-strengthened RC beam, where in again the contribution of FRP is completely neglected. The temperature rise within the insulated section is determined using the simplified equations proposed by Gao et al. [159] which are then combined with 500°C isotherm method (CEN 2004b), to predict the time-dependent moment capacity of insulated FRP-strengthened RC beams during fire exposure. Figure 2.27 shows the effect of load ratio and effect of insulation thickness on the predictions made using level II method which are compared with finite element based model predictions. It can be seen from the figures, that the results predicted using level II approach are within ±12-15% of the finite element-based predictions. Although from structural fire engineering point of view this variation is small but significant. Therefore, there are concerns about use of this method in the design offices for practical design purposes.

Thus, the above discussed review of current design guidelines in codes of practice and research document indicate that no specific fire design provisions exist for externally bonded FRP structures due to lack of information on fire response of FRP-strengthened members. For structural members that require FRP strengthening, all documents adopt a common approach, i.e., if no fire insulation is provided over the strengthening system, neglect the contribution of FRP completely for fire resistance calculation. Therefore, there is a need to develop rational fire design guidelines for use of FRP-strengthened RC members in buildings and structures.

2.7 Knowledge Gaps

Based on the state-of-the-art review, there are several drawbacks in the literature on the behavior of FRP at material level and as a component of structural system. Limited data is available on the property data of FRP at elevated temperature. Similarly, limited fire tests and numerical studies have been conducted to evaluate the fire resistance of the FRP-strengthened concrete flexural members. Majority of these experimental and numerical studies were mainly concerned with overall performance of FRP-strengthened concrete beams in fire, and therefore did not provide comprehensive understanding of the bond behavior of strengthening system, bond behavior along the length of the beam. Most of the available numerical studies did not incorporate the effect of temperature induced bond degradation or accounted using simplified assumptions. Further, the available studies did not address the effect of critical parameters on fire resistance of FRP-strengthened flexural members. The following are some of the drawbacks on behavior of FRP at material level and structural component level:

- Limited test data and analytical models are available for strength, stiffness, and bond properties of FRP at elevated temperature.
- There exists a wide variation in the available data on the high temperature strength, modulus, and bond properties of FRP. Moreover, there is a lack of reliable property relations for FRP at high temperature required for fire resistance modeling of FRP-strengthened RC structural members.
- Several fire resistance tests have been conducted to evaluate the fire response of FRP-strengthened RC beams, whereas a few fire resistance tests have been conducted on full scale FRP-strengthened RC slabs under fire conditions.
- Few numerical models are available for evaluating response of FRP-strengthened RC beams and most of them do not account for temperature induced bond degradation or involve complex modeling procedure demanding high computational effort. In particular,

there are no numerical models for evaluating the fire response of FRP-strengthened RC slabs.

- Limited information is available regarding the design of insulation configuration for achieving specific fire resistance in strengthened concrete members.
- There are no design approaches and guidelines for fire resistance design of FRP-strengthened concrete flexural members in codes and standards.

Table 2.1: Comparison of carbon, glass, and aramid fibers for different characteristics*

Parameter		Carbon	Glass	Aramid
Strength in longitudinal direction	Tensile	H	L	M
	Compressive	H	M	L
Modulus in longitudinal direction		H	L	M
Toughness		M	L	H
Impact strength		L	M	H
Density		M	H	L
Strength to weight ratio		H	L	M
Resistance to	Moisture absorption	H	H	L
	Heat	H	M	M
	Fatigue	H	L	M
	Chemical	H	M	M
	Abrasion	M	L	H
Adhesion to resin		H	H	L
Coefficient of thermal expansion		L	H	M
Conductivity		H	L	L
Melting point		H	M	L
Cost		M	L	H

Note: The above comparison and ratings are relative to each other and not to all materials.
H = Highest, M = Moderate, L = Lowest

Table 2.2: Comparison of widely available resins

Resin type	Advantages	Disadvantages
Polyesters	• Easy to use • Lowest cost • Fast curing time	• Only moderate mechanical properties • High styrene emissions in open molds • High shrinkage on curing • Limited range of working times • Decompose around 300-400°C • Poor bonding not suitable for structural applications
Vinyl-esters	• Very high chemical/ environmental resistance • Superior mechanical and thermal properties than polyesters • Excellent corrosion resistance • High fracture toughness	• Post-cure generally required for high properties • High styrene content • Expensive than polyesters • High volume shrinkage • Moderate adhesive strength • Requires specific careful surface preparation
Epoxies	• High water resistance • High resistant to wearing, cracking, and peeling • Long working times available • Environmentally stable • Temperature resistance up to 140°C in wet and 220°C in dry conditions • Low shrinkage on curing • Decompose around 400-600°C • Excellent adhesion characteristics	• Expensive • Corrosive handling • Critical mixing

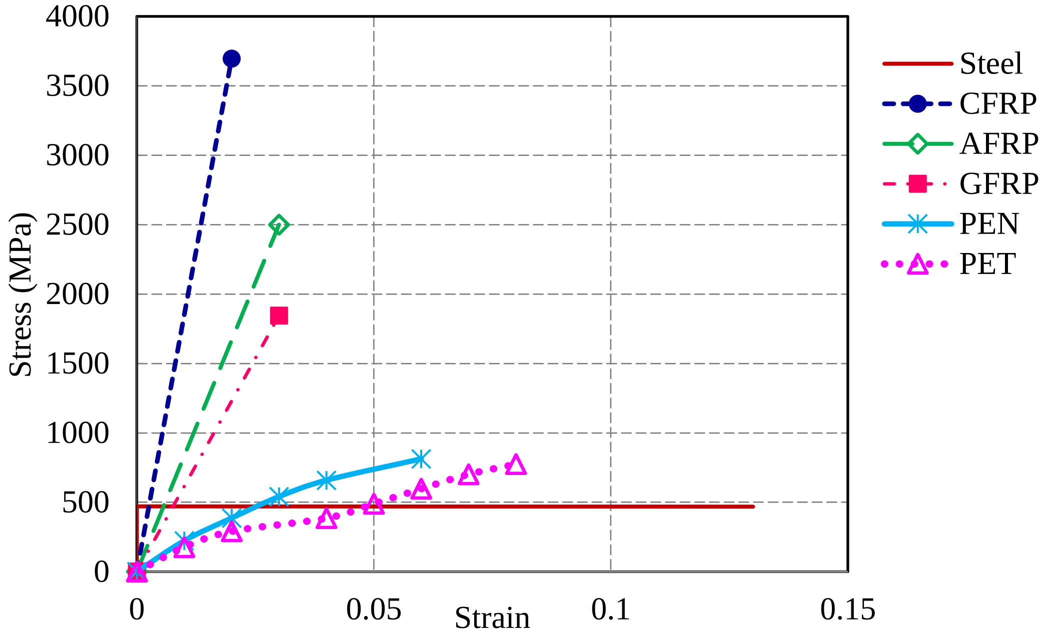

Figure 2.1: Comparison of tensile stress-strain behavior of different types of FRP composites

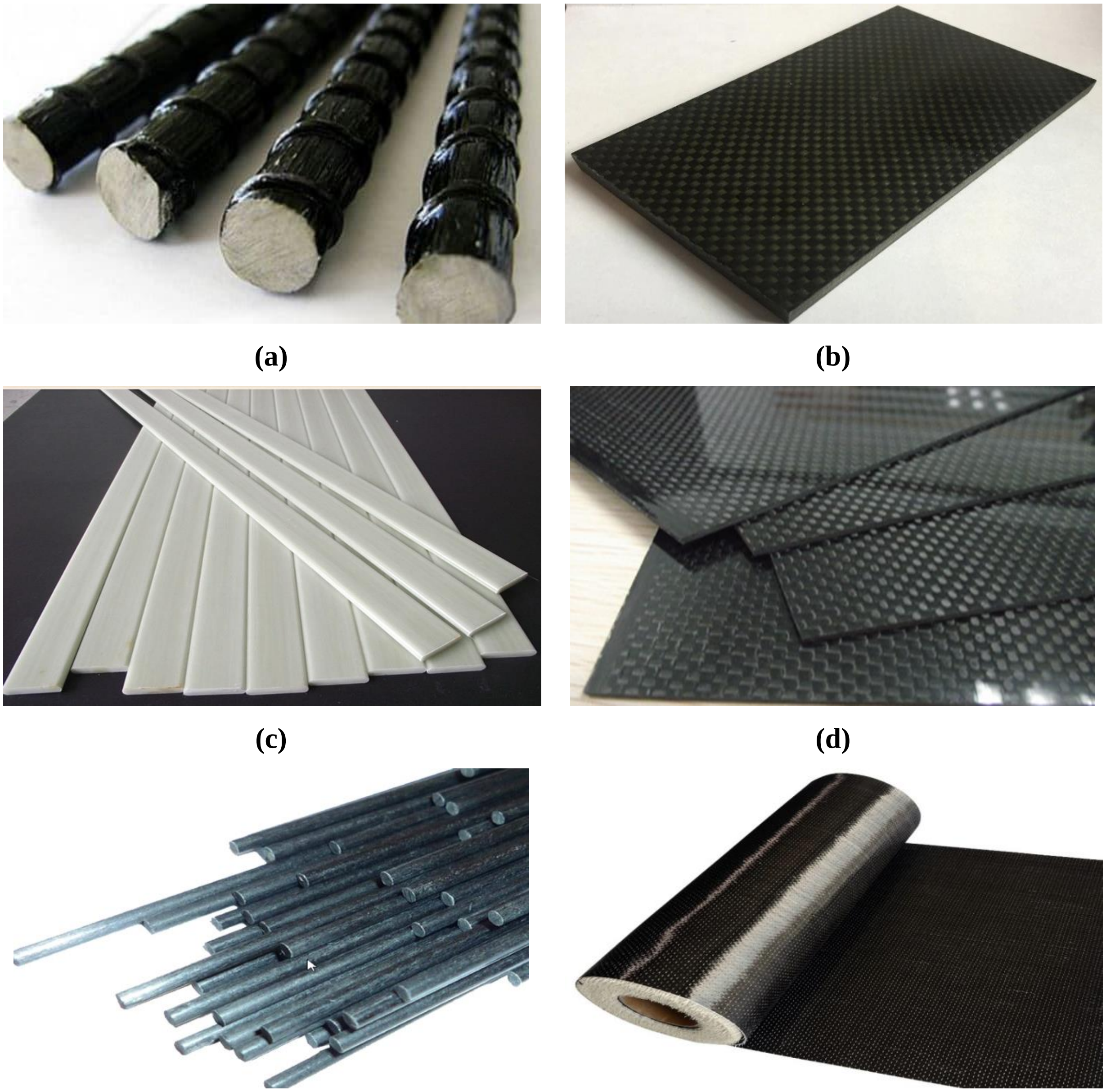

(a) **(b)**

(c) **(d)**

(e) **(f)**

Figure 2.2: Different type of FRP composite products: (a) rebars; (b) plates; (c) strips; (d) sheets; (e) rods; (f) fabric for hand lay-up

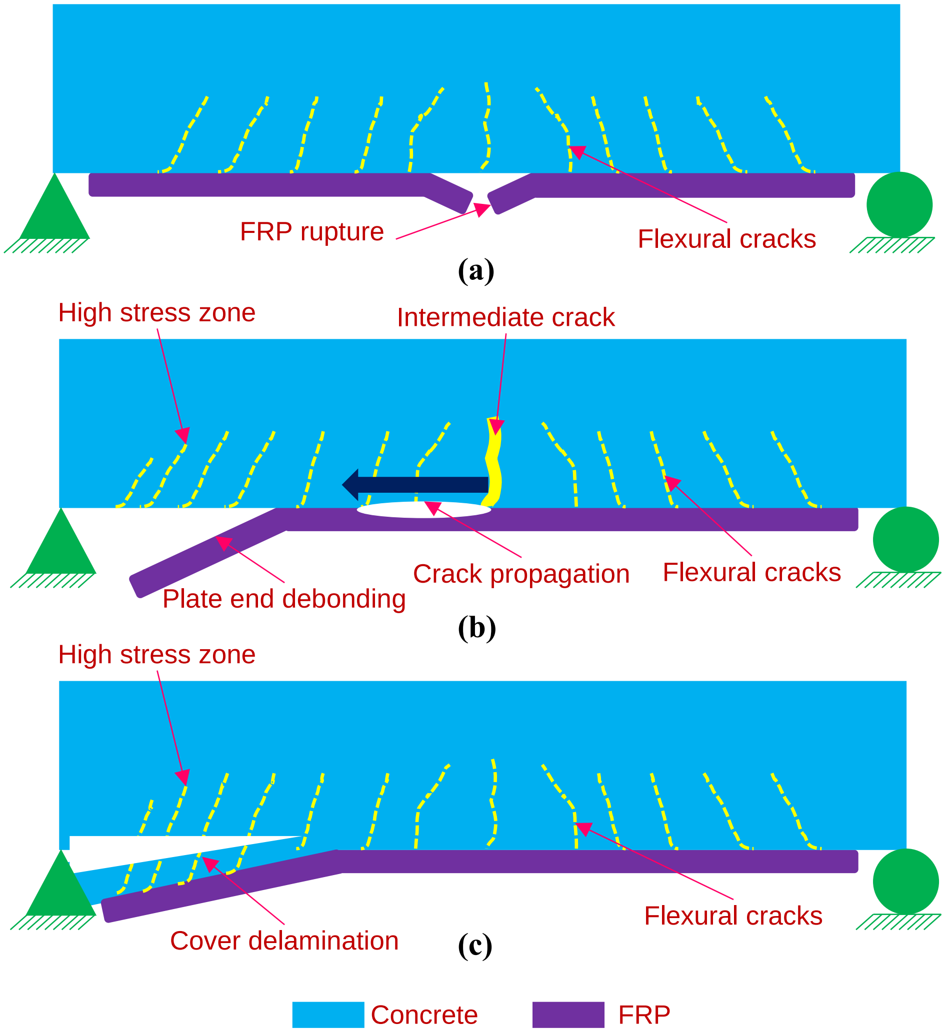

Figure 2.3: Failure modes for FRP-strengthened flexural concrete members: (a) FRP rupture; (b) plate end debonding or intermediate crack debonding; (c) cover delamination

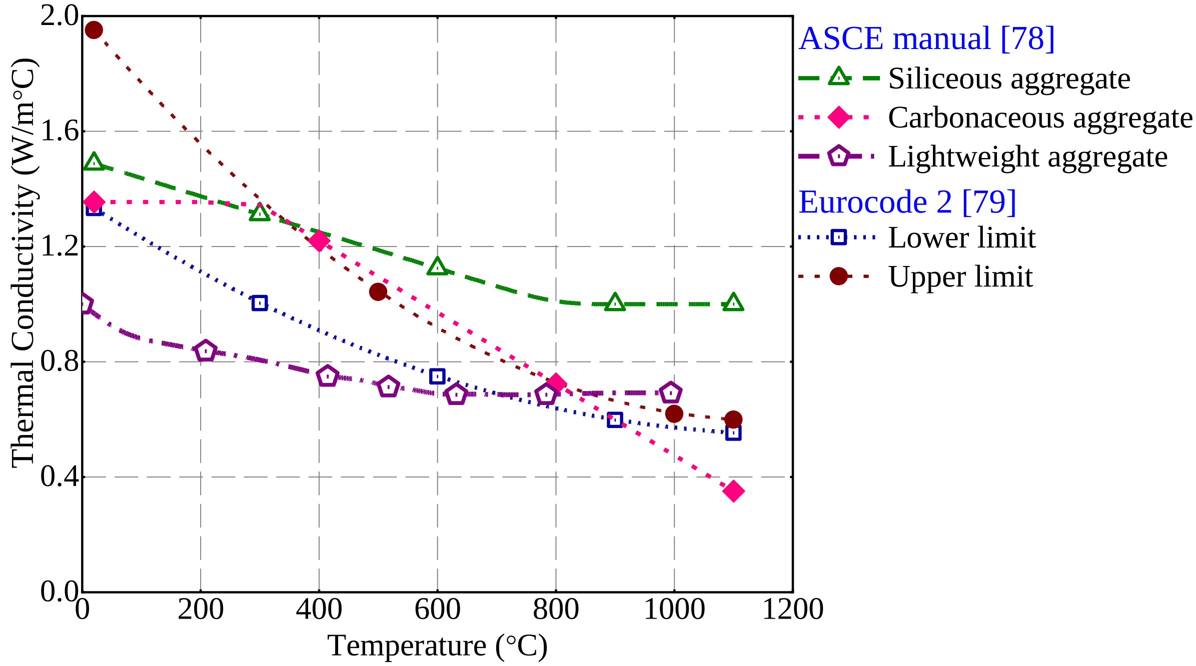

(a)

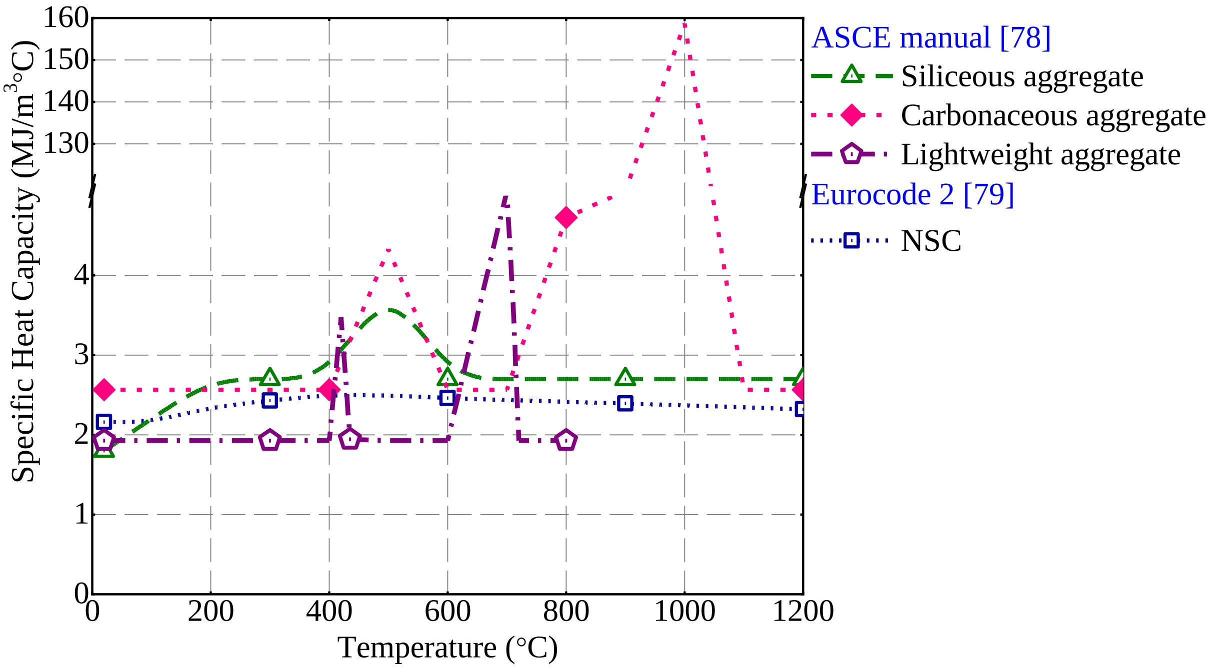

(b)

Figure 2.4: Temperature variation of thermal properties of concrete: (a) thermal conductivity; (b) specific heat capacity

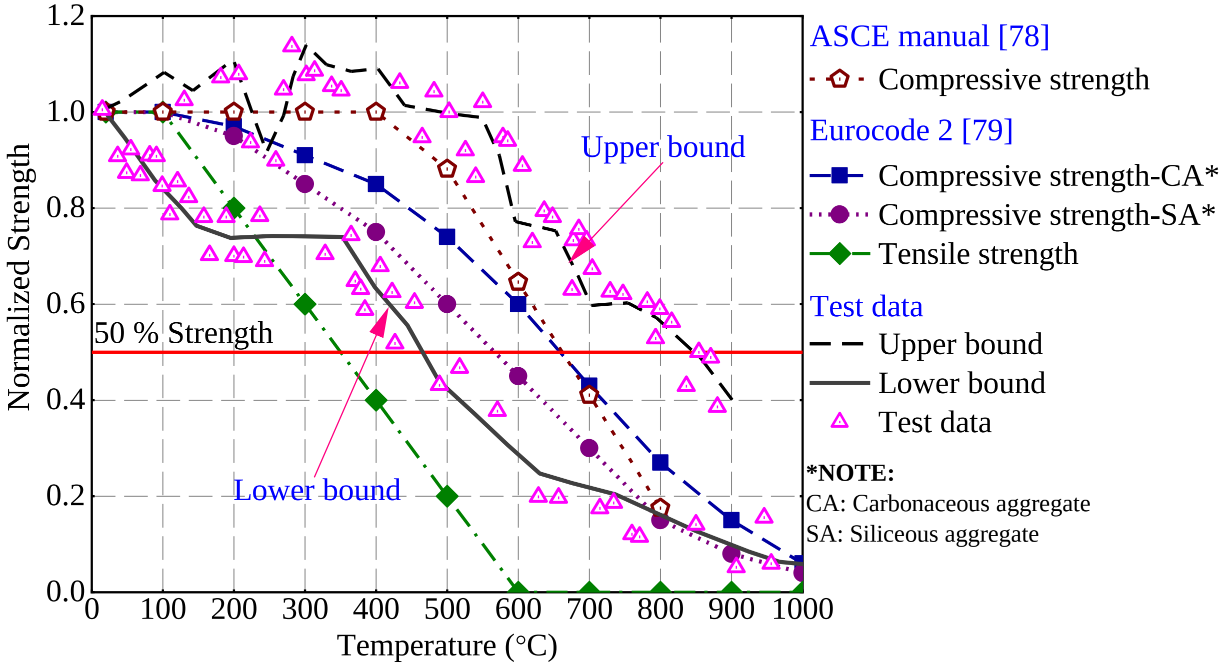

(a)

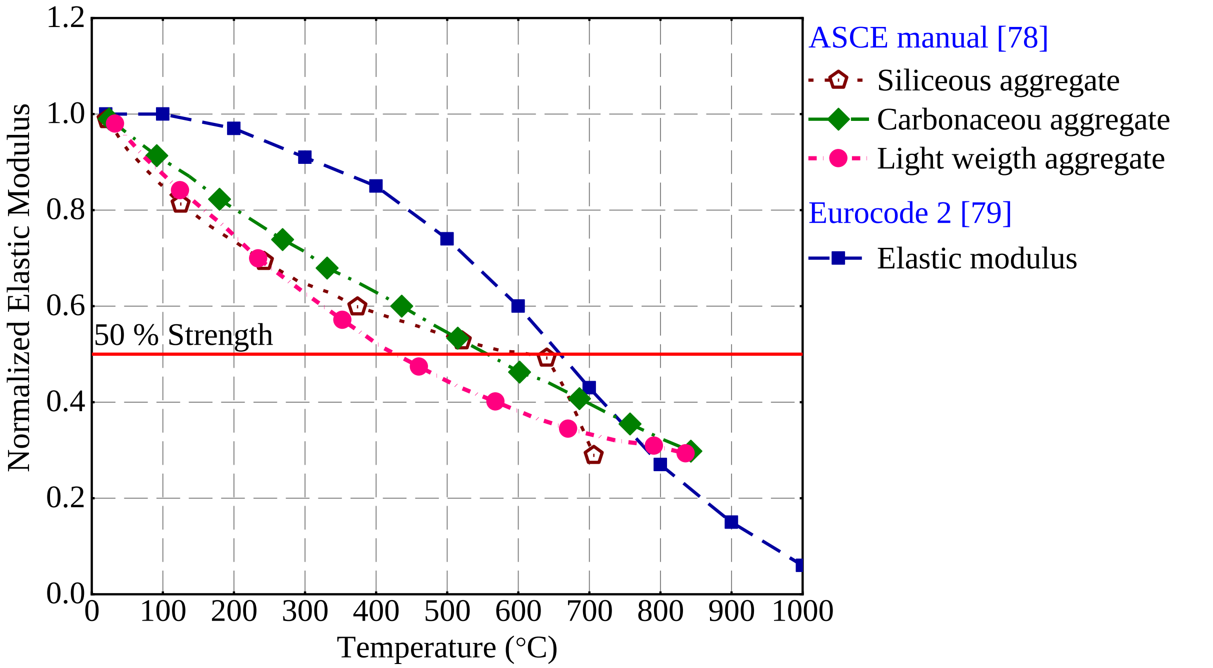

(b)

Figure 2.5: Normalized variation of mechanical properties of concrete with temperature as defined in ASCE manual and Eurocode-2: (a) compressive and tensile strength; (b) elastic modulus

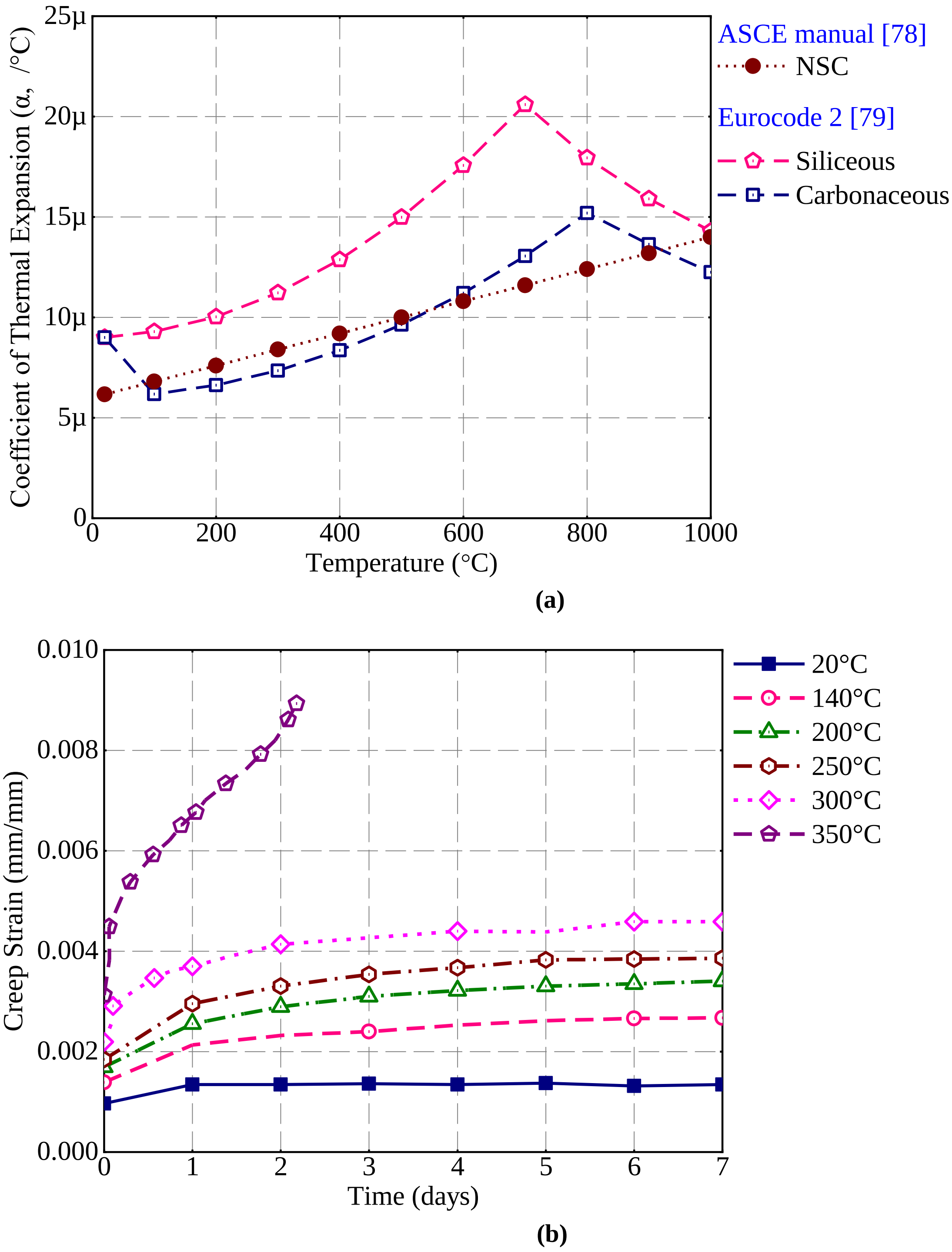

Figure 2.6: Deformation properties of concrete at different temperature levels: (a) thermal strain; (b) progression of creep strain

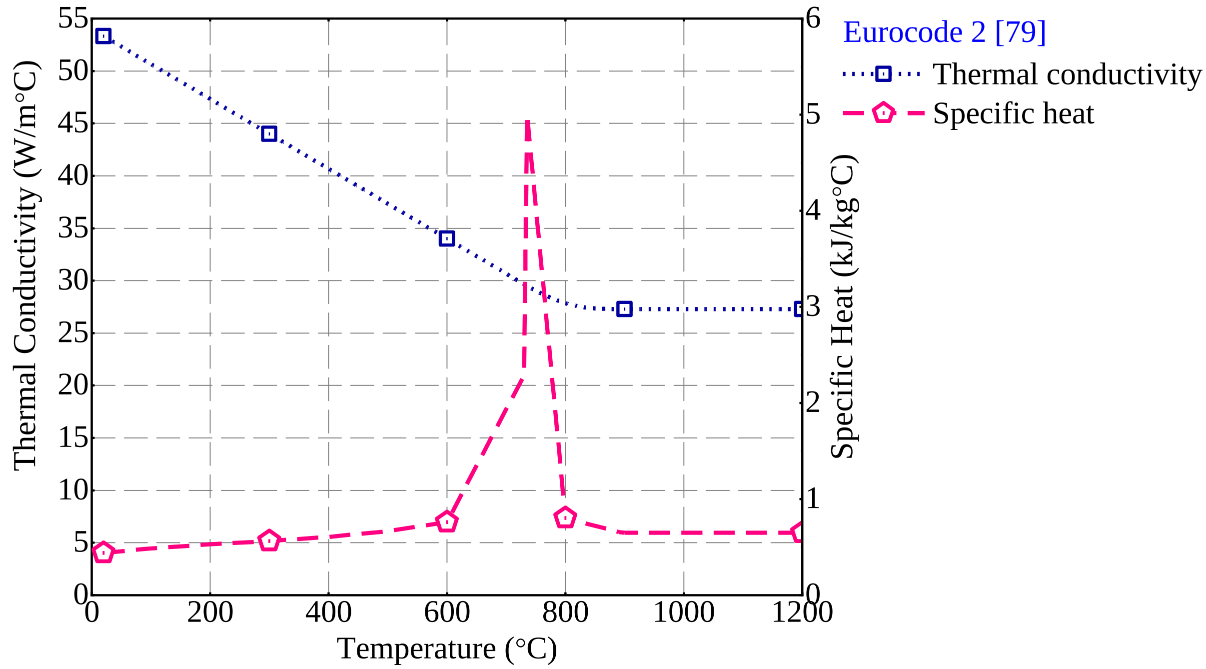

Figure 2.7: Temperature variation of thermal conductivity and specific heat of steel rebars

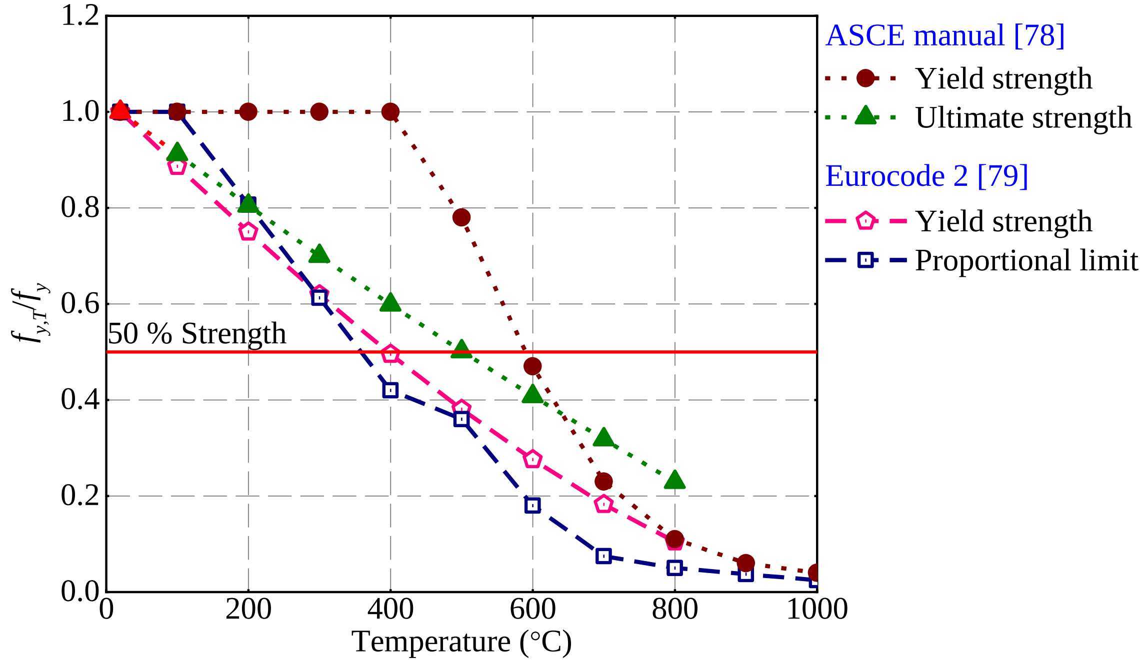

Figure 2.8: Temperature variation of yield strength and ultimate strength of steel rebars

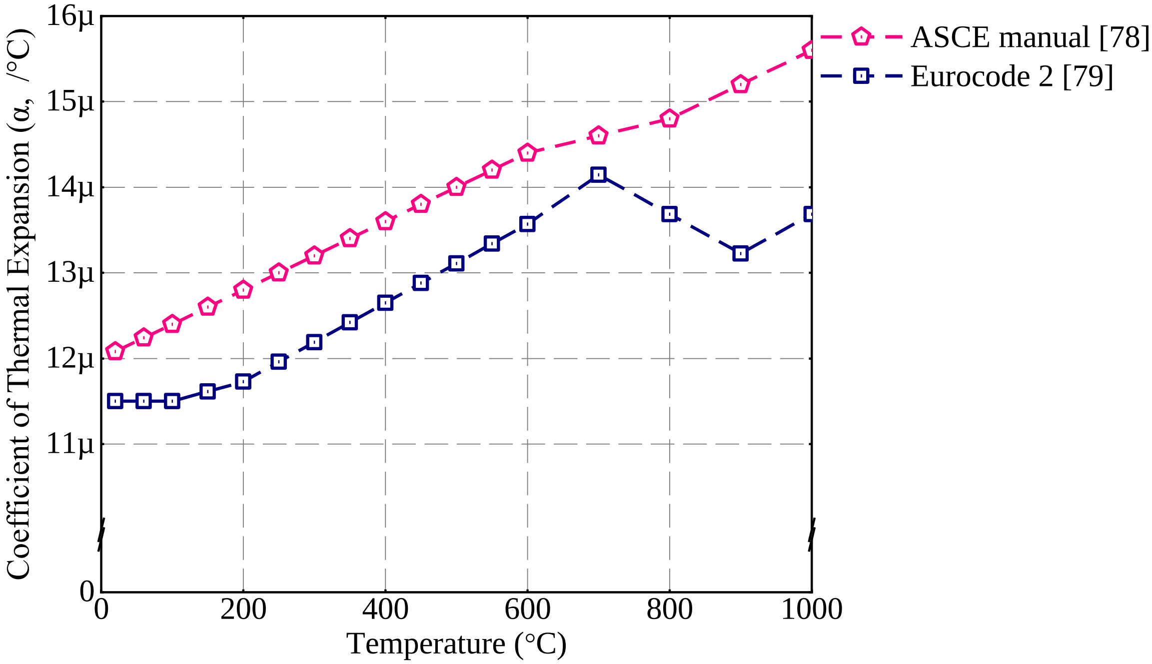

Figure 2.9: Temperature variation of coefficient of thermal expansion for steel rebars

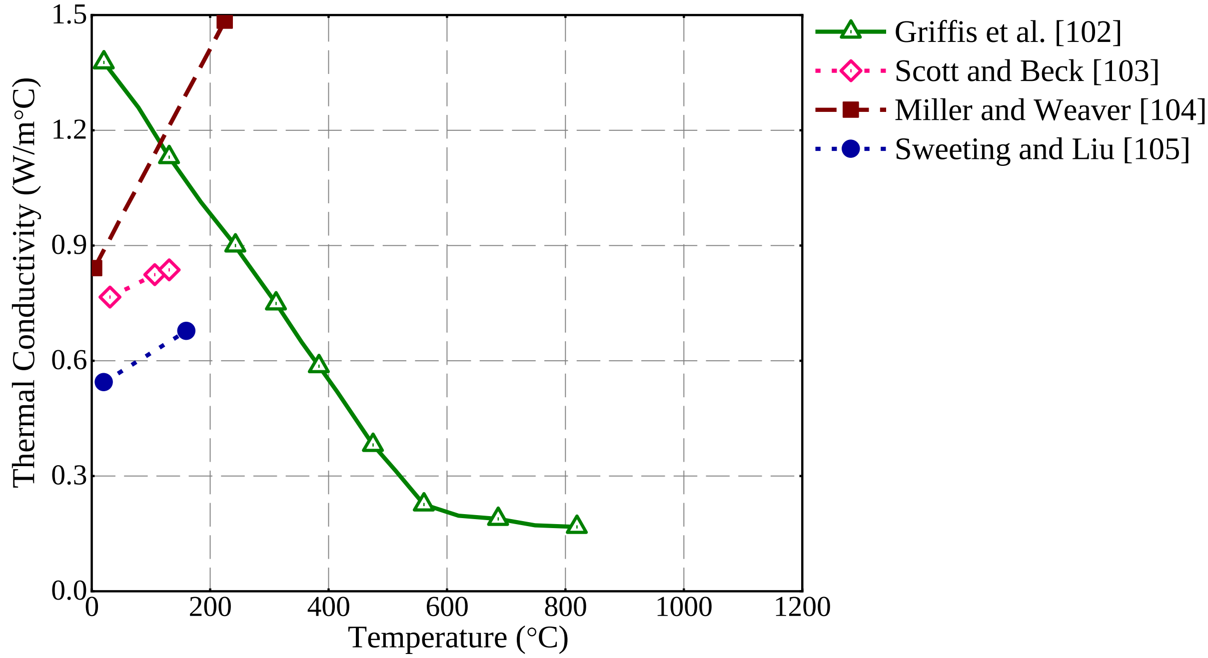

(a)

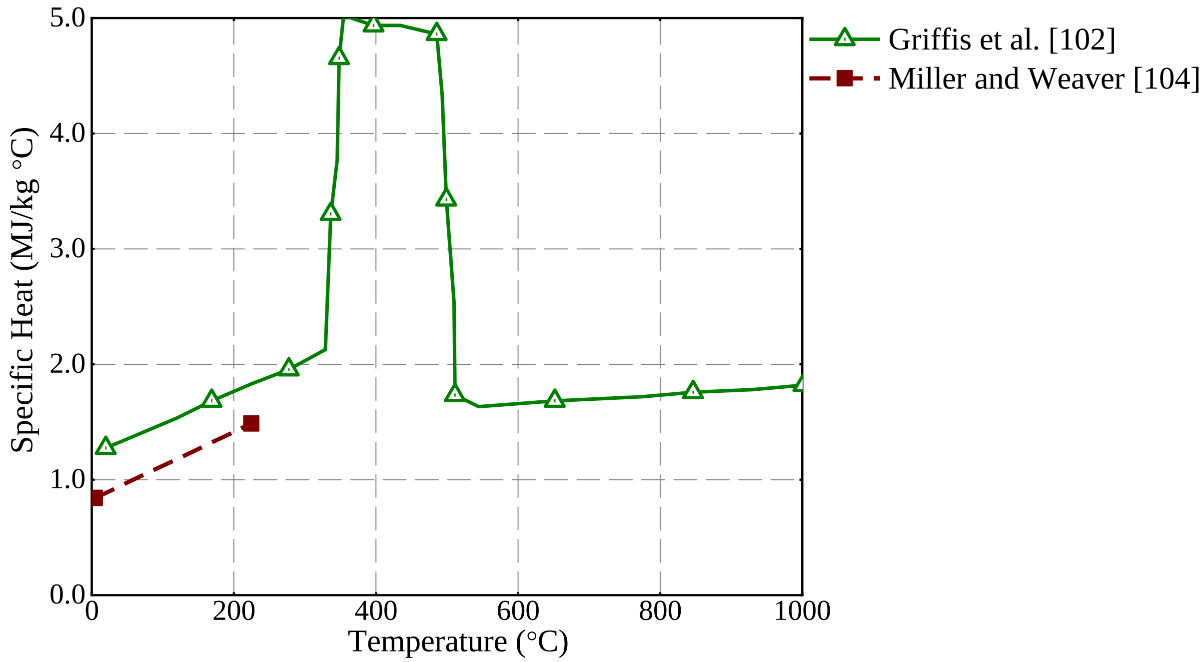

(b)

Figure 2.10: Variation of thermal properties of FRP composite materials with temperature: (a) thermal conductivity; (b) specific heat

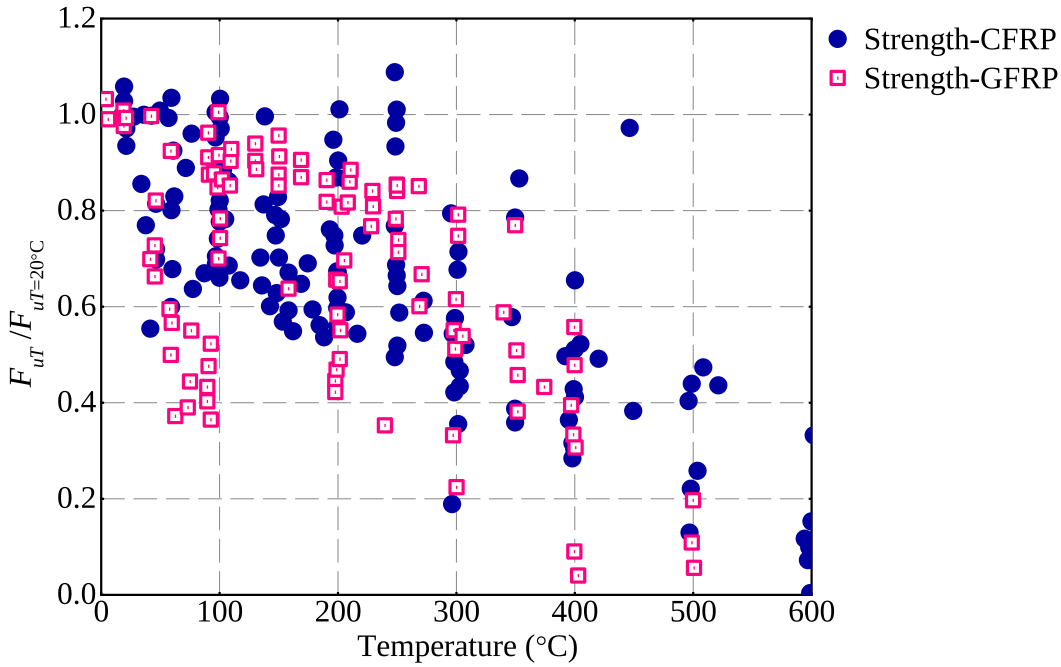

(a)

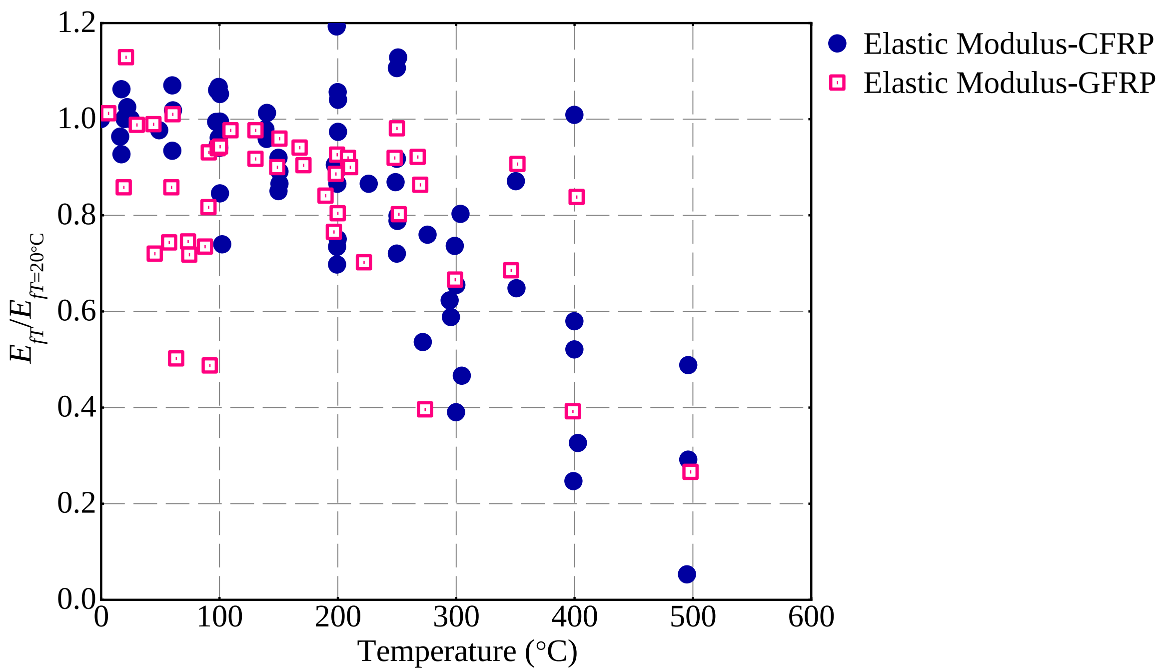

(b)

Figure 2.11: Normalized strength and elastic modulus properties of CFRP and GFRP at elevated temperatures: (a) test data for strength; (b) test data for elastic modulus; (c) relations for tensile strength; (d) relations for elastic modulus

Figure 2.11 (cont'd)

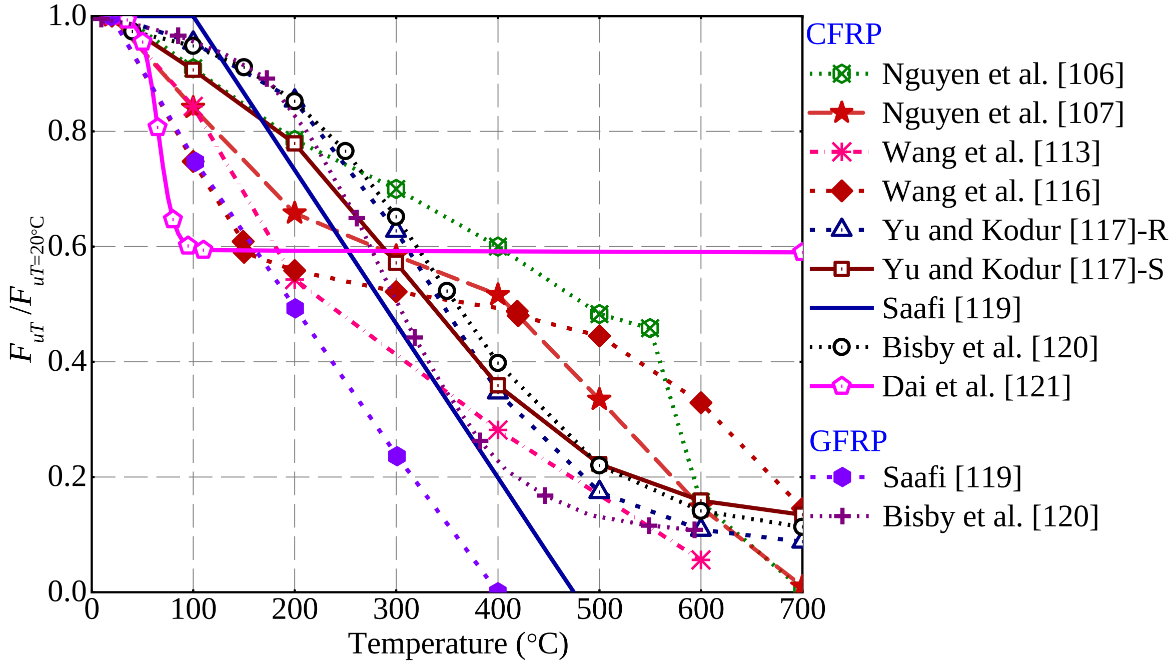

(c)

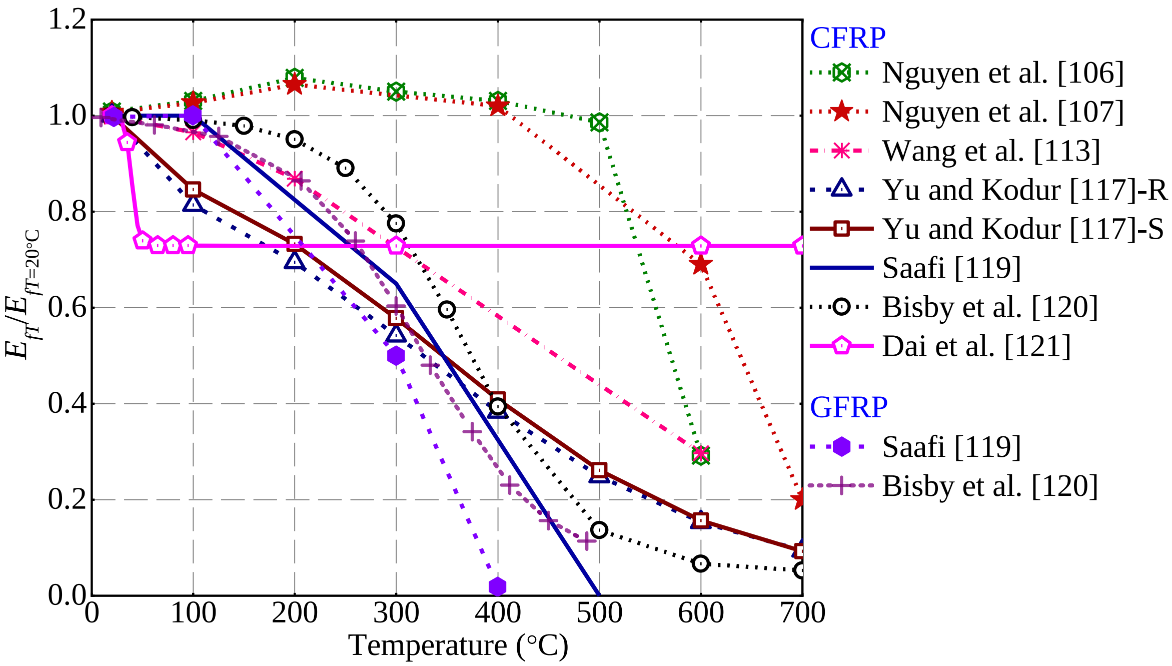

(d)

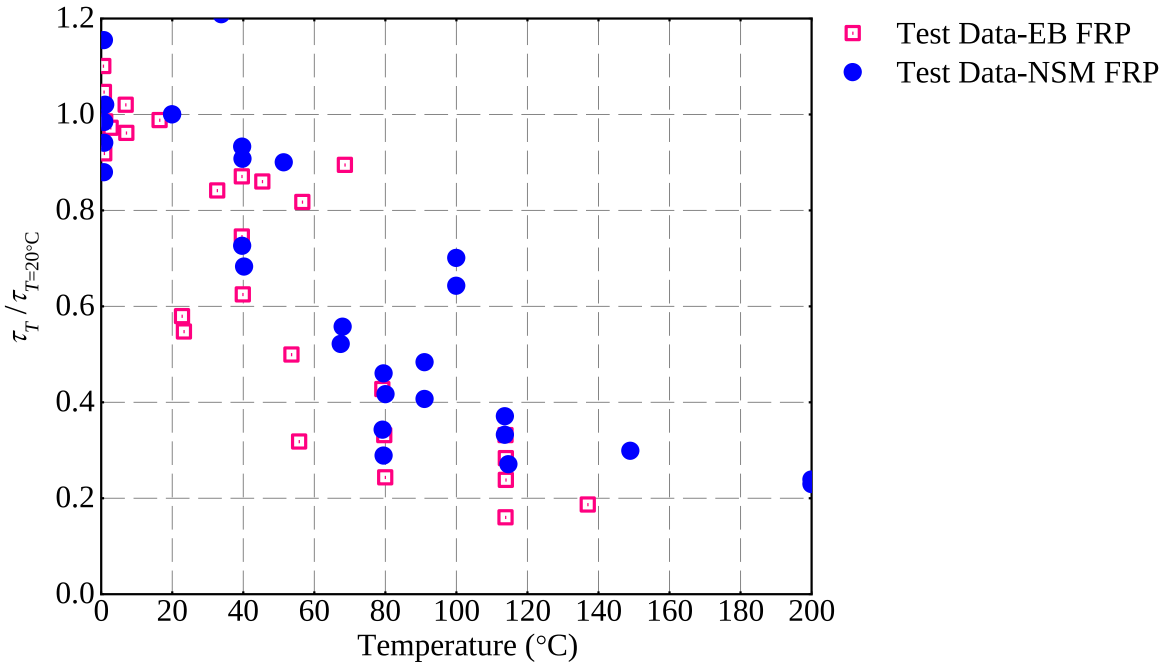

(a)

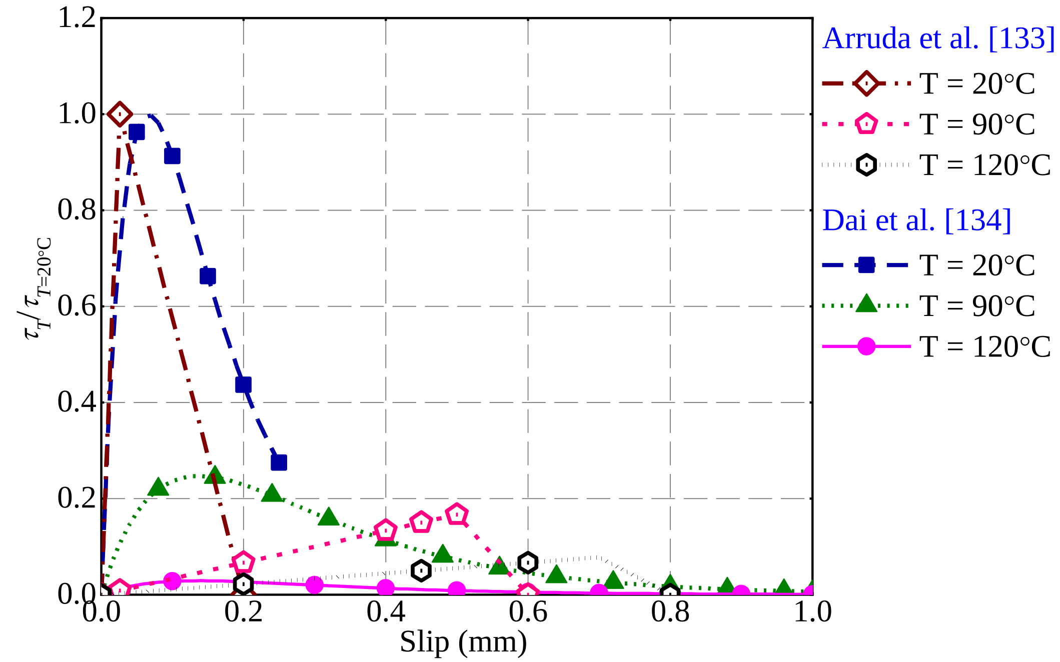

(b)

Figure 2.12: Normalized bond strength of EB and NSM CFRP at elevated temperature: (a) test data; (b) bond stress-slip relations

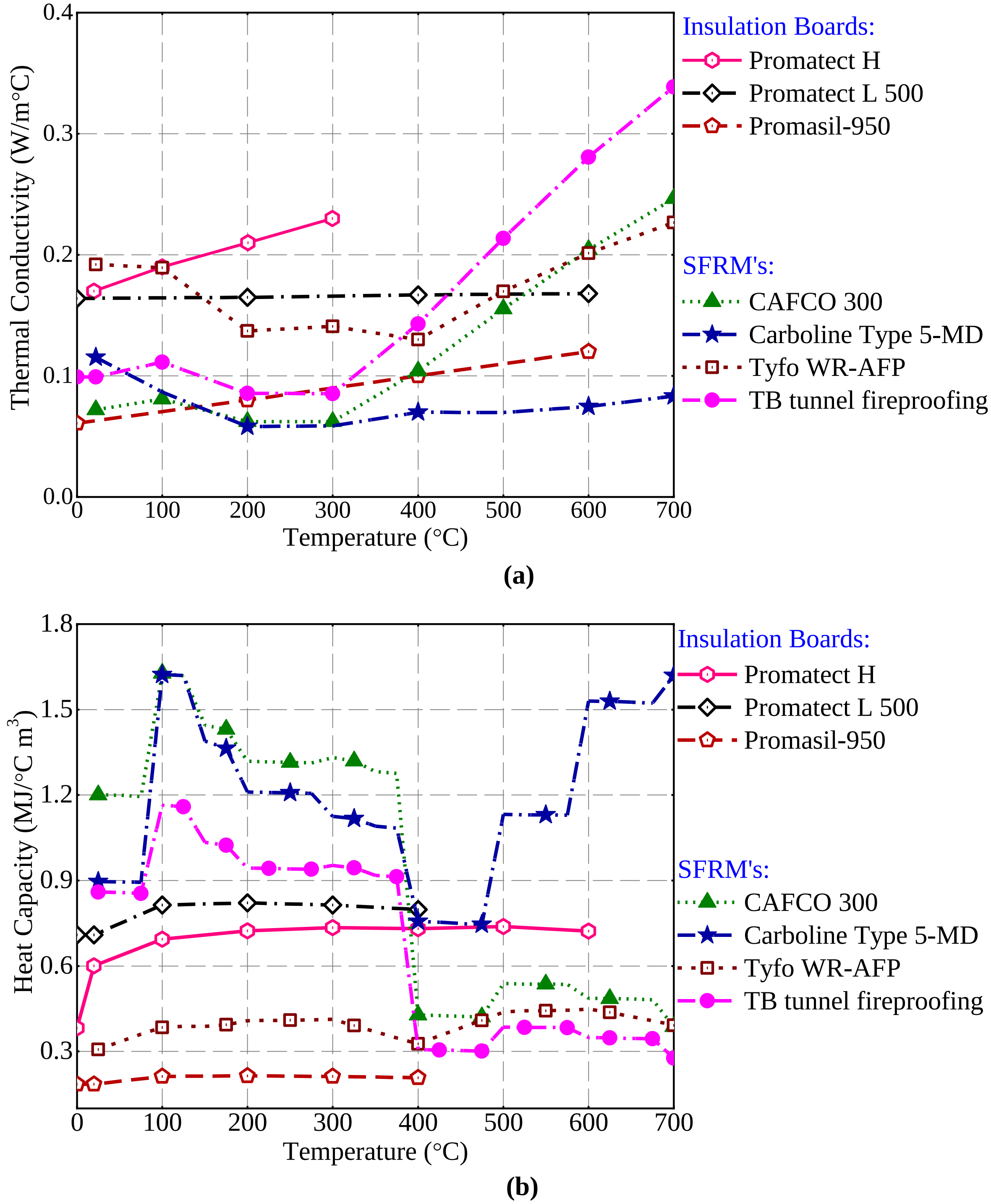

Figure 2.13: Thermal properties of different fire insulation materials at elevated temperature: (a) thermal conductivity; (b) heat capacity

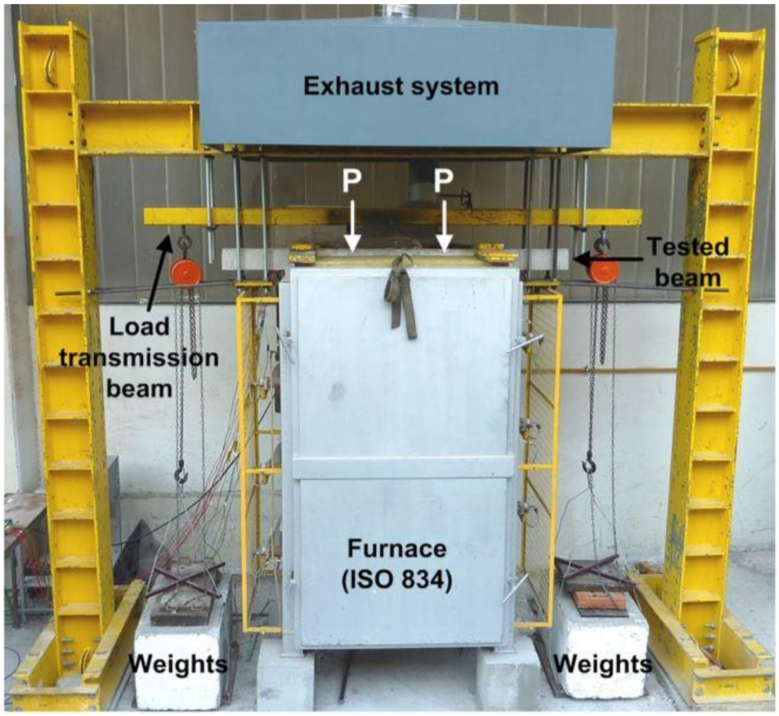

Figure 2.14: Intermediate scale furnace used for testing small scale RC beams by Firmo and Correia [149]

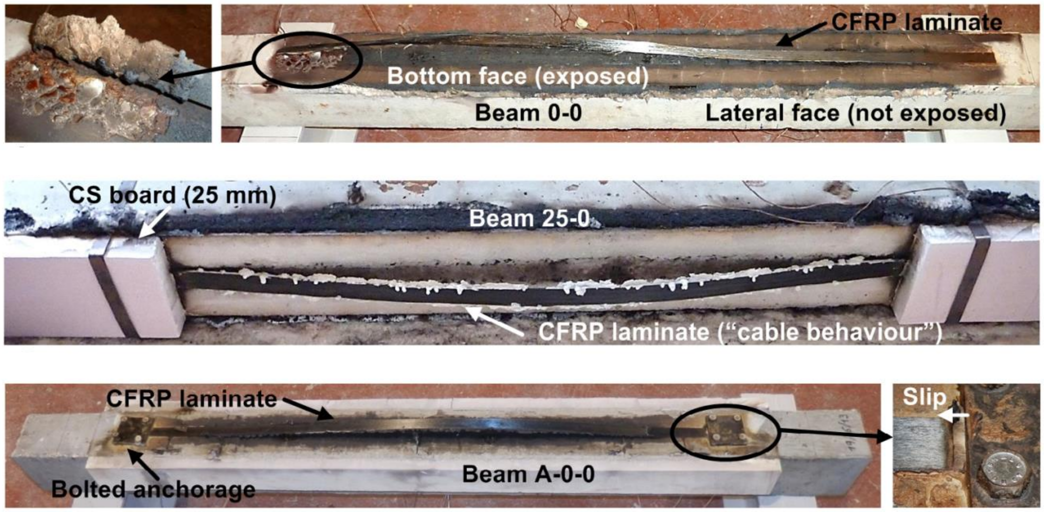

Figure 2.15: Failure modes of CFRP strengthening system in small scale FRP-strengthened RC beams as reported by Firmo and Correia [149]

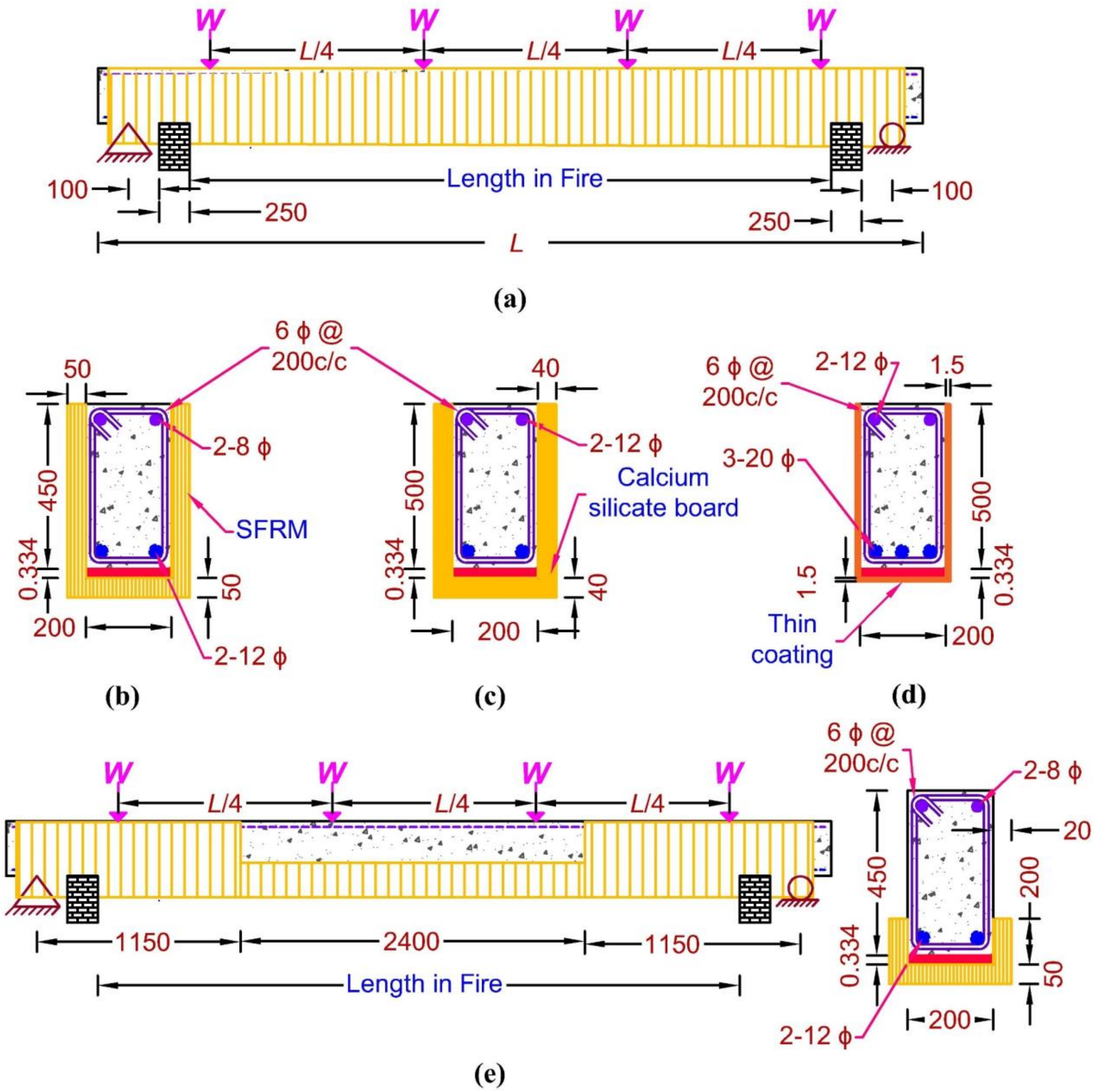

Figure 2.16: Geometrical details of the beams tested by Dong et al. [150]: (a) elevation of beams L1, L3, L4; (b, c, d) cross-section of beams L1, L3, L4; (e) elevation and cross-section of beam L2

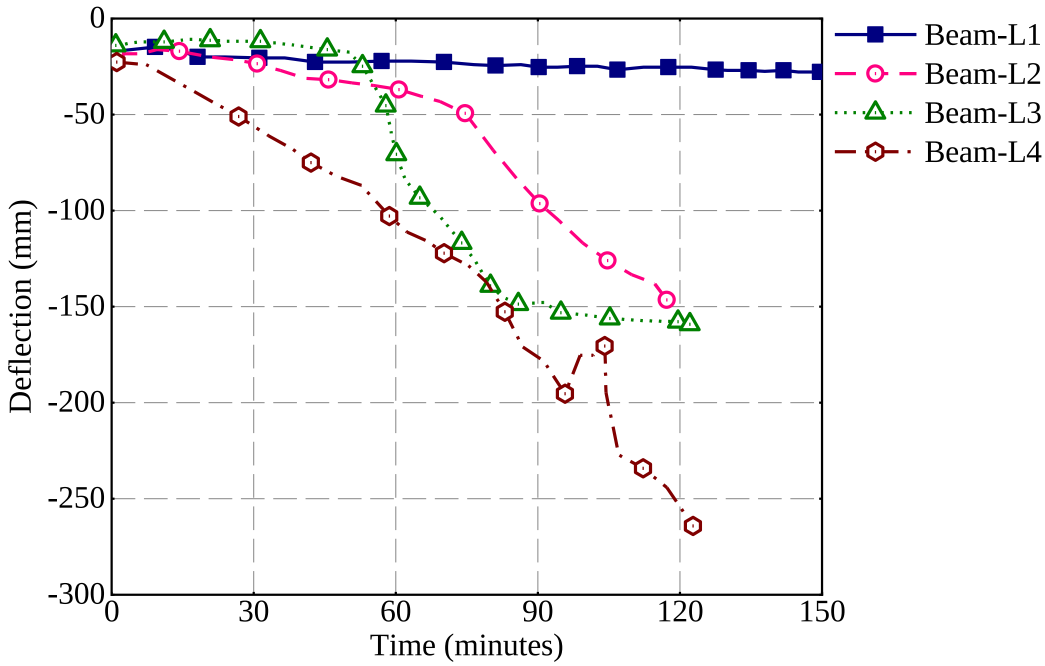

Figure 2.17: Deflection of the beams measured in fire test reported by Dong et al. [150]

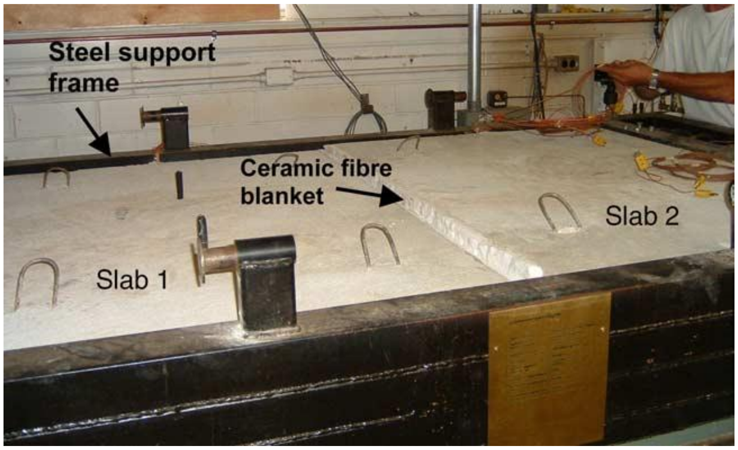

Figure 2.18: Intermediate scale furnace with two slab specimens tested at NRC (reproduced from William et al. [153])

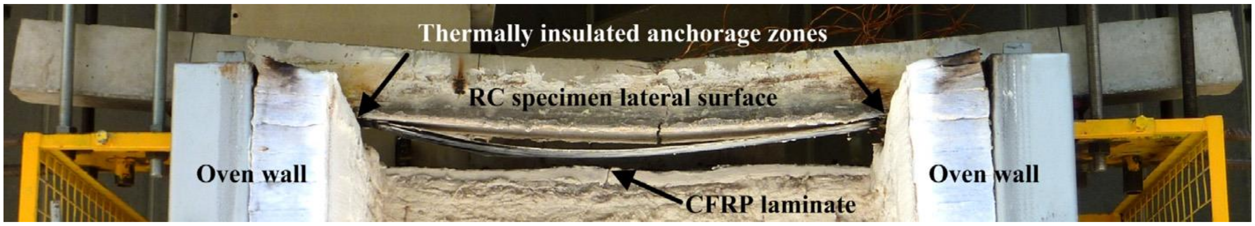

Figure 2.19: FRP-debonding due to high temperature exposure and failure of slab strip as reported by Lopez et al. [141]

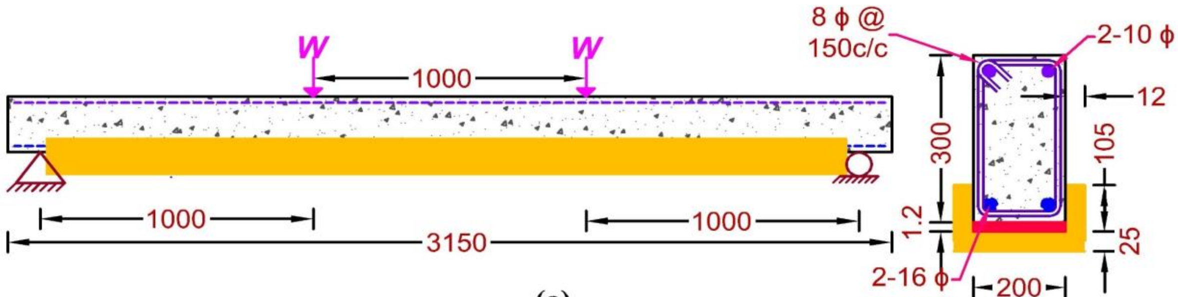

(a)

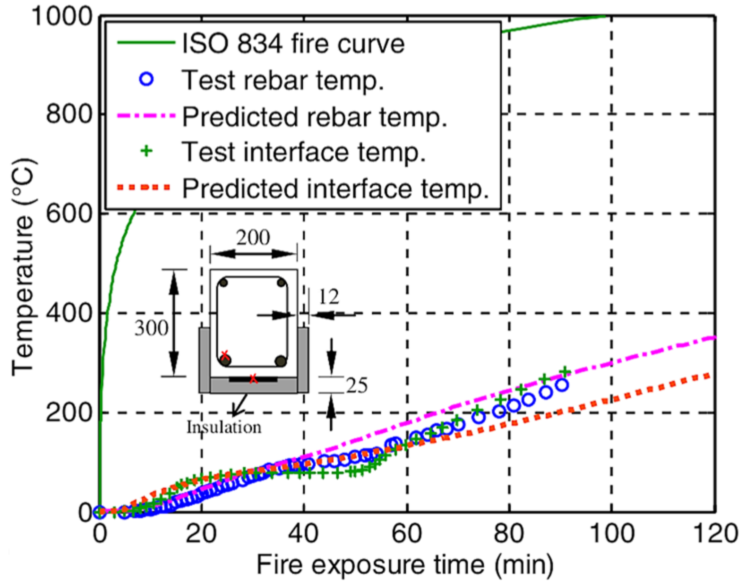

(b)

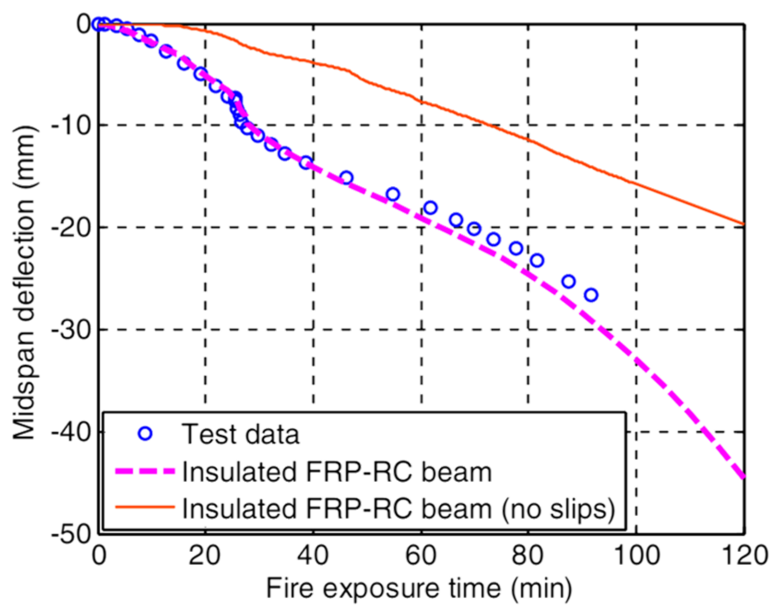

(c)

Figure 2.20: Comparison of measured and predicted results from model proposed by Dai et al. [121]: (a) geometry of beam; (b-c) thermal and structural response comparison

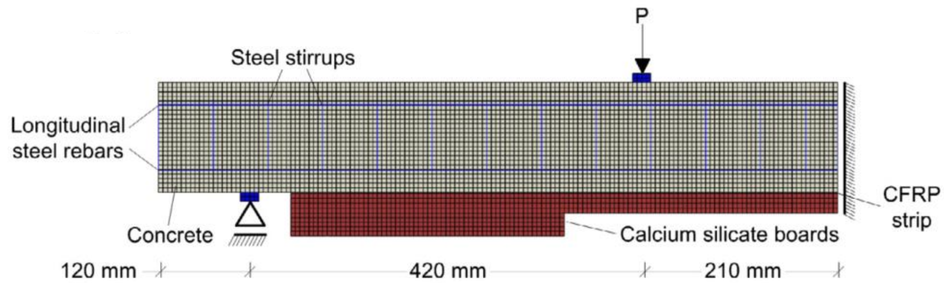

(a)

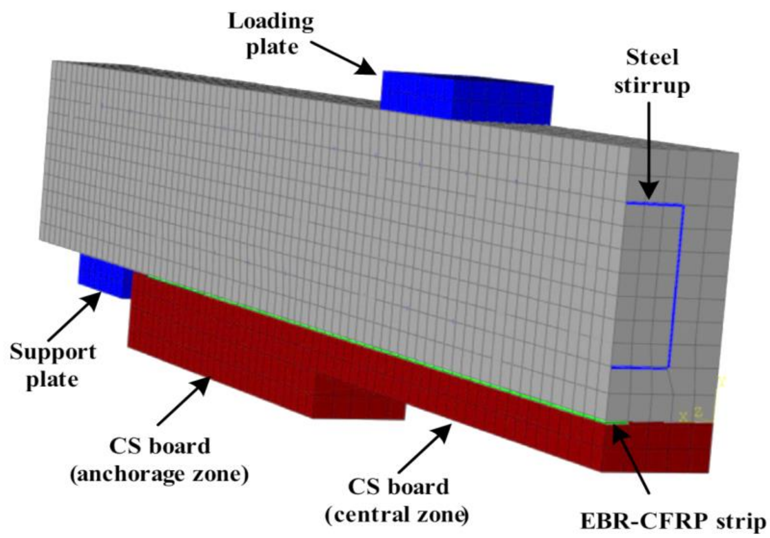

(b)

Figure 2.21: Finite element model developed by Firmo et al. [142, 157]

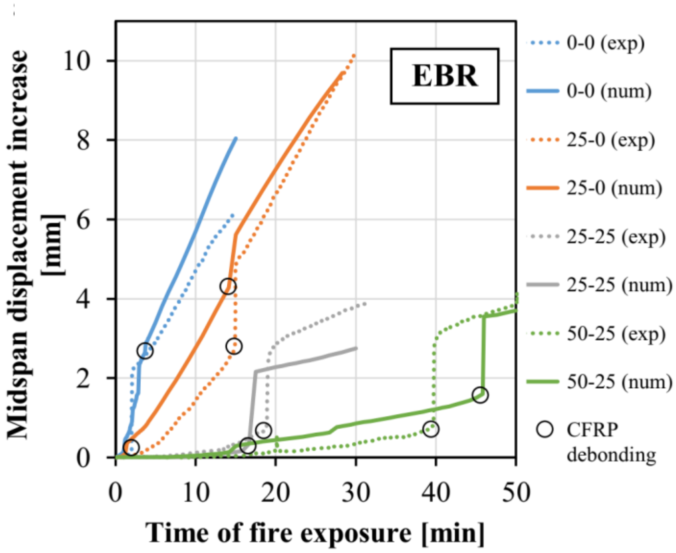

Figure 2.22: Comparison of predicted and measured deflection response as reported by Firmo et al. [157]

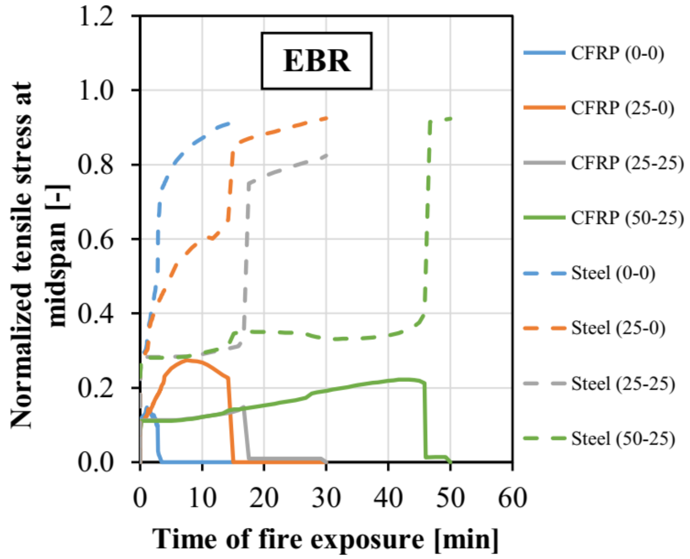

Figure 2.23: Variation of normalized tensile stress in CFRP and steel as reported by Firmo et al. [157]

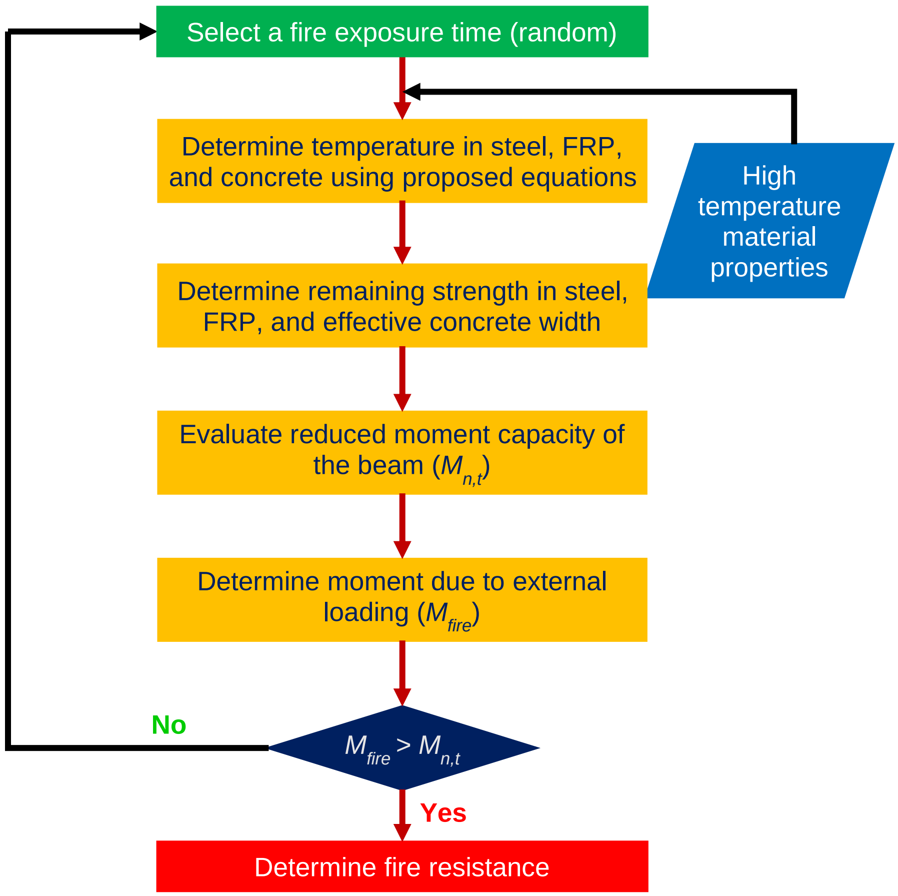

Figure 2.24: Flowchart of the rational approach proposed by Kodur and Yu [21] for evaluating fire resistance of FRP-strengthened concrete beams

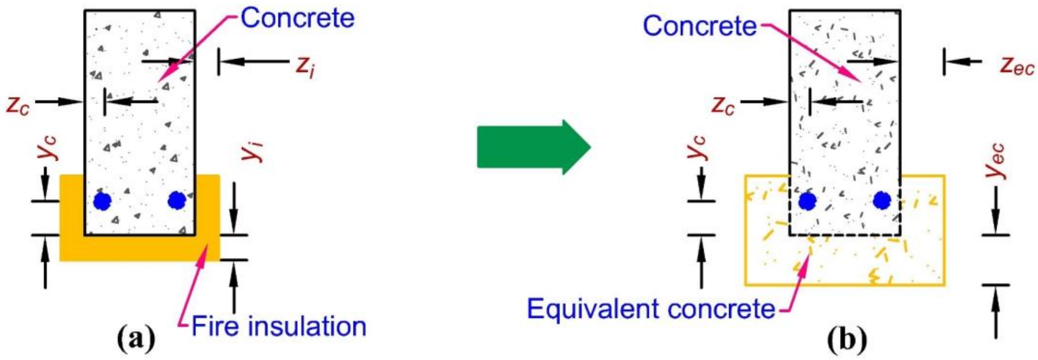

Figure 2.25: Equivalent concrete thickness method used by Kodur and Yu [21]

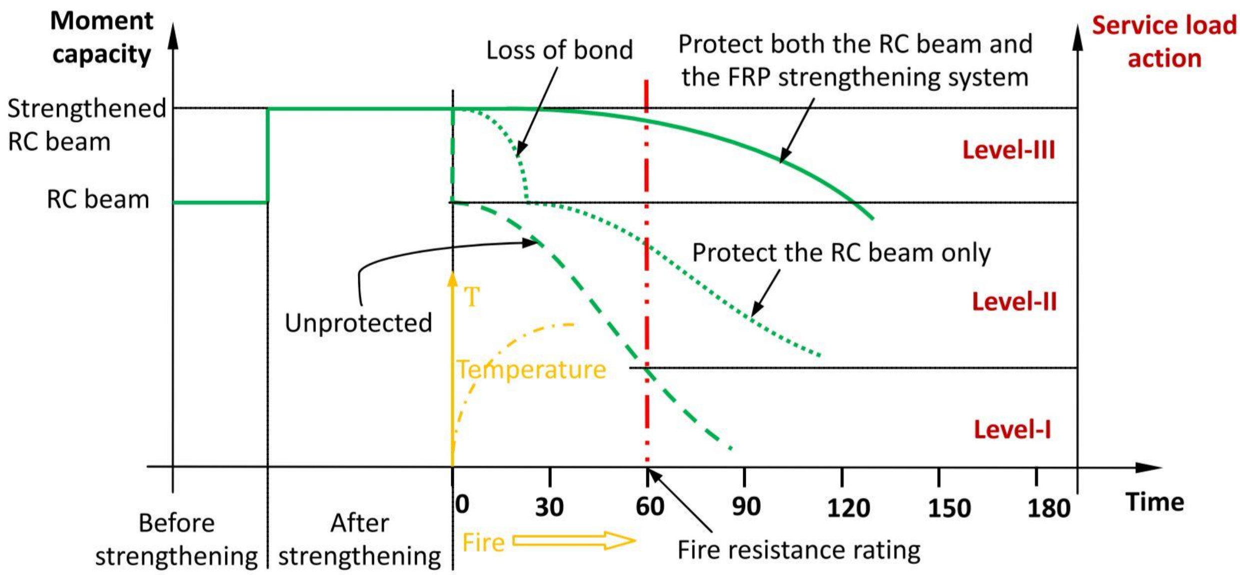

Figure 2.26: Three level procedure proposed by Gao et al. (reproduced from Gao et al. [22])

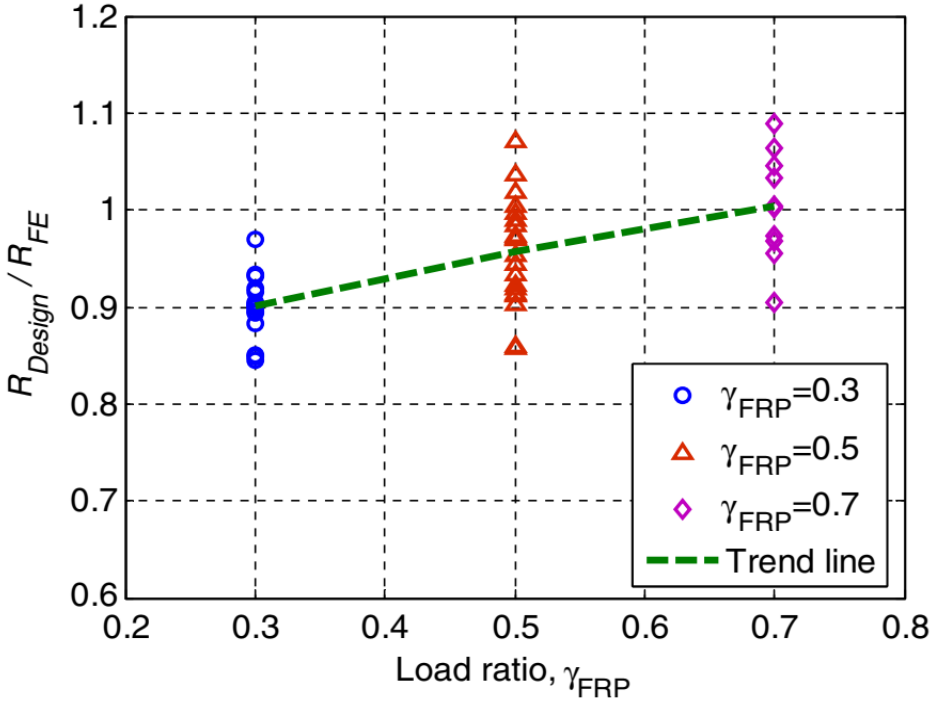

(a)

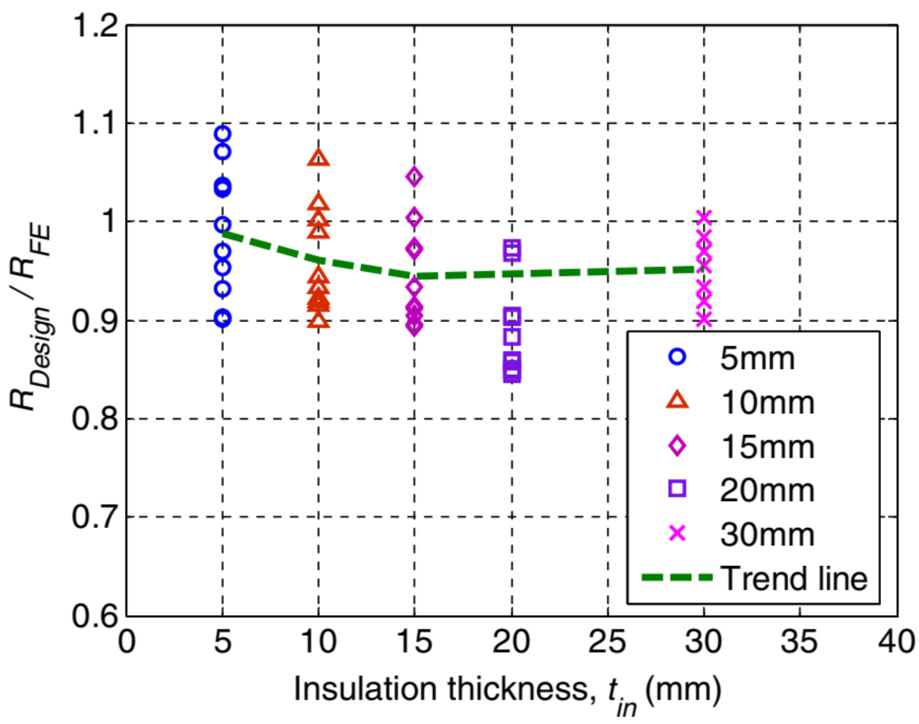

(b)

Figure 2.27: Accuracy of level II design method proposed by Gao et al. [22]: (a) effect of load ratio; (b) effect of insulation thickness (reproduced from Gao et al. [22])

CHAPTER 3

FIRE RESISTANCE TESTS

3.1 General

State-of-the-art review presented in Chapter 2 clearly indicates that limited fire tests have been conducted on FRP-strengthened concrete flexural members as compared to RC flexural members. In particular, very few fire tests have been conducted on FRP-strengthened RC slabs. Although these tests evaluated the overall fire resistance or failure times of the FRP-strengthened concrete members, only very few studies provided any insight into the behavior of FRP-strengthened RC members during fire exposure. Further, these tests do not quantify the effect of all critical factors influencing the fire resistance of FRP-strengthened concrete flexural members. To overcome some of these limitations and to generate reliable test data on fire performance of FRP-strengthened RC flexural members, fire resistance tests were carried out on a set of RC beams and slabs. Details of these tests including the fabrication, instrumentation, test procedure, and results are summarized in this chapter.

3.2 Preparation of Test Specimens

The fire resistance tests were conducted on seven CFRP-strengthened concrete flexural members comprising of five T-beams and two slabs. The beams were designated as TB1, TB2, TB3, TB4, and TB5, while the slabs were designated as S1 and S2. The design, fabrication, FRP and insulation installation, and instrumentation details of these test specimens and associated coupons for material property evaluations are described below.

3.2.1 Design and Fabrication of RC Flexural Members

The first step in the test program is the design of RC beams and slabs for fire tests. As part of this study, the RC flexural members were designed as per ACI 318M-14 [160] specifications, with dimensions closely resembling typical structural members used in buildings to increase the applicability of results. The design details of the beams and slabs are presented in Appendix B. The beams and slabs were designed with a concrete compressive strength and rebar yield strength of 35 MPa and 420 MPa, respectively. The geometrical details of the tested beams and slabs as well as their nominal capacity (based on design strength values of concrete and steel rebars) are summarized in Table 3.1, while the elevation and cross-section configuration of the beams and slabs are shown in Figure 3.1 (a-b) and Figure 3.2 (a-b), respectively.

All the T-beams were 3.96 m long and had cross-section dimensions of 432 mm × 127 mm and 254 mm × 279 mm representing flange width, flange depth, and web width, web height, respectively. The slabs were of 3.96 m span and had cross-section dimensions of 406 mm × 152 mm (width × depth). The longitudinal tensile reinforcement at the bottom comprised of 3-16 mm ϕ rebars in beams TB1 to TB4 and of 3-19 mm ϕ rebars in beams TB5. The longitudinal compressive reinforcement at the top comprised of 4-12 mm ϕ rebars in all the beams. The shear reinforcement comprised of 10 mm ϕ stirrups spaced at 152 mm c/c in the web, and 10 mm ϕ transverse rebars spaced at 305 mm c/c in the flanges, as shown in Figure 3.1 (b). The reinforcing bars were provided at a clear cover of 38 mm on all sides. In case of the slabs S1, and S2, the longitudinal and transverse reinforcement comprised of 3-12 mm ϕ rebars and 8-12 mm ϕ rebars, respectively, with a clear cover of 19 mm. Additionally, two U-shaped bent hooks are also attached to the longitudinal rebars at the top of the beams and bottom of the slab at 1 m distance on either side of the mid-span, to be used for lifting the specimens.

The beams and slabs were cast in the Civil Infrastructure Laboratory (CIL) of Michigan State University (MSU). A pictorial representation of the procedure followed in casting of the specimens is shown in Figure 3.3. Initially the plywood forms were assembled with internal dimensions similar to the dimensions that of test specimens, and the inner sides of the plywood were lubricated with three coats of oil to enable easy striping, as shown in Figure 3.3 (a-b). Following this, reinforcement cages were prepared for each beam by tying the longitudinal rebars with the stirrups and transverse rebars, while reinforcement meshes were prepared for each slab by tying the longitudinal rebars and transverse rebars. The rebars in the cages and meshes were attached with thermocouples and strain gauges, details of which are mentioned in following section. These reinforcement assemblies were then laid in the respective forms, as shown in Figure 3.3 (c-d).

Two different concrete batch mixes designated as Mix-1 and Mix-2 were used for the casting of beams and slabs. Mix-1 was used for casting of beams TB1 to TB3, while Mix-2 was used for casting of beams TB4, TB5 and slabs S1, S2. Both these mixes were supplied by Shafer Redi-Mix Inc., a local concrete batch mix plant to maintain quality control of the mixes. Table 3.2 summarizes the mix proportions for one cubic meter of concrete in each of the batch mixes. Both the concrete mixes (Mix-1 and Mix-2) were designed to achieve a compressive strength of 35 MPa and primarily comprises of Type-I Portland cement, carbonate based coarse aggregate and silica-based fine aggregates in varying proportions.

After laying the rebars in the forms, premixed concrete was poured into the forms from a concrete mix truck through hopper chute. During pouring, needle vibrators were used to ensure a compact and dense mass of concrete within the specimen and the top surface was smoothened using concrete trowel, as shown in Figure 3.3 (e-f). The T-beams and slabs were then sealed within the forms and cured for a period of 31 days. For curing the specimens were covered with 0.15 mm thick heavy duty polyethylene film. The heavy-duty plastic sheeting protects the concrete surface from dust, debris, etc., and acts as a vapor barrier thereby retaining the moisture to aid the curing process. Thereafter, the specimens were lifted out from the forms and stored at room temperature conditions for six to 21 months in CIL at MSU, before applying FRP and insulation. In addition to the test specimens, a total of forty 100 mm × 200 mm (diameter × height) cylinders and six dog-bone specimens were also cast, using the batch mix used for fabricating the beams and slabs, to measure the compressive and tensile strength of concrete at regular intervals.

3.2.2 FRP Strengthening

The above casted concrete beams and slabs were flexurally strengthened with CFRP sheet to increase their respective flexural capacity by 20% to 45%. This increase in flexural capacity of the specimens was determined based on the level of strengthening allowed in current codes of practice and the strengthening was designed as per ACI 440.2R-17 [19] specifications. Beams TB1, TB2, and TB3 were strengthened after a period of 21 months, whereas beams TB4, TB5 and slabs S1, S2 were strengthened after six months at the soffit level. The CFRP strengthening material was supplied and applied by Structural Technologies, Strongpoint LLC, USA, following recommended installation procedure, as per their field application's manual. The details of the installation procedure are described here.

To install the strengthening system, the beam and slab specimens were flipped over, and sand blasted around the soffit region to roughen the surface and partially expose the aggregates. The roughened concrete surface was cleaned using compressed air and brush. Prior to installation of CFRP sheet, a thin coat of epoxy was applied with a roller to prime the concrete surface. The prepared surface was then smoothened using a thick epoxy layer and was left to dry. The CFRP sheet was applied using the wet lay-up method, wherein the sheet was saturated with epoxy prior to its application on the concrete surface. Once fully saturated, the fabric was roller applied on the prepared concrete surface at the soffit of beams and slabs. After placement, the sheet was rolled to remove air bubbles and to ensure accurate placement i.e., to ensure that CFRP sheet is firmly embedded and adhered to surface. The applied CFRP sheet in the beam/slab was left to cure for at least 5 hours, before applying a layer of fire insulation on strengthened members. A pictorial depiction of various steps in CFRP-installation and final appearance of CFRP-strengthened beam and slab are shown in Figure 3.4.

The strength properties of CFRP sheets are summarized in Table 3.3, while the details pertaining to the dimensions of strengthening applied on each test specimens are summarized in Table 3.4. The CFRP laminate used for strengthening of beams TB1 to TB3, had a design ultimate tensile strength, design tensile modulus, and a rupture strain of 1034 MPa, 73.77 GPa, and 1.1%, respectively. Whereas the CFRP sheet used for strengthening of beams TB4, TB5 and slabs S1, S2 had a design ultimate tensile strength, design tensile modulus, and a rupture strain of 1172 MPa, 96.5 GPa, and 1.1%, respectively. The epoxy adhesive (commercial designation V-Wrap 700) used for bonding the CFRP sheets had the tensile strength, tensile modulus, and rupture strain of 60 MPa, 2.76 GPa, and 4.4%, respectively, and had a glass transition temperature (T_g) of 82°C evaluated by the manufacturer as per ASTM-D4065 specifications.

The cross-section dimensions of the CFRP sheet applied on beams TB1 to TB5 and slabs S1 and S2, are shown in Figure 3.1 (c-g) and Figure 3.2 (c-d), respectively. Beams TB1 to TB3 were strengthened by applying one layer of 170 mm wide V-wrap C200HM CFRP sheet, whereas beams TB4, TB5 and slabs S1, S2 were strengthened by applying one layer of 100 mm and 75 mm wide V-wrap C200H CFRP sheet, respectively. The cured laminate thickness of CFRP sheet for the beams and slabs was 1.02 mm. The CFRP sheet was applied over the entire unsupported length

(3.6 m) of beams and slabs and was terminated at 150 mm from the ends. The strengthening system was designed to increase the capacity of beams TB1 to TB3 by 42%, for beams TB4 and TB5 by 33%, and 23%, respectively, and for slabs S1, S2 by 40%. However, the actual yield strength of the steel rebars was much higher (*cf.* Table 3.3) than the design yield strength of 420 MPa. Therefore, the actual increase in the ultimate capacity of the concrete flexural members was 41% in beams TB1 to TB3, 28% in beam TB4, 20% in beam TB5 and 30% in slabs S1, S2. The actual ultimate capacity of the beams and slabs, and the ultimate strengthened capacity as well as the percentage increase applied increase in the respective ultimate capacity are summarized in Table 3.5.

3.2.3 Fire Insulation Application

Beams TB2 to TB5, and slabs S1, S2 were protected with a layer of fire insulation (commercial designation V-wrap FPS), to enhance their fire resistance. This fire insulation material was supplied by Structural Technologies, Strongpoint LLC, USA, and was applied by a third-party contractor following the procedure recommended by Structural Technologies LLC inc.

V-wrap FPS insulation is a spray applied cementitious material primarily comprising of vermiculite, gypsum, and Portland cement along with other additives. This insulation a density of 425 kg/m^3 and possess thermal conductivity and specific heat of 0.156 W/m-K and 1888 J/kg-K, respectively. To apply the insulation on the beams and slabs, the V-wrap FPS insulation powder was first mixed with water in ratio recommended by the manufacturer, to prepare a spray applicable mix. The mix was sprayed over the beams and slabs using a mortar sprayer attached to an electric pump. In case of beams TB1, TB2, and TB3, a thin layer of putty (epoxy mixed with silica fume) was applied to increase the adhesion between insulation and concrete. The insulation was sprayed in different spray passes (layers), with the insulation thickness not exceeding 10 mm during any single spray pass. Limiting the thickness per spray pass was required to accelerate the drying procedure between two consecutive spray passes. Special attention was paid to maintain uniform insulation thickness throughout the length of the beams and slabs. Insulation thickness was measured at several places along the beam length to ensure insulation thickness to be uniform within a tolerance range of ± 3 mm. A pictorial representation of various stages of insulation installation and typical insulated beams and slabs are shown in Figure 3.5.

The thickness and the depth of insulation applied on sides of beams TB2 to TB5 and slabs S1, S2, are shown in Figure 3.1 (d-g) and Figure 3.2 (c-d) and are summarized in Table 3.4. Beams TB2, TB3, TB4, and TB5 were insulated with 25 mm, 19 mm, 32 mm, and 19 mm, respectively thick layer of fire insulation, while slabs S1 and S2 were insulated with a 19 mm and 25 mm, thick insulation layer, respectively. Additionally, to evaluate the effect of insulation depth on the sides of the beam, the insulation was applied up to 75 mm, 112 mm, 152 mm, and 152 mm depth on sides of beams TB2, TB3, TB4, and TB5, respectively. These depth levels represent 1.5 times, 2 times, and 3 times the effective cover depth to rebars, respectively. The slabs S1 and S2 were insulated at the bottom and on the sides for its entire depth to simulate realistic scenario as applied in practice.

3.2.4 Instrumentation

During the fire tests various response parameters were measured. For this purpose, a set of sensors were installed in beams and slabs. The temperature progression was monitored at quarter and half the span length of the beams and slabs through seven K-type thermocouples installed at each of the sections, as indicated in Figure 3.1 (h) for beams and Figure 3.2 (e) for slabs. The thermocouple positions were chosen to measure temperature rise in bottom and top rebars, at mid depth of concrete, as well as at the insulation-CFRP and CFRP- concrete interfaces. The strains in the tensile and compressive rebars of the beams and in the tensile rebars of the slabs, were recorded by installing strain gauges on rebars, as indicated in Figure 3.1 (h) and Figure 3.2 (e). The vertical deflection was recorded at the mid-span of the test specimens using two displacement transducers placed along the center line at the top of the specimens. Additionally, in case of beams, the vertical deflection was also measured at one of the load extensions by attaching a displacement transducer to the top of the test frame with the wire attached to a U-hook mounted on the top of load extension as shown in Figure 3.6 (e).

3.3 Test Setup

The fire resistance tests on CFRP-strengthened RC beams and slabs were conducted at MSU's structural fire testing furnace. The testing facility is specially designed to simultaneously apply both heating and structural loading conditions, which a building structural member might encounter during a fire event. The fire furnace together with the test setup is shown in Figure 3.6. The Figure 3.6 (a, b, and c) shows the schematic layout of the furnace in plan, front view (east west elevation), and side view (north-south elevation), respectively, while Figure 3.6 (d) shows the loading arrangement on the specimens.

The testing facility comprises of a heating chamber and loading actuators mounted on steel framework which in turn is mounted on four steel columns. Each column has an overhang (cantilever) arm attached to it at 3 m from the bottom (*cf.* Figure 3.6 (b)). The heating chamber is 1.68 m high with a cross-section dimension of 3.05 m × 2.44 m and is equipped with six propane burners to provide thermal loading (heating), during a fire test. The burners can provide a maximum thermal energy of 2.5 MW and are strategically placed on the walls of the furnace to ensure uniform progression of heat within the chamber. The east and west (i.e., front and rear) walls of the furnace chamber are provided with one thermocouple, whereas the north-south side walls of the furnace are provided with two thermocouples each, to measure the temperature progression during the fire test. These thermocouples are K-type Chromel-Alumel thermocouples and are designed as per ASTM E119 specifications. Additionally, two small view ports are provided on front and rear wall of the furnace facilitate visual monitoring of the fire-exposed test specimens during fire tests.

The furnace temperature can be maintained along a desired time-temperature curve, as in a standard or design fire, by manually controlling the input gas and ventilation within the chamber. The furnace facilitates simultaneous testing of two beams or slabs under different load levels and restraint conditions, as shown in Figure 3.6 (a, c). Structural loading is applied using hydraulic loading system, which is driven by pneumatically driven hydraulic pump (*cf.* Figure 3.6 (e-f)). The hydraulic system has the capability to apply loading independently on each test specimen at the front and back. The actuators can apply a total force of 2700 kN on each specimen. Data generated during fire test such as, temperature rise, deflection, and strains in rebars, is collected using state of the art data acquisition system (Darwin Data DA100/DP120-13), which has 70 thermocouple channels, 10 strain gauge channels, and 10 displacement channels. The data acquisition system uses “DAQ32” computer program through which the measured data can be visualized on the computer screen, in real time during the fire test, and can simultaneously be recorded in a .csv file.

Figure 3.6 (e-f) shows T-beam and slab specimens mounted on the east (front) end of furnace, respectively. The specimens are lifted through the U-hooks provided on the ends of the specimen, using overhead crane. The overhead crane has a capacity of 10 ton and runs along the east-west direction along the entire lab facility. The specimens once lifted using the overhead crane, are then attached to the extension chains attached to the furnace frame and are then slowly glided using the pulley chain system as shown in Figure 3.6 (f). The specimens are lowered inside the furnace gap and are laid on the external supports using the extension chains. The external simple supports are prepared welding semicircular rods to steel sections and are placed on the overhanging arms from the four steel columns, such that the distance between the external supports 3.66 m apart from each other. Special care is taken to ensure that the top of specimen is completely in level with the top edge of the furnace, and the specimen is perfectly straight in longitudinal direction.

Once the specimens are completely in position, two 12 mm thick and 100 mm wide loading plates are placed 860 mm apart (center to center) on the top of specimens on either side of the mid-span, as shown in Figure 3.6 (a). to mark the loading points and to ensure even load distribution. Following this a covering lid is placed on the top of furnace, while any gap on sides or between top of the specimen and covering lid is filled with ceramic wool. The covering lid has four openings, through which load extension rods (loading jacks) are passed, as shown in Figure 3.6 (d). During the test, structural loading is applied on the specimens through the loading jacks attached to pneumatically controlled hydraulic actuator. The loading jacks have semicircular rods welded at its bottom end and touch the steel plates along a tangent. This arrangement ensures an even distribution of loading along the width of the specimen. The load applied on the specimens generates vertical reaction force at the external (simple) supports mounted on the overhanging arms of the columns. The generated reaction is then transferred to the columns as an axial load and bending moment. Once the specimens are mounted and loading jacks are in position, fire resistance tests are carried out using the procedure described in following section.

3.4 Fire Resistance Tests

Four different fire resistance tests were conducted to evaluate the fire resistance of strengthened concrete flexural members. The varied parameters during each of these tests are summarized in Table 3.5. Beams TB1, TB2, beams TB4, TB5, and slabs S1, S2 were tested simultaneously in first, third and fourth fire test, respectively, whereas beam TB3 was tested individually in the second fire test. Each of these fire resistance tests were carried out in two steps. At the beginning of each test, a pre-determined structural load (summarized in Table 3.5) was gradually applied on the specimens through a pneumatically driven hydraulic actuator (as explained earlier), until constant deflection was observed. Following this, the gas burners in the furnace were turned-on and the required fire temperature patterns were simulated as per the time-temperature of ASTM E119 "Standard Fire", while the structural loading on the specimens was kept constant. The beams were exposed to fire on three surfaces, i.e., two sides and soffit, while only the soffit (bottom surface) of the slabs was subjected to fire exposure

During the fire test, the specimens were simply supported at the ends with a clear span of 3.66 m and were subjected to two concentrated loads at a distance of 430 mm on either side of mid-span. Additionally, only 2.44 m of the unsupported length of specimens was exposed to fire temperatures, while the rest of the specimen was thermally protected by the walls of the furnace and by thermal blankets. This configuration was adopted to evaluate the beneficial effects of maintaining low temperature in CFRP sheet in the anchorage zones.

The total structural load applied by the actuator on each of the specimen is summarized in Table 3.5. A total load of 99 kN, 99 kN, 116 kN, 97 kN, and 128 kN was applied on beams TB1, TB2, TB3, TB4, and TB5, respectively, while a total load of 21 kN and 26 kN was applied on slabs S1 and S2, respectively. The applied load ratio for each test specimen, defined as the ratio of bending moment due to applied loading to the actual ultimate strengthened capacity of respective test specimen, is summarized in Table 3.5. As can be seen from the table, beams TB1, TB2, TB4, TB5, and slab S1 were subjected to service load levels, computed based on the respective nominal strengthened capacity, as required by ASTM E119 for fire testing condition, while beam TB3 and slab S2 were tested at a slightly higher load level (as compared to service load level) to evaluate the effect of load level on fire resistance of strengthened member.

The beams TB1, TB2, TB3 and slabs S1, S2 were exposed to ASTM E119 fire for 3 hours, whereas beams TB4, TB5 were exposed to fire for 4 hours. During the entire test duration, the deflection at the mid-span, strains, and temperatures at various locations were monitored and recorded using the data acquisition system. Except for beam TB3 which failed at 175 minutes, all the other specimens were able to support the applied loading for the entire fire exposure duration without failure.

3.5 Tests to Evaluate Material Properties

The strength properties of the constituent materials of FRP-strengthened flexural members, i.e., concrete and steel reinforcement at ambient temperature were evaluated through material property tests. In addition, the tensile strength of CFRP and CFRP-concrete interfacial bond strength in 20-80°C temperature range is also evaluated. Details of these tests are presented in this section.

3.5.1 Concrete

Concrete cylinders prepared from both the batch mixes (Mix-1 and Mix-2) were tested under uniaxial compression at 7, 14, and 28 days as well as on test day to evaluate the compressive strength of concrete. Additionally, direct tensile strength of concrete was measured at the end of 28 days through uniaxial tensile tests on three dog bone specimens. The compressive strength tests were carried out using Forney Compression Testing Machine, while tensile strength tests were carried out using 810 MTS Universal Testing Machine (UTM). The average compressive strength measured at 7, 14, and 28 days as well as the direct tensile strength at 28 days are summarized in

Table 3.2. At the end of 28 days, Mix-1 and Mix-2 yielded an average cylindrical compressive strength of 38 MPa and 43 MPa, respectively and an average tensile strength of 2.8 MPa and 3.1 MPa, respectively. Thus, it can be seen from the Table 3.1 and Table 3.2 that the 28-day strength of batch Mix-1 is slightly higher than the corresponding design strength, whereas for batch Mix-2 the average 28-day strength is significantly higher than the design strength.

3.5.2 Steel Reinforcement

The yield strength, and ultimate tensile strength of reinforcing steel bars used as tensile reinforcement in the beams and slabs was evaluated through uniaxial tensile strength test on steel rebar samples. The tests were conducted using the 810 MTS UTM. The tests were conducted on two samples each of the reinforcing bars of diameter (ϕ) 12 mm, 19 mm, and four samples of 16 mm diameter bars (one set for TB1 to TB3 and other for TB4). The average yield strength of each of these rebars is summarized in Table 3.3. The steel rebars used as tensile reinforcement in beams TB1 to TB3 (ϕ = 16 mm), TB4 (ϕ = 16 mm), TB5 (ϕ = 19 mm), and slabs S1, S2 (ϕ = 12 mm), had a yield strength of 440 MPa, 460 MPa, 450 MPa, and 545 MPa, respectively, and an ultimate tensile strength of 705 MPa, 708 MPa, 702 MPa, and 710 MPa, respectively.

3.5.3 Carbon Fiber Reinforced Polymer

For strengthening beams and slabs, two different types of CFRP sheets, namely V-Wrap C200H (for TB1, TB2, TB3) and V-Wrap C200HM (TB4, TB5, S1, and S2) were utilized. The tensile strength and CFRP-concrete interfacial bond strength of V-Wrap C200H CFRP sheets both at room temperature, i.e., 20°C and at elevated temperatures up to 80°C were evaluated. The furnace used for performing tensile and bond strength tests (details provided later), had very small cross-section area, which resulted in small gap between heating element and CFRP sheet. Due to proximity of the heating element, there were very high chances of igniting CFRP sheets at higher temperature and damaging the furnace. Therefore, due to the limitation of the equipment, only smaller temperature range was considered for the test.

To evaluate the temperature dependent tensile strength of CFRP, four coupons were tested at 20°C, and three coupons were tested at 40°C, 60°C, and 80°C each. To evaluate the interfacial bond strength, two CFRP-strengthened concrete prisms were tested at each target temperature of 20°C, 40°C, 60°C, and 80°C. A detailed test matrix showing the target temperatures and number of specimens tested during tensile and bond strength tests are shown in Table 3.6. The details of specimen size, experimental procedure and response parameters are summarized below.

(i) Tensile Strength Tests

› Test Specimens

The tensile strength tests were carried out on 13 CFRP coupons at various temperature levels. The test coupons were prepared and supplied by Structural Technologies Strongpoint LLC, as shown in Figure 3.7 (a). The CFRP coupons consisted of a single layer of V-wrap C200H high strength carbon fiber sheet impregnated with V-wrap 770 epoxy and cured for 72 hours. The coupons were 550 mm long, 25 mm wide, and 1.02 mm thick and had a nominal tensile strength and ultimate strain of CFRP coupons of 1240 MPa and 1.7% respectively, as specified by the manufacturer. Other properties of the fiber sheet, epoxy and CFRP laminate are summarized in Table 3.7.

For the tensile strength test, the CFRP coupons are gripped at the ends by the two friction clamps of the machine. The axial tensile force is transmitted to the specimen by the friction of the contacted regions between the clamps and the specimen. Although, CFRP has high tensile strength, the ends of the coupons (specimens) are susceptible to crushing under the gripping pressure of the clamps, due to the smaller width and thickness of the coupon in the contact region. Moreover, the smooth surface of CFRP leads to slippage between the clamps and coupon resulting in premature failure. Therefore, it is necessary to provide suitable anchors at the end of the coupon to facilitate proper clamping at the ends.

For achieving proper clamping at the ends' different types of anchorage configurations such as, steel pipes filled with expansive cement/epoxy, or tabs made of steel, aluminum, or composite materials are recommended in literature [67, 109, 161]. After some initial trials, it was found that the aluminum tabs provide a better gripping capability, as they generate maximum contact friction without crushing the ends of the CFRP coupons and prevents the slippage of the coupons end, thus transmitting the axial force uniformly within the CFRP coupon specimen [111, 115]. Therefore, in the current tests, aluminum tabs were used to prepare grips of the CFRP test coupons.

The aluminum tabs were 3.5 mm thick, 19 mm wide and 90 mm long, and were glued to the CFRP coupons using V-wrap 770 epoxy. To enhance the bond between the coupons and the tabs, the aluminum tabs as well as the grip portion of the CFRP coupons were roughened using coarse sandpaper and were cleaned with acetone solution, as shown in Figure 3.7 (b). Additionally, indentations were also created on the aluminum tabs, by pressing the tabs between the jaws of the universal testing machine (UTM). A schematic layout of the test specimen (coupon) a typical test specimen used to evaluate the tensile strength of CFRP at elevated temperature are shown in Figure 3.7 (c).

› Testing Equipment and Procedure

The tensile tests were carried out using a thermo-mechanical testing apparatus, shown in Figure 3.8. The setup comprises of a high-temperature MTS 653 furnace, with a maximum temperature capacity of 1400°C, mounted on an MTS 810 universal testing machine with 250 kN capacity. The furnace uses six silicon carbide heating elements arranged in three zones to generate heat. The heating elements are separated in three zones within the furnace by insulation plates to enable more uniform heating and better temperature control. The temperature rise within the furnace is controlled by an MTS 409.83 temperature controller which can increase the temperature at variable heating rates ranging from 0.1°C/minute to 100°C/minute. The controller uses a PID tuning module to monitor the temperature within the furnace to an accuracy of ±1°C. Three thermocouples, with an accuracy of 0.25%, are placed in the furnace close to the surface of the specimen to measure the surface temperature.

The tensile strength tests at the ambient and elevated temperature were carried out as per the specifications of ASTM D3039 [162]. At the start of test, one end of the specimen, sandwiched within the aluminum tabs, was clipped between jaws of UTM at the top, while the other end of the specimen was left loose between the bottom jaws of the UTM. Then the central 225 mm portion of the coupon specimen was enclosed within the furnace and exposed to a predefined target temperature within the furnace. The temperature within the furnace was increased at a variable rate ranging from 0.1°C/min to 0.5°C/minute. Once the target temperature was attained it was maintained for a duration of 3 to 5 minutes to ensure uniform temperature along the length of the coupon and steady state conditions. After the temperature stabilized which the bottom end of the specimen was gripped using the UTM jaws and then the tensile loading was applied at a rate of 2 mm/minute, as specified by ASTM D3039 [162], until failure is attained in the specimen. The elongation of CFRP in tension tests was measured as the relative displacement between the upper and the lower jaws of the UTM.

› Results and Observations for Tensile Strength Tests

All the specimens tested at various temperatures failed in brittle failure mode with rupture of fiber and cracking in the resin, as shown in Figure 3.9 (a). Moreover, failure in all the specimens initiated within the length of the specimen and not within the grips of the UTM, due to the provision of strong anchors. Additionally, at lower temperature, i.e., 20°C and 40°C, the coupons failed through brittle fracture at various locations within the length of specimen, however, at 60°C and 80°C, the failure location was always within the fire exposed portion of the specimens with CFRP splitting into bunch of fibers.

During each tension test, temperature of the specimen, load applied, and displacement of the jaws was recorded, and this data is utilized to evaluate tensile strength of CFRP coupon at each target temperature. The tensile strength was calculated by dividing the maximum applied load level when failure occurred by the original cross-sectional area of test specimen. Four specimens were tested at 20°C, and three specimens were tested at 40°C, 60°C, 80°C each. The average of three readings (four in case of 20°C) was considered as the strength of CFRP, at respective temperature. The tensile strength of each specimen measured at respective temperature as well as, the average of the tensile strength of specimens at each of the temperatures are summarized in Table 3.8.

It can be seen from Table 3.8 that at lower temperatures (20°C and 40°C) there is large scatter in the tensile strength of the specimens tested at same temperatures. However, at higher temperatures (60°C and 80°C) the scatter in tensile strength of the tested specimens is small. Such large scatter in strength values at 20°C and 40°C are common in FRP tensile strength tests and has been reported by several researchers. This can be attributed to the fact that the brittle failure of the specimens at these temperatures is due to cracking of resin, which reduces stress transfer within the fibers. The amount of cracking and resulting reduction in stress transfer in each coupon is different due to the manufacturing defects or material characteristics, and as a result, the measured ultimate load (tensile strength) is different. Despite the large scatter at 20°C and 40°C, the average of tensile strength of coupons at these temperatures is 1180.9 MPa and 1153.6 MPa, which is very close (difference of 5-7%) to the average tensile strength 1240 MPa, as recommended by the manufacturer. This indicates that the results are within the acceptable limits.

Figure 3.9 (b) shows the typical stress vs strain curve obtained from testing of the FRP coupons at elevated temperatures. The results are shown for one coupon tested at each temperature and are normalized with respect to the average tensile strength of the CFRP coupons at 20°C. The stress is calculated using the initial area of the coupons computed using the width and thickness of the coupons, measured at three different locations prior to test. The strain is computed by dividing the relative displacement between the jaws by the initial distance between them. It can be seen from the figure that at each temperature the CFRP coupons display a linear stress-strain response till abrupt failure is attained in a brittle manner. Additionally, it can be seen that the failure stress and corresponding strain at break decreases significantly with increase in temperature from 20°C to 60°C, however the decrease in stress and breaking strain is very small for the temperature increase from 60°C to 80°C.

The normalized strength ratio defined as the ultimate strength at tested temperature to the average ultimate strength at 20°C are summarized in Table 3.8 and the average strength ratio are plotted in Figure 3.9 (c). Additionally, the strength ratios measured and reported in previous studies are also shown in Figure 3.9 (c). It can be seen from the figure, that the strength decreases with increase in temperature. At 40°C, the decrease in strength is almost negligible (98% of room temperature strength), however with increase in temperature, i.e., at 60°C, the strength decreases at a faster rate and CFRP retains only 86% of its strength at 20°C. As the temperature approaches, T_g (82°C) of the polymer matrix, the CFRP further lose its tensile strength and reaches to 80% of strength at 20°C. Thus, it can be concluded that even moderate temperature rise has detrimental effect on the strength of CFRP. Moreover, these tensile strength retention factors measured in the current study are comparable with the factors previously reported factors.

(ii) *Bond Strength Test*

› Test Specimens

To evaluate the CFRP-concrete interfacial bond strength at elevated temperatures, high temperature bond tests were conducted on eight different specimens at CIL, MSU. Each test specimen comprised of four different components, namely a concrete prism of 610 mm × 100 mm × 100 mm size, with a 16 mm ϕ concentric steel rebar, a 38 mm wide carbon fiber sheet, and an aluminum plate cut in shape of a half-cylinder. The deformed steel rebar was 760 mm long with threads cut on one for a length of 90 mm, while the carbon fiber sheet was 1100 mm long. The aluminum half-cylinder plate was cut from an aluminum cuboid of 100 mm size to obtain a smooth semicircular surface (100 mm ϕ) on the top and a rectangular base at the bottom and had two bolt holes throughout its width. These four components are shown in Figure 3.10 (a) while a schematic layout of the assembled specimen is shown in Figure 3.10 (b).

As can be seen in figure, the specimen assembly comprised of half-cylinder placed on the top of the concrete prism with concentric steel rebar and a carbon fiber sheet attached to two opposing faces of the prism in an inverted U-shape. To prepare the specimen, the steel rebar was placed within the prism during casting such that, the unthreaded end was flush with the top surface of the prism, while the threaded end protruded outside the bottom end of prism. After this the half cylinder was placed on the top end of the prism and the carbon fiber sheet was attached on the two opposing faces. The carbon fiber sheet was bonded to the concrete prism for a length of 250 mm starting at 230 mm from bottom end while the top 130 mm portion of the sheet was left unbonded and was loosely passed over the half-cylinder plate and bonded on the opposite face of the prism in a similar manner, as shown in Figure 3.10 (b).

The carbon fiber sheet was applied using a two-component epoxy V-wrap 770 epoxy through wet-layup procedure, as described by the manufacturer. Prior to application of the carbon sheet, the concrete surface on either side of the prism was roughened using a belt sander and thoroughly clean using compressed air. The bond length on either side of the specimen was 250 mm, which was higher than the minimum anchorage length (111.2 mm), determined as per ACI 440.2R-17 [19] guidelines.

The concrete prisms were cast from a batch of pre-mixed concrete which comprised of Type I Portland cement, sand, and carbonate based coarse aggregates. The batch mix yielded an average cylindrical compressive strength of 37 MPa and a split tensile strength of 3.5 MPa, measured through testing of 3 cylinders each for tension and compression, after 28-days of casting. The rebars had an average yield strength of 430 MPa, determined from the tensile test of three rebar coupons. The dry carbon fiber sheet and the laminate had a tensile strength of 4830 MPa, and 1240 MPa, and elastic modulus of 227.5 GPa and 73.77 GPa, respectively, as reported by manufacturer, while the epoxy resin used for bonding the carbon fiber sheet had glass transition temperature of 82°C. These properties are summarized in Table 3.7.

› Test Equipment, Setup, and Procedure

For undertaking high temperature bond tests, a specialized test set-up, as shown in Figure 3.11 (a), was designed and fabricated. The test equipment comprises of a tension testing machine, an electric furnace to generate high temperature, and a data acquisition system. The testing machine comprises of two heavy steel beams laid horizontally and connected through a high strength extension rod on each end. A steel plate is rigidly connected using high tension bolts at the mid-span of the top and bottom beams each. These steel plates are in turn rigidly connected with two steel plates (connector plates) at the top and a U-shaped bracket at the bottom, using high tension bolts to, as shown in Figure 3.11 (a). Two washer plates are provided between the connector plates and either side anchor plate to ensure sufficient space is available for placing the half-cylinder between the anchor plates. This arrangement creates a clamping bracket for anchoring the top end of the specimen. The bond test specimen is anchored at the top end by tightly bolting the half-cylinder plate, placed between the inverted U-shaped carbon fiber sheet and top surface of prism, to the connector plates. The tight connection allows for a rigid body movement of the half-cylinder plate on the top of the specimen with the top beam. The bottom end of the specimen is anchored by bolting the steel rebar to the U-shaped steel bracket.

Two hydraulic jacks, placed on the bottom steel beam can directly apply the specified load to the top beam through high strength extension rods. When hydraulic jacks apply an increasing load, the top beam along with the half-cylinder plate (on the top of the specimen) moves upward, which in turn pulls the CFRP sheet. Since the prism is tightly anchored at the bottom, the entire tensile force (pull on CFRP) is carried by the bonded region through shear. The load applied to the specimen is measured by a pair of load cells attached to extension rods and the axial deformation of the specimen is measured through an externally placed linear variable displacement transducer (LVDT), with a range of ±38 mm and with an accuracy of 0.0254 mm. The LVDT is attached to the top loading frame through a rigid steel bracket assembly. During the test, the top beam is always maintained in a perfectly horizontal position to minimize eccentric loading during the test.

Prior to application of the load through the hydraulic jacks, the bonded region is exposed to desired temperature. The heating device comprises of a small-scale electric furnace which heats up the bonded region of the specimen. The furnace is placed on a tabletop between the top and bottom steel beams, as shown in Figure 3.11 (b). The furnace can heat the test specimen to a desired target temperature. The electric furnace comprises of cylindrical chamber with an inner diameter of 203 mm and an inner height of 254 mm. The temperature in the furnace can reach up to 1000°C, and target temperature, heating rate and stabilization duration can be programmed into the furnace through a control module. Three internal thermocouples mounted on the interior walls of furnace monitor the furnace temperature at upper, middle, and lower zones. The average reading of these three thermocouples is taken as the furnace temperature. In addition, four thermocouples (two on each bonded face) are directly attached to the specimen to monitor the actual specimen temperature during high temperature tests.

The load cells, LVDT, and specimen thermocouples are connected to a data acquisition system, wherein applied load, displacement and furnace and specimen temperatures on the specimen can be recorded every 0.01 second. Through this setup, double lap bond strength test can be conducted on FRP-strengthened concrete prism by heating the specimens to a desired temperature and then subjecting it to tensile loading.

The double lap bond strength tests were conducted at four target temperatures, i.e., 20°C, 40°C, 60°C, and 80°C. The last target temperature being the closest to the T_g of the adhesive. After anchoring the specimen at the top and bottom using the above-described procedure, the unbonded region at top of the prism and bottom 230 mm length of the prism were covered with insulation (*cf.* Figure 3.11 (b)) to prevent direct exposure to heat and subsequent temperature rise in those regions. Additionally, four K-type thermocouples were attached (two on each bonding surface) at the top and bottom of the bonded region to monitor the temperature rise at the interface. The furnace door was then closed, and heating was turned-on to attain a target temperature. The heating rate in the furnace was set to 2-5°C per minute depending on the target temperature (higher rate for higher target temperature). All tests were conducted under steady state condition, i.e., once the target temperature was attained it was maintained at that level for five minutes to ensure uniform temperature along the entire bonded region. After temperature along the bonded region stabilized, hydraulic pumps, attached to loading jacks, were turned-on and loading was applied on the specimen at a rate of 0.005±2 mm/minute until failure occurred. The temperature rise at the interface, the load applied, and the resulting deflection were recorded through a data acquisition system which are then analyzed to evaluate the load-displacement response of the bonded joint.

› Results for Bond Strength Tests

Data recorded in the above tests is utilized to evaluate the bond strength of CFRP-concrete interface at elevated temperatures. It was observed that at lower temperatures i.e., 20°C and 40°C, failure of the specimens occurred in cohesive mode, while at 60°C and 80°C, failure occurred in mixed cohesive-adhesive pattern, with a thin layer of concrete attached to the disbanded CFRP sheet. These failure patterns are shown in Figure 3.12 (a). The bond performance of CFRP-concrete system is evaluated using the average bond stress along the bonded length of the specimen [129]. The peak value of the average bond stress defined as the ratio of failure load to bonded area is taken as the bond strength of the specimen. At each target temperature two specimens were tested and the average of two values is taken as the bond strength of the CFRP-concrete interface. The load applied when the failure is reached and the computed bond strength of each specimen, as well as the average bond strength of the interface at each temperature, are summarized in Table 3.9.

It can be seen from the table that at same temperature level, the failure load from two tested specimen is nearly same indicating a minute scatter in the results. The average failure load of the specimens tested at room temperature (i.e., 20°C), is 26.13 kN, which is in close agreement with the theoretical value of failure load (27.10 kN) computed using the relation proposed by Chen and Teng (2001). Since the difference between the experimentally measured and theoretically computed failure load is only 3.3%, the measured failure load is taken as the actual failure load of the CFRP-concrete interface. At 40°C, the average failure load of the CFRP-concrete interface decreases slightly to 24.96 kN. At elevated temperatures, i.e., 60°C and 80°C, the failure load of the CFRP-concrete interface further decreases to 21.68 kN and 17.03 kN, respectively.

The load vs displacement response of a representative specimen tested at each target temperature is shown in Figure 3.12 (b). At each target temperature the load increases linearly with displacement till failure occurs in an abrupt pattern. It can be seen from the figure that at lower temperatures, the initial stiffness of the CFRP-concrete interface is nearly same, however, with increases in temperature the stiffness of the interface decreases at a faster rate. This can be attributed to the fact that with increase in temperature, the epoxy loosens which reduces the load transferring capability of the bonded joint thereby reducing the stiffness of the joint.

The bond strength of each specimen normalized with respect to average bond strength at 20°C, are summarized in Table 3.9 and the average of normalized bond strength at each temperature are plotted in Figure 3.12 (c). It can be seen from the Table 3.9 and Figure 3.12 (c) that the CFRP-concrete bond strength decreases progressively with increase in temperature. The decrease in bond strength is marginal (only 4%) at 40°C, but there is rapid decrease in bond strength to 83% and 65% of the room temperature strength at 60°C and 80°C, respectively. This deteriorating pattern in bond strength follows the same trends as reported in previous studies. Further, the bond strength retention factors reported in the previous studies are also plotted in Figure 3.12 (c). It can be seen from the figure that the bond strength retention factors measured in the current tests compare well with the previously reported trends.

3.6 Results from Fire Resistance Tests

Four fire resistance tests, designated as Test-I, Test-II, Test-III, and Test-IV, were conducted on FRP-strengthened concrete structural members, namely five beams (TB1 to TB5) and two slabs (S1, S2), to evaluate their response during fire exposure. Beams TB1 and TB2 were tested in Test-I, TB3 was tested in Test II, TB4 and TB5 were tested in Test-III, and slabs S1 and S2 were tested in Test IV. In these tests, beam TB1 was not protected with fire insulation, whereas beams TB2, TB3, TB4, TB5 and slabs S1, S2 were protected with 25 mm, 19 mm, 32 mm, 19 mm, 19 mm, 25 mm thick fire insulation, respectively. During these tests, temperatures, deflection, strains in rebars and concrete were recorded using the data acquisition system. In addition, visual observations were made through view ports to collect important information regarding beam specific events during fire test.

The data measured during these tests is utilized to analyze the performance of CFRP-strengthened concrete flexural members under combined effects of fire and structural loading. The performance is analyzed separately for beams (TB1 to TB5) and slabs (S1 and S2) through comparison of thermal response, and structural response. Through the analyses of thermal and structural response, the effect of different insulation thickness and configuration, different strengthening levels, and different load level on fire performance of CFRP-strengthened RC flexural members is evaluated. Details pertaining to the visual observations as well as the thermal and structural response of beams and slabs are presented in this section

3.6.1 Test Observations

The visual observations were made during the fire tests to record behavioral changes in specimens, such as, development of cracks in insulation, burning of epoxy, delamination of insulation or FRP, and cracking or spalling in concrete. These observations were recorded by taking videos and photographs through the two viewing ports located on front and back end of the furnace. Additionally, detailed visual observations were also taken after the natural cooldown of the specimens, to evaluate the extent of damage occurred during fire exposure.

In Test I (on beams TB1 and TB2), the epoxy in the primer putty and FRP started burning immediately within 2 minutes of start of fire exposure along the entire length of beam TB1, as shown in Figure 3.13 (a). The severe burning of epoxy lasted until 30 minutes into fire exposure and led to an increase in the size of the flames, as shown in Figure 3.13 (b), which in turn increased the temperature rise within the furnace. The severe burning of epoxy caused immediate debonding of FRP from the concrete surface, and after about 15 minutes of fire exposure, the fibers started burning as well and were completely detached from the concrete surface and broke apart from cool anchorage zones fibers. After 65 minutes into the fire test, flexural cracks started appearing at the mid-span of beam TB1, as shown in Figure 3.13 (b), indicating initiation of tensile damage in the beam due to degradation in tensile strength of concrete. Despite the crack progressions, the beam was able to support the applied loading until the end of fire exposure. The burned and detached fibers from the anchorage zone as seen after the test, are shown in Figure 3.13 (d).

In case of beam TB2, the epoxy did not start burning in the early stages of fire exposure due to the protection provided by U-shaped insulation. However, after about 25 minutes, the heat penetrated through the cracks in the insulation and softened the epoxy in the primer putty layer. As a result, the insulation at the mid-span extending up to the anchorage zone on one side fell off, exposing the primer putty coat and FRP laminate, as shown in Figure 3.14 (a). The delamination of insulation caused severe burning of epoxy which resulted in a sudden upsurge in the flames (*cf.* Figure 3.14 (a)) as well as the faster temperature rise within the furnace. After about 60 minutes of fire exposure, the remaining portion of the insulation fell off, exposing the FRP laminate to direct heat of fire. The burning of epoxy on the soffit of beam, as shown in Figure 3.14 (b), lasted until 90 minutes of fire exposure, at which point FRP was completely detached from the concrete surface and fibers had burned out. After 100 minutes, the flexural and longitudinal cracks start to appear on the sides of beam, as shown in Figure 3.14 (c), indicating tensile damage. Additionally, the FRP sheet in the center was completely cut off from the anchorage zone sheet (Figure 3.14 (d)), however, the beam survived three hours of fire exposure without any failure.

During Test II on beam TB3, behavior similar to that of beam TB2 was observed. The epoxy in primer putty layer of beam TB3 started burning after 15 minutes of fire exposure, due to heat penetration through the insulation cracks. Following this, part of the insulation delaminated after about 20 minutes of fire exposure causing upsurge in flames and temperature rise in the furnace, as shown in Figure 3.15 (a-b). The insulation delaminated completely after about 30 minutes of fire exposure, resulting in burning of epoxy and fibers in FPR which lasted until 100 minutes of fire exposure. After this, the beam continued to deflect under the applied load, however no flexural cracks were observed on the side as seen through the view port. Around 176 minutes, the loading jacks were unable to maintain constant pressure on the beam as the beam experienced significant deflection at a faster rate and suddenly failed through concrete crushing and steel yielding at the bottom, as shown in Figure 3.15 (c).

In Test III, carried out on beams TB4 and TB5, the visual observations were only noted on paper and not recorded as photographs or videos, this was due to the malfunctioning of the camera. The noted observations suggest that cracks were observed in the insulation of beams TB4 and TB5 after about 48 and 36 minutes of fire exposure, respectively. As the cracks widened and heat penetrated through these cracks, the FPR started burning after 73 and 69 minutes of fire exposure in beams TB4 and TB5, respectively. After about 175 to 180 minutes, the insulation on beam TB5 fell off which exposed the FRP directly to heat of fire. Similarly, the insulation on beam TB4 fell off after 210 minutes of fire exposure, exposing the FRP fibers to the heat of fire. Unlike in Test I and Test II, no upsurge in flames or temperature rise within the furnace was observed due to the insulation delamination. The beams survived four hours of fire exposure without any excessive deflection or strength failure. The condition of the beams TB4 and TB5 at the end of fire tests is shown in Figure 3.16 (a) and (b), respectively.

In Test IV, carried out on slabs S1 and S2, due to the relatively higher load applied on slab S2, the insulation started cracking even before the start of fire exposure. Whereas in case of slab S1, the cracks appeared on the insulation after 35 minutes of fire exposure. These cracks are shown in Figure 3.17 (a) for slab S1 and Figure 3.17 (b) for slab S2. After about 55 minutes of fire exposure, smoke was seen coming out of the insulation of both the slabs, indicating burning of polymer matrix or bonding adhesive, due to heat penetration through the cracks. The slow burning of epoxy continued as the cracks widened throughout the length of the slabs S1 and S2 until 160 minutes of fire exposure. However, there was no delamination of insulation from the soffit and sides of both the slabs. Towards the end of fire exposure, i.e., after 150 minutes, slab S2 started deflecting at a faster rate which was visible through the viewing port. However, both the slabs sustained the applied loading until the end of fire exposure without attaining failure. The condition of the slabs, i.e., detachment of FRP from the mid-span of slab S1 and splitting of FRP sheet from the anchorage zones in slab S2 are shown in Figure 3.17 (a) and (b), respectively.

3.6.2 Thermal Response

During the fire tests, the temperatures were recorded at various locations in the cross section of beams and slabs, namely FRP-concrete interface, bottom rebars (corner and middle), top rebars, mid-depth of concrete. In case of insulated beams TB2 to TB5 and slabs S1, S2, the temperature rise was also recorded at insulation-FRP interface, while in the uninsulated beam TB1, the temperature rise at the outer surface of the FRP sheet was recorded. Additionally, the gas temperature in the furnace was also recorded at eight different locations. The gas temperatures were utilized to determine the type of fire exposure during the tests, while cross-sectional temperatures were utilized to evaluate the thermal response of strengthened beams and slabs. Although the temperatures were measured at the quarter and mid-span sections, it was realized from the assessment of the test data that the temperature progression measured at both the sections follows similar trend. Therefore, only temperatures measured at the mid-span section of the beams and slabs are presented here.

(i) Furnace Fire Temperatures

Figure 3.18 shows a comparison of average furnace temperatures recorded in Test I, Test II, Test III, and Test IV with ASTM E119 [5] fire time-temperature curve. It can be seen from the figure that the furnace temperatures in all the tests are in close agreement with the ASTM E119 standard fire temperature in the early stages of fire exposure. However, after about 12-15 minutes of start of fire exposure, the furnace temperatures in all the tests start increasing at faster rate and exceed the corresponding ASTM E119 fire temperature at that time. A sudden upsurge followed by a drop in the furnace temperatures is observed in Test I and Test II at around 30 minutes and 45 minutes, respectively. This sudden increase in furnace temperature during Test I is attributed to burning of epoxy that is in FRP on uninsulated beam TB1. In Test II, the applied fire insulation on beam TB3 delaminated around minutes 30 minutes and thus, exposed the epoxy on the concrete surface leading to burning of epoxy at rapid pace. This burning of epoxy on the concrete surface increased the flame and heat within the furnace which in turn led to sudden increase in fire temperature within the furnace. The furnace temperatures during all the fire tests remain higher than the ASTM E119 fire temperature during the entire fire exposure duration. However, in all the fire tests, the difference between the cumulative area of the furnace time-temperature curve over three-hour (for Test I, Test II, and Test IV) and four hour (for Test III) duration of fire test and the intended time-temperature curve as per ASTM E119 is less than 5%. Thus, the furnace fire exposure is deemed to be acceptable as ASTM E119 Standard fire exposure for fire resistance evaluation as per ASTM E119 (2016) recommendations.

(ii) Temperature Rise at Insulation-FRP Interface

Figure 3.19 shows the temperature rise measured at insulation-FRP interface of beams TB2 to TB5, and at the outer surface of FRP in beam TB1. It can be seen from the figure that in case of uninsulated beam TB1, the temperature at the outer surface of FRP increases rapidly from the start of fire exposure, due to the direct exposure to heat of fire. The direct exposure to heat of fire results in rapid burning of epoxy along the length of the beam, which in turn further increases the temperature rise at the outer surface of FRP. The temperature at the outer surface of FRP increases beyond 750°C within 10 minutes of fire exposure, which is slightly less than the average furnace temperature (800°C) at that time. After this, the outer FRP surface temperature continues to increase rapidly at a faster rate and closely follows the average furnace temperatures.

In case of insulated beams TB2 to TB5, the insulation-FRP interface temperature increases slowly in the initial stages of fire exposure. The interface temperature in beam TB5, increases at a relatively faster rate as compared to beams TB2, TB3, and TB4. This may be due to the smaller thickness of insulation applied on beam TB5 and due to development of cracks within the insulation, near the thermocouple location, which led to increase in the heat flow to the interface resulting in faster temperature rise.

The interface temperature in beam TB4 plateaus from about 20 to 40 minutes of start of fire exposure, due to energy consumed in evaporation of free and chemically bound moisture in the insulation. However, no such plateau is observed in temperature rise at insulation-FRP interface of beams TB2, TB3, and TB5. Rather in case of beams TB2 and TB3, the insulation-FRP interface temperature increases abruptly to 850°C and 650°C after about 30 minutes and 25 minutes of fire exposure, respectively. The absence of evaporation plateau in beams TB2, TB3, and TB5 is attributed to the earlier crack formation in respective insulation layer. These cracks within the insulation result in quick evaporation of water, thereby reducing the plateau length.

The sudden upsurge in the temperature at insulation-FRP interface of beams TB2 and TB3 is attributed to the delamination of insulation along the entire length of both the beams, as confirmed through visual observations during Test I and Test II. The delamination of insulation during both the fire tests can be attributed to the putty primer coat applied on concrete surface of the beams, prior to applying the insulation. The putty layer was applied on the soffit and sides of beams TB2 and TB3, prior to spraying of insulation, to increase the adhesion between concrete and insulation. Since, the putty primer consists of epoxy polymer, it is very susceptible to elevated temperatures. As the cracks in the insulation layer of these beams widen, the heat penetration increases which leads to softening of primer and severe burning of epoxy, which in turn reduces the bond between concrete surface and insulation resulting in delamination.

Further it can be seen from Figure 3.19 that after 40 minutes, i.e., after the water evaporation plateau, the interface temperature in beam TB4 increases gradually until 180 minutes of fire exposure and then starts increasing rapidly until the end of fire exposure. This rapid increase is attributed to the widening of cracks in insulation layer, followed by localized delamination at 220 minutes which increases the interface temperature abruptly to 1000°C. Similarly, in case of beam

TB5, the insulation-FRP temperature increases gradually from 30 minutes of fire exposure until 170 minutes at which point the insulation-FRP interface temperature increases to 800°C. At 180 minutes, the interface temperature increases beyond 1000°C then follows the furnace temperature curve until the end of fire exposure. This sudden increase in temperature in both the beams was due to localized delamination of fire insulation at the mid-span of beam, which was confirmed through visual observations during the fire tests.

Figure 3.20 shows the temperatures measured at insulation-FRP interface of slabs S1 and S2. It can be seen from the figure that the interface temperature in both the slabs increases gradually in the initial stages of fire exposure (until 30 minutes) and do not experience any moisture evaporation plateau. After 30 minutes, the interface temperature in slab S2 starts increasing at a faster rate compared to that of slab S1. After 60 minutes, the interface temperature in slab S2 increases gradually until the end of fire exposure. The rapid increase in temperature between 30 to 60 minutes of fire exposure can be attributed to the increased heat flow from the cracks developed in insulation, due to higher load level applied on slab S2 during the fire test. However, a closer examination of the measured temperature rise at the quarter span (not presented here) indicates the expected trend, i.e., temperature rise in slab S1 is higher than that in slab S2, throughout the fire test duration. The insulation -FRP interface temperature in slab S1 decreases for a brief duration from 30 to 45 minutes of fire exposure and then starts increasing gradually until 120 minutes. At 120 minutes, the temperature starts increasing at a faster rate until 135 minutes of fire exposure, following this the temperature increases gradually until the end of test. The decrease in temperature after 30 minutes is due to the possible accumulation of dirt or formation of char layer on the thermocouple which hinders the measurement of actual temperature rise at the interface. Once the dirt or char layer dries out of the thermocouple at 120 minutes, the measured temperature rise increases at a faster rate to reach the actual temperature at the insulation-FPR interface and follow the same trend as that of insulation-FRP interface temperature in slab S2.

Due to the protection provided by the V-Wrap FPS fire protection system, the temperature at the FRP-concrete interface (thermocouple TC2) in both slabs remained below 300°C during the entire fire exposure duration, which is well below the decomposition temperature of polymer matrix.

(iii) Temperature Rise at FRP-Concrete Interface

The FRP-concrete interface temperature gives an indication on the condition of FRP and level of bond between FRP and concrete during the fire exposure. Figure 3.21 shows the temperatures measured at FRP-concrete interface at the mid-span of beams TB1, TB2, TB3, TB4, and TB5. As expected, due to the absence of any fire insulation, the temperature at the FRP-concrete interface in beam TB1 increases at a much faster rate and exceeds 400°C within ten minutes after the start of fire exposure, and then reaches 800°C at about 30 minutes of fire exposure. The rapid increase can also be attributed to the severe burning of epoxy on the outer surface of FRP, as mentioned earlier. The interface temperature continues to increase rapidly during the entire fire exposure duration, which leads to complete burning of epoxy and polymer matrix of FRP and as a result, FRP sheet turns into individual fibers detached from the beam.

In case of insulated beams TB2 to TB5, the interface temperature increases slowly in the initial stages of fire exposure at a relatively similar rate until 30 minutes of exposure. The FRP-interface temperature exceeds the adhesive T_g (82°C) after 30, 30, 45, and 20 minutes of fire exposure in beams TB2, TB3, TB4, and TB5, respectively. After about 30 minutes of fire exposure, the insulation delaminates from the surface of beams TB2 and TB3 and as a result the temperature at the FRP-concrete interface increases abruptly to 620°C and 780°C, respectively. The temperature at the FRP-concrete interface in beams TB2 and TB3, starts decreasing after 35 minutes and continues to decrease until 60-65 minutes, due to the formation of char layer resulting from the pyrolysis process of polymer matrix. After 65 minutes, the interface temperature increases rapidly, exceeding 950°C at 90 minutes of fire exposure and then closely follows the furnace fire temperature curve, indicating complete burning of polymer matrix and detachment of individual fibers from concrete surface.

In case of beams TB4 and TB5, the temperature at FRP-concrete interface continues to increase gradually with relatively higher temperatures in TB5 as compared to that of beam TB4, due to smaller thickness of insulation layer on TB5. At about 180 minutes of fire exposure, the interface temperature in beam TB5 increases abruptly to 800°C, due to localized delamination of fire insulation at the mid-span of beam TB5, and within 30 minutes, i.e., at 210 minutes of fire exposure, the interface temperature approaches the furnace fire temperatures. Similar behavior is observed in case of beam TB4 between 210 and 240 minutes of fire exposure.

Figure 3.20 shows the temperatures measured at FRP-concrete interface of slabs S1 and S2. The interface temperature in slabs S1 and S2 exceeds the adhesive T_g (82°C) after 35 and 40 minutes of fire exposure, respectively. A small plateau is seen in slab S2 between 25 and 35 minutes of fire exposure, possibly due to evaporation of water in insulation, resulting in slower temperature rise. Following the plateau, the interface temperature in both the slabs increases gradually at a similar pace throughout the fire exposure duration. Due to the protection provided by the V-Wrap FPS fire protection system, the temperature at the FRP-concrete interface in both slabs remained below 250°C during entire test duration, which is well below the decomposition temperature of polymer matrix.

(iv) Temperature Rise in Tension Rebars

During fire exposure, the capacity of an FRP-strengthened concrete flexural member is primarily governed by variation of strength properties of FRP and steel rebars, which are dependent on their temperature. Since strength properties of FRP degrade rapidly with increase in temperature, in the early stages of fire exposure, the applied loads (on the strengthened member) are sustained by the strength retained in steel rebars. The strength retained in steel rebars is indicated by the temperature level in the rebars, and therefore, the temperature rise was recorded in the corner and mid rebars at the bottom, throughout the test. Figure 3.22 shows the temperature rise measured at the corner and middle rebars of main tensile reinforcement (bottom rebars) of beams TB1 to TB5, as a function of fire exposure time.

It can be seen from Figure 3.22 (a-b) that the rebar temperatures in uninsulated beam TB1 increase at a relatively faster rate than that of insulated beams, throughout the fire exposure duration. In case of insulated beams TB2 to TB5, the rebar temperatures increase gradually at almost similar rate (in all the beams) in the early stages until 30 minutes of fire exposure. After 30 minutes, the rebar temperatures in beams TB2 and TB3 start increasing at a faster rate, compared to that in beams TB4 and TB5, and closely follows the rebar temperature rise in beam uninsulated TB1. The faster temperature rise is attributed to the delamination of insulation from the bottom surface of beams TB2 and TB3, as explained earlier. The temperature rise in mid-rebar of beams TB2 and TB3 is similar throughout the fire exposure duration, whereas the temperature rise in corner rebar of beam TB2 is faster and higher than that of beam TB3, even though beam TB2 has higher insulation thickness on the sides. This is attributed to the fact that insulation is extended only up to 75 mm on the sides of the beam TB2, while the insulation is extended up to 115 mm on the sided of beam TB3. Therefore, more heat penetrates from the side of beam TB2 compared to that of beam TB3 resulting in higher temperature rise in corner rebars of beam TB2.

Further it can be seen from Figure 3.22 (a-b) that in all the insulated beams, the corner and mid rebar temperatures experience a plateau at about 100°C, due to the evaporation of water from concrete. The plateau is more pronounced (longer) in mid rebars compared to that in corner rebars of all the beams. This is due to the fact that the concrete near the corner rebars is subjected to heat from two sides, i.e., bottom surface and side surface of beams. As a result, the temperature in the concrete near the corner rebar increases at a faster rate which increases the rate of water evaporation, resulting in a smaller plateau.

After overcoming the plateau, the temperature of the rebars continues to increase gradually during the entire fire exposure duration. The lowest temperature is recorded in beam TB4 due to the higher insulation thickness. The temperature in corner rebars of beams TB1, TB2, and TB3 exceeds 400°C at about 110, 120, and 130 minutes of fire exposure, respectively and then reaches 570°C at the end of fire exposure. In case of beams TB4 and TB5, the temperature in both corner and mid rebars remains below 350°C in beam TB4 and below 400°C in beam TB5, until the end of fire exposure. Thus, the maximum temperature in the main tensile reinforcement in all the beams remains below 593°C, at the end of fire exposure duration. This indicates that there is minimal degradation in the strength properties of steel rebars.

Figure 3.23 shows the time-temperature progression measured in the corner and mid rebars of slabs S1 and S2. It is clear from the figure that the temperature in the rebars increases at a very slow rate until end of fire test. Further, there is negligible difference in the temperature rise at same locations in both the slabs. This is attributed to the relatively smaller difference in the thickness of fire insulation. Moreover, the higher load level applied on slab S2 might have induced cracks in the applied insulation layer, which increased the heat flow within the section, thereby increasing temperature rise. Further, it can be seen that the temperature in steel rebars remains below 300°C in both the slabs S1 and S2, until the end of fire test. Therefore, it can be inferred that the steel rebars experience minimal degradation in their strength and modulus properties and as a result, the slabs retain most of their strength and stiffness until the end of the test.

(v) <u>Temperature Rise in Concrete</u>

Figure 3.24 compares the temperature progression measured at mid depth of concrete section, i.e., 203 mm of beams TB1 to TB5. During casting, the thermocouple positioned at the mid-depth of beam TB2 was damaged, and therefore, the temperatures were not recorded in beam TB2. It can be seen from the figure that the temperature at the mid-depth of concrete increases gradually in all the beams throughout the fire exposure duration. In the uninsulated beam TB1, the temperature rise at the mid-depth of concrete reaches 100°C after 45 minutes of fire exposure, whereas in the insulated beams TB3, TB4, and TB5 the concrete mid-depth temperature reaches 100°C after 60 minutes of fire exposure. After reaching 100°C, the temperature rise in each of the beams TB1, TB3, TB4, and TB5 sustains a plateau for about 30 minutes, due to the evaporation of water from concrete.

Further, it can be seen from the figure that after the water evaporation plateau, the mid depth temperatures in beams TB1 (uninsulated) and TB3 (25 mm thick insulation) increase at a similar rate for the remainder of fire exposure duration. This can be attributed to the delamination of insulation along the length of the beam TB3, which rendered the beam uninsulated, resulting in higher heat transmission and hence, faster temperature rise within the section. In case of beams TB4 and TB5, the mid depth temperature increased gradually until the end of fire exposure. However, at any time instant the temperature rise in beam TB4 was slightly lower than that in beam TB5, due to thicker insulation layer applied on TB4 than that on TB5. At the end of fire tests, the highest temperature recorded at the mid-depth of cross-section of beams TB1, TB3, TB4 and

TB5 was 250°C, 250°C, 250°C and 270°C, respectively. Since the strength and modulus properties of concrete start degrading only after 400°C (Lie, 1992; Eurocode-2 2004), it can be concluded that there was no loss of strength and stiffness in concrete of all the beams.

Figure 3.23 shows the temperature rise at the mid-depth of concrete in slabs S1 and S2. It can be seen from the figure that the temperature in both the slabs increases gradually at a similar rate throughout the fire exposure duration. The mid depth temperature in slabs S1 and S2 reaches 100°C after 90 minutes of fire exposure but does not experience any water evaporation plateau. At the end of fire exposure, the mid depth temperature in slabs S1 and S2 reaches 150°C, indicating the strength and modulus properties of concrete are intact throughout the duration of the fire exposure.

3.6.3 Structural Response

During the fire tests, beams TB1, TB2, TB3, TB4, and TB5, were subjected to structural loading equivalent to 51%, 51%, 60%, 56%, and 54% of their respective ultimate strengthened capacity at room temperature. While the slabs S1 and S2 were subjected to structural loading equivalent to 48% and 60% of their respective ultimate strengthened capacity (at room temperature). The structural response of the tested beams and slabs is compared in Figure 3.25, by plotting the measured mid-span deflection as a function of fire exposure time. Figure 3.25 (a) shows the mid-span deflection measured in beams, whereas Figure 3.25 (b) shows the mid-span deflections measured in slabs.

It can be seen from Figure 3.25 (a) that the deflection in uninsulated beam TB1 increases at a relatively faster rate from the start of fire exposure. Due to the direct exposure of FRP to the heat of fire in beam TB1, the composite action between FRP and concrete was completely lost within first ten minutes of fire exposure, and as a result the beam experienced faster deflection. After 10 minutes, the beam behaved as an un-strengthened RC beam subjected to higher loads, and therefore the beam TB1 deflects at relatively faster until 165 minutes of fire exposure. After 165 minutes, the temperature in rebars exceeds 400°C (*cf*. Figure 3.22), which initiates degradation of strength and modulus properties of rebars. As a result, the deflection in beam TB1 starts increasing rapidly and exceeds the deflection limit at about 180 minutes.

In case of insulated beams TB2 and TB3, the deflection increases gradually in the initial stages of fire. However, after 30 minutes of fire exposure the insulation delaminated from the soffit of the beams rendering them as FRP-strengthened uninsulated beams. Due to the delamination, the temperature rise at the FRP-concrete interface increases rapidly which causes degradation of bond between FRP and concrete which in turn reduces the composite action between FRP and concrete. Moreover, the rapid temperature rise causes rapid degradation of strength and modulus properties of FRP. As a result, the stiffness of the beams decreases resulting in faster deflection.

Further, it can be seen from the Figure 3.25 (a) that despite the same load level, the deflection in beam TB2 is lower than the deflections in beam TB1 and remains below the deflection limit until the end of fire exposure. This is attributed to the fact that the temperature rise at the FRP-concrete interface and rebars of beam TB2 was slower than that of beam TB1, which reduced the degradation in strength and modulus properties of FRP and rebar, which in turn reduces the degradation in stiffness of beam, thereby reducing deflection in beam TB2. Additionally, beam TB3 was subjected to much higher load level than that of beams TB1 and TB2, and therefore, beam TB3 had higher deflection than beam TB2.

The deflection in beam TB3 is higher than deflection in beam TB2 throughout the fire exposure duration and are similar to that of deflection in beam TB1 until 150 minutes of fire exposure. This is attributed to the fact that beam TB3 was subjected to higher load level compared to that of beams

TB1 and TB2. After 150 minutes beam TB3 starts deflecting at a much faster rate than that of beam TB1. This is attributed to the fact that after 150 minutes of fire exposure, the temperature in rebars of beams TB1 and TB3 increases beyond 400°C, which leads to degradation of strength and modulus properties of steel rebars in both the beams. The higher load levels accompanied with faster degradation in strength and modulus of steel rebars, causes beam TB3 to degrade at a much faster rate than beam TB1. The deflection in beam TB3 exceeds the deflection limit at 165 minutes of fire exposure, while the rate of deflection exceeds the rate limit in after 176 minutes of fire exposure and at the same time the beam is unable to support the applied structural loading indicating failure in strength and deflection limit states.

In case of beams TB4 and TB5, the deflection (in both beams) increases gradually at the same rate in the initial stages of fire exposure. The deflection starts increasing rapidly after about 150 minutes and 120 minutes of fire exposure, in beams TB4 and TB5, respectively. This is due to the complete degradation of CFRP-concrete interfacial bond as the interface temperature exceeds above 200°C in beam TB4 and above 250°C in beam TB5, which is significantly higher than the adhesive T_g (80°C). The degradation of bond leads to complete loss of CFRP-concrete composite action, which in turn reduces the stiffness of the beams. An important point to note here is that the deflection in beams increases rapidly at a much later stage in fire exposure, even though the temperature at the FRP-concrete interface of beams TB4 and TB5 exceeds the adhesive T_g at 44 minutes and 18 minutes of fire exposure, respectively. This infers that attainment of T_g at the interface does not lead to an immediate loss of bond between FRP-concrete, and hence, FRP continues to contribute to the strength and stiffness of beams at temperatures much higher than adhesive T_g.

In both the beams, deflection remains relatively small until the end of fire exposure, i.e., four hours. The maximum deflection at the end of four hours, in beams TB4 and TB5 was 27 mm and 40 mm, respectively. These lower deflections can be attributed to lower temperature in reinforcing bars and concrete, as discussed in previous section, which reduced degradation in strength properties of steel and concrete, which in turn reduced the deflection of the beams. Additionally, the CFRP sheets in the cooler anchorage zones of the beams remained intact. Therefore, carbon fibers detached from the beam at the mid-span, due to bond degradation, continued to carry the tensile forces through cable mechanism, thereby reducing deflection in the beams. Similar behavior was reported by Ahmed and Kodur [147], Firmo et al. [163], and Firmo and Correia [149]. Overall, both the beams TB1 and TB2 sustained applied load without failure for entire duration of fire exposure. The maximum deflection at the end of fire exposure, in beams TB1 and TB2 was 30 mm and 16 mm, respectively.

Figure 3.25 (b) compares the measured progression of deflection in slabs S1 and S2 during the entire fire exposure duration. It can be seen from the figure that deflection in both the slabs fluctuates abruptly during the entire fire test. This is attributed to the problems encountered in maintaining exact level of loading during fire test, wherein actuators with a capacity of 2720 kN were used for loading the two slabs. The hydraulic system connected to these actuators is capable of maintaining desired preset load by automatically adjusting required hydraulic pressure to match initially set pressure in the system. However, the accuracy in adjusting hydraulic pressure range goes down at very low levels of loading as compared to capacity of actuators (typically below 5% of the actuator capacity). Since, the level of applied loading on slabs S1 and S2 represented less than 1% of full capacity of these actuators, the required hydraulic pressure in these actuators was very low. Due to this low hydraulic pressure, maintaining required loading necessitated frequent manual readjustment of hydraulic pressure in the actuators throughout the fire test. This resulted in slight fluctuation in applied loading (±10% of load level on slabs).

Nevertheless, it can be seen from the figure that the deflection in slab S1 increases gradually and remains low throughout the fire test, whereas, in case of slab S2 the deflection increases very rapidly from the beginning of fire exposure despite the low temperature in concrete and steel rebars. This can be attributed to the relatively higher loading applied on the slab S2 as compared to slab S1. Due to the relatively higher loading, slab S2 experiences a surge in the deflection (runoff deflection) at about 150 minutes. However, this increase in deflection does not lead to failure of the slab S2. The maximum deflection at the end of fire exposure, in slabs S1 and S2 is 39 mm and 100 mm, respectively.

3.6.4 Fire Resistance

The fire resistance tests were carried out on the five FRP-strengthened RC T-beams and two FRP-strengthened RC slabs as per the provisions of ASTM E119 [5]. Therefore, the failure of beams is determined based on temperature, strength and deflection limit states, specified in ASTM E119 [5]. The time at which failure is attained is defined as the fire resistance of a structural member. The results from the fire resistance tests are summarized in Table 3.10.

Beams TB1, TB2, and TB3 were subjected to three hours of ASTM E119 standard fire exposure, while beams TB4 and TB4 were subjected to four hours of ASTM E119 standard fire exposure under sustained structural loading. At the end of fire exposure, the maximum temperature attained in tensile reinforcement of beams TB1, TB2, TB3, TB4, and TB5 were 570°C, 570°C, 550°C, 293°C, and 400°C, respectively. These temperatures are below the critical temperature 593°C for steel reinforcement specified in ASTM E119 [5]. This indicates that the beams ad slab did not experience thermal failure as per the ASTM E119 [5] prescriptive criteria.

The maximum mid-span deflection in beams TB1, TB2, TB3, TB4, and TB5 was recorded as 84 mm, 65 mm, 108 mm, 16 mm, and 30 mm, respectively. The deflection in beam TB2, TB4, and TB5 was much lower than the critical deflection limit of ($L_c^2/400d$ = 84 mm, where L_c is the span of the beam and d is the overall depth of beam) specified in ASTM E119 (2016), whereas deflection in beams TB1 and TB3, were close to/exceeded the critical deflection limit. However, the rate of increase of deflection in beam TB3, was much lower than the critical rate limit 3.42 mm/min. Therefore, as per ASTM E119 specifications, beams TB1 and TB2 achieved fire resistance more than three hours, beams TB3 achieved three hour of fire resistance, while beams TB4 and TB5 achieved more than four hours of fire resistance, under standard fire conditions.

During the entire fire exposure duration of three hours, the maximum temperature reached in the tensile steel rebars of slabs S1 and S2 was 316°C and 232°C, respectively. These temperatures are below the critical temperature 593°C for steel rebars as per ASTM E119 (2016) specifications. The maximum mid-span deflection in slabs S1 and S2, during the fire exposure time, was 39 mm and 101 mm, respectively. These deflection values are well below the critical limit ($L_c^2/400d$ = 219.4 mm) specified in ASTM E119 (2016). Moreover, slabs S1 and S2 sustained the applied service loads throughout fire exposure duration. Thus, both the slabs performed satisfactorily during fire exposure and achieved at least three-hour fire resistance as per ASTM E119 criterion.

3.7 Tests for Residual Capacity Evaluation

In the above fire resistance tests, beams TB1, TB2, TB4, TB5, and slabs S1, S2 were able to sustain the applied structural loading throughout the fire exposure duration without undergoing failure. Following the cool down of the beams and slabs, they were tested to evaluate the post-fire residual capacity of respective members. Details pertaining to the procedure followed and relevant response parameters measured in residual tests are presented here.

3.7.1 Test Procedure

For the residual capacity tests, the beams and slabs were allowed to cool down naturally in the furnace for 24 hours, with the temperatures in the cross-section continuously monitored. When the main tensile reinforcement rebar temperatures were below 50°C, the beams and slabs were tested under monotonic structural loading using the same test setup as used in the fire tests. During the residual capacity tests the flexural members (beams and slabs) were loaded incrementally at the rate of 5kN/minute until failure, while the compounding mid-span deflections were recorded. The results from the tests are described below, while the failure load and failure mode for each of these beams and slabs are summarized in Table 3.10.

3.7.2 Results from Residual Tests

The load-deflection response of the beams TB1, TB2, TB4, and TB5 is shown in Figure 3.26 (a). It can be seen from the figure that the mid-span deflection increases linearly with applied load in all the beams. The slope of load-deflection curves for the beams TB1, TB2 and beams TB4, TB5 changes (reduces) when the applied load exceeds 145 kN and 150 kN, respectively, indicating onset of steel yielding. Following the initiation of steel yielding, the beams TB1, TB2, TB4, and TB5 continue to deflect rapidly with increase in applied loading and attain their maximum capacity of 176 kN, 200 kN, 157 kN and 189 kN, at a mid-span deflection of 118 mm, 153 mm, 81 mm, and 78 mm, respectively. The beams TB1 and TB2 failed through yielding of steel rebars followed by concrete crushing, whereas beams TB4 and TB5 failed through yielding of steel rebars, as shown in Figure 3.27.

The loads sustained by the beams TB1, TB2, TB4, and TB5are much higher than their respective ultimate un-strengthened capacity at room temperature. The higher residual capacity can be attributed to the fact that, in both the beams, the temperature in the compressive region of concrete above the neutral axis was below 200°C and the temperature of steel rebars was way below 593°C, during the entire fire exposure duration. Hence, the concrete and steel rebars were able to retain much of their original strength and modulus properties. Additionally, the small temperature rise in the steel rebars might have increased the yield strength and ultimate tensile strength of the steel rebars due to the heating and cooling cycle. This was confirmed by testing steel rebars cut from the edges of beams TB1 and TB2 after the residual capacity tests. Hence, the lower degradation in strength and modulus of concrete and steel, increase in strength of steel rebars due to heat treatment, as well as strain hardening in steel rebars resulted in higher residual capacity of the beams.

Figure 3.26 (b) shows the total load vs deflection response of slabs S1 and S2, as recorded during the residual capacity tests. It can be seen from the figure that the deflection in both the slabs increases almost linearly with the increase in applied load up to about 30 kN. Beyond this the slope of the load-deflection curves changes and the deflection in both the slabs increases rapidly for small increase in load, indicating initiation of steel yielding. The slabs S1 and S2, attain their maximum load capacity at 41 kN and 42 kN and corresponding deflection of 112 mm and 104 mm, respectively. Both the slabs fail through yielding of steel rebars followed by crushing of concrete (only in slab S1). The failure patterns are shown in Figure 3.28.

The total load capacities of slabs S1 and S2 as obtained from the residual tests is much higher than the original un-strengthened capacity and very close to 100% ambient temperature strengthened capacity of the slabs (*cf.* Table 3.5). These high load capacities can be attributed to the fact that the temperature of the compressive region of concrete remains below 200°C and the temperature of the tensile reinforcement remains below 593°C, during entire fire exposure time. Thus, just like in the beams, concrete and steel rebars in slabs S1 and S2 retain much of their original strength. Additionally, the bond between FRP and concrete in the cooler anchorage regions is intact due to minimal temperature rise. As a result, the carbon fibers at the center continue to contribute toward the load capacity of the slabs through arch action. Thus, the residual capacity of slabs is higher than the original un-strengthened capacity.

3.8 Summary

Fire resistance tests were conducted on five FRP-strengthened RC T-beams and two FRP-strengthened RC slabs to evaluate the performance of FRP-strengthened concrete flexural members under combined effect of fire and structural loading. Results from the fire tests indicate that the presence of insulation can delay the temperature rise at the FRP-concrete interface and the steel, thereby delaying the bond degradation between FRP and concrete and reducing the degradation in strength and modulus of steel rebars. Moreover, a minimum insulation depth equivalent to twice the effective concrete cover (to rebars) on the sides of the beam reduces the temperature rise in the rebars which in turn reduces the deflection in the beams during fire exposure. Further, applying a primer putty layer prior to spraying of insulation reduces the bond between insulation and concrete surface leading to early delamination of insulation and this is due to the combustible nature of epoxy. Additionally, it was evident from the tests that applying low level of strengthening can significantly increase the fire resistance of the strengthened member, as the loads applied on these members are within the capacity of un-strengthened concrete member. Results from these tests is utilized to validate numerical model developed for evaluating performance of FPR-strengthened concrete flexural members.

Table 3.1: Geometric details of T-beams and slabs for fire resistance tests

Property			T-Beams			Slabs
Specimen designation			TB1, TB2, TB3	TB4	TB5	S1, S2
Length (m)			3.96	3.96	3.96	3.96
Clear span (m)			3.66	3.66	3.66	3.66
Cross-section (mm)			flange: 432 × 127 web: 254 × 279			400 × 152
Rebar diameter and spacing or quantity	Longitudinal	Top	4-12 mm ϕ	4-12 mm ϕ	4-12 mm ϕ	NA
		Bottom	3-16 mm ϕ		3-19 mm ϕ	3-12 mm ϕ
	Transverse		10 mm ϕ @ 305 mm c/c			8-12 mm ϕ @ 458 mm c/c
	Stirrups		10 mm ϕ @ 152 mm c/c			NA
Concrete cover thickness (mm)			38	38	38	19
Design concrete strength (MPa)			35	35	35	35
Design yield strength (MPa)			420	420	420	420
Nominal un-strengthened capacity based on design strength (kNm)			86.4	86.4	117.6	18.5

Table 3.2: Batch mix proportions of concrete used for casting the test specimens

Material/Parameter		Quantity	
		Mix-1	**Mix-2**
Cement (kg/m^3)		335	312
Fine aggregates (kg/m^3)		790	838
Coarse aggregates (kg/m^3)		1032	970
Fly ash (kg/m^3)		0	78
Water (kg/m^3)		151	140
Water/cement ratio		0.45	0.40
Air		5.5%	6.0%
Fine aggregate ratio		0.45	0.45
Fine aggregate moisture		4.00%	4.00%
Coarse aggregate moisture		1.00%	1.00%
Slump (mm)		100	100
Unit weight of concrete (kg/m^3)		2410	2340
Compressive strength (MPa)	7 days	30.9	31.8
	14 days	35.2	36.5
	28 days	38.2	43.2
Split tensile strength (MPa)	28 days	2.8	3.1

Table 3.3: Strength properties of constituent materials used in fabricating test specimens

Material	Property		Values for Test Specimens			
			TB1, TB2, TB3	TB4	TB5	S1, S2
Concrete	Compressive strength (f'_c , MPa)	28 days	38	43	43	43
		Test day	42	46	46	48
Steel	Yield strength of rebars (f_y, MPa)		440	460	450	545
FRP	Ultimate tensile strength (f_u, MPa)		1034	1172	1172	1172
	Elastic modulus (E_f, GPa)		73770	96500	96500	96500
	Rupture strain (ε_u, %)		1.4	1.1	1.1	1.1

Table 3.4: Geometrical details of materials used in strengthening and fire insulation

Test Specimen	TB1	TB2	TB3	TB4	TB5	S1	S2
Strengthening material	CFRP V-Wrap C200H			CFRP V-Wrap C200HM		CFRP V-Wrap C200HM	
No. of layers of CFRP	1						
Laminate thickness (mm)	1.00			1.02		1.02	
Width of FRP (mm)	170			100		75	
Insulation thickness (mm)	0	25	19	32	19	19	25
Insulation depth on sides (mm)	0	75	112	152	152	152	152

Table 3.5: Summary of parameter evaluated, actual capacity of test specimens, applied thermal and structural loading and applied load ratio

Test Number	**Test I**		**Test II**	**Test III**		**Test IV**	
Specimen tested	TB1	TB2	TB3	TB4	TB5	S1	S2
Parameters evaluated	Insulation thickness and configuration		Load level	Insulation thickness, strengthening levels and load level		Insulation thickness and load level	
Nominal un-strengthened capacity based on actual strength of concrete and steel rebars (kNm)	90.4		90.4	93	126	24	
Nominal strengthened capacity (kNm)	127		127	119	152	31	
Increase in flexural capacity (%)	41		41	28	20	30	
Total applied load (kN)	98	98	116	97	128	21	26
Bending moment due to applied loading (kNm)	68.5	68.5	81.2	69.4	91.5	15.0	18.6
Applied load ratio (%)	51	51	61	51	54	48	60
Fire scenario	ASTM E119						
Fire exposure duration (hours)	3		3	4		3	

Table 3.6: Test matrix for tensile strength tests and bond strength tests

Tensile Strength Test		**Bond Strength Test**	
Test Temperature	**No. of Specimens**	**Test Temperature**	**No. of Specimens**
20°C	4	20°C	2
40°C	3	40°C	2
60°C	3	60°C	2
80°C	3	80°C	2
Total Specimens	**13**	**Total Specimens**	**8**

Table 3.7: Properties* of the carbon fabric, epoxy and CFRP laminate

Material	**Ultimate tensile Strength (MPa)**	**Elastic Modulus (GPa)**	**Ultimate Strain (%)**	**Glass Transition Temperature T_g (°C)**
V-wrap C200H dry carbon sheet	4830	22.75	2.1	-
V-wrap 770 epoxy	60.7	2.76	4.4	82
V-wrap C200H cured laminate	1240	73.77	1.7	Not available

*As per manufacturer

Table 3.8: Summary of results obtained from tensile strength test of CFRP coupons at elevated temperatures

Sr. No.	Test Temperature (°C)	Failure Load (kN)	Tensile Strength (MPa)	Average Strength (MPa)	Standard Deviation (MPa)	Co-efficient of Variation (%)	Retained Stress Ratio
1	20	23.22	910.6	1180.9	267.8	22.7	0.77
2	20	37.84	1483.9				1.26
3	20	23.41	918.0				0.78
4	20	35.98	1411.0				1.19
5	40	21.78	854.1	1153.6	264.0	22.9	0.72
6	40	28.31	1110.2				0.94
7	40	38.16	1496.5				1.27
8	60	26.69	1046.7	1010.2	27.7	2.7	0.89
9	60	24.98	979.6				0.83
10	60	25.61	1004.3				0.85
11	80	24.18	948.2	928.2	15.2	1.6	0.80
12	80	22.57	885.1				0.75
13	80	24.26	951.4				0.81

Table 3.9: Summary of bond strength tests results

Sr. No.	Test Temperature	Failure Load (kN)	Bond Strength (MPa)	Average Strength (MPa)	Retained Strength Ratio	Normalized Strength Ratio
1	20°C	28.10	1.45	1.35	1.08	1.00
2	20°C	24.16	1.25		0.92	
3	40°C	24.19	1.25	1.29	0.93	0.96
4	40°C	25.73	1.33		0.98	
5	60°C	21.10	1.09	1.12	0.81	0.83
6	60°C	22.26	1.15		0.85	
7	80°C	17.43	0.90	0.88	0.67	0.65
8	80°C	16.63	0.86		0.64	

Table 3.10: Summary of the results from fire resistance tests and residual capacity tests of FRP-strengthened concrete flexural members

Flexural member	**T-Beams**					**Slabs**	
Test specimen	TB1	TB2	TB3	TB4	TB5	S1	S2
Maximum temperature in tensile reinforcement (°C)	570	570	550	293	400	316	232
Deflection at failure/ end of fire exposure (mm)	84	65	108	16	30	39	101
Fire resistance (minutes)	180*	180*	176	240*	240*	180*	180*
Failure limit state in fire test	No failure	No failure	Strength and deflection	No failure	No failure	No failure	No failure
Residual capacity (kNm)	123	140	0	110	132	29	29
Total load at failure in residual test (kN)	176	200	0	157	189	41	42
Deflection at failure in residual test (mm)	118	153	0	81	78	112	104
Failure mode in residual test	Rebar yielding with concrete crushing		NA	Rebar yielding		Rebar yielding	

* The specimen did not fail during entire fire exposure duration

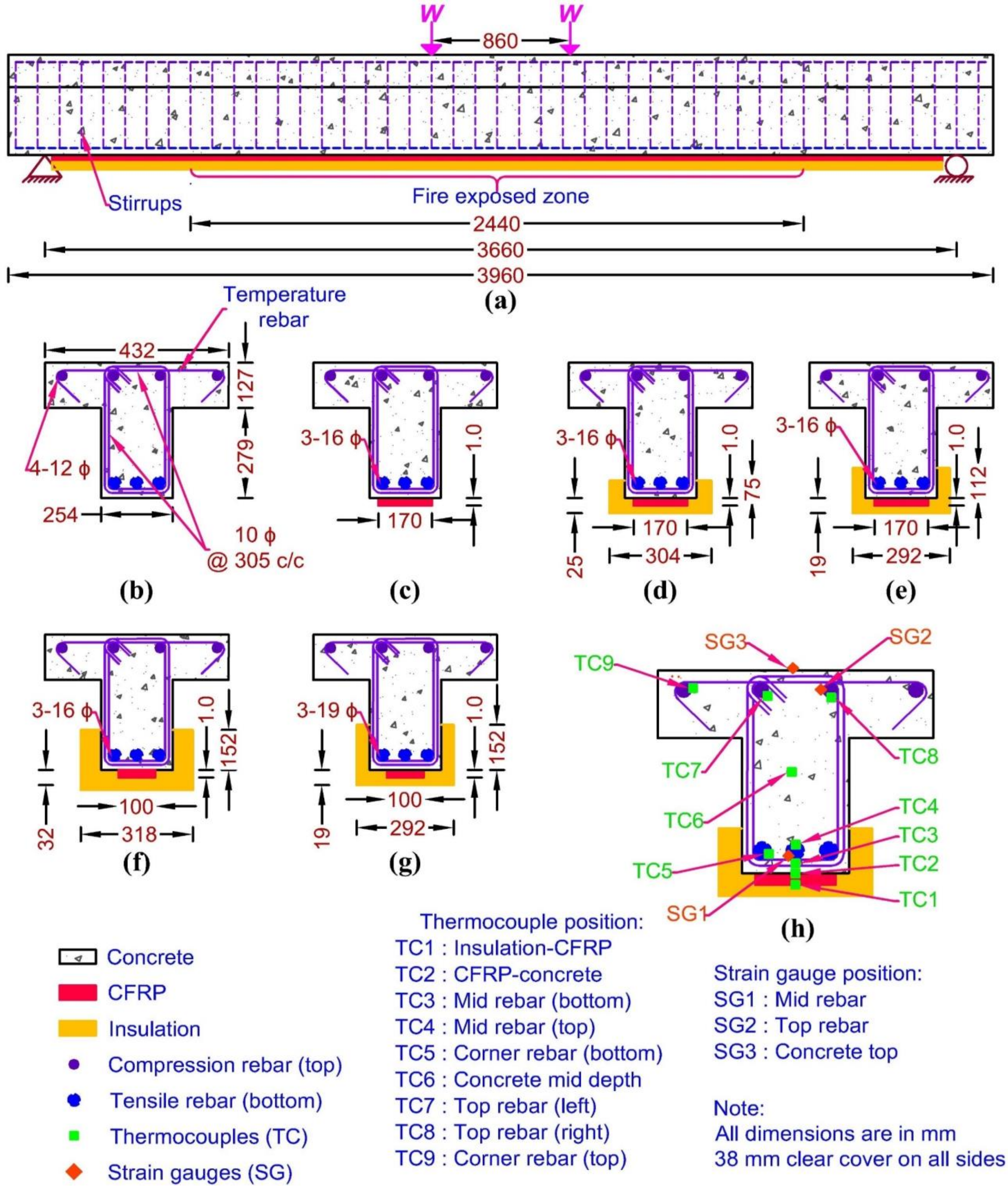

Figure 3.1: Geometrical and instrumentation details of tested beams: (a) dimensions in elevation; (b) cross-section dimensions; (c-g) FRP and insulation layout for beams TB1 to TB5; (h) thermocouple and strain gauge locations

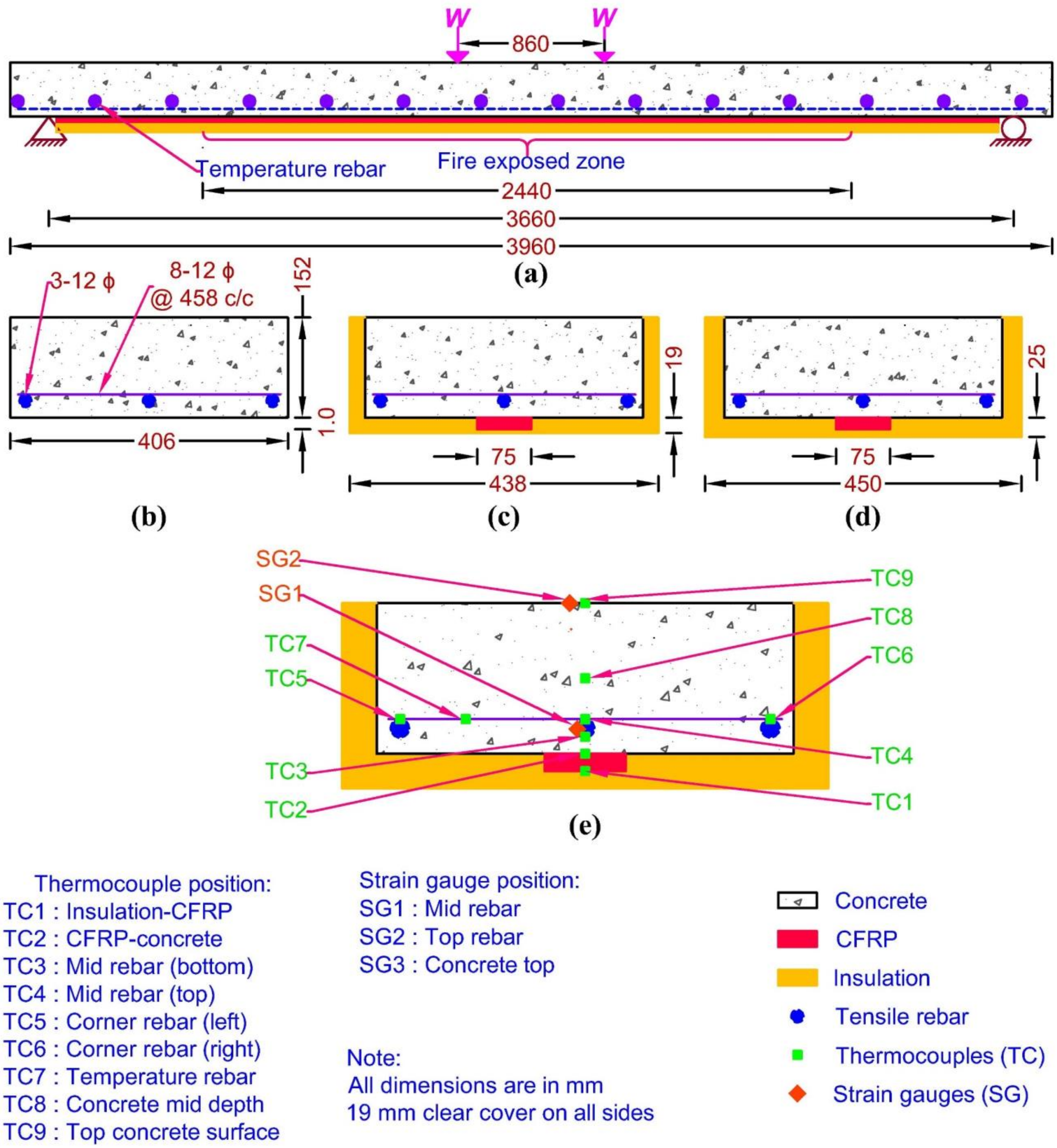

Figure 3.2: Geometrical dimensions and instrumentation details of tested slabs: (a) dimensions in elevation; (b) cross-section dimensions; (c) insulation layout for slab S1; (d) FRP and insulation layout for slab S1; (e) thermocouple and strain gauge locations

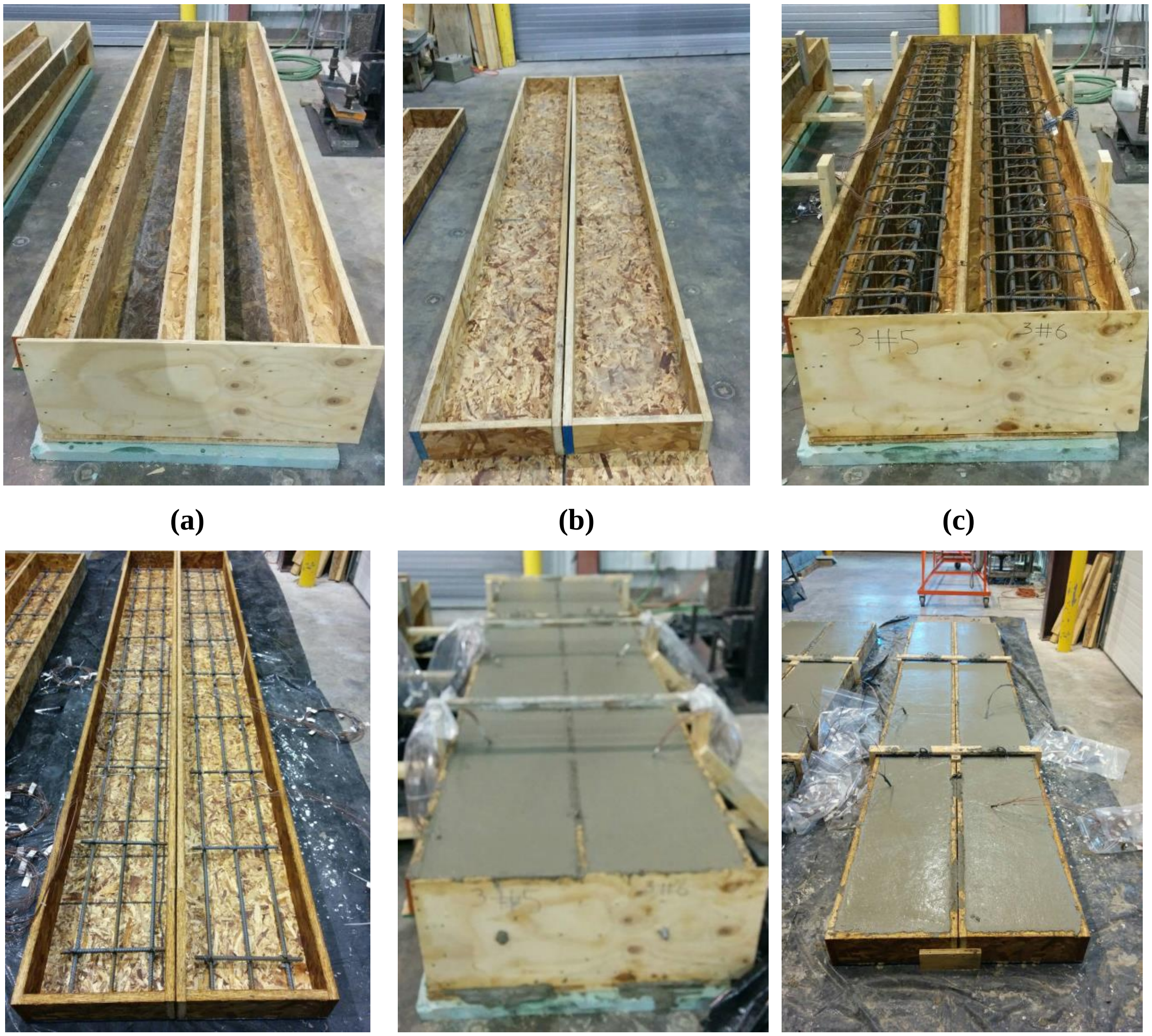

(a) (b) (c)

(d) (e) (f)

Figure 3.3: Fabrication of specimens: (a-b) formworks for T-beams and slabs; (c-d) steel cage and mesh in formworks for T-beams and slabs; (e-f) poured concrete and completed specimens

(a) **(b)**

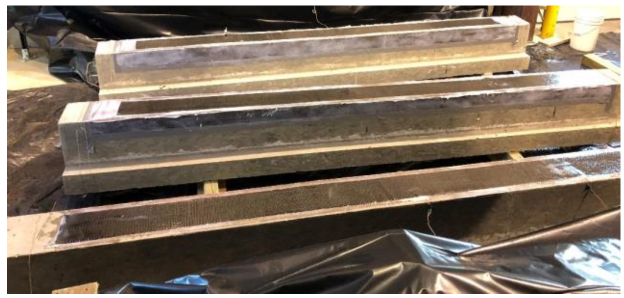

(c) **(d)**

(e) **(f)**

Figure 3.4: Stages of CFRP installation: (a) epoxy layer application on surface; (b) applying putty primer on top epoxy; (c) saturating the CFRP with epoxy; (d) roller application of CFRP; (e) completed beams with finished FRP strengthening and putty primer coat; (f) completed slab with FRP strengthening without any putty primer coat on top of FRP

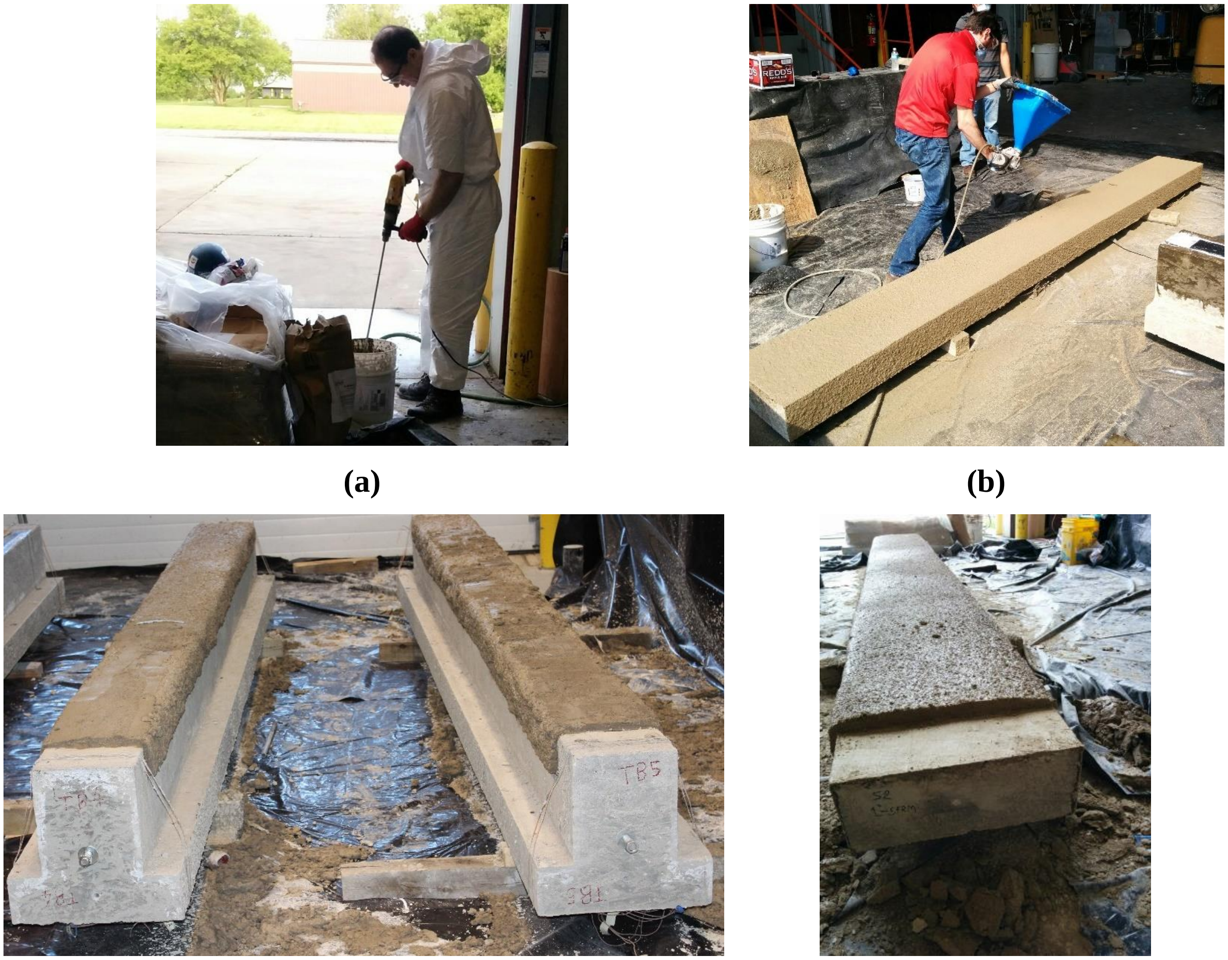

(a) (b)

(c) (d)

Figure 3.5: Different stages of installing insulation on FRP-strengthened RC beams and slabs: (a) mixing powder with water; (b) spraying on the strengthened member; (c) insulated T-beams; (d) insulated slab

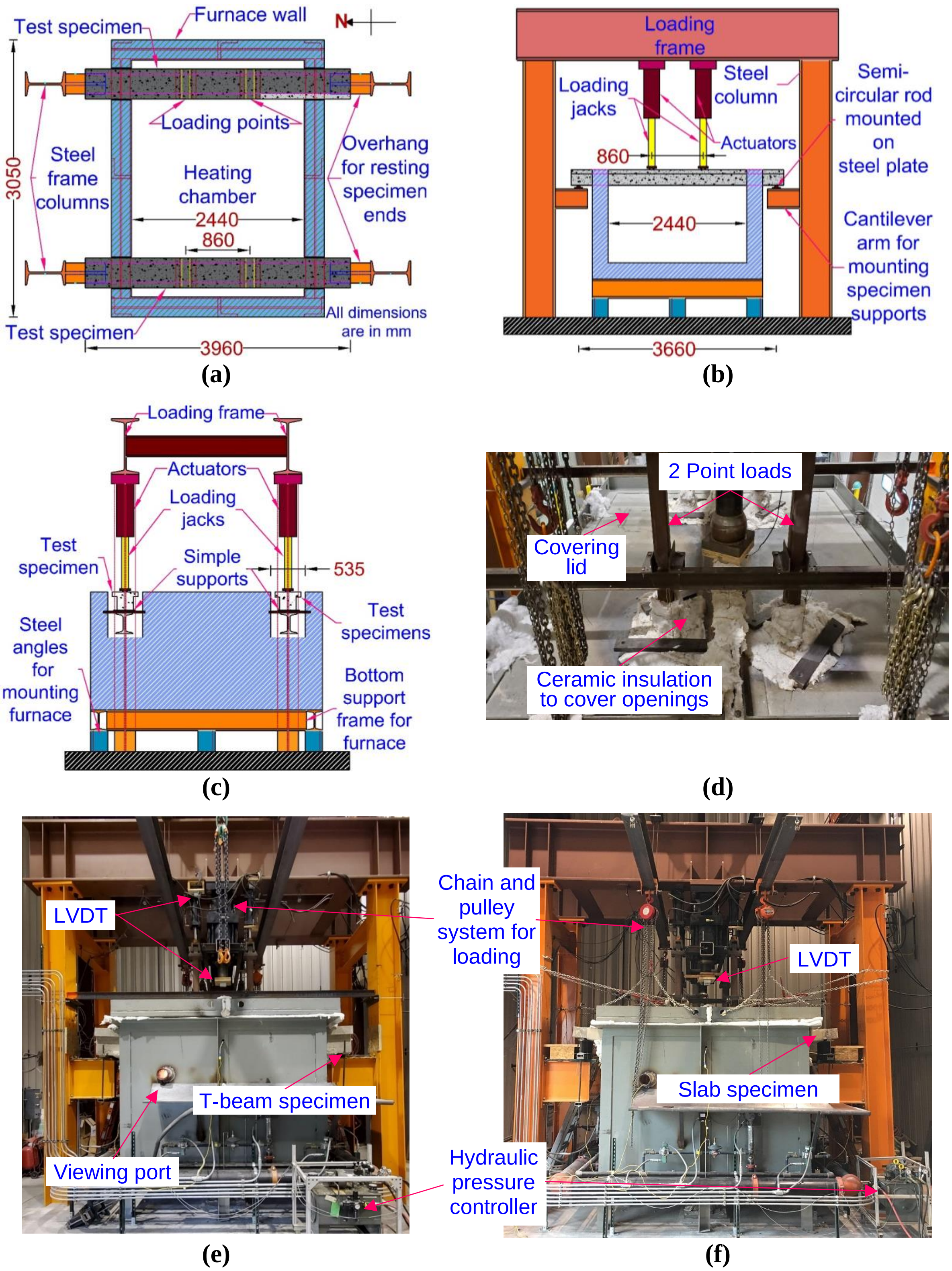

Figure 3.6: Structural fire test furnace at MSU's Civil Infrastructure Laboratory with specimen loaded: (a) plan view; (b) front view (EW elevation); (c) side view (NS elevation); (c) plan (d) loading arrangement; (e) T-beam in furnace; (f) slab in furnace

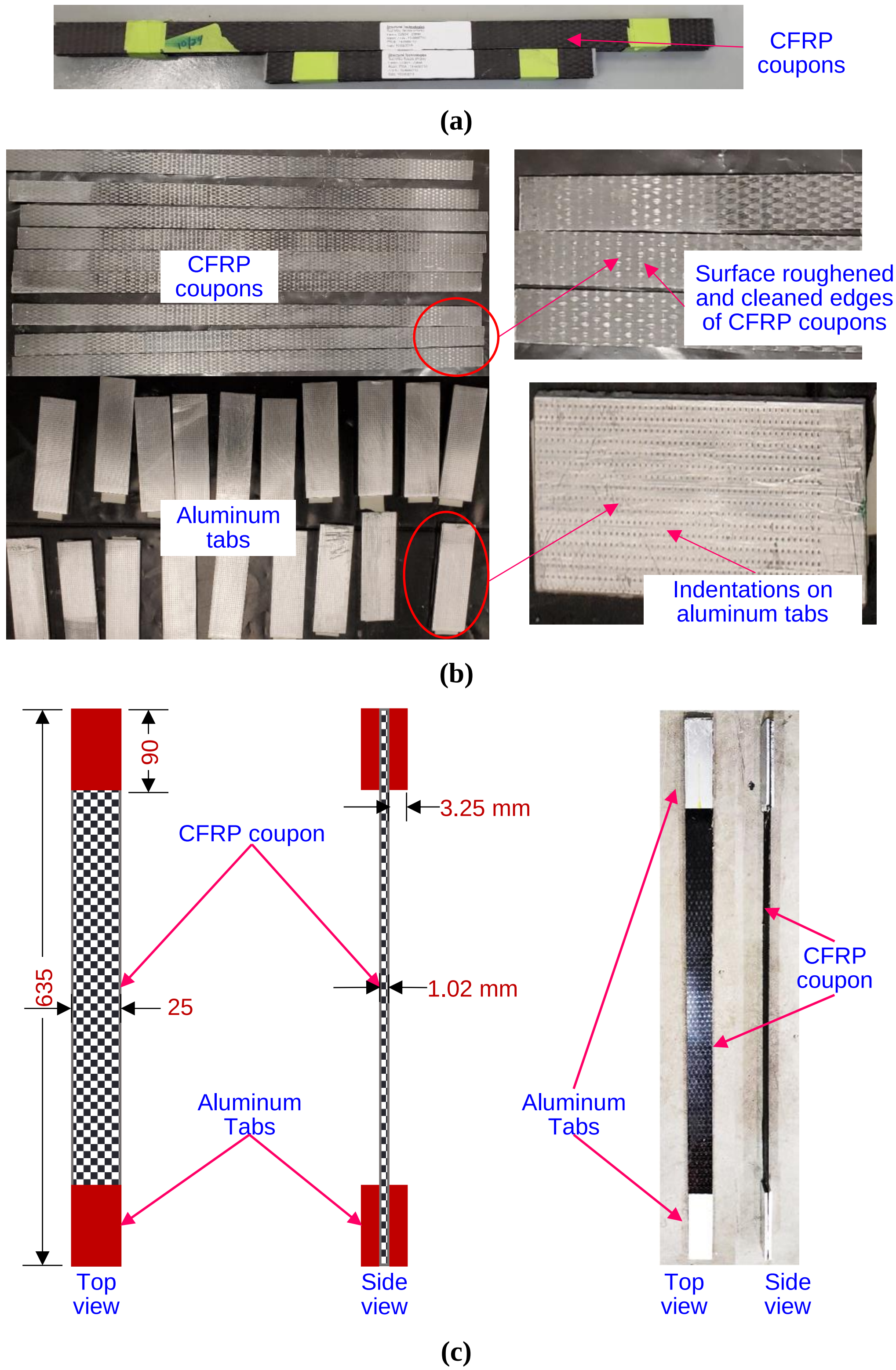

Figure 3.7: Test specimen for direct tensile tests: (a) CFRP coupons as received from Structural Technologies LLC; (b) surface roughened, and acetone cleaned CFRP coupons and aluminum tabs; (c)schematic layout and typical CFRP coupon bonded with aluminum tabs at the ends

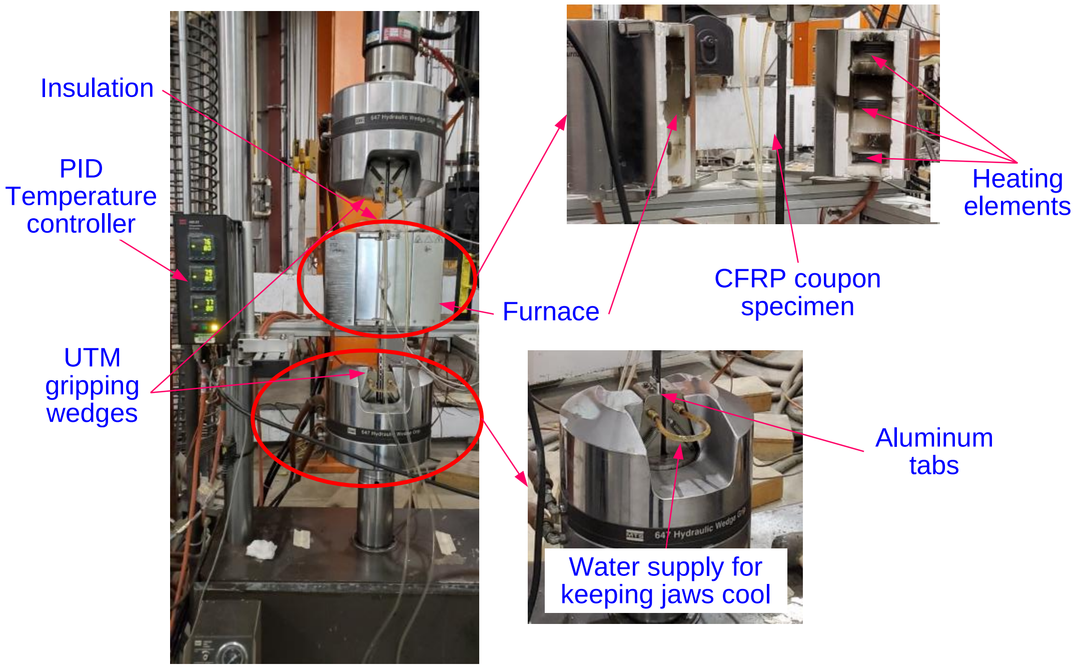

Figure 3.8: Test Set up for tensile strength tests

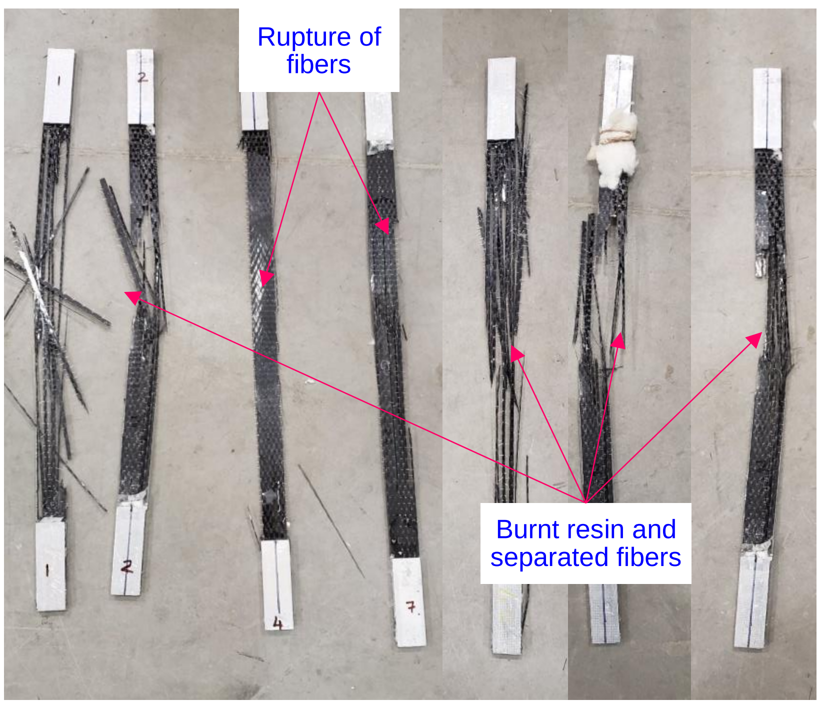

(a)

Figure 3.9: Results from the tensile strength test on CFRP coupons at elevated temperatures: (a) tested specimen with different failure modes; (b) normalized stress-strain response; (c) normalized temperature variation of tensile strength

Figure 3.9 (cont'd)

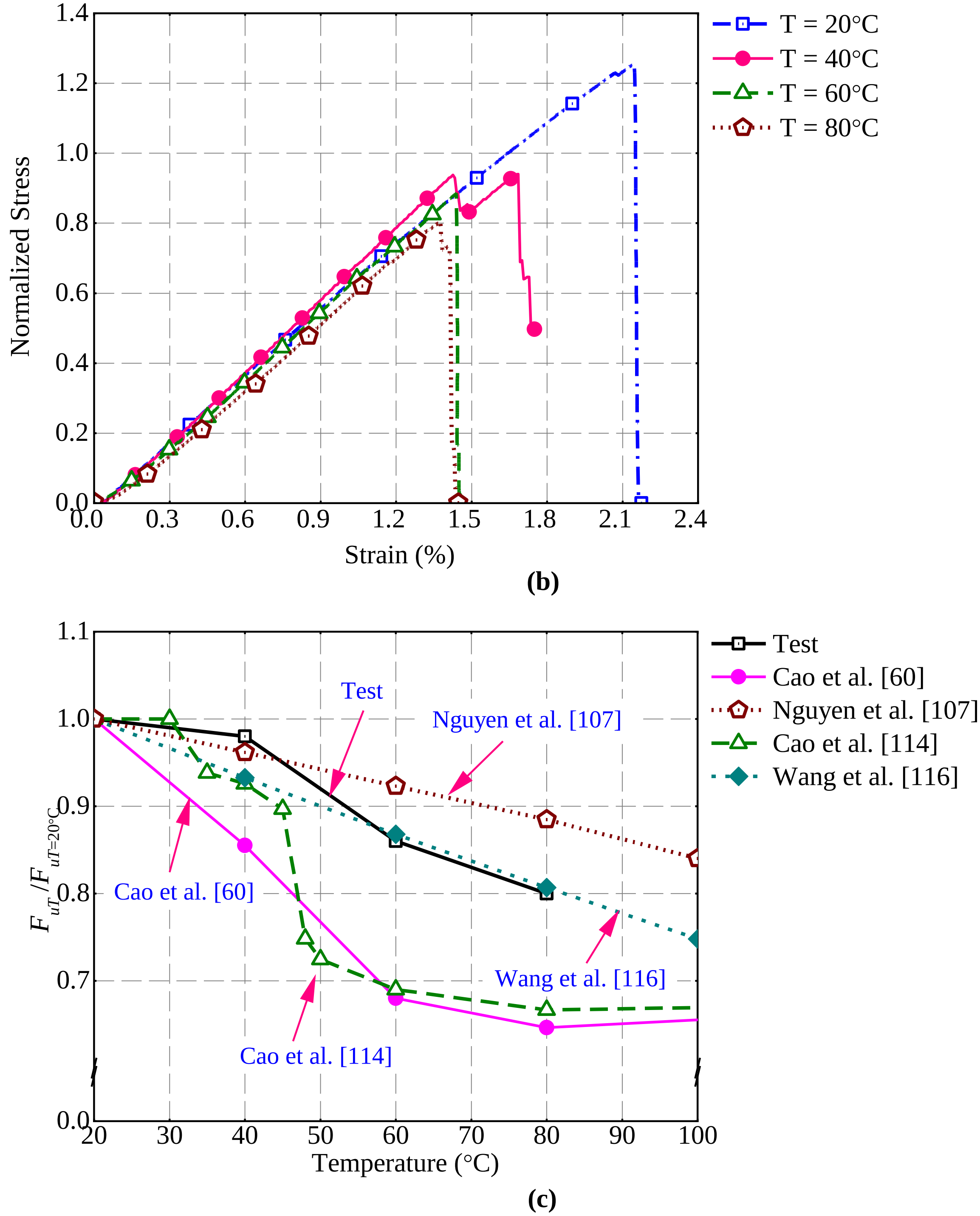

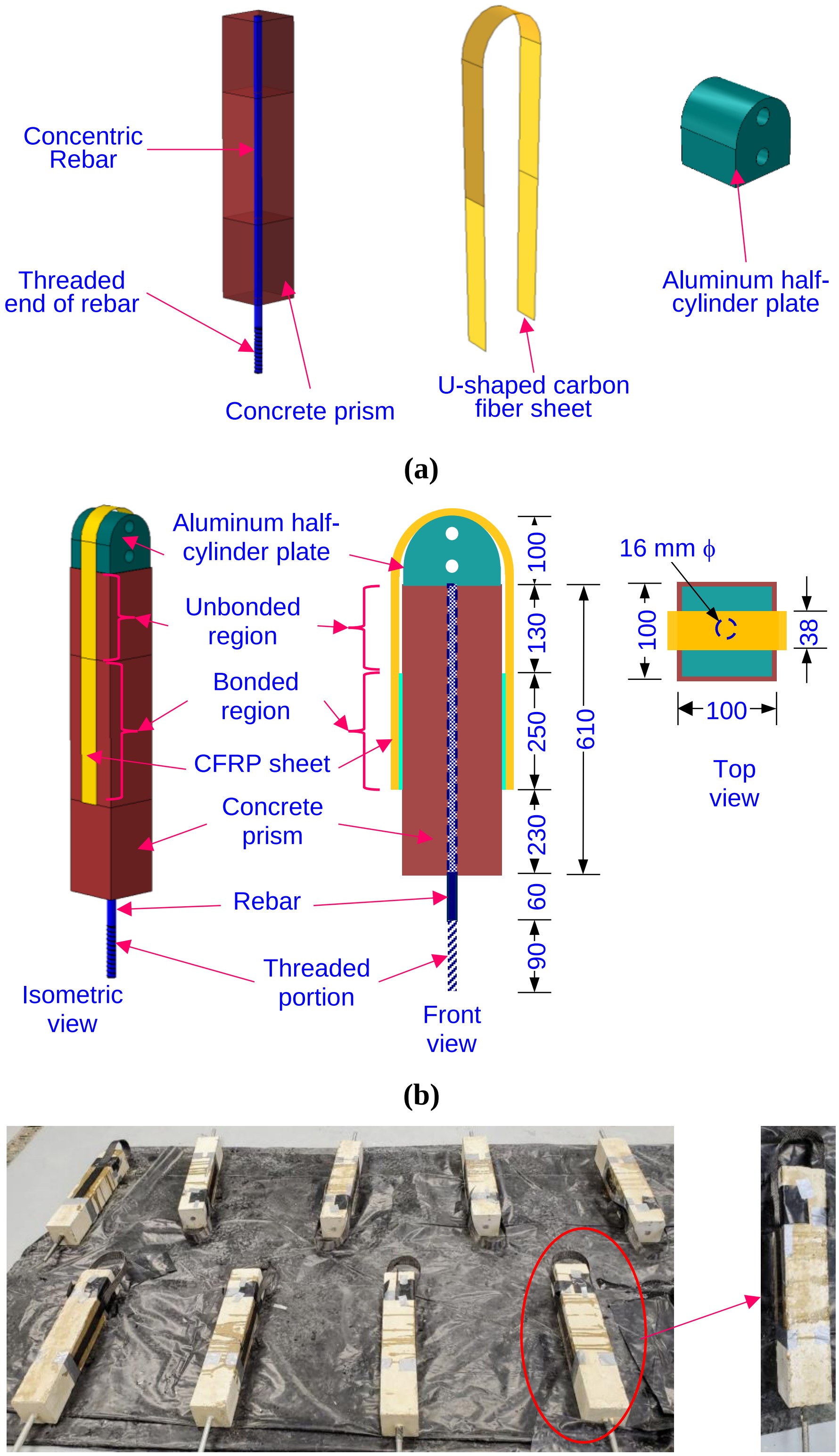

(c)

Figure 3.10: Configuration of specimen used in double lap shear tests for evaluating FRP-concrete bond strength: (a) components of specimen; (b) schematic layout; (c) typical test specimens

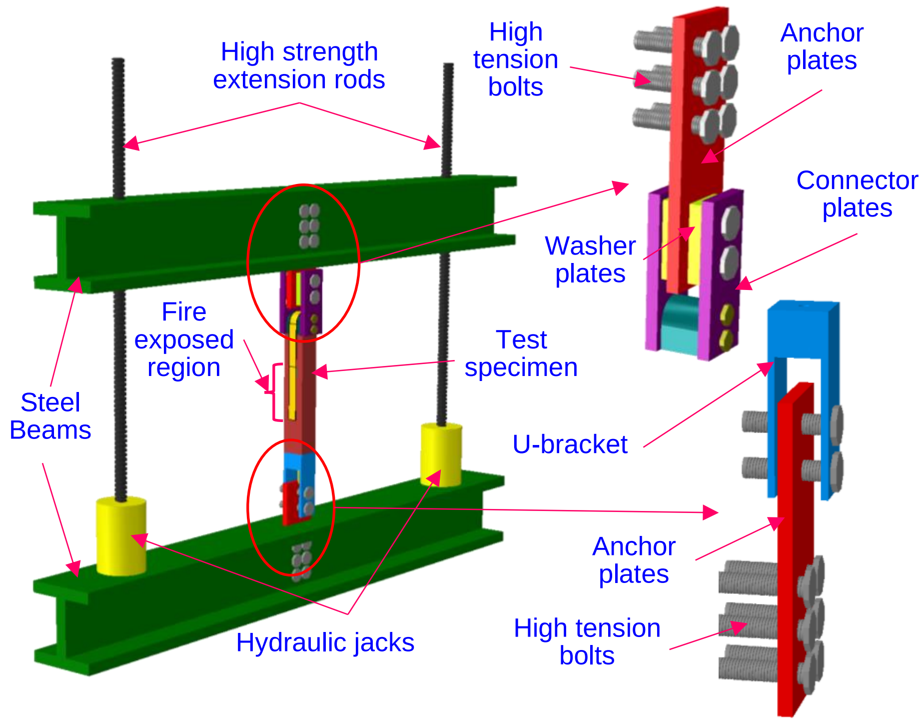

(a)

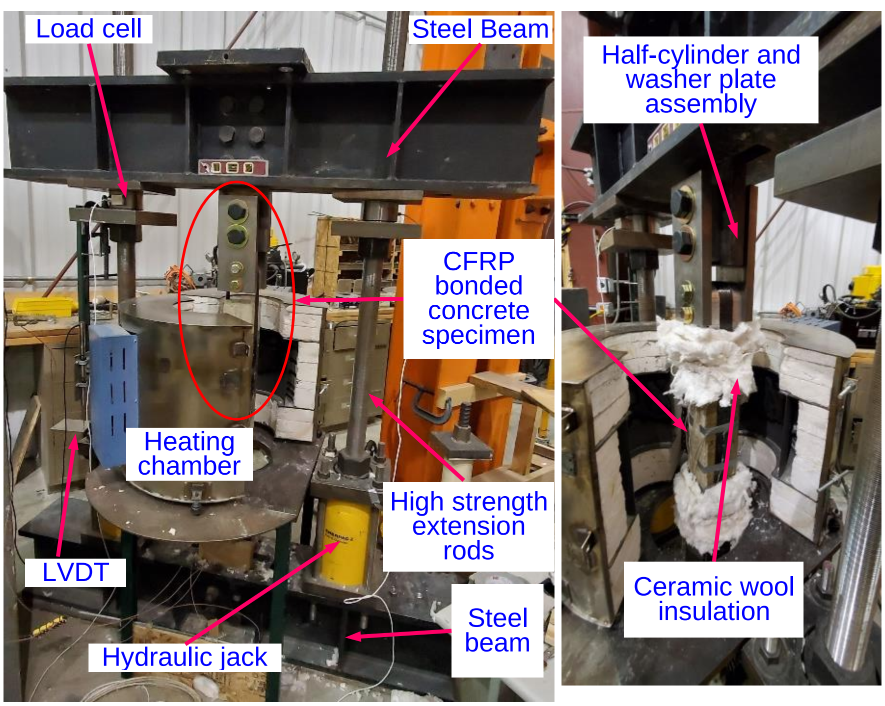

(b)

Figure 3.11: Test set up for evaluating bond strength at high temperatures: (a) schematic view; (b) experimental setup

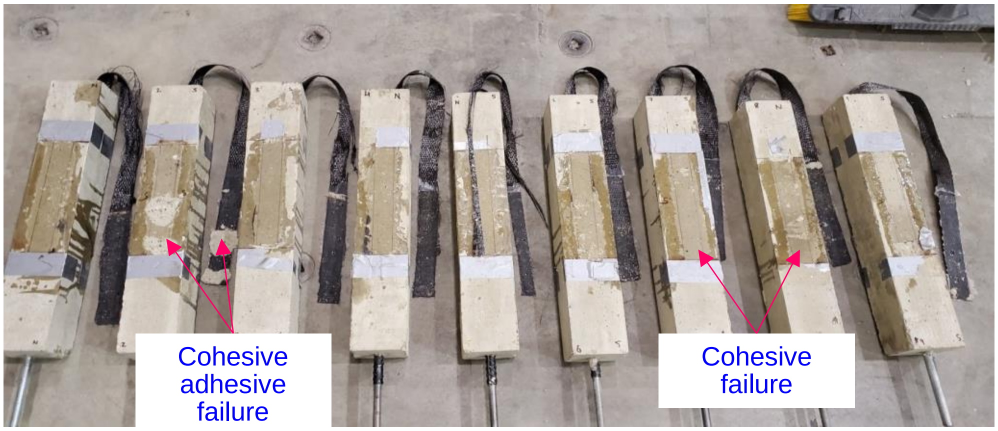

(a)

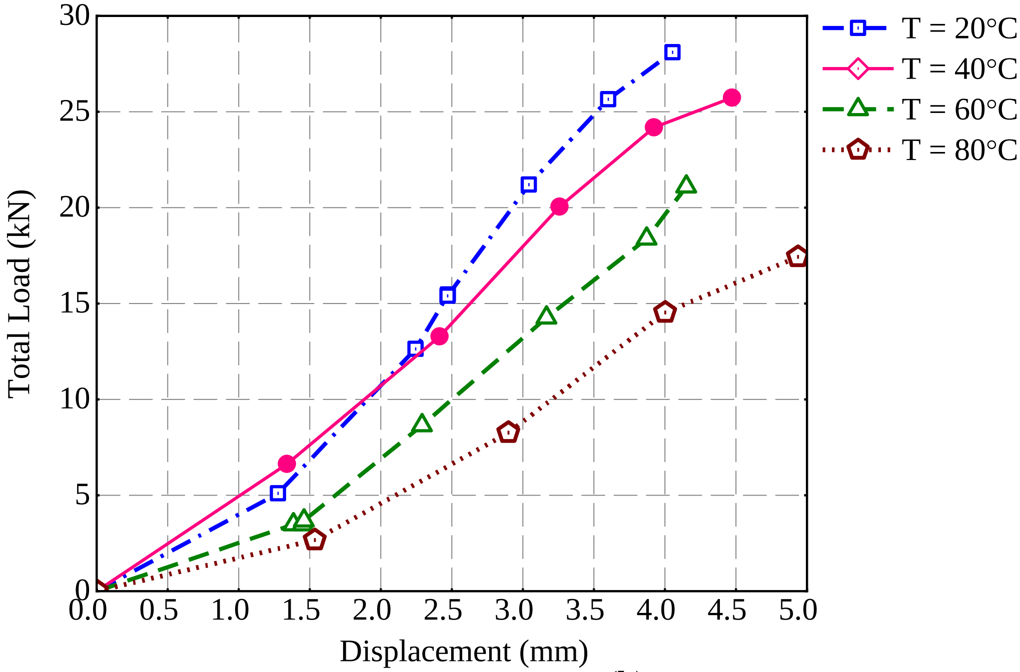

(b)

Figure 3.12: Results from the double lap shear tests: (a) tested specimens; (b) load displacement response of CFRP-concrete interface; (c) comparison of bond strength variation with temperature

Figure 3.12 (cont'd)

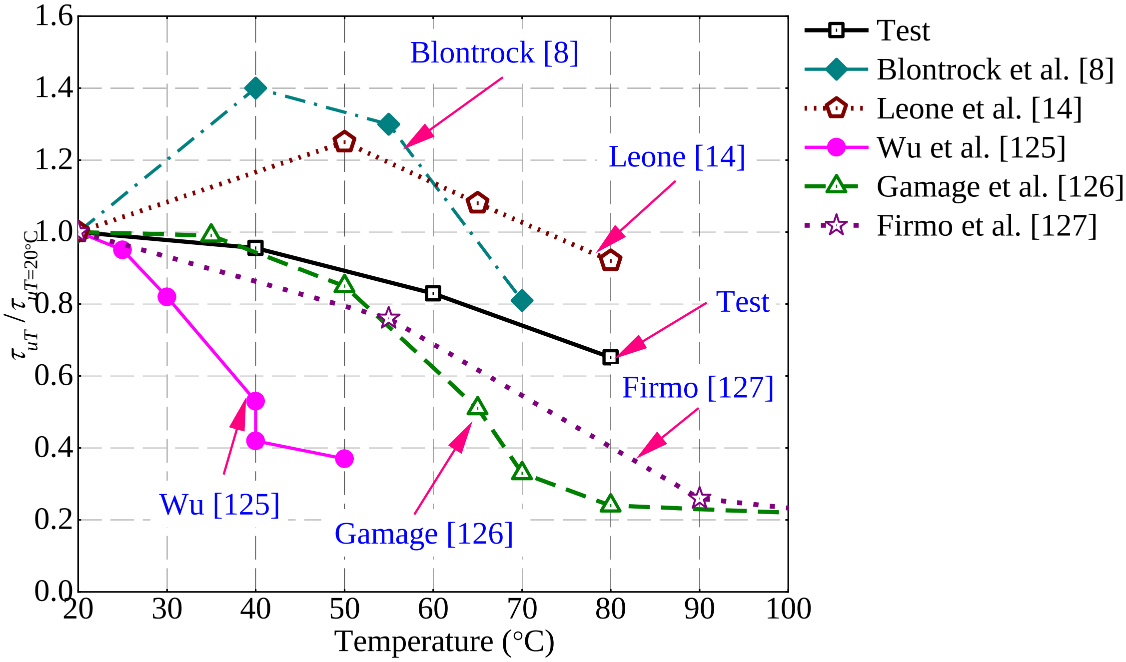

(c)

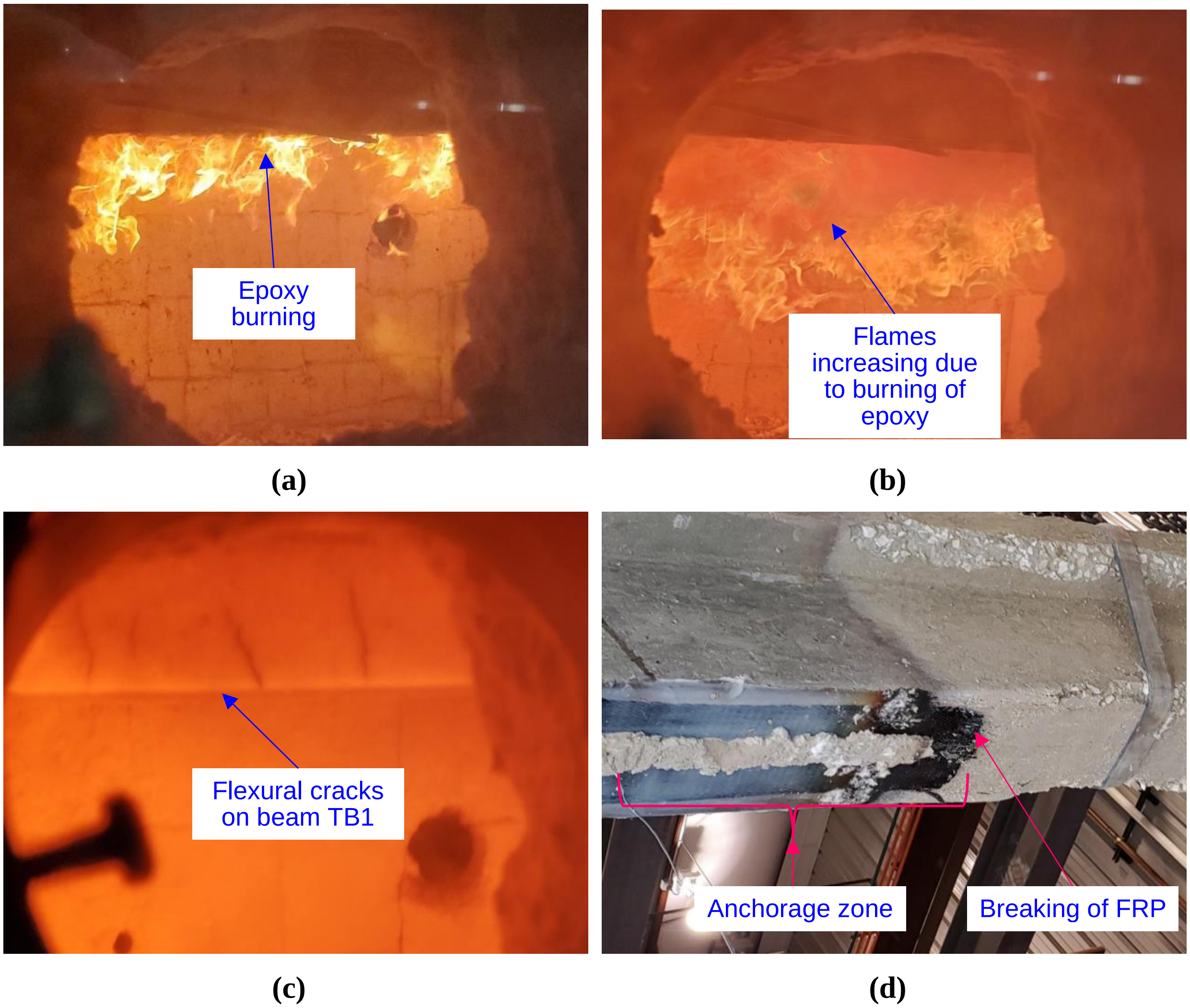

Figure 3.13: Visual observations recorded for beam TB1 during and after Test I: (a) epoxy burning along length; (b) upsurge in flames in furnace; (c) flexural cracks in beam TB1; (d) breaking of FRP from anchorage zone

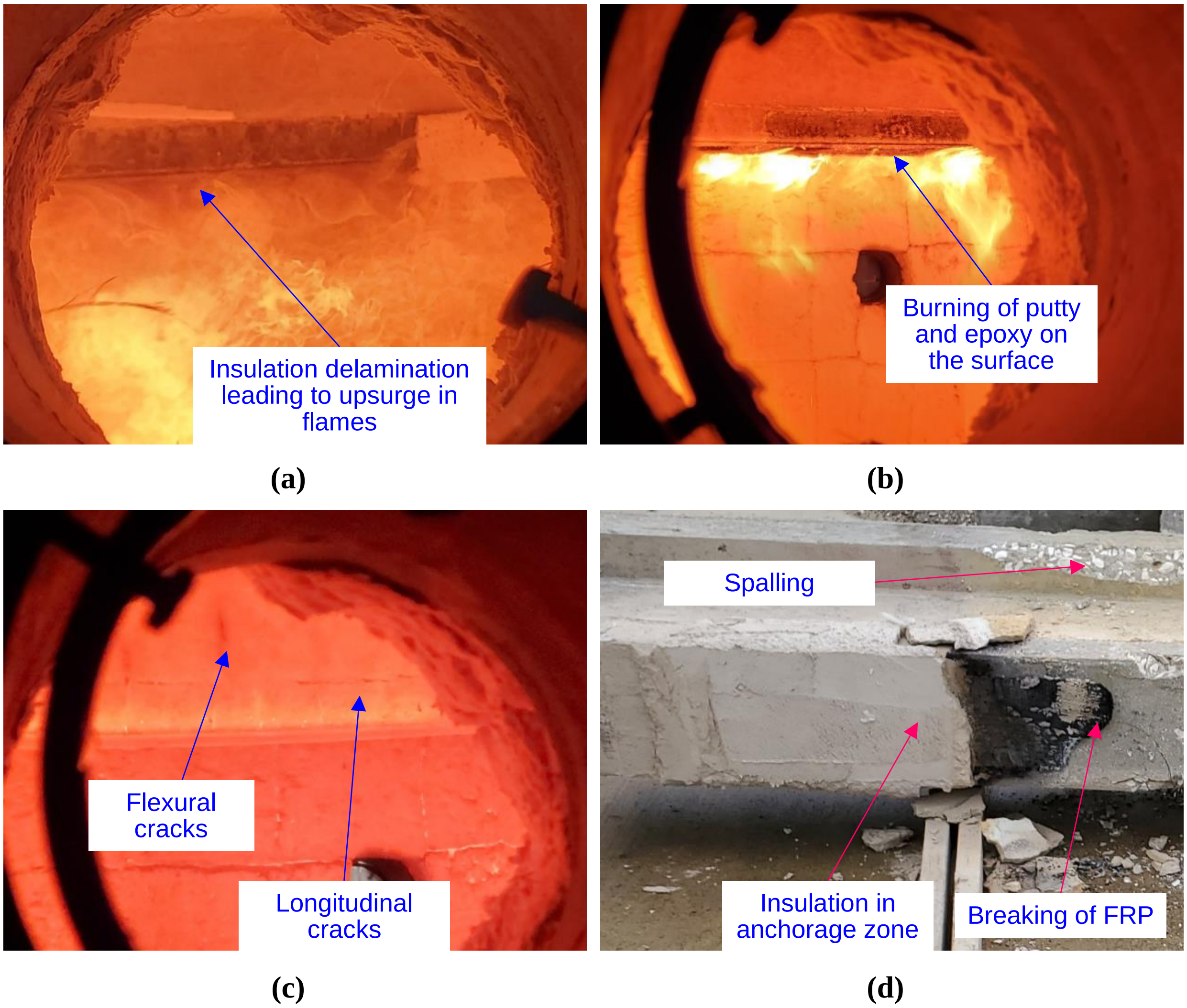

Figure 3.14: Visual observations recorded for beam TB2 during and after Test I: (a) upsurge in flames in furnace due to insulation delamination; (b) epoxy and putty layer burning along length; (c) flexural and longitudinal cracks in beam TB2; (d) breaking of FRP from anchorage zone

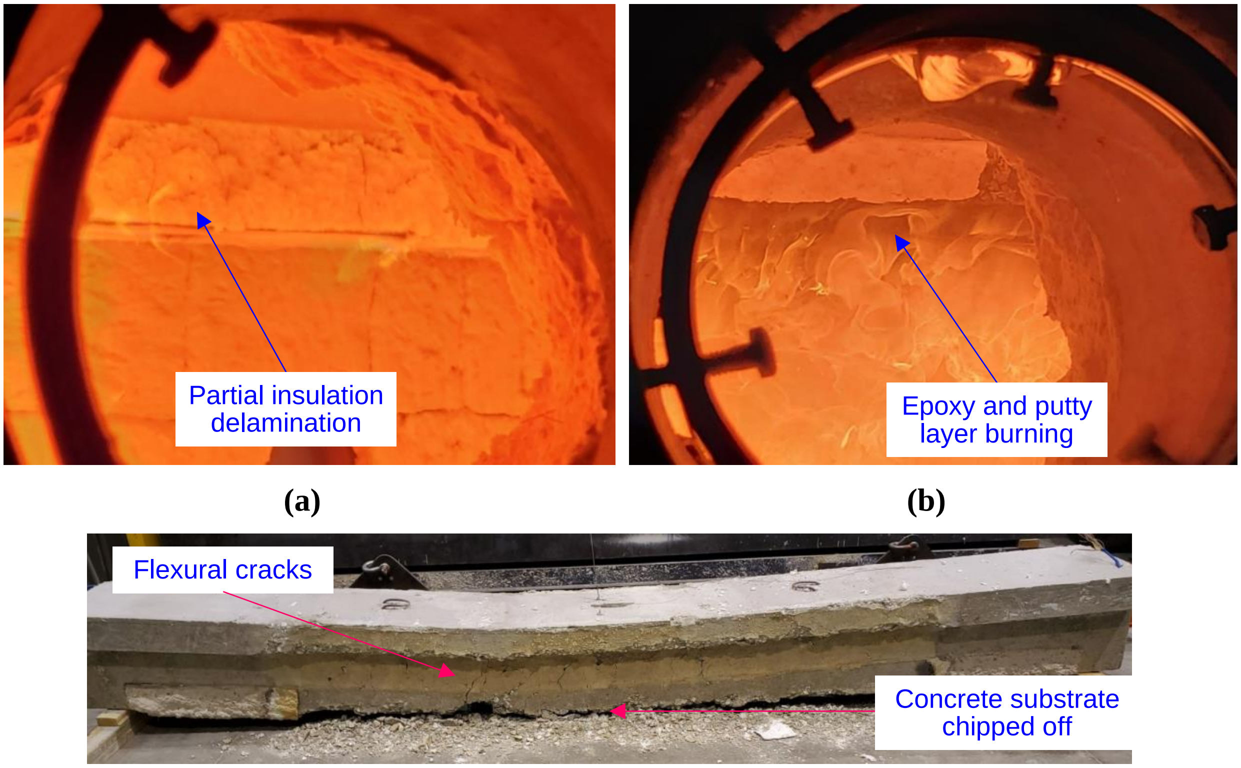

(a) **(b)**

(c)

Figure 3.15: Visual observations recorded during and after Test II: (a) epoxy burning after partial delamination of insulation along length; (b) upsurge in flames in furnace due to complete delamination; (c) failure of beam due to concrete crushing and steel yielding at bottom

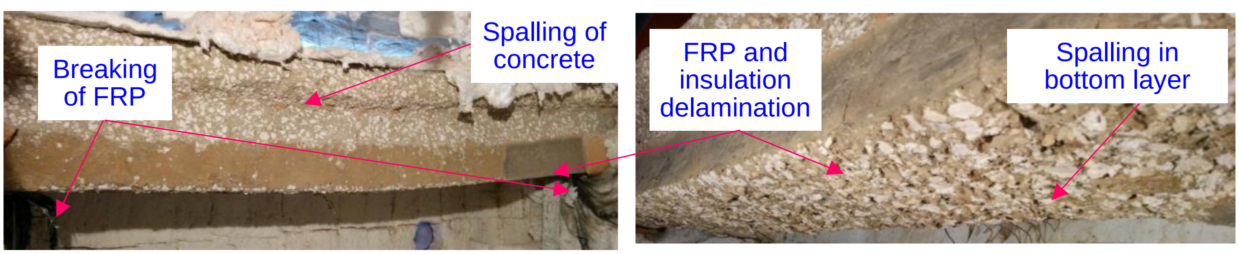

(a) **(b)**

Figure 3.16: Visual observations recorded after Test III: (a) beam TB4; (b) beam TB5

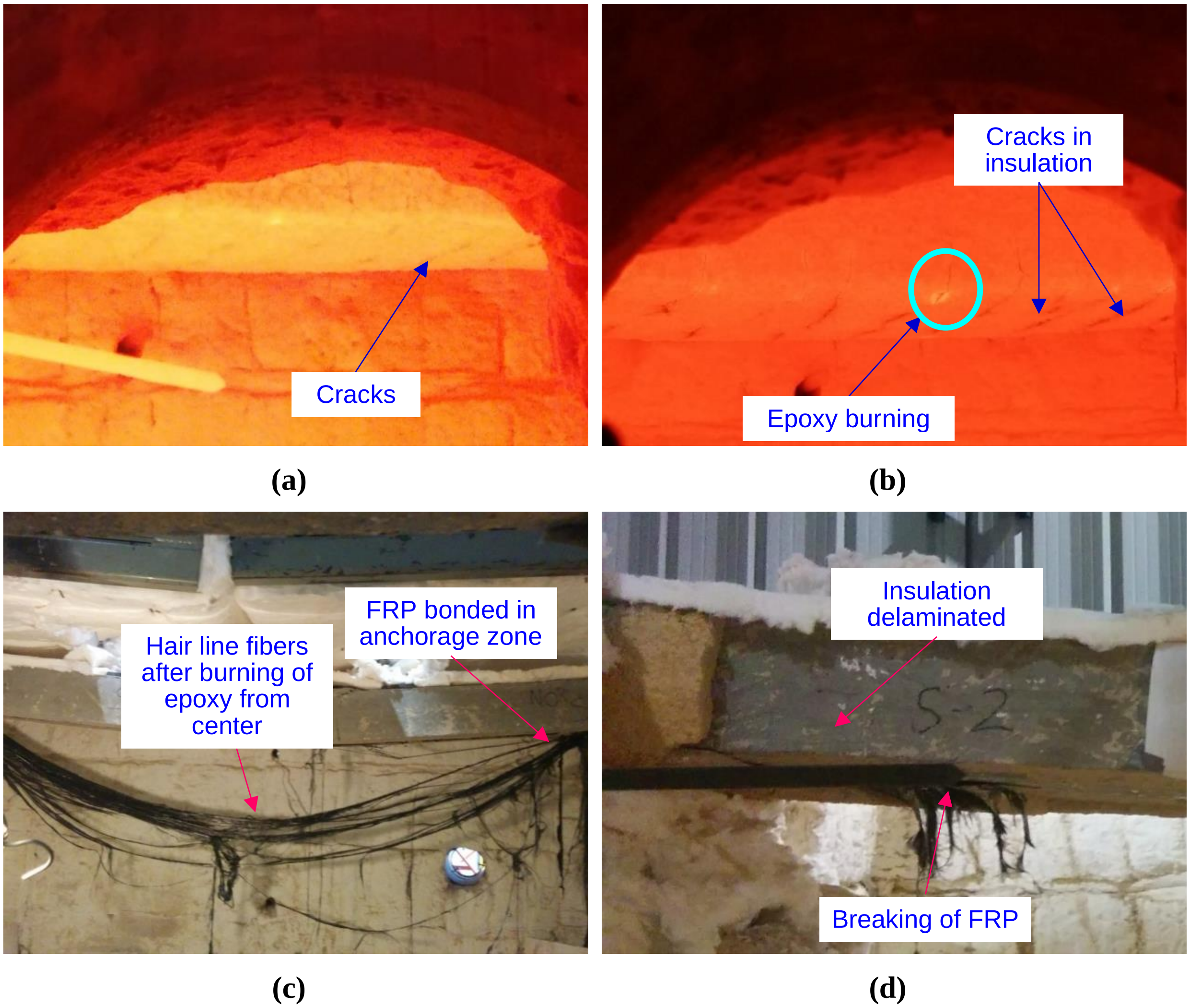

Figure 3.17: Visual observations recorded during Test IV: (a) cracks in insulation on slab S1; (b) cracks in insulation on slab S2 and slow burning of epoxy; (c) detachment of FRP from the fire exposed length of slab S1; (d) breaking of FRP from anchorage zone in S2

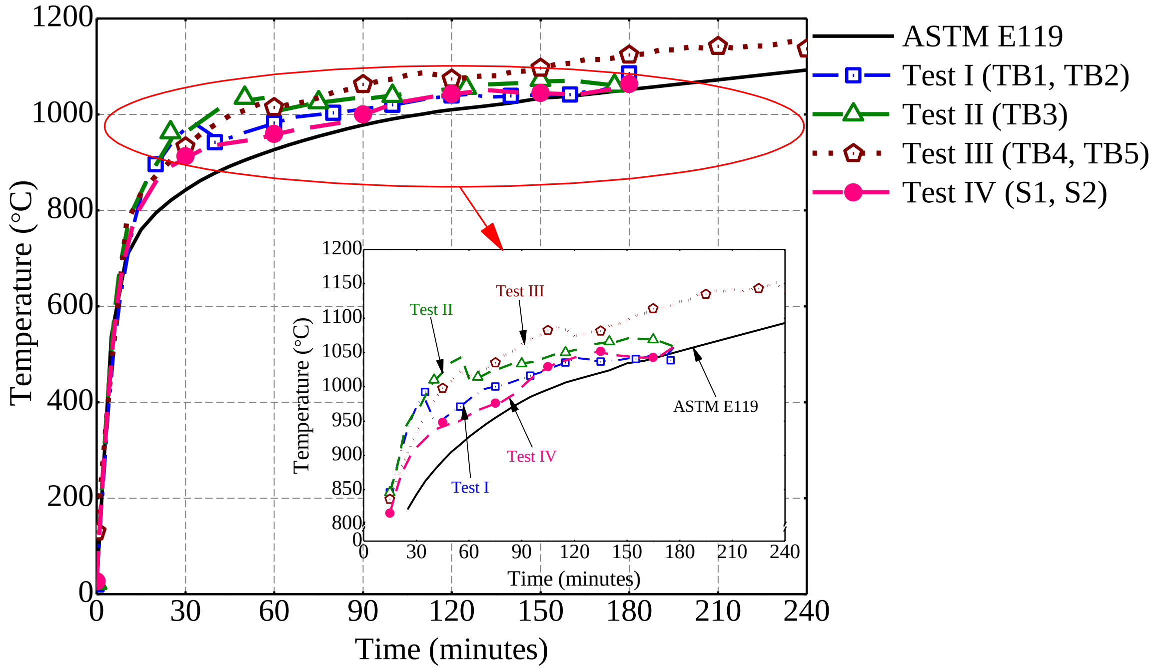

Figure 3.18: Comparison of average furnace temperatures recorded during fire tests Test I to Test IV with ASTM E119 standard fire temperatures

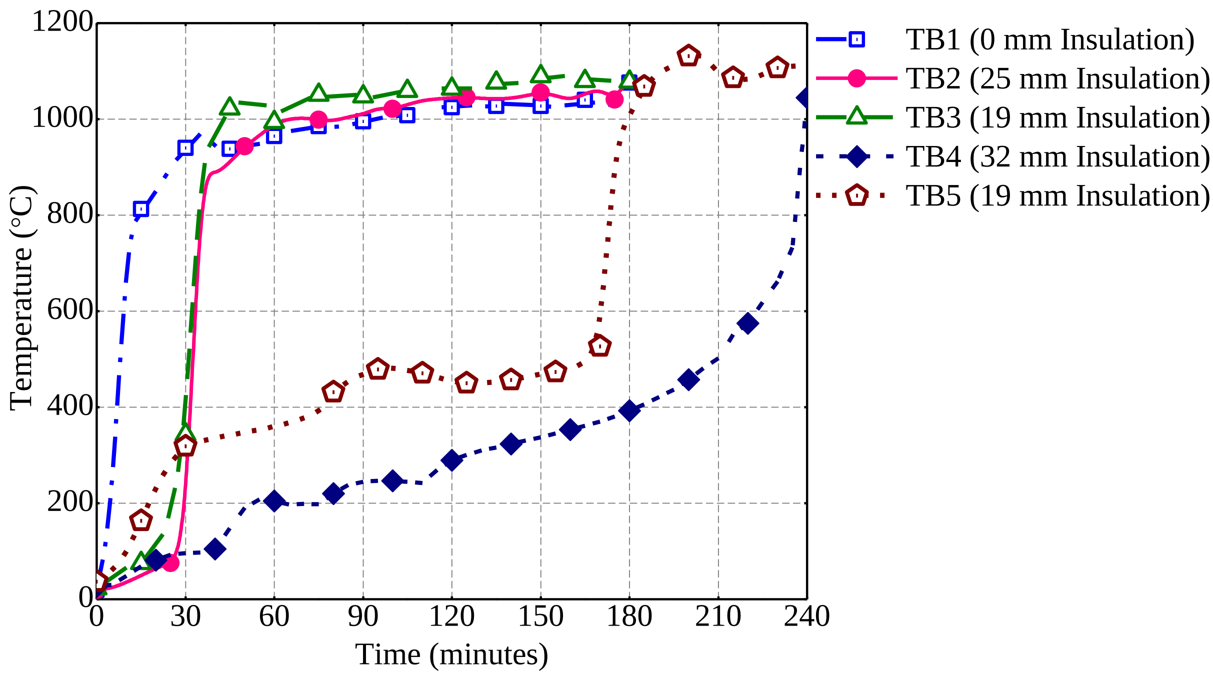

Figure 3.19: Variation of insulation-FRP interface temperatures with fire exposure time in tested beams TB1 to TB5

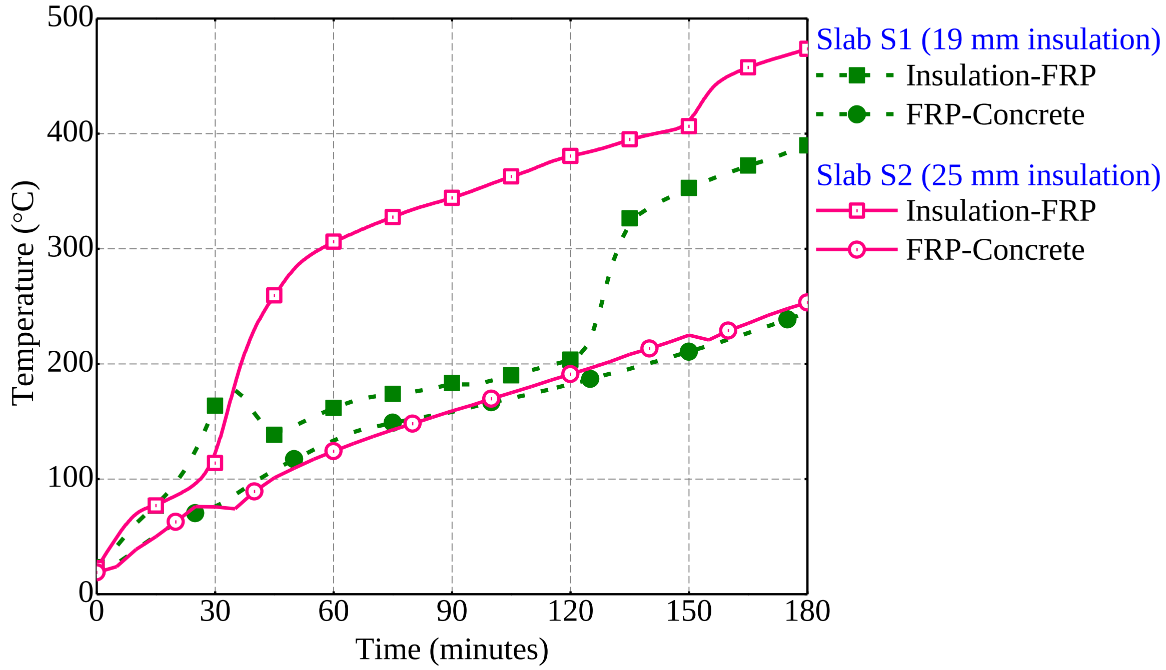

Figure 3.20: Comparison of temperature rise recorded at the insulation-FRP and FPR-concrete interfaces of slabs S1, S2 during Test IV

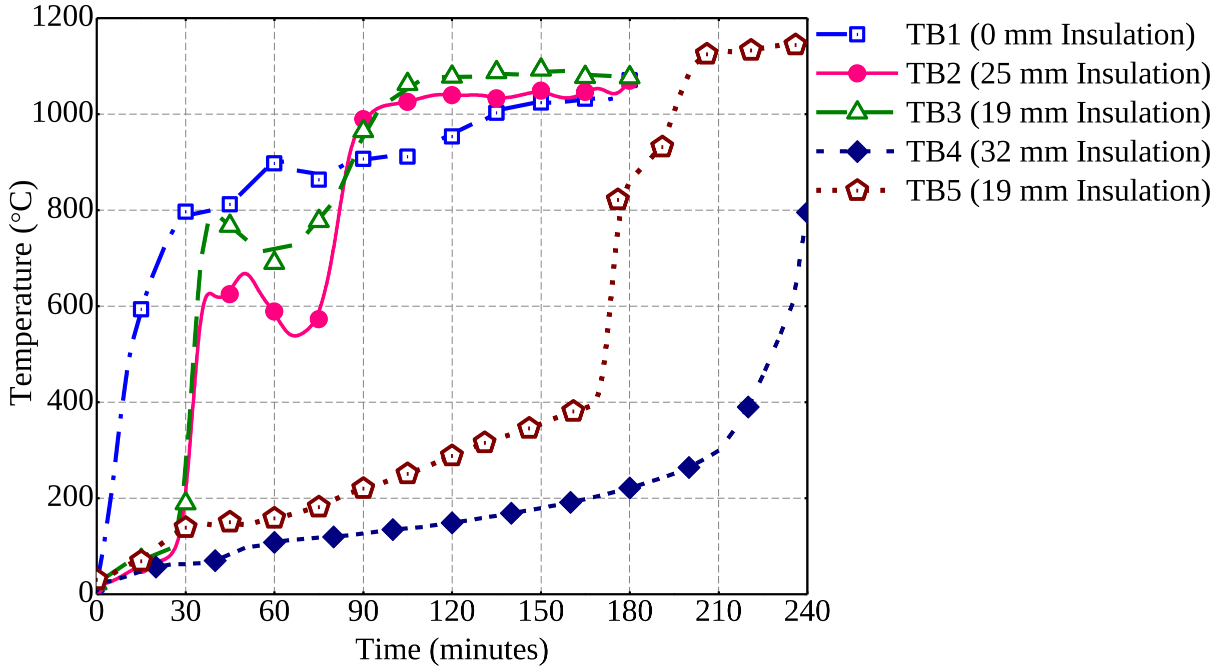

Figure 3.21: Variation of FRP-concrete interface temperatures with fire exposure time in tested beams TB1 to TB5

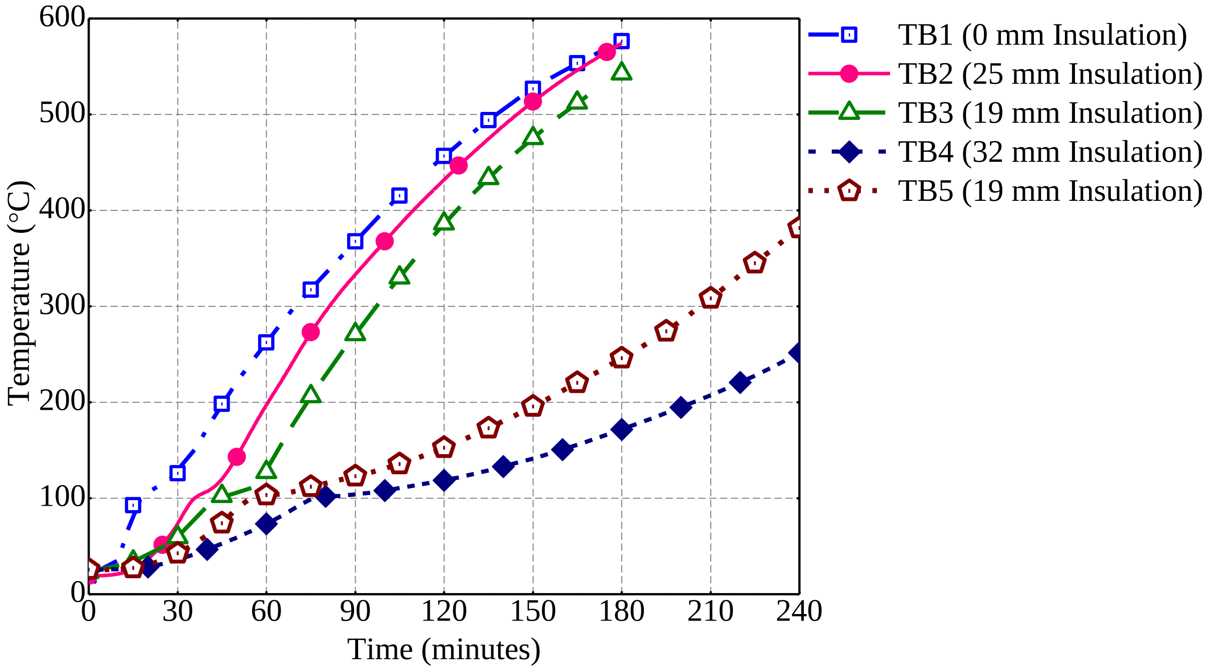

(a)

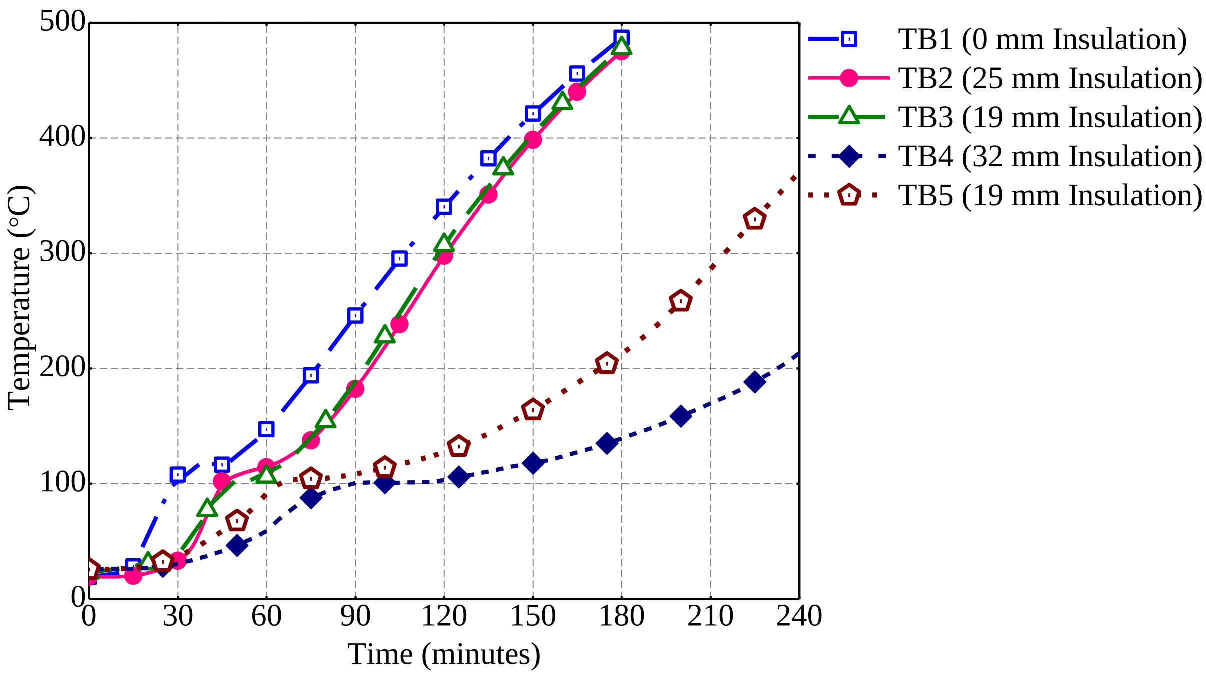

(b)

Figure 3.22: Variation of bottom rebar temperature with fire exposure time in tested beams TB1 to TB5: (a) corner rebar; (b) mid rebar

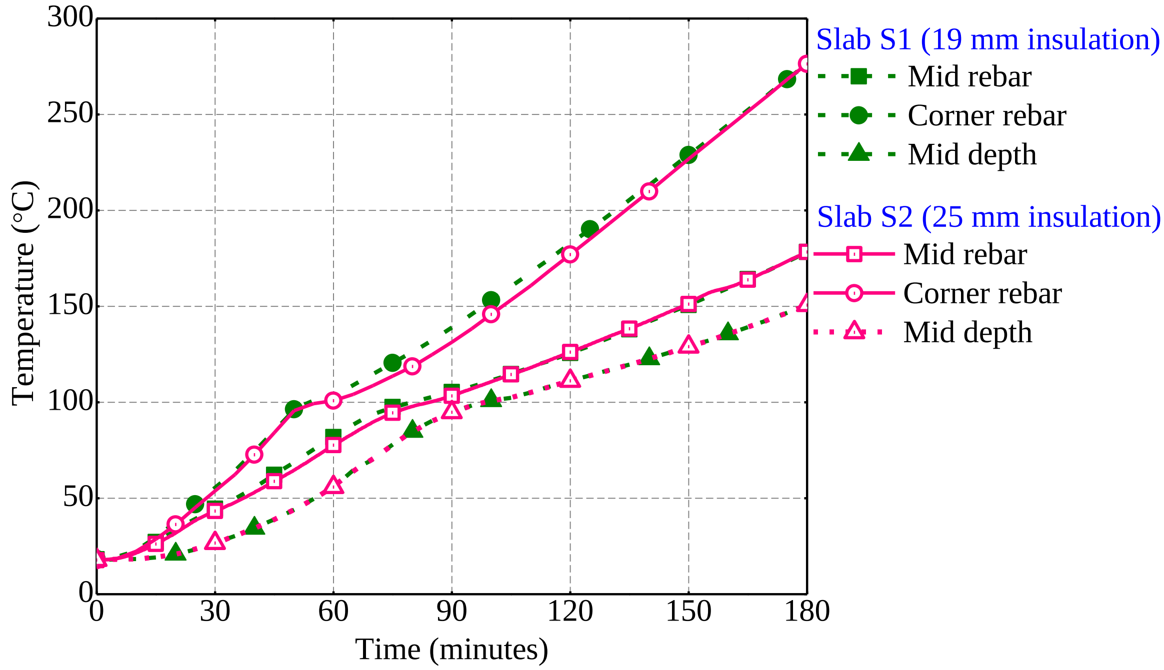

Figure 3.23: Variation of temperature at corner rebar, mid rebar, and mid-depth of tested slabs S1, S2 with fire exposure time

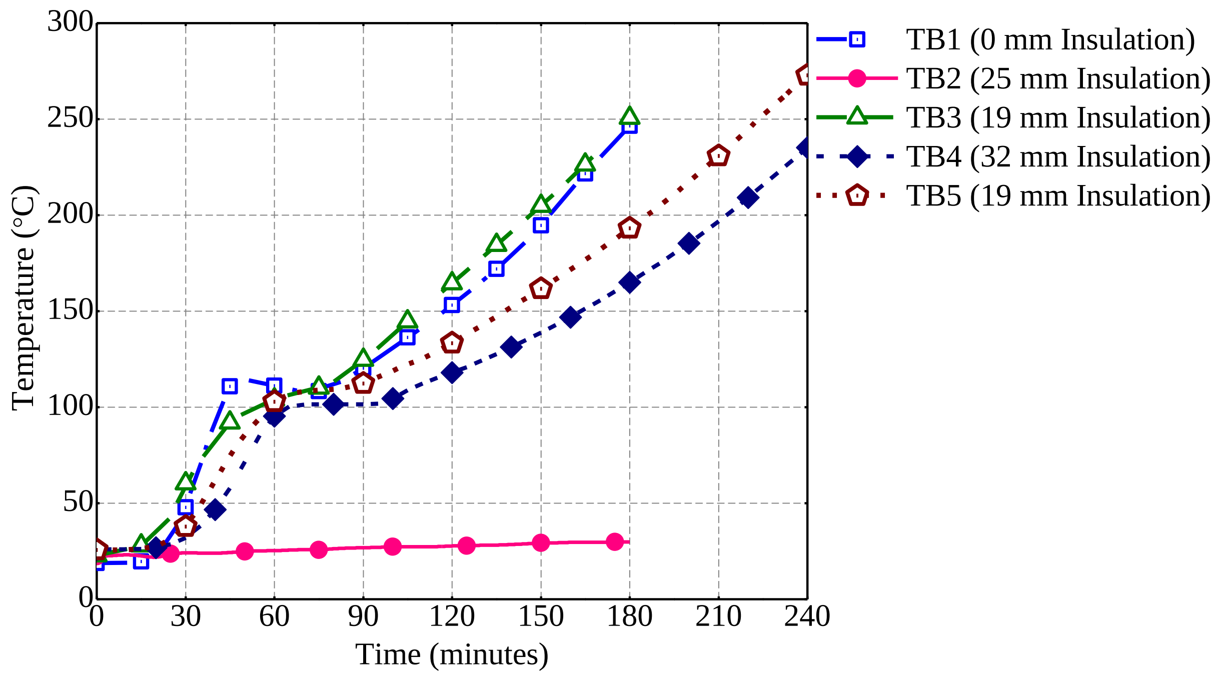

Figure 3.24: Variation of temperature at mid-depth of concrete in tested beams TB1 to TB5 with fire exposure time

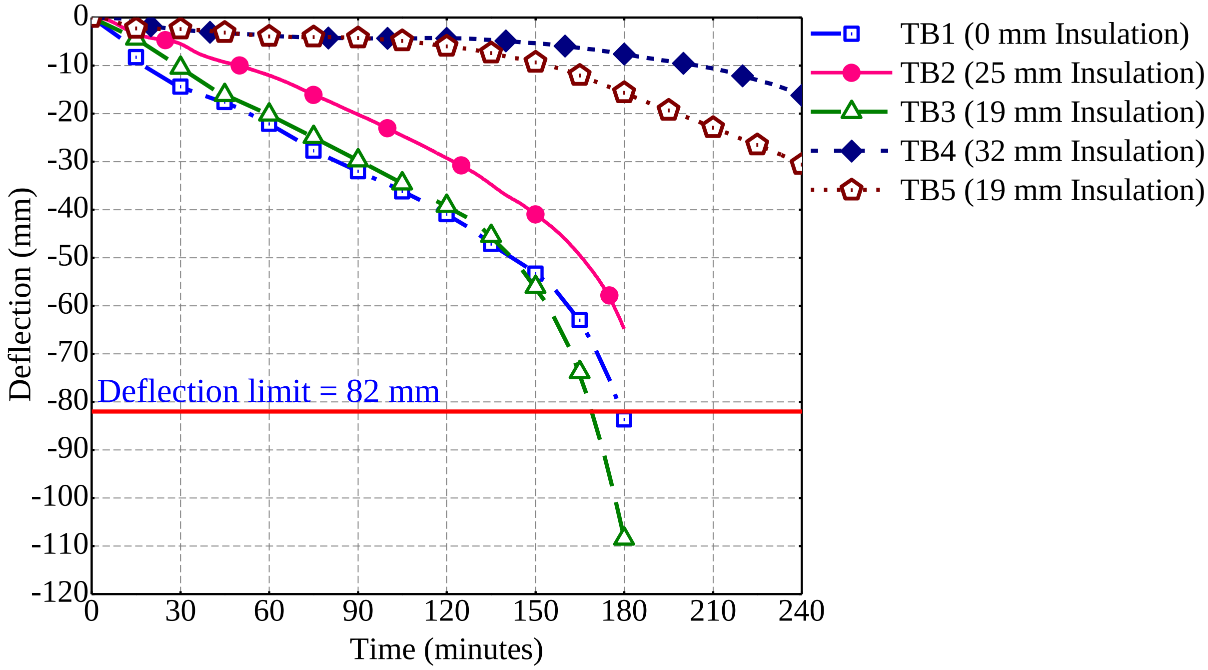

(a)

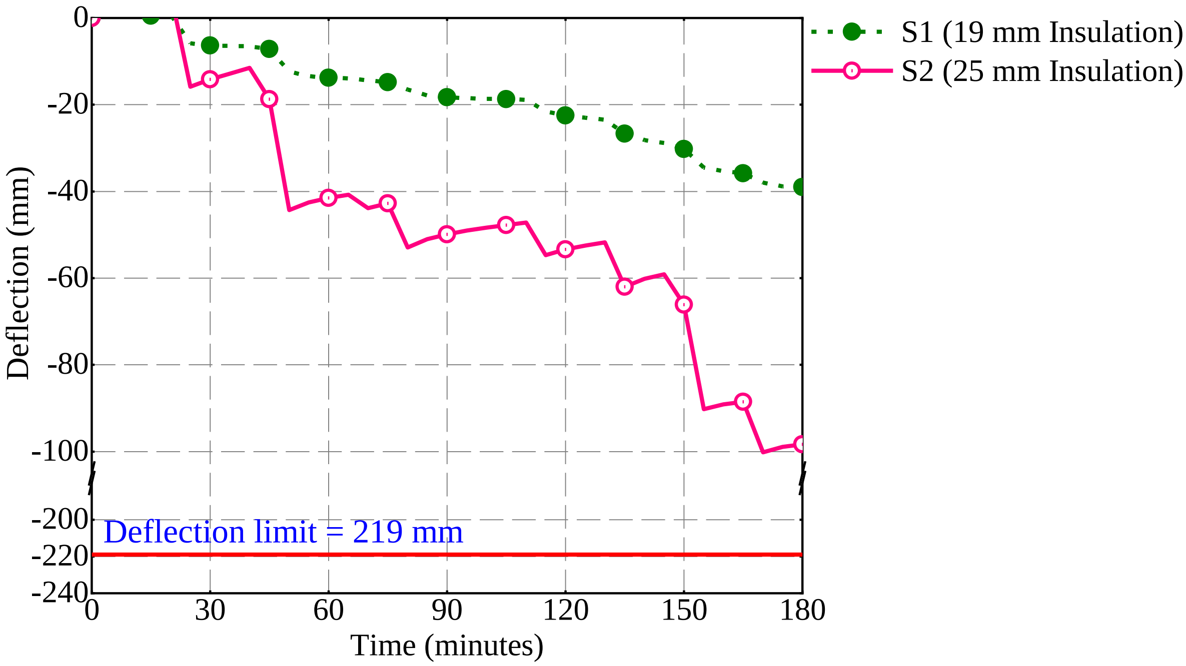

(b)

Figure 3.25: Variation of mid-span deflection with fire exposure time in tested beams and slabs: (a) beams TB1 to TB5; (b) S1, S2

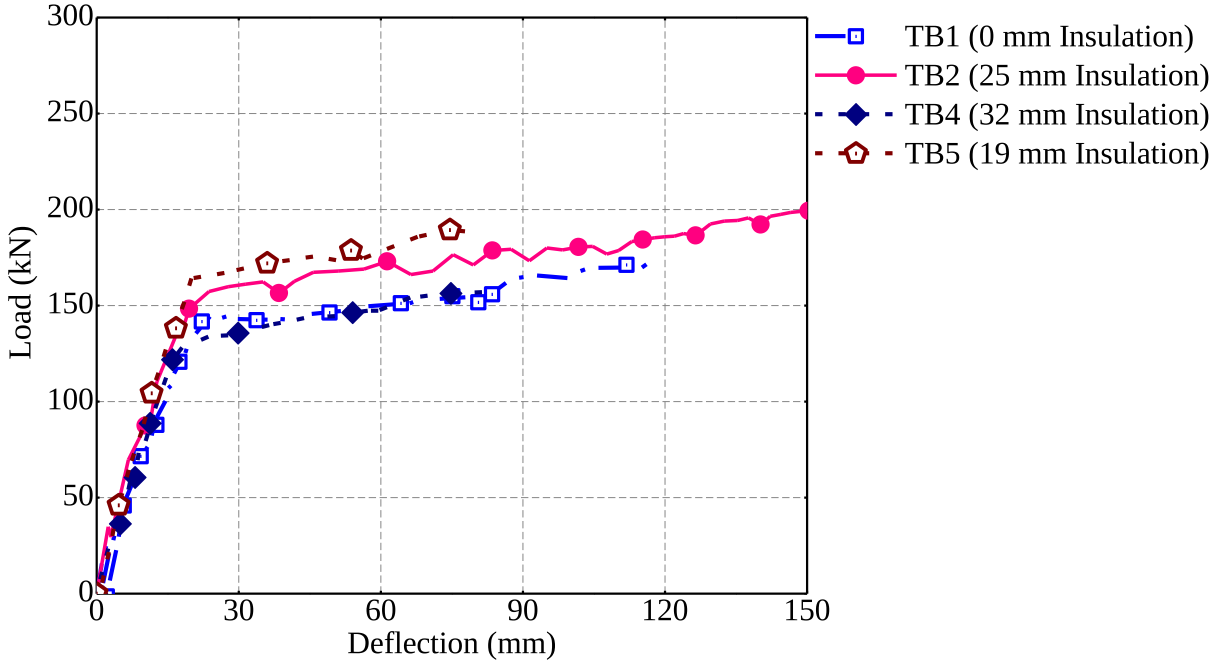

(a)

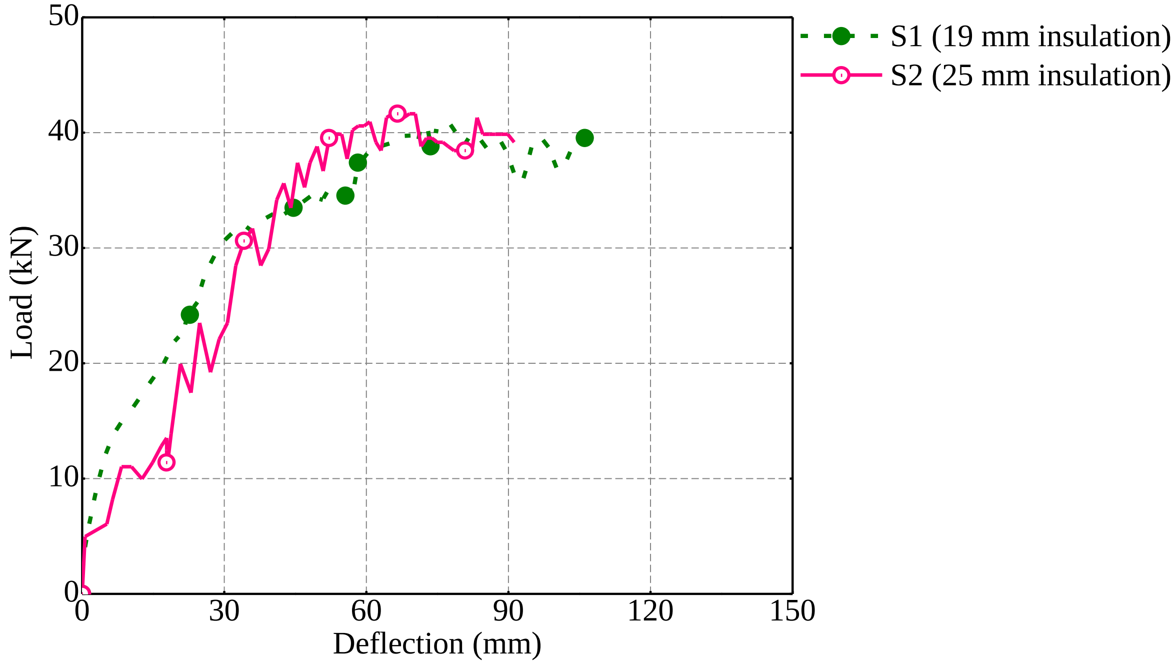

(b)

Figure 3.26: Load deflection response during residual capacity tests (a) beams TB1, TB2, TB4, and TB5; (b) slabs S1 and S2

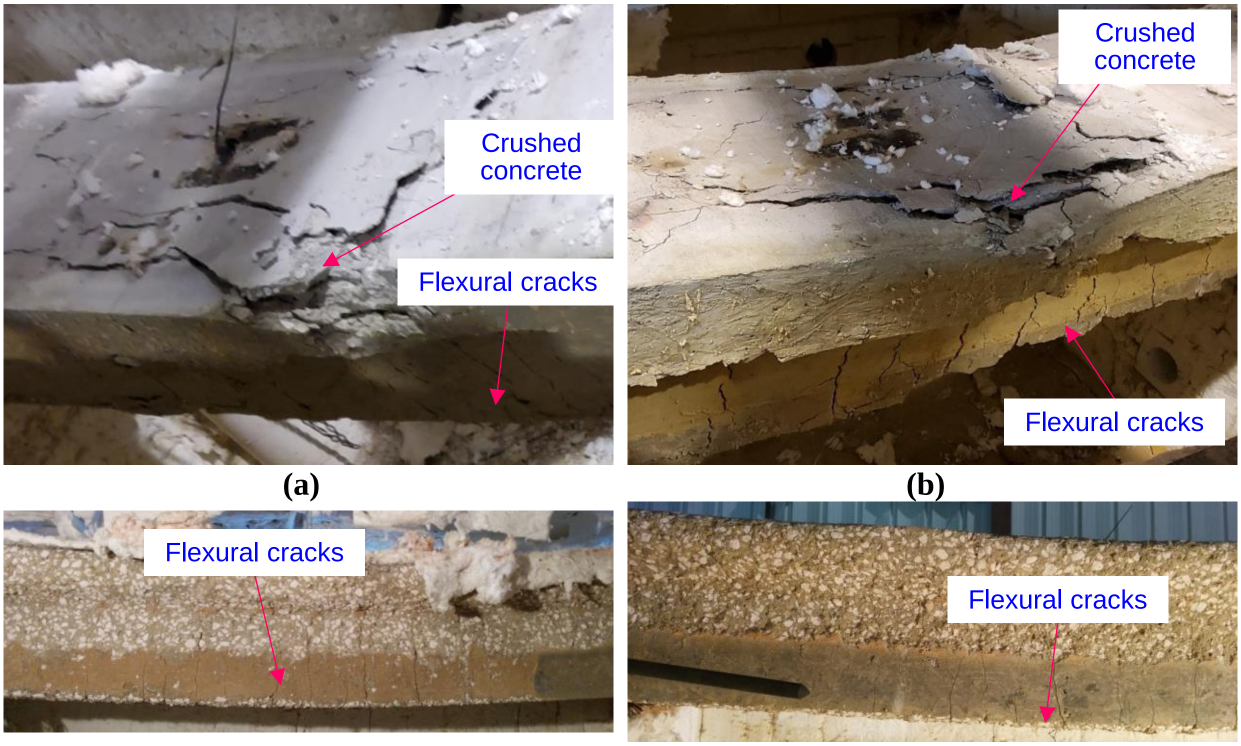

(c) (d)

Figure 3.27: Failure patterns of beams TB1, TB2, TB4, and TB5 in post fire residual capacity test: (a) concrete crushing and flexural cracks in TB1; (b) concrete crushing and flexural cracks in TB2; (c) flexural cracks in TB4; (d) flexural cracks in TB5

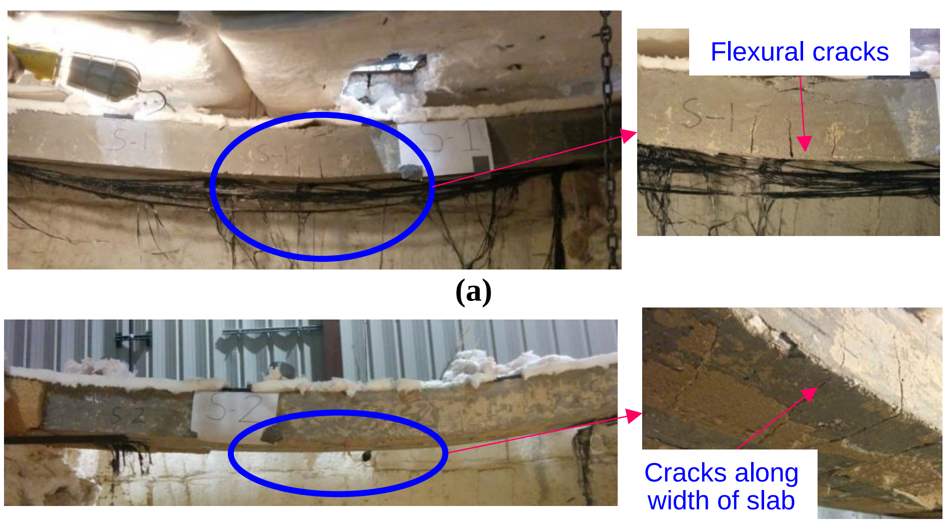

(b)

Figure 3.28: Failure patterns of tested slabs in post fire residual capacity test: (a) slab S1 with flexural cracks at center; (b) slab S2 with flexural cracks at center along the width

CHAPTER 4

NUMERICAL MODEL

4.1 General

The fire resistance tests on a structural member, although reliable, are time consuming, involve high costs, and have limitations with respect to size of specimens due to available size of furnace and loading facilities. Additionally, due to the limitation of the instrumentation (sensors) that are stable at elevated temperature, the number of response parameters that can be measured in the fire tests are limited. A practical alternative to overcome the shortcomings of a fire test is to use a numerical model for evaluating the behavior of a structural member under fire exposure. Such a numerical model must account for temperature dependent thermal and mechanical properties of the constituent materials, temperature induced bond degradation, realistic boundary and loading conditions as well as all applicable failure limit states.

The literature review presented in Chapter 2 indicated that numerical studies undertaken to evaluate fire performance of FRP-strengthened RC beams and slabs are limited. In fact, no numerical models have been developed that account for structural parameters in evaluating fire resistance of FRP-strengthened RC slabs under fire conditions. Majority of the available numerical models do not specifically account for temperature induced bond degradation or relevant failure limit states, which are critical in determining the actual fire performance of FRP-strengthened concrete flexural members. Few models that do account for temperature induced bond degradation use complex analysis procedure involving significant computational effort using commercial finite element programs, which require high computational skills to analyze and interpret the results.

To overcome some of the current drawbacks a macroscopic finite element based numerical model has been developed to evaluate the response of FRP-strengthened RC beams and slabs under the effect of fire exposure and structural loading. Detailed pertaining to the development of the numerical model together with validation of the model is outlined in following sections.

4.2 Development of Numerical Model

A macroscopic finite element based numerical model for evaluating the response of FRP-strengthened RC beams in the entire range from the linear elastic stage to collapse under fire conditions, was originally developed by Kodur and Ahmed [95] using FORTRAN program. This numerical model is further extended to predict the response of FRP-strengthened RC beams and RC slabs under combined effects of fire exposure and structural loading. The updated model specifically accounts for softening of concrete (in tension and compression), temperature induced bond degradation at the interface of FRP and concrete, and all applicable failure limit states governing fire response of FRP-strengthened RC beams and slabs.

4.2.1 General Approach

The numerical model is based on macroscopic finite element approach wherein, time dependent sectional moment curvature (M-κ) relations are utilized to evaluate the response of a FRP-strengthened RC beam/slab subjected to fire. The updated model carries out the analysis at member level (not at the section level only) and accounts for temperature dependent material nonlinearities including softening of concrete in tension and compression, bond degradation at FRP-concrete interface, and evaluated failure by considering all applicable failure limit states governing fire response of FRP-strengthened RC flexural members. The numerical procedure followed in the analysis is illustrated through a flowchart shown in Figure 4.1.

Figure 4.2 (a-b, e-f) shows the geometrical configuration as well as the loading and boundary conditions of a typical T-beam and slab that can be analyzed through the mdoel. These details are provided as an input to the model. The analysis starts by discretizing the geometry of the strutural member (*cf*. Figure 4.1). After discretization, the fire resistance analysis is carried out in small time increments of fire exposure. During each time increment a thermal analysis and structural analysis is carried out in a sequential manner to trace the fire response of the FRP-strengthened concrete flexural member.

In thermal analysis, the temperature rise and associated thermal gradients within the cross-section of the structural member are calculated. These temperatures are used to determine the level of degradation in strength and modulus properties of constitutive materials. In structural analysis, time dependent M-κ relationships are generated for each segment of the strengthened structural member. These relations are generated considering the degraded strength and modulus properties of the materials as well as the relative slip caused by temperature induced degradation of interfacial bond between FRP and concrete. The M-κ relationships are then utilized to compute the stiffness of each segment of the structural member, which forms the basis for undertaking stiffness analysis.

At each time step, the model generates various output parameters such as cross-sectional temperatures, stresses in rebars, strains, mid-span deflection and moment capacity of the structural member. The cross-sectional temperatures, mid-span deflection, and moment capacity of each segment are compared with pre-defined limiting values (discussed in the following section), to determine the failure state of the structural member. The structural member is considered to have failed when applicable failure limit state is exceeded; however, the analysis is continued until the moment capacity decreases below the moment due to applied loading. The time at which any of the applicable failure limit state is exceeded, is taken as fire resistance of the structural member.

Detailed description of thermal and structural analysis, together with applicable high-temperature material properties, as well as governing failure criterion, is outlined below.

4.2.2 Analysis Procedure

The fire resistance analysis is carried out in three main steps, namely discretization of the structural member, thermal analysis, and structural analysis. Each of these analysis steps are described in detail in this section.

(i) Discretization

At the beginning of the analysis, the length of the given structural member (beam or slab) is discretized into a number of segments along while the cross-section of each segment is discretized into a mesh of rectangular elements. The cross-section at the middle of each segment is assumed to represent the overall behavior of the segment. The descrization of a typical beam along the length and cross-section is shown in Figure 4.2 (c) and 4.2 (d), whereas the descritization of a typcial slab along the span length and across the cross-section is shown in Figure 4.2 (g) and 4.2 (h), respectively.

(ii) Thermal analysis

Following the discretization of the strengthened structural member, fire exposure condition is applied on the bottom and two sides of the beam (only at bottom for slabs), and the temperature distribution within the cross-section of the segment is determined. The fire exposure time is incremented in small time increments of 30 seconds each. The temperature of the applied fire loading at each time increement is calculated through time-temperature relation, as per standard fire curve (or any given design fire scenario). For instance, the time-temperature relation for ASTM E119 [5] standard fire is approximated by the following equation:

$$T_f = T_0 + 750\left(1-\exp\left(-3.79553\sqrt{t_h}\right)\right)+170.41\sqrt{t_h} \tag{4.1}$$

where, T_f is temperature of fire (°C); T_0 is the initial temperature (°C); t_h is time (hours). Similarly, any other fire scenarios, such as hydrocarbon fire, or parametric fire from Eurocode 2 [79] can be specified as fire exposure condition, provided the time-temperature relations are known. Additionally, design fire scenarios consisting of decay phase with linear or nonlinear cooling rate depending on the material properties of fuel and lining materials and ventilation size [101], can also be specified as fire exposure condition in the model.

Following the fire temperature computation, temperature rise in each element of the cross-section is computed. For this a two-dimensional finite element based heat transfer analysis is carried out taking into account the high-temperature thermal properties of constituent materials, namely, concrete, steel rebar, FRP, and insulation. At each time step, the temperature rise in the section is computed by establishing a heat balance at each element [164]. Heat balance condition refers to equating thermal energy generated from fire to the energy required to raise temperature of structural members surrounding the fire plus any heat losses. The heat balance condition is based on law of conservation of energy and is given as:

$$q_f = q_c + q_r + q_L \tag{4.2}$$

where, q_f is heat generated from fire; q_c and q_r are heat absorbed by the exposed surface of structure due to convection and radiation, respectively; and q_L is heat loss to the surrounding environment.

The calculations are performed over a unit length of segment assuming the temperature to be uniform over the length of segment. In the analysis, heat transfer from the fire zone to the bottom surface of the structural member/insulation is through convection and radiation mechanisms, while heat transfer within the member is through conduction. Further, the temperature at the center of each element is computed by taking the mean of temperatures at the nodes of rectangular elements, which is then provided as an input to the structural analysis.

The governing equation for transient heat conduction in isotropic material is:

$$k\nabla^2 T + Q = \rho c \frac{\partial T}{\partial t} \tag{4.3}$$

where, k is thermal conductivity (W/m°C); ρ is the density (kg/m^3); c is specific heat (J/kg°C); T is temperature (°C); t is time; Q is the internal heat source defined as the amount of heat generated per unit time per unit volume of the material, and ∇ is differential operator:

$$\nabla = \frac{\partial}{\partial x} + \frac{\partial}{\partial y} + \frac{\partial}{\partial z} \tag{4.4}$$

The convective and radiative heat flux on the boundary is given as:

$$q_c = h_c\left(T - T_E\right) \tag{4.5}$$

$$q_r = h_r\left(T - T_E\right) \tag{4.6}$$

where, h_c and h_r are the convective and radiative heat transfer coefficient (W/m^2 K^4), respectively. The radiative heat transfer coefficient is given as:

$$h_r = 4\sigma\varepsilon_s\varepsilon_f\left(T^2 + T_E^2\right)\left(T + T_E\right) \tag{4.7}$$

where, T_E is the temperature of surrounding enviornment; ε_s and ε_f are the emissivity of the exposed surface of the structural member and fire; σ is the Stefan-Boltzmann constant 5.67×10^{-8} (W/m^2 K^4). Therefore, the total heat flux on the boundary is given as:

$$q = \left(h_c + h_r\right)\left(T - T_E\right) \tag{4.8}$$

Using Fourier's law, governing heat transfer equation on boundary condition is written as:

$$-k\left(\frac{\partial T}{\partial y}n_{\mathrm{y}}+\frac{\partial T}{\partial z}n_{\mathrm{z}}\right)=-h\left(T-T_{f}\right) \tag{4.9}$$

where, n is the outward surface normal; T_f is the temperature of the fire (°C). The value of h_c, ε_f and ε_s considered in the current analysis are 25 (W/m^2 K^4), 1, and 0.8, respectively [165]. In the fire resistance analysis, the surface of a structural member is either exposed or unexposed to fire therefore, there are two different boundary conditions, namely exposed boundary condition and unexposed boundary condition, and these are given as:

exposed:

$$\begin{aligned}
&-k\left(\frac{\partial T}{\partial y}n_{\mathrm{y}}+\frac{\partial T}{\partial z}n_{\mathrm{z}}\right)=-h_{f}\left(T-T_{f}\right)\\
&-k\left(\frac{\partial T}{\partial y}n_{\mathrm{y}}+\frac{\partial T}{\partial z}n_{\mathrm{z}}\right)=h_{c}\left(T-T_{f}\right)+\sigma\varepsilon_{s}\varepsilon_{f}\left[\left(T+273\right)^{4}-\left(T_{f}+273\right)^{4}\right]
\end{aligned} \tag{4.10}$$

unexposed:

$$-k\left(\frac{\partial T}{\partial y}n_{\mathrm{y}}+\frac{\partial T}{\partial z}n_{\mathrm{z}}\right)=h_{a}\left(T-T_{a}\right) \tag{4.11}$$

where, h_f and h_a are the heat transfer coefficient of the fire exposed side and unexposed side, respectively; and the T_f and T_a are the fire exposed and unexposed side temperatures, respectively.

Galerkin finite element formulation is used for solving the above partial differential equation Eq. [4.3]. In this approach, the material property matrices (stiffness matrix K_e and mass matrix M_e) and the equivalent nodal heat flux vector (F_e) are generated for each rectangular element. These matrices are given as:

$$K_{e}=\int_{A}\left[k\frac{\partial N}{\partial x}\frac{\partial N^{T}}{\partial x}+k\frac{\partial N}{\partial y}\frac{\partial N^{T}}{\partial y}\right]dA+\int_{\Gamma}N\alpha N^{T}ds \tag{4.12}$$

$$M_{e}=\int_{A}\rho cNN^{T}dA \tag{4.13}$$

$$F_e = \int_A NQdA + \int_\Gamma N\alpha T_\alpha ds \tag{4.14}$$

where, N is the vector of shape functions; α is the h_a or h_f depending on the boundary condition; s is the distance along the boundary; and T_α is the surrounding boundary temperature (fire or ambient)

Once the element matrices are computed, they are assembled into a global system of differential equations, which is expressed as:

$$[M]\{\dot{T}\} + [K]\{T\} = \{F_n\} \tag{4.15}$$

where, [K] is the global stiffness (heat conduction/ convection) matrix; [M] is the global mass (capacitance) matrix; {F} is the equivalent nodal heat flux due to the natural boundary conditions; and {T} is the nodal vector corresponding to first order derivative of temperature with respect to time.

A finite difference procedure (θ algorithm) in the time domain is applied to solve the above equation Eq. [4.15] and this results in equation:

$$\left(M + ts\theta K\right)T_{n+1} = \left(M - ts\left(1-\theta\right)K\right)T_n + ts\left(\theta F_{n+1} + \left(1-\theta\right)F_n\right) \tag{4.16}$$

where, ts is the time step; T_n and T_{n+1} are the temperatures at the beginning and end of time step and θ is a constant parameter (value between 0 and 1) that determines the stability and accuracy of the numerical procedure applied to solve the nonlinear heat transfer equation. To achieve unconditional stability the value of θ should be ≥ 0.5 [166]. Therefore, in the proposed model the value of θ is taken as 0.5.

For unconditional stability of numerical calculations, constant θ should be greater than 0.5 [166]. Using the known temperatures at ambient condition and the above-mentioned equation Eq. [4.16], the time-temperature history at the following time step can be obtained, and this can be repeated for subsequent time steps. At each time step, an iterative procedure is required to solve Eq. [4.16] due to the nonlinearity of both thermal properties and varying boundary conditions. Detailed derivation of heat transfer equations can be found in literature [166] and is summarized in Appendix C.

(iii) Structural analysis

In the third and final step, structural response of the flexural member (beam or slab) are evaluated. The cross-sectional temperatures computed in thermal analysis are provided as an input to the structural analysis. Structural calculations, at elevated temperature exposure, are carried out using the same mesh as used for the thermal analysis [Figure 4.2 (d, h)]. The temperatures, deformations, and stresses in each element are represented by the corresponding values at the center of the element.

At the start of the structural analysis in each time step, the fire induced axial force generated in the member as well as the relative slip between FRP and concrete at each segment, due to degradation of interfacial bond, are computed using the procedure explained in next section. Following this, the M-κ relationships for each segment are generated taking into account temperature dependent degradation in mechanical properties of concrete, steel rebar, and FRP. The assumptions made for the generation M-κ relationships are enlisted below:

- Plane sections before bending remain plane after bending.
- Flexural member has a constant cross-section.
- The failure of beam is through flexural strength limit and the beam does not fail in shear strength limit.
- There is no bond-slip between steel reinforcement and concrete at various temperatures.

- FRP sheet/laminate used for strengthening of the member exhibits linear stress-strain relationship at various temperatures up to failure.
- Axial restraint force is constant along the length of the member.

The analysis starts with assuming initial values of curvature and corresponding strain in the topmost fiber of concrete. The distribution of total strain in each element of concrete, steel and FRP (which is assumed to be linear as shown in Figure 4.3) is then computed using the equation:

$$\varepsilon_t = \varepsilon_c + \kappa y \tag{4.17}$$

where, ε_t = total strain; ε_c = assumed strain at the topmost fiber in concrete; κ = assumed curvature; y =distance from uppermost fiber in concrete to the center of the element.

Once the total strain in each element of concrete, steel, and FRP is computed, the mechanical strain in each of these elements is calculated using the following formulae:

$$\varepsilon_{mec}^{c} = \varepsilon_{t}^{c} - \varepsilon_{th}^{c} - \varepsilon_{cr}^{c} - \varepsilon_{tr}^{c} \text{ (for concrete)} \tag{4.18}$$

$$\varepsilon_{mec}^{s} = \varepsilon_{t}^{s} - \varepsilon_{th}^{s} - \varepsilon_{cr}^{s} \text{ (for reinforcing steel)} \tag{4.19}$$

$$\varepsilon_{mec}^{frp} = \varepsilon_{t}^{frp} - \varepsilon_{th}^{frp} - \varepsilon_{cr}^{frp} - \varepsilon_{bi} - \varepsilon_{slip} \text{ (for FRP)} \tag{4.20}$$

where, ε_{mec} is the mechanical strain; ε_{th} is the thermal strain; ε_{cr} is the creep strain; and ε_{tr} is transient strain (exclusive to concrete); ε_{bi} is the initial strain at the soffit of the flexural member due to dead load; ε_{slip} is the strain due to slip at the interface of concrete and FRP due to the degradation of bond. The superscripts "*c*", "s" and "*frp*" represent concrete, steel rebar, and FRP, respectively. The value or expression for each of these strain components are summarized in Appendix D.

The thermal strain in concrete, steel (rebar), and FRP is a function of temperature in the element and can be computed by knowing respective coefficient of thermal expansion (which changes with temperature). In case of FRP, the thermal strain depends on the coefficient of thermal expansion which is different in transverse and longitudinal direction. The transverse direction thermal expansion coefficient is governed by matrix properties and the longitudinal direction thermal expansion coefficient is governed by the fibers orientation and fiber volume fraction. However, in a unidirectional FRP only fiber properties dominate the overall behavior (Rahman et al, 1993).

Creep strain in concrete and steel is assumed to be a function of time, temperature and stress level. The creep strain in concrete is computed based on [167] model, whereas in case of reinforcing steel, creep strain is computed based on [88] model for steel. In case of FRP, creep effects are minimal if the fibers in the FRP are oriented along the length of flexural member [138]. The creep effects of FRP can be neglected in beams or slabs strengthened for flexure as the fibers are always oriented along their longitudinal axis.

Transient strain in concrete, under fire conditions, is dependent on thermal strain and is computed using the model proposed by Anderberg and Thelandersson [93]. The initial strain resulting from the dead loads present on the flexural member, during the application of FRP strengthening, is computed through an elastic analysis of the strengthened member under dead loads [19].

Knowing the mechanical strain in each element, obtained by applying Eqs. [4.18 - 4.20], the distribution of stresses and corresponding internal forces in the cross-section of the beam/slab is computed (as shown in Figure 4.3) using temperature dependent stress-strain relationships for concrete, steel, and FRP. The internal forces are then summed to check force equilibrium in the section. For the assumed value of total strain at the top layer of concrete (ε_c), the curvature (κ) is iterated until force equilibrium and strain compatibility conditions are satisfied within a specified numerical (convergence) tolerance. Corresponding to curvature (κ) at which these conditions are satisfied, the moment due to internal forces in the section is computed. This moment and curvature represent one point in the M-κ relationship for the segment under consideration. At each time step, various points on the M-κ curves are generated for each segment of the flexural member until strain in topmost layer of concrete reaches its limiting (failure) strain, i.e., ultimate strain of concrete at any given temperature. The maximum value of the moment in the M-κ relations, determines the moment capacity of the segment of the strengthened flexural member.

The time dependent M-κ relationships generated for each segment are then used to trace the response of entire flexural member exposed to fire. At each time step, the strength and deflection of the flexural member is evaluated through a stiffness approach wherein, the updated secant stiffness of various segments of the flexural member is used. The secant stiffness matrix for each segment is based on the load (moment) level reached in the segment and is determined from the M-κ relationship generated for that particular segment. The loading vector and the secant stiffness matrix for each segment are then assembled in the form of nonlinear global stiffness/ force-displacement equation:

$$\left[K_g\right]\{\delta\}=\{P\}=\left\{P_f\right\}+\{P_s\} \tag{4.21}$$

where, $[K_g]$ is the global stiffness matrix; $\{\delta\}$ is the vector of nodal deflections; $\{P\}$ is the equivalent nodal load vector; $\{P_f\}$ is the equivalent nodal load vector due to applied loading and $\{P_s\}$ is the equivalent nodal load vector due to P-δ effect. These are second order effects resulting from axial restraint force (explained later). An iterative procedure described by Campbell and Kodur [168] is employed to solve the force-displacement equation, i.e., Eq. [4.21] and determine the strength and deflection of the flexural member.

The above described procedure for computing the strength and deflection is an improvement over the procedure followed by Ahmed and Kodur [131] in tracing the fire response of a FRP-strengthened beam. In the numerical model developed by Ahmed and Kodur [131], the maximum slip strain at a section of any segment was considered as a slip for all sections along the length of the beam. Therefore, once debonding at one of the sections (segments) occurred (computed by comparing interfacial strain with debonding strain explained in next section), complete loss of bond was considered to have occurred in the entire length of the beam, which in turn lead to an abrupt decrease in the capacity of the beam. However, this is not realistic, as the relative slip between FRP and concrete varies at each segment along the length of the beam and as a result, the moment capacity of section in each segment can be different. Hence, this approach of considering uniform slip along the entire length, although simplified analysis, provides a conservative response rather than a realistic response. Therefore, in the current version of the model, moment resulting from structural loading at any segment is compared against the moment capacity of the corresponding segment, which is computed by considering bond slip specific to that segment. Thus, a member analysis is carried out, wherein the analysis is carried out by considering entire beam or slab into account, i.e., by analyzing several cross-sections (segments) along the length of the beam (or slab), rather than analyzing an individual segment (or critical cross-section). As a result, a continuous and gradual degradation of capacity is observed as opposed to rapid and abrupt decrease, thereby providing a realistic response.

4.2.3 Modeling Bond Degradation at FRP-Concrete Interface

The bond between FRP and concrete is responsible for transfer of stresses from concrete to FRP. Therefore, if the bond between FRP and concrete interface fails, the FRP-concrete composite action is lost. This loss of composite action due to failure of bond is known as debonding failure and primarily occurs through three different failure modes namely, mode I (opening/peeling), mode II (tangential shearing), and mode III (tearing) failure modes. These failure modes are shown in Figure 4.4. Previous studies have shown that in an FRP-strengthened concrete flexural member, FRP-concrete interface is primarily subjected to normal and in-plane shear stresses. Further, due to smaller thickness of FRP sheet/plate, the bending stiffness of FRP is almost negligible as compared to that of the concrete beam, therefore normal stresses can be neglected [169]. Thus, mode II, i.e., in-plane shearing failure is primary mode of failure in FRP-strengthened concrete flexural members and must be accounted in the analysis.

At room temperature, the debonding failure is due to the shear stresses at the interface resulting from loading, however, at elevated temperature the debonding failure can also occur due to degradation of binding material. FRP is applied to RC structures using a binding material (epoxy) which being a thermosetting material, is highly susceptible to thermal degradation even at moderately low temperatures. With increase in temperature, the bond between FRP and concrete starts degrading which causes a tangential displacement in longitudinal direction (relative slip) between FRP and concrete. Due to this relative slip, the transfer of tangential shear stresses (τ) between concrete substrate and FRP reduces significantly and hence, full capacity of FRP cannot be utilized. With further increase in temperature due to fire, the degradation of bond and the resulting slip increases further, which leads to debonding of FRP and ultimately failure of strengthened member. Thus, temperature induced degradation of bond between FRP and concrete must be accounted for in fire resistance evaluation of FRP-strengthened RC structures.

Previous researchers such as, Ahmed and Kodur [131], utilized degradation of bonding adhesive's shear modulus with temperature to determine the tangential displacement, whereas Dai et al. [121], Firmo et al. [149], and Firmo et al. [157] utilized mode II cohesive laws, i.e., bond stress-slip relations to incorporate the effect the bond degradation in their analysis. The former approach by Ahmed and Kodur [131] is based on oversimplified assumptions, as the degradation of bond and resulting slip depends on various factors such as tensile strength of concrete (f_t), adhesive's T_g, stiffness of the interface, and FRP to concrete width ratio, and therefore does not accurately capture the bond-slip behavior between FRP and concrete. Whereas the latter approach involves fracture mechanics based complex cohesive zone modeling implemented using commercial software. Although, this approach simulates the behavior of FRP-concrete interface with reasonable accuracy, its implementation requires significant computational efforts as well as specific training.

To overcome the shortcomings and complexities of the above described techniques for simulating temperature induced bond degradation, a hybrid of these two procedures is implemented in the numerical model proposed in this dissertation. In this procedure, the bond stress-slip relations are used to determine the tangential displacement (δ) at each section along the length of the beam/slab, which in turn are used to determine the slip strain (ε_{slip}) in section. This slip strain (ε_{slip}) is used as one of the components of total strain at the level of FRP and is deducted from the sum of ε_{mec} and ε_{th}. Thus, the total strain at the level of FRP decreases and as a result the stress transferred to FRP is lower, thereby reducing the capacity of the strengthened member.

The temperature dependent nonlinear bond-slip relations proposed by Dai et al. [134] are used to compute the tangential displacement (relative slip) at FRP-concrete interface. These relations are based on two interfacial parameters, namely, interfacial fracture energy (G_f) and the interfacial brittleness index (B). These bond-slip relations are given as:

$$\tau_{f,T} = 2G_{f,T}B_T\left(e^{-B_T\delta} - e^{-2B_T\delta}\right) \tag{4.22}$$

with

$$\frac{G_{f,T}}{G_{f0}} = \frac{1}{2}\tanh\left[-c_2\left(\frac{T}{T_g} - c_3\right)\right] + \frac{1}{2} \tag{4.23}$$

$$\frac{B_T}{B_0} = \frac{(1-d_1)}{2}.\tanh\left[-d_2\left(\frac{T}{T_g} - d_3\right)\right] + \frac{(1+d_1)}{2} \tag{4.24}$$

where, $\tau_{f,T}$ is shear bond stress at temperature T (N mm^{-2}); δ is the interfacial slip between FRP and concrete (mm); T_g is the glass transition temperature of the adhesive (°C); T is the elevated temperature (°C); G_{f0} and $G_{f,T}$ are the interfacial fracture energy at ambient and elevated temperature (N mm^{-1}); B_0 and B_T are the interfacial brittleness index at ambient and elevated temperature (mm^{-1}); and c_2, c_3, d_1, d_2, and d_3 are constants determined from least-square regression analysis of test data with values equal to 3.21, 1.31, 0.485, 14.1, and 0.877, respectively [134].

The interfacial fracture energy (G_f) is defined as the area under the bond slip curve, and it depends on tensile strength of concrete, width ratio of FRP to concrete, and properties of bonding adhesive. The interfacial brittleness index (B) is a parameter that depends on the adhesive stiffness and governs the shape of the bond-slip curves. A high value of brittleness index represents high initial interfacial stiffness resulting in a steeper ascending and descending branch of curve. The value of interfacial fracture energy at ambient temperature (G_{f0}) is computed using the equation proposed by Lu et al. [170] given as:

$$G_{f0} = 0.308\beta_w^2\sqrt{f_t} \tag{4.25}$$

with,

$$\beta_w = \sqrt{\frac{2.25 - b_{frp}/b_c}{1.25 + b_{frp}/b_c}} \tag{4.26}$$

where, f_t is the tensile strength of concrete (N mm^{-2}); b_f is the width of FRP (mm); b_c is the width of concrete (mm); and β_w is FRP-to-concrete width ratio factor. The value of brittleness index varies from 8 to 15.1 for concrete strengths ranging from 15 to 50 MPa. Lu et al. [170] and Dai et al. [121] recommends a value of B_0 = 10.4 for all concrete strengths and conventional bonding adhesive. It is evident from the above Eqs. [4.22 - 4.26] that the bond-slip relations consider the effect of all the critical factors namely, adhesive's T_g, tensile strength of concrete (f_t) as well as the ratio of the width of FRP to concrete, which affect the bond strength relations.

A typical set of bond slip relations at elevated temperatures computed using Eqs. [4.22 - 4.26] are shown in Figure 4.5 wherein, the compressive strength of concrete (f_c' = 38.8 MPa), tensile strength (f_t = 2.8 MPa), brittleness index (B_0 = 10.4) and a conventional adhesive with T_g = 82°C [19] is considered for computations. For clear comparison, the bond strength at elevated temperatures are normalized by the peak strength at ambient temperature. It can be seen from the figure that the bond strength remains constant until 40°C. At 60°C, bond strength is reduced to 70% of strength at ambient temperature. At 70°C, i.e., close to T_g of the adhesive bond strength is reduced to 40% of that at room temperature. With further increase in temperature, the bond strength continues to degrade continuously until 120°C where bond strength is fully lost indicating complete degradation of bond between FRP and concrete.

Figure 4.6 shows the shear stress and resulting shear force for a infinetestimally small unit of length dx of a segment of length L_i. Based on the figure the average shear stress along the infinetestimally small unit can be given as:

$$\tau(dx)b_p = \frac{dN_p}{dx} \tag{4.27}$$

The average shear stress (τ_i) at the interface of FRP concrete can be computed by integrating the above equation Eq. [4.27] along the length of segment as:

$$\tau(i) = \frac{N_{frp(i+1)} - N_{frp(i)}}{L_i b_p} \tag{4.28}$$

where, $N_{frp(i)}$ is force in FRP reinforcement for segment i; L_i is the length of segment i; and b_p is the width of FRP concrete interface. The slip (δ) corresponding to the average shear stress (τ_i) is computed using the bond slip relations derived using Eqs. [4.22 - 4.26]. Following this the slip strain in the segment is then computed as:

$$\varepsilon_{slip} = \frac{\delta}{L_i} \tag{4.29}$$

4.2.4 Second Order Effects (P-δ) from Axial Force

Generally flexural members in buildings are often restrained by columns or shear walls at the ends. Therefore, when the ends of the beam/slab expand under fire conditions significant axial restraint force can develop at the supports. When the vertical deflection (δ_v) due to the applied transverse loads on the flexural member increases, the fire induced axial force (P_a) creates additional bending moment $M_a = P_a * \delta$ in the member, as shown in Figure 4.7 (c-d). Since moment M_a is generated due to the effect of vertical deflection (δ_v), which is a first order effect resulting from the transverse loads on the member, M_a is known as secondary moment and the effect is known as P-δ effect. The magnitude of the additional bending moment (M_a) is a function of axial force and stiffness of the member. M_a can have a positive or negative effect on the fire resistance of the member, and therefore, must be accounted in the numerical analysis.

To determine the amount of axial restraint generated during fire conditions and to account for the effect axial restraint force an approach recommended by Dwaikat and Kodur [171] is used and is explained here. The total axial restraint force (P_a) induced in the beam/slab can be calculated from the summation of compressive and tensile forces in each element of the cross-section, i.e.,

$$P_a = C + T = \sum \sigma_e A_e \tag{4.30}$$

where, σ_e is the stress at the center; and A_e is the area of each element in the cross-section. Since stress in each element can be computed using a given central total strain and the curvature of beam/slab, the axial force in each segment (P_{ai}) can be related to the corresponding central total strain (ε_{0i}) and the curvature (κ_i) as follows:

$$P_{ai} = f\left(\varepsilon_{0i}, \kappa_i^{ts}\right) \tag{4.31}$$

At a given time step, the axial restraint force is assumed to be the same in each segment. The curvature at the beginning of any time step (ts) is equal to the curvature in the preceding step (ts-1), and for a small increment in time the difference in the curvature is very small. Therefore, Eq. [4.31] can be expressed as:

$$P_{ai} = f\left(\varepsilon_{0i}, \kappa_i^{ts}\right) \approx f\left(\varepsilon_{0i}, \kappa_i^{ts-1}\right) \tag{4.32}$$

The axial restraint force must satisfy the compatibility condition along the span (L) of the member given as:

$$\Sigma l_i - L - \Delta = 0 \tag{4.33}$$

where, Δ is the axial expansion in the length of the flexural member, l_i is the projected length of the deformed segment I, and it can be calculated as follows:

$$l_i = \sqrt{\left(s_i\right)^2 - \left(v_{i2}^{ts} - v_{i1}^{ts}\right)^2} \approx \sqrt{\left(s_i\right)^2 - \left(v_{i2}^{ts-1} - v_{i1}^{ts-1}\right)^2} \tag{4.34}$$

where, s_i is the length of the deformed segment i, v is the vertical deflection, the subscripts i_1, i_2 indicate the end of the segment under consideration, and the superscripts (ts)and (ts-1) indicate the time step, as illustrated in Figure 4.8. Since, $s_i = (1 + \varepsilon_{0i}) * L_i$; Eq. [4.33] can be expressed as:

$$\Sigma\sqrt{\left(1+\varepsilon_{0i}\right)^2 L_i^2 - \left(v_{i2}^{ts-1} - v_{i1}^{ts-1}\right)^2} - L - \Delta = 0 \tag{4.35}$$

The axial restraint force (P_{ai}) is modified to satisfy the strain compatibility and force equilibrium conditions using the following iterative procedure:

- Assume a value of P_a for the known curvature (κ_i^{ts-1}) from preceding step, i.e., ts-1, (consider P_a = 0 at the initial time step).
- Compute the central total strain (ε_{0i}) in each segment of the flexural member.
- Compute the axial displacement (Δ) for the known value of spring stiffness (ks).
- Check compatibility along the span using Eq. [4.35].
- Update the axial force (P_a) until Eq. [4.35] is satisfied within a pre-determined tolerance value.

At the support, boundary conditions are represented by a spring with stiffness (ks). The stiffness (ks) can be assigned any value depending on the degree of restraint experienced in practical applications. Once the axial restraint force is computed through iterative procedure explained above, M-κ relationships are generated through the approach described in previous section. Finally, during the stiffness analysis, the effect of second order moments is computed as:

$$\{P_s\} = -\left[K_{geo}\right]\{\delta\} \tag{4.36}$$

where, $\{P_s\}$ is equivalent nodal vector due to P-δ effect, $[K_{geo}]$ is the geometric stiffness matrix; and $\{\delta_v\}$ is nodal displacement.

4.2.5 High-temperature Material Properties

Evaluation of fire performance of FRP-strengthened RC flexural member essentially requires temperature dependent thermal and mechanical properties of the constituent materials, i.e., concrete, reinforcing steel, FRP, and fire insulation. The thermal properties required for the heat transfer analysis include thermal conductivity, specific heat capacity, coefficient of thermal expansion (CTE), and density, while the mechanical properties required for structural analysis comprise of tensile strength, elastic modulus, stress-strain relationships, and bond-slip relations.

Reliable data on temperature dependent thermal properties of concrete and steel is available in the literature, such as ASCE manual [78] and Eurocode 2 [79]. However, limited information is available on thermal properties of FRP at ambient and elevated temperatures. For concrete and reinforcing steel, high-temperature thermal property relations proposed in ASCE manual, and Eurocode 2 are incorporated in the model. The user can select the appropriate properties for concrete based on strength (normal or high) of concrete and type of aggregate (siliceous or carbonaceous). For FRP, the temperature dependent thermal conductivity and specific heat are built into the model using the relations proposed by Griffis et al. [102]. For fire insulation, the thermal conductivity and specific heat depend on the type of material, such as gypsum board, Rockwool, SFRM, etc., used for thermal protection. Therefore, the high-temperature thermal properties of fire insulation are incorporated in the numerical model based on thermal properties generated through material property tests. All the available constitutive relations for the temperature dependent thermal and mechanical properties of concrete, steel, FRP, and insulation which are incorporated in the model, are summarized in Appendix A.

Figure 4.9 (a-b) shows the normalized variation with temperature, of thermal conductivity and specific heat, respectively, for concrete, steel, FRP, and CAFCO SFRM fire insulation. In the figure, the curves for thermal properties of concrete and steel, FRP, and fire insulation are based on relations specified in Eurocode 2 [79], Griffis et al. [102], and Kodur and Shakya [143], respectively. It can be seen from the Figure 4.9 (a), that the thermal conductivity of concrete, steel, and FRP decreases with temperature, whereas thermal conductivity of fire insulation decreases initially due to evaporation of water and then increases beyond 300°C. This is due to higher gypsum content, which has very high crystallinity [172]. The specific heat of concrete, steel, and FRP increases with temperature [Figure 4.9 (b)], whereas for fire insulation, the specific heat decreases until 400°C due to evaporation of water, after which the specific heat increases marginally due to the evaporation of chemically bound water [143]. In case of FRP, the specific heat increases around 310°C and remains constant until 510°C after which it starts decreasing. This peak plateau is due to additional heat absorbed for decomposition of the resin [102].

The values of co-efficient of thermal expansion of concrete and reinforcing steel rebars, as given in Eurocode 2 [79], are incorporated in the model. In case of FRP, the transverse direction thermal expansion coefficient (27×10^{-6}/°C), as governed by matrix properties, is higher as compared to the longitudinal direction thermal expansion coefficient (-0.09×10^{-6}/°C), as governed by fiber orientation and fiber volume fraction (Mallick 2007). In the present study, the fibers are considered to be oriented along the longitudinal axis of the flexural member. Therefore, based on the value of thermal expansion coefficient in fiber direction, the thermal strain in FRP in the longitudinal direction is assumed to be negligible.

For the high-temperature mechanical properties of concrete, relations available in ASCE manual [78] and Eurocode 2 [79] are incorporated into the model. The degradation in strength of concrete, steel, and FRP with temperature and their stress-strain response at elevated temperatures are incorporated in the model. Figure 4.10 shows the degradation in strength and elastic modulus of concrete and steel as specified in Eurocode 2 [79], and FRP Bisby et al.[120]. It can be seen from the figure that there is minimal (less than 20%) reduction in strength of concrete and steel until 400°C, whereas at the same temperature FRP loses more than 60% of its ambient temperature strength. This indicate that FRP loses strength at a higher rate as compared to concrete and reinforcing steel. Therefore, when a strengthened structural member is exposed to fire, the FRP loses much of its strength in early stages of fire. This results in a rapid reduction in the load carrying capacity of the structural member. However, the strength degradation of concrete and steel happens gradually in the later stages of fire, which is the main reason for the gradual reduction in the load carrying capacity of the structural member.

A typical set of stress-strain curves for concrete at elevated temperatures, as per the relations in Eurocode 2 [79], are shown in Figure 4.11 (a). For clear comparison, the strength at elevated temperature is normalized using the peak strength at ambient temperature. The stress-strain behavior of concrete in compression is considered as linear elastic up to $0.35f_c'$ (f_c'-peak stress). Beyond this point, the stress-strain behavior of concrete is nonlinear, i.e., the stress-strain curve consists of strain hardening and strain softening portion, which is incorporated in the model using relations proposed in Eurocode 2 [79]. Further, it can be seen from the figure that until 400°C, concrete loses less than 30% of its original strength at ambient temperature, however, at 600°C, more than 55% of the strength in concrete is lost. At about 800°C, strength in concrete reduces to 10% of its original strength at room temperature. Also, it can be seen from the figure that with the increase in temperature, ductility of concrete increases.

The stress-strain behavior of concrete in tension is linear elastic up to cracking strength followed by a softening curve. The softening stress-strain curve of concrete in tension is a two-piece bilinear curve, wherein, the first piece represents a sudden reduction of tensile stress to 60% of tensile strength and the second piece represents a linear descend of the strength to zero stress at a strain of six times cracking strain. This assumption is based on the value used by various researchers [156] for fire resistance analysis of FRP-strengthened concrete structural members. The same limit is also used in the commercially available finite element based software such as ANSYS®.

Similarly, the stress-strain behavior of reinforcing steel is defined in the model as per the relations in ASCE manual [78] and Eurocode 2 [79]. A typical set of stress-strain curves, as per the relations specified in Eurocode 2 [79], are shown in Figure 4.11 (b), wherein, the strength at elevated temperatures are normalized using the peak strength at ambient temperature for clear comparison. The stress-strain behavior is linear elastic up to the proportionality limit, after which the behavior is elastic but nonlinear until yield point, defined as the proof stress corresponding to 0.2% strain. Following the yield point, the stress-strain behavior is perfectly plastic (yield plateau) until a strain of 15% after which the stress drops to zero linearly, to a strain of 20%. It can be seen from the figure that yield stress-strain response of steel remains constant until 400°C. However, at 500°C, the strength of steel drops to 80% of original strength at room temperature, which further reduces to less than 50% at 600°C.

Published data on high-temperature mechanical properties of CFRP indicate that most of the epoxy decompose after about 300°C (Mouritz and Gibson 2006). However, fibers retain a considerable amount of strength and can contribute to strength (moment) capacity till about 500°C [109, 173]. To reflect this effect, the variation of strength and stiffness of FRP with temperature is defined based on the semi-empirical relationships proposed by Bisby et al. [120] in the temperature range of 20-1000°C. These relations have been derived by fitting a sigmoid function (a mathematical function having a smooth "S"-shaped curve) to data obtained from different tests on unidirectional composite materials, using least squares regression analysis. The stress-strain behavior of FRP is linear elastic until rupture at both ambient [19] and elevated temperature [120]. A typical set of stress-strain curves for FRP composite material at elevated temperatures, are shown in Figure 4.11 (c), wherein, the strength at elevated temperatures is normalized using the peak strength at ambient temperature for clear comparison. These stress-strain curves are based on the experimental data reported by Yu and Kodur [112].

4.2.6 Failure Criterion

At each time step, the model generates various response parameters such as cross-sectional temperatures, stresses in rebars, strains, mid-span deflection and moment capacity of the strengthened structural member. These output parameters are compared with pre-defined thermal and structural failure limit states, as specified in ASTM E119 [5], to determine the failure of the structural member. The strengthened member is considered to have failed when applicable failure limit state is exceeded; however, the analysis is continued until the moment capacity of the flexural member decreases below the moment due to applied loading. The time at which any of the applicable failure limit state is exceeded, is taken as fire resistance of the strengthened concrete member (beam or slab). The thermal and structural limit states considered for evaluating the failure are:

- The temperature of tensile reinforcing steel increases beyond 593°C.
- The average temperature on the unexposed surface of the slab exceeds 139°C or temperature at any one point exceeds 181°C above initial temperature (applicable only for slabs).
- The moment carrying capacity of the structural member falls below the applied moment due to loading.
- The mid-span deflection exceeds $L^2/400d$, and the rate of deflection exceeds $L^2/9000d$ (mm/min) limit over one minute interval where, L and d are the span length (mm) and effective depth (mm) of the structural member.

Although the failure of structural members under fire conditions is typically evaluated based on strength limit state and thermal limit state consideration, deflections also play a critical role in determining failure of horizontal structural members under fire conditions. This is due to the fact that the integrity and stability of the structural member cannot be guaranteed with excessive deformations. Fire resistance predicted using a limit on the deflection and rate of deflection will ensure safety of fire-fighters and allow safe evacuation. Thus, deflection provides a reliable evaluation of fire performance of a structural member and is considered as reliable performance index. Therefore, in addition to the insulation and strength criteria, deflection limit state, as specified in ASTM E119 [5] is also applied to evaluate the failure of strengthened structural members under fire conditions.

4.3 Model Validation

The validity of the above developed model is established by comparing response parameters predicted by the model with the response parameters measured in tests on CFRP-strengthened RC beams and slabs, under ambient and elevated temperature conditions. For this purpose, the T-beams and slabs tested at MSU in fire resistance tests carried out as a part of this dissertation (described in chapter 3) as well as the beams and slabs available in open literature are analyzed using the model. The response parameters compared for the validation include load-deflection response of the slabs tested at ambient conditions, cross-sectional temperatures, mid-span deflections and fire resistance of beams and slabs tested under fire conditions. The details of the validated beams and slabs are presented in this section.

4.3.1 Validation with Published Test Result

Four RC beams and four RC slabs are analyzed using the above developed model for validation at ambient and elevated temperature. The beams are designated as BV1, BV2, BV3, and BV4, while the slabs are designated as SV1, SV2, SV3, and SV4. Beam BV1 and slab SV1 are conventional un-strengthened RC flexural members, whereas beams BV2 to BV4 and slabs SV2 to SV4 are CFRP-strengthened RC flexural members. These beams and slabs were tested by Blontrock et al. [145] and Blontrock et al. [152], respectively. Beams BV1, BV2 and slabs SV1, SV2 were tested under ambient temperature, while the beams BV3, BV4 and slabs SV3, SV4 were tested under fire conditions. The geometrical, material property and loading details of the beams and slabs are summarized in Table 4.1 and are described below.

(i) Geometrical Configuration, Loading and Discretization Details

Figure 4.12 and Figure 4.13 shows the elevation and cross-section details of the beams BV1 to BV4 and slabs SV1 to SV4, respectively. All the beams were 3.15 m long with 200 mm wide and 300 mm deep cross-section and were reinforced with 2-10 mm ϕ steel rebars and 2-16 mm ϕ at the top and bottom, respectively. The selected slabs were 3.15 m long with 400 mm wide and 150 mm thick cross-section and were reinforced with 4 - 8 mm ϕ steel rebars in the longitudinal direction and with 6 mm ϕ rebars @ 200 mm c/c in transverse direction. The steel reinforcement in all the beams and slabs had a clear concrete cover of 25 mm.

The beams BV2 to BV4 and slabs SV2 to SV4 were strengthened with SIKA Carbodur S1012 CFRP sheet and S & P carbon sheet, respectively. The CFRP sheets were with 200 mm wide and 1.2 mm thick and were applied at the soffit of the beams and slabs using Sikadur 30 epoxy resin and Multipox epoxy resin, respectively, both having T_g of 67°C. Beams BV2 to BV4 and slab SV2 were strengthened with one layer of respective CFRP sheet, whereas slabs SV3 and SV4 were strengthened with two layers of carbon sheet.

The CFRP-strengthened RC beams BV3, BV4 and slabs SV3, SV4 were also protected with fire insulation material. Beam BV3 was protected with 25 mm thick fire insulation only at the bottom soffit along the entire span length, as shown in Figure 4.12 (c). Whereas beam BV4 was protected with 40 mm thick fire insulation on the bottom and 20 mm thick on the two sides extending up to a depth of 85 mm, only in the anchorage zones of the CFRP sheet over a length of 800 mm from either end, as shown in Figure 4.12 (d). This arrangement of insulation allows for validating the model with different insulation configuration along length. Both the beams were protected with Promatect H fire insulation which is a steam-hardened silicate plate composed of calcium silicate, cement, and some additives.

The slabs SV3 and SV4 were protected at the soffit level by using 18 mm thick Gyroc plates as an external fire insulation. These Gyroc plates were made of gypsum as a core material and were attached to the soffit of the slabs using mechanically fastened U-shaped steel profiles, as shown in Figure 4.13 (c) and (d). This arrangement of fire insulation created an empty gap of 45 mm in slabs SV3 and SV4. This gap was filled using Rockwool insulation in slab SV4. The room temperature properties of the insulation of the fire insulation material used in tests, as reported by Blontrock et al. [145, 152], are summarized in Table 4.1.

All the beams and slabs were tested under four-point loading with simply support boundary conditions. In case of ambient temperature tests, i.e., on beams BV1, BV2, and slabs SV1, SV2, the clear span between the supports (L) was 2.85 m and the distance (l_2) between the concentrated loads was 950 mm, as shown in Figure 4.12 (a-b) and Figure 4.13 (a-b). These beams and slabs were subjected to monotonic loading until failure, while load deflection response was recorded. In case of tests under fire conditions, i.e., tests on beams BV3, BV4, and slabs SV3, SV4, the clear span between the supports (L) was 3.0 m and the distance (l_2) between the concentrated loads was 1000 mm, as shown in Figure 4.12 (c-d) and Figure 4.13 (c-d). The beams and slabs were structurally loaded up to their respective service load level, as summarized in Table 4.1, and were then exposed to ISO 834 [16] standard fire conditions on the bottom surface.

For the analysis, the length of all the beams (BV1 to BV4) was discretized into 40 segments while the concrete within the cross-section of all the beams was discretized into 10 × 10 mm (width × depth) elements. The CFRP sheet attached to the soffit of beams BV2 to BV4 was discretized into 5 × 1.2 mm and the insulation attached to beams was discretized into 3 × 2 mm size rectangular elements. Similarly, the length of the slabs SV1 to SV4 was discretized into 20 segments and the concrete cross-section was discretized into 20 × 10 mm size elements. The CFRP sheets attached to the soffit of slabs SV2 to SV4 was discretized into and 10 × 1.2 mm and the insulation attached to the slabs SV3 and SV4 was discretized into 5 × 3 mm size elements. At each time step, cross-sectional temperatures (only in the analysis under fire conditions), moment capacity and mid-span deflection were evaluated.

(ii) Validation at Ambient Conditions

Beams BV1, BV2, and slabs SV1, SV2 were analyzed under two-point concentrated loading with simply supported boundary conditions, as described earlier. Based on the analysis, the moment capacity of the beams BV1, BV2 and slabs SV1, SV2, as predicted by the model is 64.7 kNm, 100 kNm, and 15 kNm, 20 kNm, respectively, which is close to the capacity reported in the tests, i.e., 64 kNm, 100 kNm for beams and 16 kNm, 19 kNm for the slabs.

The predicted and measured load-deflection response of these beams is compared in Figure 4.14. It can be seen from the figure that in the initial stages, both the beams BV1 and BV2 exhibit linear response until concrete cracking occurs at around 15 kN load. After that the mid-span deflection increases at a faster rate due to decreasing stiffness resulting from cracking in concrete. At this stage, the stresses in steel rebars in both the beams as well as the CFRP in beam BV2 increase at a faster rate until the steel rebars yield, and this can be seen in Figure 4.14 through the presence of another inflexion point on the load deflection curve. Beam BV1, which is a conventional RC beam, the moment capacity almost reaches its peak once the steel rebar enters yielding plateau. However, in FRP-strengthened beam BV2, the moment capacity keeps increasing with increased stress in FRP laminate until the ruptures. The mid-span deflection of both the beams as predicted by the model is in close agreement with the measured values, indicating the model can predict the response of RC beams with or without FRP-strengthening under ambient conditions.

Figure 4.15 shows the comparison of predicted and measured load-deflection response of slabs SV1 and SV2. It can be seen from the figure that the load-deflection response, for slabs SV1 and SV2, has two distinct points of inflection. The response of both the slabs is linear elastic up to the first point of inflection, which marks the beginning of cracking in concrete. The cracking of concrete results in increased level of stresses in steel reinforcement and CFRP until the second point of inflection, which marks the onset of yielding of steel. In case of SV1 (RC slab), the load carrying capacity of the slab reaches its peak value near the second point of inflection and the steel rebars enter a yielding plateau, resulting in ductile failure of the slab. However, in case of SV2 (CFRP-strengthened RC slab), the load carrying capacity of the slab increases beyond the point of inflection until the tensile failure of CFRP sheet, resulting in brittle failure of the slab. Further, it can be seen from Figure 4.15 that the predicted response, although largely in agreement, is slightly stiffer in initial stages as compared to the response measured in the tests. The difference can be attributed to elastic limit (modulus) of the constitutive relation and tensile strength of concrete considered in the model, which may be slightly higher as compared to the elastic limit and tensile strength of concrete used in tests. Overall, the predicted load-deflection response matches well with the measured response, indicating that the developed model can predict the response of CFRP-strengthened RC slabs under ambient conditions.

(iii) Validation at Elevated Temperature Conditions

The validity of the above model in predicting the fire response of FRP-strengthened concrete flexural members is established by comparing the predictions from the analysis with measured values in fire tests on beams BV3, BV4 and slabs SV3 and SV4, as reported by Blontrock et al. [145] and Blontrock et al. [152], respectively. During the tests, the beams and slabs were subjected to their respective service load levels which resulted in a bending moment of 40 kNm in beams and of 9.5 kNm in slabs. Only the progression of temperature in steel rebars and at CFRP-concrete interface as well as mid-span deflection were reported, and the flexural members were considered to have failed when the span to deflection ratio was equal to l/35. Further, in the tests on beams, it was reported that the CFRP-concrete composite action was lost in beams BV3 and BV4 after 18 and 39 minutes of fire exposure, respectively, and the insulation detached from the soffit of beam BV3 after 45 minutes of fire exposure, whereas in case of beam BV4, the insulation remained attached to the beam throughout the fire test duration. In case of slabs SV3 and SV4, Blontrock et al. [152] reported that interaction between CFRP and concrete surface was lost after 26 minutes and 38 minutes of fire exposure in, respectively, while the insulation in the slabs detached (fell-off) after 42 minutes and 50 minutes of fire exposure, respectively.

› Analysis Details

For the analysis, the geometrical, loading, and boundary conditions of the beams and slabs as well as the material properties of the constituent materials were considered identical to that in tests. The high temperature material properties of concrete and steel rebars follow the constitutive relations specified in Eurocode 2 [79], whereas the thermal properties of insulation follow the relations reported by Bai et al. [174] . Moreover, to evaluate the effect of detachment of insulation from the soffit of beams/slabs on the predictions from the analysis, beam BV3 was analyzed with insulation attached to the soffit throughout the fire exposure duration. Whereas slabs SV3 and

SV4, were analyzed as slabs protected with insulation until, 45 and 52 minutes of fire exposure, respectively, and then without any fire protection until failure which is determined as per above mentioned criteria.

The validation involves comparison of thermal and structural response of beams BV3, BV4 and slabs SV3, SV4. The thermal response is evaluated to determine the cross-sectional temperature, which in turn determine the degradation in strength properties of materials. Structural response is evaluated to determine the deflection and reduced capacity at any fire exposure time, which in turn is used to determine failure of the slab. These responses are validated in Figure 4.16 to Figure 4.19. Additionally, comparison of deflection in beams and slabs just prior to failure is summarized in Table 4.2.

› Thermal Response

The predicted and measured temperature rise at the CFRP-concrete interface at mid-span of beams BV3 and BV4 is compared in Figure 4.16 (a-b). The CFRP-concrete interface is protected with fire insulation in beam BV3, whereas in case of beam BV4, the interface is directly exposed to the heat of fire as insulation is provided only in the anchorage zones of beam BV4. Therefore, the interface temperature increases rapidly in beam BV4 as compared to that in beam BV3. The measured CFRP-concrete interface temperature in beam BV3 (Figure 4.16 (a)) plateaus after 30 minutes of fire exposure at 100°C due to the evaporation of water from the insulation plate. However, the predicted temperature does not experience the plateau as the water evaporation is not accounted in the model. Further, as expected the sudden increase in interface temperature at 45 minutes due to the detachment of insulation from the soffit of beam BV3 is not predicted by the model as the insulation delamination is not considered in the analysis. However, the predicted interface temperature in beam BV3 closely follow the measured temperatures until the insulation delamination. In case of beam BV4, it can be seen from Figure 4.16 (b) that the interface temperature rise predicted by model is in close agreement with that measured in test for entire fire exposure duration. This indicates that the predictions made by the model are fairly accurate

Figure 4.16 (c-d) shows the rebar temperature for beams BV3 and BV4. The rebar temperature is measured at the mid-span in beam BV3, and in the anchorage zone in beam BV4. It can be from the figure that the rebar temperature in beam BV3 increases rapidly as compared to that in beam BV4 throughout the fire exposure duration, due to the higher thickness of insulation at the soffit of beam BV4. The rebar temperature in beam BV3 plateaus for a short duration at 100°C due to moisture evaporation from concrete and then continues to increase rapidly. The rebar temperature exceeds 400°C after 80 minutes of fire exposure indicating initiation of degradation in strength properties of steel rebar. Further, it can be seen from Figure 4.16 © that the predicted temperature rise in rebar of beam BV3 is in close agreement with measured temperature rise. In case of beam BV4, the temperature increases slowly and plateaus at 100°C after 50 minutes of fire exposure due to moisture evaporation in surrounding concrete. The predicted temperature rise is in close agreement until the measured temperature rise plateaus, i.e., until 50 minutes, after which the predicted temperature continues to increase as the moisture evaporation is not accounted in the model.

Figure 4.17 (a-b) compares the predicted and measured temperature rise at the CFRP-concrete interface of slabs SV3 and SV4. It can be seen from the figure that the interface temperature in both these locations increases at a slower rate in the initial stages of fire exposure. The presence of Rockwool fire insulation in cavity of slab SV4 slows down temperature rise in the slab, and as a result, the temperatures at CFRP-concrete interface are lower than those in slab SV3. The CFRP-concrete interface temperature in slabs SV3 and SV4, increases steeply at 45 minutes and 52 minutes, respectively due to detachment of the insulation system. For comparison, the detachment of the insulation system was simulated in the analysis. The temperatures predicted by the model, with and without insulation system, compare well with the measured temperatures.

Figure 4.17 (c-d) compares the predicted and measured temperature rise in slabs SV3 and SV4. Like the interface temperature, the rebar temperature also increases slowly in slab SV4 as compared to that of slab SV3 due to the presence Rockwool insulation in cavity of slab SV4. Further, it can be seen that the predicted temperature rise in rebars of slabs SV3 and SV4 compares well with the measured values. The steel rebar temperature in both the slabs increases gradually and remain below 400°C during the entire duration of fire exposure. The temperature rise in the steel rebar predicted by the model is slightly lower than the measured values. This can be attributed to differences in high-temperature thermal property relations of concrete and insulation used in the analysis, and their actual properties in the tested slabs as well as to the presence of moisture in the concrete, which was not specifically reported by Blontrock et al. [152].

Temperatures at various locations in the concrete of beams and slabs could not be compared since Blontrock et al. [145, 152] did not report cross-sectional temperatures from the test. However, examination of concrete temperatures, predicted by the model, at various depths in beams BV3, BV4 and slabs SV3, SV4 point towards an expected trend; higher temperature at the bottom surface (closer to the fire source) and lower temperatures at distances away from the fire source. Overall, it can be seen from Figure 4.16 and Figure 4.17 that the predicted temperatures are in close agreement with the temperatures measured in the test during the entire duration of fire exposure.

› Structural Response

The predicted and measured mid-span deflection of beams BV3 and BV4 are compared in Figure 4.18 (a-b). It can be seen from the figure that for the most part of fire exposure, the predicted deflection compares well with the measured values in both the beams. Further, it can be seen that the deflection in beam BV4 (with insulation only in achorages) is almost similar to that of beam BV3 (insulation throughout the length). Analysis of the predicted results indicate that debonding of CFRP in beams BV3 and BV4 occurs after 15 and 35 minutes of fire exposure, respectively, which are close to the measured values (18 and 40 minutes of fire exposure). The small discrepancy can be attributed to a variation in bond properties used in the analysis as compared to actual properties. Nevertheless, over all model prediction of the beams deflection up to and beyond debonding point of the CFRP, matches the measured test data closely. The failure time, i.e., when span/deflection ratio is less than 1/35, predicted by the model for beams BV3 and BV4 is 92 and 82 minutes, respectively which is close to the reported values of 89 and 78 minutes, respectively.

Figure 4.19 (a-b) compares the predicted and measured progression of mid-span deflection for slabs SV3 and SV4. The deflection in both the slabs increases at a slow rate in the initial stages of fire exposure. This is attributed to the fact that there is little reduction (less than 5%) in strength and modulus of CFRP due to low level of temperature (less than 50°C) at CFRP-concrete interface. Due to presence of Rockwool fire insulation in the cavity, temperature propagation in the slab SV4 is slower, and hence, slab SV4 has slightly stiffer response as compared to slab SV3. With increase in interface temperature, bond between CFRP and concrete starts to deteriorate and as a result the composite action starts reducing after about 30 and 40 minutes of fire exposure in slabs SV3 and SV4, respectively which is slightly higher than the measured values of 26 and 38 minutes. With further increase in temperature, the composite action is completely lost which causes the slabs to behave as a conventional RC slab with higher load level thereby causing rapid rise in deflections.

The failure time predicted by the model for slabs SV3 and SV4 is 78 minutes which is slightly higher than 75 minutes as measured in the test. This may be due to the discrepancy between the actual high-temperature properties and those used in the analysis. Overall, predicted deflections follow the same trend as the measured deflections and agree reasonably well for the entire duration of fire exposure time. Therefore, the proposed macroscopic finite element model can predict the response of FRP-strengthened RC slabs under fire conditions. Further, based on the above analysis results it can be concluded that the neglecting the delamination of insulation do significantly affect the overall fire response predictions of the model.

4.3.2 Validation with Beams and Slabs Tested at MSU

To further validate the model, the FRP-strengthened RC T-beams and slabs tested as part of this dissertation at MSU are analyzed using the model. The geometrical configuration details of the tested T-beams and slabs are shown in Figure 4.20 and are summarized in Table 4.3. Additionally, material properties of the constituent materials as well as the loading details for the beams and slabs are summarized in Table 4.3. Various response parameters are compared to validate the thermal and structural response.

(i) Geometrical Configuration

The beams are designated as TB1, TB2, TB3, TB4, and TB5, while the slabs are designated as S1, S2. All the beams and slabs are 3.96 m long with a clear span of 3.66 m and are subjected to four-point loading system with simply supported boundary conditions, as shown in Figure 4.20 (a) and Figure 4.20 (c). The beams have T-shaped cross-section with dimensions shown in Figure 4.20 (b), while the slabs have a rectangular cross-section with dimensions shown in Figure 4.20 (d). Beams TB1 to TB3 are strengthened with 170 mm wide CFRP sheet, while beams TB4 and TB5 are strengthened with 100 mm wide CFRP sheet and slabs S1 and S2 are strengthened with 75 mm wide CFRP sheet. Beam TB1 is uninsulated, whereas beams TB2 to TB5 and slabs S1 and S2 are protected with fire insulation as per the configuration shown in Figure 4.20 (b) and Figure 4.20 (d), respectively.

(ii) Analysis Details

For the analysis, the cross-section of various segments along the length of the beams was discretized in to 20 mm × 20 mm quadrilateral elements which is further refined to 10 mm × 10 mm elements in the tension zone. Whereas the entire cross-section of the slabs is discretized in to 10 mm × 5 mm elements. The loading and boundary conditions of the beams and slabs are applied as per the actual test conditions. Additionally, the furnace fire temperature measured in the test were directly applied on the bottom and side surface of beams and on the bottom surface of slabs, to simulate the thermal loading. Response parameters predicted from the analysis, namely temperature rise at FRP-concrete interface, and at corner and mid rebars as well as defection and fire resistance of the beams and slabs are compared against those measured in fire tests. These response parameters are summarized in Table 4.4 and are discussed here.

(iii) Thermal Response

Figure 4.21 shows the comparison of the predicted and measured temperatures at FRP-concrete interface. In case of uninsulated beam TB1 (*cf.* Figure 4.21 (a)) the predicted temperature rise follows the same trend as the measured temperature rise throughout the fire exposure duration. However, predicted temperatures are slightly lower than the measured values throughout the fire exposure duration. This may be attributed to the severe burning of epoxy on the soffit of beam TB1, during the test, which increased the measured temperature rise in beam. These severe burning of epoxy was not accounted for in the model. After about 90 minutes of fire exposure, when the epoxy has completely burnt out, the difference between measured and predicted temperature values decreases and remains low until the end of fire exposure.

In case of insulated beams TB2 and TB3 (*cf.* Figure 4.21 (b, c)), the predicted temperatures compared well with the measured temperatures until 30 minutes of fire exposure, after which the measured temperatures increase abruptly due to the delamination of insulation which is not explicitly accounted for in the model. Similarly, in case of insulated beams TB4 and TB5 (*cf.* Figure 4.21 (d, e)), the predicted temperatures compare well with the measured values until 200 minutes and 170 minutes of fire exposure, respectively, after which the measured temperatures increased abruptly due to the delamination of insulation, which is not explicitly accounted for in the model.

Figure 4.22 shows the comparison of the predicted and measured temperatures at corner and mid steel rebars in beams TB1 to TB5. It can be seen from the figure that the predicted temperatures rise follows the same trends as that of measured temperature rise in all the beams. However, the predicted rebar temperatures are slightly lower than the measured values. In case of uninsulated beam TB1, the severe burning of epoxy on the soffit of the beam increased the heat flow within the beam cross-section which in turn increased the temperature rise at the rebar. This severe burning of epoxy was not accounted for in the model, and therefore, the predicted temperatures are lower than the measured temperatures.

In case of insulated beams TB2 and TB3, the different in the predicted and measured temperature rise at the rebars is very small in the initial stages of fire exposure. However, after 60 minutes the measured temperature rise increases at a slightly faster rate due to the delamination of insulation which is not explicitly accounted for in the model. In case of insulated beams TB4 and TB5, the higher temperatures in the test are attributed to the localized cracks in the insulation which increased the heat flow within the section which in turn lead to faster temperature rise in the section. These crack formation in the insulation was not accounted for in the numerical model. Additionally, the moisture evaporation plateau which causes a lag in the temperature rise at the rebars was also not accounted in the model. These two factors, i.e., crack formation and delamination of insulation as well as the moisture evaporation plateau causes minor discrepancies the predicted and measured values. However, the temperature rise in the rebars is less than 593°C (critical temperature for rebar due to 50% strength reduction), hence, the minor discrepancy does not significantly alter the predicted strength degradation in steel rebars.

Figure 4.23 (a-d) shows a comparison of the predicted and measured temperatures at the FRP-concrete interface and at rebars in slabs S1 and S2, respectively. It can be seen from the figure that the predicted temperature compares well with the measured temperature, with minor discrepancies. For instance, as can be seen from Figure 4.23 (a) the model slightly overpredicts the temperature rise at the FRP-concrete in slab S1 after 60 minutes of fire exposure. This may be attributed to the formation of char layer on the thermocouple resulting from the burning of epoxy which hinder the heat flow and the temperature rise at the thermocouple. This discrepancy is not in case of slab S2 (Figure 4.23 (b)) indicating the model can predict the temperature rise at the FRP-concrete interface with sufficient accuracy.

The predicted temperature rise in the rebars of the both the slabs follow the same trend as the measured temperature rise. The minor discrepancies between the predicted and measured temperature rise in the rebar can be attributed to the cracks in the insulation which increases the heat flow within the section and to the thermal properties of the insulation and concrete material used in the model which could slightly different than those in tests. Further, it can be seen from Figure 4.23 (c-d), the predicted temperature rise in steel rebars of the slabs S1 and S2, remain below 400°C, throughout the fire exposure duration. Hence, these slightly higher temperature does not affect the strength and stiffness degradation of the rebars, and therefore, does not affect the overall stiffness of the beam. Overall, it can be concluded that the model can predict the temperature rise within the cross-section of FRP-strengthened concrete flexural member with sufficient accuracy.

(iv) Structural Response

For structural response validation, the mid-span deflection, of the T-beams, predicted by the model are compared with the measured values in Figure 4.24. It can be seen from Figure 4.24 that the predicted deflection compares well with the measured values for all the beams. In the uninsulated beam TB1, the predicted deflection closely follows the measured deflection and exceeds the deflection limit at 180 minutes of fire exposure. However, the rate of deflection does not exceed the deflection rate limit, therefore the beam has not failed in deflection limit state. Similarly, in case of insulated beam TB2, TB4, TB5 the predicted values are in close agreement with the measured values throughout the fire exposure duration and remains above the deflection limit until the end of fire exposure, indicating no failure in deflection limit state. Additionally, due to the presence of insulation for a major duration of fire exposure, the temperature rise in the rebars of the beams TB4 and TB5 is very low. As a result, the degradation in strength and modulus properties of steel rebars is very low. Therefore, the deflection in beams TB4 and TB5 are very small compared to other beams.

In case of insulated beam TB3, the model slightly overestimates the deflection values as compared to the measured values between 30 and 150 minutes of fire exposure. This may be attributed to the slightly higher strength of rebar in the test than that in model. After 150 minutes the predicted deflection is slightly lower than the measured values, this may be attributed to the slightly higher temperature rise in the rebars during the test than the temperature rise predicted by the model, which slightly alters the strength degradation in rebars. As a result, the predicted deflection values exceed the deflection limit at 180 minutes which is 10 minutes more than that of 170 minutes measured in the tests. However, the rate limit is not exceeded indicating no failure in deflection limit state

Figure 4.25 shows the comparison of predicted and measured the mid-span deflection of the slabs S1 and S2. It can be seen from the figure that the predicted deflection values are in close agreement with the measured values until 130 minutes of fire exposure. After 130 minutes the model slightly underpredicts the deflection as compared to the measured values. This may be attributed to the slightly higher temperature rise in the rebars of the slab S1 measured in test than those predicted by the model. Additionally, as the applied load very small for the actuator used for load application, the applied loads on slab S1 during the test were fluctuating (*cf*. Figure 4.25 (c)) and not constant as in the model. Therefore, the deflection predicted by the model for slab S1 are slightly lower than those measured in the test.

In case of slabs S2, the predicted deflection follows the same trend as that measured in the test (Figure 4.25 (a)). However, the predicted values are much lower than the measured response until 150 minutes of fire exposure. This is attributed to major fluctuations in the applied load on slab S2 during the test, as shown in Figure 4.25 (d). The loads applied on slab S2 increases significantly than the pre-decided load value. However, these fluctuations in the load were not accounted for in the model, rather a constant value taken as the average of the loads applied during the test, was used in the model. As a result, significant fluctuations were observed in the measured deflection and the predicted deflection is lower than the measured values until 150 minutes of fire exposure. After 150 minutes, FRP-concrete interface temperature increases beyond 250°C, indicating complete loss of between FRP and concrete. As a result, the slab now behaves as reinforced concrete slab subjected to higher load levels. Therefore, the deflection in slab S2 increases rapidly at 150 minutes and then continue to increase at a gradual pace until the end of fire exposure. Like the measured deflection values, the predicted deflection in both the slabs do not exceed the deflection limit until the end of fire exposure indicating no failure. Overall, it can be concluded that the model can predicts the structural response of FRP-strengthened concrete flexural members with sufficient accuracy. Trends of the predicted deflection values for both the beams are in close agreement with the trends measured in the test.

4.3.3 Model Applicability

To illustrate the usefulness of the model in practical situations, detailed fire resistance analysis is carried out on a set of flexural members. These flexural members comprise of five CFRP-strengthened RC T-beams and two CFRP-strengthened RC slabs, tested at MSU. The geometrical, material property and loading details of these beams are presented in Chapter 3 and are briefly summarized in Section 4.3.2. The detailed response parameters generated from the analysis of the beams and slabs include degradation in moment capacity, strength contribution of CFRP and steel rebars towards the capacity of structural member, as well as distribution of temperature, strength corresponding to moment capacity, and stress corresponding to loading, cross-section of the structural member. These results are shown for the beams and slabs in Figure 4.26 to Figure 4.32 and are discussed below.

(i) Moment Capacity Degradation and Strength Contribution

The degradation in moment is an important parameter which can help determine the strength failure of the structural member, while the strength contribution helps determine what percentage of capacity is attributed to the CFRP and steel rebars as well as the time at which CFRP ceases to contribute to the capacity. Figure 4.26 and Figure 4.28 shows the degradation in moment capacity for beams TB1 to TB5 and slabs S1, S2, respectively, as a function of fire exposure time. Figure 4.27 and Figure 4.29 show the strength contribution of CFRP, steel rebars towards the capacity of beams TB1 to TB5 and slabs S1, S2, respectively, as a function of fire exposure time. The strength contribution of CFRP and steel rebars is normalized with respect to strength at room temperature. Additionally, the degradation in moment capacity of the beams and slabs, normalized with respect to respective room temperature capacity, is also plotted in Figure 4.27 and Figure 4.29.

It can be seen from the Figure 4.26 (a) that the uninsulated beam TB1 experiences rapid degradation in moment capacity in the initial 20 minutes of fire exposure followed by a gradual decrease at a relatively slower rate between 20 and 60 minutes of fire exposure. After 60 minutes the capacity of the beam remains constant until 110 minutes of fire exposure and then starts decreasing gradually until the end of fire exposure. The rapid decrease in capacity, during the initial stages of fire exposure, is attributed to the fact that the CFRP sheet is directly exposed to the heat of fire, which causes severe burning of epoxy and rapid debonding of CFRP from the soffit of beam which in turn reduces the stress transfer between CFRP and concrete. Further the higher temperature rise at interface causes rapid reduction in strength of CFRP. Due to the rapid degradation in bond and strength properties of CFRP, its contribution towards the capacity of the beam decreases rapidly, as shown in Figure 4.27 (a) and hence, the capacity of beam decreases rapidly.

After 20 minutes, the interface temperature increases beyond than 400°C (*cf.* Figure 4.21 (a)), indicating the bond between CFRP and concrete is mostly lost, however, the contribution of CFRP is completely lost only after 60 minutes of fire exposure (Figure 4.27 (a)) and the beam behaves as a RC beam. Since the temperature of rebars remains below 400°C (*cf.* Figure 4.22 (a)) there is no degradation in strength of steel rebars and thus, the capacity of beam remains almost constant until 110 minutes of fire exposure. After 110 minutes, as the rebars temperature increases beyond 400°C, the strength properties of steel start degrading. As a result, the contribution of steel towards the capacity of beam starts decreasing (Figure 4.27 (a)). Thus, the moment capacity of the beam starts decreasing gradually, and almost approaches the bending moment due to applied loading at the end of fire exposure. However, the capacity does not fall below the applied bending moment until the end of fire exposure indicating no strength failure.

In case of insulated beam TB2, the moment capacity degrades very slowly in the initial 60 minutes of fire exposure. After 60 minutes, the capacity starts degrading gradually at a relatively faster rate until 130 minutes, after which the rate of degradation increases further and remains same until the end of fire exposure. The slower degradation in the capacity, during the initial 60 minutes of fire exposure, is attributed to the lower temperature rise in the beam due to the presence of insulation. After 60 minutes, the bond between CFRP and concrete starts degrading which reduces the contribution of CFRP towards the capacity of beam, as shown in Figure 4.27 (b). As a result, the moment capacity of the beam TB2 starts decreasing at a relatively faster pace. Further, it can be seen from Figure 4.27 (b) that after 130 minutes, the contribution of CFRP to the moment capacity of the beam is almost negligible possibly due to complete degradation of bond between CFRP and concrete. Additionally, the contribution of steel rebar towards the capacity of beam also starts decreasing as the temperature in steel rebar increases beyond 400°C (*cf.* Figure 4.22 (b)). As a result, the moment capacity of beam TB2 starts decreasing at a faster rate which continues until the end of fire exposure. However, the capacity of beam remains above the bending moment due to applied loading until the end of fire exposure, indicating no strength failure.

Figure 4.26 (c) shows the moment capacity degradation in beam TB3. It can be seen from the figure that the moment capacity degradation in beam TB3 is similar to that of beam TB2, i.e., the capacity decreases slowly in the initial stages followed by a gradual decrease a relative faster pace until 120 minutes, at which point the contribution of CFRP is towards the capacity of beam completely lost, as can be seen from Figure 4.27 (c). However, after 120 minutes, the degradation of capacity in beam TB3 is slightly different than that in beam TB2. After 120 minutes, he capacity of beam TB3 remains constant until 150 minutes. This is attributed to the fact that after 120 minutes; the beam behaves as an RC beam, and the capacity of beam is due to the strength of steel rebars only. Since, the temperature of rebars is below 400°C (Figure 4.22 (c)), there is no degradation in strength of steel rebar t, thereby constant capacity. After 150 minutes the rebar temperature exceeds 400°C and as a result the contribution of steel towards the capacity of beam starts decreasing, as shown in Figure 4.27 (c). Therefore, the capacity of beams starts decreasing and ultimately falls below the bending moment due to applied loading at 180 minutes of fire exposure, indicating failure in strength limit state.

The degradation in moment capacity of beams TB4 and TB5 follow similar trend throughout the fire exposure duration. It can be seen from Figure 4.26 (d-e) that the capacity of beams TB4 and TB5 remains almost constant until 120 and 60 minutes of fire exposure, respectively. After this the capacity of the both the beams TB4 and TB5, starts decreasing at a faster rate until 150 and 120 minutes of fire exposure, respectively. This is attributed to temperature induced bond degradation (as the interface temperature exceeds T_g of epoxy) which reduces the CFRP-concrete composite action, which in turn reduces the contribution of CFRP towards the capacity (Figure 4.27 (d-e)). After 150 and 120 minutes of fire exposure, the contribution of FRP is completely lost in beam TB4 and TB5, respectively, and both the beams behave as a RC beam with insulation.

Moreover, the rebar temperature in both the beams are 400°C indicating no loss in the strength and modulus of rebars. As a result, the capacity of both the beams TB1 and TB2 remains almost constant and do not fall below the applied loading until the end of fire exposure, indicating no strength failure.

Figure 4.28 shows the degradation in moment capacity of slabs S1 and S2 as predicted by the model. It can be seen from the figure that the moment capacity of the slabs degrades in a manner similar to that of the beams. The capacity of slab S1 decreases gradually in the initial stages until 60 minutes of fire exposure. After 60 minutes, the bond between FPR and concrete is completely lost which leads to immediate reduction in contribution of CFRP (Figure 4.29 (a)) and hence, the capacity of the slab, and the slabs behaves as a RC slab. After this the capacity of the slab continues to decrease gradually at a slower rate and do not fall below the bending moment due to applied loading until the end of fire exposure, indicating no strength failure.

In case of slab S2, the capacity of slab reduces very slowly until 75 minutes of fire exposure. After this the capacity of slab starts decreasing at a faster pace until 150 minutes of fire exposure, due to the degradation of CFRP-concrete bond and due to the higher load level applied on the slab S2. The degradation of bond reduces the CFRP-concrete composite action and the contribution of CFRP towards the slab moment capacity. Whereas, due to the higher load level slab S2 experiences higher internal stresses in the cross-section and higher shear stresses at the CFRP-concrete interface. The higher internal stresses increase the rate of degradation in strength and modulus properties of the constitutive material, whereas the higher shear stresses may lead to earlier debonding of CFRP from the concrete surface thereby reducing the strength and stiffness of the slab. Moreover, higher load level produces large curvature in the slab, which increases the demand on the slab and reduces the reserve capacity. After 150 minutes, the slab behaves as a RC slab.

Since the rebar temperatures are much lower than the 400°C, owing to the thermal protection provided by insulation, there is no thermal degradation in strength and modulus of rebars and their contribution towards the capacity (Figure 4.29 (b)). The only degradation is due to higher load level which is compensated through higher curvature in the slab and higher strains in the rebar. Therefore, the capacity of slab remains above the bending moment due to applied loading indicating no strength failure.

(ii) Cross-sectional Distribution of Temperature, Strength, and Stress

Apart from the moment capacity degradation and strength contribution towards the capacity, the model can generate pictorial representation of distribution of temperature, strength at maximum capacity, and stress due to loading within the cross-section of the structural member at different time intervals during fire exposure. These outputs were generated for all the analyzed beams TB1 to TB5 and for slabs S1, S2. However, to maintain brevity, the distribution of these output parameters is shown only for beam TB2, in Figure 4.30 to Figure 4.32 and are discussed below.

Figure 4.30 shows the temperature distribution in the cross-section of beam TB2 at 0, 30, 45, 60, 120, and 180 minutes of fire exposure. The temperature distribution within the cross-section help visualize variation in thermal gradient at different time interval during the fire exposure duration, which can help determine the optimum insulation strategies for the structural member. At the start of fire exposure, the entire beam cross-section is at ambient temperature condition, as shown in Figure 4.30 (a). With the increase in fire exposure time, the temperature in the outer region of beam cross-section increases rapidly, whereas the inner core is still at room temperature condition, as can be seen from the Figure 4.30 (b-c). Therefore, in the initial stages of fire exposure, there is steep thermal gradient across the width of the beam, which can induce thermal cracks on edges of the cross-section. The temperature on the outer edges of the beam exceeds 1000°C after one hour fire exposure, whereas the temperature in the concrete region near the edges and core region increases up to 400°C and 250°C, indicating slight reduction in the thermal gradient across the width of the beam, as can be seen from Figure 4.30 (d). Further, it can be seen from Figure 4.30 (e-f), the thermal gradient across the width reduces as the temperature distribution within the beam cross-section becomes uniform with increase in fire exposure time. However, the maximum temperature in the inner core region is less than 400°C at the end of three hours of fire exposure, indicating minimal loss in the strength of concrete.

The strength distribution within the cross-section of beam TB2 corresponding to equilibrium at maximum moment capacity is shown in Figure 4.31. The strength distribution is plotted at 0, 30, 45, 60, 120, and 180 minutes of fire exposure to determine the type and amount of strength contributed by different components of the beam, i.e., concrete, top and bottom steel rebars, and CFRP. It can be seen from the figure that bottom steel rebars and CFRP contribute maximum tensile strength towards the capacity of the beam, while the tensile strength contribution from the concrete is very limited. In the initial stages the strength distribution and the depth of neutral axis is uniform along the width of the beam. However, with increase in fire exposure time, the depth of neutral axis changes along the width of the beam cross-section. Due to the initiation of CFRP-concrete bond degradation at 45 minutes of fire exposure (*cf.* Figure 4.27 (b)), the contribution of CFRP towards the capacity of beam starts decreasing, as can be seen in Figure 4.31 (c). The contribution of CFRP is almost negligible after 60 minutes (Figure 4.31 (d)), as a result the tensile strength region decreases. Therefore, to maintain equilibrium, the compressive strength region of concrete reduces. Additionally, the top two rebars which were earlier in compression now contribute towards the tensile strength region of beam. This phenomenon continues until the end of fire exposure, as a result, the compressive strength region reduces significantly and is limited to the concrete near the top surface, while rest of the beam is in tension.

Figure 4.32 shows the stress distribution due to applied loading in the cross-section of the beam TB2 at 0, 30, 45, 60, 120, and 180 minutes of fire exposure. This stress distribution helps visualize how each component of beam cross-section is stressed under the applied loading, which in turn can help determine possible cracking and spalling zones in the concrete. The stress distribution which is uniform at the start of fire exposure (Figure 4.32 (a)), becomes highly non-uniform with increase in fire exposure time (Figure 4.32 (b-f)). It can be seen from the Figure 4.32 (a-c) that the stress in CFRP increases with increase in fire exposure time. However, at 45 minutes, i.e., at the initiation of CFRP-concrete bond degradation, the stress in CFRP is almost zero. This indicates that the contribution of CFRP in resisting the applied loading, i.e., towards the stiffness of the beam is almost negligible after the initiation of bond degradation. With further increase in fire exposure time, stress in bottom steel rebars increases and as a result, the compressive region of concrete also increases. However, towards the end of fire exposure, stress in steel rebars and the compressive region of concrete reduces. Additionally, Figure 4.32 (f) indicates that significant amount (almost 85%) of concrete region below the neutral axis doesn’t contribute in resisting the applied loading.

Additionally, the predicted stress distribution can help detect spalling in concrete. Typically spalling in concrete is considered to occur due to development of pore pressure or due to thermal (compressive) stress development. The former spalling is prevalent in high strength concrete (HSC) members where water content and permeability is lower, while latter one is prevalent in both NSC and HSC and occurs in the initial 20-60 minutes of fire exposure. As can be seen from Figure 4.32 (b) compressive stresses develop in the lower portion of flange of the beam, which is identical to the spots where spalling was observed in beam TB2 during and after fire test (*cf*. Figure 3.14 (d)). This clearly demonstrates that even though spalling is not explicitly considered in the model a qualitative idea about the spalling regions can be predicted by the model.

Based on the above discussion it can be concluded that the model can predict the thermal and structural behavior of the strengthened concrete member exposed to fire with reasonable accuracy and provides useful parameter which are conducive in understanding the performance of FRP-strengthened concrete flexural members under fire exposure.

4.4 Summary

The development of a macroscopic numerical model for evaluating the fire response of FRP-strengthened concrete flexural members is presented in this chapter. The model utilizes a member level approach and evaluates the fire resistance of a FRP-strengthened concrete flexural member through a sequential thermal and structural analysis procedure. In the thermal analysis temperature distribution within the cross-section is computed. Whereas in structural analysis the temperature dependent moment curvature relations are generated, and deflection of the flexural member is computed through stiffness analysis. In the fire resistance analysis, the model accounts for high temperature thermal and mechanical properties of constituent materials, temperature induced bond degradation, material nonlinearities in concrete and steel, all high temperature strain components, and all applicable failure limit states.

To establish the validity of the developed numerical model, the thermal and structural response parameters, namely temperature, mid-span deflection and fire resistance predicted by the model are compared with the response parameters measured in tests available in literature and tests presented in previous chapter. The predicted results are in good agreement with the measured values. Based on comparison, it can be concluded that the model is capable of tracing the response of FRP-strengthened concrete flexural members from initial loading stage to failure under fire conditions, with sufficient accuracy. The model can be used to predict the fire response of strengthened flexural members with different geometry, insulation thickness and configuration, fire scenarios, and loading conditions. Hence, the model can be applied to quantify the effect of different parameters on fire response of FRP-strengthened concrete flexural member through parametric studies.

Table 4.1: Geometrical configuration, material properties, and loading details of RC beams and RC slabs tested by Blontrock et al. [145, 152] used for validation of model

Flexural member type		**Rectangular beams**				**Slabs**			
Designation		BV1	BV2	BV3	BV4	SV1	SV2	SV3	SV4
Clear span (L, m)		2.85		3.0		2.85		3.0	
Cross-section ($b_c \times d_c$, mm × mm)		200 × 300				400 × 150			
Cover to rebars (C_c, mm)		25				25			
Concrete compressive strength (f'_c, MPa)		47	46	48	47	46	44	46	47
Steel rebars	Top (#-mm)	2-10 ϕ				NA			
	Bottom (#-mm)	2-16 ϕ				4-8 ϕ			
	Yield strength (f_y, MPa)	591				557			
CFRP	Thickness (t_{frp}, mm)	NA	1.2			NA	0.2		
	Width (b_{frp}, mm)		100				200		
	Modulus of elasticity (E_f, GPa)		165				240		
	Tensile strength (f_u, MPa)		2800				3900		
	Rupture strain (ε_u, %)		1.7				1.55		
	Glass transition temperature (T_g, °C)		67				67		
Insulation	Material	NA		Promatect H		NA		18 mm Gypsum board with Cavity	18 mm Gypsum board with Rockwool
	Thickness (t_{ins}, mm)			25	40			63	
	Width (b_{ins}, mm)			200				350	
	Depth on sides (h_i, mm)			0	80			0	
	Conductivity (k_{ins}, W/m K)			0.285					
	Heat capacity (c_{ins}, J/kg°C)			875					
Applied loading	Test Condition	Ambient		Fire		Ambient		Fire	
	Fire scenario	NA		ISO 834		NA		ISO 834	
	Duration (hours)	NA		1.5				1.5	
	Structural load (kN)	Monotonic		2 × 40		Monotonic		2 × 9.1	
	Load ratio (%)	100		51		100		50	
	Distance between loads (l_2, mm)	950		1000		950		1000	

Table 4.2: Comparison of response parameters measured in tests and predicted by the model for RC beams and RC slabs tested by Blontrock et al. [145, 152]

<table>
<tr><th colspan="2" rowspan="2">Flexural member</th><th colspan="4">Rectangular beams</th><th colspan="4">Slabs</th></tr>
<tr><th>BV1</th><th>BV2</th><th>BV3</th><th>BV4</th><th>SV1</th><th>SV2</th><th>SV3</th><th>SV4</th></tr>
<tr><td rowspan="2">Maximum temperature in steel reinforcement (°C)</td><td>Test</td><td rowspan="2">NA</td><td rowspan="2">NA</td><td>490</td><td>102</td><td rowspan="2">NA</td><td rowspan="2">NA</td><td>385</td><td>145</td></tr>
<tr><td>Model</td><td>485</td><td>230</td><td>300</td><td>100</td></tr>
<tr><td rowspan="2">Moment capacity (kNm)</td><td>Test</td><td>64</td><td>100</td><td colspan="2" rowspan="2">NA</td><td>16</td><td>19</td><td colspan="2" rowspan="2">NA</td></tr>
<tr><td>Model</td><td>64.7</td><td>100</td><td>15</td><td>20</td></tr>
<tr><td rowspan="2">Deflection at failure/ end of fire exposure (mm)</td><td>Test</td><td>40</td><td>25</td><td>52</td><td>32</td><td>98</td><td>40</td><td>78</td><td>40</td></tr>
<tr><td>Model</td><td>39.5</td><td>24</td><td>51</td><td>35</td><td>100</td><td>38</td><td>75</td><td>36</td></tr>
<tr><td rowspan="2">Fire resistance (minutes)</td><td>Test</td><td colspan="2" rowspan="2">NA</td><td>85</td><td>78</td><td colspan="2" rowspan="2">NA</td><td>76</td><td>78</td></tr>
<tr><td>Model</td><td>88</td><td>80</td><td>77</td><td>72</td></tr>
<tr><td rowspan="2">Failure limit state reached</td><td>Test</td><td>Yielding</td><td>FRP rupture</td><td colspan="2" rowspan="2">Span/deflection ratio>35</td><td>Yielding</td><td>FRP rupture</td><td colspan="2" rowspan="2">Span/deflection ratio>35</td></tr>
<tr><td>Model</td><td>Yielding</td><td>FRP rupture</td><td>Yielding</td><td>FRP rupture</td></tr>
</table>

Table 4.3: Geometrical configuration, material properties, and loading details of RC flexural members tested at MSU used for validation of model

Flexural member type		**T-beams**					**Slabs**	
Designation		TB1	TB2	TB3	TB4	TB5	S1	S2
Clear span (L, m)		3.66					3.66	
Cross-section ($b_c \times d_c$, mm × mm)		flange: 432 × 127 web: 254 × 279					400 × 152	
Cover to rebars (C_c, mm)		38					19	
Concrete compressive strength (f_c', MPa)		38			46		42	
Steel rebars	Top (#-mm)	4-12 ϕ			4-12ϕ		NA	
	Bottom (#-mm)	3-16 ϕ			3-16 ϕ	3-19 ϕ	3-12 ϕ	
	Yield strength (f_y, MPa)	440			460	450	545	
CFRP	Thickness (t_{frp}, mm)	1.02			1.02		1.02	
	Width (b_{frp}, mm)	170			100		75	
	Modulus of elasticity (E_f, GPa)	73.77			96.5		96.5	
	Tensile strength (f_u, MPa)	1034			1172		1172	
	Rupture strain (ε_u, %)	1.4			1.11		1.11	
	Glass transition temperature (T_g, °C)	82			82		82	
Insulation	Material type	SFRM			SFRM		SFRM	
	Thickness (t_{ins}, mm)	0	25	19	32	19	19	25
	Width (b_{ins}, mm)	0	304	292	318	292	438	450
	Depth on sides (h_i, mm)	0	75	112	152		152	
	Conductivity (k_{ins}, W/m K)	0.154			0.154		0.154	
	Heat capacity (J/kg°C)	556460			556460		556460	
Applied Loading	Test Condition	Fire			Fire		Fire	
	Fire scenario	ASTM E119			ASTM E119		ASTM E119	
	Duration (hours)	3			4		4	
	Structural load (kN)	2 × 49		2 × 58	2 × 48	2 × 64	2 × 10.5	2 × 13
	Load ratio (%)	51	51	61	54	48	48	60
	Distance between loads (l_2, mm)	860			860		860	

Table 4.4: Comparison of response parameters measured in fire tests and predicted by the model for CFRP-strengthened RC T-beams and RC slabs tested at MSU

Flexural member		**T-beams**					**Slabs**	
		TB1	**TB2**	**TB3**	**TB4**	**TB5**	**S1**	**S2**
Maximum temperature in tensile reinforcement (°C)	**Test**	570	570	550	293	400	316	232
	Model	530	520	460	240	360	215	308
Deflection at failure/ end of fire exposure (mm)	**Test**	84	65	108	16	30	39	101
	Model	83	62	90	17	26	32	121
Fire resistance (minutes)	**Test**	>180	>180	176	>240	>240	>180	>180
	Model	>180	>180	180	>240	>240	>180	>180
Failure limit state reached	**Test**	No failure	No failure	S+D	No failure	No failure	No failure	No failure
	Model	No failure	No failure	S+D	No failure	No failure	No failure	No failure

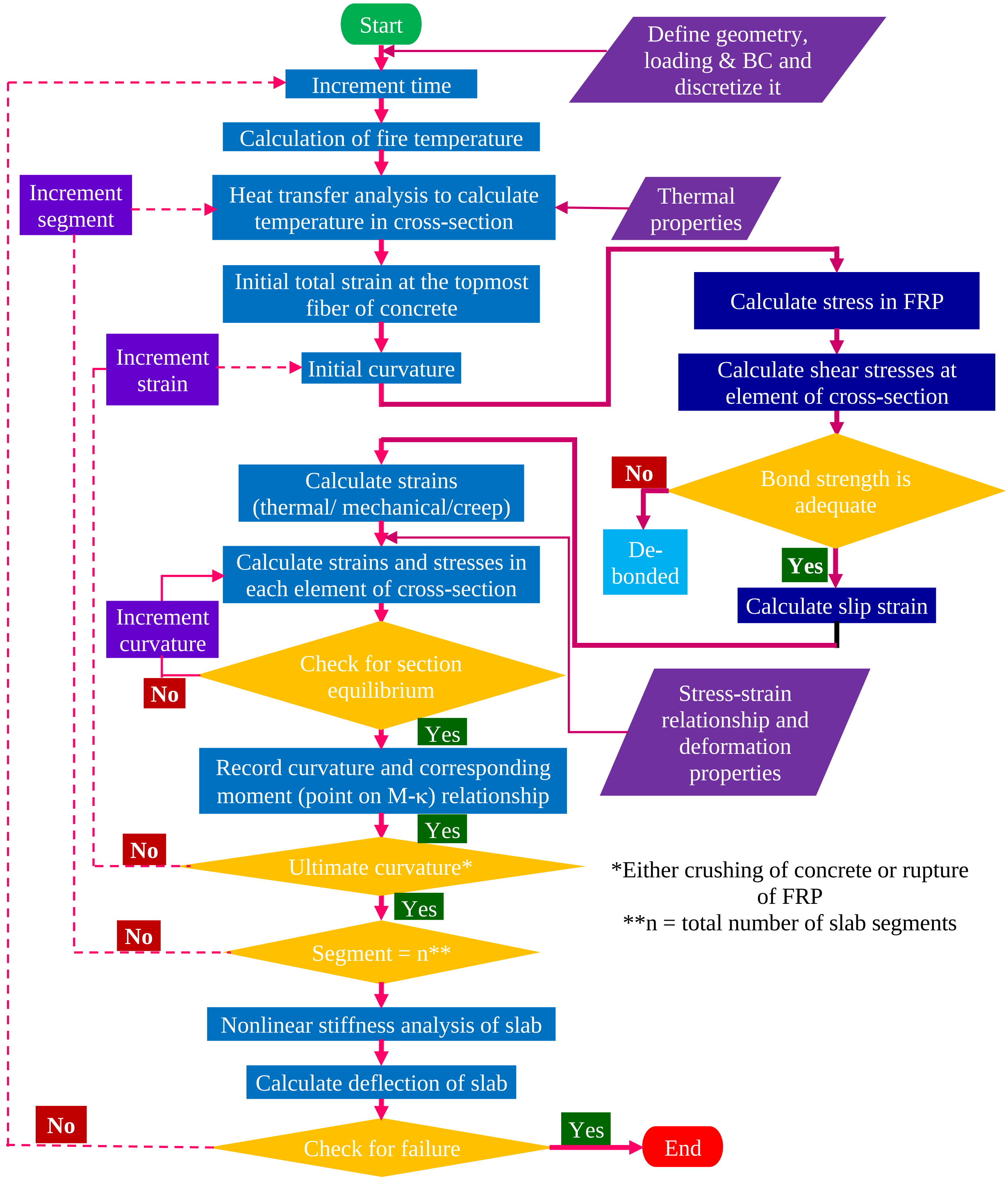

Figure 4.1: Flowchart illustrating steps in the fire resistance analysis of an FRP-strengthened RC flexural member

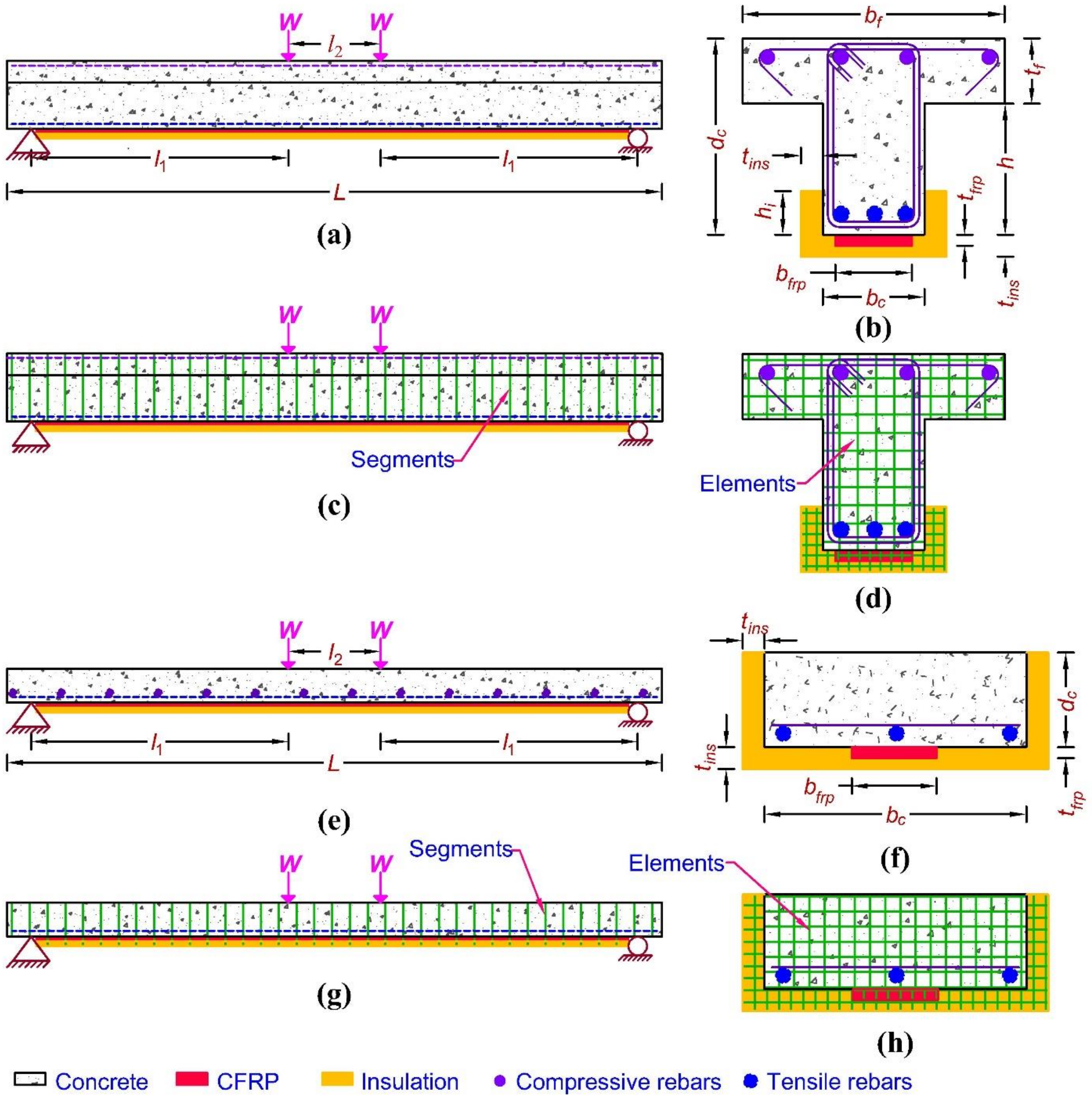

Figure 4.2: Typical beam layout and discretization of beam into segments and elements: (a) beam elevation; (b) beam cross-section; (c) discretization of beam length; (d) discretization of beam cross-section; (e) slab elevation; (g) slab cross-section; (g) discretization of slab length; (h) discretization of slab cross-section

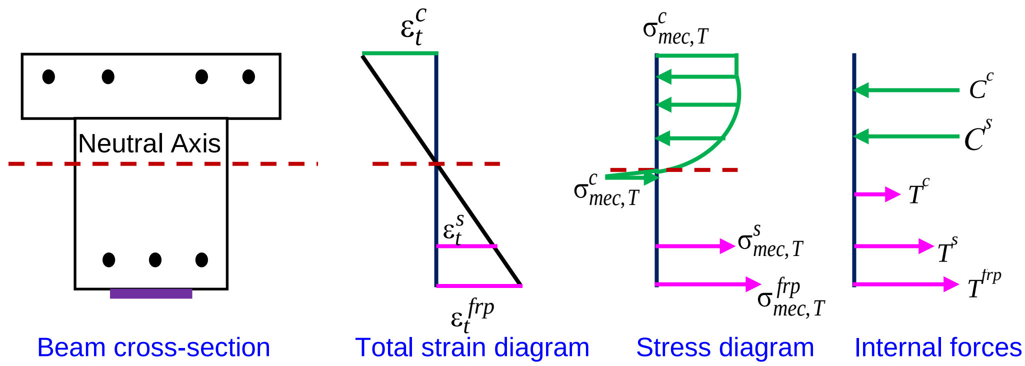

(a)

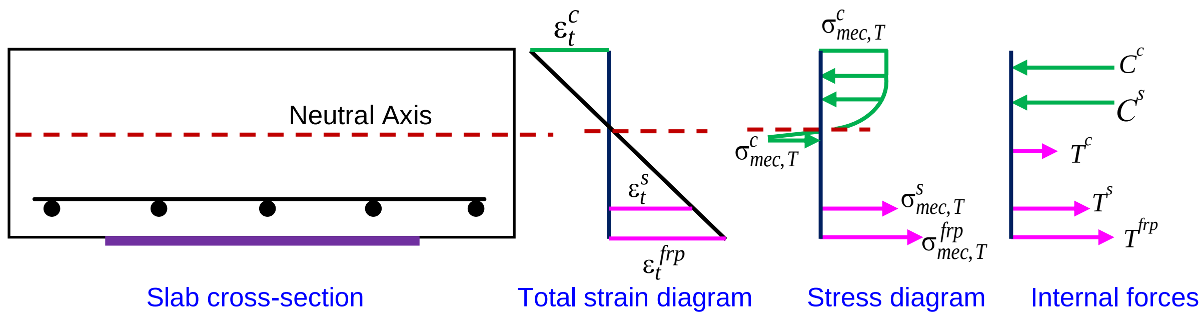

(b)

Figure 4.3: Strain compatibility and force equilibrium in the cross-section of an FRP-strengthened concrete flexural member: (a) beam; (b) slab

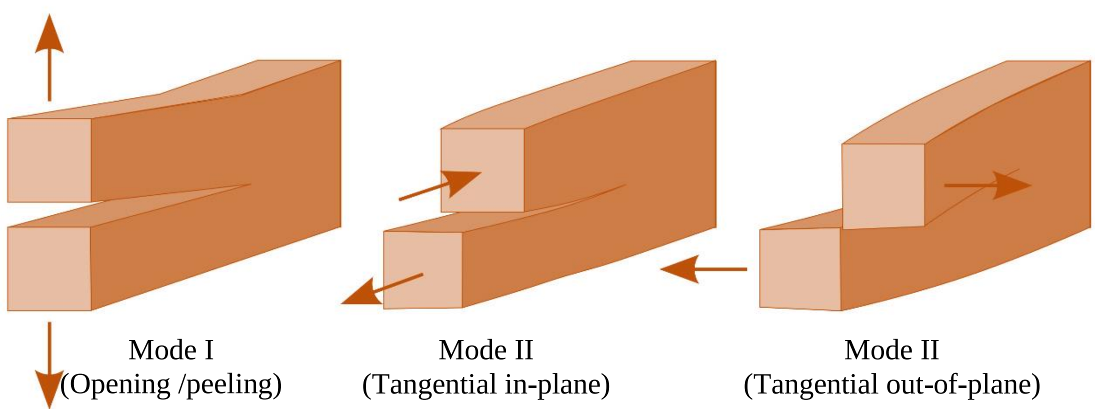

Figure 4.4: Debonding failure modes for FRP-concrete interface

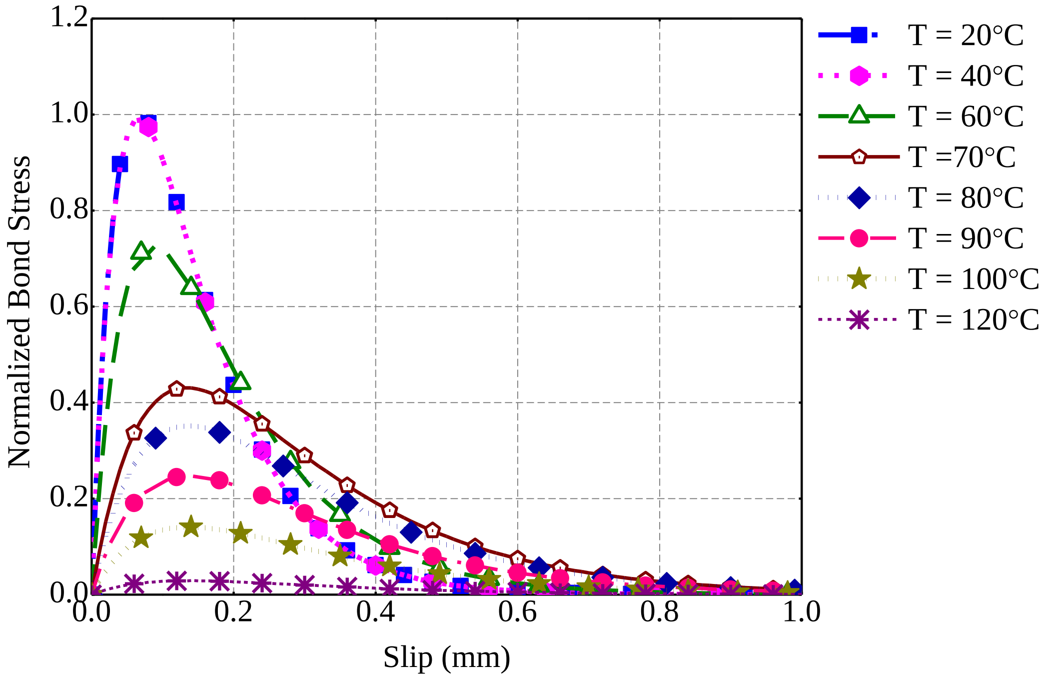

Figure 4.5: Typical bond-slip response at FRP-concrete interface at elevated temperatures

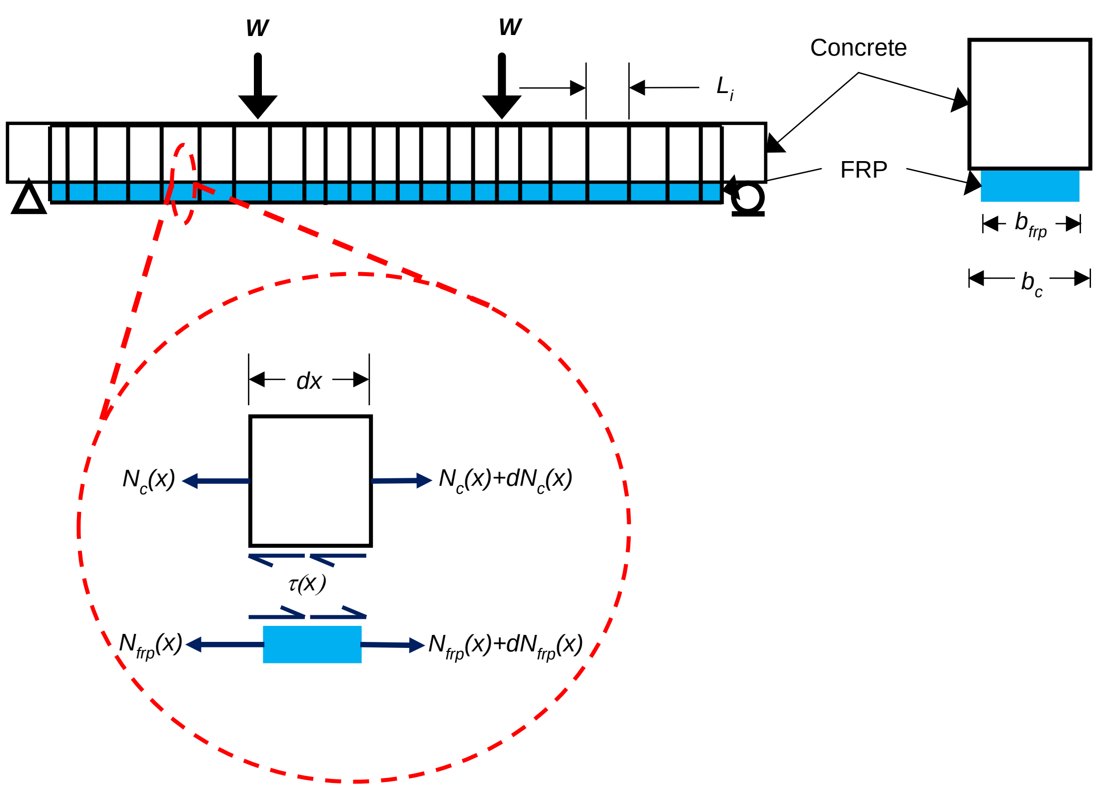

Figure 4.6: Computation of shear stress and shear force in a segment of FRP-strengthened RC flexural member

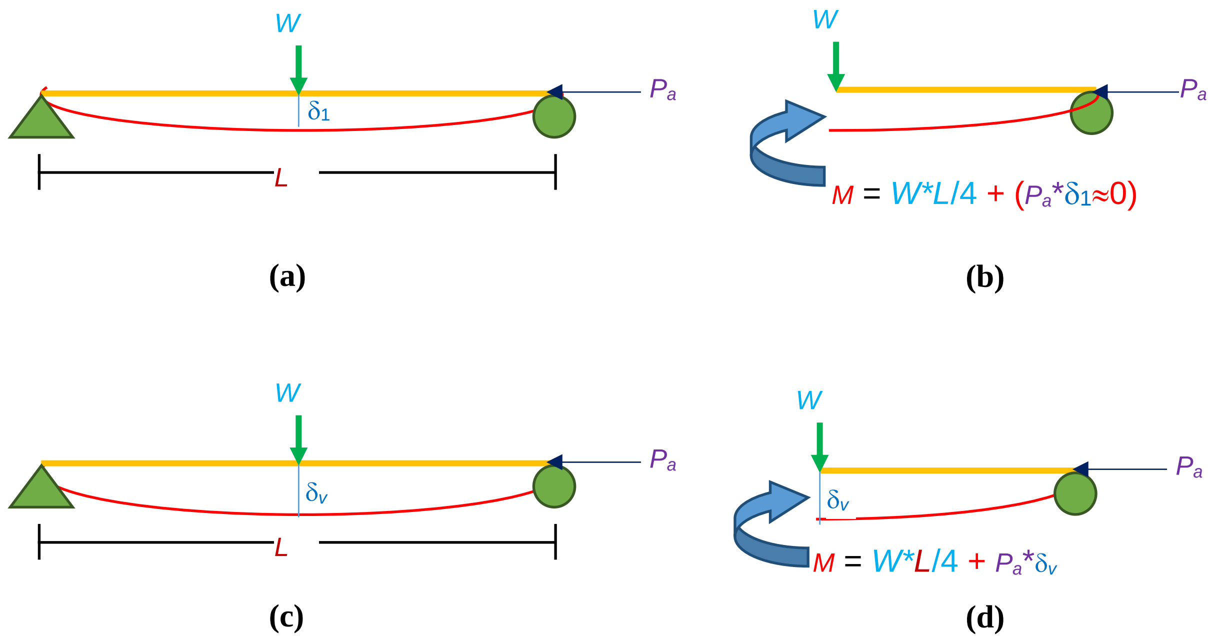

Figure 4.7: Schematic illustration of second order effects generated in a simply supported beam with axial force at ends: (a) simply supported beam with small deflection; (b) free body diagram; (c) simply supported beam with large deflection; (d) free body diagram

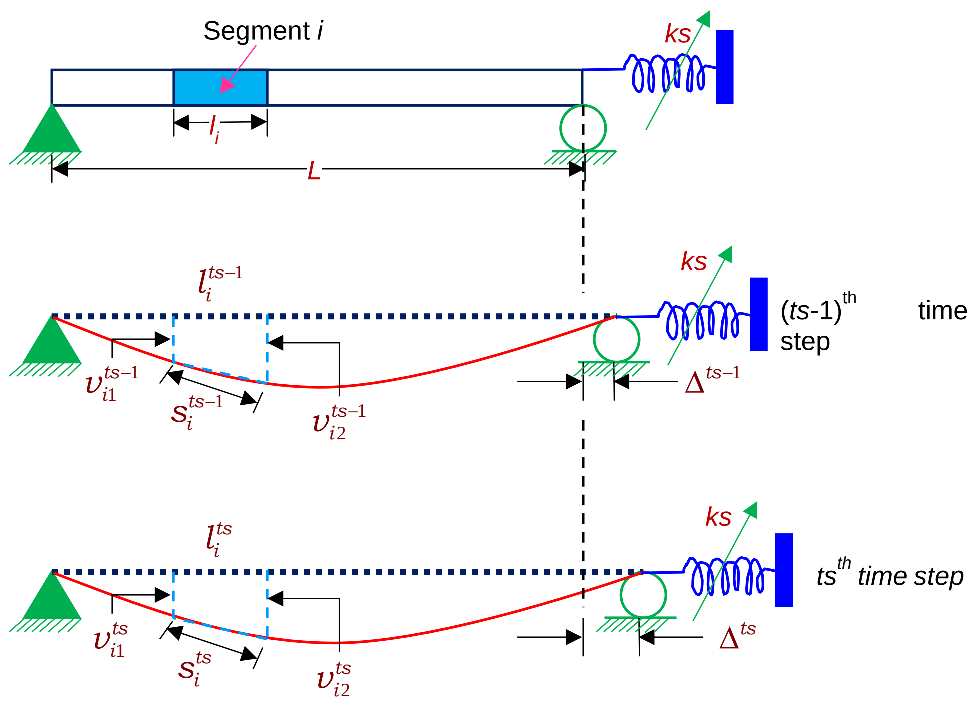

Figure 4.8: Illustration of deflected shape of flexural member at (ts-1)th and ts^{th} step for axial restraint force calculation

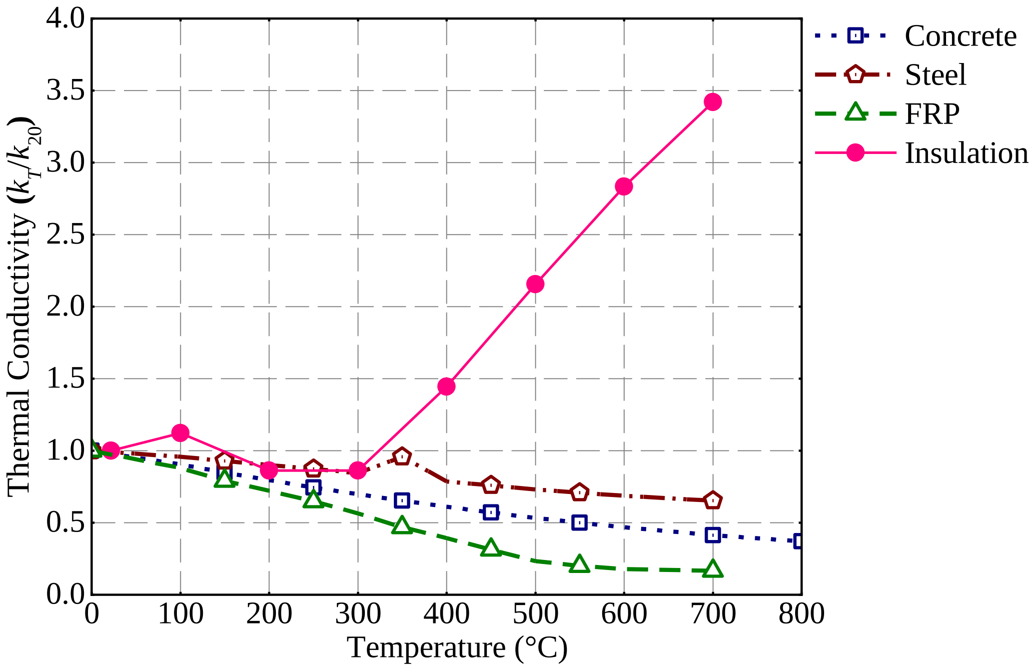

(a)

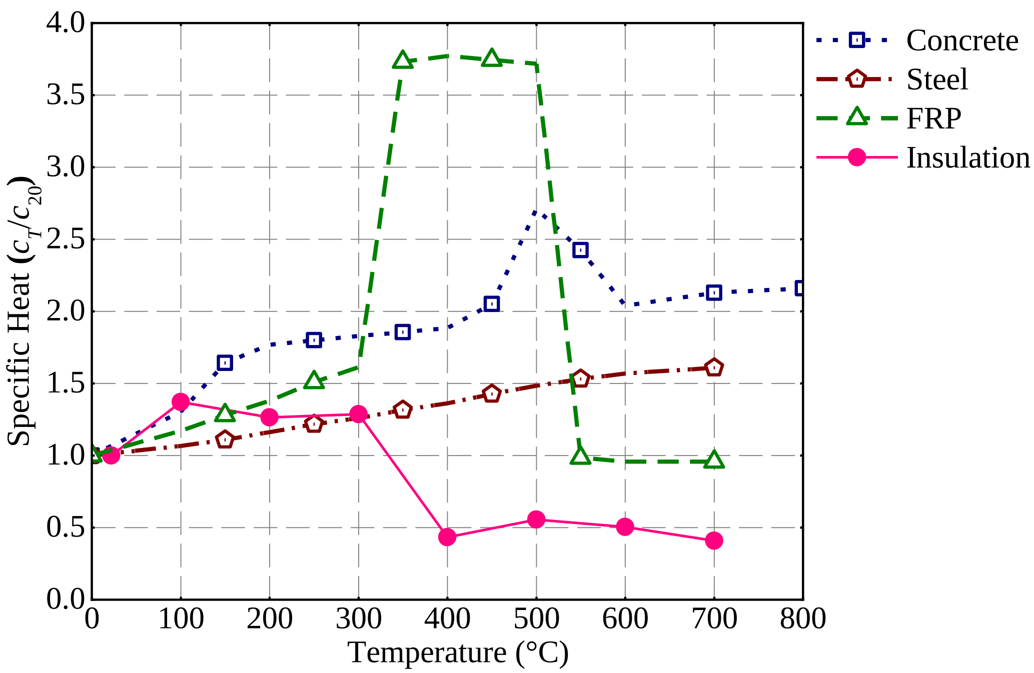

(b)

Figure 4.9: Normalized thermal properties of concrete, steel, FRP, and insulation as a function of temperature: (a) thermal conductivity; (b) specific heat

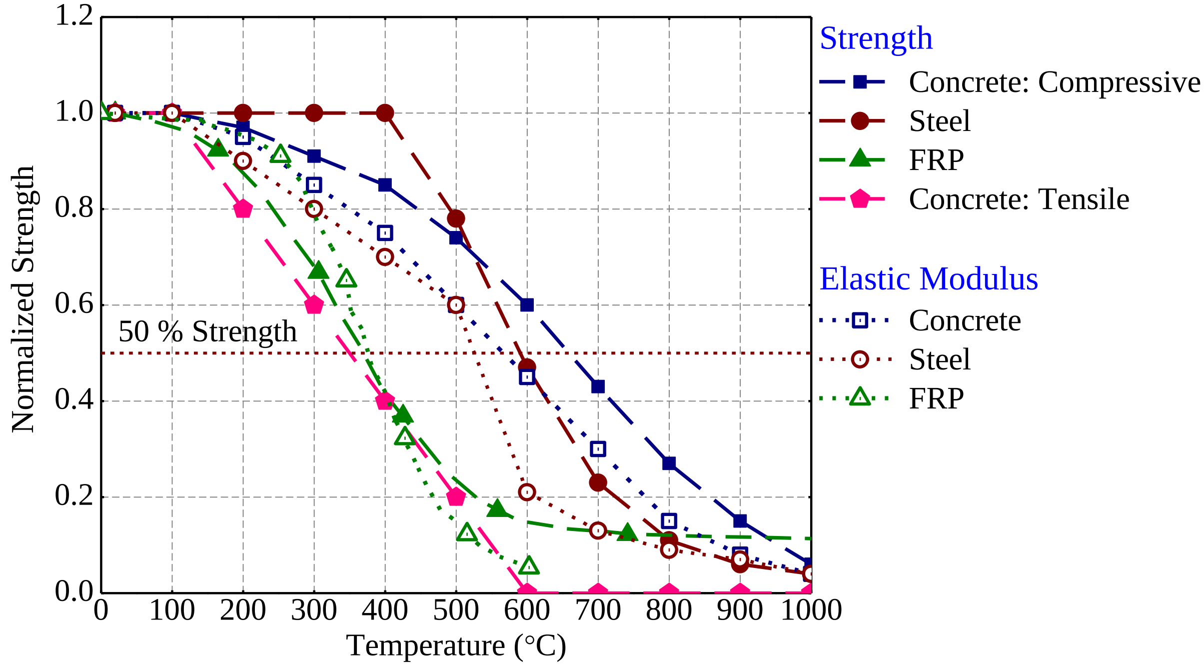

Figure 4.10: Normalized variation in strength and elastic modulus of concrete, steel, and FRP with temperature

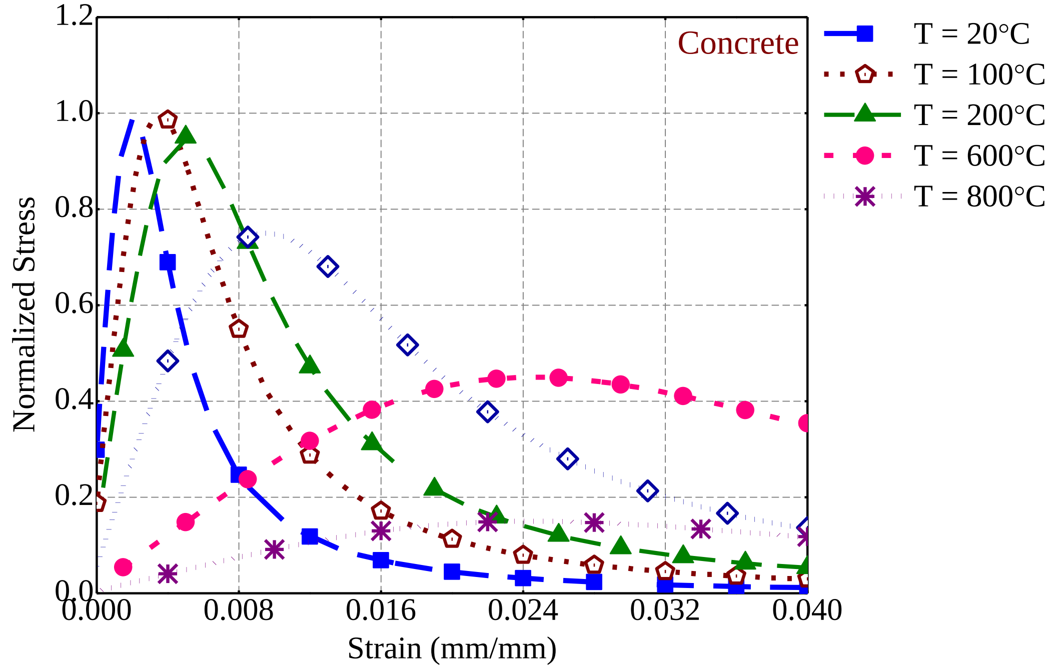

(a)

Figure 4.11: Normalized stress-strain response of different materials at elevated temperature: (a) concrete; (b) steel; (c) FRP

Figure 4.11 (cont'd)

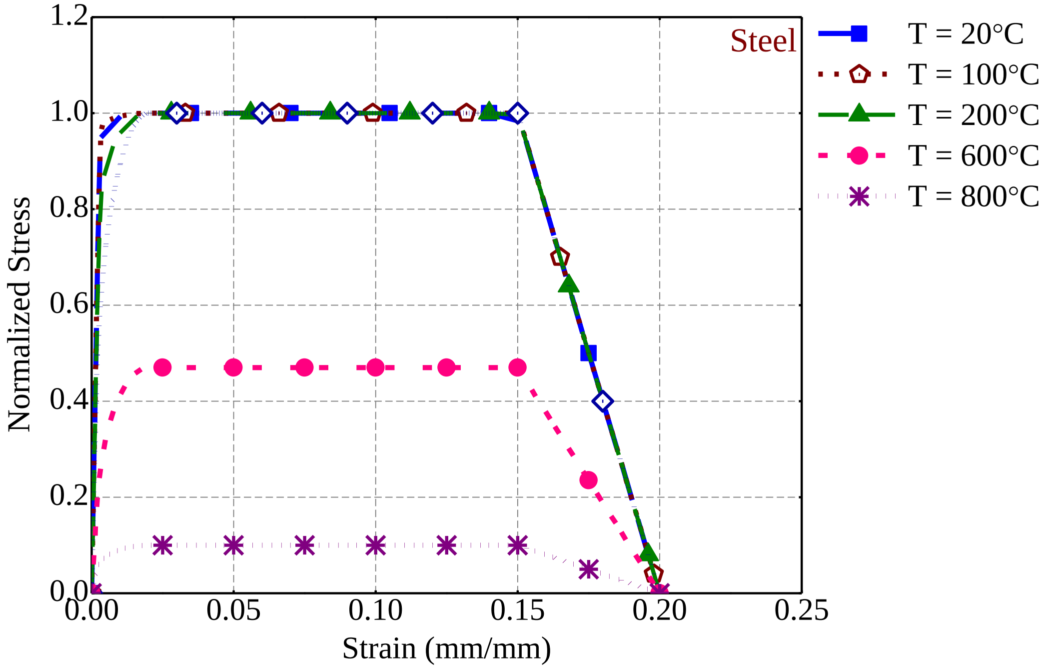

(b)

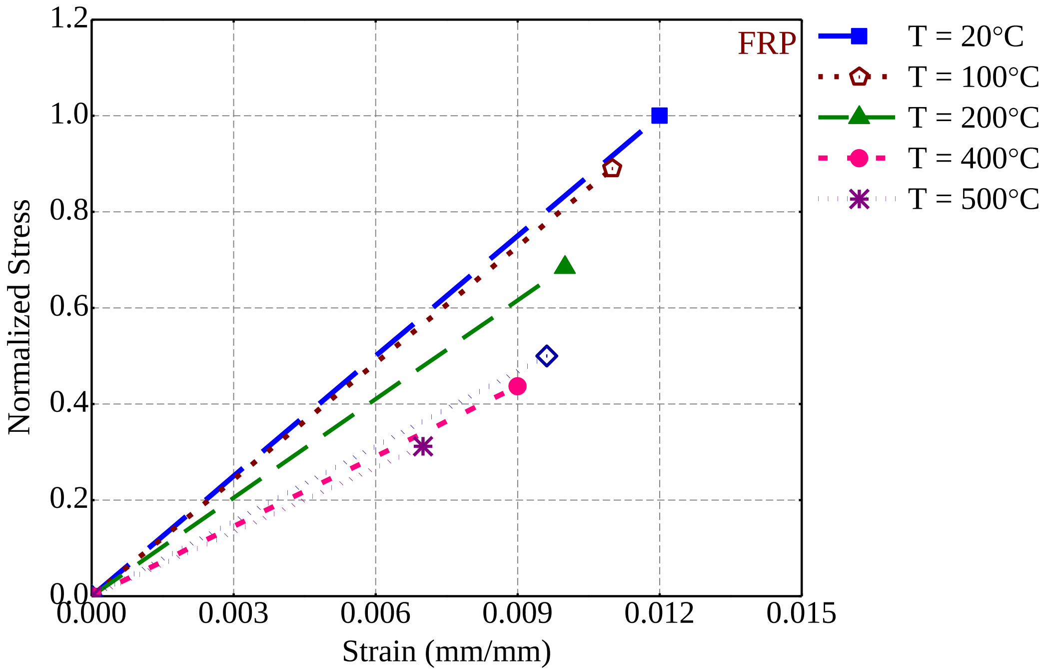

(c)

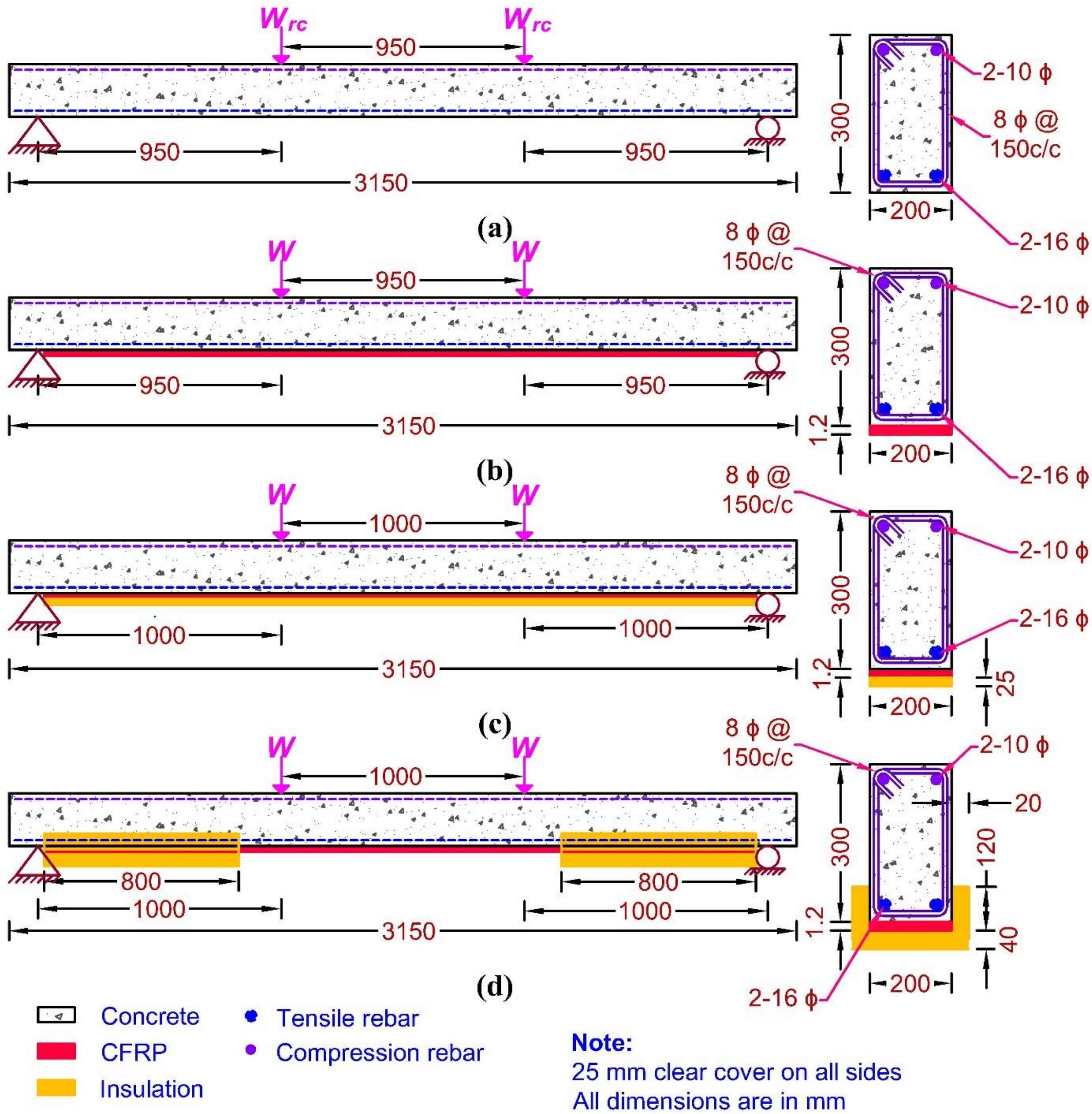

Figure 4.12: Layout and geometrical configuration of beams tested by Blontrock et al. [145] used for validation: (a) beam BV1; (b) beam BV2; (c) beam BV3; (d) beam BV4

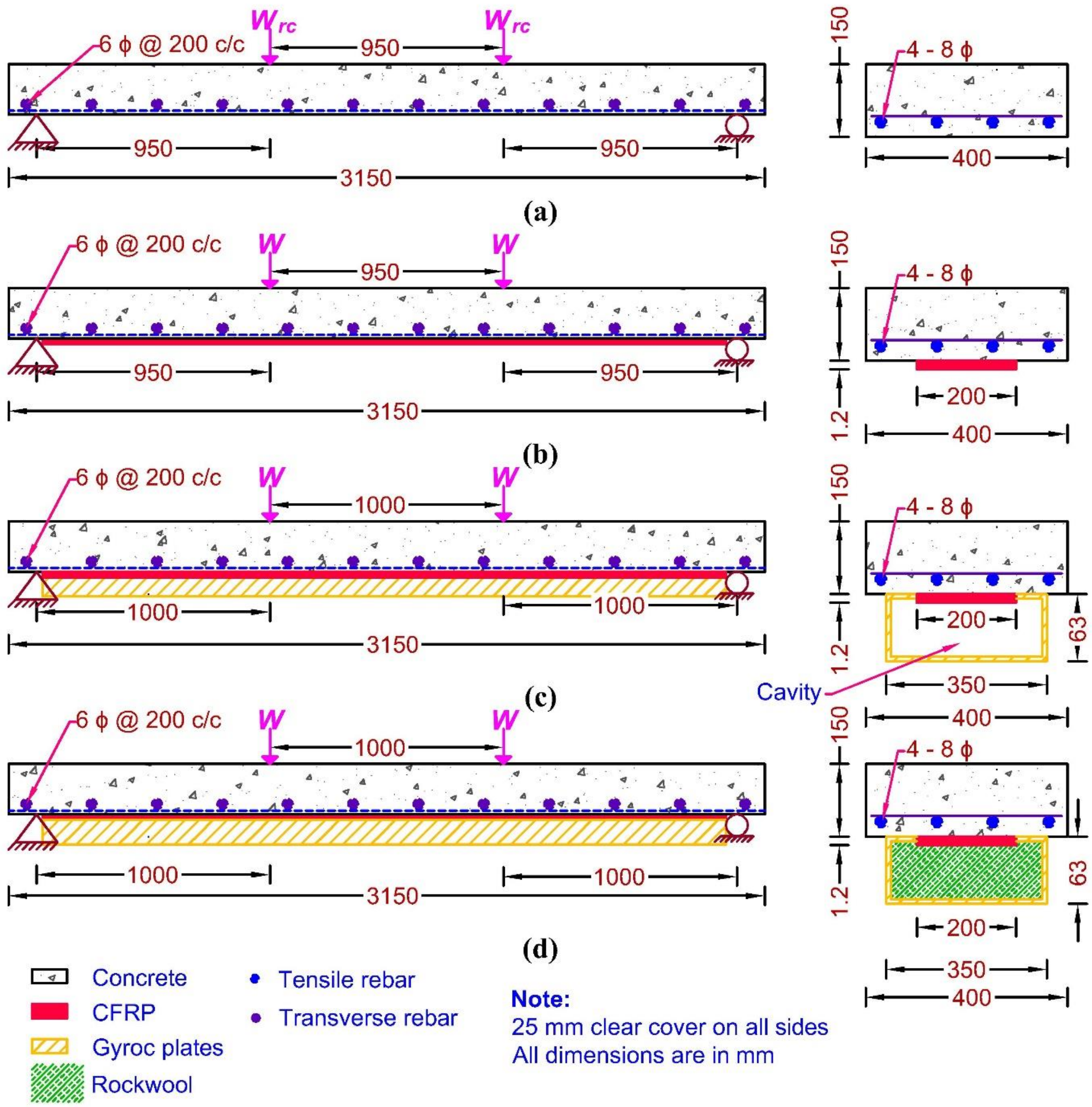

Figure 4.13: Layout and geometrical configuration of slabs tested by Blontrock et al. [152] used for validation: (a) slab SV1; (b) slab SV2; (c) slab SV3; (d) slab SV4

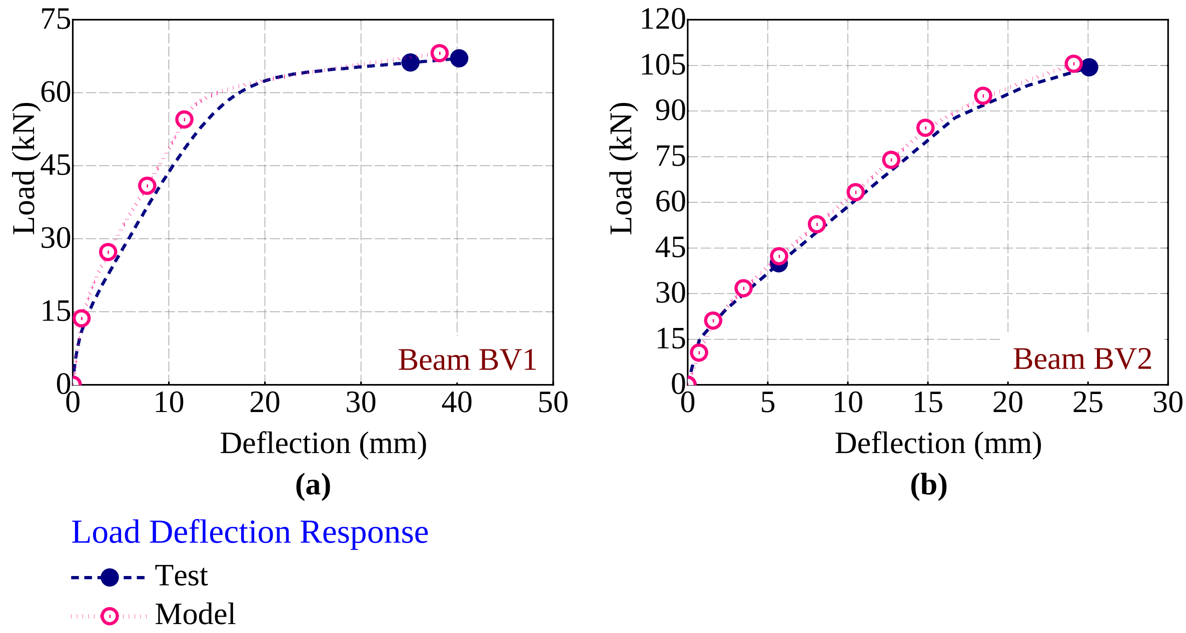

Figure 4.14: Comparison of predicted and measured load deflection response of RC beams under ambient conditions: (a) beam BV-1; (b) beam BV-2

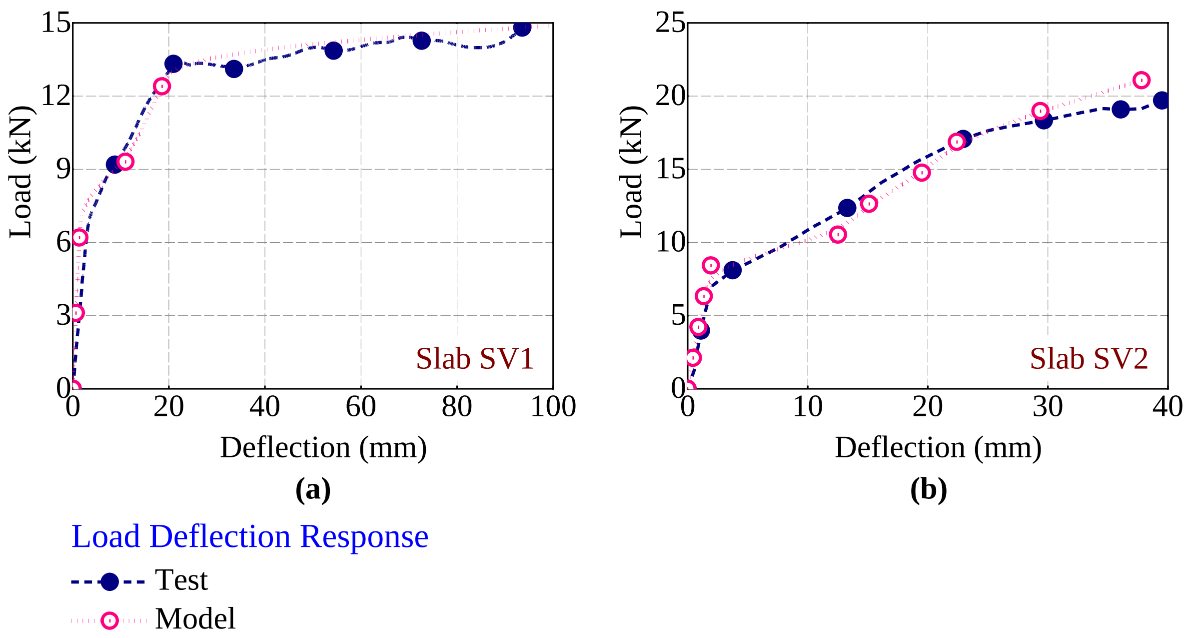

Figure 4.15: Comparison of predicted and measured load deflection response of RC slabs under ambient conditions: (a) slab SV1; (b) slab SV2

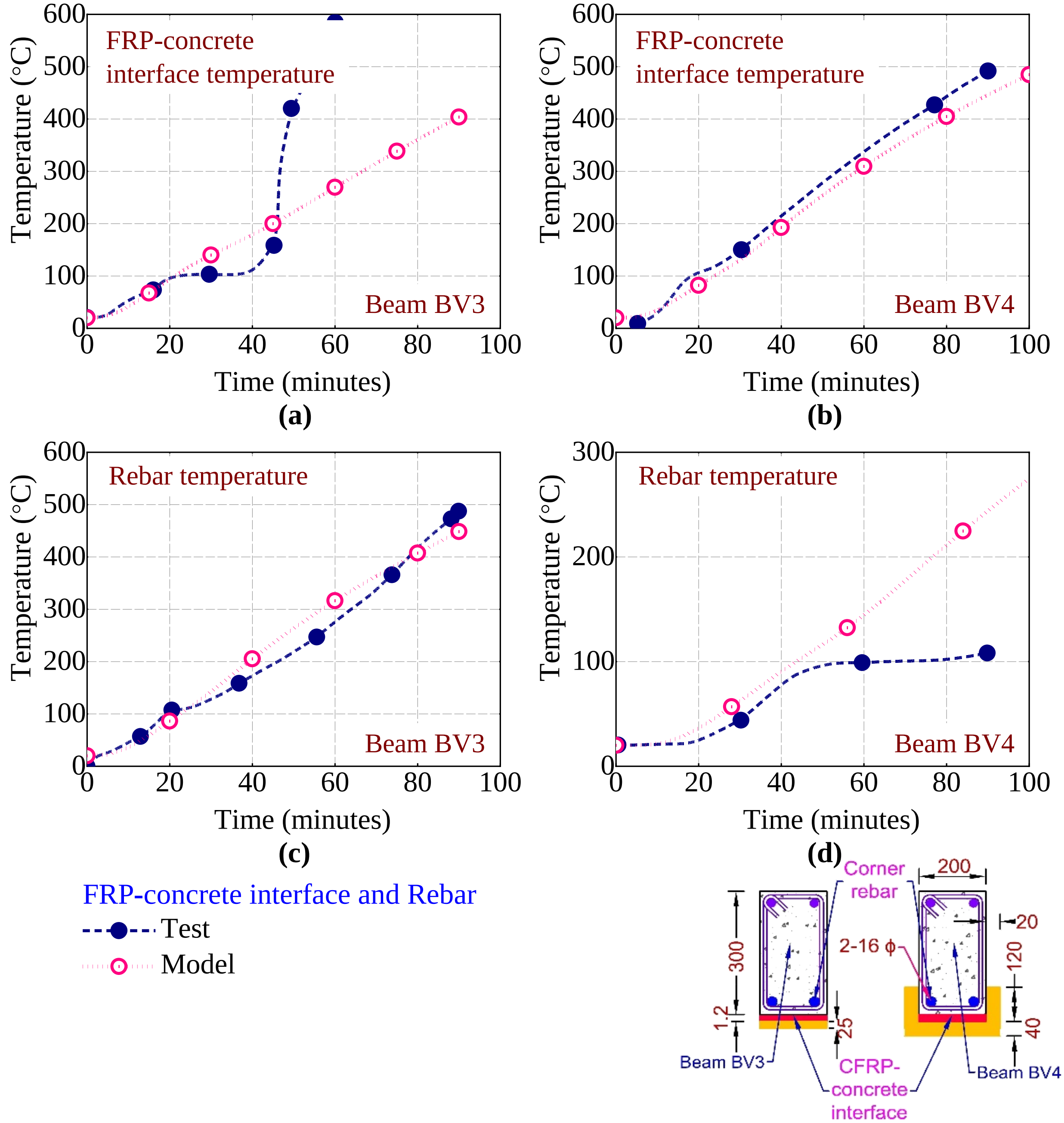

Figure 4.16: Comparison of predicted and measured thermal response of beams BV3 and BV4: (a-b) temperature rise at FRP-concrete interface; (c-d) temperature rise at corner rebar

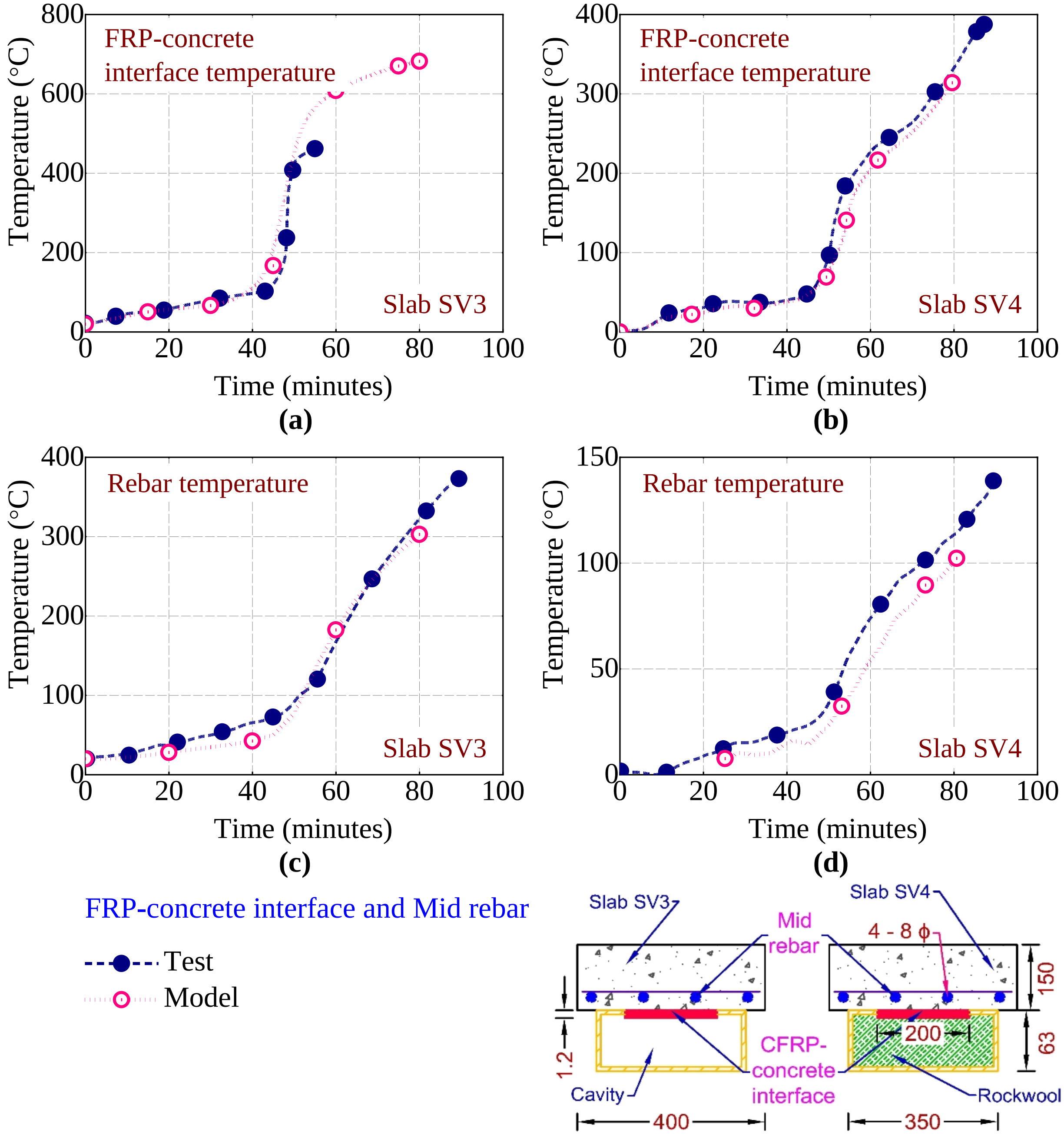

Figure 4.17: Comparison of predicted and measured thermal response of slabs SV3 and SV4: (a-b) temperature rise at FRP-concrete interface; (c-d) temperature rise at mid rebar

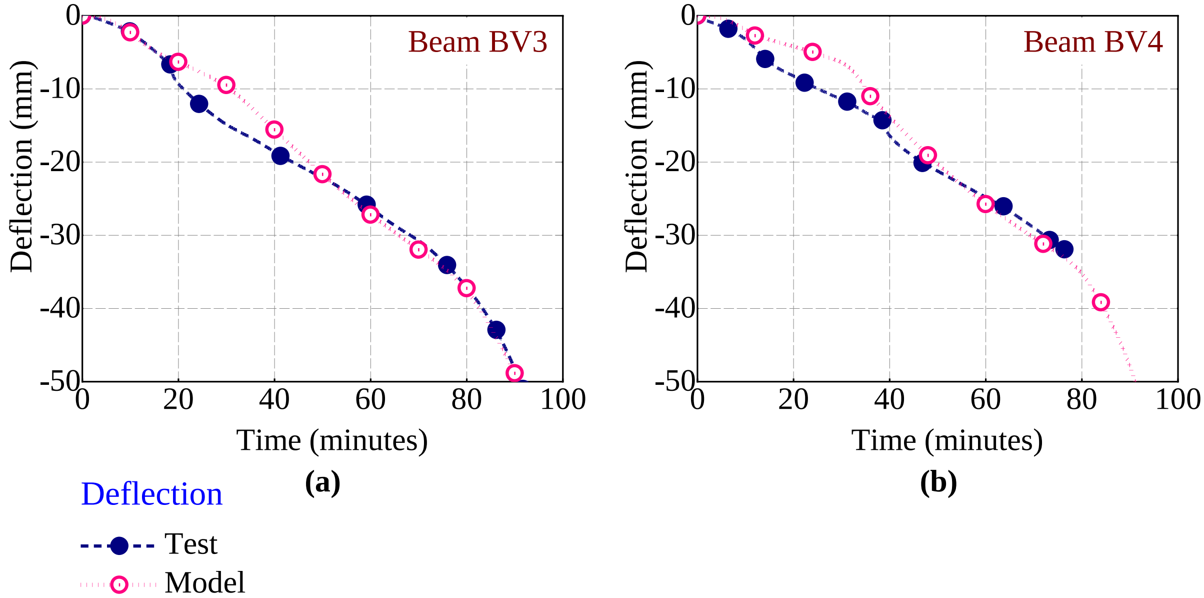

Figure 4.18: Comparison of predicted and measured mid-span deflection in beams: (a) BV3; (b) BV4

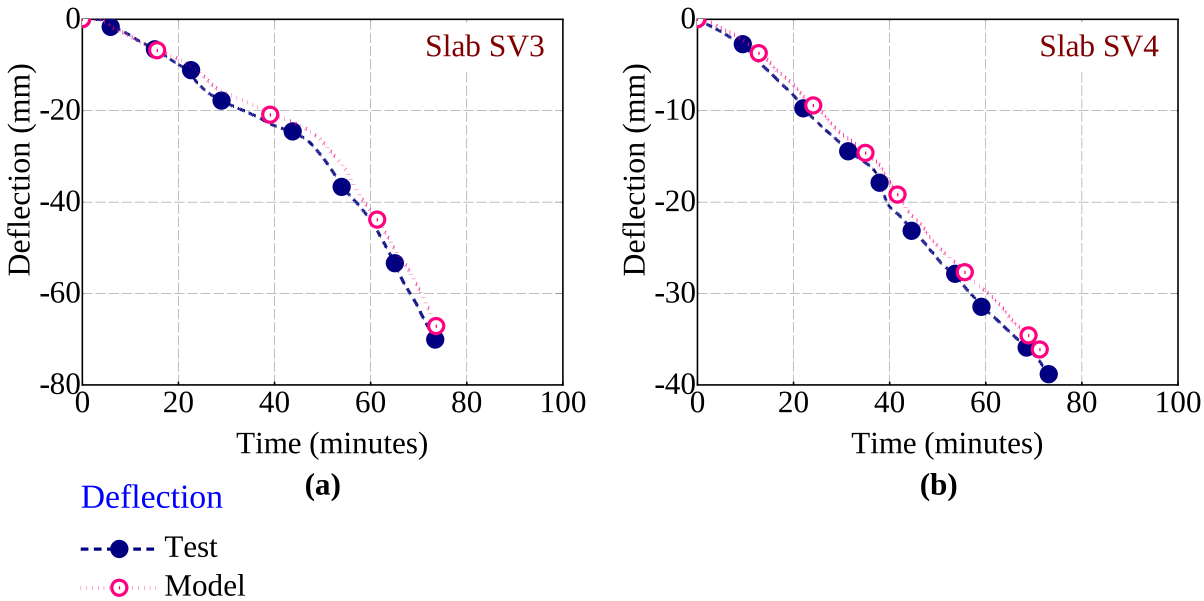

Figure 4.19: Comparison of predicted and measured mid-span deflection in slabs: (a) SV3; (b) SV4

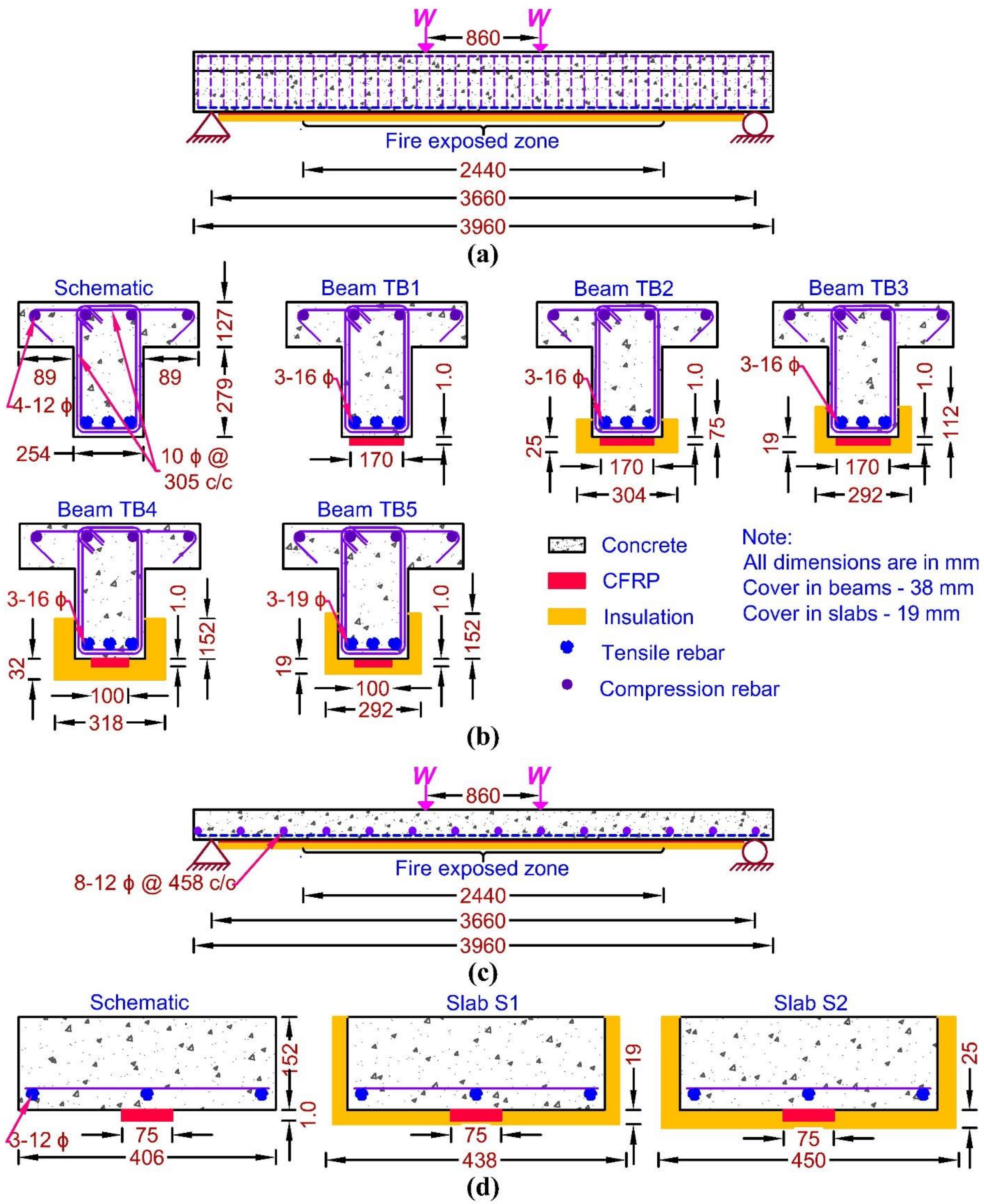

Figure 4.20: Geometrical details of beams and slabs tested at MSU: (a) elevation of a typical T-beam; (b) cross-section of beams TB1 to TB5; (c) elevation of typical slab; (d) cross-section of slabs S1 and S2

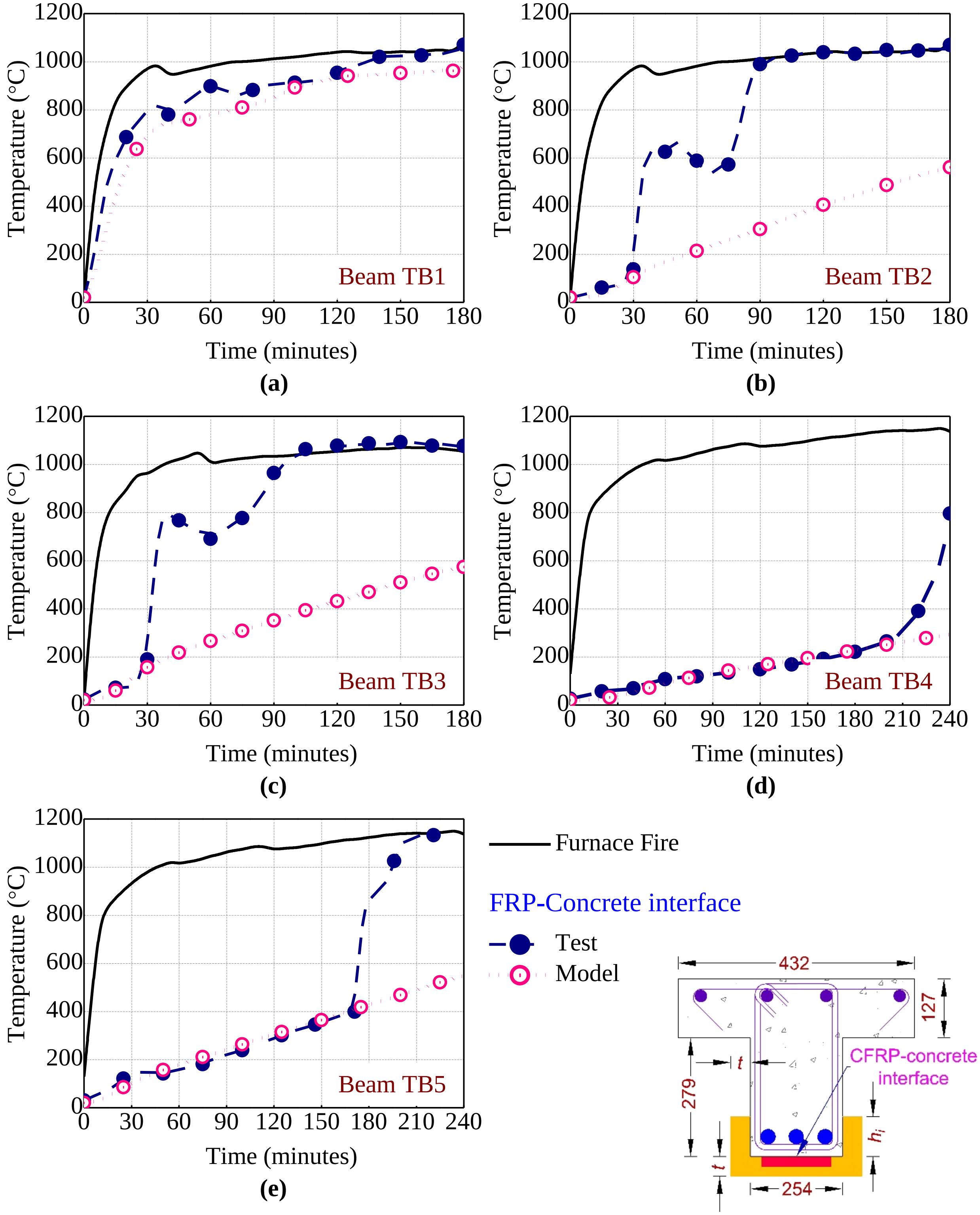

Figure 4.21: Comparison of predicted and measured temperature rise at CFRP-concrete interface at the mid-span of beams: (a) TB1; (b) TB2; (c) TB3; (d) TB4; (e) TB5

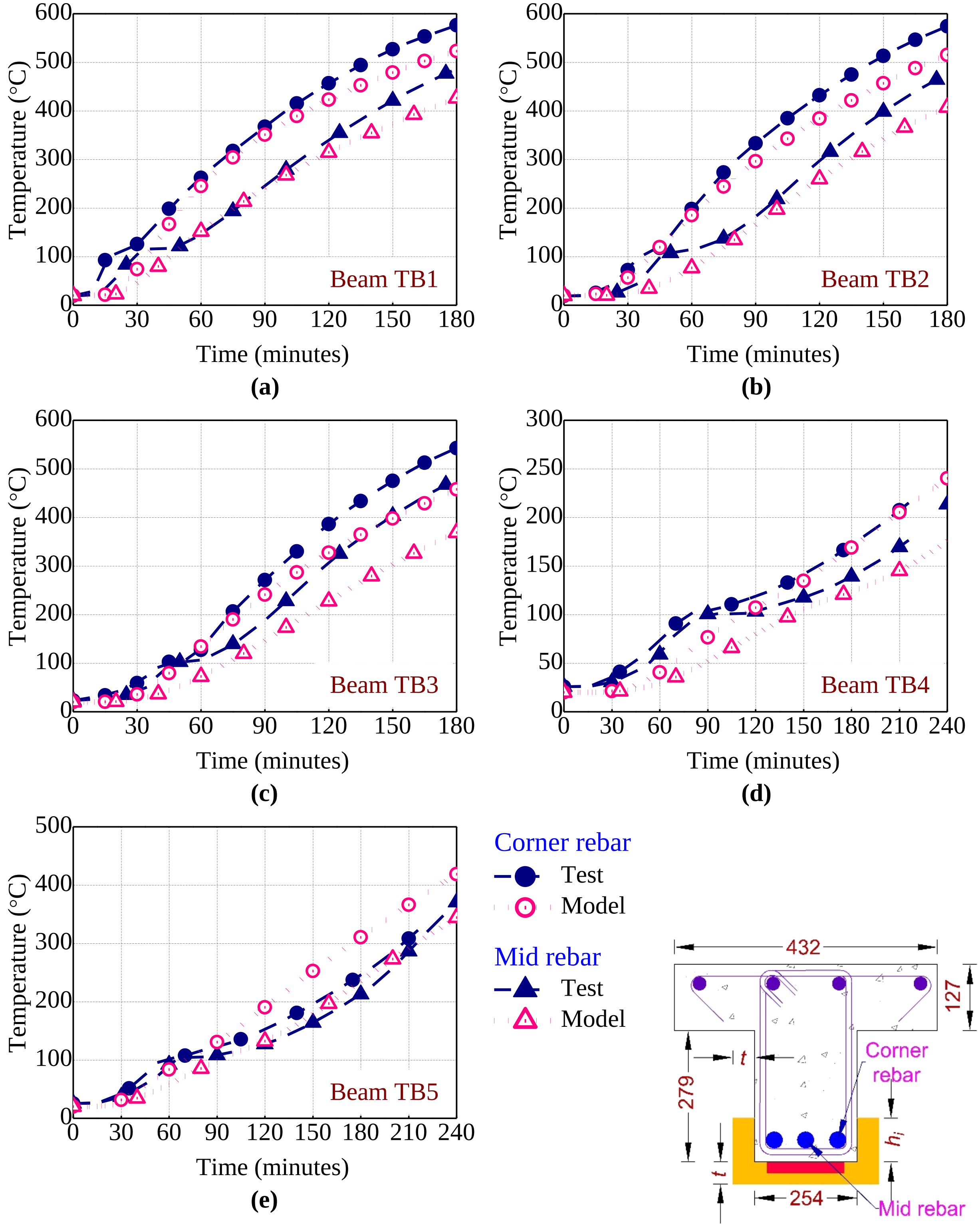

Figure 4.22: Comparison of predicted and measured temperature rise at corner and mid rebar at the mid-span of beams: (a) TB1; (b) TB2; (c) TB3; (d) TB4; (e) TB5

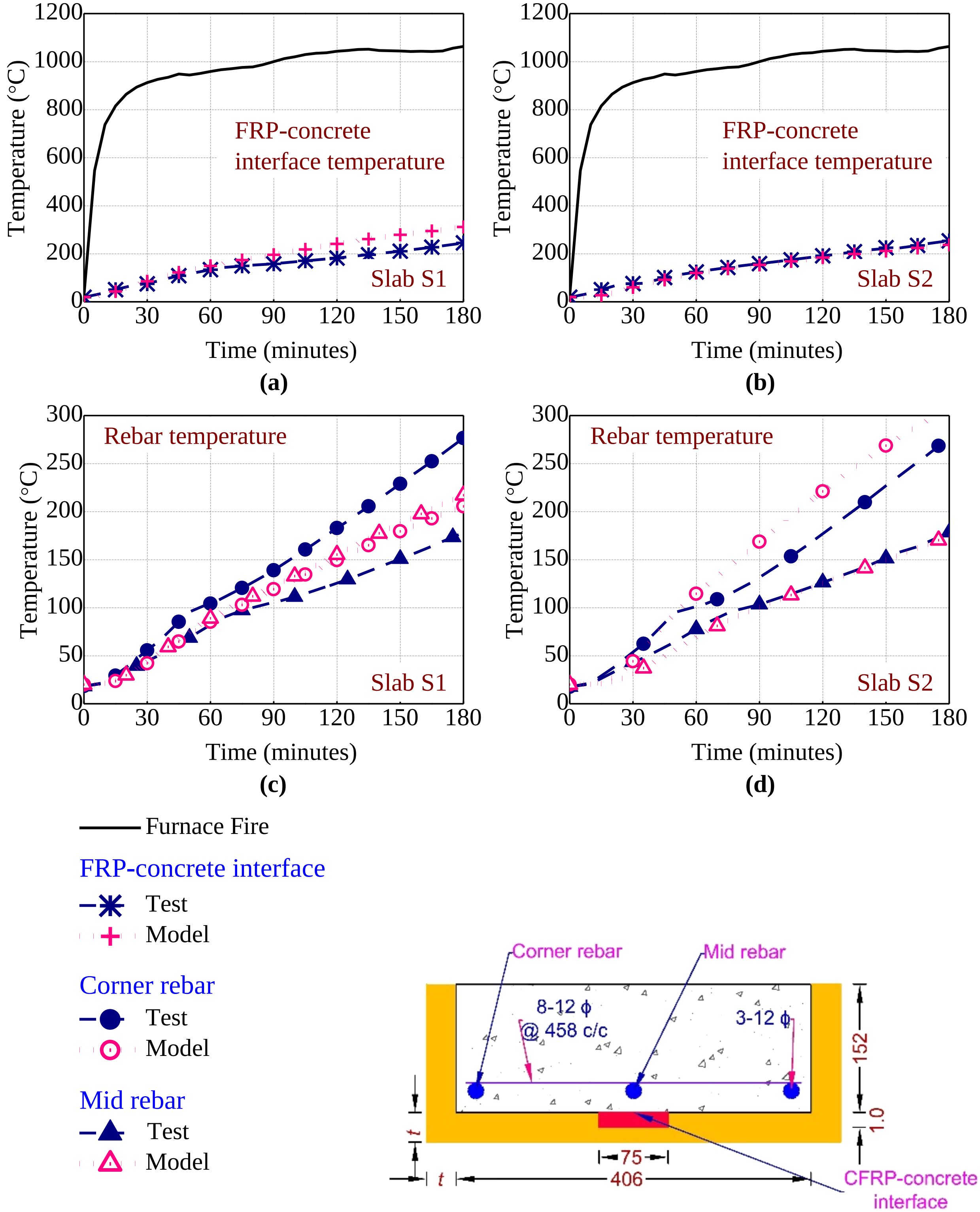

Figure 4.23: Comparison of predicted and measured temperature rise at various locations at the mid-span of slabs: (a) S1; (b) S2

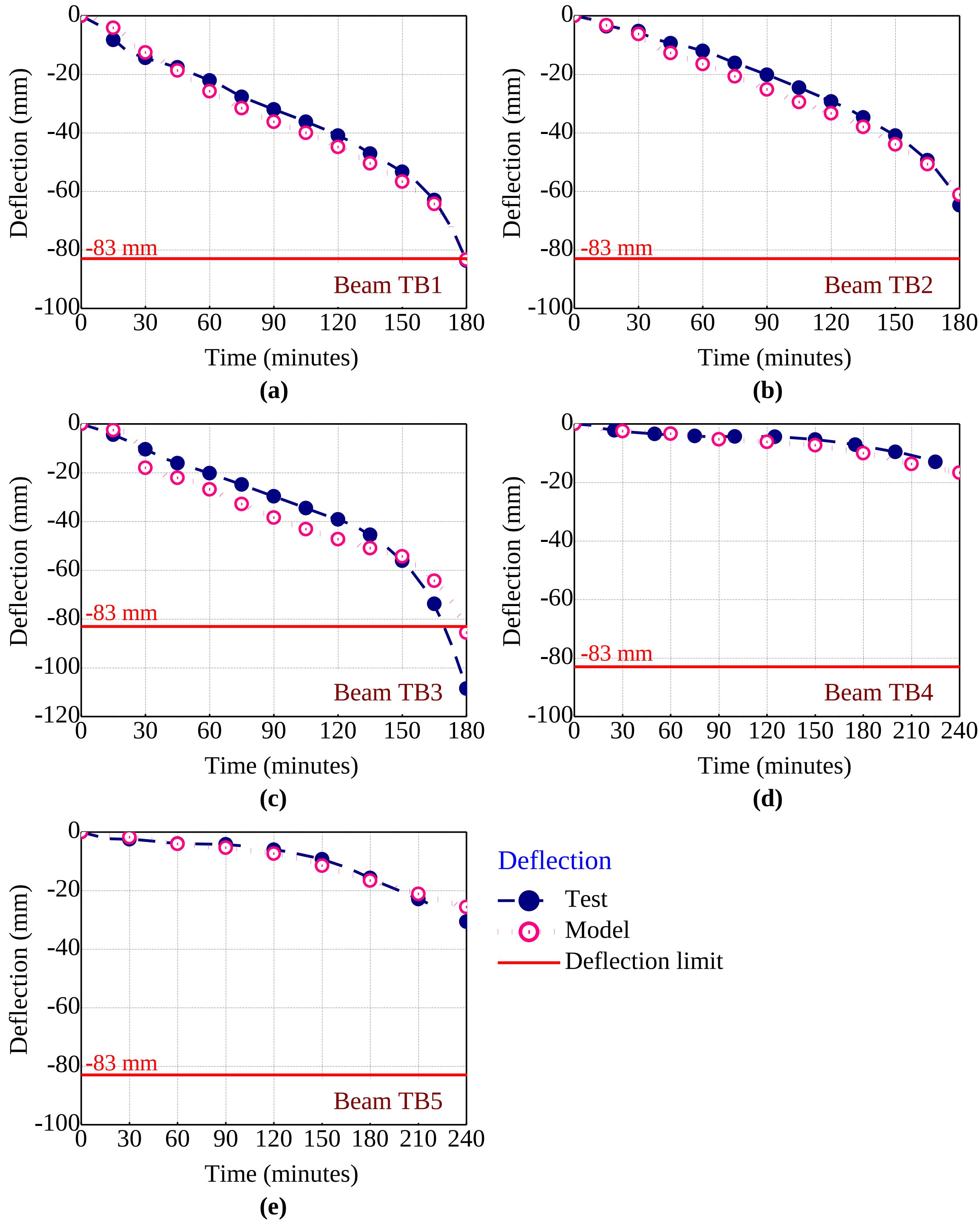

Figure 4.24: Comparison of predicted and measured mid-span deflection in beams: (a) TB1; (b) TB2; (c) TB3; (d) TB4; (e) TB5

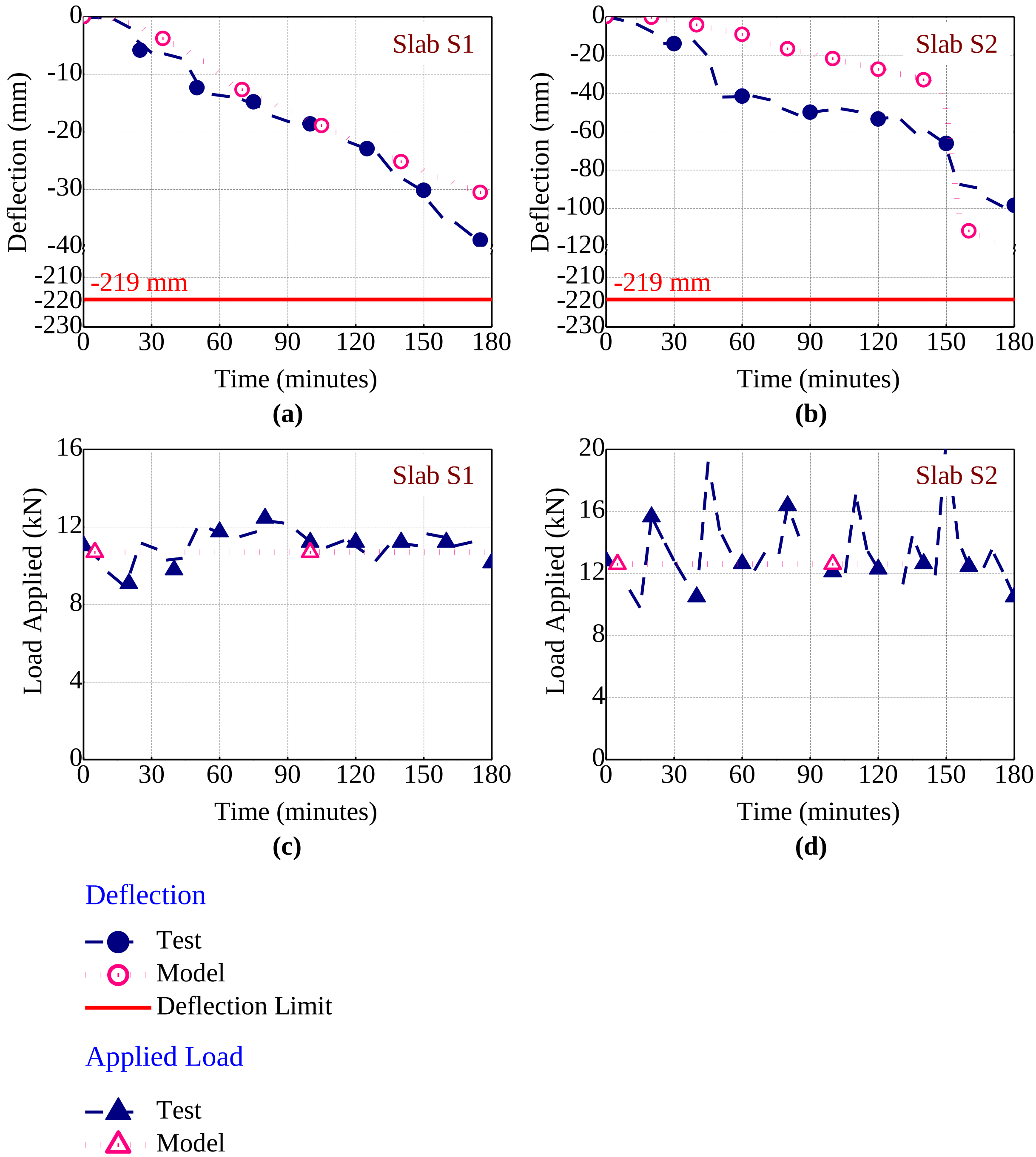

Figure 4.25: Fire resistance analysis of FRP-strengthened RC slabs: (a-b) comparison of predicted and measured mid-span deflection of slabs S1, S2; (c-d) comparison of applied load during the fire test and fire resistance analysis of slabs S1, S2

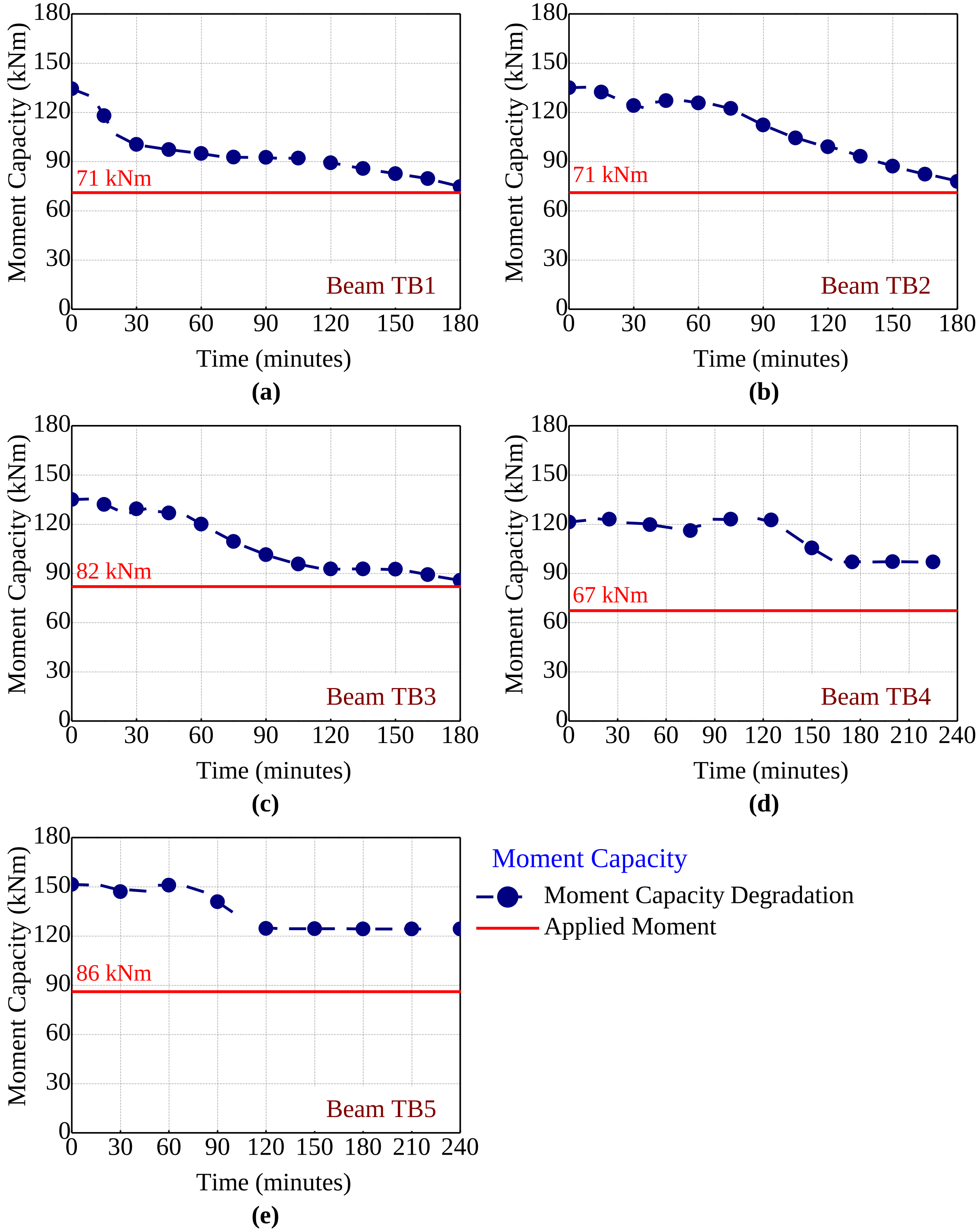

Figure 4.26: Moment capacity degradation predicted by model from the fire resistance analysis of FRP-strengthened concrete beams: (a) TB1; (b) TB2; (c) TB3; (d) TB4; (e) TB5

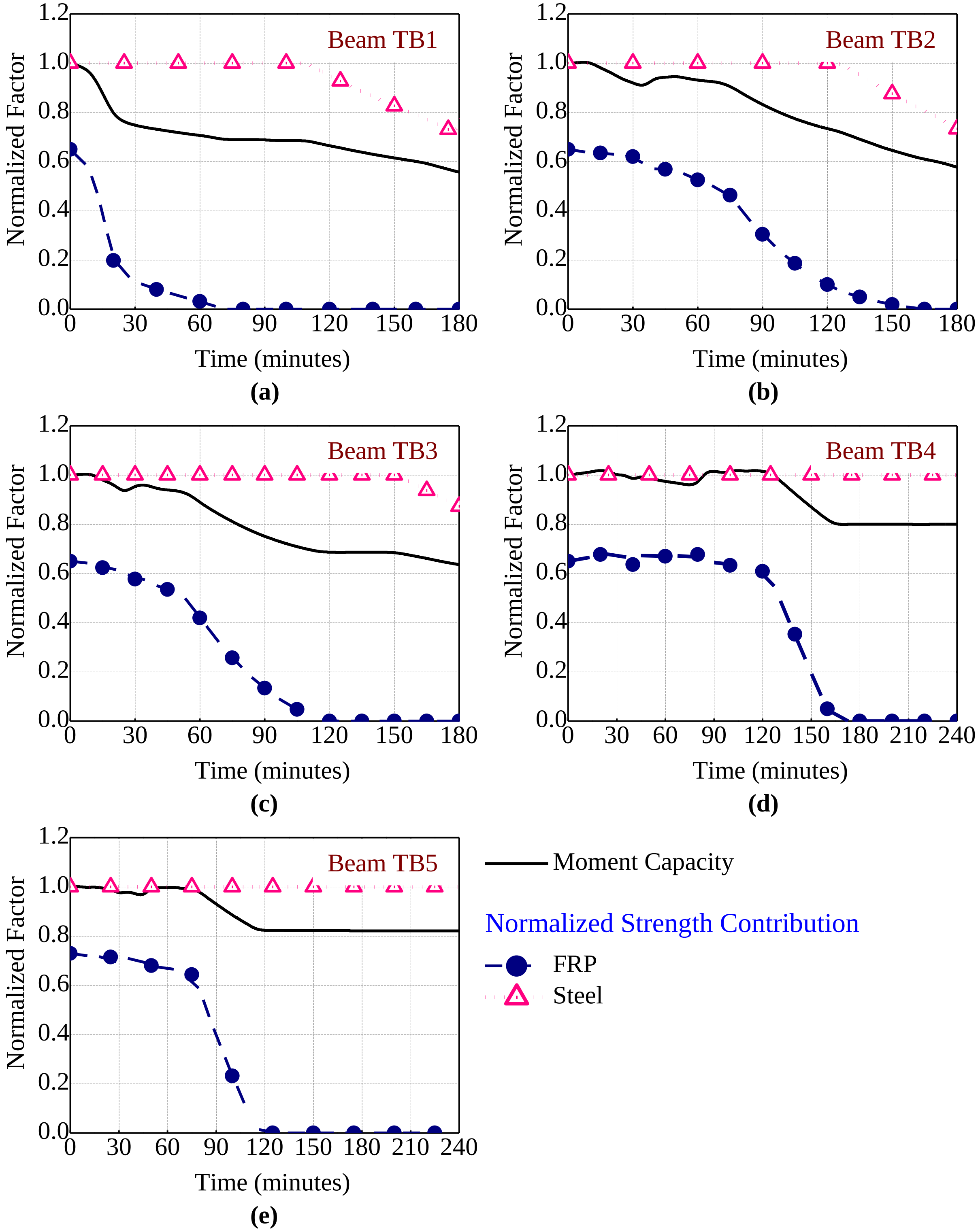

Figure 4.27: Normalized strength contribution of CFRP and steel rebar to the capacity of section at mid-span of beams TB1 to TB5 during fire exposure: (a) TB1; (b) TB2; (c) TB3; (d) TB4; (e) TB5

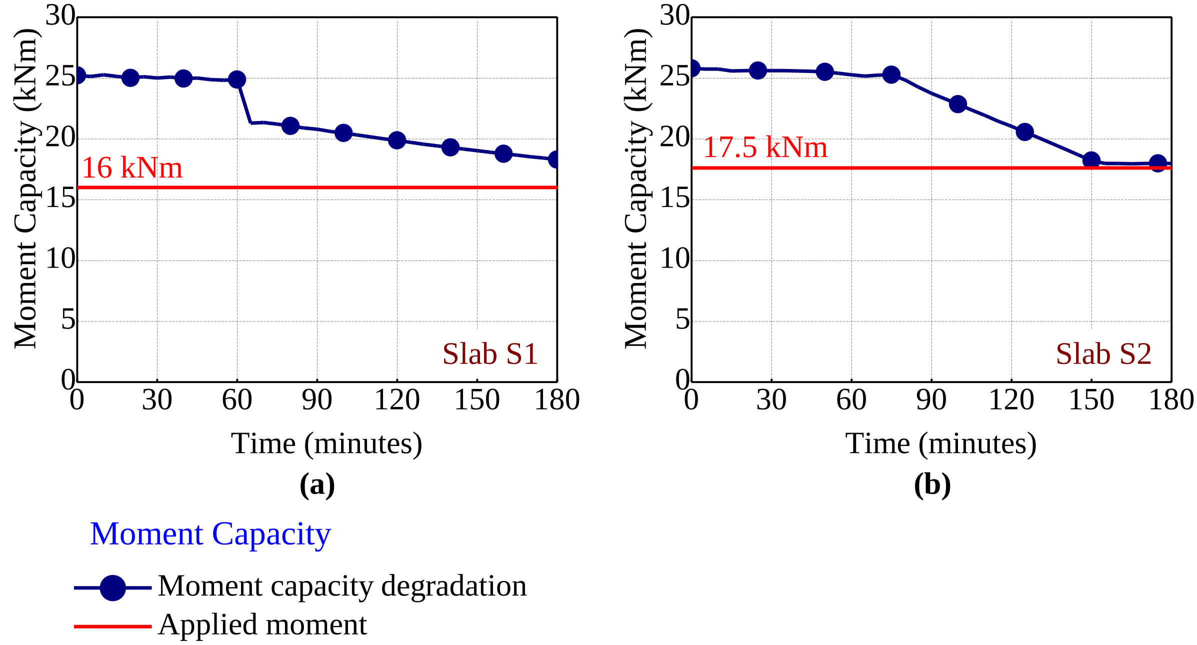

Figure 4.28: Moment capacity degradation predicted by model from the fire resistance analysis of FRP-strengthened concrete slabs: (a) S1; (b) S2

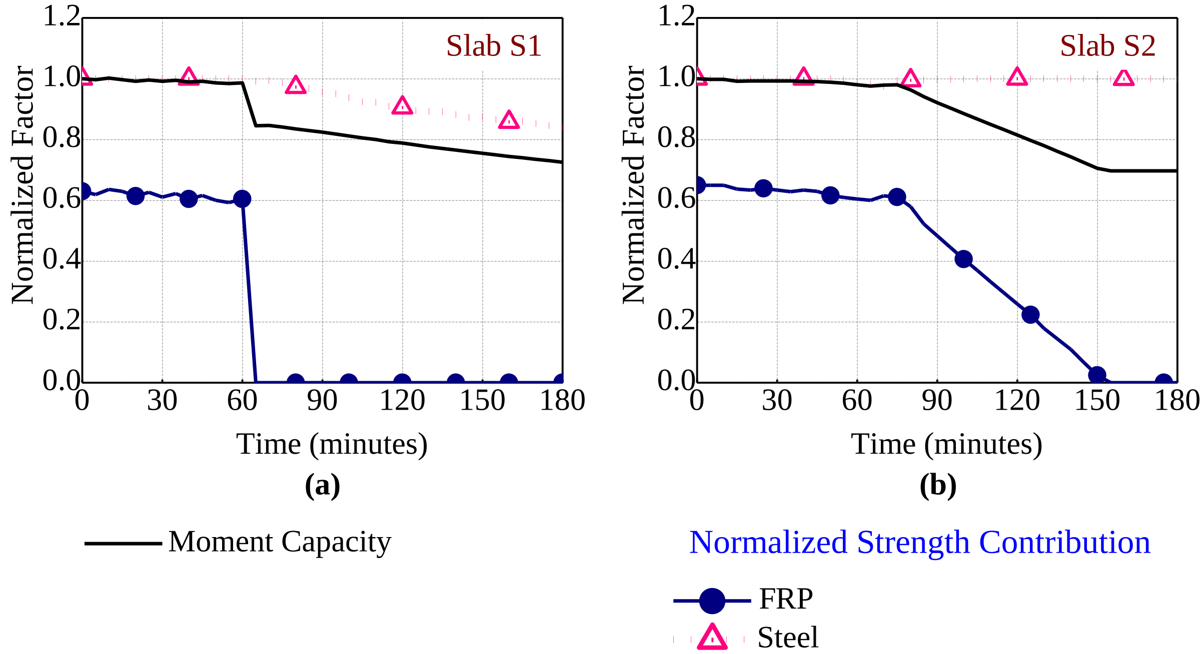

Figure 4.29: Normalized strength contribution of CFRP and steel rebar to the capacity of section at mid-span of slabs during fire exposure: (a) slab S1 (b) slab S2

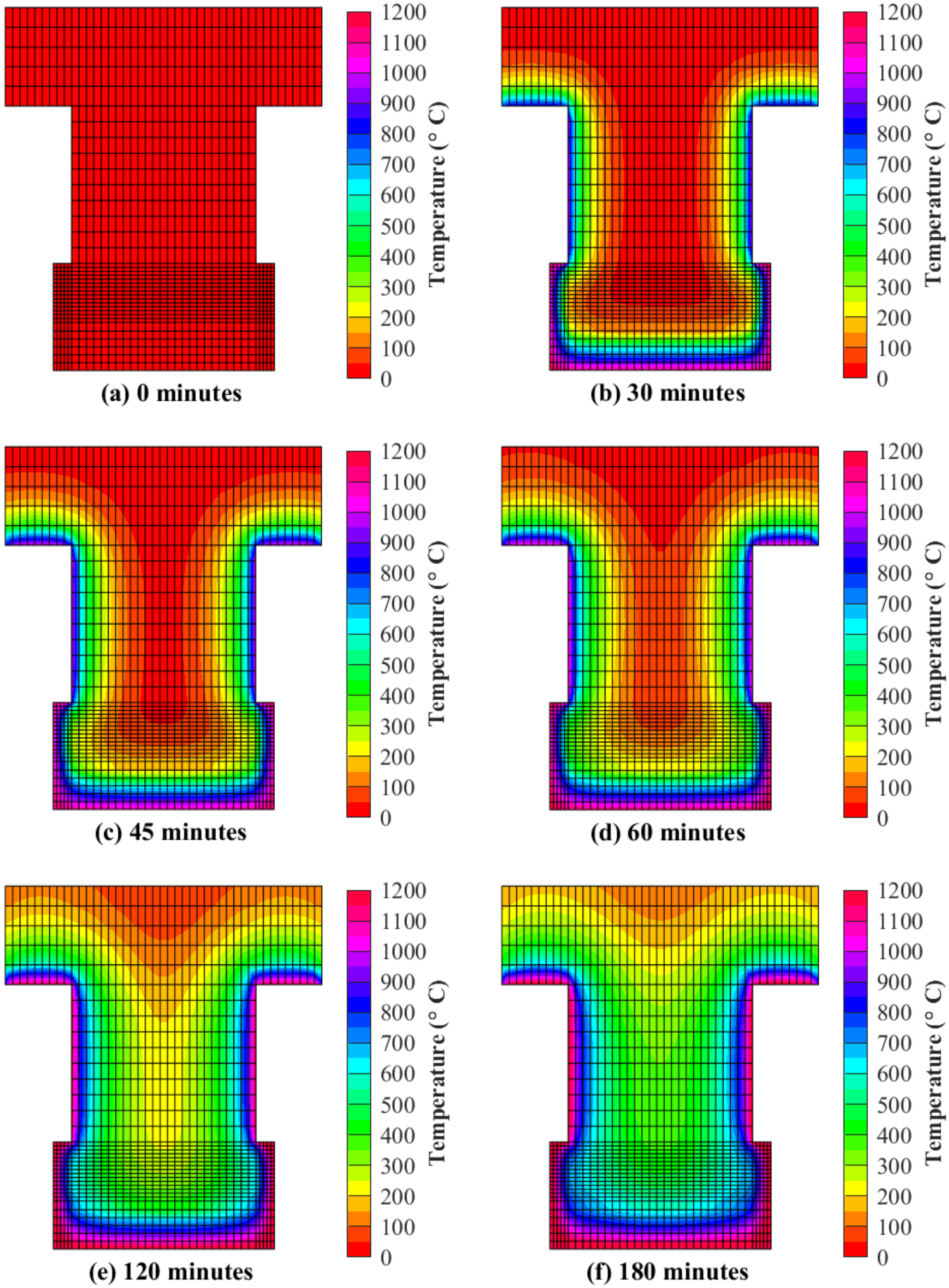

Figure 4.30: Cross-sectional temperature distribution for beam TB2 at different time intervals

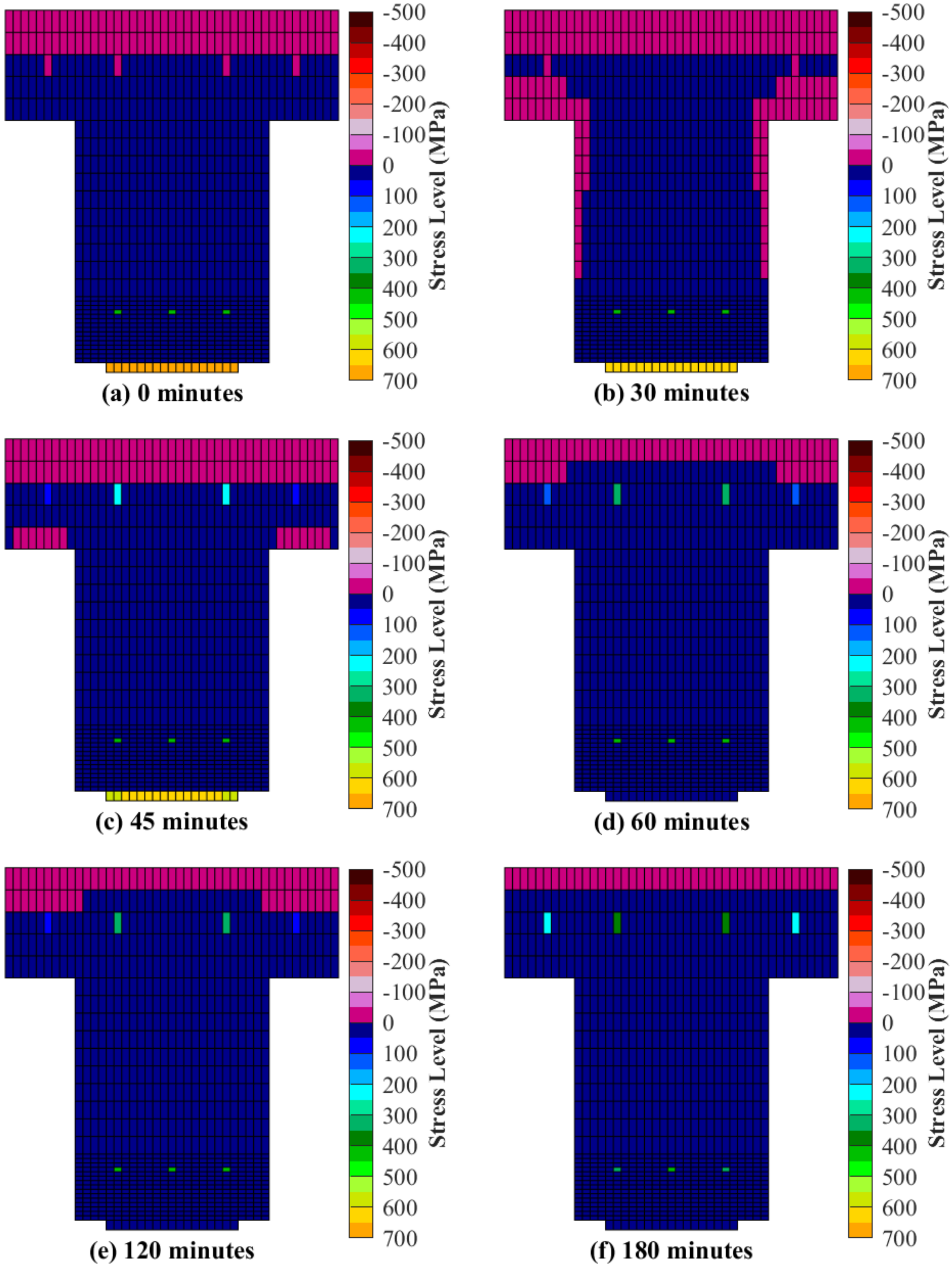

Figure 4.31: Strength distribution corresponding to moment capacity in cross-section of beam TB2 at different time intervals

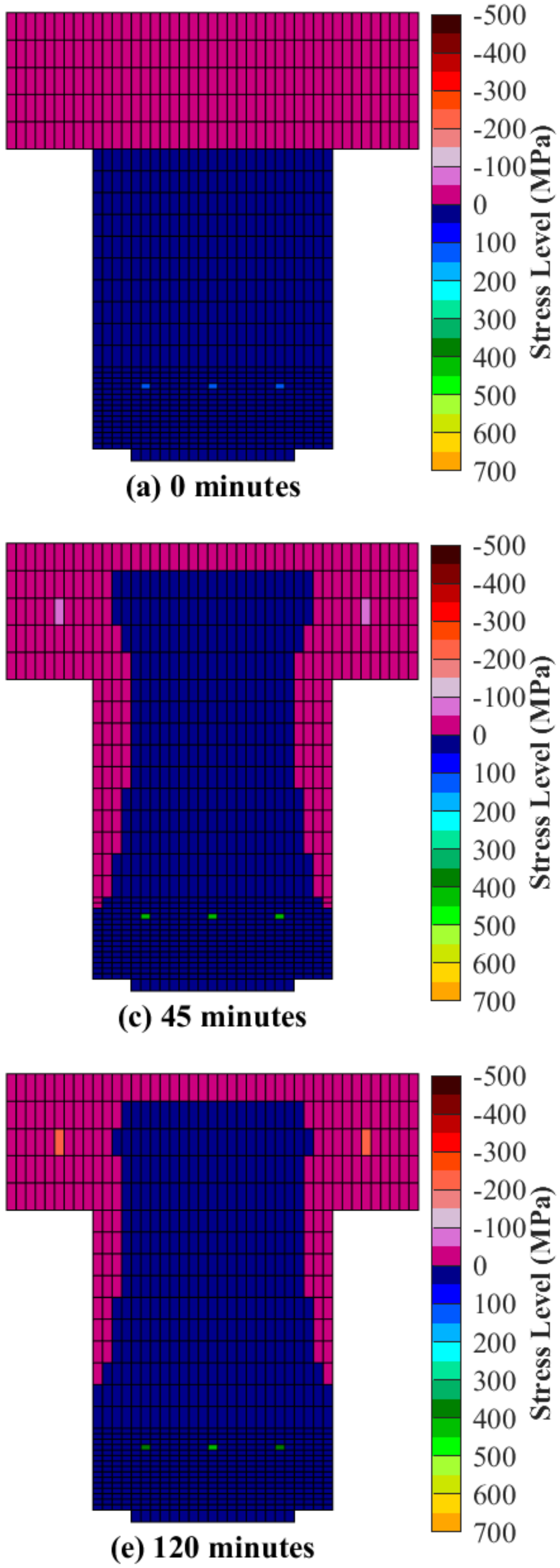

Figure 4.32: Stress distribution due to applied loading in cross-section of beam TB2 at different time intervals during fire exposure

CHAPTER 5

PARAMETRIC STUDIES

5.1 General

The literature review presented in Chapter 2 identifies several factors which influence the fire performance of FRP-strengthened concrete flexural members. These factors are interdependent which makes the fire resistance evaluation a complex task. Therefore, it is of crucial importance to quantify the effect of these factors, through a detailed parametric study, to better understand the overall performance of strengthened structural members under fire conditions. The experimental study presented in Chapter 3 attempts to evaluate the effect of few factors such as, load level, strengthening level. However, due to the limitations of the instrumentation, furnace size, loading equipment as well as the high cost involved in conducting fire tests, it is impossible to conduct numerous fire tests to quantify the influence of all the factors. Therefore, the validated numerical model presented in Chapter 4 is applied to conduct a comprehensive parametric study to evaluate the effect of various factors influencing fire performance of FRP-strengthened concrete flexural members.

Accurate fire resistance assessment of FRP-strengthened RC structural member using numerical models, require knowledge of high temperature thermal and mechanical properties of the constituent materials i.e., concrete, reinforcing steel, FRP, and insulation. A good amount of reliable data on high temperature properties and associated temperature dependent relations of concrete and reinforcing steel is available in the literature and design codes or standards. However, relatively limited data is available on high temperature strength and modulus properties of FRP in codes and standards or open literature [7]. Further, the data available on the temperature induced FRP-concrete bond degradation is also limited, that too, over a smaller temperature range.

As illustrated in Chapter 2, there exists a wide variation in the available data on high temperature properties of FRP, due to the dissimilar FRP materials, testing conditions and procedures followed in evaluating the properties of FRP. Similar to FRP, the information on high temperature thermal properties of insulation is also limited. In most cases, only the room temperature thermal properties of the insulation are provided by the manufacturer. This lack of information on high temperature thermal properties of insulation and the wide variation in limited amount of data available on high-temperature properties of FRP presents a challenge in evaluating realistic fire resistance of FRP-strengthened RC structural member.

To address this concern and to determine the influence of the available different high temperature material property relations for FRP and insulation, on fire resistance prediction, the model is first applied to undertake a numerical study on a set of FRP-strengthened RC beams in tested in fire. Thereafter, the model is applied to evaluate the effect of different parameters by varying it over a wide range by analyzing a set of FRP-strengthened RC beams and slabs. The data and results generated from these numerical and parametric studies can be applied to form guidelines for fire resistance evaluation and design of strengthened flexural members. Details of the procedure and the results from these numerical and parametric study are discussed in the following sections.

5.1.1 Numerical Studies Evaluating Effect of Material Property Relations

Numerical studies were conducted on a set of five CFRP-strengthened concrete beams tested in fire, to evaluate the effect of different property relations available for FRP and insulation on the fire resistance prediction. Results from the numerical study were then compared to the measured fire resistance of strengthened beams, to draw inferences on the effect of different property relations on fire resistance predictions. Although, the analyses were caried out for the beams, but the inferences drawn from the results are applicable for both beams and slabs. More details about the beams, analysis cases, and the analysis approach are given in the following sections.

5.1.2 Beams Selected for Evaluation

The beams selected for the analysis are taken from fire tests undertaken by different researchers, available in the literature. The beams are designated as B1, B2, B3, B4, and B5. Beam B1 was the one tested by Blontrock et al. [145]; B2 was tested by Gao et al. [151]; B3 was tested by Firmo and Correia [149]; B4 was tested by Dong et al. [150]; and B5 was tested by Zhang et al. [44] for fire resistance evaluation. All selected beams have rectangular cross-section. During the respective tests, the beams were strengthened externally with one layer of CFRP sheet and were protected with appropriate fire insulation. The layout and type of insulation on each beam is shown in Table 5.1. Beams B1 and B3 were insulated only at the bottom surface, while beams B2, B4, and B5 were insulated at the bottom and side surfaces for entire depth in beams B2 and B5, and up to 100 mm in beam B5. Details of design parameters, dimensions, material properties, and loading for the selected beams, are summarized in Table 5.1.

5.1.3 Analysis Details

To illustrate the effect of different thermal, mechanical, and bond degradation property relations of FRP on fire resistance predictions in CFRP-strengthened RC flexural members, the selected beams (B1 to B5) were analyzed in 13 different cases, C1 to C13, as described in Table 5.2. In each case, the variation of specific FRP property on fire resistance predictions was evaluated, while other properties were kept the same.

The beams were analyzed using the numerical model described in chapter 4. For this, the beams were discretized into 20 segments along the length and the cross-section of the beams was discretized into 10 × 10 mm element in the concrete region, 5 × 5 mm in the insulation region, and 5 × t_{frp} mm in FRP region, where t_{frp} is the thickness of FRP laminate or sheet. During the analysis, the beams were subjected to structural loading and fire scenario similar to that applied in the respective fire test. Accordingly, beams B1, B2, B4, and B5 were exposed to ISO 834 standard fire at the bottom and two sides, whereas beam B3 was exposed to ISO 834 fire only at the bottom surface. All the beams had simply supported end conditions, with four-point loading on beams B1 and B3, and six-point loading on beams B2, B4, and B5. The applied loading and load ratio defined as the ratio of applied load to the room temperature strengthened capacity of the beams is summarized in Table 5.1.

The room temperature material properties of the beams B1 to B5 are summarized in Table 5.1. The temperature dependent property relations for concrete and reinforcing steel, defined in ASCE manual [78] and Eurocode 2 [79] were incorporated in the model. A preliminary analysis was carried out with three different combination of property relations for concrete and steel rebars, namely, (i) ASCE manual property relations for both concrete and steel, (ii) Eurocode 2 relations for both concrete and steel, and (iii) ASCE manual relations for concrete and Eurocode 2 relations for steel rebars. Response parameters (deflections, capacity at various fire exposure times, as well as failure time) predicted from the analysis with combination (iii) were closer to the experimentally measured data. Therefore, for the analyses in the current study, the temperature dependent property relations for concrete and reinforcing steel as per ASCE manual [78] and Eurocode 2 [79], respectively, were used in the model. The temperature dependent variation in thermal conductivity and heat capacity of fire insulation is incorporated in the model depending upon the type of insulation used for thermal protection of the specific beam in the fire test and is shown in Figure 5.1. The FRP property relations incorporated in the analysis are varied based on the specific analysis case under consideration. These property relations are summarized in Table 5.2 for all the cases C1 to C13.

5.1.4 Effect of Material Property Relations-Analysis Results

Fire resistance of all the selected beams B1, B2, B3, B4, and B5 was determined for cases C1 to C13 using the strength and deflection limit state described in Chapter 4. The effect of specific FRP property relation on fire resistance prediction in each case as well as results from the analysis in these cases are discussed in following sections.

(i) Effect of Thermal Properties of FRP

Cases C1 and C2 were analyzed to evaluate the effect of temperature dependent thermal properties of FRP on fire resistance prediction. In case C1, the thermal properties of FRP were considered to be constant throughout fire exposure, whereas in case C2, the thermal properties of FRP were considered to vary with increase in temperature. Same strength and interfacial bond properties of FRP are considered in both these cases and are summarized in Table 5.2. The fire resistance time and the failure limit state exceeded for each of the five beams are compared in Table 5.3. Detailed results from the analysis of beam B1, in both these cases, are selected to illustrate the effect of thermal properties of FRP on fire resistance prediction.

Figure 5.2 compares the thermal response of beam B1, predicted in cases C1 and C2, by plotting the temperature rise in rebar and FRP-concrete interface, as a function of fire exposure time. Additionally, the temperature rise measured at these locations during the fire test is also shown in the figure. It can be seen from Figure 5.2 that the temperature rise in rebar and FRP-concrete interface predicted in both the cases, C1 and C2, is nearly identical. The lack of influence of thermal properties of FRP on predicted sectional temperatures can be attributed to the smaller cross-section of FRP sheet, as compared to the cross-section of concrete. Further, it can be seen from the figure that the temperature rise predicted in both the cases follow trends similar to that of measured temperatures. However, the predicted temperatures are slightly higher than the measured temperature. This may be attributed to the thermal properties of fire insulation incorporated in the model which may be slightly different from the actual properties. Further, there exists a plateau in the temperature rise measured at the FRP-concrete interface at 100°C, which may be attributed to the evaporation of free water in the insulation. The model does not account for such evaporation and therefore, no plateau is predicted by the model.

Figure 5.3 compares the structural response of beam B1 predicted in analysis cases C1 and C2. Figure 5.3 (a) compares the degradation in moment capacity of beam B1, as predicted in both the cases, whereas Figure 5.3 (b) compares the deflection predicted in both the cases with the measured deflections. It can be seen from Figure 5.3 that the predicted degradation of moment capacity and increase in deflections in both the cases (with and without varying thermal properties of FRP) are identical. Additionally, it can be seen from the Figure 5.3 (b) that the deflections predicted in both the cases are in close agreement with the measured values. The identical moment capacity degradation and deflection rise in both cases, C1 and C2, is attributed to the nearly identical temperature rise within the cross-section. Moreover, beam B1 fails at 108 minutes of fire exposure by exceeding the deflection limit state in both the cases (refer to Table 5.3), indicating that the beam has same fire resistance in both cases. Similar results are obtained for the other four beams (B2 to B5) analyzed in cases C1 and C2. From these results, it can be clearly concluded that thermal properties of FRP do not affect temperature rise and thus the fire resistance predictions in a fire exposed FRP-strengthened member.

(ii) Effect of Strength and Modulus Reduction Factors for FRP

The effect of different property relations, defining variation of strength and elastic modulus, on fire resistance predictions, was analyzed for different beams through cases C3, C4, C5, and C6. In these analysis cases C3 to C6, the strength and elastic modulus property reduction factors were assumed to vary as per the relations specified by Bisby et al. [120], Wang et al. [108], Dai et al. [121], and Nguyen et al. [115], respectively. These relations for strength and elastic modulus of FRP are shown in Figure 5.4. Moreover, to prevent the complete loss of FRP contribution due to temperature induced bond degradation, perfect bond was assumed at the FRP-concrete interface. Since strength relations do not affect the temperature rise in the section, the thermal response of all beams was ignored, and it was assumed that the temperature rise in beams is identical to the temperature rise measured during the respective fire test.

Fire resistance time as well as the failure limit state exceeded in each beam, analyzed for each of these cases, are compared in Table 5.3. The structural response from the analysis of beam B4, in cases C3 to C6, is used to illustrate the effect of different strength and stiffness reduction factors. Since the beam fails in strength limit state, only the degradation in moment capacity with fire exposure time is compared in Figure 5.5. It can be seen from the figure that the predicted degradation of moment capacity in all the cases is significantly different throughout the fire exposure duration.

The capacity of the beam in case C5 (when Dai et al. strength model for FRP is used) decreases rapidly in the initial stages of fire exposure and then continues to decrease at a slower rate but does not fall below the moment due to applied loading, indicating no strength failure. This is attributed to the fact that the Dai et al. model considers no reduction in strength of FRP beyond the T_g of polymer matrix. Further, the moment capacity of the beam degrades at a faster rate in case C4 (using Wang et al. model) as compared to cases C3 (using Bisby et al. model) and C6 (using

Nguyen et al. model). However, the moment capacity in case C4 falls below the applied loading at a much later time (thus higher fire resistance) as compared to cases C3 and C6. This is attributed to the faster reduction in FRP strength in cases C3 and C6, after 350°C and 500°C, respectively, as compared to reduction in strength of FRP in case C4 (*cf*. Figure 5.4 (b)).

Overall, the fire resistance predicted in cases C4 and C5 are much higher than the fire resistance predicted in cases C3 and C6. Similar results are obtained from the analysis of beams B1, B2, B3, and B5 in cases C3 to C6, and predicted fire resistance values are summarized in Table 5.3. Based on these analysis results, it can be concluded that the temperature dependent strength relations for FRP proposed by Bisby et al. [120] and Nguyen et al. [115] provide a conservative estimate of fire resistance, as compared to relations proposed by Wang et al. [108] and Dai et al. [121].

(iii) Effect of Bond-Slip Relations for FRP-Concrete Interface

The effect of different FRP-concrete bond degradation relations on fire resistance prediction in EB FRP-strengthened RC beams was analyzed in cases C7, C8, C9, C10, and C11. Case C7 considers a perfect bond between CFRP and concrete, cases C8 and C9 considers a bilinear and nonlinear bond-slip relation, respectively, as shown in Figure 5.6, whereas case C10 considers a complete loss of CFRP-concrete composite action at interface temperature beyond T_g. Cases C9 and C11 used same nonlinear bond-slip relations for simulating the temperature induced bond degradation at the FRP-concrete interface in beams B1 to B5; however, in case C9 relative slip between concrete and FRP is computed at different segments along the length of the beam, whereas in case C11, the maximum relative slip at any section along the length of the beam was taken as the relative slip throughout the length of the beam. The strength and elastic modulus reduction factors for CFRP considered in each of these cases are summarized in Table 5.2. The fire resistance predicted by the model and the failure limit state exceeded in the analysis of each beam in cases C7 to C11 are summarized in Table 5.3.

Figure 5.7 shows the geometrical and loading configuration of beam B4 for which the structural predicted structural response is compared in Figure 5.8. The degradation in moment capacity of the critical section of the beam B4 i.e., section subjected highest bending moment due to applied loading, as predicted from analysis in cases C7 to C11, is plotted against the fire exposure time in Figure 5.8 (a). Based on the loading configuration shown in Figure 5.7 (a) and the bending moment diagram shown in Figure 5.8 (a), the central 1300 mm portion of the beam is subjected to highest bending moment. Since the beam length was discretized in 10 sections each 520 mm apart, the mid-span section (section AA') as well as the section immediately before and after the mid-span (section BB') are subjected to highest bending moment due to applied loading, and are therefore, the critical sections. It was observed from the analysis that the capacity of section AA' and BB' decreases at a same rate in cases C7, C10, and C11, whereas in cases C8 and C9, the moment capacity of section BB' falls below the bending moment due to applied loading prior to that of section AA'. This is attributed to the fact that the relative slip between CFRP and concrete at a section, among other factors, depends on the distance from the applied load. Therefore, each section along the length has a different slip and as a result the reduction in stress transfer between CFRP and concrete is different, resulting in different rate of capacity degradation.

It can be seen from Figure 5.8 (a) that the capacity of the beam decreases gradually at a similar rate in all the cases C7 to C11 in the initial stages of fire exposure. After 40 minutes, the capacity of beam B4 in case C10 decreases abruptly and falls below the moment due to applied loading. This is attributed to the complete loss of strength and stiffness contribution from CFRP, after the temperature at the FRP-concrete interface exceeds the T_g of adhesive. In case C7, which considers a perfect bond between CFRP and concrete, the capacity of the beam B4 decreases slowly and reaches the moment due to applied loading after 240 minutes of fire exposure, indicating strength failure. The failure in case C7 is attributed to the temperature induced degradation in strength and modulus properties of CFRP and steel rebars.

In cases C8 and C9, where bilinear and nonlinear bond degradation relations before and after interface temperature reaches T_g are explicitly defined, the capacity of section BB' falls below the applied load bending moment after 96 and 144 minutes, respectively. The difference of failure time in cases C8 and C9 is attributed to the fact that at elevated temperature the bilinear bond-slip relation considered in case C8 is stiffer than the nonlinear bond-slip relations considered in case C9. Therefore, the capacity in case C8 decreases at a slower rate compared to that in case C9.

In case C11, the capacity of section AA' (mid-span) falls below the applied loading at 72 minutes. To illustrate the difference in cases C9 and C11, the degradation moment capacity of section AA' is also plotted in Figure 5.8 (a). It can be seen that the capacity of section AA' in case C9 falls below the applied moment after 108 minutes. The early strength failure in case C11 despite the same bond-slip relation as that in case C9, is attributed to the fact that the in case C11 the maximum slip at any section along the length of the beam is considered as the slip in all the sections of the beam. As a result, once debonding occurs at any section of the beam, the CFRP-concrete composite action is assumed to be completely lost in the entire length of the beam, which in turn leads to faster reduction in the moment capacity in each section along the beam's span. Whereas in case C9, the relative slip and resulting degradation in capacity is computed separately for each section of the beam. Therefore, the capacity of each section decreases at a different rate and falls below the bending moment due to applied loading at different times. Since section BB' attained strength failure at 96 minutes in case C9, the beam B4 is said to have attained the strength limit state at 96 minutes.

Figure 5.8 (b) compares the mid-span deflection response of beam B4 as predicted in cases C7 to C11 with the measured values. It can be seen from the figure that deflection predicted in case C9 is in close agreement with the measured deflection response, whereas the deflection in cases C7 and C8 is much stiffer than the measured values. The stiffer response in case C7 is attributed to the perfect bond between FRP and concrete, whereas the stiffer response in case C8 is attributed to the higher bond-strength required for the initiation of debonding at the CFRP-concrete interface. Due to early strength failure of the beam in case C10, the deflection is predicted only up to 40 minutes of fire exposure and is in close agreement with the measured values. In case C11, the predicted response is much softer than the measured values, i.e., higher deflection at the same time instant. This is attributed to the faster reduction in stiffness resulting from considering maximum slip at any section as the slip along the entire length of the beam, which is unrealistic. Thus, the bond-slip model proposed by Dai et al. [134] yields a better assessment of fire resistance in EB CFRP-strengthened RC beams.

To further illustrate the difference in slip computations along the length, the relative slip (mm), slip strain (%), and reduction in contribution of CFRP towards the capacity of beam B4 at section along the half-length of beam B4, as predicted in cases C9 and C11 are shown in Figure 5.9 and Figure 5.10, respectively. It can be seen from Figure 5.9 that the relative slip along the length of beam, as predicted in case C9, is almost negligible until 60 minutes of fire exposure. After 60 minutes the slip starts increasing at the sections at 520 mm and 2080 mm from the support. The faster increase in slip at these sections is attributed to the proximity of these sections to the applied loads. With the increase in fire exposure time the slip at each section along the length of the beam starts increasing with maximum increase in section BB'. Further, it can be seen that the slip at each of these sections vary significantly. With increase in relative slip at any section, the slip strain at that section increases, which in turn reduces the contribution of CFRP to capacity of the respective section, resulting in failure of section BB' at 96 minutes.

In case C11, the relative slip at all the sections is negligible until 24 minutes of fire exposure. After this the slip as well as the slip strain starts increasing uniformly at all the sections of the beam and the contribution of CFRP starts decreasing at the same rate. After 72 minutes, the slip and slip strain increases to the extent that the contribution of CFRP decreases to less than 5% at all the sections, resulting in failure premature failure.

The fire resistance predicted in case C7 (with perfect bond) for all the beams is significantly higher than the measured values as well as the fire resistance predicted in other cases C8 to C11. On the contrary, the fire resistance predicted in case C10 (with no bond after T_g) is significantly lower than the measured values. Thus, neglecting CFRP-concrete bond degradation (case C7) provides an unrealistic estimate of the fire resistance, and neglecting strength and stiffness contribution of CFRP beyond T_g (case C10) provides an over conservative estimate of fire resistance.

In cases C8, C9, and C11 with bilinear and nonlinear degradation relations, the predicted fire resistance is highest in case C8 and is lowest in case C11. However, the deflection response predicted in case C9 (nonlinear bond-slip relation) is much closer to measured values in comparison to the deflection response predicted in cases C8 and C11. Therefore, the use of Dai et al. [134] bond-slip relations lead to better fire resistance predictions. Additionally, the degradation in bond must be computed separately at each section along the length of beam and should not be idealized as the slip at the critical section.

(iv) <u>Effect of Varying Thermal Properties of Fire Insulation</u>

CFRP-strengthened concrete structural members are provided with a layer of fire insulation to increase the effectiveness of CFRP for a longer time, and to improve the fire resistance of the CFRP-strengthened RC member. Thus, fire resistance of FRP-strengthened RC members is also dictated by thickness as well as thermal properties of fire insulation. As discussed in chapter 2, the thermal properties of fire insulation vary significantly with increase in temperature (Figure 5.1), and therefore, must be accounted in the fire resistance analysis. However, most often, constant (room temperature) thermal property of fire insulation (without considering temperature dependent variation) is utilized in fire resistance analysis of FRP-strengthened RC members. Such a design consideration can lead to inaccurate fire resistance assessment. To illustrate the effect of thermal properties of insulation on fire resistance predictions, the beams B1, B2, B3, B4, and B5 are analyzed in two different cases, namely C12 and C13.

In case C12, only room temperature properties of the insulation were considered i.e., the variation of thermal properties with temperature was neglected. Whereas, in case C13, the temperature induced variation in thermal properties of fire insulation was incorporated in the model. The thermal, strength and bond degradation properties of CFRP, considered in the analysis in each case, are summarized in Table 5.2. Additionally, fire resistance time predicted from the analysis of all the beams in cases C12 and C13 are summarized in Table 5.3. It can be seen from the table that the fire resistance of all beams in case C12 is significantly higher than the fire resistance predicted in case C13.

Detailed results from thermal and structural analysis of beam B5 are used to illustrate the difference in response in these cases (C12 and C13). Figure 5.11 compares the temperature rise in rebar and FRP-concrete interface of beam B5 with the temperature rise at respective locations measured in test. It can be seen from the figure that the overall trends of temperature rise predicted in both the cases are similar to the trends measured in the test. However, the temperature rise predicted in case C12 are significantly lower than measured values, whereas the temperature rise predicted in case C13 are slightly higher than the measured values. The lower temperatures predicted in case C12 can be attributed to constant thermal properties of insulation used in the analysis, which alters the heat transfer within the section thereby, providing an in-accurate temperature rise prediction. The higher temperature rise predicted in case C13 is attributed to the increase in thermal conductivity and decrease in heat capacity of the fire insulation at high temperature (*cf.* to Figure 5.1), which increases the heat propagation within the cross-section, thereby increasing temperatures.

To compare the structural response of beam B5 predicted from the analysis in cases C12 and C13, the degradation in moment capacity and progression of deflection are plotted as a function of fire exposure time in Figure 5.12. It can be seen from Figure 5.12 (a) that although the degradation of moment capacity of beam in both the cases follow similar trends, the capacity decreases at a slower rate in case C12, as compared to that in case C13. Similarly, it can be seen from Figure 5.12 (b) that the deflection in case C13 match well to the measured values, whereas deflection response predicted in case C12 is stiffer as compared to the test data. This is attributed to the slower temperature rise in the beam in case C12, resulting from not accounting temperature induced effect on thermal properties of fire insulation, which in turn reduces the degradation of strength properties of the constituent materials. Further, the fire resistance time predicted in case C12 is 284 minutes which is significantly higher than the measured fire resistance of 199 minutes. Hence, neglecting the temperature dependence of thermal properties of fire insulation would lead to an unrealistic prediction of fire resistance in FRP-strengthened RC structural members.

5.2 Factors Influencing Fire Performance

The main factors affecting the fire performance of FRP-strengthened concrete flexural members include strengthening effect, FRP-concrete interfacial bond degradation, insulation thickness and configuration, insulation configuration in anchorage, fire scenario, load level, strengthening level, reinforcement ratio, concrete strength, aggregate type, insulation thermal properties, and axial restraints. The effect of some of these parameters such as, concrete strength, aggregate type, insulation thermal properties, axial restraints has been quantified in previous studies by Ahmed [175] and Yu [176] , however, the effect of remaining factors has been evaluated qualitatively through limited analysis or conceptual framework. Therefore, to generate data on the effect of these factors over a wide range a detailed parametric study on a set of FRP-strengthened concrete flexural members with realistic geometrical dimensions as well as realistic strengthening and load level is undertaken using the developed numerical model.

5.3 Parametric Studies

Parametric study is performed on CFRP-strengthened RC beams and CFRP-strengthened RC slabs utilizing the macroscopic finite element based numerical model developed in Chapter 4, to evaluate the influence of different parameters on the fire response. The beams and slabs considered for the analysis, the range over which the parameters are varied, and the results from the parametric study are discussed in this section.

5.3.1 Beams and Slabs for Parametric Studies

The geometrical and material property details of the beam (PB) and slab (PS) are summarized in Table 5.4. The elevation and cross-section details of the beam (PB) selected for the parametric study are shown in Figure 513. The beam is 6.0 m long and has rectangular cross-section of 254 ×

406 mm. The top and bottom longitudinal reinforcement in the beam comprises of 2-13 mm ϕ and 3-16 mm ϕ rebars, respectively, at a concrete cover of 38 mm. The shear reinforcement in the beam comprises of 10 mm ϕ stirrups provided at 150 mm c/c. The beam is strengthened in flexure by providing a 1.02 mm thick and 254 mm wide V-wrap C200HM CFRP sheet at the soffit. The beam is protected with t_{ins} mm thick V-wrap FPS fire insulation, at the soffit and on the side surfaces up to a depth of h_i mm, as measured from the bottom surface of the beam. The nominal un-strengthened capacity of the beam is M_{n_PB} = 101 kNm, which upon strengthening increased by 57% to M_{nupg_PB} = 152 kNm.

The elevation and cross-section details of the slab (PS) selected for the parametric study are shown in Figure 5.14. The RC slab is 3.5 m long with a 600 mm wide and 150 mm deep cross-section. The longitudinal reinforcement in the slab comprises of 4-13 mm ϕ rebars provided at a concrete cover of 25 mm. The slab is strengthened in flexure by providing a 1.02 mm thick and 200 mm wide V-wrap C200HM CFRP sheet at the soffit. The slab is protected with *dib* mm thick V-wrap FPS fire insulation only at the bottom surface. The nominal un-strengthened capacity of the beam is M_{n_PS} = 26 kNm, which upon strengthening increased by 57% to M_{nupg_PS} = 42 kNm.

In the parametric study, the geometrical and insulation configuration, as well as thermal and structural loading parameters of the above-described beam PB and slab PS were varied over a wide range, and as a result a total 35 beams (PB1 to PB35) and 29 slabs (PS1 to PS29) were generated. The details of the parameters varied are discussed in following section.

5.3.2 Varied Parameters and Range of Parameters

To quantify the effect of various factors on the fire performance and resistance of FRP-strengthened concrete flexural members, seven cases were analyzed for the FRP-strengthened RC beam and six cases are analyzed for the FRP-strengthened RC slab. In each of these cases one parameter was varied within a range applicable in field applications, while rest were kept constant. The specific parameter studied in each of the cases are described separately for beams and slabs.

(i) Cases for Beams

The parametric cases analyzed for CFRP-strengthened RC beam (PB) are designated as PBC1, PBC2, PBC3, PBC4, PBC5, PBC6, PBC7. The parameter varied, range of each parameter, and the beams analyzed in each of these cases are summarized in Table 5.5 and are discussed below:

- In case PBC1, the effect of CFRP strengthening is evaluated by analyzing un-strengthened and CFRP-strengthened RC beams with and without fire insulation, i.e., a total of four beams PB1 to PB4.
- In case PBC2, the effect of seven different insulation depths (h_i), ranging from 0 to 152 mm, on the sides of the beam as measured from the bottom surface of the beam is evaluated by analyzing beams PB5 to PB11.
- In case PBC3, the effect of seven different insulation thickness (t), ranging from 0 to 38 mm, applied on sides and the bottom surface was evaluated by analyzing beams PB12 to PB18.
- In case PBC4, the effect of five different load levels ranging from 30% to 70%, (in increments of 10%) is evaluated by analyzing beams PB19 to PB23.
- In case PBC5, the effect of five different fire scenarios is evaluated by analyzing beams PB24 to PB28. The five fire scenarios include, ISO 834, three parametric fires computed using Eurocode-2 (2004) provisions, and ASTM E119 fire with a cooling phase.
- In case PBC6, the effect of four different CFRP-strengthening levels, i.e., 20%, 30%, 40%, and 57%, is evaluated by analyzing beams PB29 to PB32.

- In case PBC7, the effect of three different steel reinforcement ratio ranging from 0.44% to 0.89%, with respect to area concrete, is evaluated by analyzing beams PB33 to PB35.

(ii) Cases for Slabs

The factors influencing the fire performance of CFRP-strengthened RC slabs are mostly similar to those affecting the fire performance of CFRP-strengthened RC beams. However, since slabs are not provided with insulation on the side surface, the effect of depth of insulation on sides is not evaluated here. Additionally, factors such as, strengthening level and reinforcement ratio had minimal effect similar on the fire performance of slabs, and are therefore, not evaluated here. Six parametric cases designated as PSC1, PSC2, PSC3, PSC4, PSC5, and PSC6 are analyzed for CFRP-strengthened RC slab (PS). The parameter varied in these cases are described below.

- In case PSC1, the effect of CFRP strengthening is evaluated by analyzing slabs PS1 to PS4. Slabs PS1 and PS2 are un-strengthened RC slab, whereas slabs PS3 and PS4 are CFRP-strengthened RC slabs with and without fire insulation.
- In case PSC2, the effect of six different insulation thickness (t) on the bottom surface of slab was evaluated by analyzing slabs PS5 to PS10. In all these slabs, the thickness (t) of insulation on bottom surface was varied from 0 to 38 mm.
- In case PSC3, the effect of four different load levels, i.e., 50%, 60%, 65%, and 70% is evaluated by analyzing slabs PS11 to PS14.
- In case PBC4, the effect of five different fire scenarios, similar to those in case PBC5 for beams, is evaluated by analyzing slabs PS15 to PS19.
- In case PSC5, the effect of five different width (b_{ins}) of insulation on the bottom surface of the slabs is evaluated by analyzing slab PS20 to PS24. The width of insulation considered in the analysis include 220, 240, 260, 280, 300, and 400 mm.

- In case PSC6, the effect of five different tensile strength of concrete ranging from 1.5 MPa to 3.5 MPa is evaluated by analyzing slabs PS25 to PS29.

The parameter varied, range of each parameter, and the slabs analyzed in each of aforementioned cases are summarized in Table 5.6. The details pertaining to the analysis of all the beams and slabs analyzed in the parametric study including the material properties and failure criteria considered for evaluation of fire resistance are summarized in following section.

5.3.3 Analysis Details

In the parametric study the beams (PB1 to PB35) and slabs (PS1 to PS29) were analyzed in a sequential thermo-mechanical analysis using the macroscopic numerical model developed in Chapter 4. At the start of the analysis, the length of the beams and slabs was discretized in to 20 and 10 segments, respectively. The cross-section of the beams was discretized into 16 × 5 mm elements in the concrete region, 16 × 1.02 mm in the CFRP sheet region, and 5×5 mm elements in the insulation region. Similarly, the cross-section of the slabs was discretized into 20 × 5 mm elements in concrete region, 20 × 1.02 mm in the CFRP sheet region, and 5 × 5 mm in insulation region.

The fire scenario and load ratio applied on each beam and slab is summarized in Table 5.5 and Table 5.6, respectively. During the analysis, the beams and slabs were primarily exposed to ASTM E119 fire scenario, (unless stated otherwise) and were subjected to applied loading equivalent to 50% of their respective ultimate strengthened capacity at room temperature. In the analysis, the beams and slabs were subjected to four-point loading with simply supported boundary conditions. Moreover, the beams were subjected to fire exposure on three sides, i.e., bottom surface and two sides, whereas the slabs were subjected to fire exposure only at the bottom surface.

The room temperature material property values considered in the analysis are consistent with those used in field applications. The concrete was assumed to be made up of siliceous aggregate based concrete with cylindrical compressive strength of 35 MPa, while the steel rebars had a yield strength of 460 MPa, with a yield strain of 2%. The CFRP sheet used for flexural strengthening of beams and slabs has tensile strength, elastic modulus, and ultimate strain of 1034 MPa, 73770 MPa and 1.4 %, respectively.

The temperature variation of the material properties of concrete and steel rebars was considered as per ASCE manual [78] and Eurocode 2 [79]. The temperature dependent thermal properties of insulation were based on the test data and are shown in Figure 5.1. For CFRP the temperature variation of thermal properties is considered as per Griffis et al. [102], while the strength and modulus property variation were based on the relations provided by Bisby et al. [120], as shown in Figure 5.4. The temperature induced CFRP-concrete bond degradation was accounted using the nonlinear bond-slip relations proposed by Dai et al. [134], as shown in Figure 5.6.

The output parameters generated in each time step were compared with the relevant failure limit states (strength and deflection) to determine the failure and fire resistance of the beams or slabs. The time at which the any of the failure limit state is attained is taken as the fire resistance time, however the analysis is continued until the moment capacity decreases below the bending moment due to applied loading.

5.3.4 Response Parameters from Analysis on Beams

The thermal and structural response of the beams analyzed in different cases of the parametric study are presented in Figure 5.15 through Figure 5.31. The time to attain T_g of adhesive, critical rebar temperature (593°C), strength and deflection limit state, as well as the fire resistance and the governing failure limit state attained in each beam are summarized in Table 5.7. The thermal response is presented in terms of progression of temperature at the FRP-concrete interface and corner rebar while the structural response is presented in terms of deflection and degradation in moment capacity. The effect of variation of different parameter on the response of the beams is discussed below.

(i) Case PBC1: Effect of CFRP-strengthening

Four beams, namely PB1, PB2, PB3, and PB4 were analyzed to evaluate the effect of CFRP strengthening on fire performance of RC beam. Beams PB1 and PB2 were un-strengthened RC beams, whereas beams PB3 and PB4 were CFRP-strengthened RC beams. Moreover, beams PB1 and PB3 were uninsulated, whereas beams PB2 and PB4 were provided with fire insulation. Beams PB1, PB3, and PB4 were analyzed under same load level (50% of respective ultimate capacity), whereas beam PB2 was analyzed under loading (maximum bending moment) similar to that on beam PB4, to evaluate if an insulated CFRP-strengthened RC beam can be idealized as an insulated RC beam.

Results from the analysis of beams PB1 to PB4 are summarized in Table 5.7. The thermal response of beams PB1 to PB4 is compared in Figure 5.15 by plotting the temperature rise at the CFRP-concrete interface and steel rebars as a function of fire exposure time. As explained earlier in the analysis of cases C1 and C2 in Section 5.3.3, CFRP-strengthening (due to smaller cross-section) has negligible effect on temperature rise in the section. Since all the beams have same material properties, concrete cover to the rebars, and are subjected to same fire exposure, the temperature rise in rebars of beams PB1, PB3, and beams PB2, PB4 is identical. Due to the direct exposure to heat of fire in the absence any fire protection, the temperature rise in beams PB1 and PB3 is significantly faster than that in beams PB2 and PB4. As a result, the CFRP-concrete temperature in beam PB3 exceeds T_g of adhesive with 2 minutes of fire exposure, as compared to

21 minutes in beam PB4. Moreover, the corner rebar temperature in beams PB1 and PB3 exceeds the temperature limit 593°C in 130 minutes, whereas in beams PB2 and PB4, this limit is exceeded after 239 minutes.

The structural response of beams PB1 to PB4 is illustrated by plotting the degradation in moment capacity and progression of deflection as a function of fire exposure time in Figure 5.16. Additionally, the response of an insulated RC beam subjected to structural loading equivalent to 50% of its ultimate capacity is also plotted in these figures and is denoted as beam PB2a. It can be seen from the Figure 5.16 (a) that the capacity of uninsulated RC beam PB1 remains constant until 70 minutes of fire exposure, whereas the capacity of uninsulated FRPRC beam PB3 starts degrading rapidly from the start of fire exposure. The constant capacity of beam PB1 is due to the fact that there is no degradation in strength of steel rebars, as the temperature of the steel rebars is less than 400°C. After about 75 minutes the temperature of corner rebars exceeds 400°C, and as a result the capacity of the beam PB1 starts degrading at a gradual pace and falls below the moment due to applied loading at 155 minutes, indicating strength failure. The rapid degradation in capacity of beam PB3 is attributed to the rapid degradation in the strength of CFRP as well as degradation of bond due to the faster rise in temperature at the CFRP-concrete interface resulting from direct exposure to heat of fire. After 45 minutes, the contribution of CFRP is completely lost and the beam PB3 behaves as an un-strengthened and uninsulated RC beam subjected to higher load level. As a result, the capacity of beam remains constant until 70 minutes of fire exposure, i.e., until the rebar temperatures are below 400°C and then the capacity starts degrading and falls below the moment due to applied loading at 110 minutes, indicating strength failure.

In case of insulated beams PB2, PB2a, and PB4, the capacity of un-strengthened beam PB2 remains constant until 145 minutes of fire exposure due to slower temperature rise in the rebars, and then the capacity starts degrading and falls below the moment due to applied loading at 200 minutes of fire exposure. The degradation in capacity of beam PB2a is identical to that of beam PB2, however the capacity of beam PB2a remain higher than the moment due to applied loading until the end of fire exposure, indicating no strength failure. Whereas the capacity of beam PB4 remains almost constant until 25 minutes of fire exposure and then decrease gradually until 120 minutes of fire exposure due to the temperature induced bond degradation as well as degradation in strength properties of CFRP. At 120 minutes, the composite action between CFRP and concrete is completely lost, and the beam behaves as a RC beam. Therefore, the capacity of beam PB4 remains constant until 145 minutes, then starts decreasing gradually and falls below the moment due to applied loading after 200 minutes of fire exposure.

The room temperature ultimate capacity of beam PB4 is 57% more (due to CFPR-strengthening) than that of beam PB2, consequently the bending moment due to applied loading is equivalent to 82% and 50% of the ultimate capacity of beams PB2 and PB4, respectively. Nevertheless, the beams exceed the strength limit state at the same time. This is attributed to the fact that the strength of CFRP and the CFRP-concrete interfacial bond, which contributes to the moment capacity of beam PB4, degrades rapidly at elevated temperatures, and as a result, the composite action is completely lost. After this the beam capacity is dependent on steel rebars. Since, the temperature rise in rebars of beams PB2 and PB4 is same (*cf.* Figure 5.15) the loss of strength in rebars of both the beams start at the same time, and thus, both beams exceed the strength limit state at the same time.

Figure 5.16 (b) compares the mid-span deflection of beams PB1 to PB4. The initial deflection of beams PB1, PB2, PB3, and PB4, i.e., before the start of fire exposure, is 12 mm, 26 mm, 22 mm, 22 mm, respectively. It can be seen from the figure that the uninsulated beams PB1, PB3 deflect at the same rate in the initial stages of fire exposure. After about 20 minutes, beam PB3 starts deflecting at a faster rate as compared to the beam PB1. This can be attributed to two reasons, first the strength and modulus properties of CFRP reduces rapidly due to direct exposure to heat of fire. Second after 10 minutes, strain distribution in the beam cross-section due to applied loading becomes nonlinear with compressive strains at the level of CFRP (as shown in Figure 5.17 (b)). Since CFRP is inactive in compression, the contribution of CFRP in resisting the applied loading is completely lost, which in turn reduces the stiffness of the beam, thereby causing faster deflection. It is worth mentioning that in beam PB3, the complete loss of composite action due to debonding of CFRP occurs after 45 minutes of fire exposure (as seen in Figure 5.16 (a)), while the reduction in stiffness of the beam due to compressive strain at the level of CFRP starts after10 minutes, which are both much later than the time (2 minutes) at which interface temperature exceeds adhesive T_g. Thus, the contribution of CFRP towards the strength and stiffness of beam is lost at the interface temperature much higher than T_g. Finally, the deflection and rate of deflection in beam PB3 exceeds the deflection limit state at 105 minutes of fire exposure. While, the un-strengthened beam PB1 exhibits stiffer response and deflects gradually until 105 minutes fire exposure, after then starts deflecting rapidly exceeding the deflection limit state at 145 minutes of fire exposure

In case of insulated beams PB2 and PB4 the deflection response is identical throughout the fire exposure duration. However, the deflection response of beam PB2a is much stiffer than that of beams PB2 and PB4, due to the lower applied load level on beam PB2a. The deflection in beam PB2a does not exceeds the deflection limit indicating no failure. The identical deflection is attributed to the fact that in both the beams, the applied structural loading and the cross-sectional temperature rise resulting from fire exposure is same. Since the temperature rise in both the beams is same the degradation in strength and modulus properties of steel rebars is same and therefore, the resulting deflection is same. Thus, the insulated CFRP-strengthened RC beam PB4 behaves similar to that of the insulated un-strengthened RC beam PB2. Both the beams deflect gradually in the initial stages until 150 minutes of fire exposure. After 150 minutes the beams start deflecting at a faster rate and exceed the deflection limit state after 190 minutes of fire exposure.

The governing failure limit state attained, and corresponding fire resistance time achieved in each beam is summarized in Table 5.7. Since all the beams attained deflection limit state prior to strength limit state, the beams are considered to have failed in deflection limit state. Therefore, deflection is the governing limit state. It can be seen from the Table 5.7 that the uninsulated and un-strengthened RC beam PB1 has higher fire resistance than the uninsulated and CFRP-strengthened RC beam PB3, while CFRP-strengthened beam PB4 protected with fire insulation has higher fire resistance than that of beam PB1. Thus, it is essential to provide external fire insulation to achieve satisfactory fire resistance in CFRP-strengthened RC beams. Further, it can be seen from Table 5.7 that fire resistance of uninsulated beams PB1 and PB3 is higher than the time to attain critical rebar temperature in these beams, while the fire resistance of insulated beams PB2 and PB4is significantly higher than the time to attain critical rebar temperature. Thus, time to attain critical rebar temperature does not provide an accurate estimate of fire resistance time in any of the beams. Additionally, it can be inferred from the analysis of beams PB2 and PB4, that in an insulated CFRP-strengthened RC beam, the CFRP has negligible effect on the deflection response of the beam, and therefore, an insulated CFRP-strengthened RC beam can be idealized as an insulated un-strengthened RC beam.

(ii) <u>Case PBC2: Effect of depth of insulation on side surfaces</u>

As determined in previous case, CFRP-strengthened RC beams are required to be provided with external fire protection to achieve satisfactory fire resistance. Since beams are subjected to fire from three sides, a U-shaped insulation configuration has been recommended in previous studies (Ahmed and Kodur, 2011; Yu and Kodur, 2013). However, there are no specific guidelines regarding optimum depth of insulation on sides of beams. To evaluate the optimum depth of insulation on the sides of a beam, seven CFRP-strengthened RC beams, designated as PB5, PB6, PB7, PB8, PB9, PB10, and PB11 were analyzed in this case. All these beams were insulated at the bottom and side surfaces with 19 mm thick fire insulation. The depth (h_i) of insulation on the sides, as measured from the bottom surface, was varied from 0 to 152 mm as summarized in Table 5.5. The depth of insulation is incremented in multiples of concrete cover (C_c = 38 mm) to the steel reinforcing bars, i.e., C_c, 1.5*C_c, 2*C_c, 2.5*C_c, 3*C_c, 4* C_c rounded up to the nearest multiple of an inch.

The temperature rise at the center of CFRP-concrete interface as well as at the mid-rebar of the beams is primarily influenced by the heat transfer from the bottom surface of the beam. Since the thickness of insulation at the bottom surface is same in all the beams, the heat transfer and consequently the temperature rise at the CFRP-concrete interface and the mid-rebar locations (not shown in the thesis) is same in all the beams. Therefore, the thermal response of the beams is evaluated by plotting the temperature rise in the corner steel rebars of the beams, as a function of fire exposure time in Figure 5.18. It can be seen from the figure that the temperature in the corner rebar of beams PB5 to PB11 increases monotonically and follows similar trend throughout the fire exposure duration. The rebar temperature increases at a relatively faster rate in beams with smaller depth of insulation (PB5 to PB8), and at a slower rate in beams with larger depth of insulation (PB9 to PB11) on the sides. Consequently, the rebar temperature exceeds the critical rebar temperature of 593°C, after 190, 205, 220, and 239 minutes in beams PB5, PB6, PB7, and PB8, respectively. This indicates that the strength and modulus properties of corner rebars in these beams degrade by more than 50% of its room temperature values. In case of beams PB9, PB10, and PB11 the rebar temperature remains below 550°C until the end of fire exposure. This indicates that the degradation in strength and modulus properties of corner rebars in these beams is less than 50%. Additionally, the difference in temperature rise at the corner rebars of beams PB9 to PB11 is very negligible. Thus, increasing the depth of insulation on the sides of beams beyond a certain optimum depth has no major influence on the temperature rise in rebars.

To evaluate the structural response, the degradation in moment capacity of beams PB5 to PB11 with fire exposure time is shown in Figure 5.19 (a). It can be seen from the figure that the capacity degradation trends are similar in beam PB5, PB6, and PB7, and in beams PB8 to PB11, throughout the fire exposure duration. The capacity of all the beams remains constant until 25 minutes of fire exposure, after this the capacity decreases gradually for a short duration followed by a rapid decrease due to the degradation of CFRP-concrete interfacial bond. The degradation in capacity of beams PB6 to PB8 and beams PB9 to PB11 is identical until the loss of FRP-concrete composite action in them, i.e., until 120 minutes and 135 minutes, respectively.

After the loss of composite action, the capacity of beams PB5, PB6, and PB7 continue to decrease gradually and falls below the moment due to applied loading at 155, 170, and 185 minutes of fire exposure, respectively, indicating strength failure. This is attributed to the fact that by the time the composite action in these beams is lost, the rebar temperature has exceeded 400°C, and therefore, the strength properties of rebars have started degrading resulting in failure. In beams PB8 to PB11, the capacity remains constant until the rebar temperatures are below 400°C. The capacity then starts decreasing slowly and falls below the bending moment due to applied loading in beams PB8, PB9, and PB10 at 200, 220, and 240 minutes of fire exposure. The capacity of beam PB11 remains higher than the applied moment until the end of fire exposure indicating no failure. Thus, with every increment in depth of the insulation on the side surface of the beams, the time to attain strength limit state increases by 10%.

To further evaluate the strength response of the beams PB5 to PB11, the mid-span deflection is plotted against the fire exposure time in Figure 5.19 (b). It can be seen from the figure, that all the beams deflect in a similar manner, throughout the fire exposure duration. Further, it can be seen that the deflection response of the beams become stiffer with each increment in depth of insulation on the side surfaces. The deflection in all the beams is same in the initial stages until 25 minutes of fire exposure, after which the beams start deflecting gradually at a different rate, fastest in beam PB5 and slowest in beam PB11. The beams continue to deflect gradually until the temperature in corner rebars is below 400°C. Once the rebar temperature exceeds 400°C, the deflection in all the beams starts increasing at a faster rate. Consequently, the deflection and rate of deflection exceed the deflection limit state after 150, 160, 175, 190, 215, and 230 minutes in beams PB5, PB6, PB7, PB8, PB9, and PB10, respectively, as shown in Figure 5.19 (b). These times are slightly less than the time to attain the strength limit state in the respective beams. Thus, the fire resistance of all these beams is determined through deflection limit state and are summarized in Table 5.7. Additionally, it can be inferred that 76 mm (2*C_c) depth of insulation on the sides of the beam is sufficient to attain 3 hours of fire resistance, as in beam PB8.

(iii) Case PBC3: Effect of thickness of insulation on soffit and side surfaces

Apart from the depth of insulation on the sides, thickness of insulation is another major factor which governs the fire resistance of FRP-strengthened beams. Therefore, to develop optimum thickness of insulation (t_{ins}) seven different beams, namely PB12 to PB18 were analyzed in case

PBC3. In all these beams, the thickness (t_{ins}) of insulation on sides and the bottom surface (*cf.* Figure 5.13) was varied from 0 to 38 mm (in multiples of quarter inch), as described in Table 5.5, while the depth (h_i) of insulation on the sides was maintained at 76 mm (2*C_c). In beam PB12 the thickness (t) of insulation is 0 mm at the bottom and 19 mm on the sides to evaluate the effect of insulating only the sides of the beam.

The temperature rise at the CFRP-concrete interface of beams PB12 to PB18 is plotted as a function of fire exposure time in Figure 5.20 (a), to evaluate thermal response of the beams. As expected, the presence of insulation impedes the temperature rise at the CFRP-concrete interface and increases the time to reach adhesive T_g. The interface temperature in beam PB12 exceeds the adhesive T_g in 2 minutes and follows the ASTM E119 fire curve (like beam PB3), due to direct exposure to fire in the absence of insulation. In beams PB13 and PB14, the interface temperature increases at relatively faster rate compared to beams PB15 to PB18 and exceeds the T_g after 7 and 14 minutes of fire exposure, respectively. In beams PB15 to PB18, the interface temperature follows similar trends and increase gradually throughout the fire exposure duration with slowest in beam PB18 (38 mm thick insulation). Further it can be seen from the figure that beyond 19 mm the difference in temperature rise at interface is decreases, with increase in thickness of insulation. Thus, CFRP-strengthened concrete RC beams must be provided with at least 19 mm thick insulation layer, where maintaining interface temperature below adhesive T_g is critical for structural performance.

The temperature rise in the corners rebars of beams PB12 to PB18 is plotted as a function of fire exposure time in Figure 5.20 (b). In all the beams, the rebar temperature increases gradually and follows similar trends throughout the fire exposure duration. As expected, the rate of temperature rise decreases with increase in insulation thickness. For instance, the rebar temperature exceeds 400°C at 90, 105, and 120 minutes of fire exposure in beams PB12, PB13, and PB14, respectively. Whereas in beams PB15, PB16, PB17, and PB18, the rebar temperature exceeds 400°C after 135, 150, 165, and 175 minutes of fire exposure, respectively. Thus, the degradation of strength and modulus properties of corner rebars starts much earlier in beams PB12 to PB15 as compared to that in beams PB15 to PB18.

It can be seen from the figure that in beams PB12 to PB14, after 120 minutes (i.e., beyond 400°C) the difference in rebar temperatures increases significantly. As a result, the rebar temperature in these beams exceeds critical temperature (593°C) between 150 and 210 minutes of fire exposure. However, in case of the beams PB15 to PB18, the difference in temperature rise is very minimal throughout the fire exposure duration. The rebar temperature exceeds the critical rebar temperature after 239 minutes of fire exposure in beam PB15, whereas in beams PB16 to PB18, the rebar temperature remains below 560°C until end of fire exposure. Thus, even 19 mm thick insulation is sufficient to maintain the rebar temperature below critical temperature level for four hours of ASTM E119 fire exposure. Further, to evaluate the effect of providing insulation only on the sides of the beam surface the temperature rise in corner rebars of beam PB12 is compared with that of completely uninsulated beam PB3. It can be seen from the figure that the provision insulation on the sides of beams delays the temperature rise in rebars by almost 15 minutes, i.e., 12%. Thus, the degradation in strength and modulus properties of rebars can be slightly delayed by providing insulation on the sides of the beam.

To evaluate the structural response the degradation in moment capacity of beams PB3, PB12 to PB18 is plotted against the fire exposure time in Figure 5.21 (a). As expected, the rate of in moment capacity degradation decreases with the increase in thickness of insulation. It can be seen from the figure that due to the absence of insulation on the bottom surface, the degradation in moment capacity of beam PB12 is identical to that of beam PB3 until 75 minutes of fire exposure. The capacity of beam PB12 remains constant until 90 minutes of fire exposure, and then starts decreasing gradually (as rebar temperature exceeds 400°C) and attains strength limit state after 125 minutes of fire exposure, which is 15 minutes later than that of beam PB3. The slightly higher time to attain strength limit state in beam PB12 is attributed to the presence of insulation on the sides of beam which reduces the temperature rise in the rebars. Thus, providing insulation on the sides of the beam can increase the failure time by 15 minutes based on strength limit state.

In case of insulated beams PB13 to PB18, the moment capacity degradation follows trends similar to that of beam PB4 in case PBC1, throughout the fire exposure duration. The capacity of the beams PB13 to PB18 can be discretized into four stages. In the first stages, the capacity remains almost constant for a short duration, depending on the thickness of insulation, in the initial stages of fire exposure. In the second stage the capacity starts decreasing gradually due to degradation in strength and modulus properties of CFRP as well as due to the temperature induced degradation of CFRP-concrete interfacial bond. Once the CFRP-concrete composite action is completely lost at the end of second stage, the capacity of the beams remains constant until the rebar temperature remains below 400°C which marks the end of third stage. In the fourth stage, the capacity starts degrading slowly due to degradation in strength and modulus of steel rebars and then falls below the bending moment due to applied loading.

In case of beams PB13, PB14, PB17, and PB18 the duration of third stage (i.e., constant capacity) is very small, as the by the time the CFRP-concrete composite action is lost in these beams the rebar temperature is close to 400°C. Therefore, although the rate of capacity degradation changes, the capacity continues to decrease gradually until it falls below the applied moment. Additionally, in case of beams PB15 to PB18, the capacity increases slightly at the start of second stage and then starts degrading gradually. The slight increase is attributed to the fluctuations in the strength contribution of CFRP towards the capacity of beams, as shown in Figure 5.22, due to the development of higher strains at the level of CFRP resulting from the softening of material at elevated temperatures. Further, it can be seen from the figure that the time to reach the strength limit state increases by greater than 15% for each increment in the thickness of insulation between beams PB12 to PB15, however, for beams PB15 to PB18, the increase in time to attain strength limit state is less than 10% for each increment in thickness of insulation. Thus, it can be concluded that beyond 19 mm the effect of increase in thickness of insulation on failure due to strength limit state is very minimal.

To further evaluate the effect of thickness of insulation, the mid-span deflection is plotted as a function of fire exposure time in Figure5.21 (b). It can be seen from the figure that the deflection all the beams follows similar trends throughout the fire exposure duration. Beam PB12 (uninsulated at the bottom surface) experience deflection identical to that of beam PB3 in the initial stages of fire exposure. However, after 15 minutes beam PB12 exhibits slightly stiffer behavior compared to that of beam PB3. This is attributed to the fact that after 10 minutes, the contribution of CFRP towards the stiffness of the beam is completely lost, in both beams PB3 and PB12, due to compressive strains developed at the level of CFRP, as explained in case PBC1. As a result, the stiffness of beam is completely dependent of steel rebars. Since the rebar temperatures are different in both the beams, due to the presence of insulation on the sides of beam PB12, the deflection response of both the beams is different.

In case of insulated beams PB13 to PB18, the deflection response is similar to that of beam PB4 (case PBC1) and becomes stiffer with each increment in the thickness of insulation. In all the beams, the deflection remains almost constant in the initial stages, and then experience a sharp increase due to loss of stiffness contribution of CFRP because of compressive strains due to loading. Following this the deflection starts increasing gradually until at a slower rate until the rebar temperature exceeds 400°C, at which point the deflection starts increasing rapidly and exceeds the deflection limit state indicating failure. In all the beams, the deflection limit state is attained 10 minutes prior to that of strength limit state. Therefore, all the beams have failed in deflection limit state, as per ASTM E119 failure criterion. Additionally, as observed in degradation of moment capacity, the difference in the deflection decreases with increase in thickness of insulation beyond 19 mm. Even with 19 mm thick insulation, the beam PB15 can achieve more than three hours (almost 190 minutes) of fire resistance. Thus, providing insulation thickness higher than 19 mm would not be optimal for the beam utilized in the parametric study.

(iv) Case PBC4: Effect of applied load level

In case PBC4, the effect of five different load levels, namely 30%, 40%, 50%, 60%, and 70, was evaluated by analyzing beams PB19, PB20, PB21, PB22, and PB23 under same fire exposure. The applied structural load levels were determined with respect to the ultimate strengthened capacity of the CFRP-strengthened RC beam PB at room temperature. These load levels correspond to 50%, 65%, 82%, 99%, and 115% of the ultimate un-strengthened capacity of RC beam PB at room temperature.

Results from the analysis indicate that load level has no effect on the thermal response of the beams but has significant influence on the structural response. To demonstrate the deterioration resulting from the applied loading in beams PB19 to PB23 the stress distribution at the mid-span cross-section of each beam is also plotted in Figure 5.23. In the figure, the layer of CFRP at the bottom is magnified by a factor of 10 for better visualization.

It can be seen from Figure 5.23 that in the initial stages, the stress distribution in all the beams is uniform. Even at the start of fire exposure, the bottom rebars and CFRP experience higher stresses in beams subjected to higher load levels. For instance, at the start of fire exposure the stress in the rebars and CFRP of beam PB19 (30% load level) is between 100-150 MPa and 0-50 MPA, respectively, whereas in case of beam PB22 (60% load level) the stress in rebar and CFRP is between 350-400 MPa and 100-150 MPa, respectively. Further, it can be seen from the figure that after one hour of fire exposure, the stress in CFRP of beams PB19 to PB21, reduces to zero, whereas at the same the stress in CFRP of beams PB22 and PB23 is between 0-50 MPa and 50-200 MPa, respectively. This is attributed to the fact that after 35 to 40 minutes of fire exposure, compressive strains are generated at the level of CFRP in beams PB19 to PB21, due to relatively smaller curvature resulting from lower loads (as explained in case PBC1 in Section 5.5.4 (i)), however in beam PB23 tensile strains are generated due to large curvatures resulting from higher loads. Additionally, it can be seen from the Figure 5.23 (a, b, c) that stress in rebars of the beams PB19, PB20, and PB21 is less than the yield strength (460 MPa) until 180 minutes of fire exposure, whereas in beams PB22 and PB23 (Figure 5.23 (d, e)), the stress is very close to or equal to the yield strength of the rebars from the start of fire exposure. Thus, it can be inferred that the rebars of CFRP-strengthened RC beams subjected to smaller load levels (less than the un-strengthened capacity of beam), do not yield due to applied loading, whereas at higher load levels, the rebars start yielding irrespective of the temperature rise.

To evaluate the structural response of beams PB19 to PB23, the degradation in moment capacity and deflection is plotted as a function of fire exposure time in Figure 5.24 (a). It can be seen from the figure that the rate of degradation of moment capacity as well as the deflection of the beams increases with increasing load levels. This is attributed to the fact that higher load levels increase the demand on the beam which leads to higher internal stresses, as shown in Figure 5.23, which in turn leads to faster degradation of the strength and stiffness properties of the materials. The degradation of strength properties results in faster degradation of moment capacity, while the degradation of stiffness properties produces large curvatures, resulting in faster and larger deflections.

It can be seen from the Figure 5.24 (a) that the moment capacity of all the beams PB19 to PB23 degrade in a manner similar to that of beam PB4 in case PBC1. The degradation in moment capacity of these beams is identical, until the onset of CFRP-concrete bond degradation, after which the capacity of beams subjected to higher loads degrades at a faster rate due to faster degradation of CFRP-concrete interfacial bond. The faster degradation of CFRP-concrete bond in beams with higher applied loads is attributed to the high shear stresses generated at the CFRP-concrete interface, which increases the relative slip between CFRP and concrete resulting in degradation of interfacial bond and faster capacity degradation. After the complete loss of composite action, the capacity degradation is identical in beam PB19 to PB22. Due to lower load levels, beam PB19 does not attain strength limit state, whereas beams PB20, PB21, and PB22 attain strength limit state after 235, 200, and 145 minutes of fire exposure, respectively. In case of beam PB23 the moment due to applied loading is much higher than the capacity of the un-strengthened RC beam, therefore, the beam attains strength limit state during the CFRP-concrete composite degradation after 50 minutes of fire exposure. Thus, the applied load levels affect the rate of bond degradation in insulated and CFRP-strengthened RC beams which in turn affect the capacity degradation.

The progression deflection in beams PB19 to PB23 is plotted against the fire exposure time in Figure 5.24 (b). It can be seen from the figure that beams PB19, PB20, and PB21 deflect, at different rate due to the different applied load levels, but in a manner similar to that of beam PB4 in case PBC1. Deflection in beam PB19 is much lower than deflection limit until the end of fire exposure, whereas deflection in beams PB20 and PB21 exceed deflection limit state after 220 and 190 minutes, respectively. In case of beams PB22 and PB23 deflection increases sharply after the onset of CFRP-concrete bond degradation at 25 minutes and exceed the deflection limit after 50 and 45 minutes of fire, respectively. This is attributed to the fact that after the onset of CFRP-concrete bond degradation the deflection is primarily governed by the stiffness of steel rebars. The higher load levels increase the strains in the bottom steel rebars beyond the yield strain. The yielding of the bars reduces stiffness of beam resulting in large curvatures and faster deflection in the beam. Although the deflection limit is exceeded in beam PB22, the limit of rate of increase in deflection is not exceeded. Therefore, only beams PB20, PB21, and PB23 failed in deflection limit state.

To evaluate the fire resistance of beams PB19 to PB23, the time to attain strength and deflection limit state are summarized in Table 5.7. It can be seen from the table that the fire resistance time decreases with increase in applied load levels, and therefore, the influence of load ratio should be accounted for design under fire conditions and the applied loads should be kept less than 50% of ultimate strengthened capacity and 80% less than ultimate un-strengthened capacity to achieve three hours of fire resistance.

(v) <u>Case PBC5: Effect of fire scenarios</u>

In case PBC5, the effect of five different fire scenarios (FS) was evaluated by analyzing beams PB24 to PB28. Beam PB24 was exposed to ISO 834 fire exposure, while beams PB25 to PB28 were exposed to four different fire scenarios namely DF1, DF2, DF3, and DF4. Additionally, the effect of ASTM E119 fire scenario was also compared here by using results of beam PB4. Fire scenarios DF1, DF2, and DF3 are short, medium, and long severe design fire scenarios, while DF4 is ASTM E119 fire scenario which has a cooling phase. These fire scenarios are shown in Figure 5.25. It can be seen from the figure that the ASTM E119 and ISO 834 standard fire curves are almost identical until 60 minutes, after which the temperature in ISO 834 increase a slightly higher rate compared to ASTM E119 fire. The temperature rise in DF1, DF2, and DF3, was computed using Eurocode 1 (EN 1991-1-2 2002) provisions representing a wide range of compartment characteristics including fuel load and ventilation conditions. The temperature rise in DF1, DF2, and DF3 peaks at after 60, 90, 120 minutes of fire exposure, respectively and then cools down linearly to 20°C at a rate of -10°C/minute, after 120 minutes representing a slow burnout fire. The temperature rise in DF4 follows ASTM E119 fire curve for 120 minutes followed by linear cooling to room temperature at the rate -10°C/minute.

The thermal response of beams PB4, and PB24 to PB28 is compared in Figure 5.26 by plotting the temperature rise at the CFRP-concrete interface and corner rebar against the fire exposure time. As expected, the exposure to higher intensity fire scenarios DF1, DF2, and DF3 in beams PB25, PB26, and PB27 leads to rapid increase in the temperature at all locations within the cross-section compared to that of ASTM E119, ISO 834, and DF4 fire scenarios in beams PB4, PB24, and PB28, respectively. The temperature in beams PB25, PB26, and PB27 starts decreasing gradually after attaining peak temperatures due to the onset of the cooling phase. Consequently, the rebar temperatures in these beams remain below the critical rebar temperature of 593°C until the end of fire exposure. The temperature in beams PB4 and PB24 increases continuously at the same rate throughout the fire exposure duration while the temperatures in beam PB28 increases for almost 130-150 minutes and then starts decreasing due to the presence of decay phase. Therefore, the rebar temperature in beams PB4 and PB24 exceeds the critical temperature after 239 and 230 minutes of fire exposure, respectively, whereas the rebar temperature in beam PB28 remain below 500°C until end of fire exposure.

Figure 5.27 (a) shows degradation in moment capacity of beams PB4, PB24 to PB28, as a function of fire exposure time. It can be seen from figure that the moment capacity of beams PB25 to PB27 subjected to DF1, DF2, and DF3, fire scenarios degrade at a faster rate compared to that of beams PB4, PB24, and PB28 subjected to ASTME119, ISO834, and DF4 fire scenario. The capacity degradation is identical in beams PB25 to PB27, however only beams PB26 and PB27 attain the strength limit state at 160 minutes of fire exposure. Similarly, the capacity degradation is identical in beams PB4, PB24, and PB28, however, the only beams PB4 and PB24 fail in the strength limit state after 195 and 200 minutes of fire exposure, respectively. Beams PB25 and PB28 starts recovering the capacity after 120 and 150 minutes of fire exposure, respectively, due the decrease in temperature of the rebars, which leads to recovery of strength in rebars. Thus, fire scenarios significantly affect the rate of capacity degradation of CFRP-strengthened RC beams.

The progression of mid-span deflection of beams PB4, and PB24 to PB28 are compared in Figure 5.27 (b). The deflection profiles show that all the beams deflect in a similar manner, however, like in the case of capacity degradation, beams PB25 to PB28 (exposed to DF1 to DF3) deflect at a faster rate compared to that of beams PB4, PB24, and PB28. The deflection is almost same in beams PB25 to PB27, and identical in beams PB4, PB24, and PB28. However, only beams PB4, PB24, PB26, and PB27 exceed the deflection limit state after 190, 185, 145, and 150 minutes of fire exposure, respectively. Deflection in beams PB25 and PB28 starts reducing after 150 and 200 minutes of fire exposure due to the recovery of strength and stiffness of concrete and steel during the cooling phase of fire. Thus, fire scenarios significantly affect the deflection and rate of increase in deflection of CFRP-strengthened RC beams.

The time to attain FRP T_g, critical rebar temperature, strength and deflection limit state, as well as the fire resistance time are summarized in Table 5.7. Beams PB25 and PB28 did not attain strength or deflection limit state until end of fire exposure, and therefore, these beams have more than four hours of fire resistance. The beams PB4, PB24, PB26, and PB28 attained deflection limit state prior to strength limit state, and therefore, the failure and fire resistance time of the beams is governed by deflection limit state. Among the beams that failed during fire exposure, beam PB26 (subjected to DF2) has the lowest fire resistance of 145 minutes, whereas beam PB4 has the highest fire resistance of 190 minutes. The above discussion clearly infers that the fire scenario has significant effect on the thermal and structural response, as well as the fire resistance of the strengthened concrete beams, and in most cases the strengthened beams have lower fire resistance in severe design fire scenarios compared to that of standard fire scenarios.

(vi) Case PBC6: Effect of strengthening level

In case PBC6, the effect of four different strengthening level was evaluated by analyzing beams PB29 to PB32. To change the level of strengthening beams PB29, PB30, PB31, and PB32 were strengthened with a CFRP sheet of 100, 150, 200, and 254 mm, respectively, which increases the ultimate capacity of these beams by 20%, 30%, 40%, and 57%, respectively. All the beams were analyzed under same load level equivalent to 50% of their respective capacity, as summarized in Table 5.5. The applied loads on beams PB29, PB30, PB31, and PB32 correspond to 63%, 69%, 75% and 82% of the un-strengthened RC beam. Thus, beam with highest strengthening level has highest applied load level for the un-strengthened RC beam.

The strengthening level has no major influence on the thermal response of the beams. Therefore, only structural response is compared here. Figure 5.28 (a) shows the degradation in moment capacity of beams PB29 to PB32 as a function of fire exposure time. It can be seen from the figure that until the onset of CFRP-concrete bond degradation, the capacity of all beams degrades very slowly at a similar rate. After the initiation of bond degradation, the beams with higher strengthening level experience faster reduction in capacity as compared to the beams with lower strengthening level, at same level of CFRP-concrete bond degradation. This is attributed to the fact that in beams with high strengthening level CFRP is a major contributor to the capacity, therefore, any small reduction in CFRP-concrete composite action results in significant reduction in the capacity of the beam.

After complete loss CFRP-concrete composite action, the degradation in capacity of all the beams is identical, as it is governed by strength of steel rebars. Since, the applied loads on beams with higher strengthening level are much higher than the reserved capacity of the un-strengthened RC beam, the beam PB32 (highest strengthening level) attains strength limit state first (200 minutes) while beam PB29 with lowest strengthening level does not attain strength limit state until the end of fire exposure.

The deflection response of beams PB29 to PB32 is shown in Figure 5.28 (b). The deflection trends in all the beams are similar to that of beam PB4 in case PBC1. All the beams deflect at same rate until 35 minutes of fire exposure, after which the rate of deflection increases with increase in strengthening level of the beams. This is attributed to the fact after 35 minutes CFRP does not contribute towards the stiffness of beam due to the compressive strains at the level of CFRP resulting from applied loading. Therefore, after 35 minutes all the beams deflect as an un-strengthened RC beam whose stiffness depends on stiffness of rebars. Since the load levels due to load applied on beams PB29 to PB32 are different for an un-strengthened RC beam, the beams deflect at a different rate. For instance, beam PB32 (highest strengthening level) deflects faster and attains deflection limit state at 190 minutes, while the beam PB29 (lowest strengthening level) deflects slowly and attains deflection limit state at 235 minutes.

The fire resistance time and failure mode for beams PB29 to PB32 are summarized in Table 5.7. It can be seen from the table that fire resistance of the beams decreases with increase in strengthening level. All the beams failed in deflection limit state prior to strength limit state. Based on the above discussion it can be inferred that the strengthening level has significant effect on the capacity degradation and deflection of CFRP-strengthened RC beams and therefore must be accounted in fire design.

(vii) Case PBC7: Effect of steel reinforcement ratio

In case PBC7, the effect of three different steel reinforcement ratio (ρ) with respect to area concrete was evaluated by analyzing beams PB33 to PB35, wherein the reinforcement ratio was varied from 0.44% to 0.89%. Beams PB33, PB34, and PB35 were reinforced with two, three, and four rebars of 16 mm diameter, respectively, which correspond to ρ value of 0.44%, 0.67%, and 0.89%, respectively. The strengthening level was maintained at 43% in all these beams by providing different width of CFRP sheet as described in Table 5.5 and were subjected to same load levels equivalent to 50% of the ultimate strengthened capacity.

Results from the analysis indicate that the steel reinforcement ratio has no effect on the temperature rise in the cross-section of the beams but has considerable effect on structural response. To evaluate the structural response the degradation in moment capacity and progression of mid-span deflection are plotted as a function of fire exposure time in Figure 5.29. It can be seen from the Figure 5.29 (a) that the capacity of all the beams degrade at a different rate throughout the fire exposure duration, whereas the deflection response of the beams is relatively same.

Despite same temperature rise at the CFRP-concrete interface and same relative slip between CFRP and concrete, the rate of CFRP-concrete bond degradation is significantly different in all these beams. To highlight this difference in rate of CFRP-concrete bond degradation, the strength contribution of CFRP (normalized with strength at room temperature) towards the capacity of respective beam is plotted in Figure 5.30. It can be seen from the figure that the CFRP continue to contribute until 160 minutes of fire exposure in beam PB33, whereas the CFRP contribution is completely lost after 135 and 100 minutes of fire exposure in beams PB34 and PB35, respectively. This can be attributed to the compressive strains generated at the level of CFRP in beams PB34 and PB35 after 135 and 100 minutes, respectively, due to relatively smaller curvatures developed in them to maintain equilibrium. The compressive strains inhibit the stress transfer between CFRP and concrete and as a result the contribution of CFRP is completely lost earlier in beams PB34 and PB35. Thus, reinforcement ratio has significant effect on the rate of CFRP-concrete bond degradation in beam, which in turn affect the degradation of capacity in beams. Nevertheless, the capacity of beams PB33, PB34, and PB35 attain the strength limit state after 205, 220, and 220 minute of fire exposure, respectively, i.e., within 15 to 20 minutes of each other. The higher time in beam PB34 and PB35 is due to the high ρ value which increases the reserve capacity of un-strengthened RC beams as compared to that of beam PB33.

The deflection response of beams PB33, PB34, and PB35, as shown in Figure 5.29 (b), follows trends similar to that of beam PB4 in case PBC1. The deflection response of beams PB34 and PB35 is almost similar throughout the fire exposure duration and is slightly stiffer than the beam PB33 due to higher ρ value. The beams PB33, PB34, and PB35 exceed the deflection limit state after 190, 210, and 220 minutes of fire exposure, respectively. Thus, increasing the reinforcement value beyond certain limit does not yield a stiffer deflection response in CFRP-strengthened RC beams.

The fire resistance time of beams PB33 to PB35 and governing failure limit state are summarized in Table 5.7. It can be seen from the table that the fire resistance time increase with in steel reinforcement ratio. However, the increase very minimal at very high ρ value. Beam PB33 has lowest fire resistance of 190 minutes, whereas beam PB35 has highest fire resistance of 220 minutes. All the beams failed in deflection limit state. Based on the above discussion it can be inferred that the steel reinforcement ratio influences the rate of CFRP-concrete bond degradation significantly, however the influence on fire resistance is less than 10% which further reduces to less than 4% at very reinforcement ratio.

5.3.5 Response Parameters from Analysis on Slabs

Results from the parametric study on slabs are presented in Figure 5.31 to Figure 5.41 and are summarized in Table 5.8. A preliminary analysis of the results show that temperature rise at the rebars in the central region is higher than that in the corner rebars. Therefore, the effect of different parameters on thermal response is analyzed by plotting temperature rise at the at the FRP-concrete interface and mid rebar as a function of fire exposure time., while the effect on structural response is analyzed by in plotting the degradation in moment capacity and deflection as a function of fire exposure time. The details are discussed in following sections.

(i) Case PSC1: Effect of CFRP-strengthening

In case PSC1, the effect of CFRP strengthening was evaluated by analyzing slabs PS1 to PS4. Slabs PS1 and PS2 were un-strengthened RC slab, whereas slabs PS3 and PS4 were CFRP-strengthened RC slabs with and without fire insulation. Additionally, slabs PS1 and PS3 were uninsulated slabs, whereas slabs PS2 and PB4 were protected with fire insulation. As in the case of beams, slabs PS1, PS3, and PS4 are analyzed under same load level (50% of respective ultimate capacity), whereas slab PS2 was analyzed under loading equal to that on slab PS4, which corresponds to 78% of ultimate capacity of slab PS2 at room temperature. This was done to evaluate if an insulated CFRP-strengthened RC slab can be idealized as an insulated RC slab. The thermal and structural response of these slabs are plotted in Figure 5.31 and Figure 5.32, respectively.

Results from the analysis indicate that like in the case of beams, the CFRP-strengthening has negligible effect on the temperature rise in the cross-section of the slabs, as shown in Figure 5.31. The temperature rise in almost identical slabs PS1, PS3, and in slabs PS2, PS4. The temperature rise in slabs PS1 and PS3 is faster than the temperature rise in slabs PS2 and PS4, due to the direct exposure to fire. Consequently, the FRP-concrete interface temperature exceeds FRP T_g, and rebar temperature exceeds the critical temperature (593°C) in slab PS3, within 2 minutes and 150 minutes of fire exposure, respectively, whereas in case of insulated slab PS4 the interface temperature exceeds T_g after 12 minutes, but the rebar temperature remains below 410°C until the end of fire exposure. Thus, the critical rebar temperature is not attained in insulated slabs PS2 and PS4.

The structural response shown in Figure 5.32 indicates that the effect of CFRP-strengthening on structural response is more pronounced in case of uninsulated slabs PS1 and PS3, compared to that in insulated slabs PS2 and PS4. The capacity of un-strengthened RC slab PS1, as shown in Figure 5.32 (a), remains constant until 60 minutes of fire exposure due to minimal degradation in the strength properties of rebar. After 60 minutes, the temperature of rebars increases beyond 400°C which initiates degradation in the strength of rebars, and as a result, the capacity of slab PS1 starts decreasing gradually and attains strength limit state after 175 minutes of fire exposure.

The capacity of CFRP-strengthened RC slab PS3 decreases rapidly from the start of fire exposure due to the degradation of strength properties of CFRP and degradation of CFRP-concrete bond. After 30 minutes, the CFRP-concrete composite action is completely lost in slab PS3 and the slab behaves as an un-strengthened RC slab. As a result, the capacity of slab PS3 starts decreasing after 60 minutes of fire exposure and falls below the moment due to applied loading after 110 minutes of fire exposure.

In case of insulated slabs, the capacity of un-strengthened RC slab PS2 remains constant throughout the fire exposure duration of four hours, due to minimal degradation in strength of rebars. The capacity of CFRP-strengthened RC slab PS4 remains constant until 25 minutes, i.e., until the onset of CFRP-concrete bond degradation, and then degrades gradually until 75 minutes of fire exposure, i.e., until complete loss of CFRP-concrete composite action. After 75 minutes, the capacity of remains constant similar to that of slab PS2, until the end of fire exposure. Thus, the insulated slabs do not fail in strength limit state.

Similar trends are observed in the deflection profiles of the slabs PS1 to PS4 shown in Figure 5.32 (b). It can be seen from the figure that slabs PS1 and PS3 deflect at a similar rate until 30 minutes of fire exposure. After 30 minutes, the uninsulated RC slab PS1 exhibit much stiffer response compared to that of uninsulated CFRP-strengthened RC slab PS3. Nevertheless, none of the slabs PS1 and PS3 attain deflection limit state. In case of insulated slabs PS2 and PS4, both the slabs exhibit identical deflection response throughout the fire exposure duration, which is much stiffer than that of slab PS1. Therefore, none of the slabs PS2 and PS4 attain deflection limit state until the end of fire exposure.

The time to attain FRP T_g, critical temperatures in rebar, as well as fire resistance time and failure limit state are summarized in Table 5.8. The uninsulated slabs PS1 and PS3 have 175 and

110 minutes of fire resistance, respectively, based on strength limit state. Since the insulated slabs PS2 and PS4 did not attain any of the failure limit state until the end of four hours of fire exposure, their fire resistance was more than four hours.

(ii) *<u>Case PSC2: Effect of insulation thickness</u>*

In case PSC2, six CFRP-strengthened slabs PS5 to PS10 were analyzed to evaluate the effect of different insulation thickness (t_{ins}) at the bottom surface of the slabs. Slab PS5 was an uninsulated slab, whereas slabs, PS6, PB7, PS8, PS9, and PS10 were protected with 6, 12-, 19-, 25-, and 38-mm thick insulation on the bottom surface.

The thermal response of the slabs PS5 to PS10 is shown in Figure 5.33. As expected, the increase in insulation thickness reduces the temperature rise in the slab cross-section. For instance, the interface temperature exceeds the FRP *Tg* after 2 minutes in uninsulated slab PS5, whereas in insulated slabs PS6, PS7, PS8, PS9, and PS10 the interface temperature exceeds FRP *Tg* after 6, 12, 21, 30, 42, and 55 minutes, respectively. Similarly, the rebar temperature exceeds critical temperature of 593°C after 110 minutes in uninsulated slab PS5, whereas in the insulated slabs the rebar temperature remains below 550°C, until the end of fire exposure. Further, it can be seen from the figure that the effect of increasing the insulation thickness is more pronounced in slabs PS5, PS6, PS7, and PS8, whereas difference in thermal response of slabs PS8, PS9, and PS10 is very marginal. For instance, the rebar temperatures in slab PS5 reduces from 750°C to 320°C in slab PS8, i.e., more than 55%, at the end of 240 minutes of fire exposure. However, the rebar temperature between slabs PS8 to PS10 is from 320°C to 200°C, i.e., less than 35%. Moreover, even with 12 mm thick insulation the rebar temperatures remain close to 400°C until the 240 minutes of fire exposure, indicating minimal loss in the strength of rebars until 240 minutes.

Therefore, providing an insulation layer of at least 12 mm thickness can enhance the thermal performance of CFRP-strengthened RC slab.

The structural response of slabs PS5 to PS10 is compared in Figure 5.34. The degradation in moment capacity of uninsulated slab PS5, as shown in Figure 5.34 (a) is identical to that of slab PS3 (shown Figure 5.34 (a)). Therefore, slab PS5 attains strength limit state after 110 minutes, due to rapid degradation in CFRP-concrete bond in the first 30 minutes followed by strength degradation in rebars after 60 minutes of fire exposure.

In case of insulated slabs PS6 to PS10, the presence of insulation delays the onset of CFRP-concrete bond degradation as well as the complete loss of CFRP-concrete composite action. For instance, the CFRP-concrete bond degradation starts between 20 minutes and 90 minutes in slabs PS6 to PS10 as compared to 2 minutes in case of slab PS5. Consequently, capacity of insulated slabs PS6 to PS10 remains constant for a longer duration in the initial stages. Similarly, the FRP-concrete composite action is completely lost in the insulated slabs between 50 and 120 minutes, as compared to 30 minutes in slab PS5. As a result, the dependence of capacity of insulated CFRP-strengthened slabs on the strength of rebars start after at least 50-120 minutes of fire exposure. In case of insulated slab PS6, the rebar temperature exceeds after 400°C after 150 minutes. As a result, the capacity of slab starts degrading gradually, and therefore, slab PS6 attains strength limit state after 239 minutes. For the insulated slabs PS7 to PS10, the rebar temperatures remain below 410°C, therefore, the capacity of slabs PS7 to PS10 remains constant and do not attain strength limit state until end of four hours of fire exposure.

The deflection profiles of the slabs PS5 to PS10 shown in Figure 5.34 (b) indicate that the increase in thickness of insulation stiffens the deflection response of the slabs. The highest deflections are observed in case of uninsulated slab PS5 (similar to that of slab PS3) and lowest in slab PS10. The deflection increases rapidly in uninsulated slab PS5 compared to that of insulated slabs PS6 to PS10. The difference in deflection response is more pronounced in increasing the thickness of insulation from 0 to 19 mm, i.e., from slabs PS5 to PS8, whereas the difference in deflection response of slabs PS8 to PS10 is negligible. The deflection in slab PS6 increases rapidly towards the end of fire exposure whereas the deflection in slabs PS7 to PS10 increases at gradual pace throughout the fire exposure duration. The higher deflection in insulated slabs PS6, PS7, and PS8 are attributed to the faster degradation in stiffness of rebars resulting from temperature rise. Nevertheless, none of the slabs PS5 to PS10, attain the deflection limit state until the end of fire exposure or strength failure. Thus, deflection is not a governing failure criterion for slabs PS5 to PS10.

The fire resistance time of slabs PS5 to PS10 and governing failure mode are summarized in Table 5.8. The fire resistance time of slabs PS5 and PS6 is 110 and 239 minutes, respectively, determined as per strength limit state. Since, the remaining slabs PS7 to PS10 insulated with 12-38 mm thick insulation, did not fail in strength or deflection limit state, they have more than four hours of fire resistance. Thus, providing insulation thickness of at least 12 mm can help achieve four hours of fire resistance in CFRP-strengthened RC slab based on the strength, deflection and critical rebar temperature criteria. Since, slabs are often required to have at least three hours of fire resistance, providing insulation thickness higher than 12 mm would not be optimum.

(iii) Case PBC3: Effect of load level

In case PSC3, four different slabs, PS11 to PS14 were analyzed to evaluate the effect of different load levels. All the slabs had same geometrical and insulation configuration, and the concentrated loads were applied at distance of 1.5 m from the end supports as shown in Figure 5.14. The applied loads on slabs PS11, PS12, PS13, and PS14 generated maximum bending equivalent 50%, 60%, 65%, and 70% of room temperature ultimate strengthened capacity of the respective slab. Load levels smaller than 50% were not considered in the analysis, because the slab can sustain 50% load level for four hours of fire exposure (as seen in case PSC1). As in the case of beams, the applied load levels only affect the structural response of the slabs, which is compared here.

Figure 5.35 (a) shows the degradation in moment capacity of the slabs PS11 to PS14 as a function of fire exposure time. As expected, the moment capacity decreases at a faster rate with increase in applied load levels. Consequently, the time to attain strength limit state decreases with increase in applied loads. For instance, the slab PS12, which is subjected to 60% load level, attains strength limit state after 230 minutes of fire exposure, whereas slab PS13 and PS14 subjected to 70% and 80% load levels attains strength limit state after 40 and 30 minutes of fire exposure, respectively. Further, it can be seen from the figure that the rate of moment capacity degradation increases during the CFRP-concrete bond degradation phase. Thus, the load levels affect the rate of CFRP-concrete bond degradation in insulated CFRP-strengthened RC slabs.

Figure 5.35 (b) shows the deflection profiles of the slabs PS11 to PS14, as a function of fire exposure time. As expected, the deflection and rate of rise in deflection increases with increase in load level, due to the high stresses generated in the section. The higher stresses results in rapid degradation in strength of constitutive materials. Moreover, at higher load levels, the steel rebars starts yielding, which in turn reduces stiffness of the slab. As a result, the deflection in slabs increases rapidly. Nevertheless, none of the slabs PS11 to PS14 failed in deflection limit state.

Table 5.8 summarizes the fire resistance time and governing failure mode for slabs PS11 to PS14. Slab PS11 has more than four hours of fire resistance as it did not attain strength or deflection limit state until the end of four hours of fire exposure. Whereas slabs PS12, PS13, and

PS14 has a fire resistance of 230, 40, and 30 minutes, respectively, based on strength limit state. It can be seen that the fire resistance decreases with increase in load levels. Therefore, effect of load levels must be considered in the fire design of CFRP-strengthened concrete slabs.

(iv) Case PBC4: Effect of fire scenarios

Fire severity in realistic fire scenarios is often much more severe than the standard fire scenarios. To compare the performance of CFRP-strengthened concrete slabs under different fire scenarios, slabs PS15 to PS19 were analyzed in case PBC4. All the slabs had geometry, insulation, and loading configuration identical to that of slab PS4. However, the fire scenarios considered in the analysis of slabs PS15, PS16, PS17, PS18, and PS19 included, ISO 834 standard fire exposure as well as design fire scenarios DF1, DF2, DF3, and DF4, respectively. These fire scenarios are explained in case PBC5 and shown in Figure 5.26. The thermal and structural response of these slabs is compared in Figure 5.36 and Figure 5.37, respectively. Additionally, the response of slab PS4 is also shown in these figures to compare the effect of ASTM E119 standard fire exposure.

It can be seen from the Figure 5.36, that the temperature increases at a faster rate in cross-section of slabs subjected to design fire scenarios DF1 to DF3, i.e., slabs PS16 to PS18, as compared that in slabs PS15, PS19, and PS4, which are subjected to standard fire scenarios. The temperature in slabs PS16 to PS19 starts decreasing after attaining peak temperature due to the presence of decay phase. Further, it can be seen that the mid-rebar temperature in slabs PS16 to PS19 remains below 400°C throughout the fire exposure duration, indicating no strength loss in rebars. In slabs PS4 and PS15, which are subjected to standard fire exposure, the temperature increases continuously at almost identical rate throughout the fire exposure duration and the rebar temperature exceeds 400°C after 215 minutes of fire exposure, indicating initiation of strength loss.

Figure 5.37 (a) shows the degradation in moment capacity of slabs PS4, and PS15 to PS19 as a function of fire exposure time. Due to faster temperature rise in slabs PS16 to PS18, their capacity starts degrading earlier as compared to that of slabs PS4, PS15, and PS19. However, the rate of degradation is similar in all the slabs. The CFRP-concrete composite action is lost after 45 minutes in slabs PS16 to PS18 and after 60 minutes in slabs PS4, PS15, and PS19. After the loss of composite action, the capacity of the slabs remains constant and above the moment due to applied loading until the end of fire exposure, i.e., 4 hours, indicating no failure.

The deflection profiles of slabs PS4, and PS15 to PS19 are shown in Figure 5.37 (b). It can be seen from the figure that the slabs PS16 to PS18 starts deflecting at a faster rate as compared to slabs PS4, PS15, and PS19. The faster increase in deflection is attributed to the rapid increase in temperature which leads to faster degradation of CFRP-concrete bond which in turn reduces the stiffness of the slabs. The deflection in slabs PS4 and PS15 increases at a similar rate throughout the fire exposure duration, whereas the deflection in slabs PS16 to PS19 starts decreasing (i.e., recovery) to reduction in temperature of steel rebars and concrete in from the cooling phase of fire scenarios DF1, DF2, DF3, and DF4. None of the slabs attain deflection limit state until the end of fire exposure.

Since the slabs PS4, and PS15 to PS19 did not fail in strength or deflection limit state, until four hour of fire exposure duration, the slabs are considered to have more than four hours of fire resistance, as summarized in Table 5.8. Thus, fire severity and fire scenarios can influence the temperature rise in the cross-section and can influence the structural response of the slabs, but the fire resistance not significantly affected.

(v) <u>Case PBC5: Effect of width of insulation</u>

Six CFRP-strengthened RC slabs designated as PS20 to PS25 were analyzed in case PSC5, to evaluate the effect of width (*b_ins*) of insulation applied on the bottom surface of slab. The slabs PS20, PS21, PS22, PS23, PS24, and PS25 were protected with 200, 250, 300, 400, 450, and 500 mm wide and 12 mm thick layer of insulation on the bottom surface. The thermal and structural response of these slabs is discussed below.

The temperature rise in the cross-section of slabs PS20 to PS25 at 5, 60, 90, and 120 minutes as well as at respective failure time are shown in Figure 5.38 (a-f). Additionally, to compare the response of these slabs (PS20 to PS25) with that of a slab protected with insulation throughout its width, temperature rise in cross-section of slab PS4 analyzed in case PSC1, are also shown in Figure 5.38 (g). As can be seen from the figure the thickness of insulation layer covering the CFRP sheet in all the slabs (PS4, PS20 to PS25) is same, therefore, temperature rise at the CFRP-concrete interface is same in all the slabs. The corner rebars are at a distance of 32 mm from either edge of the slab. Therefore, the width of insulation in slabs PS20 to PS22 is not wide enough to provide protection to region of concrete beneath the corner rebars, whereas in slabs PS23 to PS25 the insulation covers a small portion of concrete on the inner edge of corner rebars. Therefore, the temperature rise in corner rebars of slabs PS20 to PS22 is identical. Similarly, the temperature rise in slabs PS23 to PS25 is also identical and slightly lower than that of slabs PS20 to PS22. Since the insulation in slab PS4 provides protection along the entire width of the concrete. Therefore, the temperature rise in corner rebars of slabs PS20 to PS25 is significantly higher than that in slab PS4, throughout the fire exposure duration. The temperature of corner rebars in slabs PS20 to PS22 increases beyond critical rebar temperature (593°C) after 230 minutes of fire exposure, whereas in slabs PS23 to PS25 and PS4, the corner rebars' temperature remains below the critical temperature until the end of fire exposure.

The varying width of insulation in slabs PS20 to PS25 changes the temperature rise in the mid-rebars. Therefore, temperature rise in mid-rebars of these slabs as well as slab PS4 are plotted in Figure 5.39, as a function of fire exposure time. It can be seen from the figure that the temperature increases at a faster rate for slabs PS20 to PS22, i.e., slabs with smaller insulation width as compared to slabs with larger width of insulation, i.e., slabs PS23 to PS25. This is attributed to the fact that for smaller insulation width, the concrete region beneath the mid-rebars is directly exposed to fire resulting in faster temperature rise. There is a significant difference in temperature rise in mid-rebars of slabs PS20, PS21, and PS22, whereas temperature rise in the mid-rebars of slabs PS23 to PS25 is very much similar to that in slab PS4. This indicates that the increasing the insulation width from 200 mm to 250 mm, 300 mm, and 400 mm has significant effect on the thermal response of the slab, However, beyond 400 mm, i.e., almost 100 mm more than the distance of the mid-rebar from the edge of slabs, the difference in thermal response is negligible. Despite the rapid temperature rise in all the slabs PS20 to PS22, the mid-rebars temperature increases beyond 593°C only in slab PS20, whereas in remaining slabs the rebar temperature remains below 550°C, and thus does not exceed the critical temperature of 593°C.

The degradation in moment capacity of slabs PS20 to PS25, and PS4 is plotted against the fire exposure time in Figure 5.40 (a). The trends of moment capacity degradation are similar in slabs PS20 to PS25. It can be seen from the figure that the degradation in moment capacity resulting from degradation of CFRP-concrete bond starts earlier in slabs with smaller width of insulation (i.e., PS20 to PS23), as compared to that of slabs with larger width of insulations (PS4, PS24, and PS25). The CFRP-concrete composite action in slabs PS20 to PS25 is lost between 45 and 60 minutes of fire exposure. Following the complete loss of composite action, the capacity of slabs PS20 to PS24 remains constant until 80 minutes, whereas the capacity of slab PS25 remains constant until 90 minutes of fire exposure. After this the capacity of slabs PS20 to PS25 starts decreasing gradually and attains strength limits between 135 and 230 minutes, which is much earlier than slab PS4 (>240 minutes). Thus, reducing the width of the insulation can lead to early strength failure in CFRP-strengthened RC slabs.

The deflection response of slabs PS4, and PS20 to PS25 is compared in Figure 5.40 (b). The slabs PS20 to PS25, starts deflecting at a faster rate as compared to that of slab PS4. Further, it can be seen that the deflection response becomes stiffer with increase in width of insulation. The larger insulation width decreases the temperature rise in the cross-section which in turn reduces the degradation in strength and stiffness of the rebars, thereby reducing the stiffness degradation of the slabs. Despite the faster increase in deflection none of the slabs attain deflection limit state until failure.

The fire resistance time and the governing failure limit state for slabs PS20 to PS25 are summarized in Table 5.8. Slabs PS20, PS21, PS22, PS23, PS24, and PS25 have fire resistance of 135, 155, 165, 175, 195, and 230 minutes, respectively, determined as per strength limit state. Thus, the fire resistance increases with increase in width of insulation. The fire resistance times of slabs PS20 to PS25 are 22-109% more than the uninsulated CFRP-strengthened RC slab PS2 (110 minutes) but are 4-44% lower than the fire resistance of slab PS4 (>240 minutes). Thus, width of insulation on the bottom surface of the slab has significant influence on the fire resistance of the slabs. Providing insulation wide enough to cover the concrete beneath all the rebars can enhance provide more than 3 hours of fire resistance in CFRP-strengthened RC slabs.

(vi) <u>Case PBC6: Effect of tensile strength of concrete</u>

As seen in case C7 to C11, temperature induced bond degradation is a critical factor governing the fire response of CFRP-strengthened concrete structural members. Among other factors, the bond degradation is highly dependent on the tensile strength of concrete in the layers just CFRP-sheet. However, the effect of tensile strength of concrete on the rate of bond degradation and hence, the fire response of strengthened concrete structures has not been quantified. Therefore, in case PSC6, the effect of tensile strength of concrete on fire response of strengthened concrete structures was evaluated by analyzing slabs PS26 to PS30. The geometry and insulation configuration of these slabs was identical to that of slab PS4. However, during the structural analysis, the tensile strength of concrete was considered as 1.5, 2.0, 2.5, 3.0, and 3.5 for slabs PS26, PS27, PS28, PS29, and PS30, respectively. As seen in case PSC3, the CFRP-concrete bond governs the behavior of slabs at higher load level. Therefore, to highlight the effect of concrete tensile strength on rate of bond degradation and the fire response of slabs, structural loading equivalent to 60% of ultimate room temperature strengthened capacity of slab PS4 was applied on slabs PS26 to PS30.

The thermal response of the slabs is not affected by the tensile strength and is therefore, not discussed here. The structural response is analyzed by plotting degradation in moment capacity and deflection as function of fire exposure time in Figure 5.41. It can be seen from Figure 5.41 (a) that there is almost negligible effect of tensile strength on the rate of moment capacity degradation. The higher tensile strength in slabs PS29 and PS30, increases the stiffens of the CFRP-concrete bond and thus, delays the complete loss of CFRP-concrete composite action. Nonetheless, all the slabs attain strength limit state after 230 minutes of fire exposure. Thus, the tensile strength of concrete can maintain the CFRP-concrete composite action for a slightly longer duration but cannot influence the overall time to strength limit.

The deflection profiles of the slabs PS26 to PS30, as shown in Figure 5.41 (b) indicate that the tensile strength of concrete significantly influences the rate of deflection of strengthened slabs. It can be seen from the figure that with increase in tensile strength, the rate of deflection decreases.

For instance, slabs PS29 and PS30 exhibit significantly stiffer response between 45 and 120 minutes of fire exposure as compared to that of slabs PS26 to PS28. The stiffer response is attributed to the increase in stiffness of the CFRP-concrete bond due to the higher tensile strength of concrete. However, once the CFRP-concrete composite action is completely lost, all the slabs have identical deflection and rate of deflection. Moreover, none of the slabs attain deflection limit until the failure through strength limit state.

The slabs PS26 to PS30 have identical fire resistance time, achieved through strength limit state, as summarized in Table 5.8. Thus, the tensile strength of concrete influences the bond degradation and rate of deflection but does not affect the overall fire resistance of strengthened concrete slabs.

5.4 Summary

The macroscopic finite element based numerical model developed in Chapter 4 was applied to conduct a set of numerical and parametric studies. The numerical studies were conducted to evaluate suitable high temperature property relations of CFRP, and insulation required for accurate assessment of fire resistance using a numerical model. A total of 12 cases were analyzed in the numerical study. Based on the analysis in the numerical study, it can be concluded that temperature variation of thermal properties of CFRP have negligible effect on the fire resistance prediction and therefore, can be neglected. Whereas the temperature variation of thermal properties of insulation has significant influence on the fire response prediction, and therefore, must be properly accounted in fire resistance analysis. Further, the strength and elastic modulus property relations proposed by Bisby et al. [120] and the nonlinear bond degradation relations proposed by Dai et al. [134] provide a realistic estimate of fire resistance of CFRP-strengthened RC flexural members. Additionally, it can be concluded that the relative slip must be calculated separately at each section along the length of the strengthened flexural member rather than idealizing slip at the critical section as the slip along the entire length of the member.

The parametric studies were conducted to evaluate the effect of different parameters on the fire response of CFRP-strengthened RC beams and slabs. A total of 35 beams and 29 slabs were analyzed to evaluate the influence of different parameters on the fire response of strengthened flexural members. Based on the parametric study on the CFRP-strengthened RC beams and slabs, it can be concluded that an insulated CFRP-strengthened RC beam or RC slab can be idealized as an insulated RC beam or RC slab. The factors significantly influencing the fire response of CFRP-strengthened RC beams include insulation thickness and depth on the sides, load level, and fire scenario. Whereas factors such as, strengthening level and steel rebar reinforcement ratio moderately influence the fire response of CFRP-strengthened RC beams. Additionally, it can be concluded from the parametric studies that the deflection limit is the primary governing criterion for determining failure of the beams. Similarly, the factors significantly influencing the fire response of CFRP-strengthened RC slabs, include insulation thickness, width of insulation, and load levels. Whereas fire scenario and tensile strength of concrete have negligible influence on the fire response of CFRP-strengthened RC slabs. Additionally, strength limit state is the major governing criterion for CFRP-strengthened RC slabs.

The inferences drawn from the results of the numerical studies can provide a designer with suitable property relations intending to carry out rational fire resistance assessment of CFRP-strengthened RC flexural members. The data generated in parametric study can be utilized to develop guidelines for fire design, and for enhancing the fire resistance of CFRP-strengthened RC flexural members. Further, the data developed can be utilized to train machine learning models for predicting fire resistance of strengthened concrete flexural members, as shown in chapter 6.

Table 5.1: Geometrical and material property details of beams selected for analysis

Parameter/Property			**B1** [145]	**B2** [151]	**B3** [149]	**B4** [150]	**B5** [44]
Clear span (L, m)			3.0	6.0	1.5	5.2	4.4
Cross-section ($b_c \times d_c$, mm × mm)			200 × 300	200 × 500	100 × 120	200 × 500	250 × 400
Steel rebar diameter	Top (mm)		2-10 ϕ	2-12 ϕ	2-6 ϕ	2-12 ϕ	2-12 ϕ
	Bottom (mm)		2-16 ϕ	2-16 ϕ	2-6 ϕ	2-16 ϕ	2-22 ϕ
Cover to rebars (C_c, mm)			25	20	10	20	25
Compressive strength concrete (f_c' , MPa)			47	23	37	30.7	40
Steel	Yield strength (f_y, MPa)		591	375	470	372	363
	Elastic Modulus (E_s, GPa)		205	200	193	210	210
FRP	Type		CFRP	CFRP	CFRP	CFRP	CFRP
	$t_{frp} \times b_{frp}$ (mm × mm)		1.2 × 100	0.334 × 200	1.4 × 20	0.334 × 200	0.167 × 250
	Modulus of Elasticity (E_f, GPa)		165	160	189	260	200
	Tensile strength (f_u, MPa)		2800	4030	2076	4030	3455
	Glass transition temperature (T_g, °C)		65	73	47	73	85
Insulation	Material type		Promatect H	CS board	Promatect L 500	CS board	SFRM
	Thickness (t_{ins}, mm)		25	40	25	40	10
	Density of insulation (ρ_{ins}, kg/m^3)		870	244.7	450	250	500
	Thermal conductivity (k_{ins}, W/m K)		0.175	0.0603	0.09	0.061	0.125
	Specific heat (J/ kg°C)		840	790	815	740	1036
	Scheme/ config-uration	Concrete	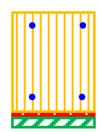	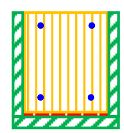	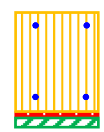	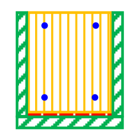	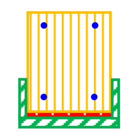
		FRP					
		Insulation					
		Steel rebar					
Fire scenario (FS)			ISO 834	ISO 834	ISO 834	ISO 834	ISO 834
Load applied (kN)			2 × 40.6	4 × 30.2	2 × 6.1	4 × 33	4 × 25.5
Load Ratio (%)			45	52.2	36	63	50

Table 5.2: Description of cases C1 to C13 analyzed in numerical studies

Case No.	Description of effect of property evaluated	Thermal properties of FRP	Strength and modulus properties of FRP	Bond degradation relations	Thermal properties of insulation
C1	Effect of **thermal properties** of FRP	Constant with respect to temperature	Bisby et al. [120]	Dai et al. [134]	Varying with temperature
C2		Varying with temperature			
C3	Effect of different **strength and elastic modulus** relations of FRP	Varying with temperature	Bisby et al. [120]	Perfect bonding	Varying with temperature
C4			Wang et al. [108]		
C5			Dai et al. [121]		
C6			Nguyen et al. [115]		
C7	Effect of different **bond degradation relations**	Varying with temperature	Bisby et al. [120]	Perfect bonding	Varying with temperature
C8				Lu et al. [170]	
C9				Dai et al. [134]	
C10				No bond after interface temperature exceeds T_g of adhesive	
C11				Dai et al. [134] (slip only at critical section)	
C12	Effect of **thermal properties of insulation**	Varying with temperature	Bisby et al. [120]	Dai et al. [134]	Constant with respect to temperature
C13					Varying with temperature

Table 5.3: Comparison of fire resistance and failure mode of beams B1 to B5 evaluated in cases C1 to C13

Beam No.	**Case No.**	**C1**	**C2**	**C3**	**C4**	**C5**	**C6**	**C7**	**C8**	**C9**	**C10**	**C11**	**C12**	**C13**
	Effect of property evaluated	**Thermal properties of CFRP**		**Strength properties of CFRP**				**Bond degradation relations**					**Thermal properties of insulation**	
B1	Fire resistance (minutes)	108	108	136	144	320	108	136	108	108	108	108	120	108
	Failure limit state	D	D	S	S	S	S	S	D	D	D	D	S	D
B2	Fire resistance (minutes)	112	112	184	112	180	144	184	100	112	48	60	208	112
	Failure limit state	S+D	S+D	S	S	S	S	S	S+D	S+D	S	D	S	S+D
B3	Fire resistance (minutes)	138	138	336	164	>400	278	336	135	138	58	150	160	138
	Failure limit state	S	S	S	S	NF	S	S	D	D	S	S	S	S
B4	Fire resistance (minutes)	152	152	244	296	>320	248	244	144	152	40	56	196	152
	Failure limit state	S+D	S+D	S	S	NF	S	S	D	D	S	D	S	S+D
B5	Fire resistance (minutes)	196	196	204	200	228	196	204	196	196	196		284	196
	Failure limit state	D	D	S + D	S	S	S	S + D	D	D	D		S+D	D

Note: **S**: Strength limit state; **D**: Deflection limit state

Table 5.4: Geometrical configuration and material property details of the RC beam and RC slab considered for parametric study

Property			**Beam**	**Slab**
Designation			PB	PS
Clear span (L, m)			6.0	3.5
Cross-section ($b_c \times d_c$, mm × mm)			254 × 406	600 × 150
Concrete cover thickness (C_c, mm)			38	25
Concrete compressive strength (f'_c, MPa)			35	35
Aggregate in concrete			Siliceous	Siliceous
Steel rebars	Longitudinal rebars (number – diameter)	Top	2-13 mm ϕ	NA
		Bottom	**nts**-16	4-13 mm ϕ
	Stirrup diameter (mm)			
	Yield strength (f_y, MPa)		460	460
	Elastic modulus (E_s, GPa)		210	210
FRP	Thickness (t_{frp}, mm)		1.02	1.02
	Width (b_{frp}, mm)		$\boldsymbol{b_{frp}}$	200
	Modulus of elasticity (E_f, GPa)		73.770	73.770
	Tensile strength (f_u, MPa)		1034	1034
	Rupture strain (ε_u, %)		1.4	1.4
	Glass transition temperature (T_g, °C)		82	82
Insulation	Thickness at the bottom and sides (mm)		$\boldsymbol{t_{ins}}$	$\boldsymbol{t_{ins}}$
	Depth on the sides (mm)		$\boldsymbol{h_i}$	0
	Thermal conductivity (k_{ins}, W/°C m)		0.154	0.154
	Specific heat capacity (J/°C m^3)		556460	556460

Note: ***nts***, $\boldsymbol{b_{frp}}$, $\boldsymbol{t_{ins}}$, $\boldsymbol{h_i}$ are varying for beams and slabs analyzed in parametric study and are defined in Table 5.5 for beams and Table 5.6 for slabs

Table 5.5: Critical factors studied in parametric study on CFRP-strengthened RC beam

Case name and factor evaluated	Beam name	*nts*	ρ_s	b_{frp}	*FRP SL*	Insulation t_{ins}	Insulation h_i	*Applied Moment*	*Applied LL*	*Fire scenario*
Unit	(#)	#	(%)	(mm)	(%)	(mm)		(kNm)	(%)	
PBC1 CFRP-strengthening	PB1	3	0.67	0	**-**	0	0	46	50	ASTM E119
	PB2					19	76	76	82	
	PB3			254	**57**	0	0	76	50	
	PB4					19	76			
PBC2 Insulation depth on sides	PB5	3	0.67	254	57	19	**0**	71	50	ASTM E119
	PB6						**38**			
	PB7						**57**			
	PB8						**76**			
	PB9						**102**			
	PB10						**127**			
	PB11						**152**			
PBC3 Insulation thickness at soffit and sides of beam	PB12	3	0.67	254	57	**0**	76	71	50	ASTM E119
	PB13					**6**				
	PB14					**12**				
	PB15					**19**				
	PB16					**25**				
	PB17					**32**				
	PB18					**38**				
PBC4 Load level	PB19	3	0.67	254	57	19	76	**43**	**30**	ASTM E119
	PB20							**57**	**40**	
	PB21							**71**	**50**	
	PB22							**86**	**60**	
	PB23							**100**	**70**	
PBC5 Fire scenario	PB24	3	0.67	254	57	19	76	71	50	**ISO 834**
	PB25									**DF1**
	PB26									**DF2**
	PB27									**DF3**
	PB28									**DF4**
PBC6 Strengthening level	PB29	3	0.67	**100**	**20**	19	76	56	50	ASTM E119
	PB30			**150**	**30**			61		
	PB31			**200**	**40**			66		
	PB32			**254**	**57**			71		
PBC7 Steel rebar ratio	PB33	**2**	**0.44**	128	43	19	76	44	50	ASTM E119
	PB34	**3**	**0.67**	190				65		
	PB35	**4**	**0.89**	254				85		

Note: ***FRPSL***: FRP strengthening level; ***LL***: load level; ***FS***: fire scenario; t_{ins}: thickness of insulation at bottom and sides; h_i: depth of insulation on sides of beam; b_{frp}: width of FRP; ρ_s: steel reinforcement ratio (A_{st}/bd); ***nts***: number of tensile rebars

Table 5.6: Critical factors studied in parametric study on CFRP-strengthened RC slab

<table>
<tr><th rowspan="2">Case name and factor evaluated</th><th rowspan="2">Slab name</th><th rowspan="2">Concrete tensile strength (f_t)</th><th colspan="2">Insulation</th><th colspan="2">Applied</th><th rowspan="2">Fire scenario</th></tr>
<tr><th>Thickness (t_{ins})</th><th>Width (b_{ins})</th><th>Moment</th><th>Load level (LL)</th></tr>
<tr><td>Unit</td><td>(#)</td><td>(MPa)</td><td colspan="2">(mm)</td><td>(kNm)</td><td>(%)</td><td></td></tr>
<tr><td rowspan="4">PSC1
CFRP-strengthening</td><td>PS1</td><td rowspan="4">1.5</td><td>0</td><td>0</td><td>13</td><td>50</td><td rowspan="4">ASTM E119</td></tr>
<tr><td>PS2</td><td>12</td><td>600</td><td>22</td><td>78</td></tr>
<tr><td>PS3</td><td>0</td><td>0</td><td rowspan="2">22</td><td rowspan="2">50</td></tr>
<tr><td>PS4</td><td>12</td><td>600</td></tr>
<tr><td rowspan="6">PSC2
Insulation thickness at soffit and sides of beam</td><td>PS5</td><td rowspan="6">1.5</td><td>0</td><td rowspan="6">600</td><td rowspan="6">22</td><td rowspan="6">50</td><td rowspan="6">ASTM E119</td></tr>
<tr><td>PS6</td><td>6</td></tr>
<tr><td>PS7</td><td>12</td></tr>
<tr><td>PS8</td><td>19</td></tr>
<tr><td>PS9</td><td>25</td></tr>
<tr><td>PS10</td><td>38</td></tr>
<tr><td rowspan="4">PSC3
Load level</td><td>PS11</td><td rowspan="4">1.5</td><td rowspan="4">12</td><td rowspan="4">600</td><td>22</td><td>50</td><td rowspan="4">ASTM E119</td></tr>
<tr><td>PS12</td><td>26</td><td>60</td></tr>
<tr><td>PS13</td><td>30</td><td>70</td></tr>
<tr><td>PS14</td><td>35</td><td>80</td></tr>
<tr><td rowspan="5">PSC4
Fire scenario</td><td>PS15</td><td rowspan="5">1.5</td><td rowspan="5">12</td><td rowspan="5">600</td><td rowspan="5">22</td><td rowspan="5">50</td><td>ISO 834</td></tr>
<tr><td>PS16</td><td>DF1</td></tr>
<tr><td>PS17</td><td>DF2</td></tr>
<tr><td>PS18</td><td>DF3</td></tr>
<tr><td>PS19</td><td>DF4</td></tr>
<tr><td rowspan="6">PSC5
Width of insulation</td><td>PS20</td><td rowspan="6">1.5</td><td rowspan="6">12</td><td>200</td><td rowspan="6">22</td><td rowspan="6">50</td><td rowspan="6">ASTM E119</td></tr>
<tr><td>PS21</td><td>250</td></tr>
<tr><td>PS22</td><td>300</td></tr>
<tr><td>PS23</td><td>400</td></tr>
<tr><td>PS24</td><td>450</td></tr>
<tr><td>PS25</td><td>500</td></tr>
<tr><td rowspan="5">PSC6
Concrete tensile strength</td><td>PS26</td><td>1.5</td><td rowspan="5">12</td><td rowspan="5">600</td><td rowspan="5">26</td><td rowspan="5">60</td><td rowspan="5">ASTM E119</td></tr>
<tr><td>PS27</td><td>2.0</td></tr>
<tr><td>PS28</td><td>2.5</td></tr>
<tr><td>PS29</td><td>3.0</td></tr>
<tr><td>PS30</td><td>3.5</td></tr>
</table>

Table 5.7: Summary of results obtained from parametric studies of CFRP-strengthened RC beams

Case name and Factor evaluated	Beam name	Time to Attain				Fire resistance	Failure limit state
		FRP T_g	Rebar temperature > 593°C	Strength limit state	Deflection limit state		
Unit	(#)	(minutes)				(minutes)	(S/D)
PBC1 CFRP-strengthening	PB1	-	129	155	145	**145**	**D**
	PB2		239	200	190	**190**	
	PB3	2	129	110	105	**105**	
	PB4	21	239	200	190	**190**	
PBC2 Insulation depth on sides	PB5	20	191	155	150	**150**	**D**
	PB6		205	170	160	**160**	
	PB7	21	221	185	175	**175**	
	PB8		239	200	190	**190**	
	PB9		n.a.	220	215	**215**	
	PB10			240	230	**230**	
	PB11			n.a.	n.a.	**>240**	**n.f.**
PBC3 Insulation thickness at soffit and sides of beam	PB12	2	152	125	120	**120**	**D**
	PB13	7	183	155	145	**145**	
	PB14	13	215	180	170	**170**	
	PB15	21	239	200	190	**190**	
	PB16	30	n.a.	220	210	**210**	
	PB17	41		235	225	**225**	
	PB18	51		n.a.	235	**235**	
PBC4 Load level	PB19	21	239	n.a.	n.a.	**>240**	**n.f.**
	PB20			235	225	**225**	**D**
	PB21			200	190	**190**	**D**
	PB22			145	n.a.	**145**	**S**
	PB23			50	45	**45**	**D**
PBC5 Fire scenario	PB24	21	230	195	185	**185**	**D**
	PB25	15	n.a.	160	150	**150**	**D**
	PB26	13		n.a.	n.a.	**>240**	**n.f.**
	PB27	13		160	145	**145**	**D**
	PB28	21		n.a.	n.a.	**>240**	**n.f.**
PBC6 Strengthening level	PB29	21	n.a.	n.a.	235	**235**	**D**
	PB30			230	220	**220**	
	PB31			215	210	**210**	
	PB32		239	200	190	**190**	
PBC7 Steel reinforcement ratio	PB33	21	239	205	190	**190**	**D**
	PB34			220	210	**210**	
	PB35			225	220	**220**	

Note: S: strength; **D**: deflection; **n.f.**: no failure; **n.a.**: not achieved until end of fire exposure

Table 5.8: Summary of results obtained from parametric studies of CFRP-strengthened RC slabs

Case name and Factor evaluated	Beam name	Time to Attain				Fire resistance	Failure limit state
		FRP T_g	Rebar temperature > 593°C	Strength limit state	Deflection limit state		
Unit	(#)	(minutes)				(minutes)	(T/S/D)
PSC1 CFRP-strengthening	PS1	n.a.	145	175	n.a.	**175**	**S**
	PS2		n.a.	n.a.		**>240**	**n.f.**
	PS3	2	145	110		**110**	**S**
	PS4	12	n.a.	n.a.		**>240**	**n.f.**
PSC2 Insulation thickness at soffit and sides of beam	PS5	2	155	110	n.a.	**110**	**S**
	PS6	6	n.a.	239		**239**	
	PS7	12		n.a.		**>240**	**n.f.**
	PS8	30					
	PS9	55					
	PS10	42					
PSC3 Load level	PS11	12	n.a.	n.a.	n.a.	**>240**	**n.f.**
	PS12			230		**230**	**S**
	PS13			40		**40**	
	PS14			30		**30**	
PSC4 Fire scenario	PS15	12	n.a.	n.a.	n.a.	**>240**	**n.f.**
	PS16	7					
	PS17	7					
	PS18	8					
	PS19	12					
PSC5 Width of insulation	PS20	12	231	135	n.a.	**135**	**S**
	PS21		233	155		**155**	
	PS22		237	165		**165**	
	PS23		n.a.	175		**175**	
	PS24		n.a.	195		**195**	
	PS25		n.a.	230		**230**	
PSC6 Concrete tensile strength	PS26	12	n.a.	n.a.	n.a.	**>240**	**n.f.**
	PS27						
	PS28						
	PS29						
	PS30						

Note: S: strength; **D**: deflection; **n.f.**: no failure; **n.a.**: not achieved until end of fire exposure

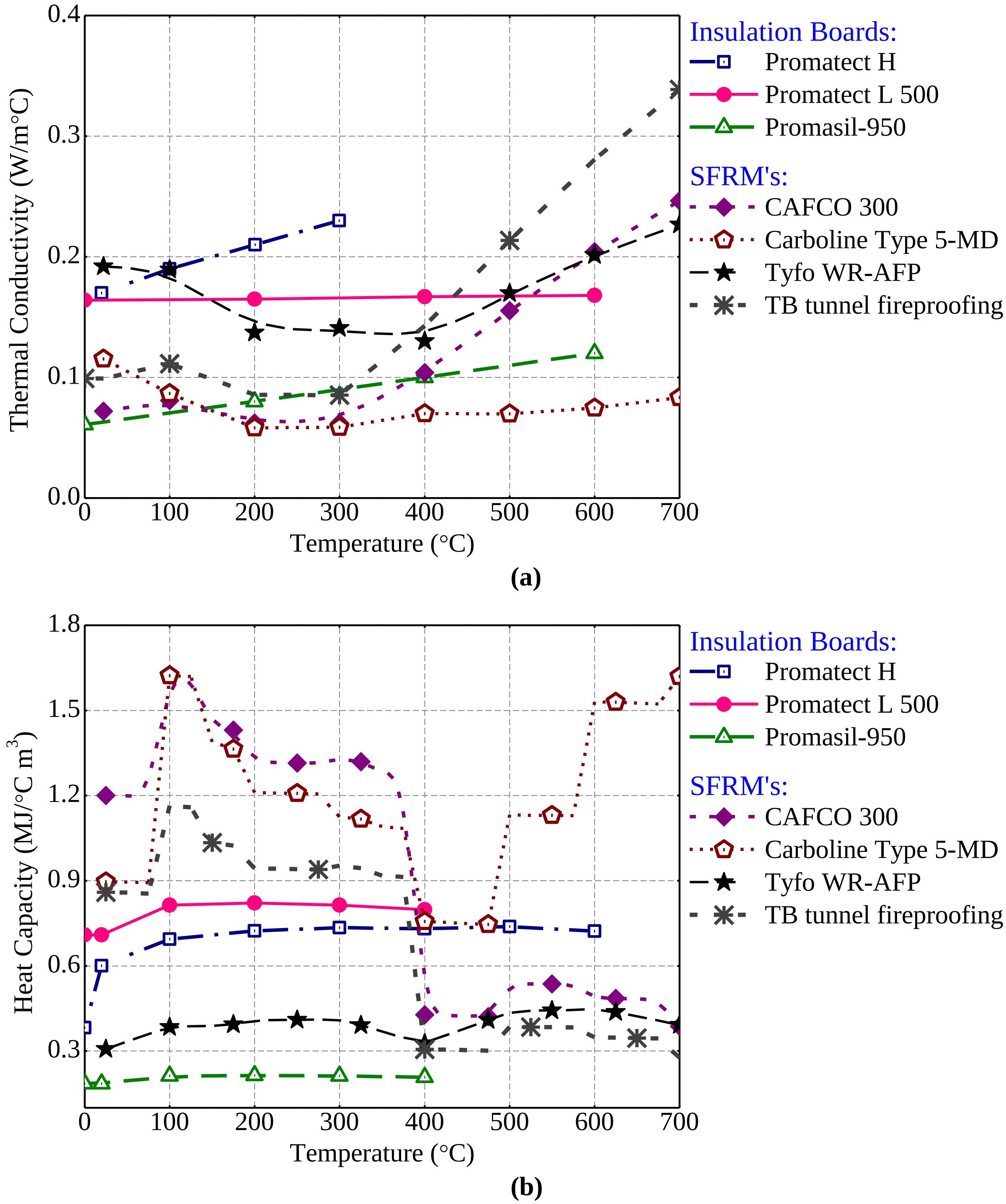

Figure 5.1: High temperature thermal properties of various fire insulation materials considered in numerical studies: (a) thermal conductivity; (b) heat capacity

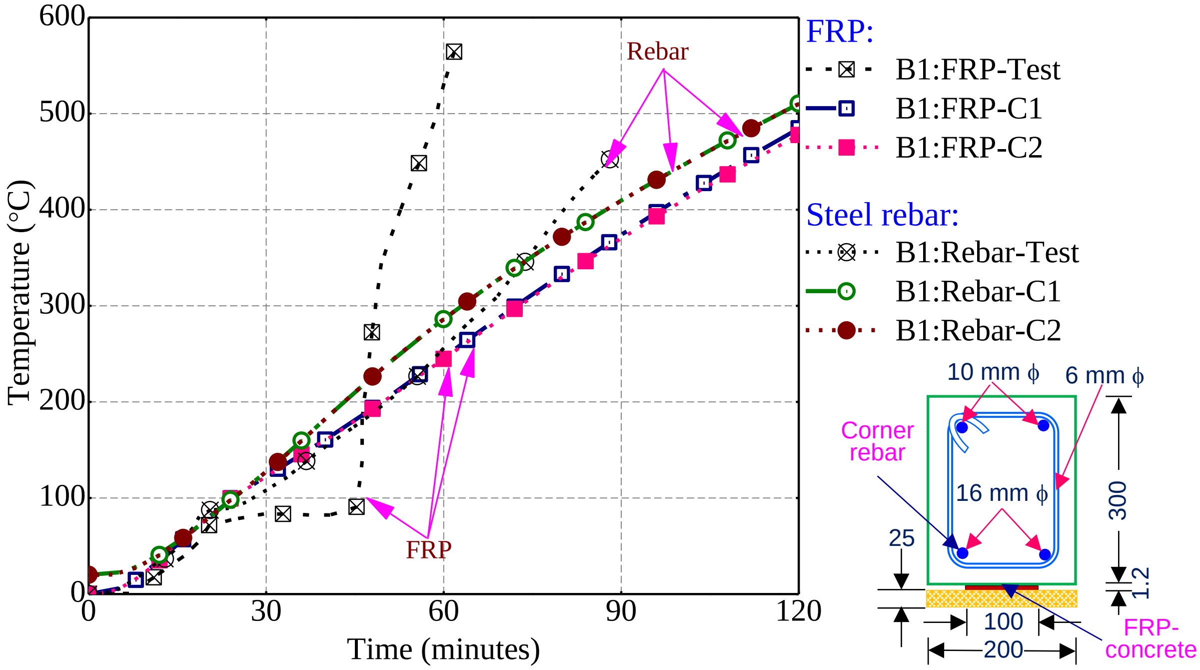

Figure 5.2: Effect of temperature dependence of thermal properties of FRP on temperature rise in steel rebar and FRP-concrete interface in beam B1

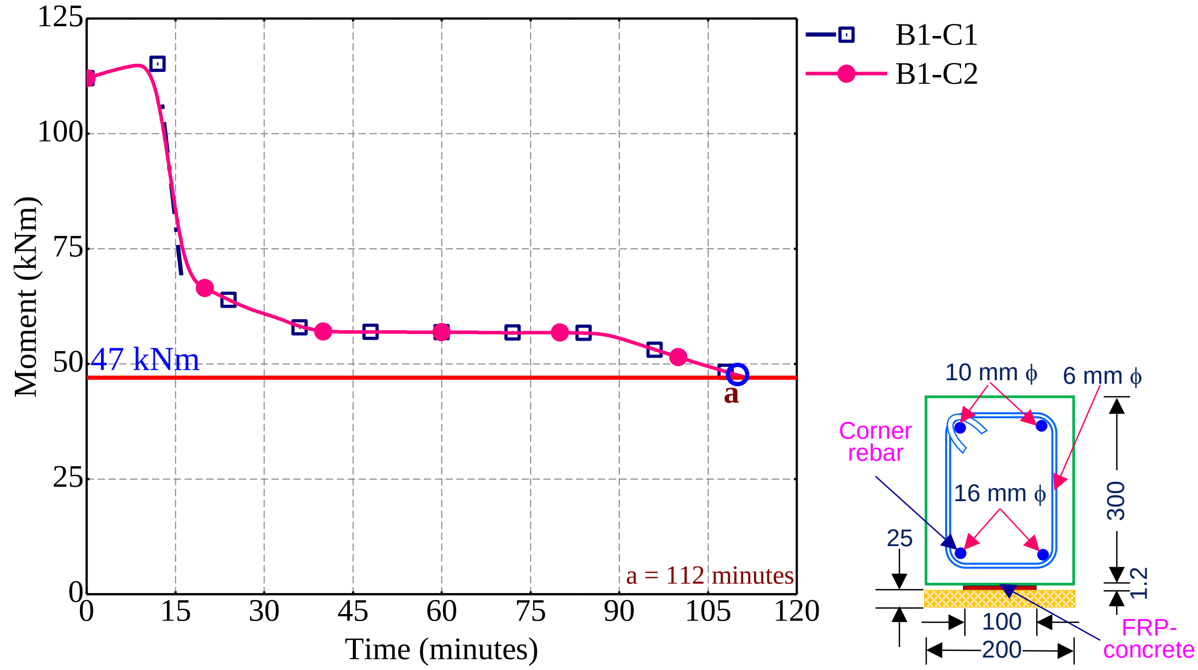

(a)

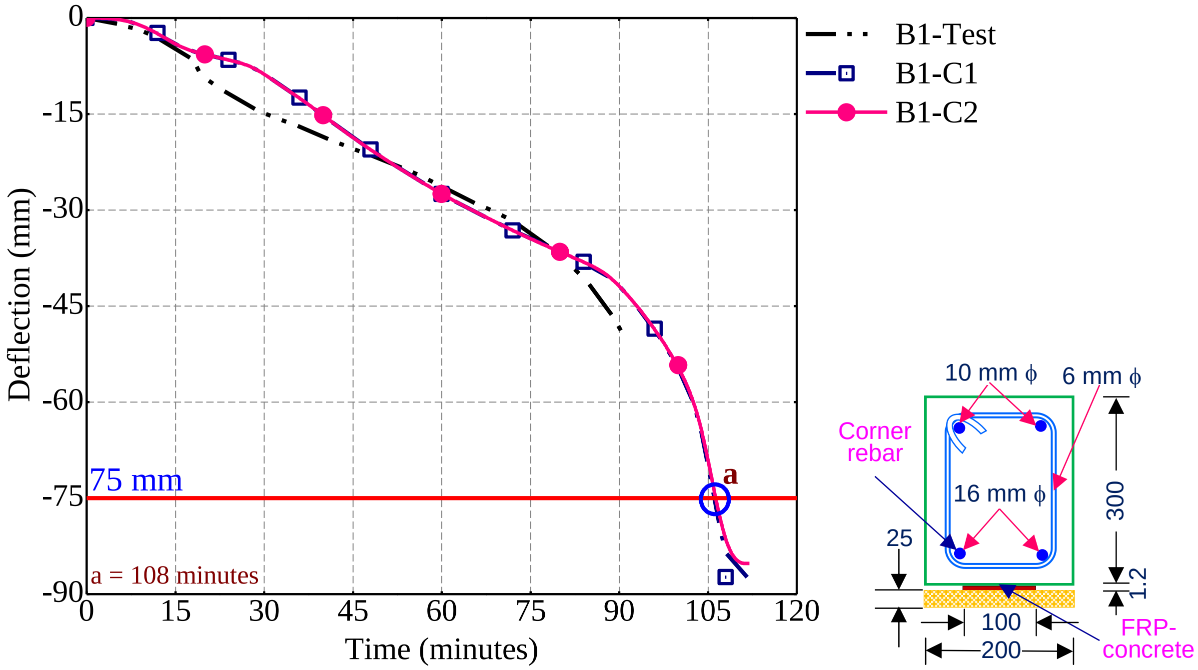

(b)

Figure 5.3: Effect of high temperature thermal properties of CFRP on structural response of beam B1: (a) degradation of moment capacity; (b) deflection

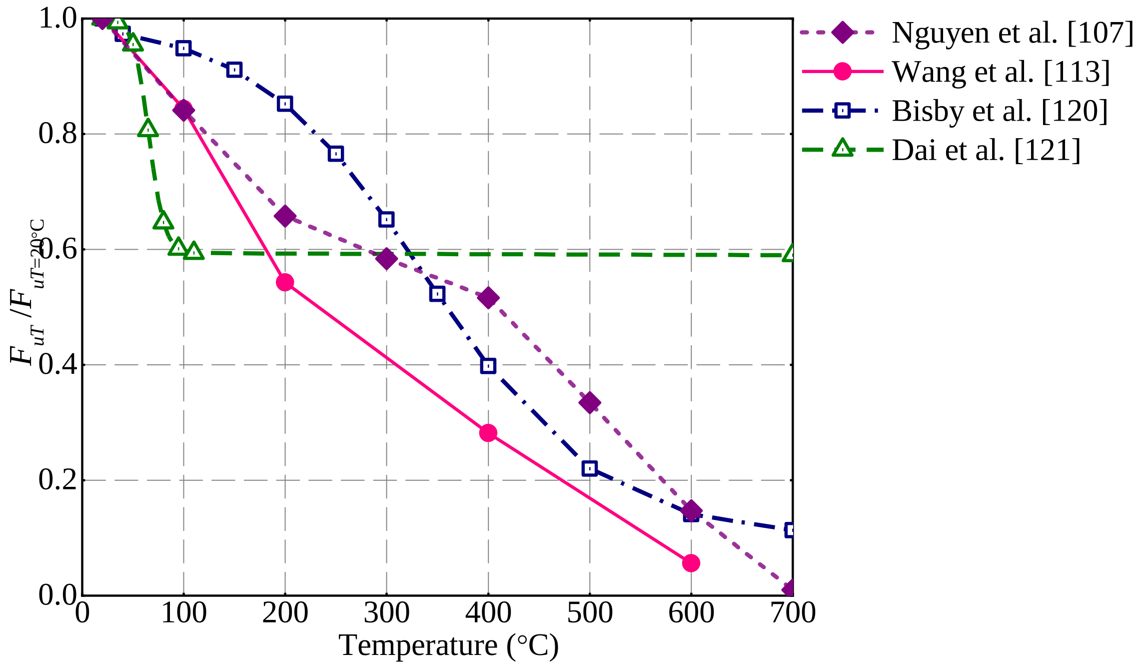

(a)

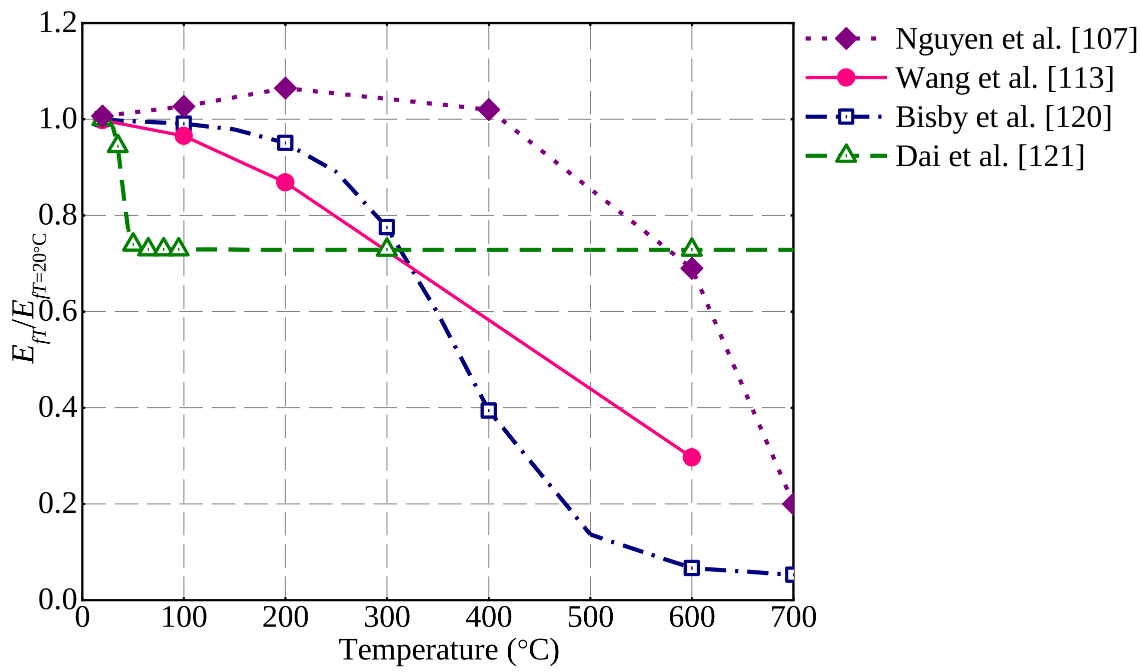

(b)

Figure 5.4: Normalized strength property relations of CFRP considered for analysis in cases C3 to C6: (a) relations for tensile strength (b) relations for elastic modulus

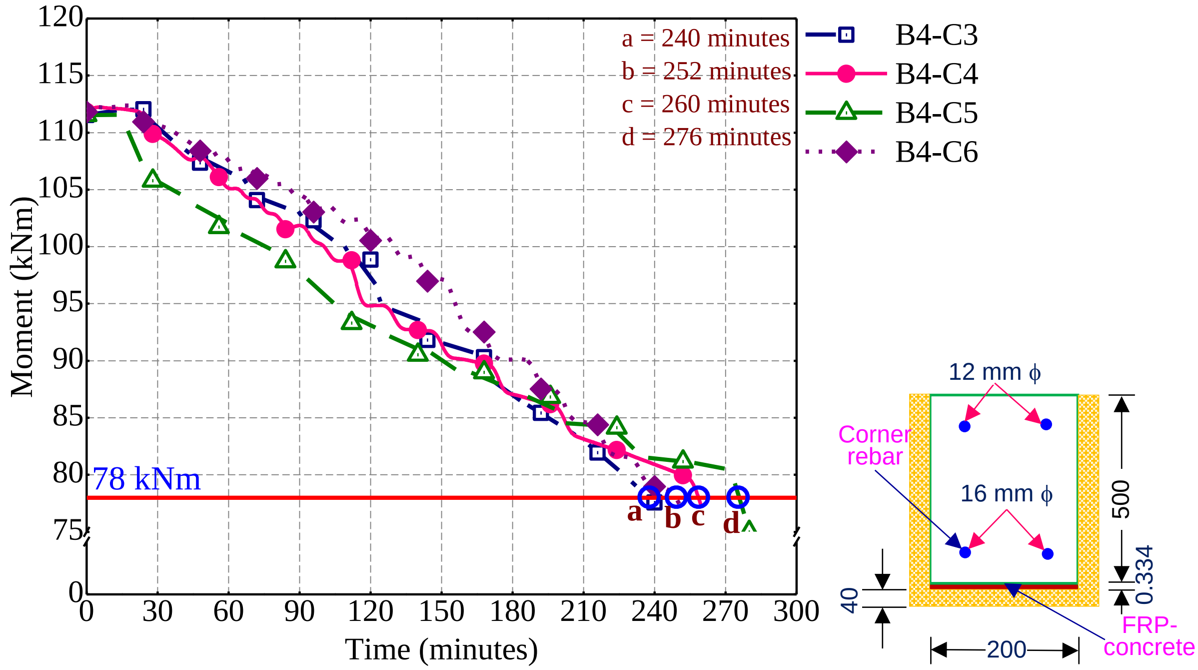

Figure 5.5: Effect of different temperature dependent strength and elastic modulus relations for CFRP on degradation in moment capacity at mid-span of beam B4

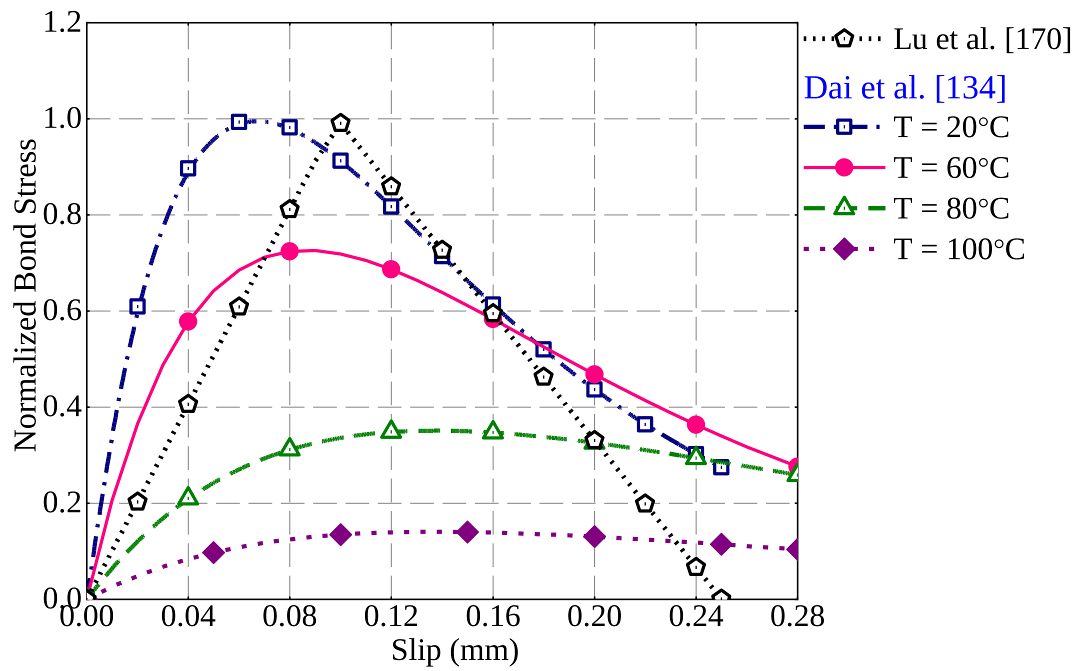

Figure 5.6: Normalized bilinear and nonlinear bond stress vs slip relations for externally bonded CFRP at ambient and elevated temperatures

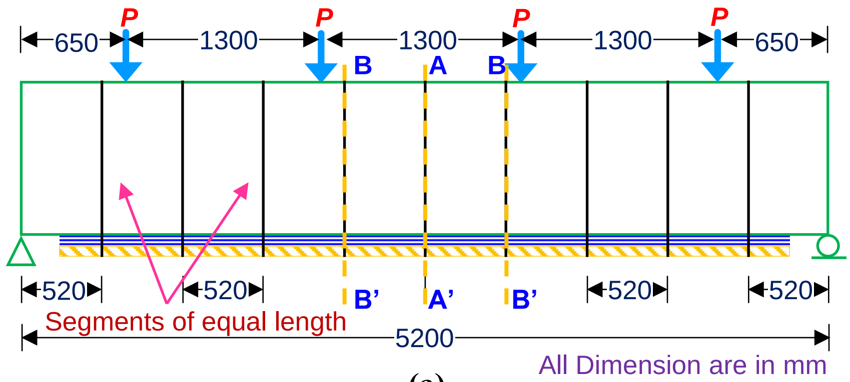

(a)

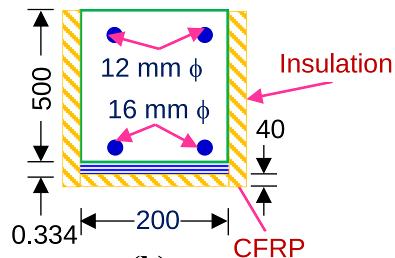

(b)

Figure 5.7: Geometrical layout and details of segments along the length of beam B4: (a) Elevation; (b) cross-section

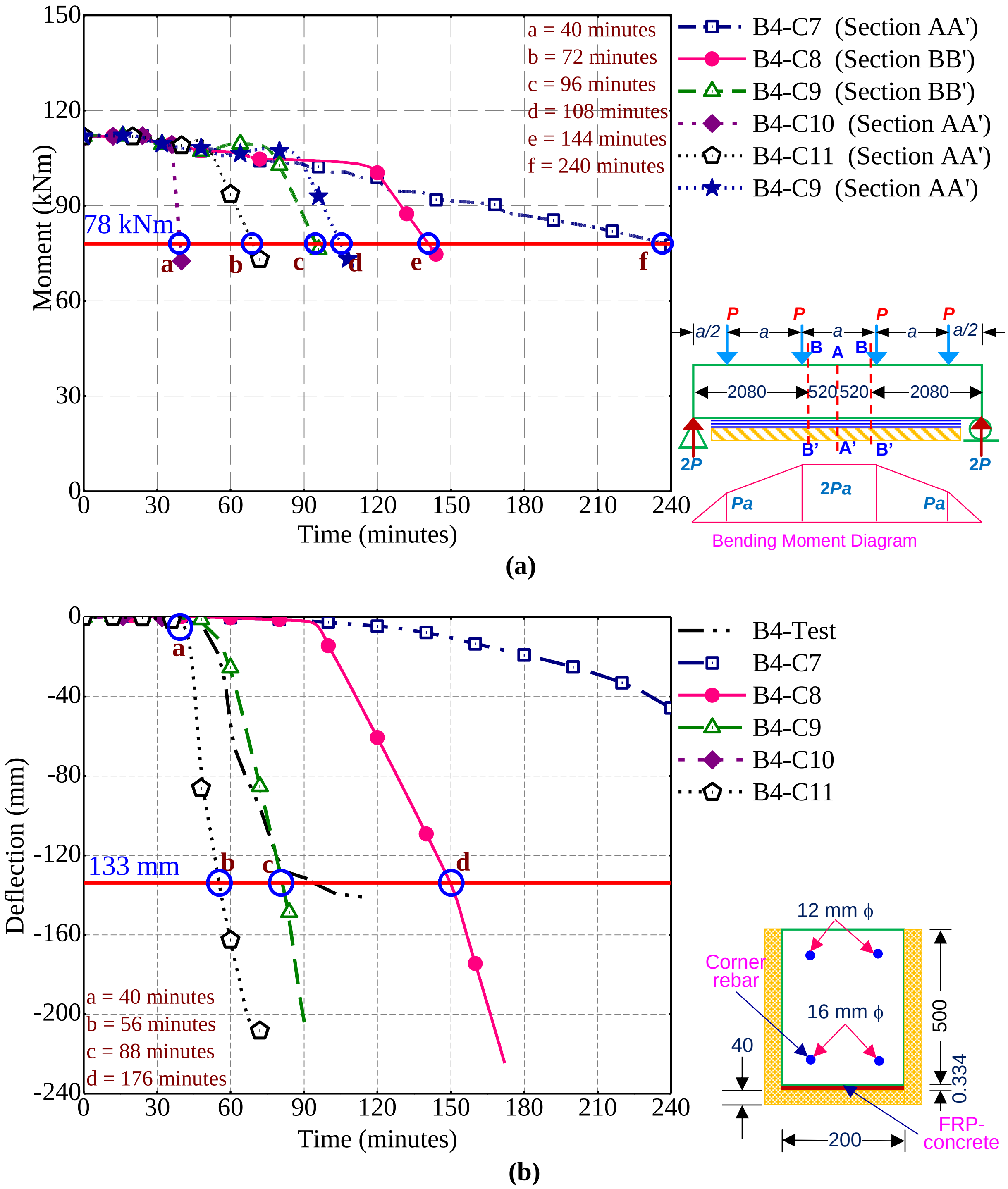

Figure 5.8: Effect of different bond-slip relations and bond-slip evaluation procedure in flexural member on structural response of beam B4: (a) degradation of moment capacity; (b) mid-span deflection

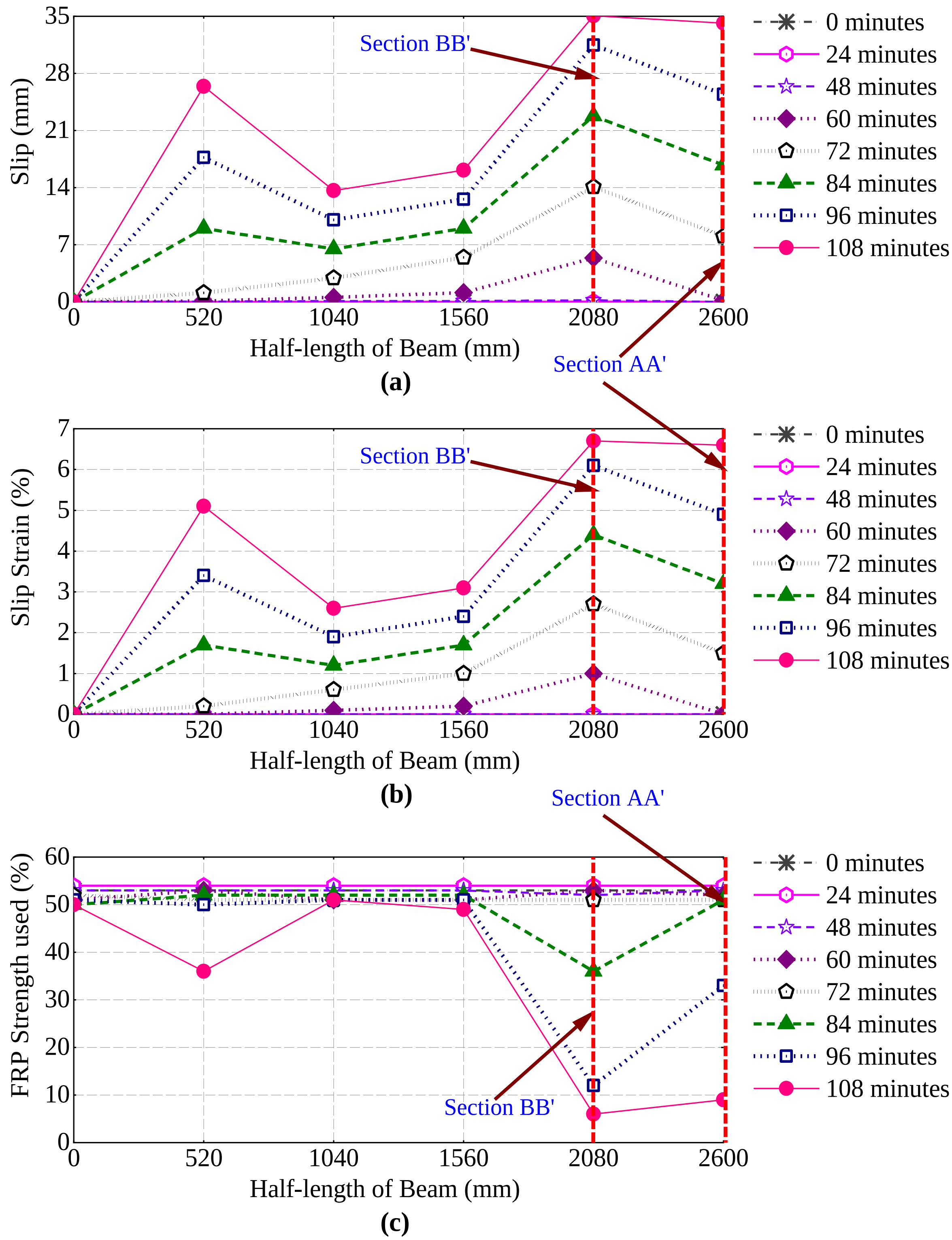

Figure 5.9: Results from the bond slip analysis at various sections along the length of beam B4 analyzed in case C9: (a) total slip; (b) slip strain; (c) strength of CFRP used (only half-length portion is shown)

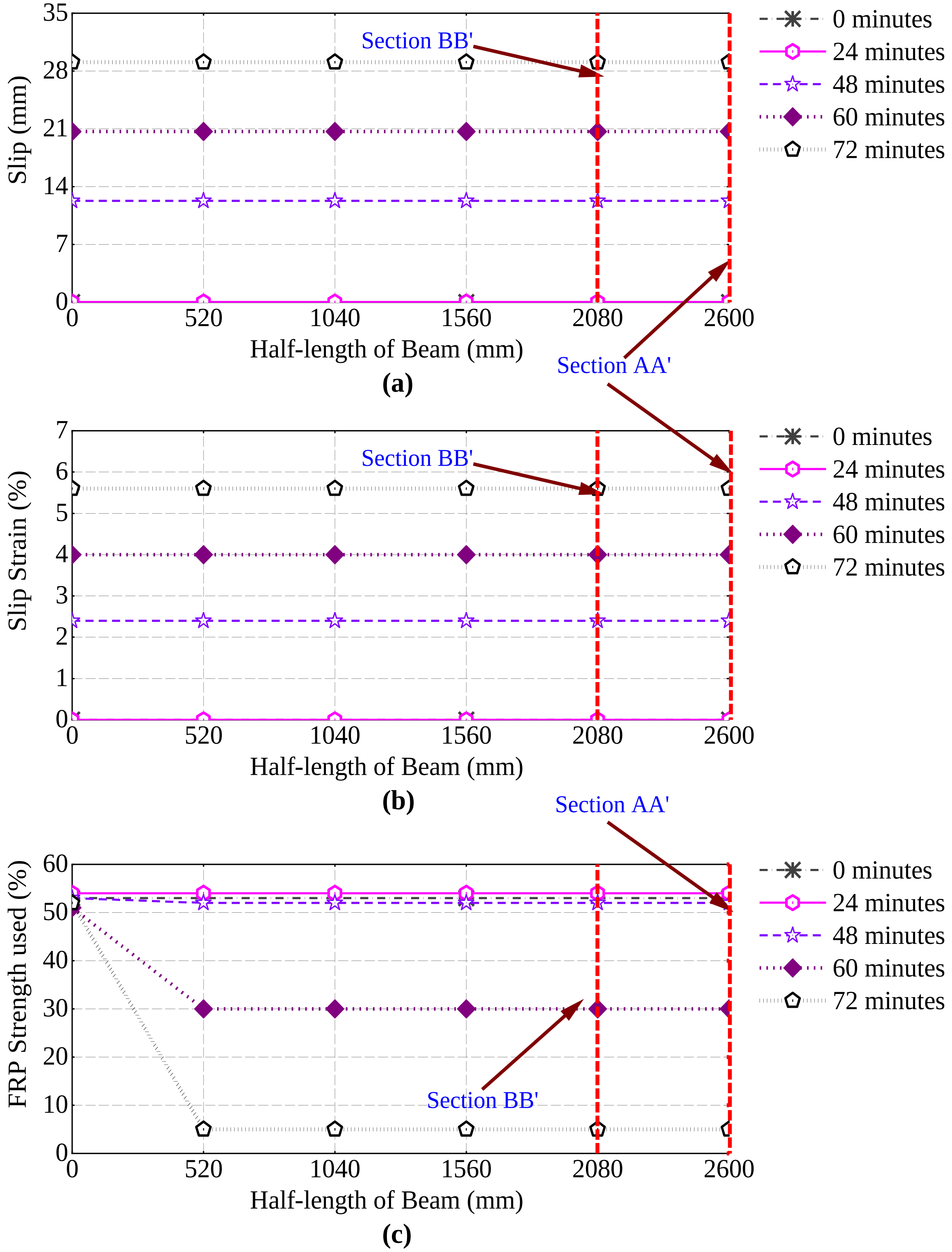

Figure 5.10: Results from the bond slip analysis at various sections along the length of beam B4 analyzed in case C11: (a) total slip; (b) slip strain; (c) strength of CFRP used (only half-length portion is shown)

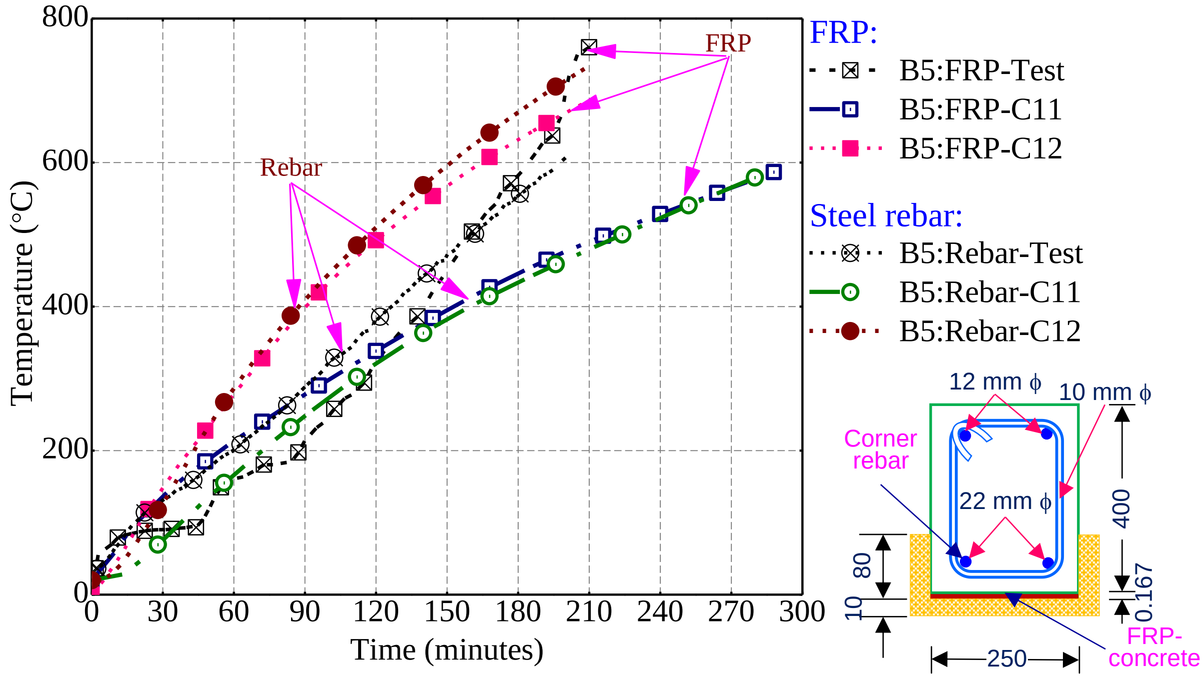

Figure 5.11: Effect of considering or neglecting temperature variation of thermal properties of fire insulation materials on temperature rise in steel rebars and FRP-concrete interface of beam B5

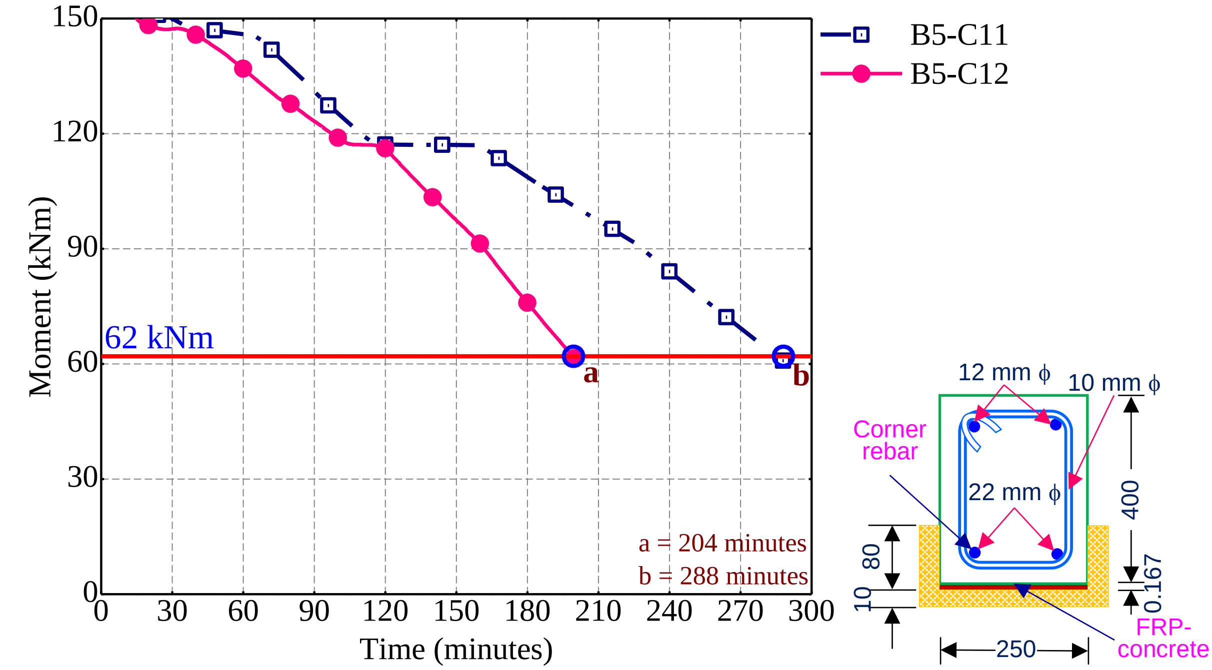

(a)

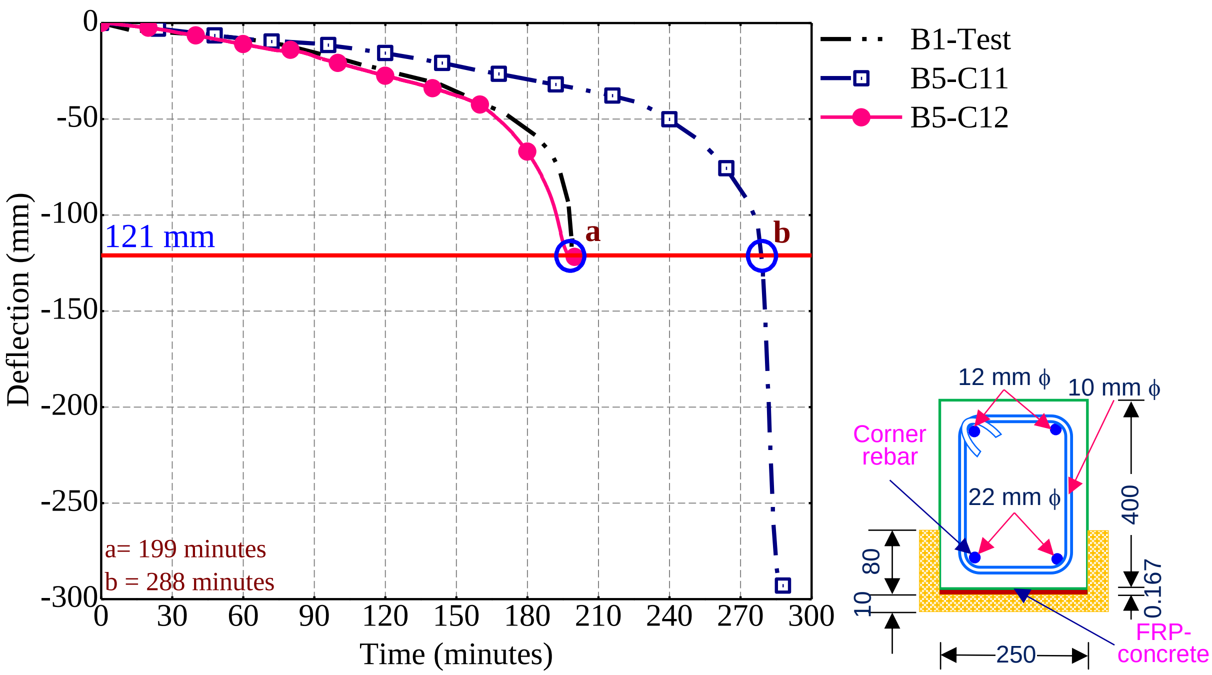

(b)

Figure 5.12: Effect of considering or neglecting temperature variation of thermal properties of fire insulation materials on structural response of beam B5: (a) degradation of moment capacity; (b) deflection

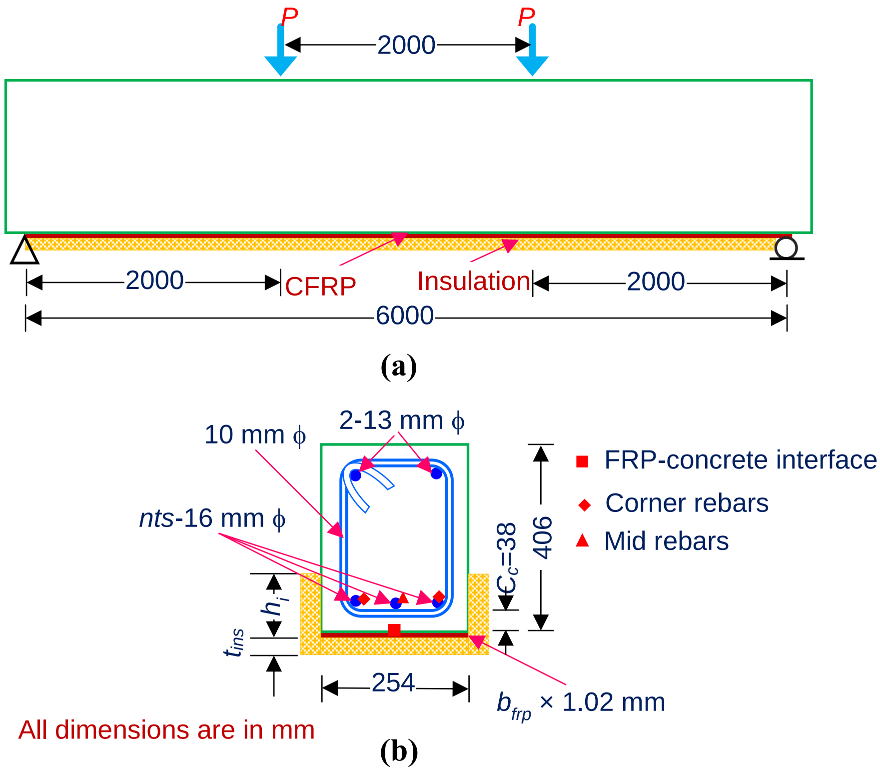

Figure 5.13: Geometrical configuration of RC beam used for the parametric studies: (a) elevation; (b) cross-section

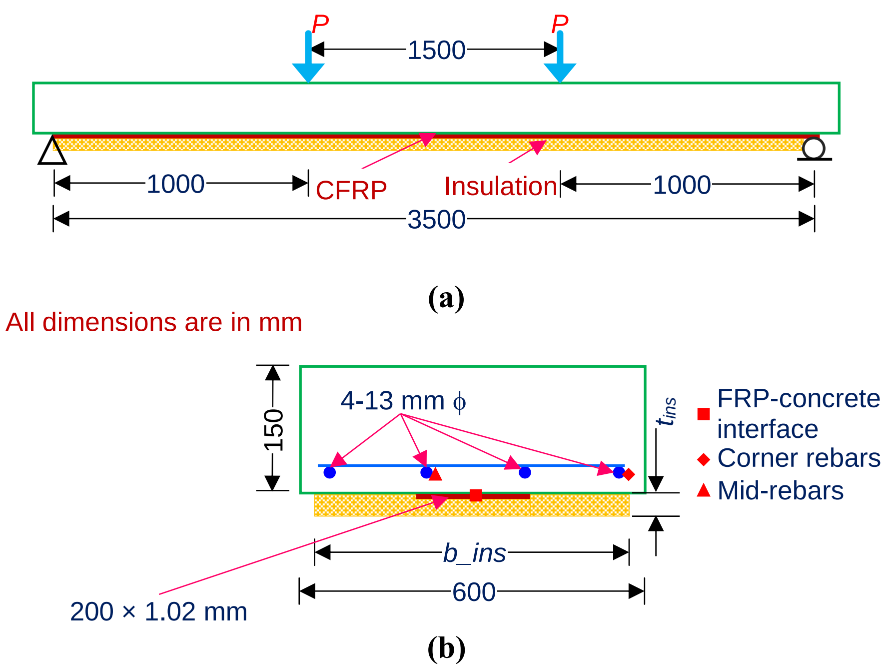

Figure 5.14: Geometrical configuration of RC slab used for the parametric studies: (a) elevation; (b) cross-section

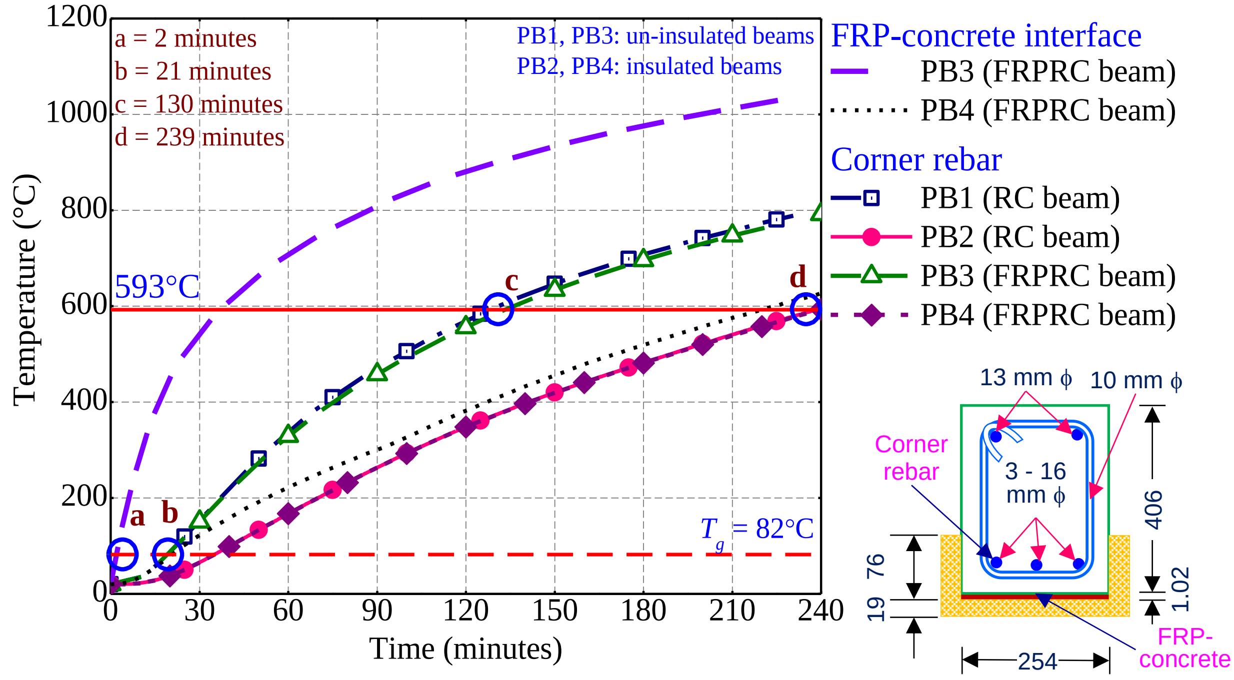

Figure 5.15: Effect of CFRP-strengthening on temperature rise in cross-section of beams PB1 to PB4 analyzed in case PBC1

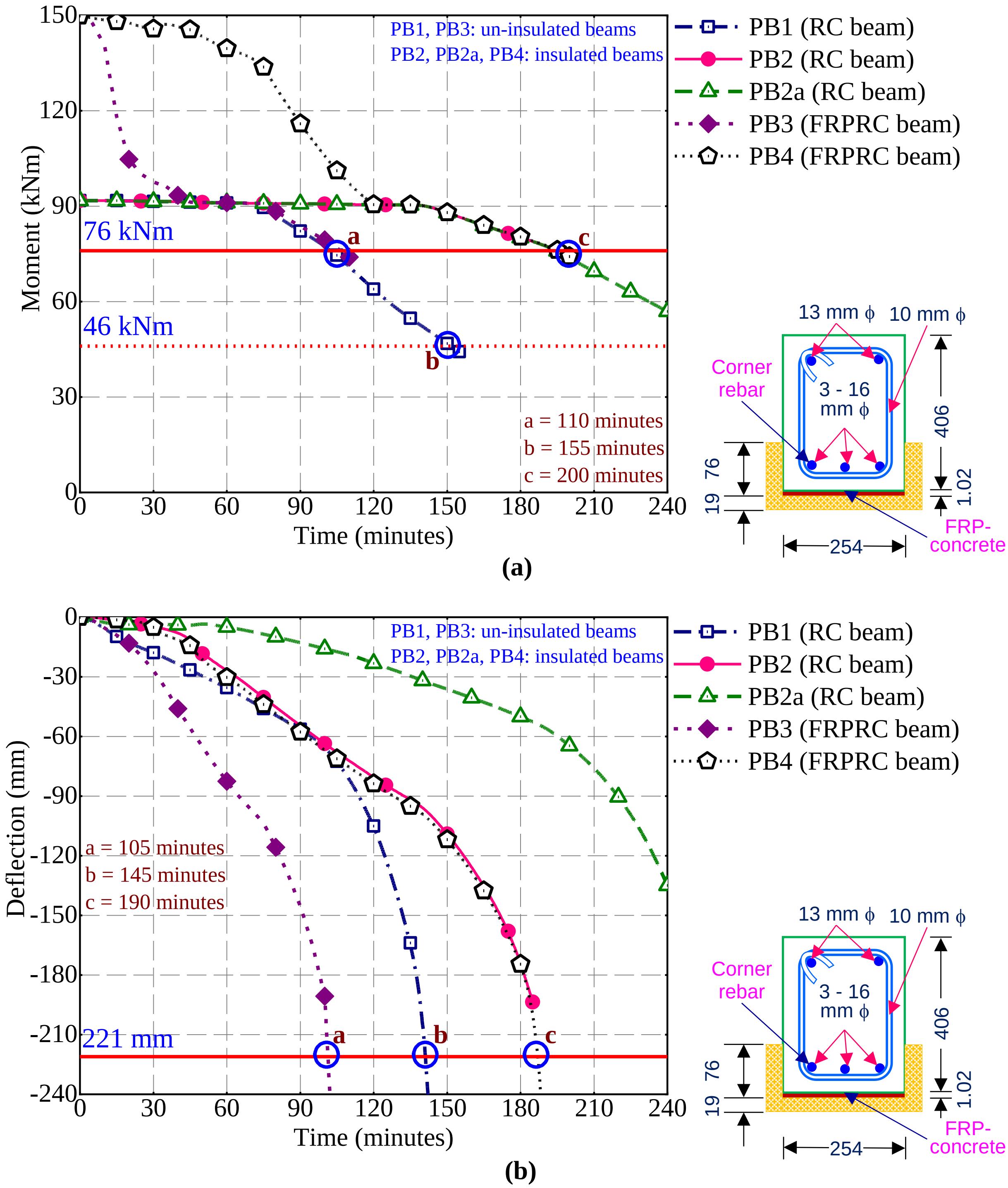

Figure 5.16: Structural response of beams PB1 to PB4 analyzed in case PBC1: (a) degradation in moment capacity; (b)mid-span deflection

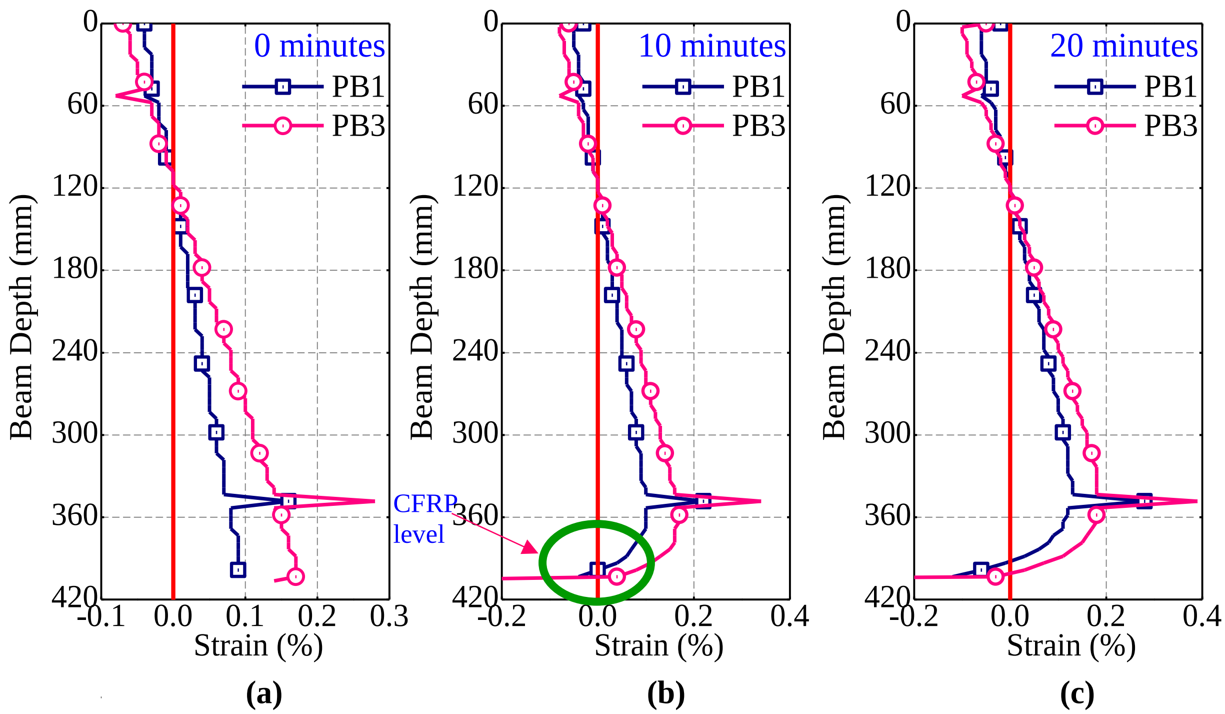

Figure 5.17: Distribution of strains due to applied loading along the depth of beams in early stages of fire exposure: (a) 0 minutes; b) 10 minutes; (c) 20 minutes

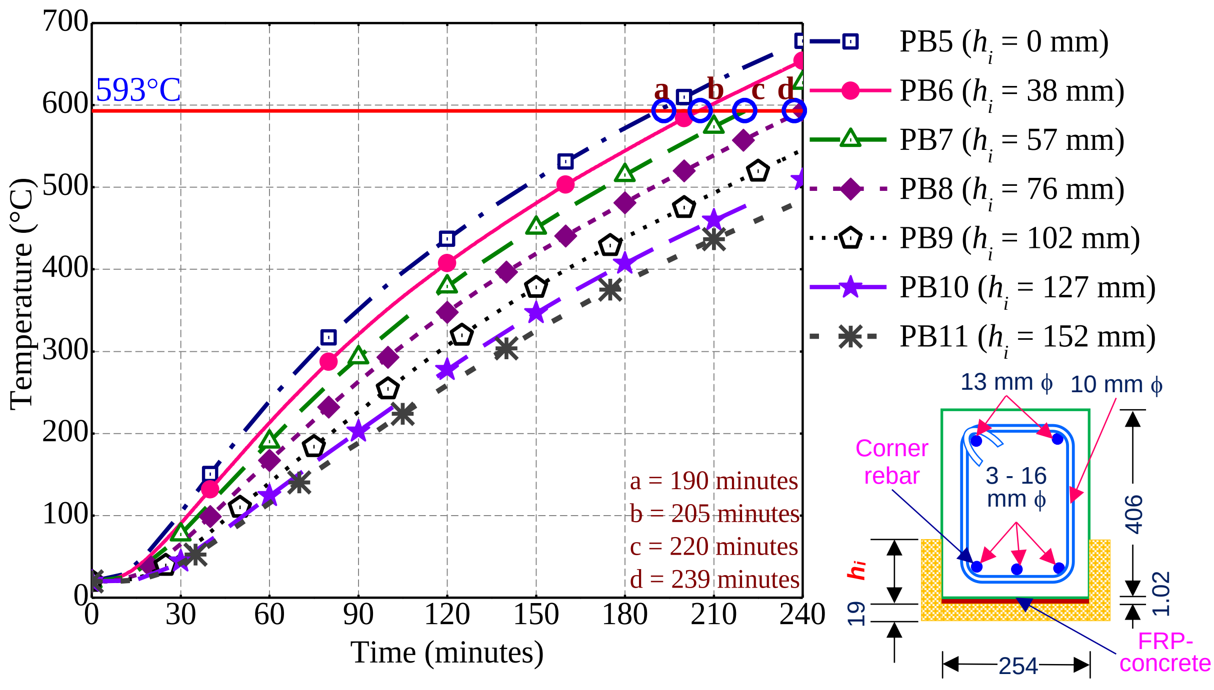

Figure 5.18: Effect of depth of insulation along the sides surfaces of beam on temperature rise in corner rebar of beams PB5 to PB11 analyzed in case PBC2

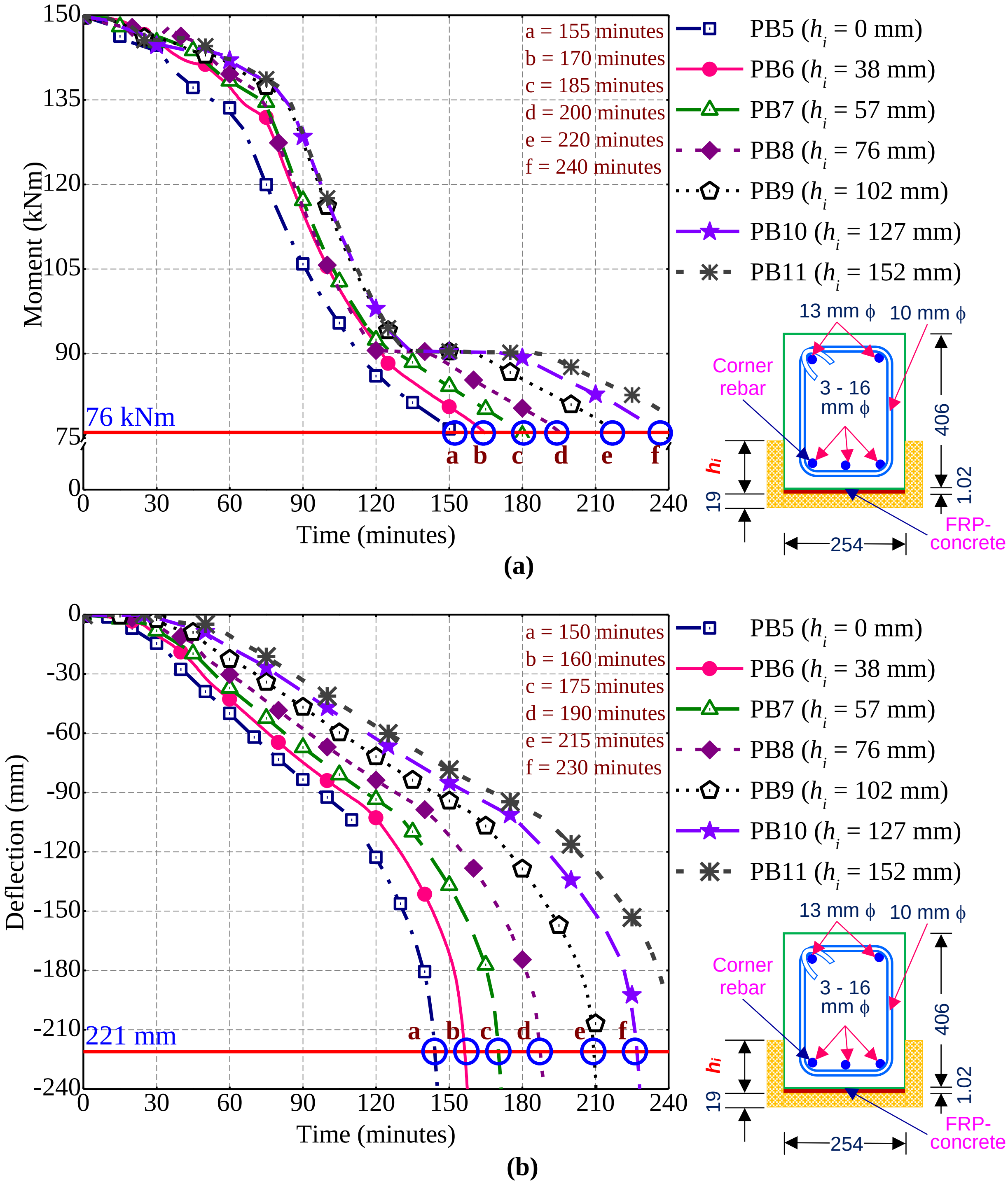

Figure 5.19: Effect of depth of insulation along the sides on structural response of beams PB5 to PB11 analyzed in case PBC2: (a) degradation in moment capacity; (b) mid-span deflection

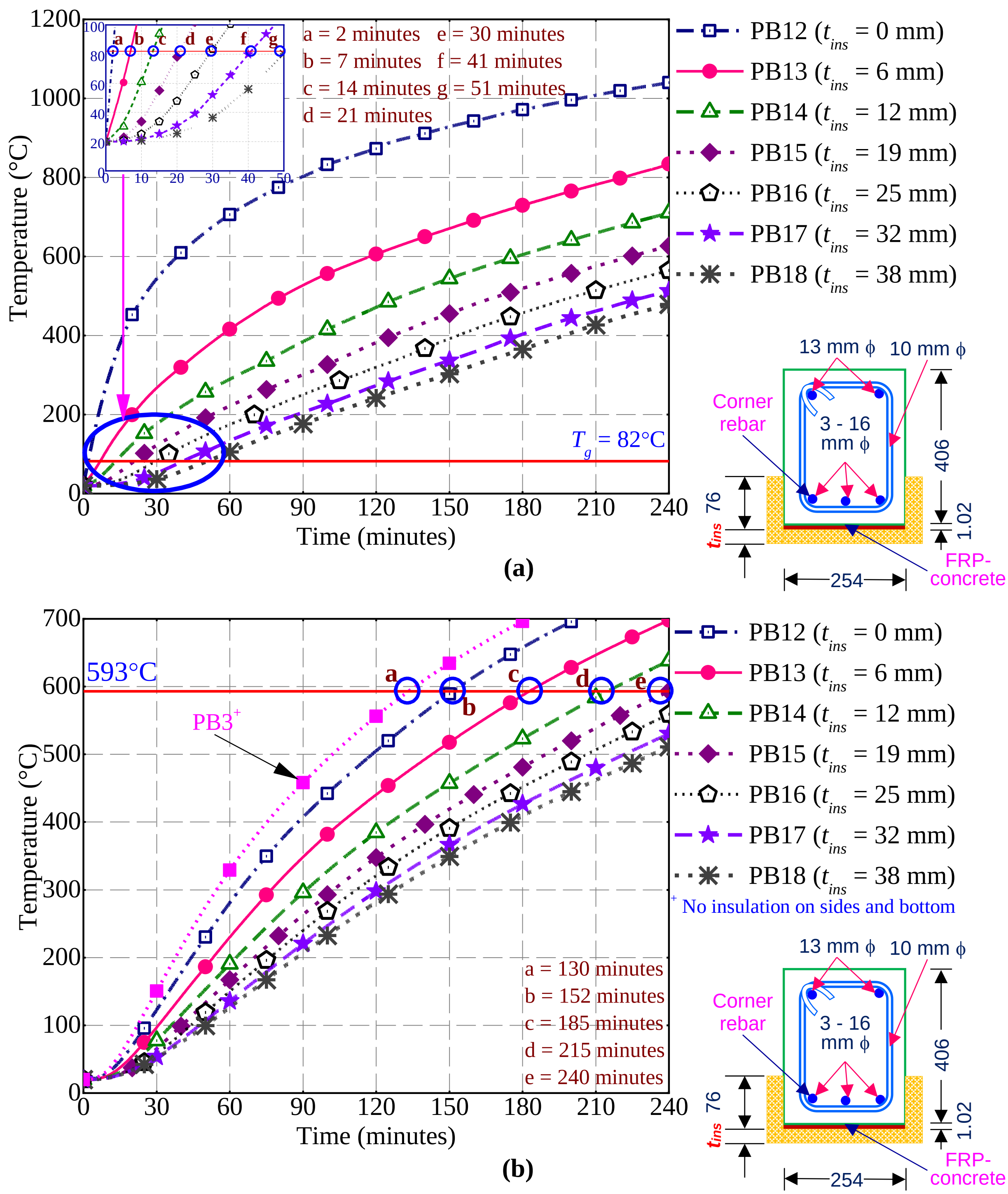

Figure 5.20: Effect of thickness of insulation on temperature rise in beams PB12 to PB18 analyzed in case PBC3: (a) FRP-concrete interface; (b) corner rebar

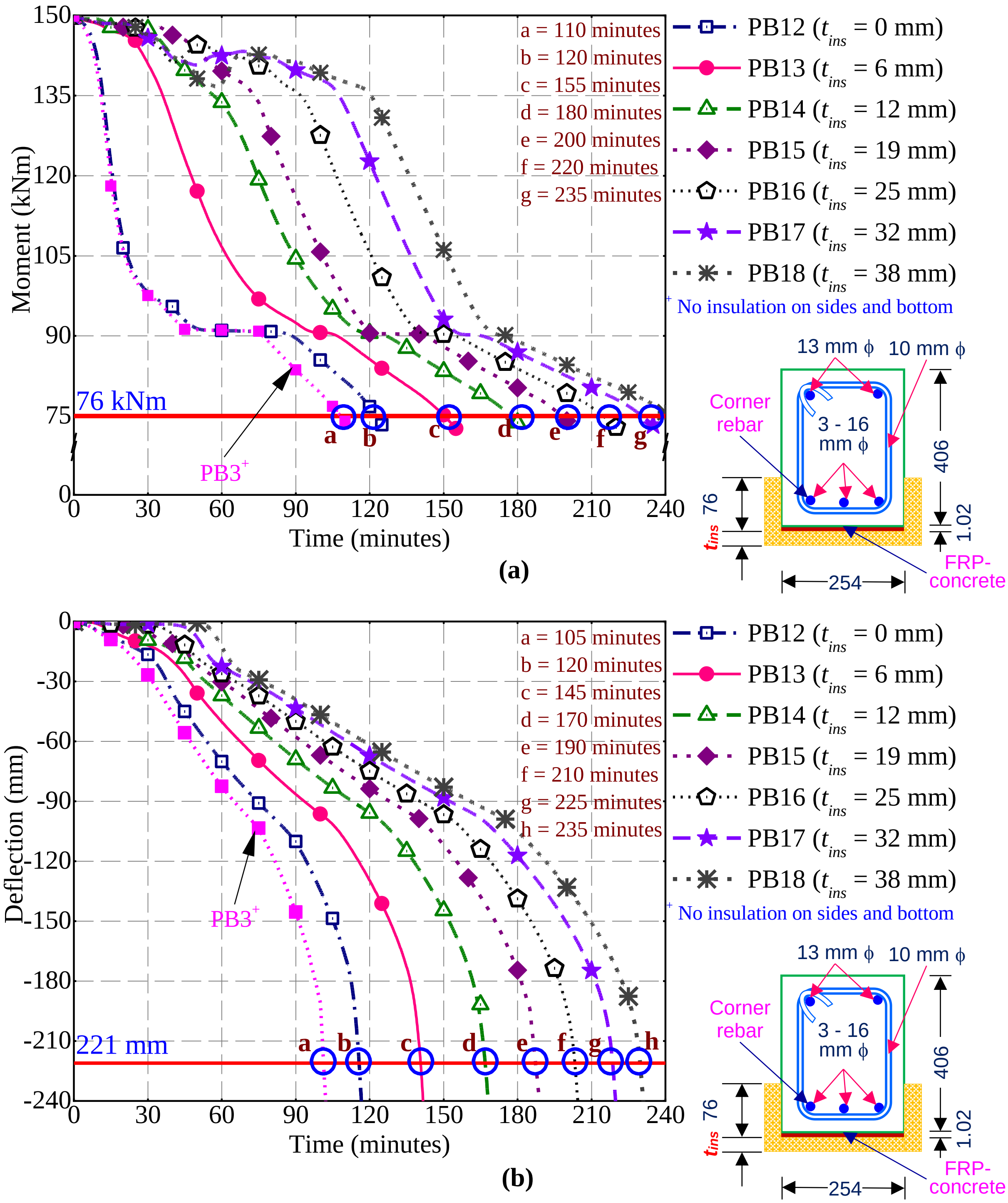

Figure 5.21: Effect of thickness of insulation on structural response of beams PB12 to PB18 analyzed in case PBC3: (a) degradation in moment capacity; (b) mid-span deflection

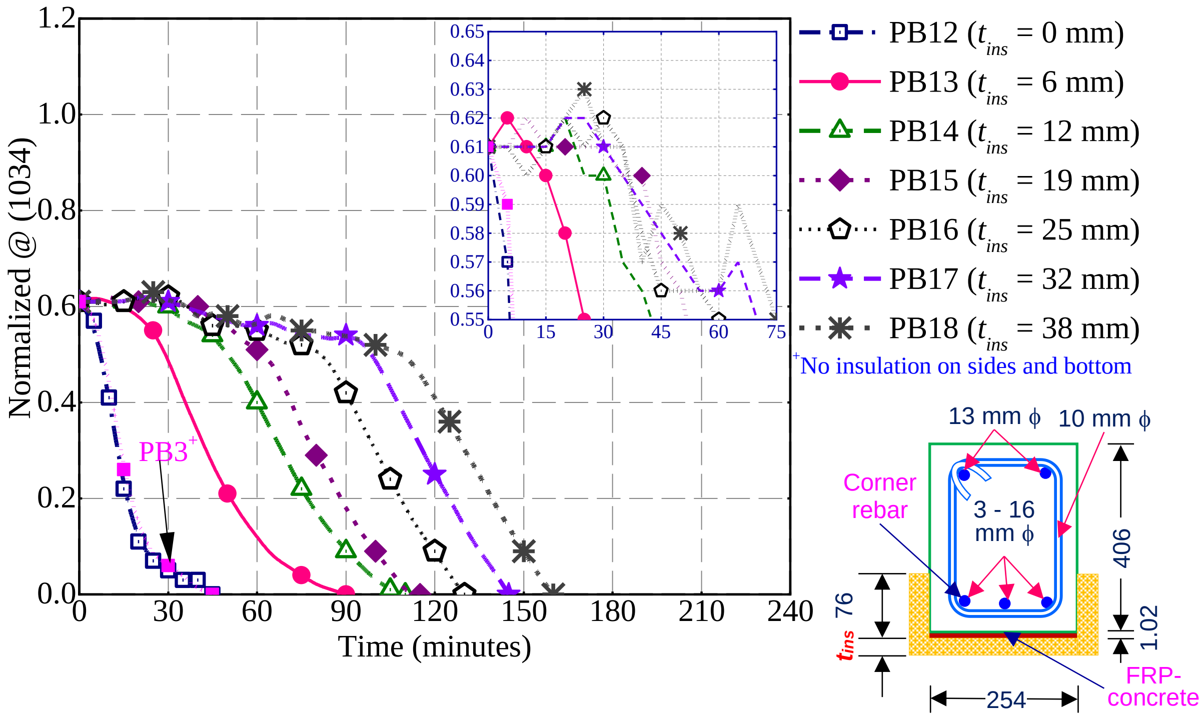

Figure 5.22: Strength contribution of CFRP towards the capacity of mid-span sections in beams PB12 to PB18 normalized with respect to strength at ambient temperature

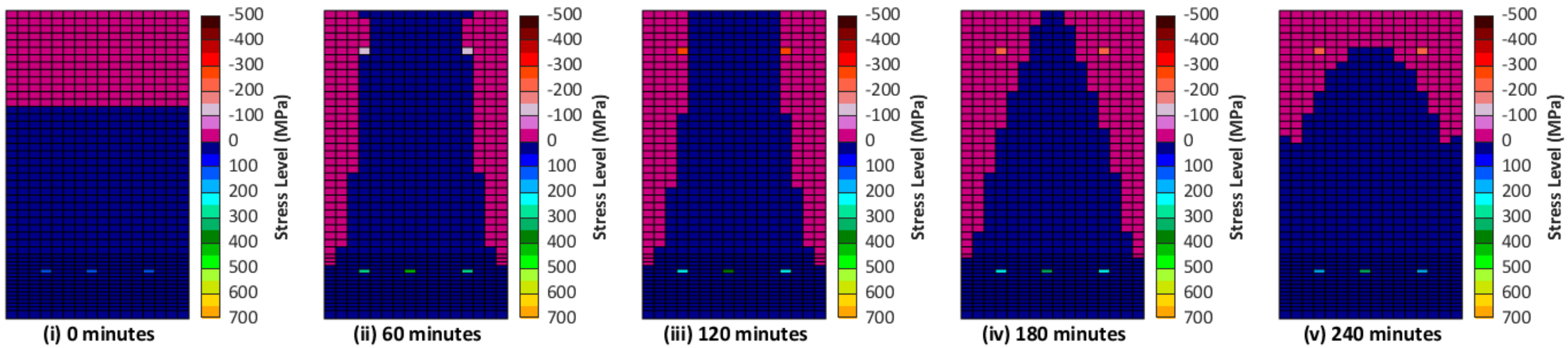

(a)

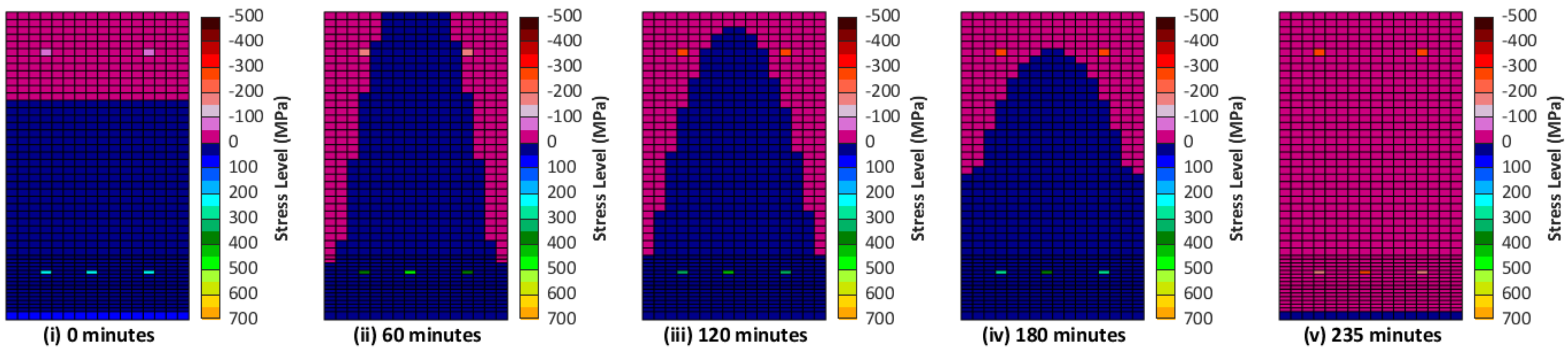

(b)

Figure 5.23: Stress distribution due to applied loading at each one-hour interval until failure in the cross-section at mid-span of beams analyzed in case PBC4: (a) PB19; (b) PB20; (c) PB21; (d) PB22; (e) PB23

Figure 5.23 (cont'd)

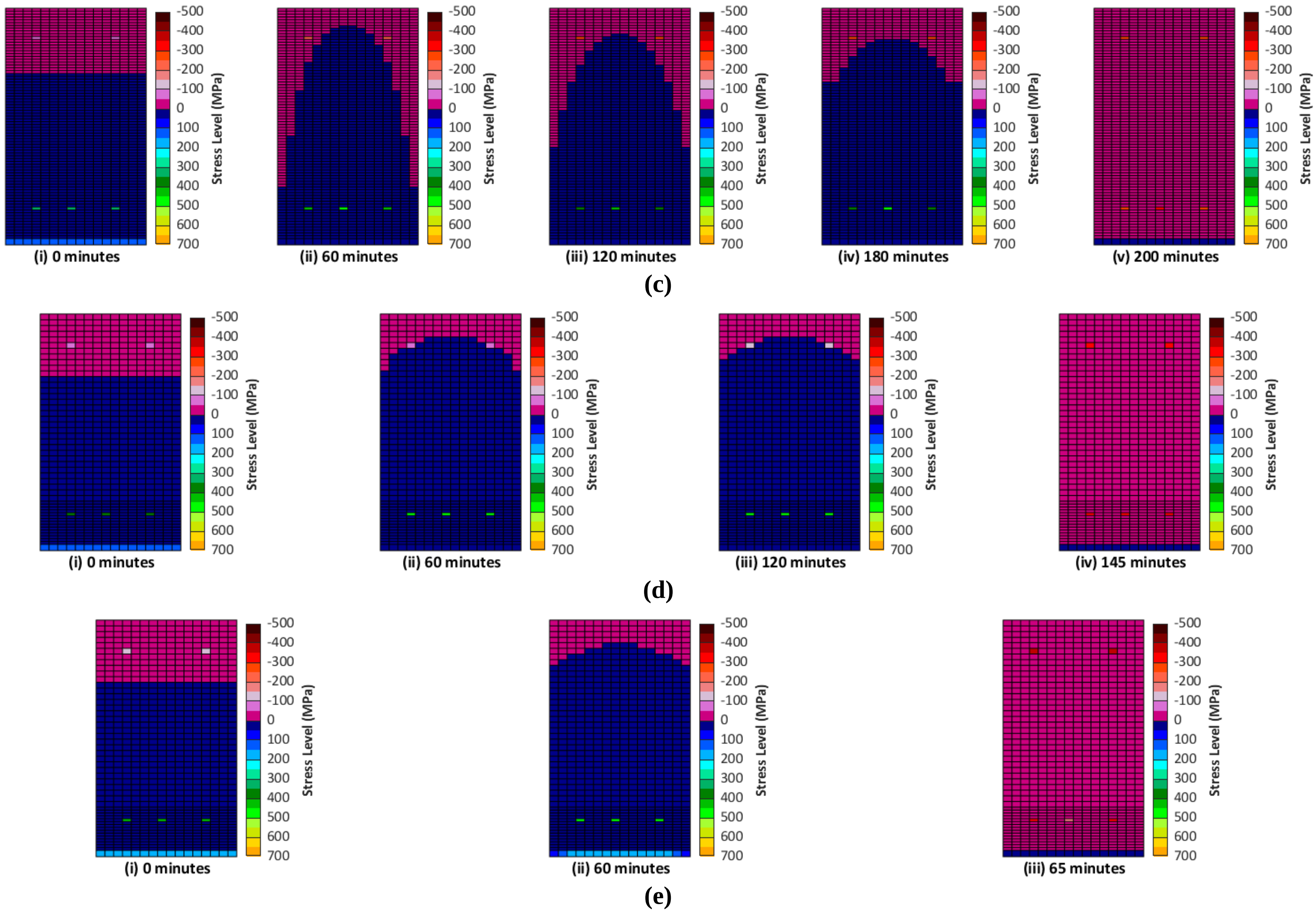

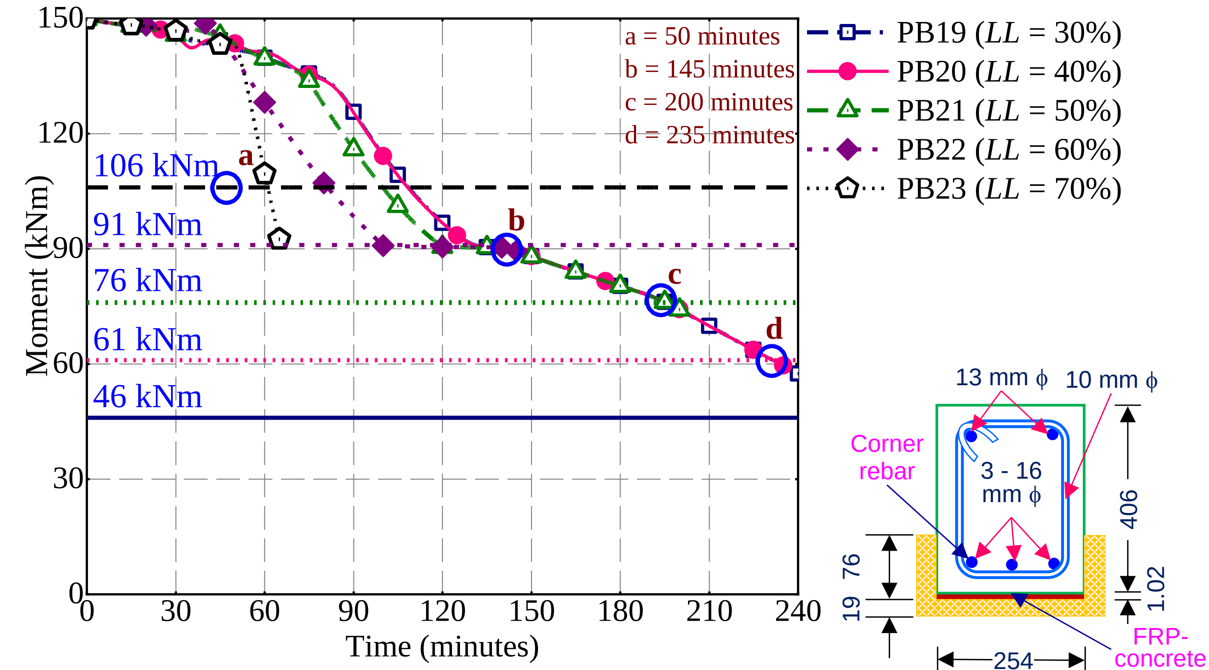

(a)

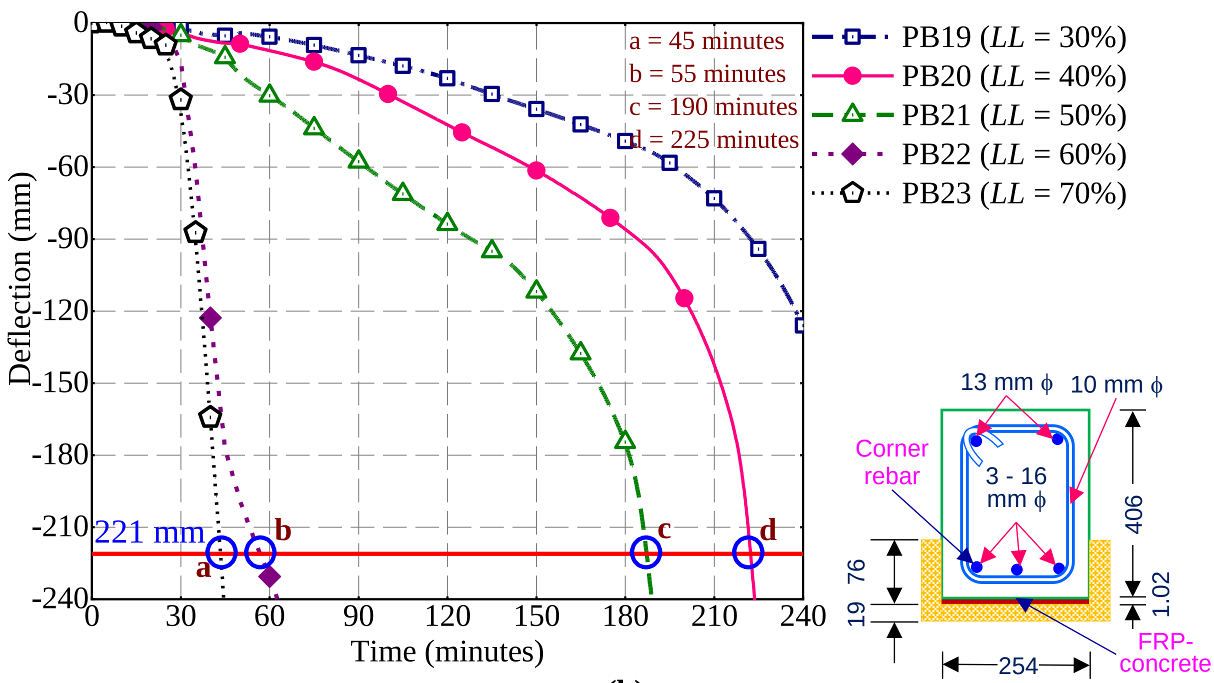

(b)

Figure 5.24: Effect of applied load level on structural response of beams PB19 to PB23 analyzed in case PBC4: (a) degradation in moment capacity; (b) mid-span deflection

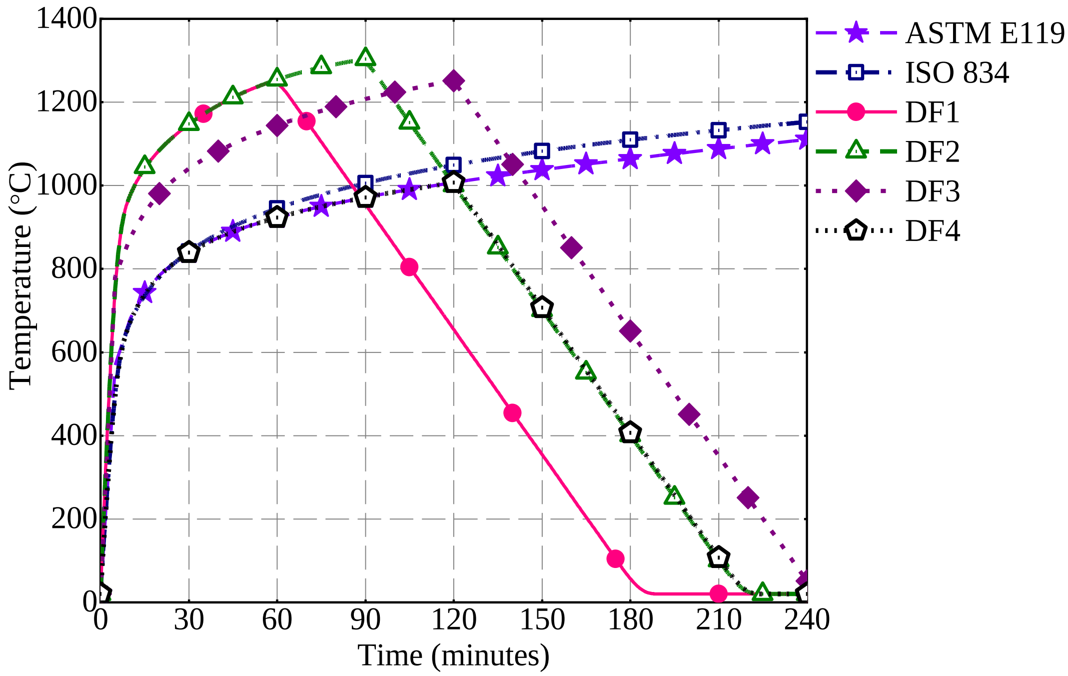

Figure 5.25: Time-temperature curves of different fire scenarios used in parametric study on FRP-strengthened concrete flexural members (cases PBC5 and PSC4)

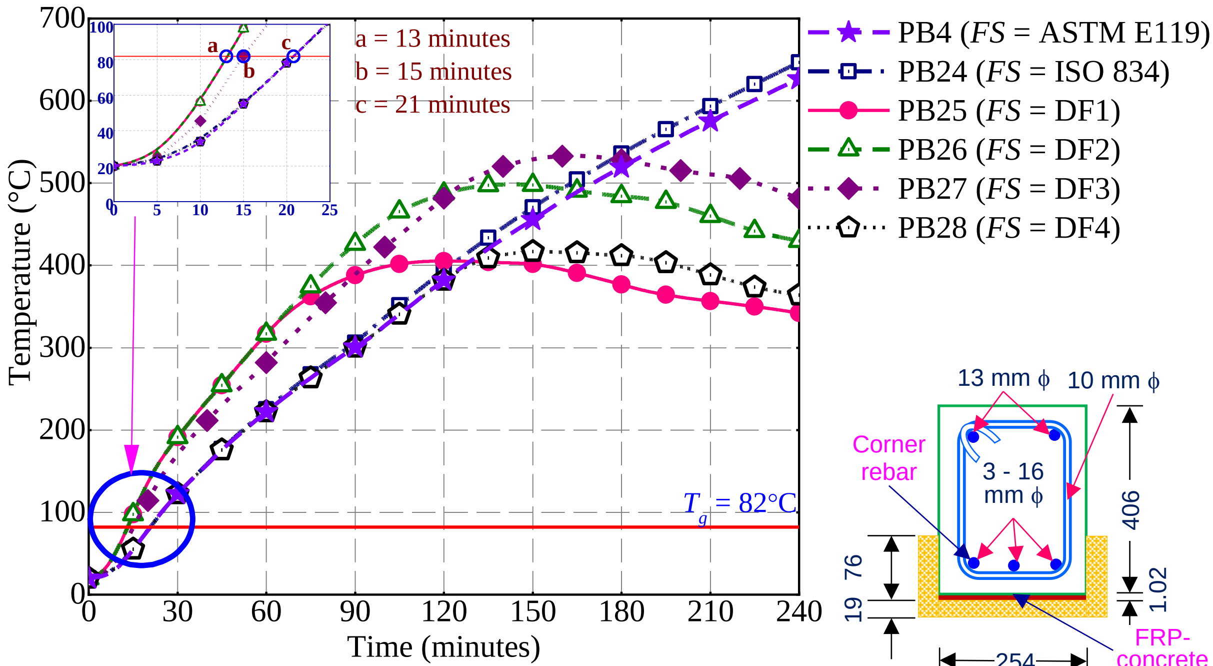

(a)

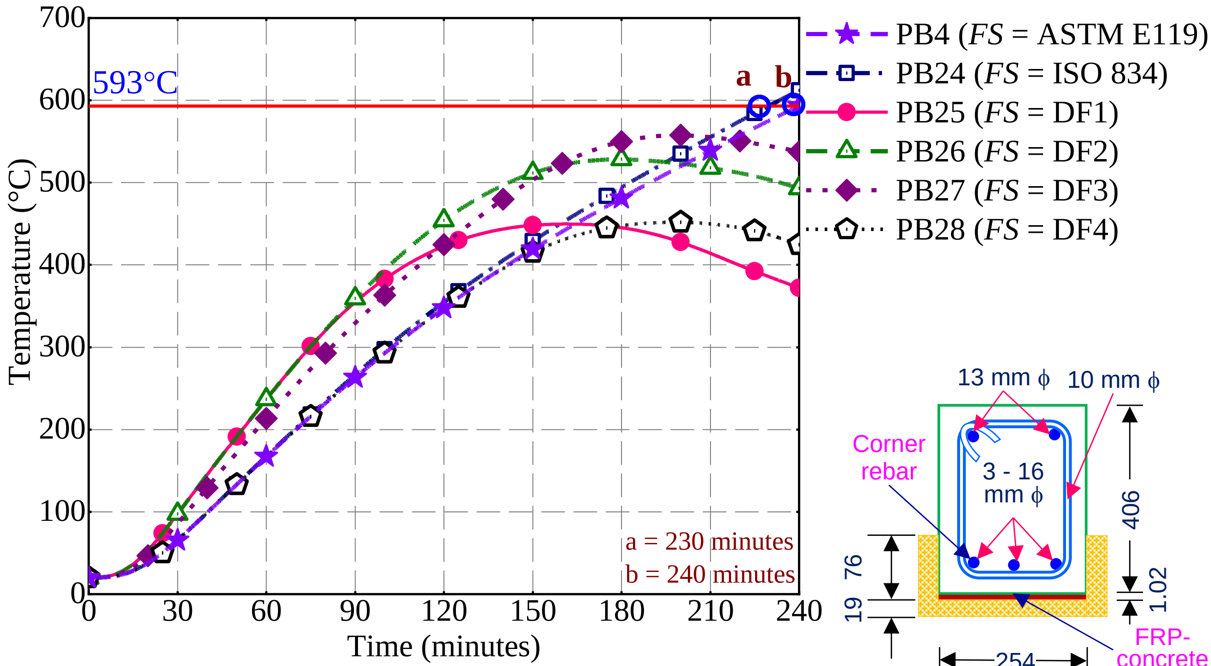

(b)

Figure 5.26: Effect of different fire scenarios on temperature rise in beams PB4, PB24 to PB28: (a) FRP-concrete interface; (b) corner rebar

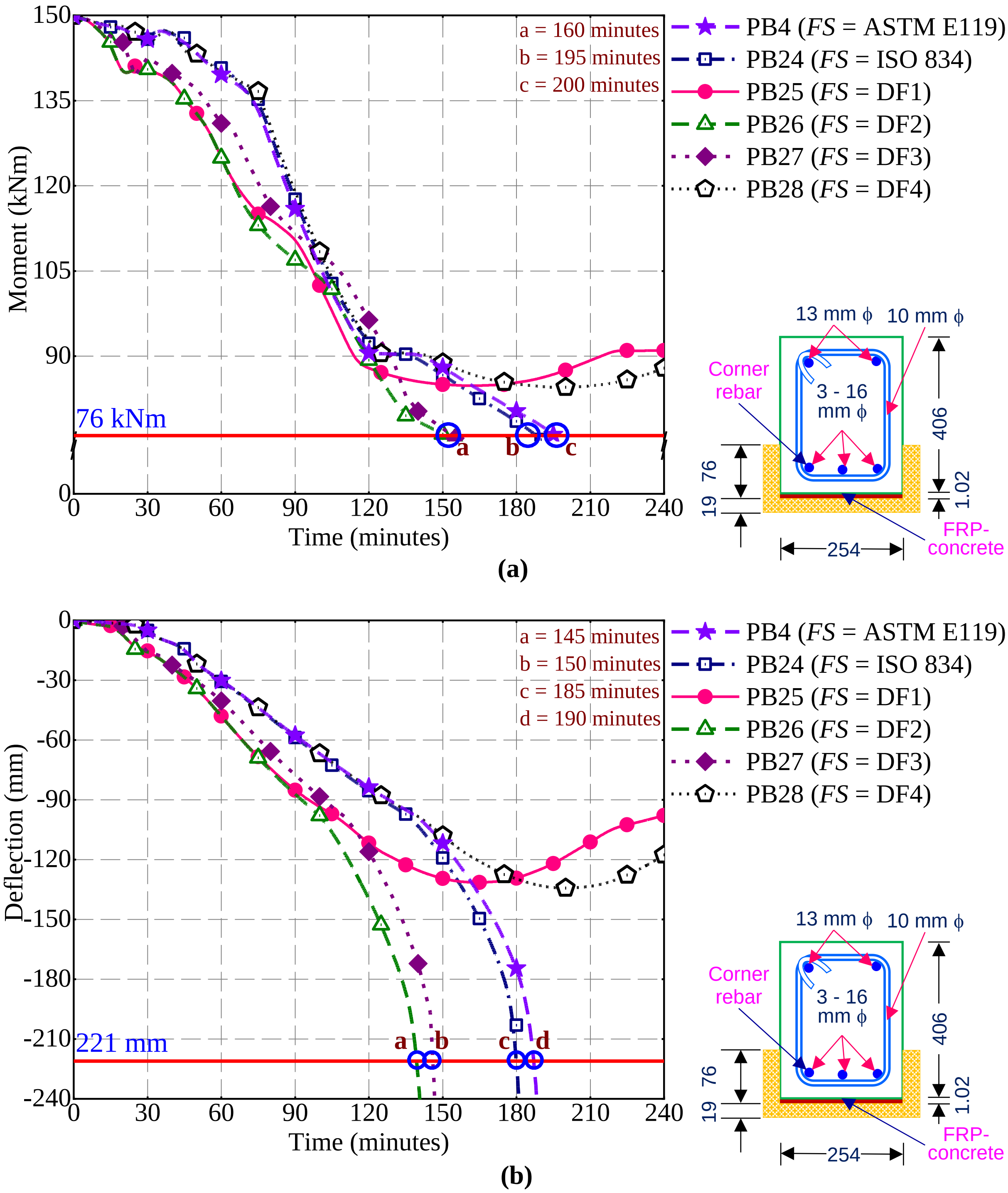

Figure 5.27: Effect of different fire scenarios on structural response of beams PB4, PB24 to PB28: (a) moment capacity degradation; (b) mid-span deflection

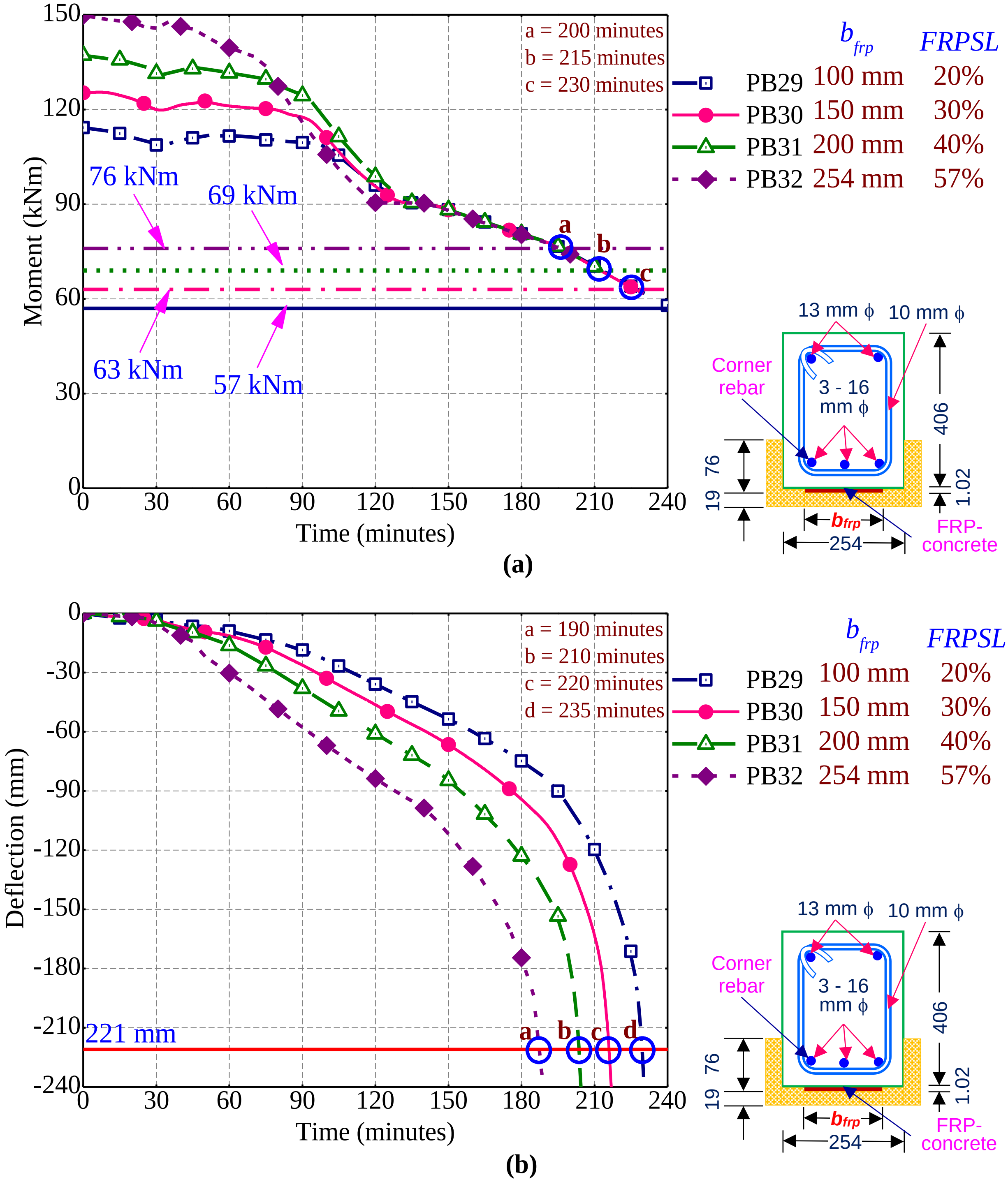

Figure 5.28: Effect of CFRP-strengthening level on structural response of beams PB29 to PB32 analyzed in case PBC6: (a) degradation in moment capacity; (b) mid-span deflection

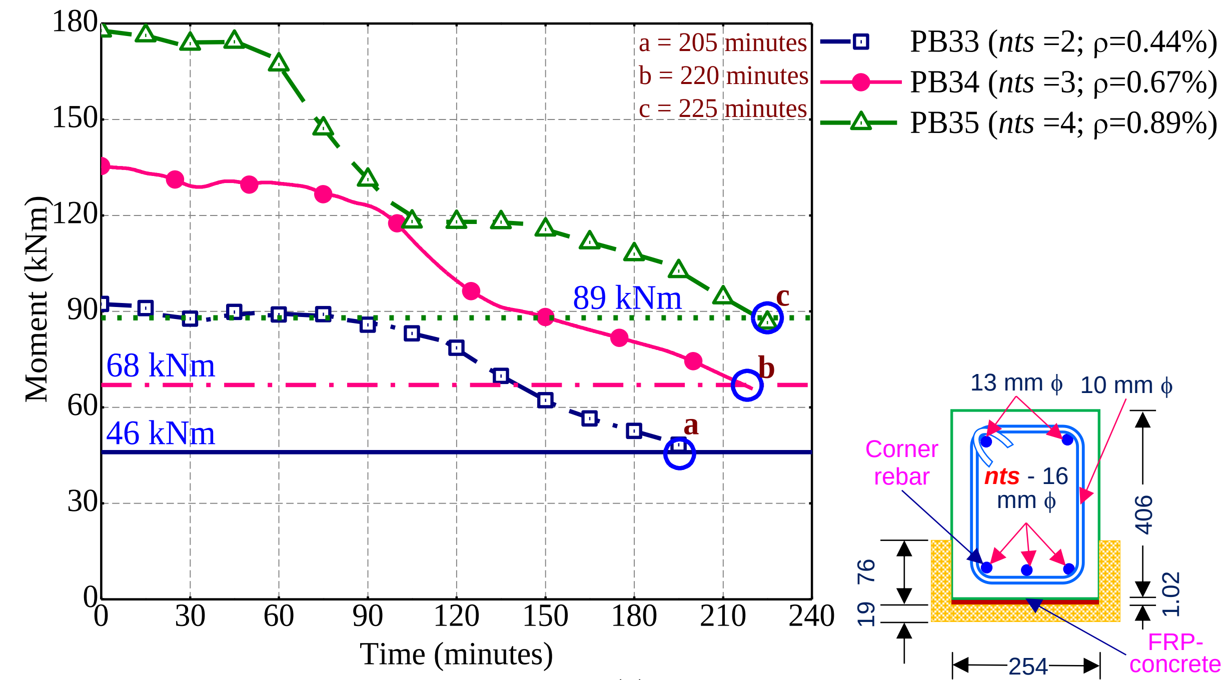

(a)

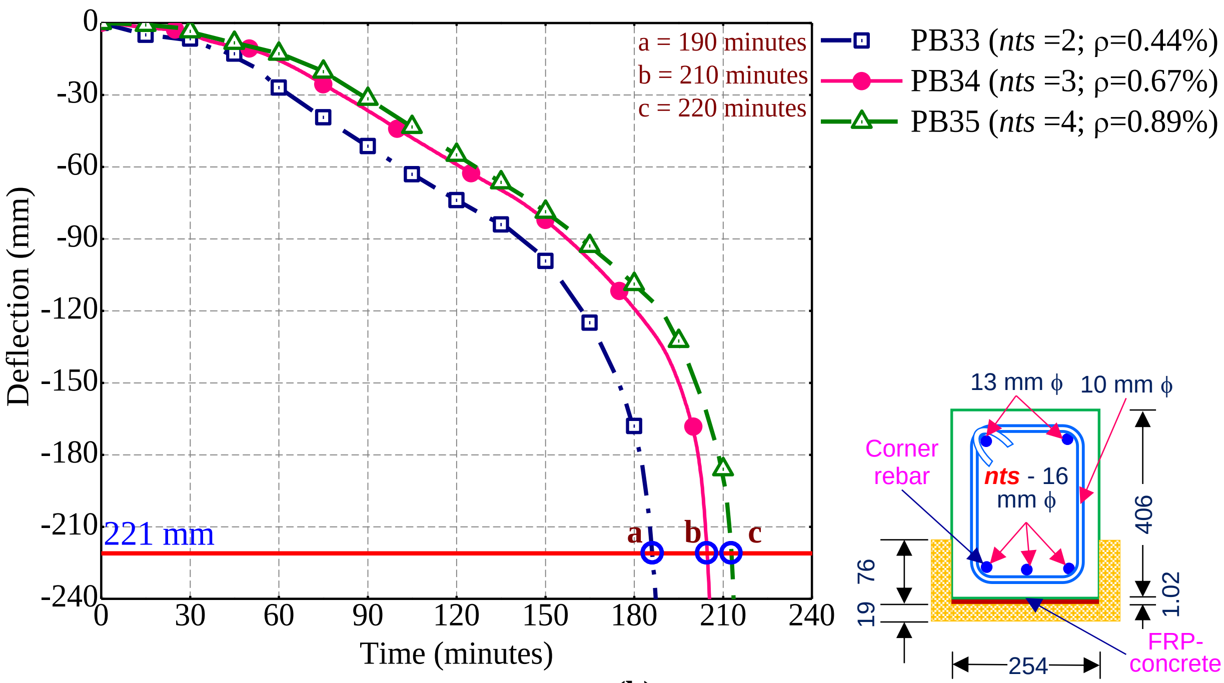

(b)

Figure 5.29: Effect of steel reinforcement ratio on structural response of beams PB33 to PB35 analyzed in case PBC7: (a) degradation in moment capacity; (b) mid-span deflection

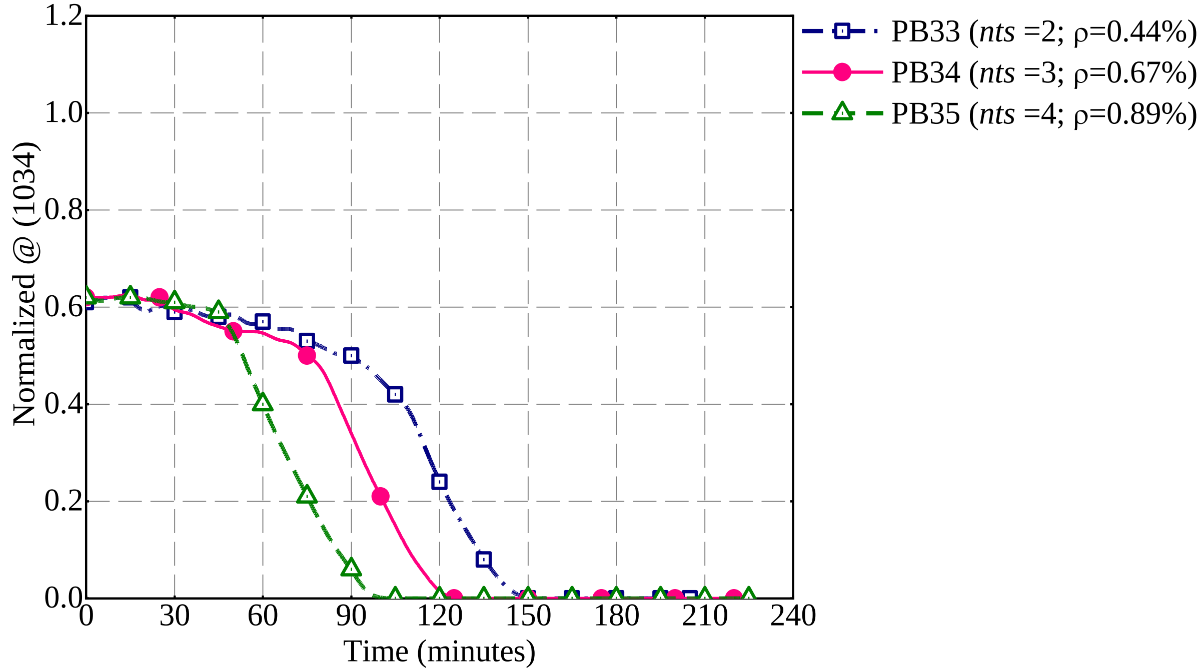

Figure 5.30: Normalized strength contribution of CFRP towards the capacity of beams PB33, PB34, and PB35 analyzed in case PBC7

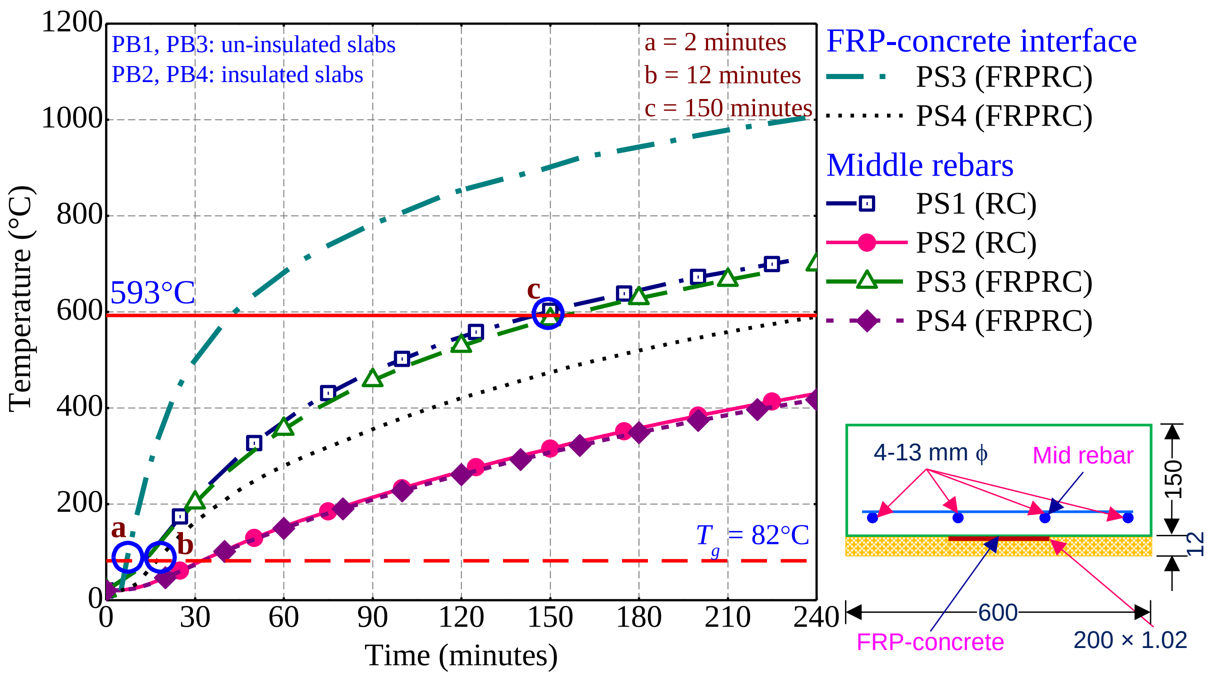

Figure 5.31: Effect of CFRP-strengthening on temperature rise in cross-section of slabs PS1 to PS4 analyzed in case PSC1

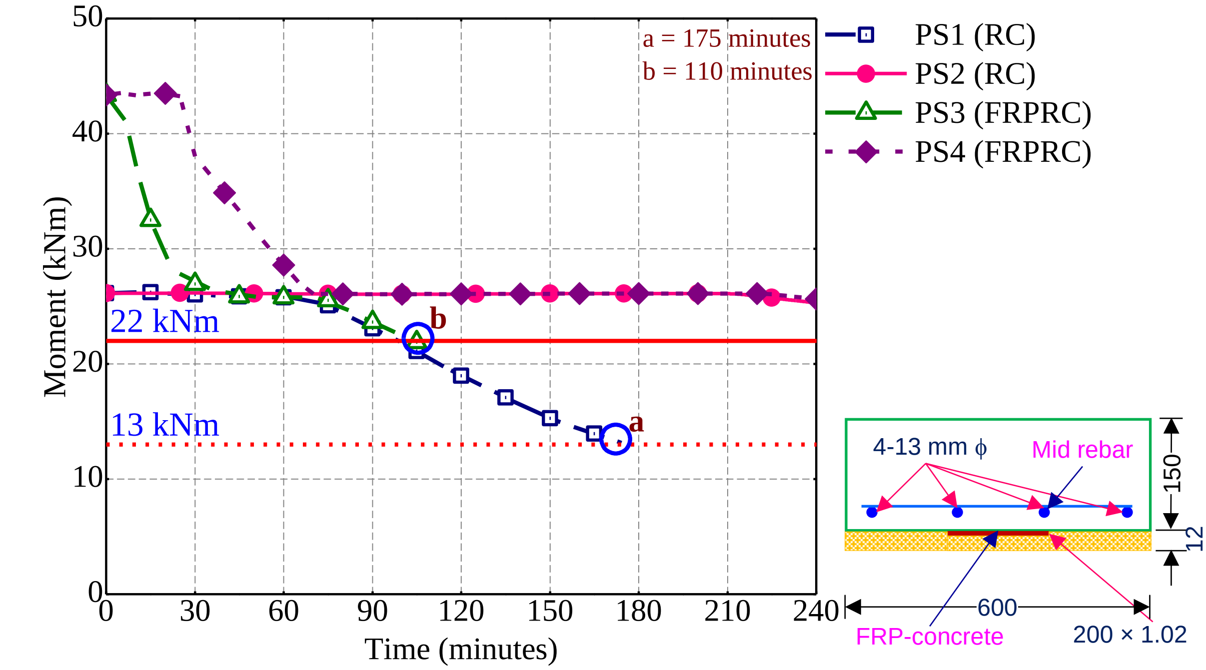

(a)

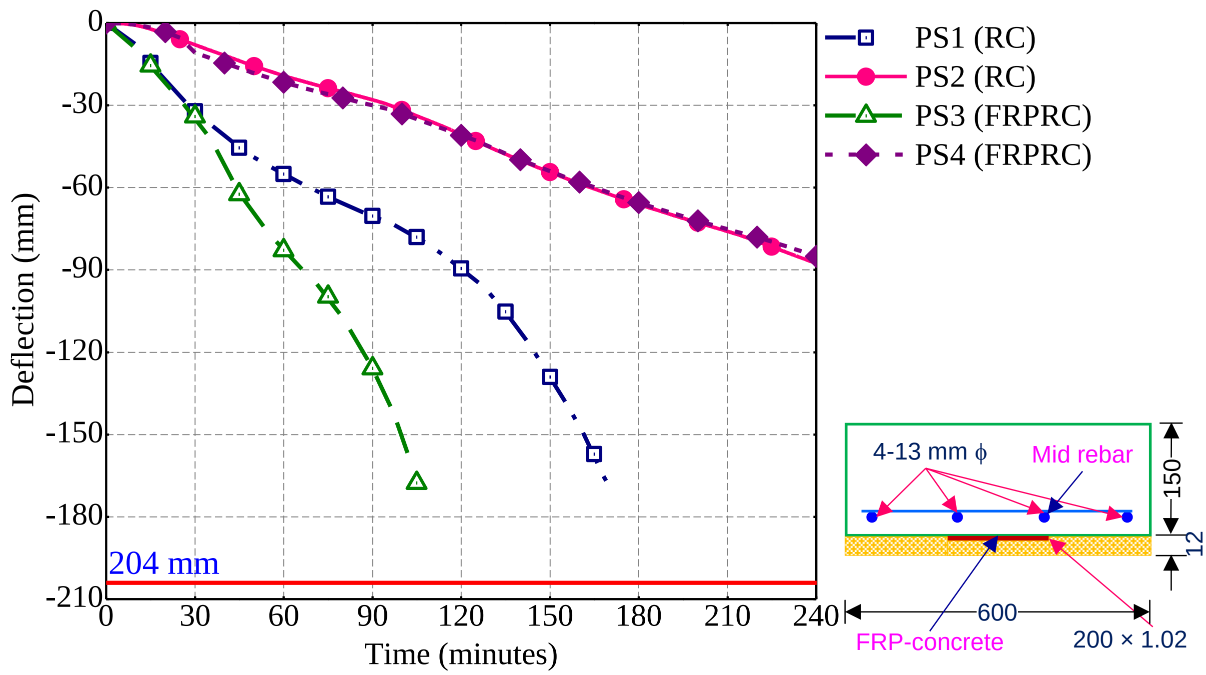

(b)

Figure 5.32: Effect of CFRP-strengthening on structural response of slabs PS1 to PS4 analyzed in case PSC1: (a) degradation in moment capacity; (b) deflection

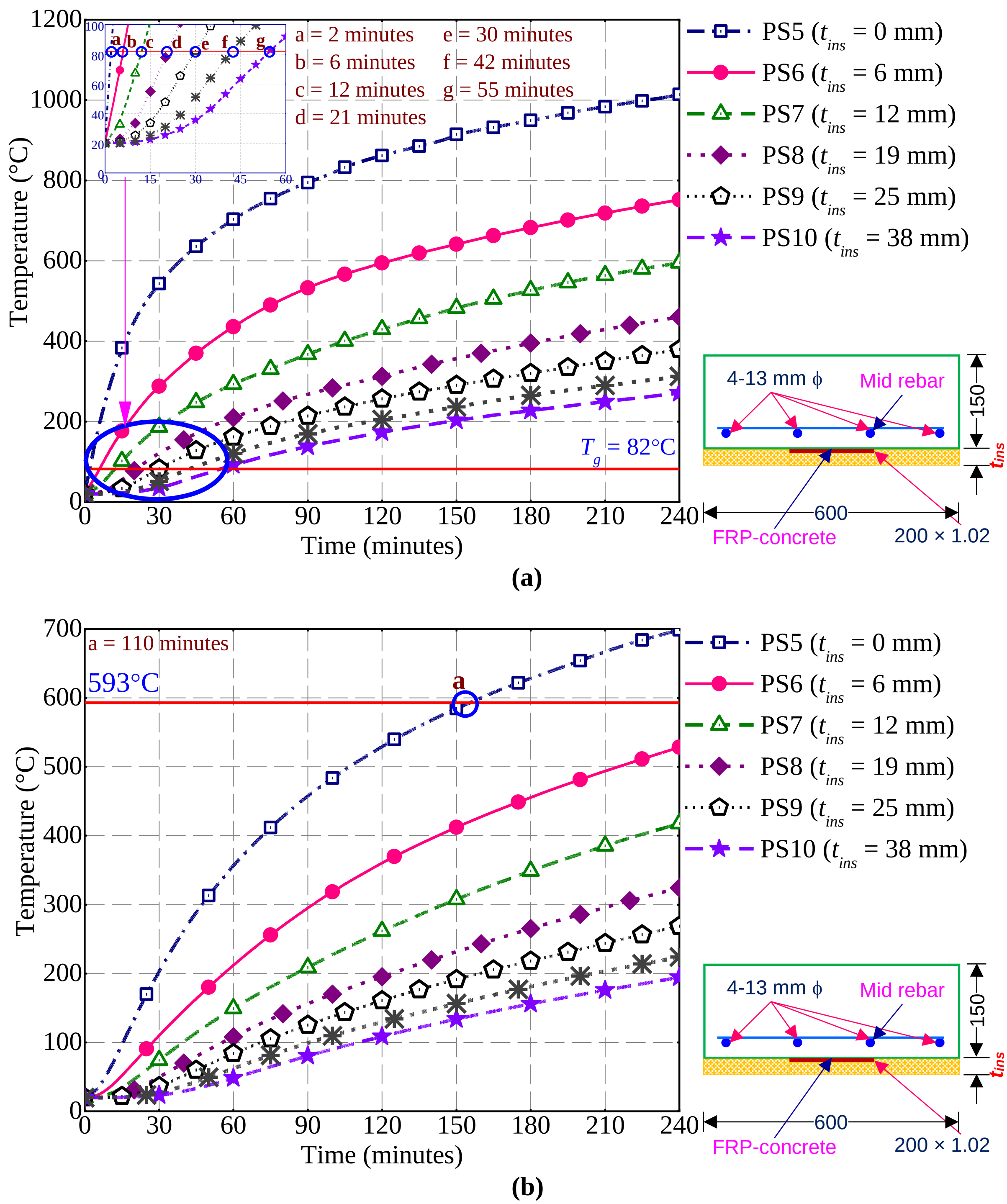

Figure 5.33: Effect of thickness of insulation on temperature rise in slabs PS5 to PB10 analyzed in case PSC2: (a) FRP-concrete interface; (b) mid rebars

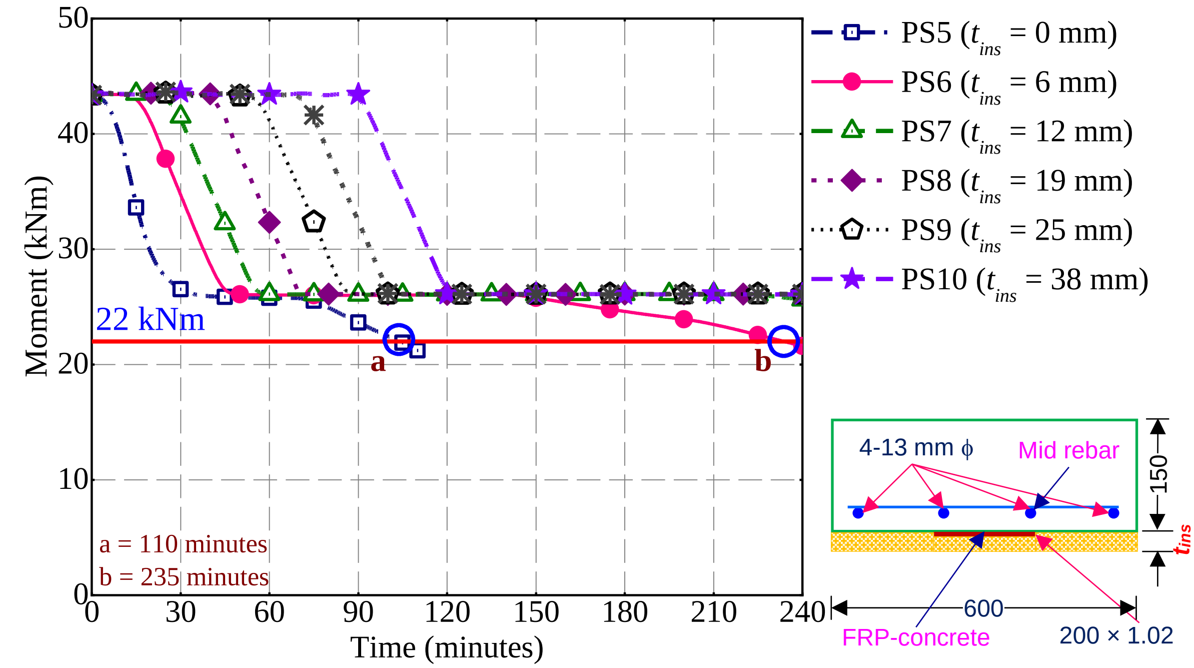

(a)

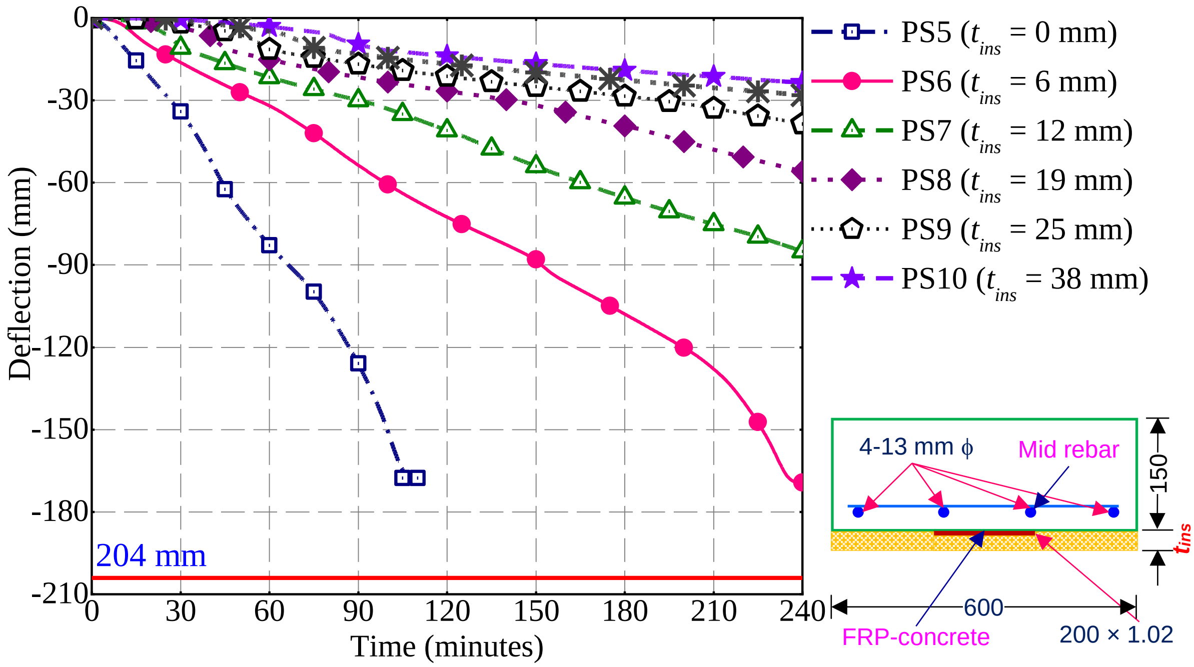

(b)

Figure 5.34: Effect of thickness of insulation on structural response of slabs PS5 to PB10 analyzed in case PSC2: (a) degradation in moment capacity; (b) deflection

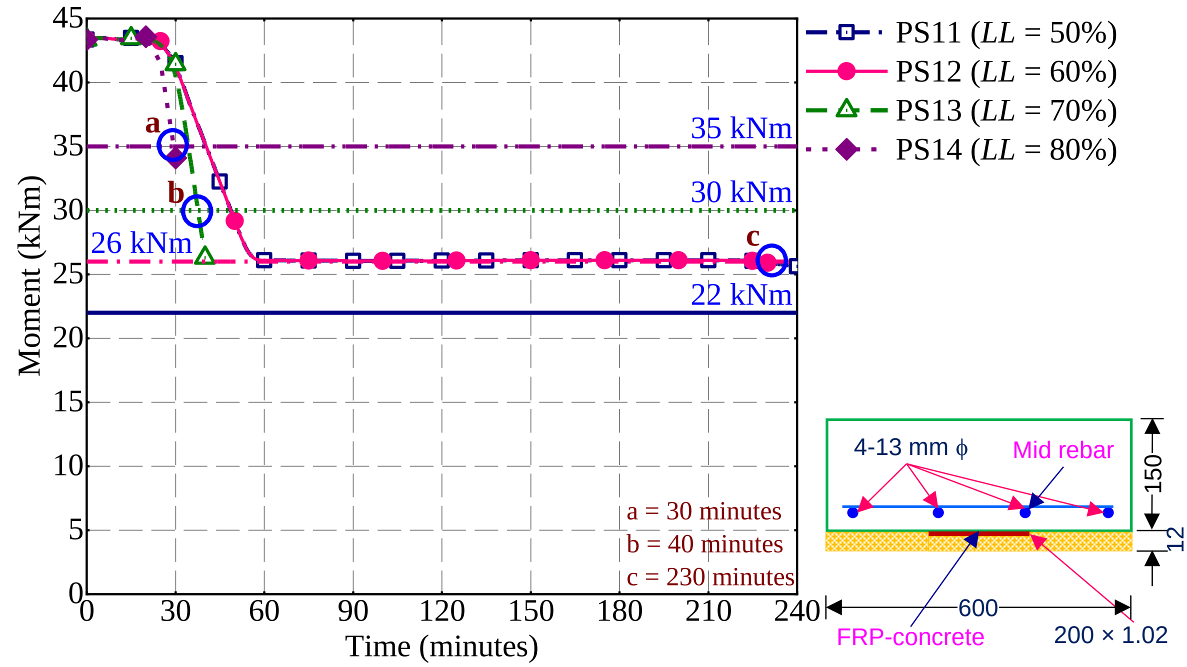

(a)

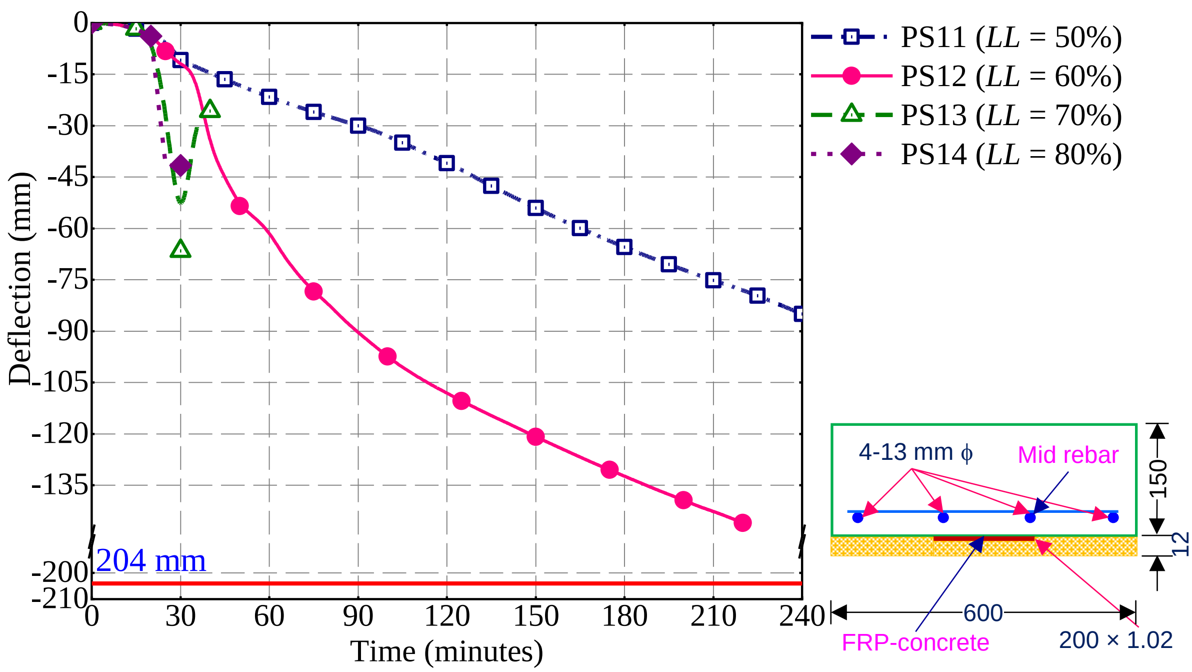

(b)

Figure 5.35: Effect of applied load level on structural response of slabs PS11 to PS14 analyzed in case PSC3: (a) degradation in moment capacity; (b) deflection

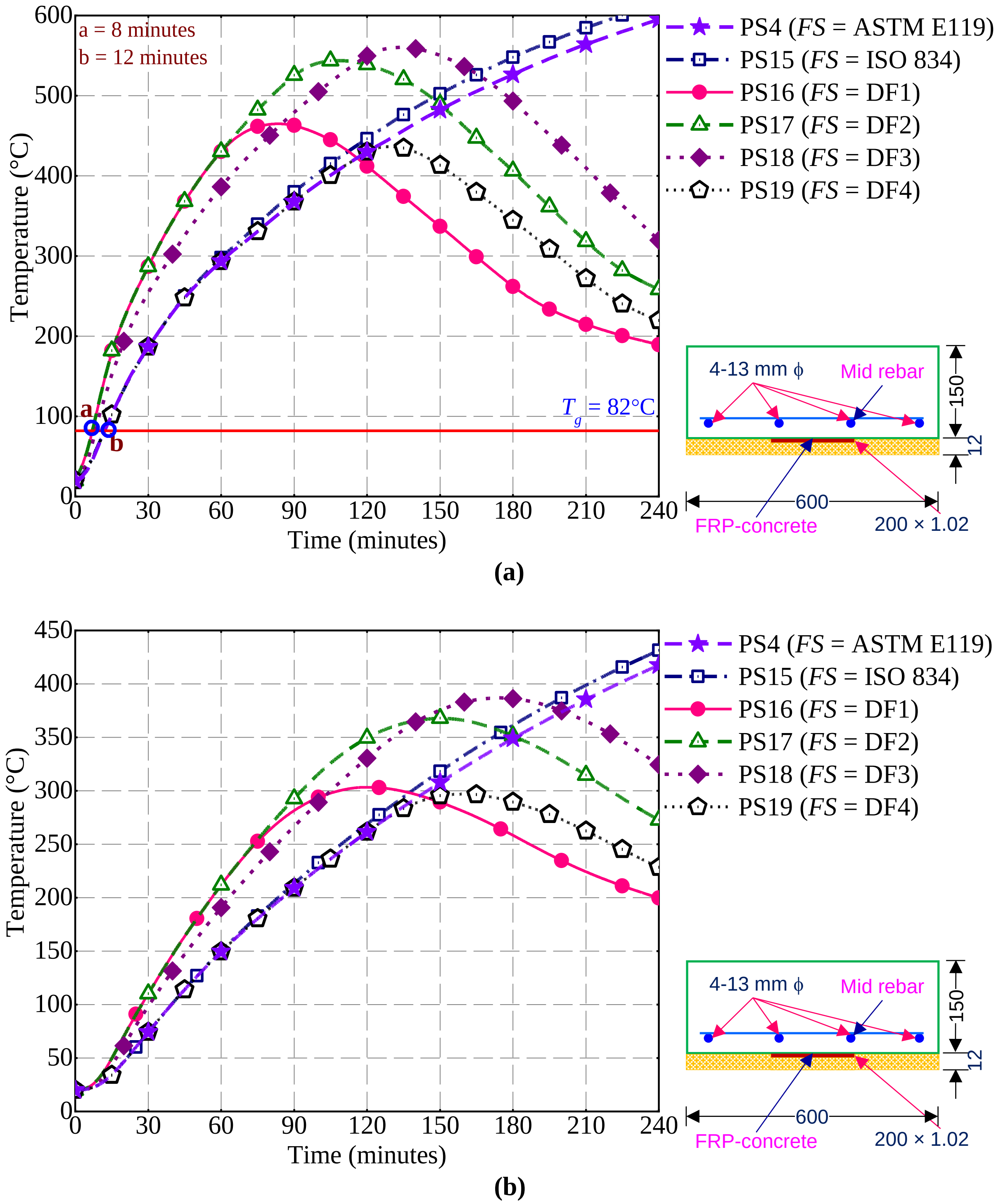

Figure 5.36: Effect of different fire scenarios on temperature rise in slabs PB4, PS15 to PS19 at: (a) FRP-concrete interface; (b) mid rebars

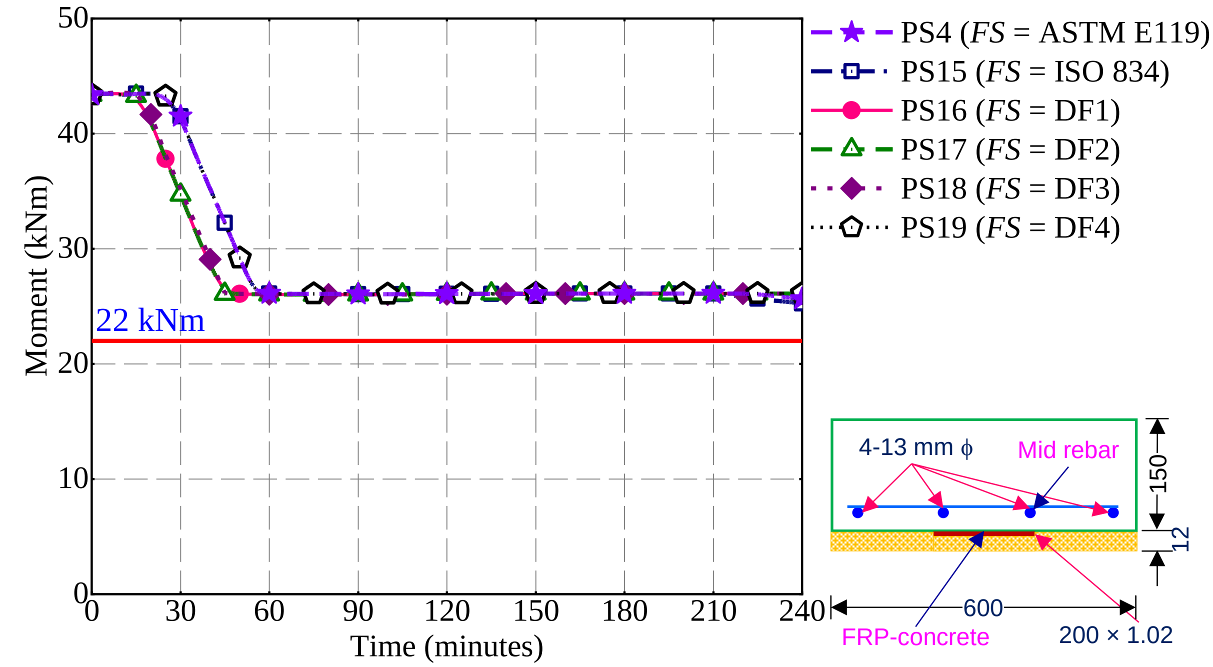

(a)

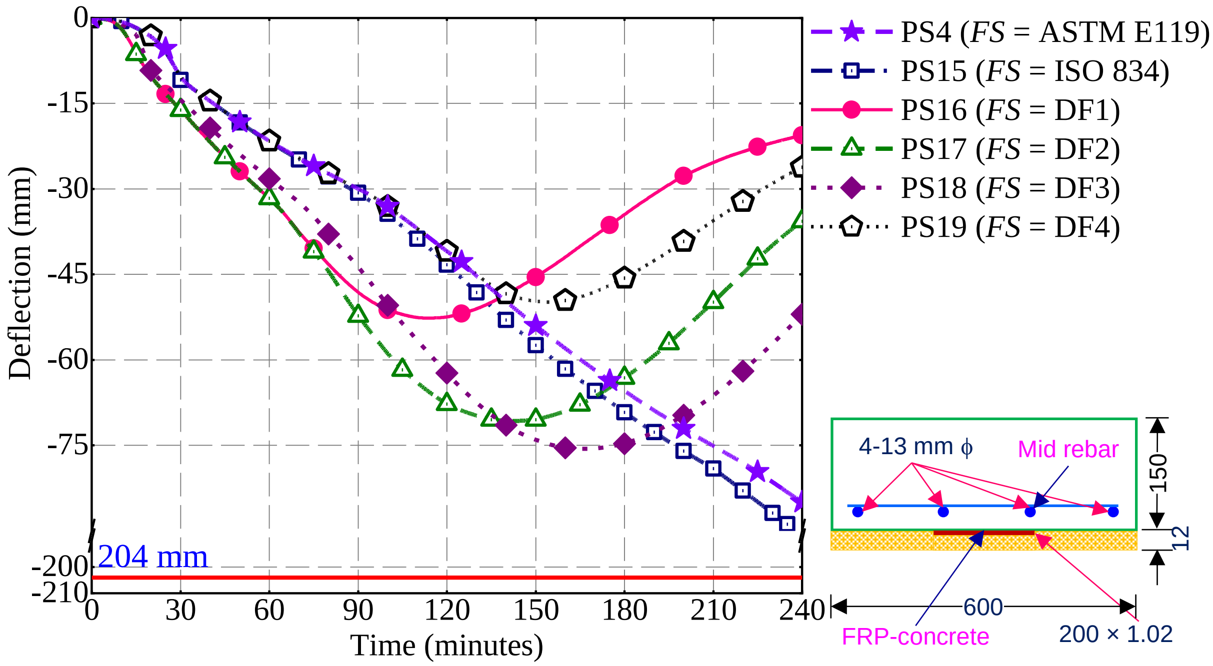

(b)

Figure 5.37: Effect of different fire scenarios on structural response of slabs PB4, PS15 to PS19 analyzed in case PSC4: (a) degradation in moment capacity; (b) deflection

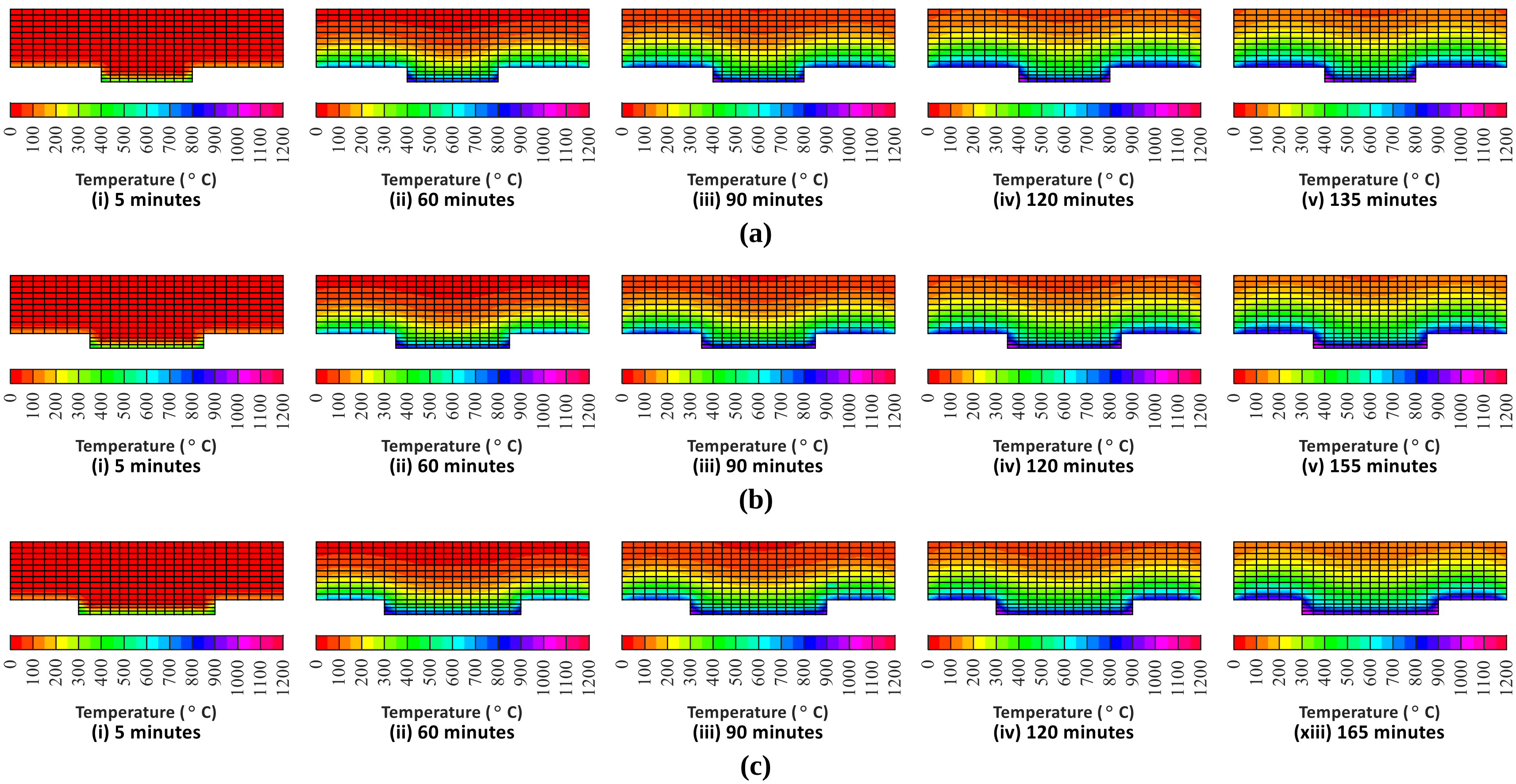

Figure 5.38: Effect of insulation width applied at the slab soffit on the temperature rise in cross-section of slabs analyzed in case PSC5 and in slab PS4: (a) PS20; (b) PS21; (c) PS22; (d) PS23; (e) PS24; (f) PS25; (g) PS4; (h) representative

Figure 5.38 (cont'd)

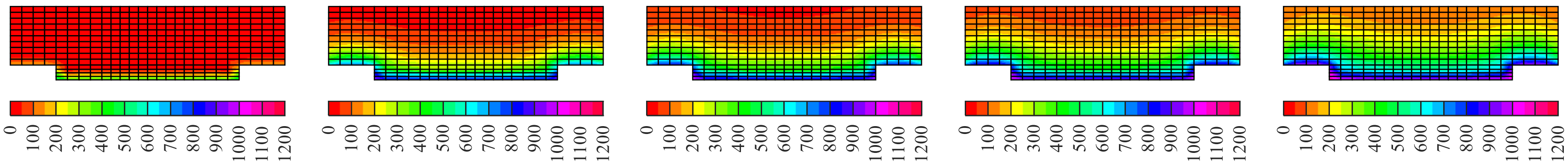

Temperature (° C) (i) 5 minutes | Temperature (° C) (ii) 60 minutes | Temperature (° C) (iii) 90 minutes | Temperature (° C) (iv) 120 minutes | Temperature (° C) (v) 175 minutes

(d)

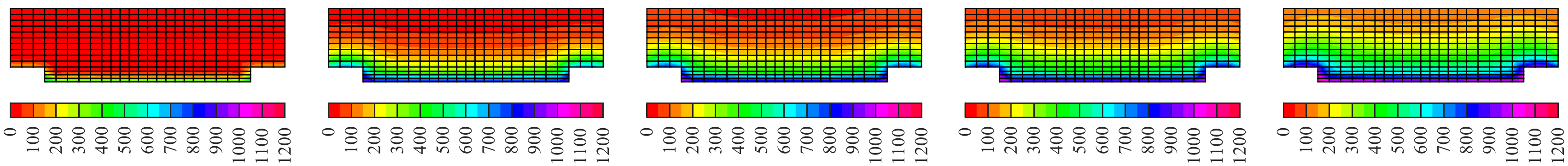

Temperature (° C) (i) 5 minutes | Temperature (° C) (ii) 60 minutes | Temperature (° C) (iii) 90 minutes | Temperature (° C) (iv) 120 minutes | Temperature (° C) (xv) 195 minutes

(e)

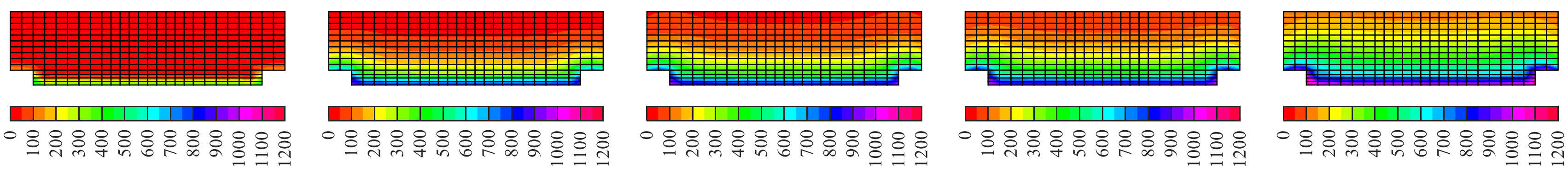

Temperature (° C) (i) 5 minutes | Temperature (° C) (ii) 60 minutes | Temperature (° C) (iii) 90 minutes | Temperature (° C) (iv) 120 minutes | Temperature (° C) (v) 230 minutes

(f)

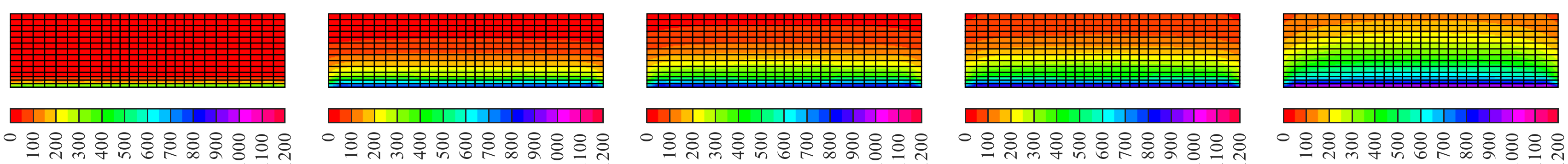

Temperature (° C) (i) 5 minutes | Temperature (° C) (ii) 60 minutes | Temperature (° C) (iii) 90 minutes | Temperature (° C) (iv) 120 minutes | Temperature (° C) (v) 240 minutes

(g)

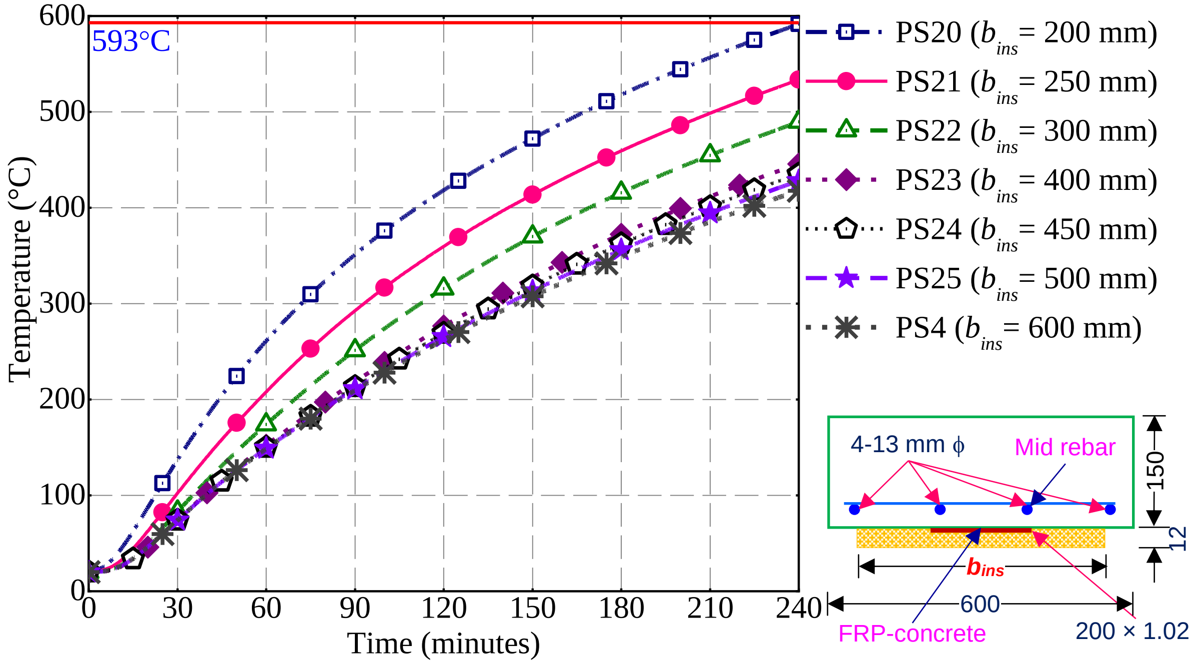

Figure 5.39: Effect of width of insulation applied at the soffit of slabs on the temperature rise at the mid rebars of slabs PS4, PS20 to PS25 analyzed in case PSC5

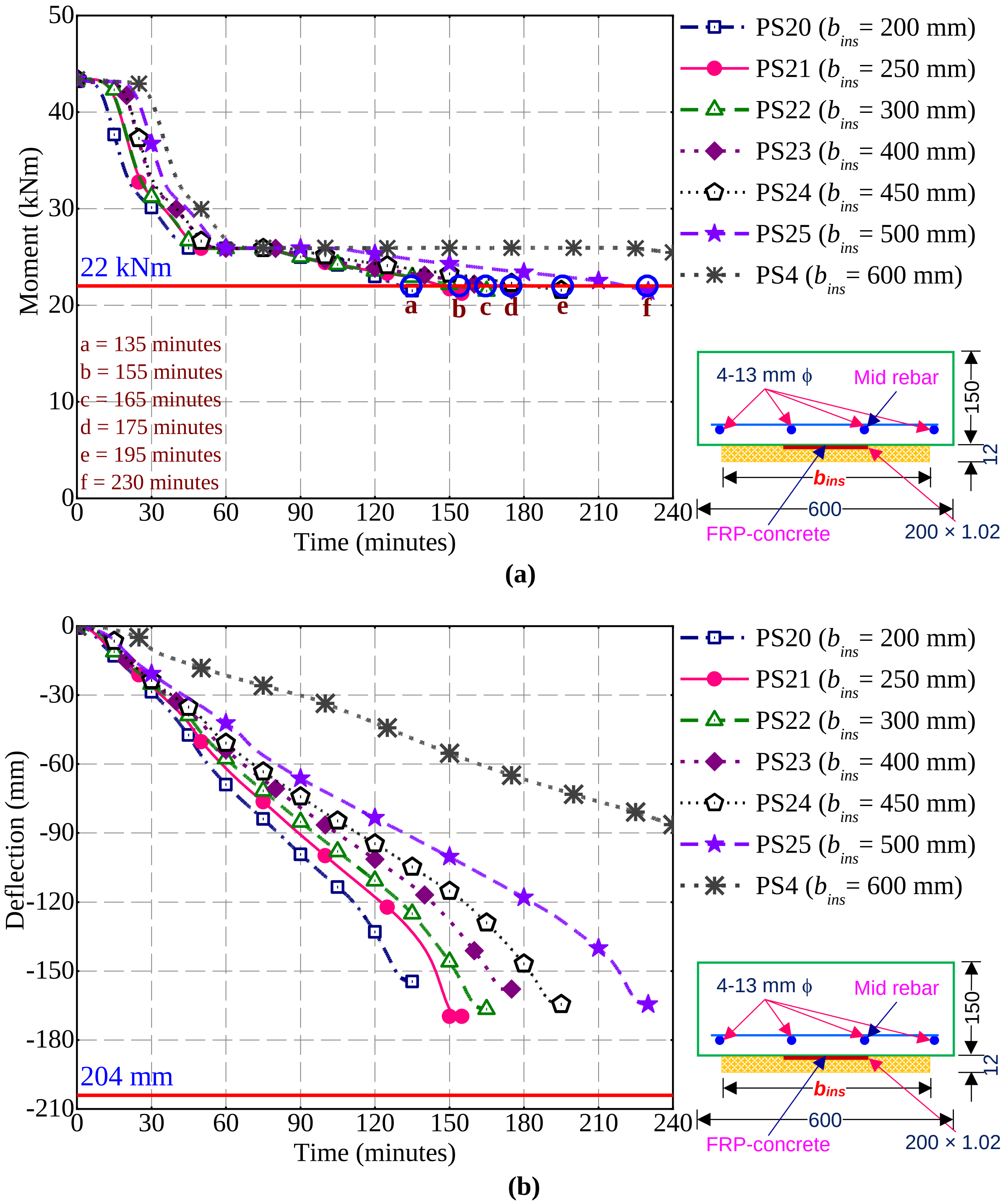

Figure 5.40: Effect of width of insulation applied at soffit of slabs on structural response of slabs PS4, PS20 to PS25 analyzed in case PSC5: (a) degradation in moment capacity; (b) deflection

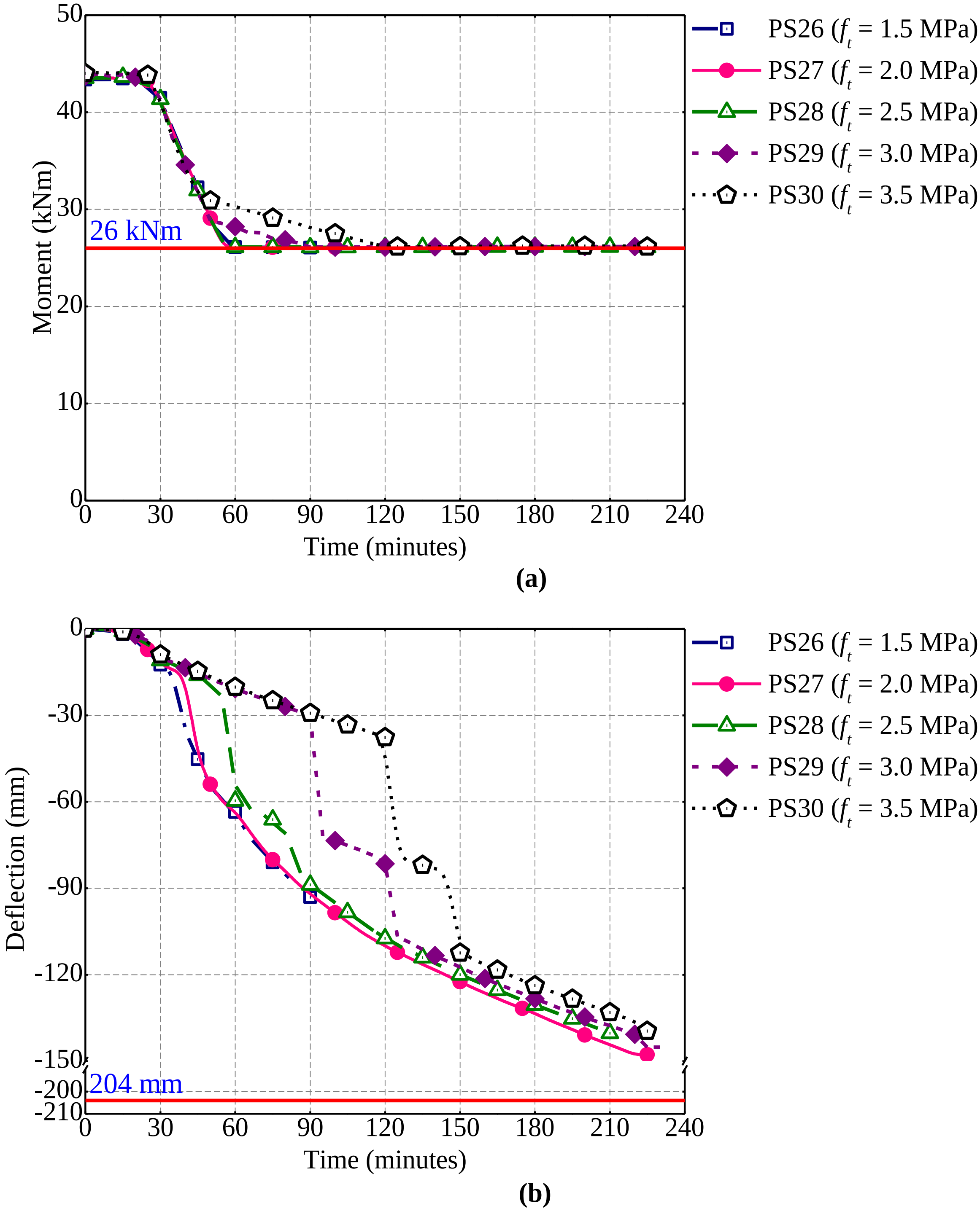

Figure 5.41: Effect of room temperature tensile strength of concrete on structural response of slabs PS26 to PS30 analyzed in case PSC6: (a) degradation in moment capacity; (b) deflection

CHAPTER 6

AUTONOMOUS FIRE RESISTANCE PREDICTION OF FRP-STRENGTHEEND BEAMS

6.1 General

The parametric studies presented in chapter 5 clearly indicate that fire performance of FRP-strengthened concrete structural members is influenced by several factors, and this makes the fire resistance assessment a formidable task. Therefore, despite several experimental and numerical studies on evaluating the fire performance of FRP-strengthened concrete beams, there are very few simplified approaches for fire design of strengthened concrete structures. Rather, as described in Chapter 2, the ACI 440.2R-17 [19] recommends neglecting the contribution of FRP towards the capacity while evaluating the fire resistance. However, as observed in Chapters 3, 4, and 5, this assumption is over conservative, especially in cases where the strengthened member is protected by fire insulation. This lack of simplified approaches pertaining to fire design of strengthened concrete members, hinders the use of FRP for structural application.

As mentioned in previous chapters, fire resistance assessment through standard fire tests is laborious, costly, and time consuming. Further, the fire tests have practical limitation on the available equipment and conditions that can be simulated in laboratory environment. Moreover, these tests are meant to validate/test a specific hypothesis making the results less applicable to general scenario. Alternatively, the computationally demanding microscopic numerical models developed in ABAQUS®/ANSYS® or the macroscopic numerical model presented in this thesis (*cf.* Chapter 4) can provide a detailed analysis of the fire performance of strengthened structural members over the entire loading range and a reasonably accurate estimate of fire resistance.

However, the predictions from the numerical models are highly sensitive to variations in input parameters, such as high temperature material property relations and bond-slip relations. The use of these models is time consuming and require special training. Moreover, design engineers are often interested in determining the fire resistance rather than analyzing the structural response throughout the loading range. Therefore, use of these numerical models for regular design is impractical.

Another alternative is the use of rational approach proposed by Yu and Kodur [21] or the three-stage design approach proposed by Gao et al. [22] as described in Chapter 2. These approaches use simplified equations for computing temperature and moment capacity of the FRP-strengthened section at different time intervals, respectively. While the former approach neglects the FRP-concrete bond degradation, the latter approach neglects FRP completely in uninsulated cases or considers contribution of FRP only until T_g of adhesive is reached, both of which are unrealistic. Thus, these approaches use oversimplified assumptions, and do not account for all factors affecting fire performance of FRP-strengthened concrete beams. Moreover, these approaches involve lengthy calculations which reduces their applicability in design offices. These factors necessitate the development of more coherent, all inclusive, and ready to use tool for fire resistance evaluation of FRP-strengthened concrete structural members. To develop such a simplified approach a machine learning (ML) based artificial intelligence (AI) model is developed. For this purpose, a dataset of the available fire tests on FRP-strengthened concrete beams is compiled and then different ML algorithms are applied after systematic feature engineering and hyperparameter tuning.

6.2 ML in Civil Engineering: State-of-the-art

Over the past few decades, ML based AI models have emerged as an efficient technique for mapping the input features to the output of a phenomenon under consideration, without explicitly programming the exact relation between them. These models implement various ML algorithms such as support vector regression (SVR), random forest (RF), extreme gradient boosting (XGB), and artificial neural network (ANN) or evolutionary techniques such as genetic programming (GP). These algorithms identify and learn the underlying complex patterns of interconnectivity between parameters in a previously known dataset. As such, the ML based AI models can overcome the complexities associated with large variability and interdependence of input features and predict the response parameters efficiently. Owing to these advantages, the ML based AI models have been extensively used in various sub-domains of civil engineering, ranging from structural, traffic, geotechnical, and construction engineering. These studies are summarized in various state-of-the-art reviews [177–181].

Within the structural engineering domain, ML based techniques are being applied for various applications, such as design optimization[182, 183], earthquake engineering [184–188], structural health monitoring [189–191], material property evaluation of concrete [192–194], damage detection in structures [195–198], predicting performance of FRP-strengthened concrete structural members [199–204].

In fire engineering field, the ML techniques such as ANNs have been used for predicting accuracy of automatic fire detection systems [205], profiling compartment fire and wildfire dynamics [206, 207], as well as for flame identification and smoke detection [208, 209]. Decision trees (DT) algorithm were used by [210, 211] to assess the fire dynamics and fire risk, respectively. RF models have been implemented by [212, 213] flame image processing and to analyze spontaneous combustion of coal, respectively. These researchers showed that RF algorithm can be robustly deployed to complex fire environments with high prediction capability.

The use of ML based AI models for structural fire engineering computations is rather limited. For instance, Al-Khaleefi et al. [214], Lu et al. [215], and Lazarevska et al. [216] used ML models for predicting fire resistance of steel concrete composite columns, steel columns, steel frames, and eccentrically loaded composite columns, respectively. Similarly, Erdem [217] predicted moment capacity of RC slabs under fire exposure using ML model, while McKinney and Ali [218] predicted fire resistance and spalling in HSC columns using two different ML models. These ML models were primarily developed using simplified ANN algorithms with one hidden layer and were trained over dataset available from fire tests or numerical modeling.

Implementation of other ML algorithms such as, SVM in structural fire engineering has been very limited. For instance, Chen et al. [219] used SVM algorithm for predicting temperature rise in fire damaged concrete beams and columns, while Wei et al. [220] used SVM for evaluating fire risk in buildings. Recently, Naser [221–223] used hybrid combination of ANN and GP to develop expression for temperature dependent constitutive relations for construction materials, for predicting fire induced spalling in HSC columns, and for predicting fire resistance of RC beams and columns, respectively.

The aforementioned studies clearly demonstrated the potential of contemporary ML techniques for solving the complex problems related to determination of structural fire resistance. Further, the review clearly indicates that the ML based AI models can be a useful aid to predict response parameters in situations where testing and numerical modeling are not feasible or practical and can save substantial amount of time as well as human effort. Therefore, different ML algorithms are applied to develop ready to use models for computing fire resistance of FRP-strengthened concrete flexural members. The details of different algorithms considered for developing the models as well as the final models are provided in following sections.

6.3 ML Algorithms

Machine learning (ML) gives computers the ability to learn without any explicit programming. Based on the type of dataset available for training, ML can be classified as supervised or unsupervised learning. Supervised learning involves learning the relation between the input and labeled outputs of a given dataset and is used for classification or regression. Whereas unsupervised learning involves learning the pattern from a dataset with unlabeled outputs and is primarily used for clustering or dimensionality reduction. Figure 6.1 shows a graphical representation of ML techniques and algorithms. In this chapter, regression based supervised learning algorithms are applied on a dataset (described in following section) to develop models for predicting fire resistance of FRP-strengthened flexural members. Three different ML algorithms namely support vector regression (SVR), random forest regressor (RFR), and deep neural networks (DNN) are utilized to develop a model for predicting fire resistance of FRP-strengthened concrete members. These algorithms are briefly described here.

6.3.1 Support Vector Regression

The SVR algorithm is an extension of Support Vector Machine (SVM) algorithm developed by Vapnik [224] for pattern classification problems with multi-dimensional inputs. In SVR the relation between input and output variables of a dataset is approximated through optimization, i.e., by minimizing the loss function [224, 225]. The loss function is $\in$-insensitive, i.e., insensitive to error tolerance as described below.

The training in SVR begins by transforming the input variables (x) of the dataset to a higher-dimension feature space using a user specified nonlinear kernel function, such as polynomial, sigmoidal, Gaussian radial basis kernel, or hyperbolic tangent. In the higher-dimension space, the data is distributed sparsely as compared to that in original space. Following this linear regression is performed in this space using a linear objective function $y = f(x,w)$ given as:

$$y = f\left(x,w\right) = \sum_{j=1}^{n} w_j \varphi_j\left(x\right) + b_t \tag{6.1}$$

where, x is the input variables vector; w is the weight vector; φ_j is the nonlinear mapping (kernel) function; and b_t is the bias term which can be eliminated if the mean of x is 0. The estimation accuracy is measured using Vapnik's ε-insensitive loss function L_ε given as:

$$L_\varepsilon\left(y, f\left(x,w\right)\right) = \begin{cases} 0 & \text{, if } \left|y - f\left(x,w\right)\right| \le \in \\ \left|y - f\left(x,w\right)\right| - \in, & \text{otherwise} \end{cases} \tag{6.2}$$

where, ϵ is the user specified error tolerance (width of the insensitive zone) and governs the number of support vectors. A bigger value of ε leads to more support vectors. Vapnik's function (Eq. [6.2]) defines an ∈-tube, wherein the loss (error) is zero if the predicted value is within the tube, and if the predicted value is outside the tube, the loss is equal to the magnitude of difference between predicted value and ε. Figure 6.2 shows a pictorial representation of the hyperplane and ε-tube. In the figure, ξ_j and ξ_j^* are the non-negative slack variables giving the distance between edge of ∈-tube and measured values lying above or below the ε-tube, respectively, i.e.:

$$\begin{aligned} \left|y - f\left(x,w\right)\right| - \in = \xi & \text{ for data above } \in\text{-tube} \\ \left|y - f\left(x,w\right)\right| - \in = \xi^* & \text{ for data below } \in\text{-tube} \end{aligned} \tag{6.3}$$

The performance of SVR is bound by an empirical risk given as:

$$R_{emp}^{\varepsilon}(w) = \frac{1}{kp}\sum_{j=1}^{kp} L_{\varepsilon}\left(y_j, f\left(x_j, w\right)\right) \tag{6.4}$$

where, kp is the number of data points. The objective function $y = f(x,w)$ defining the hyperplane is determined through an optimum approach with the goal of minimizing the empirical risk functional given by Eq. [6.4] and the norm of weight vector w, such that for each input (x_j) the output $f(x_j, w)$ is within Euclidian distance ε from the actual value (Fang et al., 2008), i.e.,:

$$\begin{aligned} \min: R &= \frac{1}{2}\|w\|^2 + C\left(\sum_{j=1}^{kp} L_{\varepsilon}\left(y_j, f\left(x_j, w\right)\right)\right) \\ &= \frac{1}{2}\|w\|^2 + C\left(\sum_{j=1}^{kp} \xi + \sum_{j=1}^{kp} \xi^*\right) \end{aligned} \tag{6.5}$$

with constraints:

$$\begin{cases} y_j - f\left(x_j, w\right) \leq \in + \xi_j \\ y_j - f\left(x_j, w\right) \leq \in + \xi_j^* \\ \xi_j, \xi_j^* \geq 0,\ j = 1, 2, 3 \ldots k \end{cases} \tag{6.6}$$

where, C is the regularization parameter defined by user to control the trade-off between weight vector norm $||w||$ and the SVR model error. A large value of C reduces SVR approximation error by penalizing large errors.

It is evident from Eqs. [6.1 to 6.6] that the generalization performance of a SVR is largely dependent on the selection of optimum values for ε, C and the parameters of the nonlinear mapping (kernel) function (φ_j). These values must be calibrated to obtain the optimum objective function which reliably connects the input and output variable in a dataset. Furthermore, Eq. [6.5] and Eq. [6.6] indicate that SVR involves solving a linearly constrained quadratic programming which has optimal and unique global solution. Moreover, SVR employs the structural risk minimization principle and search techniques which eliminate kernel evaluations, thereby resulting in good generalization accuracy even for a small dataset and higher computational efficiency, respectively (Kecman, 2001). Campbell and Ying

6.3.2 Random Forest Regressor (RFR)

Random forest (RF) is the most versatile and powerful ML algorithm developed by Breiman [226] for classification and regression problems. The RF algorithm used for regression is termed as random forest regressor (RFR) and it assimilates several hundreds or thousands of decision trees (DT) through ensemble methods, such as bagging, random patches etc. Each DT consists of a root node, decision branch resulting in sub-tree node or leaf nodes, i.e., target outputs, and this assimilation of DTs is known as forest. The final output of the RFR is predicted by bagging or bootstrap aggregating (taking average of) the result of each individual DT, respectively [227].

Figure 6.3 shows the structure of a typical RFR model trained for a given training dataset $\boldsymbol{T}$ = ([X], {Y}) consisting of P number of datapoints, where [X] is the input matrix consisting of N input features; and {Y} is the target output vector. As can be seen from the figure, the RFR comprises of n_{tree} number of DTs, each trained over bootstrap datasets (n_d). The prediction from all the n_{tree} DTs is assimilated and averaged to make the final prediction. The detailed procedure is as follows.

The training starts by acquiring (forming) n_d datasets (T_j, j = 1, 2, …, n_d) from the original dataset $\boldsymbol{T}$ each consisting of N input features and the output vector. Each T_j bootstrap dataset comprises of randomly selected K datapoints such that K<P, and labeled as in-bag datapoints, while remaining P-K datapoints are considered out-of-bag (OOB) datapoints [226]. The random selection ensures that the datapoints in each dataset are different. Liaw and Wiener [228] recommends randomly selecting only two-thirds of the total P datapoints, i.e., K = 2P/3 as in-bag datapoints.

Following this n_{tree} DTs are grown simultaneously through the classification and regression trees (CART) model. For each DT in RFR only a small subset of input features m_{try} ($m_{try} < N$) are selected randomly for splitting at each node. The number of input features m_{try} is kept constant throughout the growth of the tree and the forest. The size of each DT is controlled either by specifying depth of the tree (d_t) or by limiting the minimum number of datapoints available for comparison at a decision node (n_p). Thus, each tree grows to its maximum size without pruning.

Each of the generated tree is utilized to make prediction for the OOB datapoints, which are then aggregated to make the final prediction $\hat{y}_j^{\text{OOB}}$ for the OOB datapoints. The predicted value is then used to compute the prediction error given as:

$$\begin{aligned} \text{MSE}_{\text{OOB}} &= n_{tree}^{-1} \sum_{j=1}^{n_{tree}} \left(y_j - \hat{y}_j^{\text{OOB}} \right)^2 \\ R_{\text{RF}}^2 &= 1 - \text{MSE}_{\text{OOB}} \big/ \hat{\sigma}_y^2 \end{aligned} \tag{6.7}$$

where, MSE_{OOB} is the mean squared error of the OOB data prediction; y_j is the actual value of the targe output in the OOB dataset; R_{RF}^2 is the R-squared values of the OOB data, and $\hat{\sigma}_y^2$ is the variance of the predicted value of OOB data [228]. Further, the influence of each variable on the output, i.e., variable importance is quantified by measuring the increase in prediction error due to random permutation of a particular variable while other variables remain unchanged [226, 229]. Finally, the RF model is tested on a new dataset ***TE*** which was not a part of the training dataset ***T*** to perform predictions.

Based on the above description it is evident that the values three variables namely, n_{trees}, n_d, and m_{try} needs to be optimized to obtain satisfactory performance. Although, the DTs in RFR are generated using the CART technique and the final prediction is through bagging of prediction from the DTs, RFR is significantly different from that of regular DTs or bagging approach. The difference stems from the fact that a large number of trees (ideally $n_{tree} \geq 500$/ twice the number of datapoints) are simultaneously grown in RFR at each node. Further, the RFR involves two-stage randomization, i.e., random selection of training datapoints in the bootstrap datasets and random selection of input features for splitting at each node. Additionally, it is easier to compute the importance of variable based on OOB error.

The large value n_{tree} helps to minimize the generalization error and the reduce possibility of overfitting the training data, and as a result, the RFR model can efficiently identify the complex relation between the features of training dataset. Whereas, the two-stage randomization, results in independent and dissimilar trees which reduces the variance of the final ensemble prediction, thereby resulting in a powerful prediction model [228–231].

Moreover, the random selection of in-bag datapoints leaves the OOB datapoints which can be directly used as validation test set as they are not involved in training or generating the tree, which reduces the splitting of dataset into training and validation test datapoints. Additionally, the availability of variation index of each input feature helps identify the importance of each feature, which can help understand the phenomenon better [232].

6.3.3 Deep Neural Network

Artificial neural networks (ANN) are supervised learning models inspired by mammalian brains that have capacity to learn, compute, and adapt from a given dataset and make predictions for a new dataset. A typical ANN primarily comprises of an input layer and an output layer which are connected through one or more hidden layers. Each layer of ANN consists of several processing units known as neurons, which are interconnected across the layers, resembling the neuron network in mammalian brains capable of processing information [233].

ANN are highly powerful algorithm which can solve highly nonlinear problems with relative ease and efficiency. The hidden layers within the ANN structure identify/fit complex relations between the input and output variables, and the number of hidden layers govern the performance of the ANN models. For instance, too many hidden layers increase the complexity and variance of the model and resulting in overfitting, whereas too few hidden layers can lead to low variance and high bias resulting in underfitting. Therefore, ANNs are classified on the basis number of hidden layers. For instance, an ANN with one hidden is known as single layer perceptron whereas an ANN with two hidden layers is known as multi-layered perceptron (MLP-ANN). Similarly, ANNs with more than two hidden layers are referred as "Deep Neural Network" (DNN) and are used for deep learning [234].

Apart from the number of hidden layers, another major difference between a single or multilayer perceptron and DNN stems from the type of first layer in the network. Ideally in a perceptron of MLP-ANN the first layer is an input layer wherein number of neurons are equal to the number of input variables. However, in a DNN model, the first layer is a hidden layer with implicit input layer. Here the number of neurons is defined to specify the scale/dimension to which the input variables need to be transformed. Therefore, number of neurons in the first layer of DNN model can be equal to or higher than number of input features, usually $2m+1$, where m is number of input features [235].

Figure 6.4 shows a pictorial representation of the structure of a typical DNN model comprising of first layer with implicit input layer, two hidden layers, and one output layer. The first layer and the implicit input layer are denoted as F1, and I1, respectively, while the three hidden layers in between are denoted HL1, HL2, and the final layer, i.e., output layer is denoted as O1. Each layer consists of several neurons, which are interconnected across the layers. Before transmitting the output from neurons in one layer to the neurons in subsequent layers, they are passed through linear or nonlinear activation functions such as, Sigmoid, rectified linear unit (ReLu), TanH, Step, scaled exponential linear units (SELU), ELU, etc.

The activation function determines if a particular neuron in any layer must be activated, provides a nonlinear output for the neuron and channels it to neurons in other layers. Further, it can be seen from the figure that the information flows only in one direction, i.e., from first layer to last (output) layer via hidden layers. Such a neural network (NN) in which the information flows only in one direction, is termed as fully connected feed forward NN. The procedure for developing a DNN model is briefly explained below.

At the start of the analysis, the input features [X] = $\{x_1, x_2, x_3, \ldots, x_n\}$ together with certain assumed weights $\{w_i\}$ and biases $\{b_i\}$associated with input features are provided to the implicit input layer (I1). The input features are multiplied with the associated weights and the associated biases are added to the weighted product. These weighted inputs together with the biases are linearly combined and provided to the neurons in first layer (F1) after passing through an activation function. Thus, each neuron in the first layer (F1) gets a different set of inputs.

The inputs of neurons in the layer F1 are again linearly combined after adding biases to the product of weights and inputs which are transformed through an activation function and transmitted to the neurons in the hidden layer (HL1). The information or inputs at neurons in layer HL1 are processed in this manner and transferred to the neurons in subsequent hidden layer HL2. Finally, the neuron in the layer O1 (output layer) receives the outputs from the neurons of the layer HL2 and after processing it produces the output. The output of any neuron in hidden layer and output layer is given as:

$$
\begin{aligned}
h_i^n &= H\left(\sum_{k=1}^{N} w_{ik}^n x_k + b_i^n\right) \\
o_l &= f\left(\sum_{j=1}^{N} w_{lj} h_j^n + b_l\right)
\end{aligned}
\tag{6.8}
$$

where, i, j, k, l denotes the neuron number; n denotes the hidden layer number; x denotes the input variables; H and f are activation functions; h_i and o_l are the outputs of i^{th} and l^{th} neuron in n^{th} hidden layer and output layer, respectively; w_{ik}, w_{lj} are the weights associated with the neurons in n^{th} hidden layer and output layer, respectively; b_i and b_l are the biases or threshold terms associated with the neurons in n^{th} hidden layer and output layer, respectively, and N denotes the total number of neurons in a particular layer under consideration.

The output produced by the layer O1 are then compared with the actual output of the training data and the value of selected error function (described in section 6.5.4) is estimated. The weights and biases are then updated during training through optimization algorithm, such as gradient descent technique, Adam algorithm, etc., with a goal of minimizing error function. The entire procedure is repeated iteratively until convergence, i.e., smallest possible value of error function is achieved. During each iteration (known as epochs), the model is trained several times on small a subset of datapoints, defined by batch size. The number of epochs required for convergence depends on the DNN structure and learning rate, which are progressively optimized through different strategies. Upon satisfactory validation, the final model is applied on the test data to evaluate the performance of model on unknown dataset.

Based on the above discussion it is evident that the performance of DNN is governed by several parameters such as DNN structure, i.e., number of hidden layers, number of neurons in each layer, type of activation function, type of loss function, batch size, optimizer, and number of iterations (epochs). The value of these parameters must be optimally tuned such that sufficient accuracy is obtained on both training and test datasets and all the connectivity structures and activation functions are differentiable.

Although, DNN can identify highly nonlinear or complex relations, they have several disadvantages. For instance, the implementation of DNN is somewhat difficult than that of SVR or RFR as several parameters needs to be optimized to get satisfactory accuracy. Moreover, DNN employs local search or optimization techniques which often gets trapped in local minima rather than going for the global minima. This makes the DNN and ANN a stochastic algorithm resulting in different model when trained several times on the same dataset. Additionally, visualization of DNN is extremely difficult, as the exact relations between the inputs and outputs of the neurons is unknown. Therefore, DNN are often used as a last choice of ML algorithm for developing predicting models [236].

6.4 Analysis Methodology

The ML algorithms described in section 6.3 are implemented to develop ready to use tools for predicting fire resistance of FRP-strengthened RC beams. The ML algorithms, i.e., SVR, RFR, and DNN were implement using Python programming language using "ScikitLearn [237]" library. Additionally, "Keras [238]" application programing interface (API) of "TensorFlow" library were also used for implementing the DNN model. The steps involved in developing the fire resistance prediction models through ML algorithms are as follows:

- Compile the database on fire resistance of FRP-strengthened RC beams to be used for training by reviewing the available experimental or numerical studies and real-world observations.

- Apply data preprocessing techniques, such as feature engineering and feature scaling on the independent input variables which governs the dependent variable i.e., fire resistance of FRP-strengthened members.
- Split the dataset into “training set” and “test set”.
- Apply hyperparameter tuning to optimize the parameters for the selected algorithm.
- Validate the performance of the algorithm using the parameters selected in previous test, over the training dataset through k-fold cross-validation techniques.
- Apply the model on the unseen test data to evaluate the accuracy and performance of the developed model using performance metrics.

6.4.1 Database Compilation and Preprocessing

The accuracy of the any ML algorithm based predictive model depends on the quality of the dataset and quantity of datapoints available in the dataset used for training the model. For the training of different ML based models, a comprehensive review of studies evaluating fire response of EB CFRP-strengthened RC beams as presented in Chapter 2, was utilized for preparing the dataset.

The dataset subsequently referred as Dataset-E comprised of 49 datapoints based on the experimental studies evaluating the fire resistance of EB CFRP-strengthened concrete beams available in literature including the one presented in Chapter 3. The dataset comprised of all the geometrical details of the beam, such as type and size of the cross-section, diameter of top and bottom rebars, cover thickness, cross-section of FRP, thickness and configuration of insulation. Moreover, the ambient temperature strength properties of concrete, steel reinforcement, and FRP, as well as thermal properties of insulation were provided in the dataset. Additionally, the applied loading and fire exposure, as well as the time of failure and the deflection at failure were recorded in the dataset.

In the dataset, the beams had varying features in terms of cross-section (rectangular and T), reinforcement ratio, level of strengthening, applied load ratio, and presence of external fire protection etc. Only beams that were tested under ASTM E119 [5] or ISO 834 [16] standard fire exposures were included in the dataset. Of the 49 experimentally tested beams, 20 were reported to have failed during the fire test and the failure time is considered as the ultimate fire resistance time of the beam. In case of remaining 29 beams, the fire test was stopped prior to failure, and the time which the test was stopped is considered as the minimum fire resistance time of the respective beam.

(i) Feature Engineering

Feature engineering refers to feature generation and feature extraction. The input features are combined to yield a new feature that has greater influence on the phenomenon being modeled, i.e., fire resistance. Whereas feature extraction involves reducing the number of input features to a manageable number such that the reduced features can still accurately describe the original dataset and govern the fire resistance of FRP-strengthened beams. As described above, the initial dataset had 29 different input parameters. Several features were combined based on domain expertise of the author to reduce the number of input parameters. Additionally, a preliminary correlation matrix was developed to determine features with high correlation. Through this feature engineering the number of input features were reduced to a total of 16 parameters.

These input parameters include, length of beam (L), area of concrete (A_c), total area of tensile steel reinforcement (A_s), area of FRP (A_f), cover to steel reinforcement (C_c), compressive strength of concrete (f_c), yield strength of steel rebars (f_y), ultimate tensile strength of FRP (f_u), glass transition temperature of FRP (T_g), thickness of insulation (t_{ins}), depth of insulation on sides of beams (h_i), thickness of insulation in anchorages (anc_t_{ins}), density of insulation (ρ_{ins}), thermal conductivity of insulation (k_{ins}), specific heat of insulation (c_{ins}), and total applied load (P). While the fire resistance time was taken as the output parameter of the dataset. Table 6.1 summarizes the values of these 16 input parameters and the output parameter used in Dataset-E.

(ii) Statistical Analysis

A statistical analysis of the above described 16 input features in the Dataset-E was carried out and the values of various statistical parameters such as mean, median, maximum, minimum, standard deviation, and coefficient of variation were provided in the Table 6.2. It can be seen from the table that except for the strength of concrete and tensile strength of steel rebars, all the input parameters have high value of standard deviation and coefficient of variation (>40%). This indicates that the data is spread out on a sufficiently wide range. Therefore, the ML algorithms can be trained on large range of values for different input parameters.

The low variation in the strength of concrete and steel rebars is attributed to the fact that FRP-strengthening is often carried out on structural members made of normal strength concrete (NSC), i.e., 20 MPa to 55 MPa [160] primarily reinforced with conventional steel rebars of strength 420MPa to 500 MPa. NSC with strength between 20 MPa - 55 MPa experience same degradation in strength and modulus properties at elevated temperatures. Similarly, reinforcing steel with strength between 420 MPa - 500 MPa have same behavior at elevated temperatures. Since the maximum and minimum values of strength of concrete and steel rebars are close to these ranges, the low variation in their values will not affect the training or performance of ML algorithms.

Further, the skew and kurtosis value of the input parameters were computed to determine the normality of the distribution and are summarized in Table 6.2. These values indicate that f_y, f_u, and

c_{ins} are negatively skewed, whereas the remaining parameters are positively skewed. However, the value of skewedness of all the parameter is very close to zero. Moreover, the kurtosis value which determines the outlier of a given dataset, of all the parameters except A_f and k_{ins}, are much lower than 3. Therefore, the distribution of the input parameters can be considered to be close to normal distribution, thus encompassing a wide range of values of different parameters.

To visualize the spread of each input parameter histograms were plotted for each of the parameter in Figure 6.5. Moreover, a frequency distribution curve of each input parameters is also shown in Figure 6.5. In the figure, the frequency signifies the number of times a particular value of the respective variable is repeated in the dataset. It can be seen from the figure that distribution of A_f and k_{ins} is highly skewed in positive direction, whereas the remaining variables have almost normal distribution.

Additionally, a correlation matrix of the whole Dataset-E is shown in Figure 6.6, wherein the Spearman's correlation coefficient ranging from -1 to 1 is plotted using appropriate color scheme. The values (colors) closer to +1 or -1 indicate a positive or negative, i.e., direct, or inverse monotonic relation between the variables, whereas the values (colors) closer to 0 indicate there is no relation between the variables. It can be seen from the figure, that there exists a good correlation between the geometrical features of the beam, the applied loading, and the fire resistance (failure time) of the beam, while there is least correlation between fire resistance and strength concrete and strength of FRP.

(iii) <u>*Feature Scaling*</u>

In case of supervised learning for regression, ML algorithms are trained using datasets which primarily comprises of numbers. Algorithms, such as SVR and ANN/DNN which compute the distance between the data are highly sensitive to the relative scale of input features. The input features with higher value ranges are assigned higher weights as compared to input features with lower value ranges. As a result, the parameters with higher value range starts dominating the behavior of the prediction model. For instance, if the input parameters of Dataset-E (Table 6.1) are directly used for training ML algorithms, the algorithms would assign higher weights to area of concrete, length of beam, specific heat of concrete, and assign lower weights to the thermal conductivity and thickness of insulation.

Thus, unscaled range of input parameters result in an unequal weighting of the features, while unscaled output parameters result in spurious error gradients. These conditions often lead to unstable learning process or failure of the learning process. Moreover, the uneven dimensions of the input and output parameters makes it difficult to select a suitable tolerance factor for evaluating convergence of the model. Additionally, the convergence rate of the algorithm functions decreases, and the optimization function do not work correctly when unscaled input features are used. Therefore, it is necessary to either scale or normalize the features of the dataset using scaling techniques.

To ensure stable and faster learning and to treat all the input features of similar weights, each of the input variables in Dataset-E were standardized using standard scaler also known as Gaussian normalization technique. The Gaussian normalization standardizes the values of the input variables such that it varies from -1 to +1 and has the mean and variance close to 0 and 1, respectively. The new value of the input variable is determined using:

$$x_{norm} = \frac{x - \mu}{\sigma} \tag{6.9}$$

where, x is the original value of input variable; x_{norm} is the new value of input variable x; μ is the mean of the original values of input parameter x; σ is the standard deviation of the original values of the input parameter. This operation was carried out using the “StandardScaler” function available in the “Scikitlearn” library.

(iv) Train-Test Split

Following the scaling of the features in Dataset-E, the dataset was randomly split into training data and test data. Among the datapoints available in Dataset-E, 80% of the datapoints of the parent dataset were selected randomly for training the ML algorithms. While remaining 20% datapoints were used for testing the performance of developed model. Similar split ratio or a ratio close to that has been used in several previous studies [239, 240]. The division resulted in 39 datapoints for training and 10 datapoints for testing. Although the dataset was split randomly, special care was taken to ensure that the training and testing dataset are representative of the respective parent datasets. The training dataset comprised of widespread values of the input features which encompassed all the values between the two extremes.

6.4.2 Hyperparameter Tuning

As described in section 6.3 there are several parameters in for each algorithm which govern their performance. To obtain optimal values of these parameters for each algorithm, hyperparameter tuning analysis was carried out using the “GridSearchCV” function available in “Scikitlearn [237]” library. The details of the different parameters optimized in each algorithm are described below:

(i) Parameter Tuning for SVR

The performance of SVR depends on the values of $\in$ (error tolerance), C (error regularization) and the parameter of kernel function. In the current analysis following different combinations were evaluated:

- Kernel function: linear, polynomial, radial basis function (RBF), sigmoid

- Error regularization parameter (C): 0.5, 1, 5, 10, 15
- Degree of polynomial: 2, 3, 4, 5
- Constant term in polynomial: 0.01, 0.5, 0.1, 1, 5, 10
- Gamma parameter for RBF: automatic, scaled
- ε: 0.1, 0.5, 1

(ii) <u>Parameter Tuning for RFR</u>

The performance of RFR is primarily governed by two parameters namely, the number of DTs (n_{tree}) to be generated and maximum number of input features (m_{try}) to be used for splitting a node. However, the RFR model builder in "Scikitlearn" library of python provides control over various other parameters, such as the minimum number of samples for splitting at node (n_s), and depth of tree (d_t). Therefore, in the current study following parameters were optimized:

- Number of trees (n_{tree}): 100, 200, 300, 500, 1000
- Maximum number of samples in each sub-dataset (K): 0.33, 0.66, 0.75, 0.99
- maximum number of input features for splitting a node (m_{try}): 2, 3, 7, 8 ,10, 12, 15
- Maximum depth of tree (d_t): 10, 50, 100, unbound
- Minimum samples for splitting at a node (n_s): 2, 6, 8, 10, 12, 15

(iii) <u>Parameter Tuning for DNN</u>

The hyperparameter tuning using the "GridSearchCV" function helps optimize only the loss function, the optimization algorithm, activation function, batch size, and number of epochs. Therefore, following range were considered for each of these parameters were tried:

- Activation function: ReLu, Sigmoid, Tanh, SELU, ELU
- Kernel initializer: Standard normal distribution, constants initialization, Lecun normal

- Loss function: mean squared error (MSE), mean absolute percentage error (MAPE), mean absolute error (MAE)
- Batch size: 10, 15, 20, 25, 30
- Epochs: 500, 1000, 1500, 2000, 2500

The DNN structure was determined through a separate process, wherein DNN models with different combinations of the number of hidden layers, number of neurons in each layer were trained using a tenfold cross-validation analysis. Values of the batch size, epochs, activation function, and loss function were derived from the above grid search analysis and following combination of number of hidden layers and number of neurons in first layer as well as hidden layers:

- Number of hidden layers: 1, 2, 3, 4
- Number of neurons in first layer: 21, 25, 26, 30, 33, 35, 50
- Number of neurons in each hidden layer: 5, 10, 15, 20, 25, 26, 30, 33

Models with different combination of the aforementioned parameter values was evaluated. In each of these models, a ten-fold cross-validation scheme, explained in following section, was implemented to determine the optimal value of the parameters.

6.4.3 Ten-Fold Cross-Validation Scheme

The training data procured at the start of the analysis is further discretized into training data and validation During the hyperparameter tuning, the DNN models are trained on the training data and are evaluated on validation data. Once the optimal parameters are determined, the final model is then evaluated on the test data. Since the dataset is randomly discretized into training, validation, and test data, the available data points for training the model reduces significantly, which in turn makes the trained model more biased towards the randomly selected training data. To overcome this bias in the model as well as to train the model over a limited data points, a *k*-fold cross-validation procedure is implemented, where *k* refers to the number of groups the given data is divided into. Ideally, k = 10, provides a reasonably accurate and all-round performance of the model [239, 241] therefore, in the current study ten-fold cross-validation scheme was used.

In this scheme, the training data is first shuffled randomly and then divided into 10 groups (folds). For each unique group, one group is held out as test data set, while the model is trained on remaining (*k*-1, i.e., 10-1) 9 groups. The trained model is then evaluated on the one group which was held out as test data set. The process is repeated for each group so that the model is trained and validated on the data in each group. Thus, each data group is held out at least once and the model is trained on each data group (*k*-1) = 9 times. After each performance evaluation of the trained model on the test data set, the evaluation score and parameter values are retained, while the model is discarded. Finally, the optimal parameters are selected from the combination which has highest evaluation score.

6.4.4 Performance Evaluation Metrics

The performance and accuracy of the developed models was quantitatively evaluated through three different performance metrics, namely Pearson correlation coefficient (R), coefficient of determination (R^2), and root mean square error (RMSE). The mathematical formulation for these error measures is as follows:

$$R = \frac{\sum_{i=1}^{n}\left(A_i - A_{mean}\right)\left(P_i - P_{mean}\right)}{\sum_{i=1}^{n}\left(A_i - A_{mean}\right)^2 \sum_{i=1}^{n}\left(P_i - P_{mean}\right)^2} \tag{6.10}$$

$$R^2 = 1 - \frac{\sum_{i=1}^{n}(P_i - A_i)^2}{\sum_{i=1}^{n}(A_i - A_{mean})^2} \tag{6.11}$$

$$RMSE = \sqrt{\frac{\sum_{i=1}^{n}(P_i - A_i)^2}{n}} \tag{6.12}$$

where, A_i is the actual value of the fire resistance; P_i is the predicted value of the fire resistance; A_{mean} and P_{mean} are the average values of the actual and predicted fire resistance; and n is the number of datapoints. In these metrics, a higher value of R and R^2 ranges between -1 to 1 and 0 to 1, respectively. A higher value of R and R^2, closer to 1 is considered a good correlation. The value of RMSE is scale dependent and is very sensitive to outliers. A lower value of RMSE is considered as favorable and indicative of good performance [242].

6.5 Results and Discussion

Based on the above described hyperparameter tuning and ten-fold cross-validation analysis procedure, the specific parameters for training SVR, RFR, and DNN ML algorithms were determined. The performance metrics for each model on the training and test dataset are summarized in Table 6.3. The selected parameters for each algorithm and the trained models as well as the performance metrics as determined on the test data are discussed here.

6.5.1 Selected Parameters for SVR Model

Based on the above described hyperparameter tuning analysis, it was observed that the fourth-degree polynomial kernel function, with a constant value of 5 provided a better performance than that of the gaussian radial bias function. Additionally, a small value of error regularization (C) value and $\in$-tube diameter resulted in better training evaluation score for the SVR algorithm.

Therefore, the final prediction model based on SVR algorithm was trained using a fourth-degree polynomial kernel with a constant parameter of 5 and with C = 0.5 and $\in$-tube of diameter 1 minute. These value of 1 minute helped encompass majority of the datapoints.

Figure 6.7 (a-b) shows the prediction performance of the SVR algorithm-based model on the training dataset and test dataset procured from Dataset-E. It can be seen from the figure that the model achieved a value of 0.94 and 0.89 for R and R^2, respectively on the training dataset, and value of 0.94 and 0.86 for test dataset. The value of the two coefficients of determination on the unseen dataset are reasonably high indicating good performance of the prediction model. These values indicate that the training and test dataset are very close. However, the RMSE value of the model was observed to be almost 19 minutes and 16 minutes over the training and test dataset, respectively. The RMSE is relatively very high indicating a possible error 15 to 20 minutes in the fire resistance prediction.

6.5.2 Selected Parameters for RFR Model

For the RFR algorithm based predictive model the optimum values of the two primary hyper parameters i.e., n_{tree}, and m_{try}, were found to be 200 and 15, respectively. Moreover, from the ten-fold cross-validation and grid search functions it was observed that unbounded (no control on depth) DTs with each sub-dataset containing 33 % of the total samples and using at least two samples for splitting a node resulted in optimal performance.

Figure 6.7 (c-d) shows the prediction performance of the RFR algorithm-based model on the training and test data split obtained from the Dataset-E. It can be seen from the figure that fire resistance predicted made by the developed model are very close to the actual values measured in respective fire tests, for both the training dataset and test dataset. The value of performance measures R, R^2, and RMSE are .96, 0.92, and 16 minutes for the training dataset, and 0.91, 0.79, 20 minutes for the test dataset, respectively. The higher accuracy obtained in the training as compared to test, indicate possible overfitting of the model on the training dataset. Moreover, the RMSE values on both training and test dataset are similar to that of SVR model, indicating possible error of 16 to 20 minutes in fire resistance prediction.

6.5.3 Selected Parameters for DNN Model

The optimal DNN structure as determined from the experimentation analysis consisted of first layer with implicit input layer, two hidden layers (HL1) and (HL2) and one output layers, each consisting of 35, 26, 7, and 1 neuron, respectively. The weight and biases for the input features in each neuron were initialized through Lecun normal technique which produces weight that are randomly selected values multiplied with the variance 1/number of input units used in weight tensor. The weighted input features in one layer were transferred to the subsequent layer through SELU activation function. The model was trained for 1000 epochs, with a batch size of 25, i.e., at every iteration, model was trained for number of samples/25 times, over randomly selected 25 datapoints. During each iteration, MSE loss function was utilized to evaluate the performance of the model on validation dataset.

The aforementioned hyperparameters and DNN structure were used to train the final model on training dataset and performance of the model was determined through predictions made by the model on test dataset (which was completely unseen by the model). Figure 6.7 (e-f) compares the measured fire resistance with those predicted by DNN model for the training and test dataset.

It can be seen from the figure that the predicted values are in close agreement with measure values for both the training and test datasets. The R and R^2 values are 0.99 and 0.98 for the training datasets, and 0.96 and 0.91 for the test dataset, respectively. These values are higher than those obtained in SVR or RFR models. Moreover, the RMSE value of the DNN models is 6 minutes and

12 minutes for the training and test datasets, respectively, which are much lower than the SVR and RFR models. Thus, the DNN model can predict fire resistance of CFRP-strengthened RC beams with reasonable accuracy and has good generalization potential. The slightly smaller value of R and R^2 on test data is attributed to the smaller dataset used for training the model. Further, it can be seen from Table 6.3 that among the three algorithms used for developing predictive models, DNN offers most accurate predictions.

6.5.4 Training ML model on Larger Dataset

The SVR, RFR, and DNN models discussed in the previous sections were able to predict the fire resistance of CFRP-strengthened RC beams with an error margin of 12 minutes to 20 minutes based on RMSE for predicted values of test dataset. The difference between the RMSE for the predicted values of training and test dataset ranges from 2 minutes to 6 minutes. This error margin indicates that the models are slightly overfitting the training data and are therefore, not able to generalize the predictions for a larger range of input parameters variable. The slight overfitting may be attributed to the smaller number of datapoints used for training the model.

To evaluate if addition of more datapoints will improve the model predictions, the dataset-E was supplemented with 29 datapoints based on parametric studies presented in Chapter 5. The addition of datapoints increased the total number of datapoints to 78, thereby resulting in a new dataset denoted as Dataset-EN. This new dataset was again pre-processed and then was split into training set and test set. All the three ML algorithms, i.e., SVR, RFR, and DNN were trained over this new training dataset and performance was evaluated over the test dataset.

Figure 6.8 compares the measured and predicted values for the training and test dataset for ML algorithms-based prediction models, while the performance metrics are summarized in Table 6.3. It can be seen from the figure and Table 6.3, that when trained over Dataset-EN, the performance of both SVR and RFR in terms of R and R^2 increases for both training and test datasets. However, RMSE of these models decreases for prediction on the training datasets and increases for prediction on test dataset procured from Dataset-EN. This indicates that the models are overfitting on the training dataset. Similarly, in case of DNN model the performance in terms of R and R^2 remains same for the prediction on training and test dataset whereas, the RMSE value increases for both the training dataset and test dataset. This indicates that the DNN model is also overfitting the training dataset procured from Dataset-EN.

The overfitting and high value of RMSE of the models is attributed to the fact that new datapoints added to Dataset-E were based on a parametric study, wherein majority of the parameters such as the length, cross-section dimension, cover thickness, area of reinforcement or insulation thickness is same for majority of the datapoints. This results in a smaller spread of the input parameter which in turn increase chances of overfitting on the training dataset. Further, any small change in one or two parameters can result in very high RMSE values as it is very sensitive to the outliers as well as the scale of the data. Therefore, the models must be trained on a large dataset encompassing the variation of different input parameters over a wide range. However, the performance evaluation in term of R and R^2 clearly indicates that the performance of the model can increase substantially with the increase in number of datapoints.

6.6 Limitation of the Model

The efficiency of any machine learning model depends on the size and quality of the selected dataset used for training as well as the distribution of input features within the dataset. In the current study, results from fire tests on CFRP-strengthened concrete beams were utilized for training the model. So far, few studies have been reported in literature for evaluating the fire resistance of CFRP-strengthened concrete beams, due to several limitations, such as test equipment needs, cost, etc. Of the available studies only 49 of them were tested under similar fire exposure, loading levels, and insulation configuration. Therefore, only these 49 data points have been used for training the model.

The readers of this thesis are to realize that the developed ML algorithm-based prediction models are valid for the range of input features presented in Figure 6.5 and summarized in Table 6.2. Since the range and frequency of some of the features is very small the developed models are applicable over a smaller range of values of input features and the efficiency of the model, based on different performance metrics is almost 90-95%.

Currently, the purpose of this chapter is to demonstrate the potential of machine learning based algorithms for developing models to predict the fire resistance of CFRP-strengthened concrete beams. While the developed models are valid for the given range of input features, better and reliable models can be developed by increasing the pool of the training dataset by conducting more fire tests on strengthened beams. Additionally, the results from numerical studies can also be utilized in the dataset to increase the variability of the input features. Further, genetic algorithms in conjunction with machine learning can be implemented on the larger dataset to generate equations for computing fire resistance of FRP-strengthened beams, which can be directly used by practicing engineers and researchers.

6.7 Summary

The development of ML algorithms-based predictive models for predicting fire resistance of CFRP-strengthened RC beams is presented in this chapter. For this purpose, a comprehensive database was compiled by collecting results from the fire tests on CFRP-strengthened RC beams available in literature. The dataset was utilized to train the algorithms, wherein 16 different input features were taken as input for training and fire resistance time was taken as the output. Different governing parameters for each model were determined through extensive hyperparameter tuning in conjunction with the ten-fold cross-validation analysis scheme. Based on the results presented in this chapter following conclusions can be drawn:

- Predictive models based on SVR, RFR, and DNN algorithms can predict fire resistance of CFRP-strengthened RC beams with reasonable accuracy. Therefore, ML algorithms can be used for developing autonomous models for predicting the fire resistance of CFRP-strengthened RC beams.
- Among the three, DNN algorithm offers maximum prediction accuracy on unseen dataset with R and R2 score of 0.96 and 0.91, respectively. While RFR algorithm offer lowest prediction accuracy with R and R2 score of 0.91 and 0.79, respectively.
- The prediction accuracy and generalization potential of the ML based models is highly governed by the size of input parameter vector, number of datapoints in the dataset, as well as the range of input parameters. To develop models with higher accuracy, a larger dataset with wide spread of input parameters must be used to train the algorithms.

Table 6.1: Summary of Dataset-E used for training the ML algorithms

Beam Name	L	A_c	C_c	A_s	A_f	f_c	f_y	f_u	T_g	t_{ins}	h_i	ρ_{ins}	k_{ins}	c_{ins}	Ld	anc t_{ins}	FR
B1	3	60000	25	402	0	48	591	0	0	0	0	0	0	0	61	0	90
B2	3	60000	25	402	0	46	591	0	0	0	0	0	0	0	61	0	90
B3	3	60000	25	402	120	44	591	2800	52	25	0	870	0.175	840	81	25	76
B4	3	60000	25	402	120	47	591	2800	52	40	80	870	0.175	840	81	40	90
B5	3	60000	25	402	120	45	591	2800	52	25	80	870	0.175	840	81	25	92
B6	3	60000	25	402	120	46	591	2800	52	0	0	870	0.175	840	81	40	76
B7	3	60000	25	402	120	48	591	2800	52	25	0	870	0.175	840	81	25	90
B8	3	60000	25	402	120	44	591	2800	52	25	0	875	0.125	840	81	25	91
B9	6	100000	20	402	67	23	375	4030	73	40	500	245	0.06	790	121	40	84
B10	3.7	103124	38	851	0	52	450	0	0	0	0	0	0	0	100	0	180
B11	3.7	103124	38	851	460	52	450	986	82	25	100	351	0.116	700	140	25	180
B12	1.5	12000	10	57	0	26	542	0	0	0	0	0	0	0	10	0	69
B13	1.5	12000	10	57	60	26	542	2742	55	0	0	0	0	0	16	0	60
B14	1.5	12000	10	57	60	26	542	2742	55	25	0	475	0.058	687	16	25	90
B15	1.5	12000	10	57	60	26	542	2742	55	25	0	870	0.164	712	16	25	89
B16	1.5	12000	10	57	60	26	542	2742	55	40	0	475	0.058	687	16	40	208
B17	1.5	12000	10	57	60	26	542	2742	55	40	0	870	0.164	712	16	40	181
B18	1.3	12000	15	57	0	37	546	0	0	0	0	0	0	0	7	0	50
B19	1.3	12000	15	57	28	37	546	2076	47	0	0	0	0	0	23	0	15
B20	1.3	12000	15	57	28	37	546	2076	47	0	0	450	0.09	815	23	25	31
B21	1.3	12000	15	57	28	37	546	2076	47	25	0	450	0.09	815	23	25	32
B22	1.3	12000	15	57	28	37	546	2076	47	25	0	450	0.09	815	23	50	50
B23	1.3	12000	15	57	28	37	546	2076	47	25	0	450	0.09	815	23	75	75
B24	1.3	12000	15	57	28	37	546	2076	47	50	0	450	0.09	815	23	75	80
B25	1.3	12000	15	57	28	37	546	2076	85	25	0	450	0.09	815	23	50	74
B26	1.3	12000	15	57	28	37	546	2076	47	0	0	0	0	0	23	0	12
B27	1.3	12000	15	57	28	37	546	2076	47	25	0	450	0.09	815	23	50	61
B28	4.7	90000	20	402	33	31	372	4030	73	50	450	1000	0.12	500	80	50	149

Table 6.1 (cont'd)

B29	4.7	90000	20	402	33	31	372	4030	73	20	200	1000	0.12	500	80	50	117
B30	5.2	100000	20	943	33	31	372	4030	73	40	500	250	0.061	740	132	40	120
B31	5.2	100000	20	943	33	31	372	4030	73	1.5	500	600	0.06	800	132	1.5	123
B32	4.4	100000	25	760	0	40	364	0	0	0	0	0	0	0	76	0	129
B33	4.4	100000	25	760	42	40	364	3455	85	10	80	500	0.126	1036	102	10	199
B34	3	45000	19	157	0	30	500	0	0	0	0	0	0	0	48	0	77
B35	3	45000	19	157	60	30	500	2742	75	20	300	550	0.13	1080	48	20	100
B36	3	45000	19	157	60	30	500	2742	75	35	300	550	0.13	1080	48	35	108
B37	3	45000	19	157	60	30	500	2742	75	50	300	550	0.13	1080	48	50	127
B38	3	45000	19	157	60	30	500	2742	75	20	300	1650	0.67	800	48	20	92
B39	3	45000	19	157	60	30	500	2742	75	35	300	1650	0.67	800	48	35	114
B40	3	45000	19	157	60	30	500	2742	75	50	300	1650	0.67	800	48	50	104
B41	3	45000	19	157	60	30	500	2742	75	20	300	475	0.058	900	48	20	86
B42	3	45000	19	157	60	30	500	2742	75	35	300	475	0.058	900	48	35	128
B43	3	45000	19	157	60	30	500	2742	75	50	300	475	0.058	900	48	50	128
B44	3.7	60800	19	339	77	43	500	1172	80	19	152	425	0.156	1200	21	19	180
B45	3.7	60800	19	339	77	43	500	1172	80	25	152	425	0.156	1200	26	25	180
B45	3.7	125730	38	603	173	38	440	1034	82	0	0	0	0	0	98	0	180
B46	3.7	125730	38	603	173	38	440	1034	82	25	75	425	0.156	1200	98	25	180
B47	3.7	125730	38	603	173	38	440	1034	82	19	112	425	0.156	1200	116	19	176
B48	3.7	125730	38	603	102	43	460	1172	82	32	152	425	0.156	1200	97	32	240

Note: **The table is compiled using data from these studies** [44, 145, 147–151, 243, 244]**.**
L: length of beam (m); A_c: Area of concrete (mm^2); C_c: concrete cover (mm); A_s: Area of steel (mm^2); A_f: Area of FRP (mm^2); f_c: compressive strength of concrete (MPa); f_y: yield strength of steel (MPa); f_u: tensile strength of FRP (MPa); T_g: glass transition temperature of polymer (°C); t_{ins}: thickness of insulation at midspan (mm); h_i: depth of insulation on sides (mm); ρ_{ins}: density of insulation (kg/m^3); k_{ins}: thermal conductivity of insulation (W/mK); c_{ins}: specific heat of insulation (J/kg°C); ***Ld***: total load applied on beams (kN); anc_t_{ins}: thickness of insulation in anchorages (mm); ***FR***: fire resistance time (minutes).

Table 6.2: Statistical analysis of the input features in Dataset-E

Statistical Quantity	Mean (μ)	Median	Maximum value	Minimum value	Standard deviation (σ_{std})	Skewness	Kurtosis
L (m)	2.86	3	6	1.26	1.23	42.90	0.29
A_c (mm^2)	55170	45000	125730	12000	38228.35	69.29	0.45
C_c (mm)	21.08	19	38	10	8.15	38.67	0.91
A_s (mm^2)	318.95	157.08	942.48	56.55	274.91	86.19	0.87
f_c (mm^2)	67.83	60	460	0	71.95	106.07	3.42
f_y (MPa)	36.18	37	52	23	7.56	20.90	0.24
F_u (MPa)	503.22	500	591	364	68.63	13.64	-0.72
T_g (°C)	2125.03	2741.7	4030	0	1167.11	54.92	-0.44
t_{ins} (mm)	56.5	55	85	0	26.18	46.34	-1.17
d_{ins} (mm)	21.71	25	50	0	16.23	74.75	0.05
ρ_{ins} (kg/m^3)	119.7	0	500	0	156.58	130.81	1.13
k_{ins} (W/mK)	511.72	450	1650	0	413.07	80.72	1.03
c_{ins} (J/kg°C)	0.12	0.09	0.67	0	0.15	120.20	2.82
L_d (kN)	682.98	815	1200	0	397.04	58.13	-0.78
$Anct_{ins}$ (mm)	58.918	48	140	7.2	37.56	63.75	0.52
FR (minutes)	26.61	25	75	0	19.70	74.03	0.31

Table 6.3: Performance metrics of SVR, RFR, and DNN model trained on Dataset-E and Dataset-EN

ML Algorithm	Performance metrics	Dataset-E		Dataset-EN	
		Training dataset	Test dataset	Training dataset	Test dataset
SVR model	R	0.94	0.94	0.99	0.95
	R^2	0.89	0.86	0.98	0.89
	RMSE	18.9	16.2	8.9	21.8
RFR model	R	0.96	0.91	0.98	0.94
	R^2	0.92	0.79	0.96	0.84
	RMSE	16.1	20.2	12.7	22.9
DNN model	R	0.99	0.96	0.98	0.96
	R^2	0.98	0.91	0.97	0.91
	RMSE	6.3	12.7	11.6	17.2

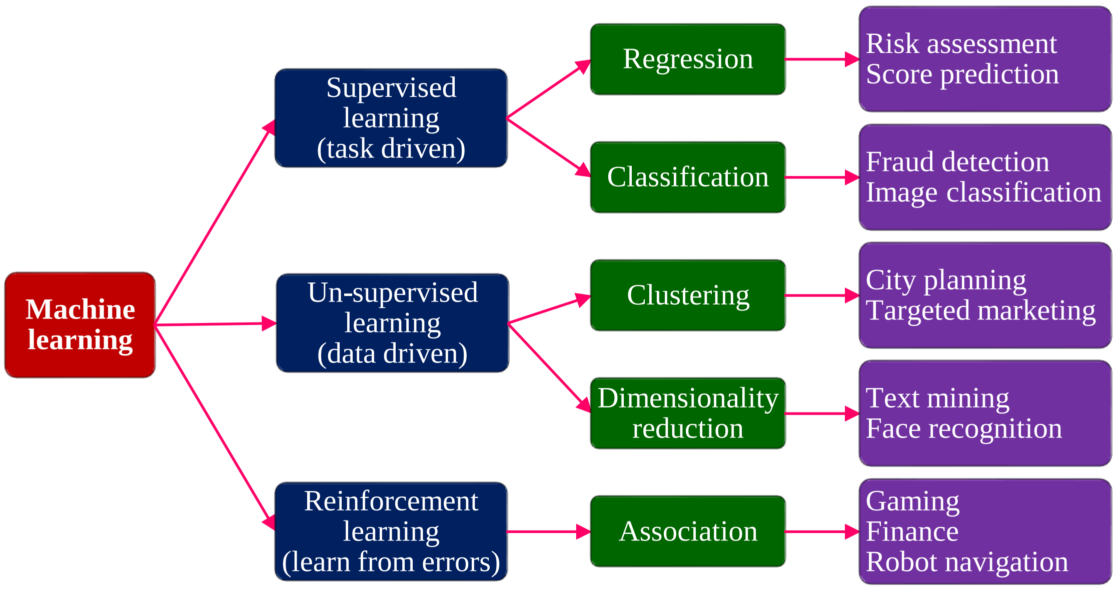

Figure 6.1: Type of machine learning and machine learning algorithms

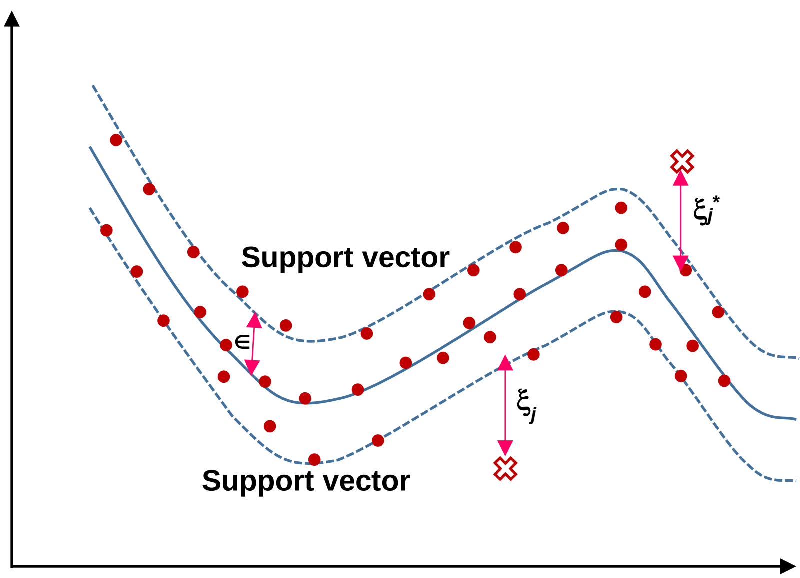

Figure 6.2: Pictorial representation of ∈-tube used in support vector regression algorithm

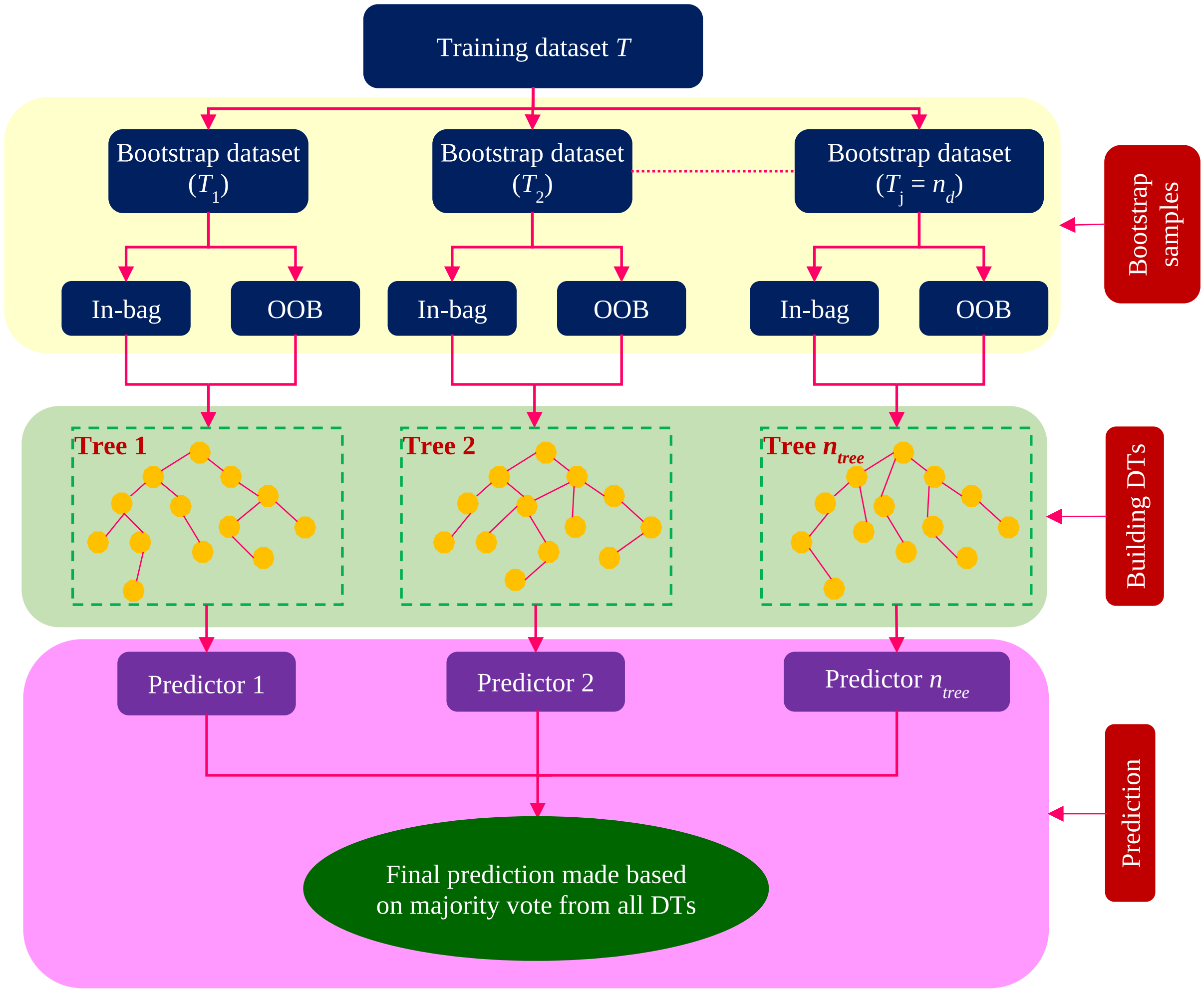

Figure 6.3: Structure of a random forest regressor

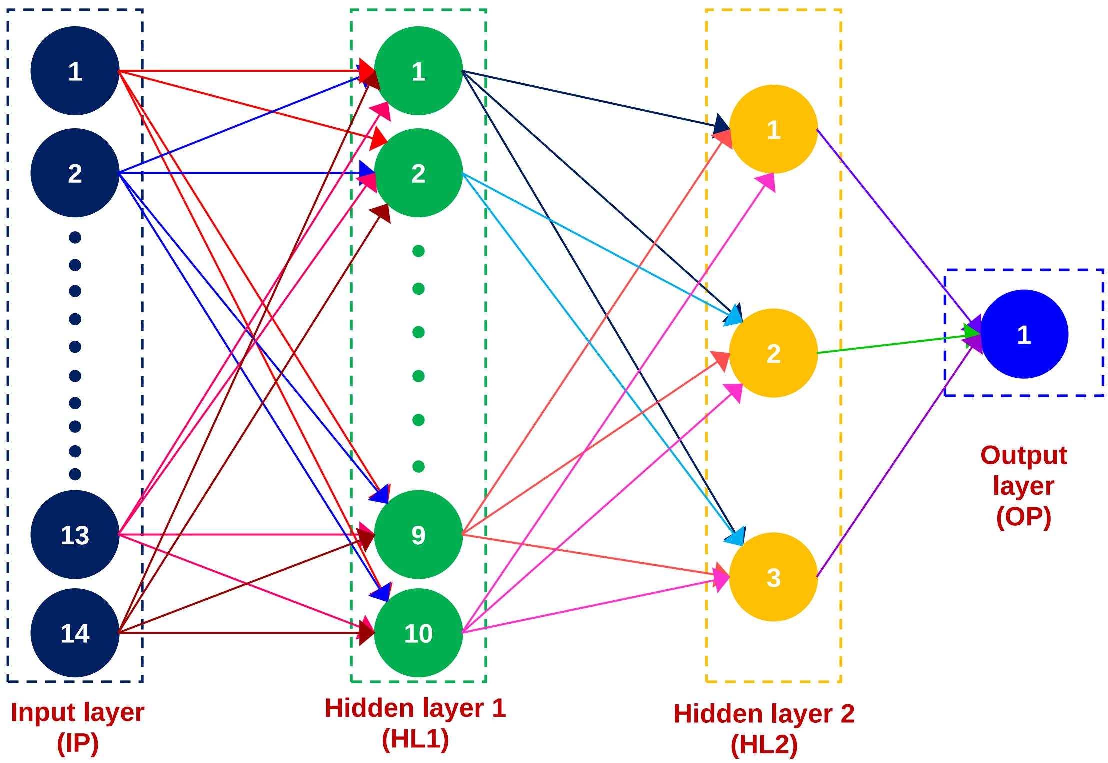

Figure 6.4: Typical structure of a deep neural network

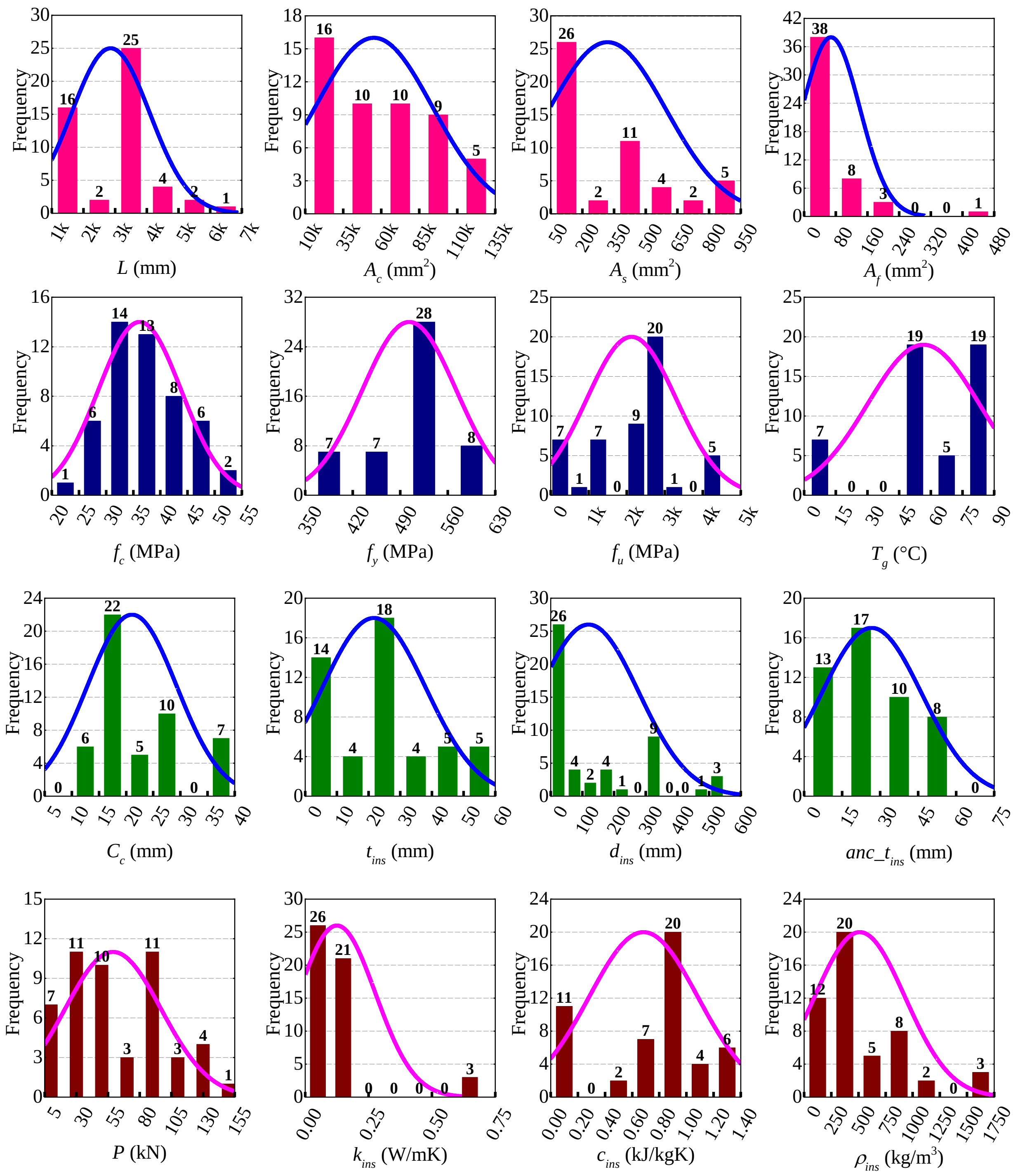

Figure 6.5: Frequency distribution of the input parameters in the Dataset-E

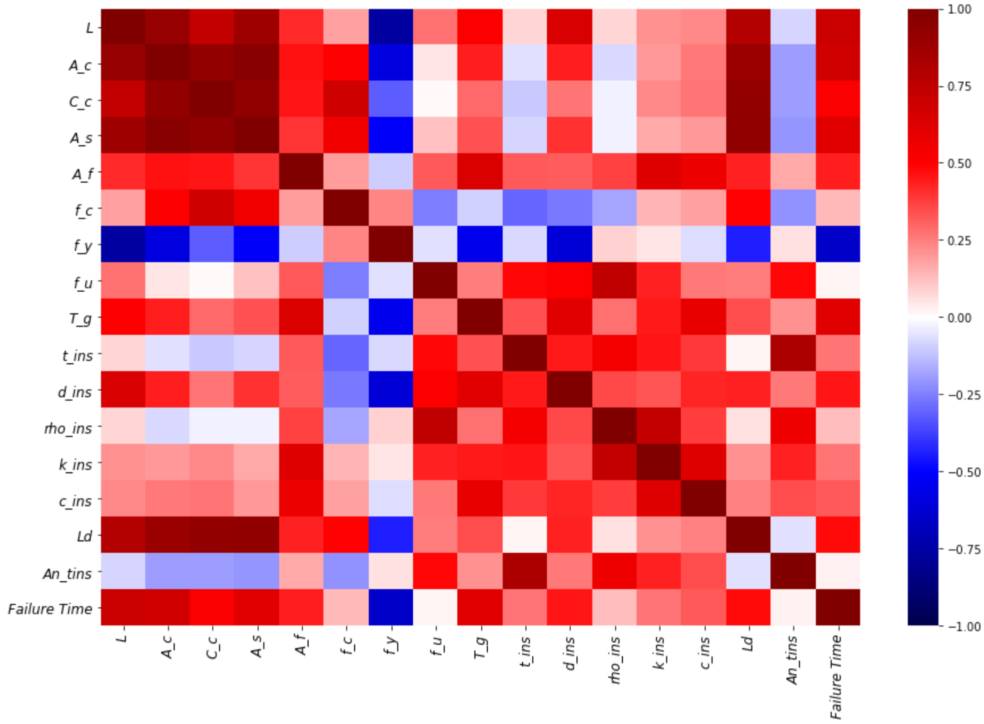

Figure 6.6: Correlation matrix for the input parameters of the dataset

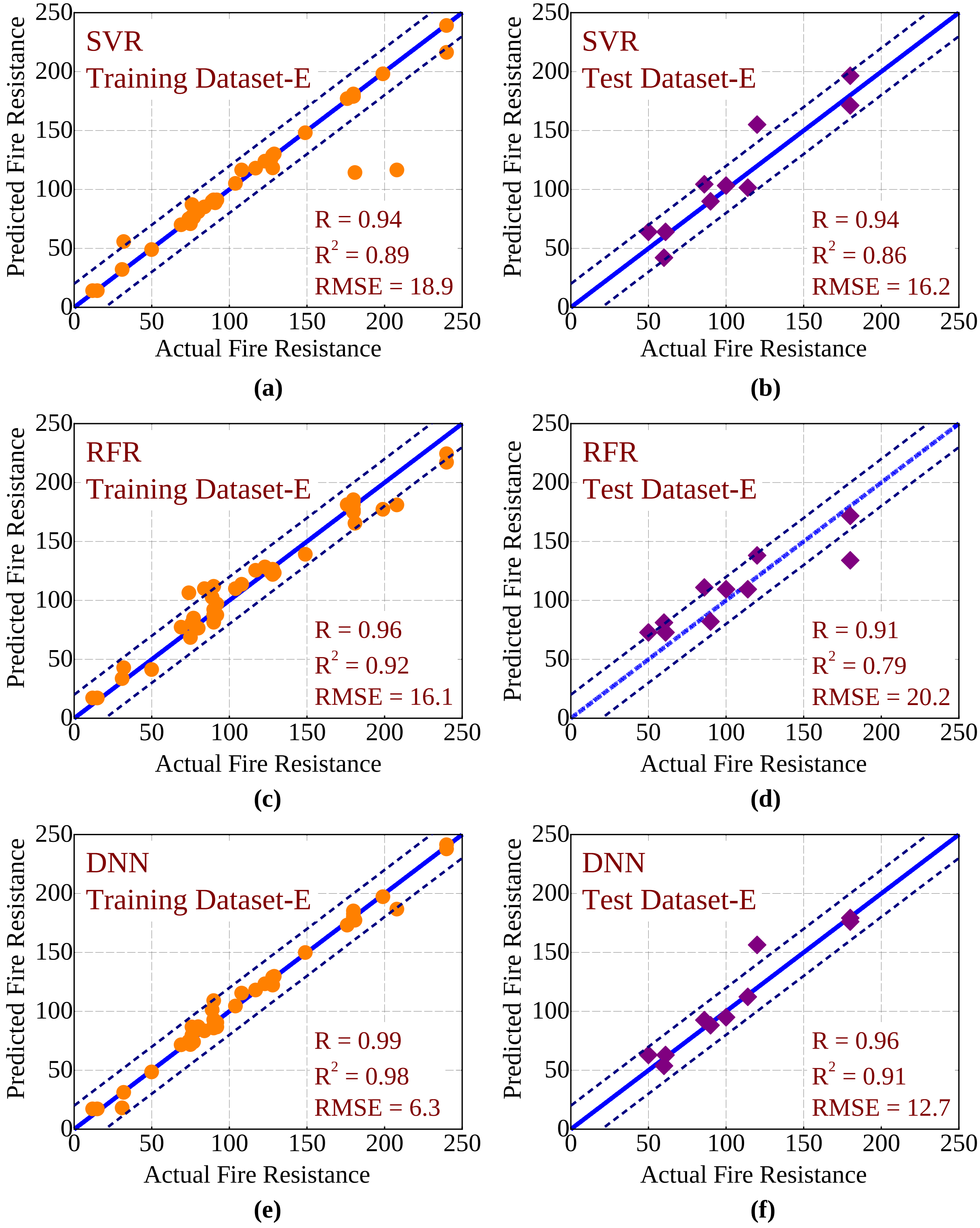

Figure 6.7: Comparison of actual fire resistance time with those predicted using ML based models trained over Dataset-E: (a) SVR- training data; (b) SVR- test data; (c) RFR- training data; (d) RFR- test data; (e) DNN- training data; (f) DNN- test data

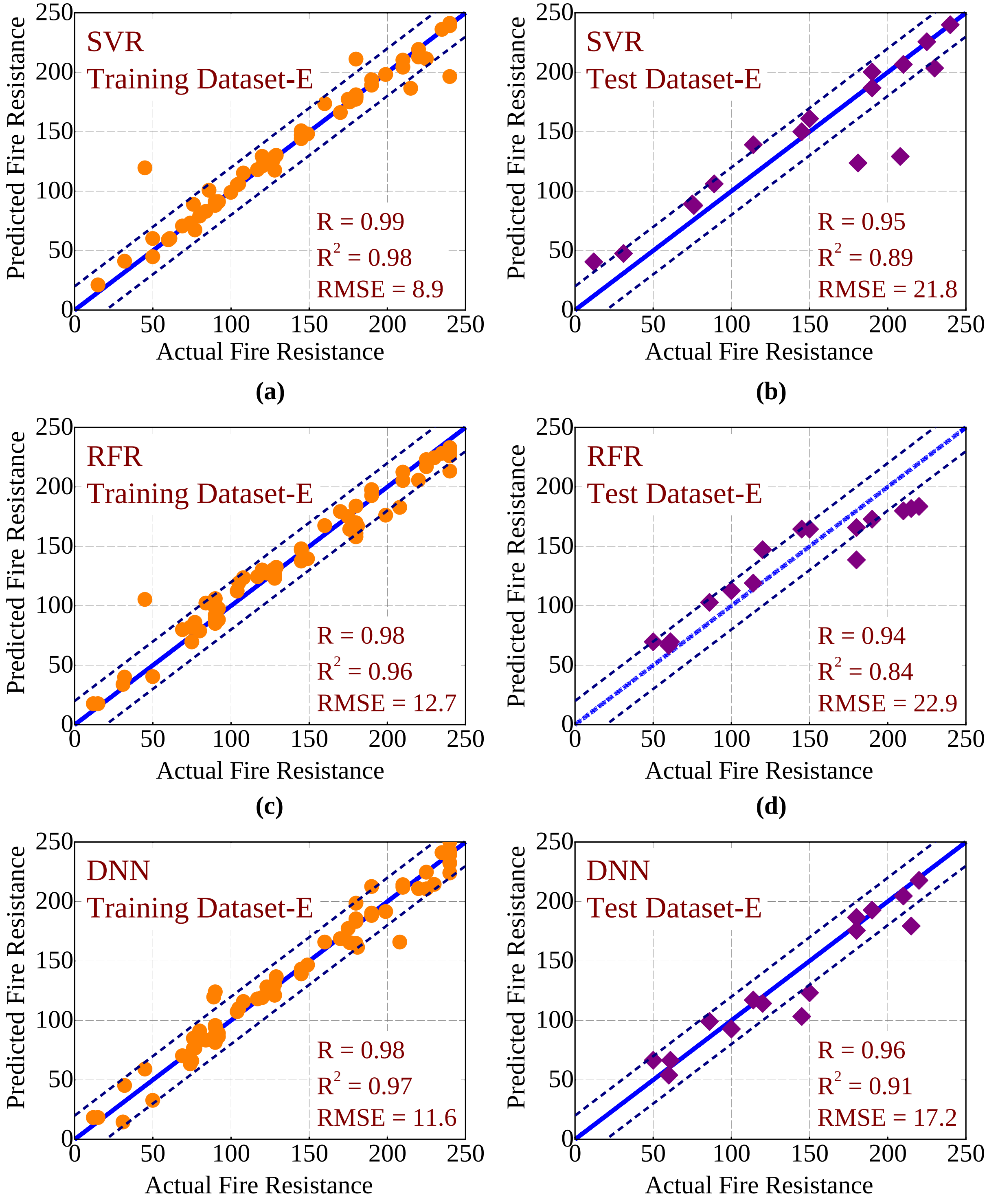

Figure 6.8: Comparison of actual fire resistance time with those predicted using ML based models trained over Dataset-EN: (a) SVR- training data; (b) SVR- test data; (c) RFR- training data; (d) RFR- test data; (e) DNN- training data; (f) DNN- test data

CHAPTER 7

CONCLUSIONS

7.1 General

This dissertation presents a comprehensive study on the response of FRP-strengthened concrete flexural members under combined effects of structural loading and fire exposure. An elaborate literature review was conducted on the mechanical properties of FRP materials and on fire response of FRP-strengthened RC flexural members. Through this extensive literature review the current level of understanding and knowledge gaps pertaining to fire performance of strengthened structural members was enumerated. Both experimental and numerical studies were undertaken to develop a thorough understanding on fire performance of FRP-strengthened concrete flexural members and to address the knowledge gaps identified in literature review.

As part of experimental studies, uniaxial tension tests were carried out at different temperatures to evaluate high temperature tensile strength of CFRP, while double lap shear tests were conducted through an innovative test set up to evaluate the bond strength of CFRP-concrete interface at elevated temperatures. Further, full scale fire tests were conducted on five CFRP-strengthened RC T-beams and two CFRP-strengthened RC slabs. Data from the tests was utilized to gauge the effect of insulation thickness and configuration, strengthening level, load level and fire exposure time on fire resistance of CFRP-strengthened concrete flexural members.

As part of numerical studies, a macroscopic finite element based numerical model, previously developed for FRP-strengthened concrete beams was extended to evaluate the response of FRP-strengthened RC slabs under combined effects of fire exposure and structural loading. The model utilizes a member level approach and evaluates the fire resistance of an FRP-strengthened concrete flexural member through a sequential thermal and structural analysis procedure. In the thermal analysis temperature distribution within the cross-section is computed. Whereas in structural analysis the temperature dependent moment curvature relations are generated, and deflection of the flexural member is computed through stiffness analysis.

The updated model accounts for material nonlinearities including softening of concrete in tension and compression, various strain components, properties of constituent materials at elevated temperature, temperature induced bond degradation at FRP-concrete interface, and all applicable failure limit states governing fire response of FRP-strengthened RC flexural members. The developed numerical model was validated by comparing the predicted the thermal and structural response parameters with the response parameters measured in tests available in open literature and tests conducted at MSU.

The validated model was further applied to establish suitable high temperature material properties of FRP, and insulation required for fire resistance analysis of strengthened flexural members through a numerical study on fire tested beams. Further, the model was applied to conduct a set of parametric studies on strengthened beams and slabs to quantify the effect of critical factors influencing fire performance of FRP-strengthened concrete members. Finally, three different machine learning (ML) algorithms, namely support vector regression (SVR), random forest regression (RFR), and deep neural network (DNN) were implemented to develop a ready to use tool for computing fire resistance of FRP-strengthened beams. The algorithms were trained over a dataset compiled using the fire resistance tests on FRP-strengthened RC beams available in open literature. Additionally, the information generated from the parametric studies was also utilized in developing a larger dataset for training the ML algorithms.

7.2 Key Findings

Based on the information presented in this dissertation, following key conclusions are drawn:

1) The fire performance of FRP-strengthened concrete flexural members is a complex phenomenon which is influenced by several factors. Limited experimental and numerical studies are undertaken on fire response of FRP-strengthened concrete flexural members. In particular there are no numerical models to evaluate fire resistance of strengthened RC slabs, taking into account thermal and structural response. Additionally, limited information is available regarding the high temperature mechanical properties of FRP. Moreover, the available information is case specific and there exists a wide variation in it.
2) The high temperature uniaxial tension test and double shear tests indicate that tensile strength and FRP-concrete interfacial bond strength decreases rapidly with increase in temperature. The tensile strength decreases by 20% at a temperature close to the T_g of polymer matrix. Whereas the interfacial bond strength decreases by almost 35% at a temperature close to the T_g of the bonding adhesive.
3) Results from the fire tests on FRP-strengthened beams indicate that FRP-strengthened RC beams can attain three hours fire resistance without any insulation provided the applied structural load is less than 50% and 75% of the ultimate strengthened capacity and un-strengthened capacity of the RC beam, respectively. Further, the tests indicate that FRP-strengthened RC beams and slabs can provided with at least 19 mm thick insulation and subjected to service load level can achieve up to four and three hours of fire resistance, respectively, under ASTM E119 standard fire exposure.
4) The proposed macroscopic finite element based numerical model is capable of tracing the response of FRP-strengthened concrete flexural members from pre-loading stage to

collapse under fire. The model utilizes a member level approach (an improvement over sectional level analysis) and can account for different geometrical cross-section, different insulation configuration and thickness, loading type and fire exposure. Further, the model incorporates high temperature material properties of constitutive materials, namely concrete, steel rebars, FRP, and insulation, including different types of relations for temperature induced interfacial bond degradation and temperature induced material nonlinearity. The thermal and structural response predicted by the model are in close agreement with those measured in the fire tests.

5) Results from the experimental and numerical studies indicate that fire insulation, fire scenario, and applied load level are the critical factors that substantially influence the fire response of strengthened flexural members. Whereas the strengthening level and reinforcement ratio has moderate effect on the fire performance of strengthened concrete flexural members.

6) Regarding insulation it can be concluded from the from the experimental and numerical studies that thickness, configuration, and application strategy of the insulation has significant influence on the fire performance of FRP-strengthened concrete flexural member.

    - An uninsulated FRP-strengthened concrete flexural member has lower fire resistance than that of un-strengthened uninsulated concrete flexural member. Whereas a strengthened and un-strengthened concrete flexural member has same fire resistance, when protected with fire insulation and subjected to identical structural loading and fire exposure.

- Additionally, it can be inferred that a minimum depth on insulation equivalent to twice the concrete cover on the side surface can help achieve at least three hours of fire resistance in FRP-strengthened beams.
- Further it can be concluded that provision of primer putty layer prior to spraying of insulation layer reduces the bond between insulation and concrete surface.

7) The high temperature material properties of FRP and insulation including temperature induced FRP-concrete bond degradation used as an input to numerical models have significant influence on fire resistance assessment of strengthened concrete flexural members.
    - The thermal properties of FRP have negligible effect, whereas temperature dependent mechanical property relations for FRP and the thermal properties of insulation have significant effect of fire response evaluation of strengthened flexural member. Therefore, their temperature dependence must be considered in the fire resistance analysis.
    - The FRP-concrete bond degradation significantly affects the fire performance of strengthened concrete members. The contribution of FRP towards the stiffness of the structural members is lost much earlier than towards the capacity of the member.
    - The member level analysis indicates that the relative slip resulting from bond degradation must be computed separately at each section along the length of the beam rather than idealizing slip at the critical section as the slip along the entire length of the member.
8) The proposed ML based predictive models are highly effective in predicting fire resistance of strengthened concrete beams with or without insulation. Among the different algorithms

used in this study the DNN algorithm provides relatively accurate estimate of fire resistance on known and unknown datasets. The proposed autonomous models can be directly used by design engineers and practitioners, as a ready to use tool for predicting fire resistance of FRP-strengthened concrete beams.

7.3 Recommendations for Future Work

The research presented in this dissertation has advanced the state-of-the-art with respect to fire response of FRP-strengthened concrete flexural members. However additional research is needed to gain further insights into some of the complexities related to the behavior of strengthened concrete members under fire conditions. The following are some of the key recommendations for future research in this area:

- Due to a large variability in the available FRP sheets and bonding adhesive materials, additional experimental data is needed to evaluate the interaction of different bonding adhesives with concrete, especially the effect of geopolymer and cementitious material-based adhesives used for applying FRP to concrete surface on the fire response of strengthened members must be evaluated.
- Test data on fire response of FRP-strengthened concrete flexural members under different design fire scenarios, different insulation layout along length and in anchorages, different strengthening layouts (in slabs), different restraint conditions and with different sensors capable of measuring FRP-concrete interfacial strains is required.
- Further work is required to incorporate advanced features into the proposed numerical model namely, cracking in insulation, moisture evaporation in concrete and insulation, and pyrolysis in FRP. Moreover, the model needs to be modified to evaluate shear response of

strengthened concrete flexural members under fire conditions as well as to evaluate the fire resistance of flexural members strengthened using geopolymer bonded fiber sheet.

- Test data and numerical studies are required to evaluate the fire resistance of two-way RC slabs strengthened with FRP.
- More work is required to develop performance based rational design methodology which accounts for all the parameters influencing the fire resistance of strengthened concrete flexural members including temperature induced bond degradation and different fire scenarios.
- In recent year, biopolymers are being used in construction industry, due to their numerous advantages such as, sustainability, cost effectiveness, lightweight characteristics, appreciable specific strength, biodegradability, environmental friendliness of renewable materials and health and safety of manufacturer and consumers. Therefore, there is merit to use of natural fiber reinforced biopolymer composites for strengthening applications, which must be explored.

7.4 Research Impact

Over the past few decades, FRP materials have emerged as promising and cost-effective solution for strengthening and retrofitting of concrete structures. The advantages such as high strength to weight ratio, ease of application, and durability make FRP a primary choice over other traditional materials such as steel plates, concrete, etc. However, the poor performance of FRP under fire conditions due to the sensitivity of polymer matrix to high temperatures, hinders the application of FRP in buildings, where satisfactory fire resistance of structural member is a primary requirement. Fire performance evaluation of FRP-strengthened flexural members is a complicated task, which is governed by several factors. While the design codes and standards recommend neglecting FRP for fire design of strengthened concrete members, the rational approaches available in open literature either neglect important factors such as temperature induced bond degradation or use over simplified equations derived through several assumptions.

The experimental and numerical studies presented in this dissertation provide a comprehensive evaluation of the response of FRP-strengthened concrete flexural members under fire conditions. These studies have helped establish a fundamental understanding on the fire performance of strengthened concrete flexural members. Further, these experimental and numerical studies have quantified the effect of several critical factors, such as insulation configuration and thickness, load levels, fire scenario, strengthening level, and reinforcement ratio, influencing the fire response of strengthened beams and slabs. Moreover, the material property tests provide innovative test methods for evaluating the tensile strength and FRP-concrete interfacial bond strength at elevated temperatures. These studies indicate that insulated FRP-strengthened concrete beams and slabs can sustain service loads for at least four and three hours, respectively. Thus, it is apparent from these studies that external fire protection is required to achieve satisfactory fire resistance in strengthened flexural members.

Additionally, the numerical model presented in this study provides an effective alternative to costly and time-consuming fire resistance tests for evaluating the fire performance of FRP-strengthened concrete flexural members. The model accounts for different geometry, insulation configuration, high temperature material properties, temperature inducted FRP-concrete bond degradation and all applicable failure limit states. Moreover, the stress and strain distribution in the cross-section of the beam due to applied loading as well as due to the maximum capacity of cross-section can be used for carrying out post-fire stability analysis on the strengthened members.

Thus, the model can be used to conduct detailed fire resistance analysis and performance-based fire design of FRP-strengthened concrete flexural members.

Moreover, the ML algorithms based predictive models demonstrate the potential of implementing AI for fire resistance evaluation of the FRP-strengthened concrete members. The predictive models developed using different ML algorithms by training over the dataset compiled from fire resistance tests on strengthened beams, available in open literature, can be effectively used for determining fire resistance of FRP-strengthened beams in practical design scenarios and developing code provisions.

APPENDICES

APPENDIX A

ELEVATED TEMPERATURE MATERIAL PROPERTIES

This Appendix provides a summary of high temperatures material property, including thermal, mechanical, and deformation property relations for concrete, steel, FRP, and insulation, as specified in ASCE manual [78] and Eurocode 2 [79] or any other test data. Thermal properties include specific heat, thermal conductivity, and density, while the strength properties include compressive/tensile strength, elastic modulus. Some documents, such as ASCE manual provides specific heat capacity instead of providing separate relations for specific heat and density. Additionally, the constitutive relations for deformation properties such as, thermal expansion (for concrete and steel), creep strain, transient strain (only for concrete) are also provided.

Table A.1: Notations and units to be considered for each property unless stated otherwise

Property	Notations	Units	Remarks
Compressive strength of concrete	$f'_{c,T}$	MPa	
Creep strain	$\varepsilon_{x,cr,T}$		
Density	$\rho_{x,T}$	kg/m^3	
Heat capacity	$\rho_{x,T}c_{x,T}$	J/m^3°C or kJ/m^3°C	
Specific heat	$c_{x,T}$	J/kg°C	
Temperature	T	°C	
Tensile strength of concrete	$f_{t,c,T}$	MPa	
Tensile strength of FRP	$F_{u,T}$	MPa	
Thermal conductivity	$k_{x,T}$	W/m°C	
Thermal strain	$\varepsilon_{x,th,T}$	-	
Transient strain	$\varepsilon_{x,tr,T}$		
Yield strength of steel	$f_{y,T}$	MPa	

Note: Subscript ***x*** must be replaced by the type of material: concrete (*c*); steel (*s*); FRP (*frp*) and insulation (ins), and subscript (*T*) indicates the temperature level *T*

A.1 CONCRETE

A.1.1 Thermal Properties

(i) As per Eurocode 2

Eurocode 2 [79] provides separate relations for defining variation of specific heat and density of concrete with temperature, and these relations are not categorized on the basis of aggregate.

Table A.2: Specific heat capacity and thermal conductivity of concrete as per Eurocode 2

Property	Type of Aggregate	Temperature Range (°C)	Constitutive relations
Specific Heat $c_{c,T}$ (J/kg°C)	*Siliceous and Carbonaceous*	$20 \le T \le 100$	$c_{c,T} = 900$
		$100 \le T \le 200$	$c_{c,T} = 900 + (T - 100)$
		$200 \le T \le 400$	$c_{c,T} = 1000 + (T - 200)/2$
		$400 \le T \le 1200$	$c_{c,T} = 1100$
Density $\rho_{c,T}c_{c,T}$ (kg/m^3)		$20 \le T \le 115$	$\rho_{c,T} = \rho_{20°C}$
		$115 \le T \le 200$	$\rho_{c,T} = \rho_{20°C}(1 - 0.02(T - 115)/85)$
		$200 \le T \le 400$	$\rho_{c,T} = \rho_{20°C}(0.98 - 0.03(T - 200)/200)$
		$400 \le T \le 1200$	$\rho_{c,T} = \rho_{20°C}(0.95 - 0.07(T - 400)/800)$
Thermal Conductivity $k_{c,T}$ (W/m°C)		*Upper Limit:* $20 \le T \le 1200$	$k_{c,T} = 2 - 0.2451(T/100) + 0.0107(T/100)^2$
		Lower Limit: $20 \le T \le 1200$	$k_{c,T} = 1.36 - 0.136(T/100) + 0.0057(T/100)^2$

(ii) As per ASCE Manual

ASCE manual [78] provides constitutive relations for the specific heat capacity and thermal conductivity of concrete which is further categorized based on type of coarse aggregate used in batch mix of concrete. The relations for these properties are summarized in the table below.

Table A.3: Specific heat capacity and thermal conductivity of concrete as per ASCE manual

Property	Type of Aggregate	Temperature Range (°C)	Constitutive relations
Specific Heat Capacity $\rho_{c,T}c_{c,T}$ (J/m^3°C)	*Siliceous*	$0 \le T \le 200$	$\rho_{c,T}c_{c,T} = (0.005T + 1.7) \times 10^6$
		$200 \le T \le 400$	$\rho_{c,T}c_{c,T} = 2.7 \times 10^6$
		$400 \le T \le 500$	$\rho_{c,T}c_{c,T} = (0.013T - 2.5) \times 10^6$
		$500 \le T \le 600$	$\rho_{c,T}c_{c,T} = (-0.013T + 10.5) \times 10^6$
		$T \ge 600$	$\rho_{c,T}c_{c,T} = 2.7 \times 10^6$
	Carbonaceous	$0 \le T \le 400$	$\rho_{c,T}c_{c,T} = 2.566 \times 10^6$
		$400 \le T \le 410$	$\rho_{c,T}c_{c,T} = (0.1765T - 68.034) \times 10^6$
		$410 \le T \le 455$	$\rho_{c,T}c_{c,T} = (-0.05043T + 25.00671) \times 10^6$
		$455 \le T \le 500$	$\rho_{c,T}c_{c,T} = 2.566 \times 10^6$
		$500 \le T \le 635$	$\rho_{c,T}c_{c,T} = (0.01603T - 5.44881) \times 10^6$
		$635 \le T \le 715$	$\rho_{c,T}c_{c,T} = (0.005T - 100.90225) \times 10^6$
		$715 \le T \le 785$	$\rho_{c,T}c_{c,T} = (-0.22103T + 176.07343) \times 10^6$
		$T \ge 785$	$\rho_{c,T}c_{c,T} = 2.566 \times 10^6$
	Lightweight	$0 \le T \le 400$	$\rho_{c,T}c_{c,T} = 1.930 \times 10^6$
		$400 \le T \le 420$	$\rho_{c,T}c_{c,T} = (0.0772T - 28.95) \times 10^6$
		$420 \le T \le 435$	$\rho_{c,T}c_{c,T} = (-0.1029T + 46.706) \times 10^6$
		$435 \le T \le 600$	$\rho_{c,T}c_{c,T} = 1.930 \times 10^6$
		$600 \le T \le 700$	$\rho_{c,T}c_{c,T} = (0.03474T - 18.9140) \times 10^6$
		$710 \le T \le 720$	$\rho_{c,T}c_{c,T} = (-0.1737T + 126.994) \times 10^6$
		$T \ge 720$	$\rho_{c,T}c_{c,T} = 1.93 \times 10^6$
Thermal Conductivity $k_{c,T}$ (W/m°C)	*Siliceous*	$0 \le T \le 800$	$k_{c,T} = -0.000625T + 1.5$
		$T \ge 800$	$k_{c,T} = 1.0$
	Carbonaceous	$0 \le T \le 293$	$k_{c,T} = 1.355$
		$T \ge 293$	$k_{c,T} = -0.001241T + 1.7162$
	Lightweight	$0 \le T \le 600$	$k_{c,T} = -0.000395833T + 0.925$
		$T \ge 600$	$k_{c,T} = 0.6875$

A.1.2 Strength Properties of Concrete

(i) As per Eurocode 2

$$\sigma_c = \frac{3\varepsilon f'_{c,T}}{\varepsilon_{c1,T}\left(2+\left(\frac{\varepsilon}{\varepsilon_{c1,T}}\right)^3\right)}, \varepsilon \le \varepsilon_{cu1,T}$$

For $\varepsilon_{c1(T)} < \varepsilon \le \varepsilon_{cu1(T)}$, the Eurocode permits the use of linear as well as nonlinear descending branch in the numerical analysis. For the parameters in this equation refer to Table A.4.

Table A.4: Values for parameters of the high temperature stress-strain relations of NSC

T (°C)	Normal strength concrete					
	Siliceous Aggregate			Carbonaceous Aggregate		
	$\frac{f'_{c,T}}{f'_{c,20°C}}$	$\varepsilon_{c1,T}$	$\varepsilon_{cu1,T}$	$\frac{f'_{c,T}}{f'_{c,20°C}}$	$\varepsilon_{c1,T}$	$\varepsilon_{cu1,T}$
20	1	0.0025	0.02	1	0.0025	0.02
100	1	0.004	0.0225	1	0.004	0.023
200	0.95	0.0055	0.025	0.97	0.0055	0.025
300	0.85	0.007	0.0275	0.91	0.007	0.028
400	0.75	0.01	0.03	0.85	0.01	0.03
500	0.6	0.015	0.0325	0.74	0.015	0.033
600	0.45	0.025	0.035	0.6	0.025	0.035
700	0.3	0.025	0.0375	0.43	0.025	0.038
800	0.15	0.025	0.04	0.27	0.025	0.04
900	0.08	0.025	0.0425	0.15	0.025	0.043
1000	0.04	0.025	0.045	0.06	0.025	0.045
1100	0.01	0.025	0.0475	0.02	0.025	0.048
1200	0	-	-	0	-	-

(ii) <u>As per ASCE Manual</u>

$$\sigma_c = \begin{Bmatrix} f'_{c,T}\left[1-\left(\frac{\varepsilon-\varepsilon_{\max,T}}{\varepsilon_{\max,T}}\right)^2\right], \varepsilon \le \varepsilon_{\max,T} \\ f'_{c,T}\left[1-\left(\frac{\varepsilon_{\max,T}-\varepsilon}{3\varepsilon_{\max,T}}\right)^2\right], \varepsilon > \varepsilon_{\max,T} \end{Bmatrix}$$

$$f'_{c,T} = \begin{Bmatrix} f'_c & 20 \le T \le 450 \\ f'_c\left[2.011 - 2.353\left(\dfrac{T-20}{1000}\right)^2\right] & 450 < T \le 874 \\ 0 & T > 874 \end{Bmatrix}$$

$$\varepsilon_{\max,T} = 0.0025 + (6.0T + 0.04T^2) \times 10^{-6}$$

A.1.3 Deformation Properties

› **Thermal Expansion**

(i) As per Eurocode 2

Eurocode 2 [79] quantifies thermal expansion through thermal strain variation with temperature which is categorized on the basis of aggregates.

Table A.5: Thermal strain of concrete as per Eurocode 2

Concrete Type	Temperature Range (°C)	Constitutive relations
Siliceous Aggregate	$20 \le T \le 700$	$\varepsilon_{c,th} = -1.8\times10^{-4} + 9\times10^{-6}T + 2.3\times10^{-11}T^3$
	$700 \le T \le 1200$	$\varepsilon_{c,th} = 14\times10^{-3}$
Carbonaceous Aggregate	$20 \le T \le 805$	$\varepsilon_{c,th} = -1.2\times10^{-4} + 6\times10^{-6}T + 1.4\times10^{-11}T^3$
	$805 \le T \le 1200$	$\varepsilon_{c,th} = 12\times10^{-3}$

The above thermal strains are relative to length at 20°C, therefore, with a reference of 20°C the modification factor for coefficient of thermal expansion (α) can be calculated as:

$$f_\alpha(T) = \frac{\alpha(T)}{\alpha(20)} = \frac{\varepsilon(T)/\Delta T}{\varepsilon(20)} = \frac{\varepsilon(T)/(T-20)}{\varepsilon(20)}$$

(ii) As per ASCE Manual

ASCE manual [78] provides same relation for carbonaceous and siliceous aggregate based concrete for thermal expansion in terms of coefficient of thermal expansion as given below:

$$\alpha_c = (0.008T + 6) \times 10^{-6}$$

› **Creep Strain as per Anderberg and Thelandersson** [93]

$$\varepsilon_{c,cr} = \beta_1 \frac{\sigma}{f'_{c,T}} \sqrt{t} e^{d(T-293)}$$

where, ε_{cr} is creep strain; β_1 is a constant with value = 6.28×10^{-6} $s^{-0.5}$; $f'_{c,T}$ is compressive strength of concrete at elevated temperature; σ is stress in concrete at current temperature.

› **Transient Strain as per Harmathy** [167]

$$\varepsilon_{c,tr} = k_2 \frac{\sigma}{f'_{c,20}} \varepsilon_{th}$$

where, ε_{tr} is transient strain; k_2 is a constant with value ranging between 1.8 and 2.35; $f'_{c,20}$ is compressive strength of concrete at ambient temperature; σ is stress in concrete at current temperature.

A.2 REINFORCING STEEL

A.2.1 Thermal Properties

ASCE manual [78] provides relations for high temperature thermal properties of steel rebars in form of specific heat capacity and thermal conductivity, whereas, Eurocode 2 [79] provides relations for thermal conductivity and specific heat only, as Eurocode 2 assumes density of steel to be constant with temperature.

(i) As per Eurocode 2

Table A.6: Thermal properties of steel rebars as per Eurocode 2

Property	Temperature Range (°C)	Constitutive relations
Specific Heat $c_{s,T}$ (J/kg°C)	$20 \le T \le 600$	$c_{c,T} = 425 + 7.73\times10^{-1}T - 1.69\times10^{-2}T^2 + 2.22\times10^{-6}T^3$
	$600 \le T \le 735$	$c_{c,T} = 666 + 13002/(738 - T)$
	$735 \le T \le 900$	$c_{c,T} = 545 + 17820/(T - 731)$
	$900 \le T \le 1200$	$c_{c,T} = 650$
Thermal Conductivity $k_{s,T}$ (W/m°C)	$20 \le T \le 800$	$k_{s,T} = 54 - 3.33\times10^{-2}T$
	$800 \le T \le 1200$	$k_{s,T} = 27.3$

(ii) As per ASCE Manual

Table A.7: Thermal properties of steel rebars as per ASCE manual

Property	Temperature Range (°C)	Constitutive relations
Specific Heat Capacity $\rho_{s,T}c_{s,T}$ (J/m³°C)	$0 \le T \le 650$	$\rho_{s,T}c_{s,T} = (0.004T + 33)\times10^6$
	$650 \le T \le 725$	$\rho_{s,T}c_{s,T} = (0.068T - 38.3)\times10^6$
	$725 \le T \le 800$	$\rho_{s,T}c_{s,T} = (-0.086T + 73.35)\times10^6$
	$T \ge 800$	$\rho_{s,T}c_{s,T} = 4.55\times10^6$
Thermal Conductivity $k_{s,T}$ (W/m°C)	$20 \le T \le 900$	$k_{s,T} = 48 - 0.022T$
	$T \ge 800$	$k_{s,T} = 28.2$

A.2.2 Strength Properties

(i) As per ASCE Manual

$$\varepsilon_s \le \varepsilon_p \quad \sigma_s = \frac{f(T,0.001)}{0.001}\varepsilon_s$$

$$\varepsilon_s > \varepsilon_p \quad \sigma_s = \frac{f(T,0.001)}{0.001}\varepsilon_p + f(T,\varepsilon_s - \varepsilon_p + 0.001) - f(T,0.001)$$

where,

$$f(T,x) = 6.9(50 - 0.04T)[1 - \exp((-30 + 0.03T)\sqrt{x})]$$

$$\varepsilon_p = 4 \times 10^{-6} f_{y,20}$$

where, ε_s is strain in steel reinforcement, respectively, and $f_{y,20}$ is the yield strength of reinforcing steel (MPa) at room temperature.

(ii) As per Eurocode 2

$$\varepsilon_s \le \varepsilon_{sp,T} \quad \sigma_s = \varepsilon_s E_{s,T}$$

$$\varepsilon_{sp,T} < \varepsilon_s \le \varepsilon_{sy,T} \quad \sigma_s = f_{sp,T} - c + (b/a)(a^2 - (\varepsilon_{sy,T} - \varepsilon_s)^2)^{0.5}$$

$$\varepsilon_{sy,T} < \varepsilon_s \le \varepsilon_{st,T} \quad \sigma_s = f_{sy,T}$$

$$\varepsilon_{st,T} < \varepsilon_s \le \varepsilon_{su,T} \quad \sigma_s = f_{sy,T}\left(1 - \frac{\varepsilon_s - \varepsilon_{st,T}}{\varepsilon_{su,T} - \varepsilon_{st,T}}\right)$$

$$\varepsilon_s > \varepsilon_{su,T} \quad \sigma_s = 0.00$$

where,

$$\varepsilon_{sp,T} = \frac{f_{sp,T}}{E_{s,T}}, \varepsilon_{sy,T} = 0.02, \varepsilon_{st,T} = 0.15, \varepsilon_{su,T} = 0.2 \qquad a^2 = (\varepsilon_{sy,T} - \varepsilon_{sp,T})(\varepsilon_{sy,T} - \varepsilon_{sp,T} + \frac{c}{E_{s,T}})$$

$$b^2 = c(\varepsilon_{sy,T} - \varepsilon_{sp,T})E_{s,T} + c^2 \qquad c^2 = \frac{(f_{sy,T} - f_{sp,T})^2}{(\varepsilon_{sy,T} - \varepsilon_{sp,T})E_{s,T} - (f_{sy,T} - f_{sp,T})}$$

The values of $f_{sp,T}$, $f_{sy,T}$ and $E_{s,T}$ can be obtained from Table A.8.

Table A.8: Reduction factor for yield strength, proportional limit, elastic modulus of steel

Steel temperature T (°C)	$\frac{f_{y,T}}{f_{y,20°C}}$	$\frac{f_{sp,T}}{f_{y,20°C}}$	$\frac{E_{s,T}}{E_{s,20°C}}$
20	1	1	1
100	1	1	1
200	1	0.807	0.9
300	1	0.613	0.8
400	1	0.42	0.7
500	0.78	0.36	0.6
600	0.4	0.18	0.31
700	0.23	0.075	0.13
800	0.11	0.05	0.09
900	0.06	0.0375	0.0675
1000	0.04	0.025	0.045
1100	0.02	0.0125	0.0225
1200	0	0	0

A.2.3 Deformation Properties

› **Thermal Expansion**

(i) As per ASCE Manual

ASCE manual [78] provides the thermal expansion of steel rebars in terms of coefficient of thermal expansion as per the relations below:

$$20°C \le T \le 1000°C \quad \alpha_s = [0.004(T+12)]\times 10^{-6}$$

$$T \ge 1000°C \quad \alpha_s = 16\times 10^{-6}$$

(ii) As per Eurocode 2

Eurocode 2 [79] defines the thermal expansion in reinforcing steel rebars in terms of thermal strain as per the relations described below:

$$20°C \le T \le 750°C \quad \varepsilon_{s,th} = 1.2\times10^{-5}T + 0.4\times10^{-8}T^2 - 2.416\times10^{-4}$$

$$750°C \le T \le 860°C \quad \varepsilon_{s,th} = 11\times10^{-3}$$

$$860°C \le T \le 1200°C \quad \varepsilon_{s,th} = 2\times10^{-5}T - 6.2\times10^{-3}$$

A.3 CARBON FIBER REINFORCED POLYMER

A.3.1 Thermal Properties

› **Specific Heat**

In the following relations the specific heat of CFRP ($c_{frp,T}$) has the units of kJ/kg°C.

$$0°\text{C} \le T \le 325°\text{C} \quad c_{frp,T} = 1.25 + \frac{0.95}{325}T$$

$$325°\text{C} \le T \le 343°\text{C} \quad c_{frp,T} = 2.2 + \frac{2.8}{18}(T - 325)$$

$$343°\text{C} \le T \le 510°\text{C} \quad c_{frp,T} = 5.0 + \frac{-0.15}{167}(T - 343)$$

$$510°\text{C} \le T \le 538°\text{C} \quad c_{frp,T} = 4.85 + \frac{-3.59}{28}(T - 510)$$

$$538°\text{C} \le T \le 3316°\text{C} \quad c_{frp,T} = 1.265 + \frac{1.385}{2778}(T - 538)$$

$$T \ge 3316°\text{C} \quad c_{frp,T} = 0$$

› **Density**

In the following equations, density ($\rho_{frp,T}$) has units of (g/cm^3) and T is in ℃.

$$0°\text{C} \le T \le 510°\text{C} \quad \rho_{frp,T} = 1.6$$

$$510°\text{C} \le T \le 538°\text{C} \quad \rho_{frp,T} = 1.6 + \frac{-0.35}{28}(T - 510)$$

$$538°\text{C} \le T \le 1200°\text{C} \quad \rho_{frp,T} = 1.25$$

› **Thermal conductivity**

$$0°\text{C} \le T \le 500°\text{C} \quad k_{frp,T} = 1.4 + \frac{-1.1}{500}T$$

$$500°\text{C} \le T \le 650°\text{C} \quad k_{frp,T} = 1.4 + \frac{-0.1}{150}(T - 500)$$

$$T \ge 650°\text{C} \quad k_{frp,T} = 0.2$$

A.3.2 Strength and Elastic Modulus Properties

The values of tensile strength ($f_{f,T}$) and elastic modulus ($E_{f,T}$) of FRP can be obtained from Table A.9.

Table A.9: Recommended relations for defining degradation of strength and stiffness of FRP

Property	Proposed by	Relation
Strength	Bisby (2003)	$\frac{f_{f,T}}{f_{f,20°\text{C}}} = \left(\frac{1-a_\sigma}{2}\right)\tanh\left(-b_\sigma\left(T - c_\sigma\right)\right) + \left(\frac{1+a_\sigma}{2}\right)$ $a_\sigma = 0.1;\ b_\sigma = 5.83\times10^{-3};\ c_\sigma = 339.54$
Elastic modulus	Bisby (2003)	$\frac{E_{f,T}}{E_{f,20°\text{C}}} = \left(\frac{1-a_E}{2}\right)\tanh\left(-b_E\left(T - c_E\right)\right) + \left(\frac{1+a_E}{2}\right)$ $a_E = 0.05;\ b_E = 8.68\times10^{-3};\ c_E = 367.41$

A.3.3 Bond Properties

The following equations provide the bond stress-slip for FRP (proposed by Dai et al. []).

$$\tau_{f,T} = 2G_{f,T}B_T\left(e^{-B_T\delta} - e^{-2B_T\delta}\right)$$

where,

$$\frac{G_{f,T}}{G_{f0}} = \frac{1}{2}\tanh\left[-c_2\left(\frac{T}{T_g} - c_3\right)\right] + \frac{1}{2}$$

$$\frac{B_T}{B_0} = \frac{\left(1-d_1\right)}{2}.\tanh\left[-d_2\left(\frac{T}{T_g} - d_3\right)\right] + \frac{\left(1+d_1\right)}{2}$$

and,

$$G_{f0} = 0.308\beta_w^2\sqrt{f_t}$$

$$\beta_w = \sqrt{\frac{2.25 - b_f / b_c}{1.25 + b_f / b_c}}$$

where, $\tau_{f,T}$ is shear bond stress at temperature T (N mm^{-2}); δ is the interfacial slip between FRP and concrete (mm); T_g is the glass transition temperature of the adhesive (°C); T is the elevated temperature (°C); G_{f0} and $G_{f,T}$ are the interfacial fracture energy at ambient and elevated temperature (N mm^{-1}); B_0 and B_T are the interfacial brittleness index at ambient and elevated temperature (mm^{-1}); and c_2, c_3, d_1, d_2, and d_3 are constants determined from least-square regression analysis of test data with values equal to 3.21, 1.31, 0.485, 14.1, and 0.877, respectively.

A.4 INSULATION

A.4.1 Thermal Conductivity

Table A.10: Thermal conductivity of different insulation materials at elevated temperatures

Tempe -rature	Promatect H	Promatect L 500	Promasil 950	CAFCO 300	Carboline Type 5-MD	Tyfo WR AFP	TB tunnel fireproofing
(°C)	(W/m°C)	(W/m°C)	(W/m°C)	(W/m°C)	(W/m°C)	(W/m°C)	(W/m°C)
20	1.00	1.00	1.03	0.07	0.12	0.19	0.10
100	1.12	1.01	1.15	0.08	0.09	0.19	0.11
200	1.24	1.05	1.31	0.06	0.06	0.14	0.09
300	1.35	1.01	1.47	0.06	0.06	0.14	0.09
400	1.35	1.02	1.63	0.10	0.07	0.13	0.14
500	1.35	0.94	1.79	0.16	0.07	0.17	0.21
600	1.35	1.73	1.95	0.20	0.07	0.20	0.28
700	1.35	1.75	2.11	0.25	0.08	0.23	0.34

A.4.2 Heat Capacity

Table A.11: Heat capacity of different insulation materials at elevated temperatures

Tempe -rature	Promatect H	Promatect L 500	Promasil 950	CAFCO 300	Carboline Type 5-MD	Tyfo WR AFP	TB tunnel fireproofing
(°C)	(MJ/°C m^3)	(MJ/°C m^3)	(MJ/°C m^3)	(MJ/°C m^3)	(MJ/°C m^3)	(MJ/°C m^3)	(MJ/°C m^3)
20	0.38	0.71	0.19	1.20	0.90	0.31	0.86
100	0.60	0.81	0.21	1.63	1.62	0.38	1.16
200	0.69	0.82	0.21	1.32	1.21	0.41	0.94
300	0.72	0.81	0.21	1.33	1.12	0.41	0.95
400	0.73	0.80	0.21	0.43	0.76	0.33	0.31
500	0.73	0.78	0.20	0.54	1.13	0.44	0.39
600	0.74	0.77	0.20	0.49	1.53	0.45	0.35
700	0.72	0.75	0.20	0.39	1.62	0.39	0.28

APPENDIX B

DESIGN AND LOAD CALCULATIONS

This Appendix summarizes the design and load calculations for the CFRP-strengthened RC beams and slabs tested as part of this dissertation, described in Chapter 3.

B.1 Design of T-beams

Five RC T-beams designated as TB1, TB2, TB3, TB4, and TB5 were designed as per ACI 318 [160] and strengthened with CFRP sheet as per ACI 440.2R-17 [19]. Design procedure followed for design of beam TB1 is shown here.

B.1.1 Geometrical Configuration and Material Properties of T-beams

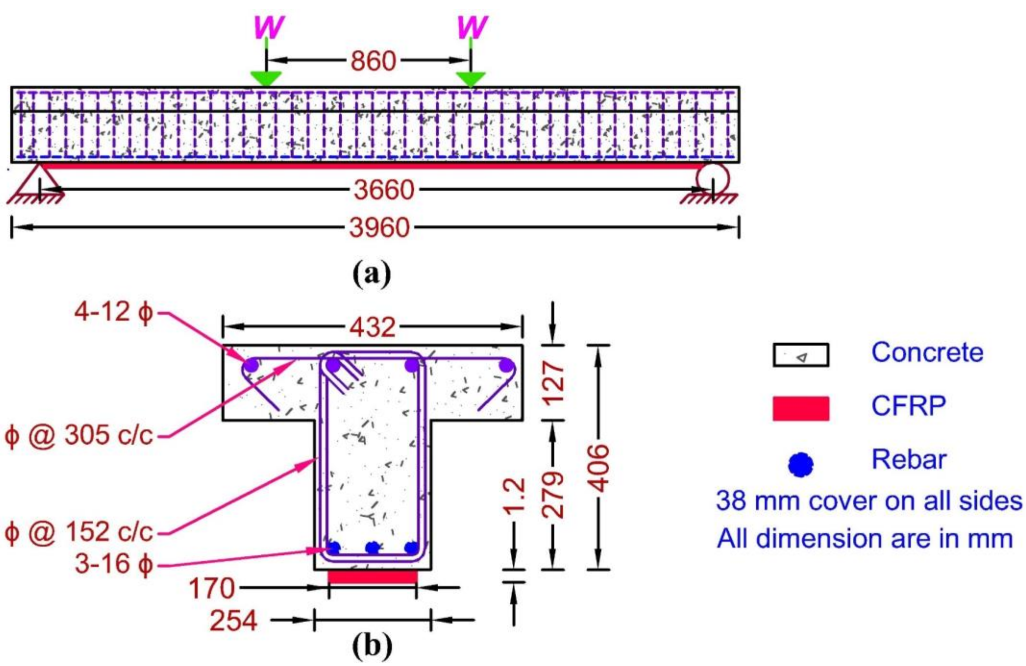

Figure B.1: Geometrical configuration of beam TB1: (a) elevation (b) cross-section

Figure B.1 shows the geometrical dimensions of the T-beam considered in the design, whereas Figure B.2 shows the shear force and bending moment diagram for beam B1 based on the loading configuration in the fire tests. The material and geometrical properties of beam TB1 are summarized in Table B.1.

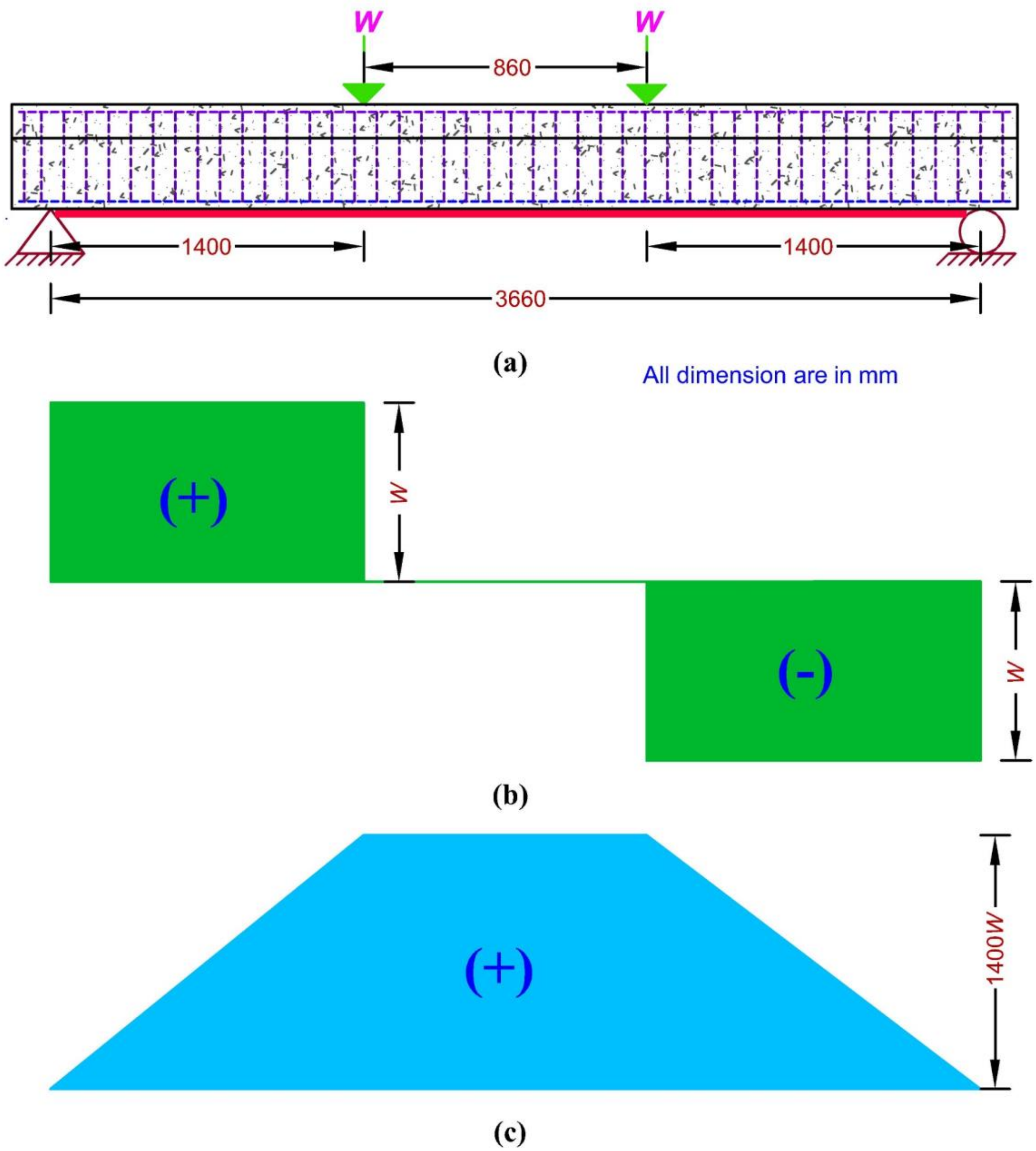

Figure B.2: Shear force and bending moment diagram for beam TB1

Table B.1: Geometrical and material property details of T-beams

Material Properties				Geometrical Dimensions					
Parameter		Value	Unit	Parameter	Value	Unit	Parameter	Value	Unit
Concrete	Strength (f'_c)	38	MPa	Length of beam (L)	3660	mm	Bottom rebars (nts-ϕ_b)	3-16	#-mm
	strain (ε_{cu})	0.003		Width of flange (b_f)	432	mm	Top rebars (ncs-ϕ_t)	4-12	#-mm
Steel rebars	Modulus (E_s)	201	GPa	Width of web (b_c)	254	mm	Stirrup (ϕ_s)	10	mm
	Yield strength (f_y)	440	MPa	Thickness of flange (t_f)	127	mm	CFRP thickness (t_{frp})	1.02	mm
CFRP sheet	Strength (F^*_{fu})	1034	MPa	Total depth of beam (d_c)	406	mm	Width of CFRP (b_{frp})	170	mm
	Ultimate strain (ε^*_{fu})	0.014		Clear cover (C_c)	38	mm	Number of layers of CFRP (n_f)	1	#
	Modulus (E_f)	73.77	GPa	Height of web (h)	279	mm	Environmental factor (EF)	0.95	

B.1.2 Calculations for Design of RC T-Beam

Assumption: Assume a stirrup spacing of 152 mm, transverse reinforcement spacing of 305 mm, and steel yields

› **Preliminary calculations**

Effective cover (ec):	$ec = C_c + \phi_s + 0.5*\phi_b =$	56	mm
Effective depth (d):	$d = d_c - ec =$	350	mm
Modulus of concrete (E_c):	$E_c = 4700\sqrt{f'_c} =$	28973	MPa
Area of steel (A_s):	$A_s = \pi\phi_b^2/4 =$	603.19	mm^2
Yield strain of steel (ε_y):	$\varepsilon_y = f_y / E_s =$	0.0022	
Steel-concrete modular ratio (m):	$m = E_s / E_c =$	6.93	

› Depth of neutral axis

Height of stress block (a):	$a=\left(A_s f_y\right)/\left(0.85*b_c*f_c'\right)=$	19.02	mm	
Check for beam to be designed as T-beam / rectangular	Is $a>t_f$	**No**		Beam to be designed as **rectangular beam** with b_f as width of section
Block parameter based on f_c' (β_1)	$\beta_1=0.85-\left(0.05\times\left(f_c'-28\right)/7\right)=$	0.78		$f_c' < 55$
Depth of neutral axis (c):	$c = a/\beta_1 =$	24.43	mm	

› Moment capacity of RC T-beam

Nominal moment capacity (M_n):	$M_n=A_s\times f_y\times\left(d-0.5\times a\right)\times10^{-6}=$	**90.4**	**kNm**	Nominal moment capacity
Strain in tension steel rebars (ε_{st}):	$\varepsilon_{st} = 0.003 \times (d - c)/c =$	0.040		$\varepsilon_{st} > \varepsilon_y \Rightarrow$ **Steel yields** Assumption is correct
Strength reduction Factor (φ):	$\varphi =$	0.9		
Ultimate resisting Moment (M_u):	$M_u = M_n \times \varphi =$	**81.3**	**kNm**	
Ultimate load that can be applied as per loading configuration (P_u):	$P_u=M_u/1.4=$	58.1	kN	Bending moment diagram shown in Figure B.1 (c)
Maximum nominal shear force at distance d from the end of support (P_n):	$P_n=P_u/\varphi=$	**64.6**	**kN**	Ultimate load divided by reduction factor

› Shear capacity

Shear capacity by concrete (V_c):	$V_c=0.17\times\sqrt{f_c'}\times b_c\times d=$	93.16	kN	
Area of stirrups (A_v):	$A_v=2\times\left(\phi_s\right)^2\times\pi/4=$	157	mm^2	Vertical area of stirrups
Shear capacity by stirrups (V_s):	$V_s=A_v\times f_y\times d/s=$	159.15	kN	Assuming s = 152 mm
Total shear capacity of beam (V_n):	$V_n = V_c + V_s =$	**252.3**	**kN**	$V_n > P_n$ $\therefore$ **Satisfied**
Design shear capacity of beam (V_u):	$= V_u = 0.75 \times V_n$	189	kN	

› Check for minimum flexural reinforcement

Minimum reinforcement ratio (ρ_{min}):	$\rho_{min}=\max\left\{0.25\times\sqrt{f_c'}/f_y, 1.4/f_y\right\}=$	0.0030	$1.4/f_y$ is higher
Reinforcement provided (ρ):	$\rho = A_s/b_c*d =$	0.007	$\rho > \rho_{min}$ $\therefore$ **Satisfied**

› **Check for minimum shear reinforcement**

Shear reinforcement ratio (r_s):	$r_s = A_{v,min}/s =$	1.033	
Ratio 1 for minimum shear check (r_1):	$r_1 = 0.062\sqrt{f_c'}\,b_c/f_y =$	0.22	
Ratio 2 for minimum shear check (r_2):	$r_2 = 0.35 b_c/f_y =$	0.20	
Check for minimum shear reinforcement:	Is $r_s > \max\{r_1, r_2\}$	Yes	**∴ Minimum shear reinforcement ratio is Satisfied**

› **Check for overhang and transverse reinforcement spacing**

Spacing of transverse reinforcement:		305	mm	Spacing < (5 × t_f)
Check for transverse rebar spacing (5 × t_f):	= 5 × 127 =	635	mm	∴ **OK**
Check for width of flange (0.25 × L):	= 0.25 × 3660 =	915	mm	b_f < (0.25 × L) ∴ **OK**
Check for flange thickness (0.5 × b_c):	= 0.5 × 254 =	127	mm	t_f ≥ (0.5 × b_c) ∴ **OK**
Width of overhang (O_f):	= (b_f - b_c)/2 =	89	mm	
Check 1 for overhang (8 × t_f):	= 8 × 127 =	1016	mm	Check1 > O_f ∴ **OK**

B.1.3 Design of CFRP Strengthening

› **Preliminary calculations**

Depth to FRP (d_f):	$d_f = d_c + 0.5 * t_{frp} =$	406.51	mm
Area of FRP (A_f):	$A_f = b_{frp} \times t_{frp} =$	173.4	mm^2
FRP-concrete modular ratio (n):	$n = E_f / E_c =$	2.54	
Design FRP Strength (F_{fu}):	= EF × (F^*_{fu}) =	982.3	MPa
FRP Rupture Strain (ε_{fu}):	= EF × (ε^*_{fu}) =	0.0133	

› Check for limiting strain

Maximum allowable rupture strain (ε_{ru}):	$\varepsilon_{ru} = 0.9 \times \varepsilon_{fu} =$	0.0120	
FRP design strain (ε_{fd}):	$\varepsilon_{fd} = 0.41 \times \sqrt{\left(f_c' / n_f E_f t_{frp} \right)} =$	0.0092	

Since $\varepsilon_{ru} > \varepsilon_{fd}$, $\therefore$ **Debonding** controls the design of the FRP system

Limiting strain:	$\varepsilon_{fd} =$	0.0092	

› Un-strengthened cracked section analysis for existing strain

Modular factor (k_1):	$k_1 = -\rho_s m + \sqrt{\left((\rho_s m)^2 + 2(\rho_s m) \right)} =$	0.263	
Cracked moment of inertia (I_{cr}):	$I_{cr} = \left(bd^3/3 \right) k_1^3 + m \times A_s \times d^2 (1 - k_1)^2 =$	390616925	mm^4
Self-weight (w_{DL}):	$w_{DL} = 25 \times \left((b_f \times t_f) + (b_c \times h) \right) \times 10^{-6} =$	3.14	N/mm
Moment due to dead loads (M_{DL}):	$M_{DL} = w_{DL} \times L^2 / 8$	6161398.65	Nmm
Initial Strain (ε_{bi}):	$\varepsilon_{bi} = M_{DL} \left(d_f - kd \right) / \left(I_{cr} E_c \right) =$	0.00017	

› Iteration for design of strengthening system

Assumed depth of N A (c_{as}):	$c_{as} = 0.25 * d =$	101.50	mm
Effective strain at level of FRP (ε_{fe}):	$\varepsilon_{fe} = 0.003 \times \left(d_f - c_{as} \right) / c_{as} =$	0.21	

Effective strain cannot exceed the limiting strain $\therefore$ **ε_{fe} = 0.0092**

Effective strain in concrete (ε_c):	$\varepsilon_c = \left(\varepsilon_{fe} + \varepsilon_{bi} \right) \times c_{as} / \left(d_f - c_{as} \right) =$	0.0013		
Effective strain in steel (ε_s):	$\varepsilon_s = \left(\varepsilon_{fe} + \varepsilon_{bi} \right) \times \left(d - c_{as} \right) / \left(d_f - c_{as} \right) =$	0.0079		$\therefore \varepsilon_s > \varepsilon_y$
Effective stress in FRP (F_{fe}):	$F_{fe} = E_f \times \varepsilon_{fe} =$	679.7	MPa	
Effective Stress in steel (f_s):	$f_y = E_s \times \varepsilon_s =$	440	MPa	
Strain corresponding to (f_c'):	$\varepsilon_c' = 1.7 \left(f_c' / E_c \right) =$	0.0022		
Force Resultants (β_1)	$= \left(4\varepsilon_c' - \varepsilon_c \right) / \left(6\varepsilon_c' - 2\varepsilon_c \right) =$	0.81		

Force Resultants (α_1)	$=\left(3\varepsilon_c' \times \varepsilon_c - \varepsilon_c^2\right) / \left(3\beta_1 \varepsilon_c'^2\right) =$	0.92	
Actual depth of NA (c_a)	$=\left(A_s f_s + A_f F_{fe}\right) / \alpha_1 \beta_1 f_c' b_f =$	32.63	mm
Difference between c_a and c_{as}	$c_a - c_{as} =$	-68.87	

After 10 iterations the actual depth of NA is determined **c_a = 49.6 mm**

Force Resultants (β_1)	$=\left(4\varepsilon_c' - \varepsilon_c\right) / \left(6\varepsilon_c' - 2\varepsilon_c\right) =$	0.71	
Force Resultants (α_1)	$=\left(3\varepsilon_c' \times \varepsilon_c - \varepsilon_c^2\right) / \left(3\beta_1 \varepsilon_c'^2\right) =$	0.67	

› **<u>Moment capacity computation</u>**

Nominal moment capacity due to steel (M_{ns}):	$M_{ns} = A_s \times f_s \times \left(d - 0.5 \times c \times \beta_1\right) \times 10^{-6} =$	**88.2**	**kNm**
Nominal moment capacity due to FRP (M_{nf}):	$M_{nf} = A_f \times F_{fe} \times \left(d - 0.5 \times c \times \beta_1\right) \times 10^{-6} =$	**45.85**	**kNm**
FRP strength reduction factor (Ψ):	$\Psi =$	0.85	
Total nominal moment capacity due to steel and FRP (M_{n_upg}):	$M_{n\_upg} = M_{ns} + \Psi M_{nf} =$	**127.21**	**kNm**
Ultimate resisting Moment (M_u)	$M_u = \varphi M_{n\_upg} =$	**114.5**	**kNm**
Increase in Capacity	$= 100 \times \left(M_{n\_upg} - M_n\right) / M_n =$	**41**	**%**
Maximum Nominal load as per loading (P_n):	$P_n = M_{n\_upg} / 1.4 =$	**91**	**kN**
Ultimate load that can be applied as per loading configuration (P_u):	$P_u = M_u / 1.4 =$	82	kN
Applied load ratio based on loading mentioned in Chapter 3 (lr)	$lr = P / P_n = 49/91 =$	**51**	**%**

The above-described procedure is followed to design the strengthened beams TB2 to TB5.

B.2 Design of RC Slab

Two RC slabs designated as S1 and S2, were designed as per ACI 318 (2014) and strengthened with CFRP sheet as per ACI 440.2R (2017). Design procedure followed for design of slab S1 is shown here.

B.2.1 Geometrical Configuration and Material Properties of slabs

The material properties and geometrical dimensions of the slab considered in the design and load calculations are summarized in Table B.1, while the cross-section details are shown in Figure B.3, below.

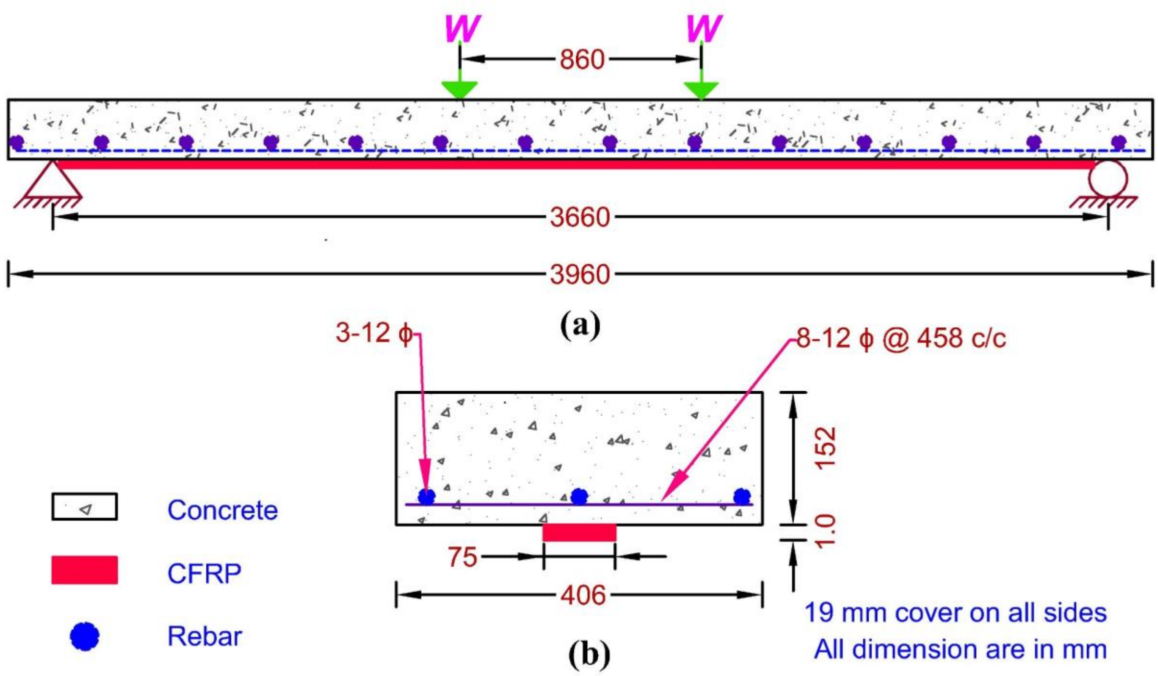

Figure B.3: Geometrical configuration of slab S1 (a) elevation (b) cross-section

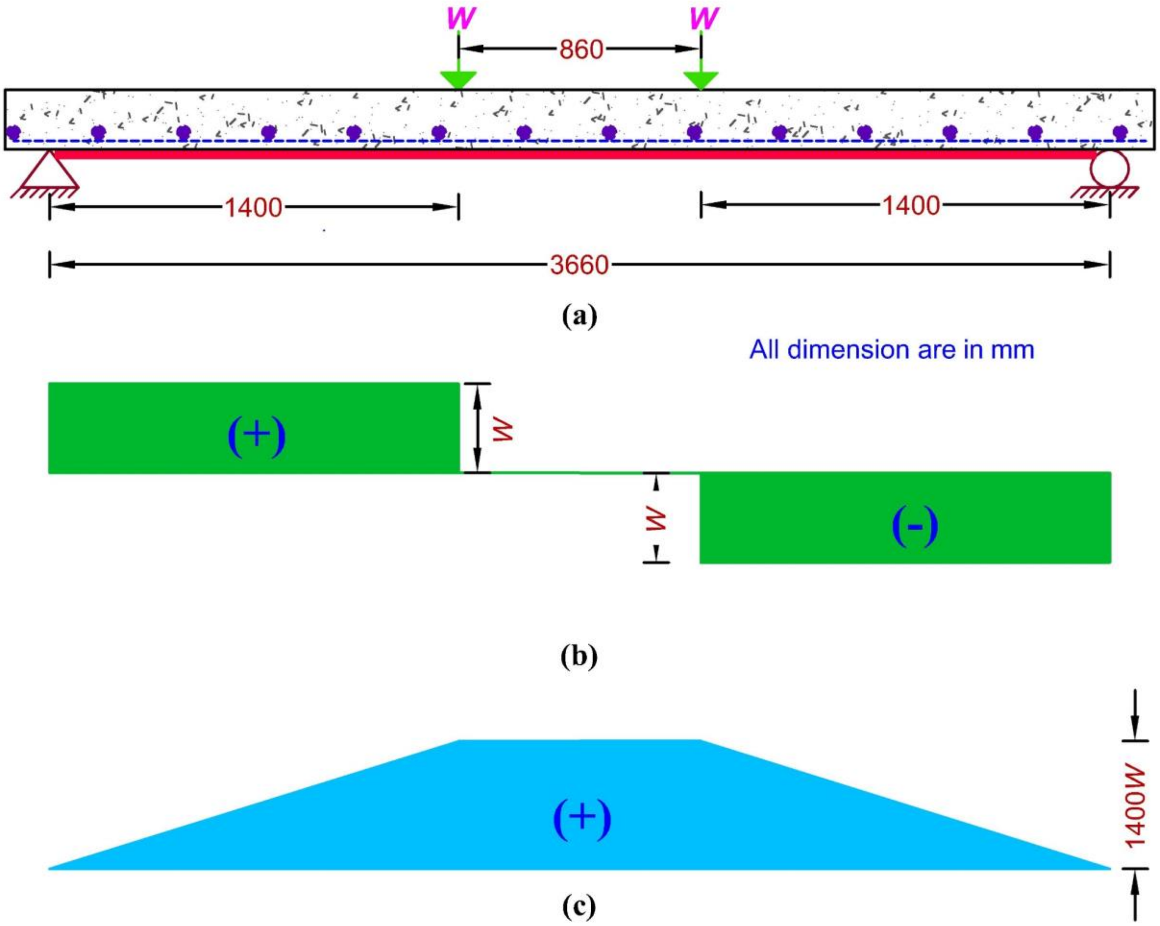

Figure B.4: Shear force and bending moment diagram for slab S1

Table B.2: Geometrical and material property details of slabs

Material Properties				Geometrical Dimensions					
Parameter		Value	Unit	Parameter	Value	Unit	Parameter	Value	Unit
Concrete	Strength (f_c')	43	MPa	Length of slab (L)	3660	mm	CFRP thickness (t_{frp})	1.02	mm
	Strain (ε_{cu})	0.003		Width of slab (b_c)	406	mm	Width of CFRP (b_{frp})	75	mm
Steel rebars	Modulus (E_s)	210	GPa	Depth of slab (d_c)	152	mm	Number of layers of CFRP (n_f)	1	#
	Yield Strength (f_y)	545	MPa	Clear cover (C_c)	19	mm	Environmental factor (EF)	0.95	
CFRP sheet	Strength (F_{fu}^*)	1172	MPa	Bottom rebars (nts-ϕ_b)	4-12	#-mm			
	Ultimate Strain (ε_{fu}^*)	0.011		Temperature rebars (ncs-ϕ_t)	4-12	#-mm			
	Modulus (E_f)	96.50	GPa						

B.2.2 Calculations for Design of RC T-Beam

Assumption: Assume a stirrup spacing of 152 mm, transverse reinforcement spacing of 305 mm, and steel yields

› **Preliminary calculations**

Effective cover (ec):	$ec = C_c + \phi_s + 0.5 * \phi_b =$	25	mm
Effective depth (d):	$d = d_c - ec =$	127	mm
Modulus of concrete (E_c):	$E_c = 4700\sqrt{f_c'} =$	30900	MPa
Area of steel (A_s):	$A_s = \pi\phi_b^2/4 =$	368.2	mm^2
Yield strain of steel (ε_y):	$\varepsilon_y = f_y / E_s =$	0.0026	
Steel-concrete modular ratio (m):	$m = E_s / E_c =$	6.80	

› **Depth of neutral axis**

Height of stress block (a):	$a=(A_s f_y)/(0.85*b_c*f_c')=$	13.5	mm	
Block parameter based on f_c' (β_1)	$\beta_1=0.85-(0.05\times(f_c'-28)/7)=$	0.74		$f_c' < 55$
Depth of neutral axis (c):	$c = a/\beta_1 =$	18.2	mm	

› **Moment capacity of RC T-beam**

Nominal moment capacity (M_n):	$M_n = A_s\times f_y\times(d-0.5\times a)\times10^{-6} =$	**24.1**	**kNm**	Nominal moment capacity
Strain in tension steel rebars (ε_{st}):	$\varepsilon_{st} = 0.003 \times (d - c)/c =$	0.0179		$\varepsilon_{st} > \varepsilon_y \Rightarrow$ **Steel yields**
Strength reduction Factor (φ):	$\varphi =$	0.9		Assumption is correct
Ultimate resisting Moment (M_u):	$M_u = M_n \times \varphi =$	**21.7**	**kNm**	
Ultimate load that can be applied as per loading configuration (P_u):	$P_u = M_u/1.4 =$	15.5	kN	Bending moment diagram shown in Figure B.1 (c)
Maximum nominal shear force at distance d from the end of support (P_n):	$P_n = P_u/\varphi =$	**17.2**	**kN**	Ultimate load divided by reduction factor

› **Shear capacity**

Shear capacity by concrete (V_c):	$V_c = 0.17\times\sqrt{f_c'}\times b_c\times d =$	57.4	kN	
Total shear capacity of beam (V_n):	$V_n = V_c =$	**57.4**	**kN**	$V_n > P_n$ $\therefore$ **Satisfied**
Design shear capacity of beam (V_u):	$= V_u = 0.75 \times V_n =$	43	kN	

› **Check for minimum flexural reinforcement**

Minimum reinforcement ratio (ρ_{min}):	$\rho_{min} = \max\{0.25\times\sqrt{f_c'}/f_y, 1.4/f_y\} =$	0.0026		$1.4/f_y$ is higher
Reinforcement provided (ρ):	$\rho = A_s/b_c*d =$	0.007		$\rho > \rho_{min}$ $\therefore$ **Satisfied**

B.2.3 Design of CFRP Strengthening

› **Preliminary calculations**

Depth to FRP (d_f):	$d_f = d_c + 0.5 * t_{frp} =$	152.51	mm
Area of FRP (A_f):	$A_f = b_{frp} \times t_{frp} =$	76.5	mm^2
FRP-concrete modular ratio (n):	$n = E_f / E_c =$	3.12	
Design FRP Strength (F_{fu}):	$= EF \times (F^*_{fu}) =$	1113.4	MPa
FRP Rupture Strain (ε_{fu}):	$= EF \times (\varepsilon^*_{fu}) =$	0.0105	

› **Check for limiting strain**

Maximum allowable rupture strain (ε_{ru}):	$\varepsilon_{ru} = 0.9 \times \varepsilon_{fu} =$	0.0094	
FRP design strain (ε_{fd}):	$\varepsilon_{fd} = 0.41 \times \sqrt{\left(f_c' / n_f E_f t_{frp} \right)} =$	0.0086	

Since $\varepsilon_{ru} > \varepsilon_{fd}$, $\therefore$ **Debonding** controls the design of the FRP system

Limiting strain:	$\varepsilon_{fd} =$	0.0086	

› **Un-strengthened cracked section analysis for existing strain**

Modular factor (k_1):	$k_1 = -\rho_s m + \sqrt{\left((\rho_s m)^2 + 2(\rho_s m) \right)} =$	0.267	
Cracked moment of inertia (I_{cr}):	$I_{cr} = \left(bd^3/3 \right) k_1^3 + m \times A_s \times d^2 (1 - k_1)^2 =$	26842568	mm^4
Self-weight (w_{DL}):	$w_{DL} = 25 \times \left((b_f \times t_f) + (b_c \times h) \right) \times 10^{-6} =$	1.54	N/mm
Moment due to dead loads (M_{DL}):	$M_{DL} = w_{DL} \times L^2/8 =$	3024196.6	Nmm
Initial Strain (ε_{bi}):	$\varepsilon_{bi} = M_{DL} \left(d_f - kd \right) / \left(I_{cr} E_c \right) =$	0.00043	

› **Iteration for design of strengthening system**

Assumed depth of N A (c_{as}):	$c_{as} = 0.25 \times d =$	31.8	mm
Effective strain at level of FRP (ε_{fe}):	$\varepsilon_{fe} = 0.003 \times \left(d_f - c_{as}\right) / c_{as} =$	0.011	

Effective strain cannot exceed the limiting strain $\therefore$ **ε_{fe} = 0.0086**

Effective strain in concrete (ε_c):	$\varepsilon_c = \left(\varepsilon_{fe} + \varepsilon_{bi}\right) \times c_{as} / \left(d_f - c_{as}\right) =$	0.0024		
Effective strain in steel (ε_s):	$\varepsilon_s = \left(\varepsilon_{fe} + \varepsilon_{bi}\right) \times \left(d - c_{as}\right) / \left(d_f - c_{as}\right) =$	0.0071		$\therefore \varepsilon_s > \varepsilon_y$
Effective stress in FRP (F_{fe}):	$F_{fe} = E_f \times \varepsilon_{fe} =$	827	MPa	
Effective Stress in steel (f_s):	$f_y = E_s \times \varepsilon_s =$	545	MPa	
Strain corresponding to (f'_c):	$\varepsilon'_c = 1.7\left(f'_c / E_c\right) =$	0.0024		
Force Resultants (β_1)	$= \left(4\varepsilon'_c - \varepsilon_c\right) / \left(6\varepsilon'_c - 2\varepsilon_c\right) =$	0.75		
Force Resultants (α_1)	$= \left(3\varepsilon'_c \times \varepsilon_c - \varepsilon_c^2\right) / \left(3\beta_1 \varepsilon'^2_c\right) =$	0.89		
Actual depth of NA (c_a)	$= \left(A_s f_s + A_f F_{fe}\right) / \alpha_1 \beta_1 f'_c b_f =$	22.67	mm	
Difference between c_a and c_{as}	c_a - c_{as} =	-9.1		

After 10 iterations the actual depth of NA is determined **c_a = 24.10 mm**

Force Resultants (β_1)	$= \left(4\varepsilon'_c - \varepsilon_c\right) / \left(6\varepsilon'_c - 2\varepsilon_c\right) =$	0.73
Force Resultants (α_1)	$= \left(3\varepsilon'_c \times \varepsilon_c - \varepsilon_c^2\right) / \left(3\beta_1 \varepsilon'^2_c\right) =$	0.80

› **Moment capacity computation**

Nominal moment capacity due to steel (M_{ns}):	$M_{ns} = A_s \times f_s \times \left(d - 0.5 \times c \times \beta_1\right) \times 10^{-6} =$	**23.5**	**kNm**
Nominal moment capacity due to FRP (M_{nf}):	$M_{nf} = A_f \times F_{fe} \times \left(d - 0.5 \times c \times \beta_1\right) \times 10^{-6} =$	**9.05**	**kNm**
FRP strength reduction factor (Ψ):	$\Psi =$	0.85	
Total nominal moment capacity due to steel and FRP (M_{n_upg}):	$M_{n\_upg} = M_{ns} + \Psi M_{nf} =$	**31.2**	**kNm**
Ultimate resisting Moment (M_u)	$M_u = \varphi M_{n\_upg} =$	**28.1**	**kNm**

Increase in Capacity	$=100\times\left(M_{n\_upg}-M_n\right)/M_n=$	**30**	**%**
Maximum Nominal load as per loading (*P_n*):	$P_n=M_{n\_upg}/1.4=$	**22.3**	**kN**
Ultimate load that can be applied as per loading configuration (*P_u*):	$P_u=M_u/1.4=$	**20.1**	kN
Applied load ratio based on loading mentioned in Chapter 3 (*lr*)	$lr=P/P_n=10.5/22.3=$	**48**	**%**

The above-described procedure is followed to design the strengthened slab S2.

APPENDIX C

FINITE ELEMENT FORMULATION

To solve the heat and mass transfer problems, the cross-section of the beam segment is divided into rectangular elements as shown in Figure 5.1. Since the dependent variable (the variable to be computed) in the two problems is scalar, Q4 (quadrilateral element that has four nodes) element is used in the analysis. Due to the nonlinearity of both problems, the integrations in Eqns. (5.11) through (5.13) are evaluated numerically using Gaussian quadrate integration technique. The vector of shape functions for Q4 element can be written as:

$$N = \begin{bmatrix} (1-s)(1-t)/4 \\ (1+s)(1-t)/4 \\ (1+s)(1+t)/4 \\ (1-s)(1+t)/4 \end{bmatrix}$$

where: s and t are transformed coordinates as shown in Figure C.1. The analysis is generally carried out using four Gauss points and the element stiffness matrix (Ke), mass matrix (Me) and nodal heat or mass flux (Fe) are evaluated at every Gauss point. Those values of the element matrices at the four Gauss points are summed to form the element material property matrices which are used for the subsequent steps in the analysis.

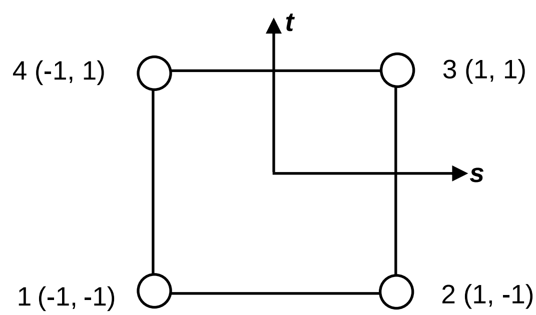

Figure C.1: Q4 element in transformed coordinates

REFERENCES

REFERENCES

[1] Bakis, C. E., Bank, L. C., Brown, V. L., Cosenza, E., Davalos, J. F., Lesko, J. J., Machida, A., Rizkalla, S. H., & Triantafillou, T. C. (2002). "**Fiber-Reinforced Polymer Composites for Construction—State-of-the-Art Review.**" *Journal of Composites for Construction*, 6(2), 73–87.

[2] Barros, J. A. O., Dias, S. J. E., & Lima, J. L. T. (2007). "**Efficacy of CFRP-Based Techniques for the Flexural and Shear Strengthening of Concrete Beams.**" *Cement and Concrete Composites*, 29(3), 203–217.

[3] Oehlers, D. J., Haskett, M., Wu, C., & Seracino, R. (2008). "**Embedding NSM FRP Plates for Improved IC Debonding Resistance.**" *Journal of Composites for Construction*, 12(6), 635–642.

[4] Rashid, R., Oehlers, D. J., & Seracino, R. (2008). "**IC Debonding of FRP NSM and EB Retrofitted Concrete: Plate and Cover Interaction Tests.**" *Journal of Composites for Construction*, 12(2), 160–167.

[5] ASTM E119. (2016). "**Standard Test Methods for Fire Tests of Building Construction and Materials.**" *Ed., ASTM Committee-E05*, ASTM International: West Conshohocken, PA, United States.

[6] Kodur, V. K. R. (1999). "**Fire Resistance Requirements for FRP Structural Members.**" *in Proceedings of Annual Conference - Canadian Society for Civil Engineering*, 1, 83–94.

[7] Firmo, J. P., Correia, J. R., & Bisby, L. A. (2015). "**Fire Behaviour of FRP-Strengthened Reinforced Concrete Structural Elements: A State-of-the-Art Review.**" *Composites Part B: Engineering*, 80, 198–216.

[8] Blontrock, H., Matthys, S., Taerwe, L., & Matthys, S. (1999). "**Properties of Fiber Reinforced Plastics at Elevated Temperatures with Regard to Fire Resistance of Reinforced Concrete Members.**" *in ACI Special Publication*, SP-188, 43–54.

[9] Naser, M. Z. Z., Hawileh, R. A. A., & Abdalla, J. A. A. (2019). "**Fiber-Reinforced Polymer Composites in Strengthening Reinforced Concrete Structures: A Critical Review.**" *Engineering Structures*, 198, 109542.

[10] Bourbigot, S. & Flambard, X. (2002). "**Heat Resistance and Flammability of High Performance Fibres: A Review.**" *Fire and Materials*, 26(4–5), 155–168.

[11] Ashby, M. F. & Jones, D. R. H. (1998). "**The Light Alloys.**" *in Engineering Materials 2: An Introduction to Microstructures, Processing and Design, Eds., Ashby* & *Jones*, Butterworth-Heinemann: Oxford, 3 ed., 100–112.

[12] Mouritz, A. P. & Gibson, A. G. (2006). "**Fire Properties of Polymer Composite Materials.**" *Ed., Gladwell*, 143; Springer: AA Dordrecht, Netherlands.

[13] Kodur, V. K. R. & Baingo, D. (1998). "**Fire Resistance of FRP Reinforced Concrete Slabs.**" Ottawa, ON, Canada.

[14] Leone, M., Matthys, S., & Aiello, M. A. (2009). "**Effect of Elevated Service Temperature on Bond between FRP EBR Systems and Concrete.**" *Composites Part B: Engineering*, 40(1), 85–93.

[15] Denton, S. R. (2001). "**Analysis of Stresses Developed in FRP Plated Beams Due to Thermal Effects.**" *in Proceedings of the International Conference on FRP Composites in Civil Engineering,* 527–536.

[16] ISO 834. (2019). "**Fire Resistance Tests — Elements of Building Construction.**" *Ed., ISO/TC 92/SC 2 Fire Containment*, International Standards: Vernier, Geneva Switzerland.

[17] FIB Bulletin 14. (2001). "**Externally Bonded FRP Reinforcement for RC Structures.**" *Ed., fib Task Group 9.3,* International Federation for Structural Concrete (Fib): Lausanne, Switzerland.

[18] CSA S806-2012. (2017). "**Design And Construction Of Building Structures With Fibre-Reinforced Polymers.**" *Ed., Standards Council of Canada*, 2nd ed.; Canadian Standards Association Group: Mississauga, Ontario, Canada.

[19] ACI 440.2R-17. (2017). "**Guide for the Design and Construction of Externally Bonded FRP Systems for Strengthening Concrete Structures.**" *Ed., ACI Committee 440*, American Concrete Institute: Farmington Hills, MI, United States.

[20] ACI 216.1-14. (2007). "**Code Requirements for Determining Fire Resistance of Concrete and Masonry Construction Assemblies.**" *Ed., ACI Committee 216*, American Concrete Institute: Farmington Hills, MI, United States.

[21] Kodur, V. K. R. & Yu, B. (2016). "**Rational Approach for Evaluating Fire Resistance of FRP-Strengthened Concrete Beams.**" *Journal of Composites for Construction,* 20(6), 04016041.

[22] Gao, W. Y., Dai, J.-G., & Teng, J. G. (2018). "**Three-Level Fire Resistance Design of FRP-Strengthened RC Beams.**" *Journal of Composites for Construction,* 22(3), 05018001.

[23] Hollaway, L. (1990). "**Polymer, Fibre and Composite Material Properties and Manufacturing Techniques.**" *in Polymers and Polymer Composites in Construction, Ed., Hollaway,* Thomas Telford Ltd.: London, England, 5–31.

[24] Bank, L. C. (2006). "**Composites for Construction : Structural Design with FRP Materials.**" John Wiley & Sons Inc.: Hoboken, New Jersey, United States.

[25] Schwartz, M. M. (1997). "**Composite Materials, Volume I: Properties, Non-Destructive Testing, and Repair.**" 1st ed.; Prentice Hall: Hoboken, NJ, United States.

[26] Hollaway, L. C. (2010). "**A Review of the Present and Future Utilisation of FRP Composites in the Civil Infrastructure with Reference to Their Important In-Service Properties.**" *Construction and Building Materials*, 24(12), 2419–2445.

[27] Kurtz, S. & Balaguru, P. (2001). "**Comparison of Inorganic and Organic Matrices for Strengthening of RC Beams with Carbon Sheets.**" *Journal of Structural Engineering*, 127(1), 35–42.

[28] Toutanji, H., Zhao, L., & Zhang, Y. (2006). "**Flexural Behavior of Reinforced Concrete Beams Externally Strengthened with CFRP Sheets Bonded with an Inorganic Matrix.**" *Engineering Structures*, 28(4), 557–566.

[29] Toutanji, H. & Deng, Y. (2007). "**Comparison between Organic and Inorganic Matrices for RC Beams Strengthened with Carbon Fiber Sheets.**" *Journal of Composites for Construction*, 11(5), 507–513.

[30] Bakharev, T. (2005). "**Durability of Geopolymer Materials in Sodium and Magnesium Sulfate Solutions.**" *Cement and Concrete Research*, 35(6), 1233–1246.

[31] Zheng, W., Chen, W., Xu, W., & Wang, Y. (2009). "**Experimental Research on Alkali-Activated Slag High Temperature Resistant Inorganic Adhesive Pasting CFRP Sheets on Surface of Concrete.**" *Journal of Building Structures*, 30(4), 138–144.

[32] Zhang, H. Y., Kodur, V., Qi, S. L., Cao, L., & Wu, B. (2014). "**Development of Metakaolin–Fly Ash Based Geopolymers for Fire Resistance Applications.**" *Construction and Building Materials*, 55, 38–45.

[33] Davidovits, J. (1989). "**Geopolymers and Geopolymeric Materials.**" *Journal of Thermal Analysis*, 35(2), 429–441.

[34] Andini, S., Cioffi, R., Colangelo, F., Grieco, T., Montagnaro, F., & Santoro, L. (2008). "**Coal Fly Ash as Raw Material for the Manufacture of Geopolymer-Based Products.**" *Waste Management*, 28(2), 416–423.

[35] Buchwald, A., Hohmann, M., Posern, K., & Brendler, E. (2009). "**The Suitability of Thermally Activated Illite/Smectite Clay as Raw Material for Geopolymer Binders.**" *Applied Clay Science*, 46(3), 300–304.

[36] Andini, S., Cioffi, R., Colangelo, F., Ferone, C., Montagnaro, F., & Santoro, L. (2011). "**Characterization of Geopolymer Materials Containing MSWI Fly Ash and Coal Fly Ash.**" *Advances in Science and Technology*, 69, 123–128.

[37] Ferone, C., Colangelo, F., Cioffi, R., Montagnaro, F., & Santoro, L. (2011). "**Mechanical Performances of Weathered Coal Fly Ash Based Geopolymer Bricks.**" *Procedia Engineering*, 21, 745–752.

[38] Menna, C., Asprone, D., Ferone, C., Colangelo, F., Balsamo, A., Prota, A., Cioffi, R., & Manfredi, G. (2013). "**Use of Geopolymers for Composite External Reinforcement of RC Members.**" *Composites Part B: Engineering*, 45(1), 1667–1676.

[39] Kong, D. L. Y. Y., Sanjayan, J. G., & Sagoe-Crentsil, K. (2007). "**Comparative Performance of Geopolymers Made with Metakaolin and Fly Ash after Exposure to Elevated Temperatures.**" *Cement and Concrete Research*, 37(12), 1583–1589.

[40] Bernal, S. A., Rodríguez, E. D., Mejía de Gutiérrez, R., Gordillo, M., & Provis, J. L. (2011). "**Mechanical and Thermal Characterisation of Geopolymers Based on Silicate-Activated Metakaolin/Slag Blends.**" *Journal of Materials Science*, 46(16), 5477–5486.

[41] Zhang, H. Y., Kodur, V., Qi, S. L., & Wu, B. (2015). "**Characterizing the Bond Strength of Geopolymers at Ambient and Elevated Temperatures.**" *Cement and Concrete Composites*, 58, 40–49.

[42] Zhang, H. Y., Kodur, V., Wu, B., Yan, J., & Yuan, Z. S. (2018). "**Effect of Temperature on Bond Characteristics of Geopolymer Concrete.**" *Construction and Building Materials*, 163, 277–285.

[43] Yan Zhang, H., Kodur, V., Wu, B., *et al.* (2016). "**Comparative Thermal and Mechanical Performance of Geopolymers Derived from Metakaolin and Fly Ash.**" *Journal of Materials in Civil Engineering*, 28(2), 04015092.

[44] Zhang, H. Y., Lv, H. R., Kodur, V., & Qi, S. L. (2018). "**Comparative Fire Behavior of Geopolymer and Epoxy Resin Bonded Fiber Sheet Strengthened RC Beams.**" *Engineering Structures*, 155, 222–234.

[45] Scott, D. W., Lai, J. S., & Zureick, A.-H. (1995). "**Creep Behavior of Fiber-Reinforced Polymeric Composites: A Review of the Technical Literature.**" *Journal of Reinforced Plastics and Composites*, 14(6), 588–617.

[46] Takeda, K., Mitsui, Y., Murakami, K., Sakai, H., & Moriyasu, N. (1996). "**Flexural Behaviour of Reinforced Concrete Beams Strengthened with Carbon Fibre Sheets.**" *Composites Part A-Applied Science and Manufacturing*, 27, 981–987.

[47] Toutanji, H. A. & Gómez, W. (1997). "**Durability Characteristics of Concrete Beams Externally Bonded with FRP Composite Sheets.**" *Cement and Concrete Composites*, 19(4), 351–358.

[48] Chaallal, O., Nollet, M.-J., & Perraton, D. (1998). "**Strengthening of Reinforced Concrete Beams with Externally Bonded Fiber-Reinforced-Plastic Plates: Design Guidelines for Shear and Flexure.**" *Canadian Journal of Civil Engineering*, 25(4), 692–704.

[49] Khalifa, A., Gold, W. J., Nanni, A., & M.I., A. A. (1998). "**Contribution of Externally Bonded FRP to Shear Capacity of RC Flexural Members.**" *Journal of Composites for Construction*, 2(4), 195–202.

[50] Dortzbach, J. (1999). "**Carbon Fiber Reinforcing Polymers as Negative Moment Reinforcing in Repair of Composite Steel Parking Deck.**" *ACI Symposium Publication*, 188, 417–428.

[51] Grace, N. F., Sayed, G. A., Soliman, A. K., & Saleh, K. R. (1999). "**Strengthening Reinforced Concrete Beams Using Fiber Reinforced Polymer (FRP) Laminates.**" *ACI Structural Journal*, 96(5), 865–875.

[52] Mayo, R., Nanni, A., Watkins, S. E., Barker, M. G., & Boothby, T. E. (1999). "**Strengthening of Bridge G-270 with Externally Bonded CFRP Sheets.**" *in SP-188, 4th International Symposium on Fiber Reinforced Polymer Reinforcement for Reinforced Concrete Structures*, 429–440.

[53] Green, M. F., Bisby, L. A., Beaudoin, Y., & Labossière, P. (2000). "**Effect of Freeze-Thaw Cycles on the Bond Durability between Fibre Reinforced Polymer Plate Reinforcement and Concrete.**" *Canadian Journal of Civil Engineering*, 27(5), 949–959.

[54] Kachlakev, D. & McCurry, D. D. (2000). "**Behavior of Full-Scale Reinforced Concrete Beams Retrofitted for Shear and Flexural with FRP Laminates.**" *Composites Part B: Engineering*, 31(6–7), 445–452.

[55] Grace, N. F. (2001). "**Strengthening of Negative Moment Region of Reinforced Concrete Beams Using Carbon Fiber-Reinforced Polymer Strips.**" *ACI Structural Journal*, 98(3), 347–358.

[56] El-Hacha, R., Wight, R., & Green, M. (2001). "**Prestressed Fibre-Reinforced Polymer Laminates for Strengthening Structures.**" *Progress in Structural Engineering and Materials*, 3(2), 111–121.

[57] Neale, K. W. (2000). "**Strengthening Reinforced Concrete Structures with Externally-Bonded Fibre Reinforced Polymers.**" *Progress in Structural Engineering and Materials*, 2(2), 133–138.

[58] Waldron, P., Byars, E. A., & Dejke, V. (2001). "**Durability of FRP in Concrete: A State of the Art.**" *in International Workshop on Composites in Construction*, 92–101.

[59] Pellegrino, C. & Modena, C. (2002). "**Fiber Reinforced Polymer Shear Strengthening of Reinforced Concrete Beams with Transverse Steel Reinforcement.**" *Journal of Composites for Construction*, 6(2), 104–111.

[60] Yang, X. & Nanni, A. (2002). "**Lap Splice Length and Fatigue Performance of Fiber-Reinforced Polymer Laminates.**" *ACI Materials Journal*, 99(4), 386–392.

[61] Shahrooz, B. M., Boy, S., & Baseheart, T. M. (2002). "**Flexural Strengthening of Four 76-Year-Old T-Beams with Various Fiber-Reinforced Polymer Systems: Testing and Analysis.**" *ACI Structural Journal*, 99(5), 681–691.

[62] Green, M. F., Dent, A. J. S., & Bisby, L. A. (2003). "**Effect of Freeze–Thaw Cycling on the Behaviour of Reinforced Concrete Beams Strengthened in Flexure with Fibre Reinforced Polymer Sheets.**" *Canadian Journal of Civil Engineering*, 30(6), 1081–1088.

[63] Ashour, A. ., El-Refaie, S. ., & Garrity, S. . (2004). "**Flexural Strengthening of RC Continuous Beams Using CFRP Laminates.**" *Cement and Concrete Composites*, 26(7), 765–775.

[64] Shahrooz, B. M. & Boy, S. (2004). "**Retrofit of a Three-Span Slab Bridge with Fiber Reinforced Polymer Systems--Testing and Rating.**" *Journal of Composites for Construction*, 8, 241–247.

[65] Teng, J. G., Lam, L., & Chen, J. F. (2004). "**Shear Strengthening of RC Beams with FRP Composites.**" *Progress in Structural Engineering and Materials*, 6(3), 173–184.

[66] Zhang, Z., Hsu, C.-T. T., & Moren, J. (2004). "**Shear Strengthening of Reinforced Concrete Deep Beams Using Carbon Fiber Reinforced Polymer Laminates.**" *Journal of Composites for Construction*, 8(5), 403–414.

[67] Cao, S., Wu, Z., & Wang, X. (2009). "**Tensile Properties of CFRP and Hybrid FRP Composites at Elevated Temperatures.**" *Journal of Composite Materials*, 43(4), 315–330.

[68] Phan, L. T. & Carino, N. J. (1998). "**Review of Mechanical Properties of HSC at Elevated Temperature.**" *Journal of Materials in Civil Engineering*, 10(1), 58–65.

[69] Phan, L. T. & Carino, N. J. (2003). "**Code Provisions for High Strength Concrete Strength-Temperature Relationship at Elevated Temperatures.**" *Materials and Structures*, 36(2), 91–98.

[70] Cheng, F.-P., Kodur, V. K. R., & Wang, T.-C. (2004). "**Stress-Strain Curves for High Strength Concrete at Elevated Temperatures.**" *Journal of Materials in Civil Engineering*, 16(1), 84–90.

[71] Kodur, V. K. R., Wang, T. C., & Cheng, F. P. (2004). "**Predicting the Fire Resistance Behaviour of High Strength Concrete Columns.**" *Cement and Concrete Composites*, 26(2), 141–153.

[72] Gawin, D., Pesavento, F., & Schrefler, B. A. (2004). "**Modelling of Deformations of High Strength Concrete at Elevated Temperatures.**" *Materials and Structures*, 37(4), 218–236.

[73] Khaliq, W. & Kodur, V. (2012). "**High Temperature Mechanical Properties of High-Strength Fly Ash Concrete with and without Fibers.**" *ACI Materials Journal*, 109(6), 665–674.

[74] Li, L. Y. & Purkiss, J. (2005). "**Stress-Strain Constitutive Equations of Concrete Material at Elevated Temperatures.**" *Fire Safety Journal*, 40(7), 669–686.

[75] Shin, K. Y., Kim, S. B., Kim, J. H., Chung, M., & Jung, P. S. (2002). "**Thermo-Physical Properties and Transient Heat Transfer of Concrete at Elevated Temperatures.**" *Nuclear Engineering and Design*, 212(1–3), 233–241.

[76] Youssef, M. A. & Moftah, M. (2007). "**General Stress-Strain Relationship for Concrete at Elevated Temperatures.**" *Engineering Structures*, 29(10), 2618–2634.

[77] Kodur, V. K. R. & Sultan, M. A. (2003). "**Effect of Temperature on Thermal Properties of High-Strength Concrete.**" *Journal of Materials in Civil Engineering*, 15(2), 101–107.

[78] Lie, T. T. (1992). "**Structural Fire Protection: ASCE Manual of Practice No. 78.**" *Ed., ASCE Committee on Fire Protection*, ASCE: New York, NY, United States.

[79] Eurocode 2. (2004). "**EN 1992-1-2 Eurocode 2: Design of Concrete Structures, Part 1-2: General Rules - Structural Fire Design: British Standard.**" *Ed., European Committee for Standardization*, CEN: Brussels, Belgium.

[80] Harmathy, T. Z. (1973). "**Design of Concrete Masonry Walls for Fire Endurance.**" *in Behavior of Concrete under Temperature*, SP-39, 179–203.

[81] Kodur, V. K. R. & Lie, T. T. (1995). "**Fire Performance of Concrete-Filled Hollow Steel Columns.**" *Journal of Fire Protection Engineering*, 7(3), 89–98.

[82] Lie, T. T. & Kodur, V. K. R. (1996). "**Thermal and Mechanical Properties of Steel-Fibre-Reinforced Concrete at Elevated Temperatures.**" *Canadian Journal of Civil Engineering*, 23(2), 511–517.

[83] Saad, M., Abo-El-Enein, S. A., Hanna, G. B., & Kotkata, M. F. (1996). "**Effect of Silica Fume on the Phase Composition and Microstructure of Thermally Treated Concrete.**" *Cement and Concrete Research*, 26(10), 1479–1484.

[84] Khan, M. I. (2002). "**Factors Affecting the Thermal Properties of Concrete and Applicability of Its Prediction Models.**" *Building and Environment*, 37(6), 607–614.

[85] Khoury, G. A., Majorana, C. E., Pesavento, F., & Schrefler, B. A. (2002). "**Modelling of Heated Concrete.**" *Magazine of Concrete Research*, 54(2), 77–101.

[86] Kodur, V. K. R., Dwaikat, M., & Dwaikat, M. (2008). "**High-Temperature Properties of Concrete for Fire Resistance Modeling of Structures.**" *ACI Materials Journal*, 105(5), 517–527.

[87] Schneider, U. (1988). "**Concrete at High Temperatures - A General Review.**" *Fire Safety Journal*, 13(1), 55–68.

[88] Harmathy, T. Z. (1967). "**A Comprehensive Creep Model.**" *Journal of Basic Engineering*, 89(3), 496–502.

[89] Kodur, V. K. R. & Alogla, S. M. (2017). “**Effect of High-Temperature Transient Creep on Response of Reinforced Concrete Columns in Fire.**” *Materials and Structures*, 50(1), 27.

[90] Alogla, S. M. (2019). “**Response of Reinforced Concrete Columns under Temperature Induced Transient Creep Strain.**” Michigan State University.

[91] Khoury, G. A., Grainger, B. N., Sullivan, P. J. E., Khoury, G. A., Sullivan, P. J. E., & Grainger, B. N. (1985). “**Strain of Concrete during First Heating to 600°C under Load.**” *Magazine of Concrete Research*, 37(133), 195–215.

[92] Kodur, V. K. R. R. & Harmathy, T. Z. (2016). “**Properties of Building Materials.**” *in SFPE Handbook of Fire Protection Engineering*, Springer: New York, NY, United States, 3rd ed., 277–324.

[93] Anderberg, Y. & Thelandersson, S. (1976). “**Stress and Deformation Characteristics of Concrete: Experimental Investigation and Material Behaviour Model.**” *in Bulletin of Division of Structural Mechanics and Concrete Construction*, Bulletin54, 1–86.

[94] Harmathy, T. Z. (1983). “**Fire Severity: Basis of Fire Safety Design.**” *in ACI Symposium Publication*, 115–150.

[95] Kodur, V. K. R. & Ahmed, A. (2010). “**Numerical Model for Tracing the Response of FRP-Strengthened RC Beams Exposed to Fire.**” *Journal of Composites for Construction*, 14(6), 730–742.

[96] Phan, L. T. (1996). “**Fire Performance of High-Strength Concrete: A Report of the State-of-the-Art.**” Gaithersburg, MD, United States.

[97] Phan, L. T., Lawson, J. R., & Davis, F. L. (2001). “**Effects of Elevated Temperature Exposure on Heating Characteristics, Spalling, and Residual Properties of High Performance Concrete.**” *Materials and Structures*, 34(2), 83–91.

[98] Kodur, V. K. R. & Phan, L. (2007). “**Critical Factors Governing the Fire Performance of High Strength Concrete Systems.**” *Fire Safety Journal*, 42(6–7), 482–488.

[99] Panedpojaman, P. & Intarit, P. (2016). “**Maximum Temperature Prediction for Concrete Sections during Cooling Phase.**” *KKU Engineering Journal*, 43(S2), 294–298.

[100] Bisby, L. A. (2005). “**Fire Behaviour of Fibre-Reinforced Polymer (FRP) Reinforced or Confined Concrete.**”

[101] Buchanan, A. H. & Abu, A. K. (2016). “**Structural Design for Fire Safety.**” 2nd ed.; John Wiley & Sons Ltd.: West Sussex, England.

[102] Griffis, C. A., Masumura, R. A., & Chang, C. I. (1981). “**Thermal Response of Graphite Epoxy Composite Subjected to Rapid Heating.**” *Journal of Composite Materials*, 15(5), 427–442.

[103] Scott, E. P. & Beck, J. V. (1992). "**Estimation of Thermal Properties in Epoxy Matrix/Carbon Fiber Composite Materials.**" *Journal of Composite Materials*, 26(1), 132–149.

[104] Miller, J. R. & Weaver, P. M. (2003). "**Temperature Profiles in Composite Plates Subject to Time-Dependent Complex Boundary Conditions.**" *Composite Structures*, 59(2), 267–278.

[105] Sweeting, R. D. & Liu, X. L. (2004). "**Measurement of Thermal Conductivity for Fibre-Reinforced Composites.**" *in Composites Part A: Applied Science and Manufacturing*, 35(7–8), 933–938.

[106] Kumahara, S., Masuda, Y., Tanano, H., & Shimizu, A. (1993). "**Tensile Strength of Continuous Fiber Bar under High Temperature.**" *in American Concrete Institute, ACI Special Publication*, SP138, 731–742.

[107] Sumida, A., Fujisaki, T., Watanabe, K., & Kato, T. (2001). "**Heat Resistance Of Continuous Fiber Reinforced Plastic Rods.**" *in FRPRCS-5: Fibre-Reinforced Plastics for Reinforced Concrete Structures Volume I*, Thomas Telford Ltd.: London, England, 557–565.

[108] Wang, Y. C., Wong, P. M. H., & Kodur, V. (2007). "**An Experimental Study of the Mechanical Properties of Fibre Reinforced Polymer (FRP) and Steel Reinforcing Bars at Elevated Temperatures.**" *Composite Structures*, 80(1), 131–140.

[109] Cao, S., Wang, X., & Wu, Z. (2011). "**Evaluation and Prediction of Temperature-Dependent Tensile Strength of Unidirectional Carbon Fiber-Reinforced Polymer Composites.**" *Journal of Reinforced Plastics and Composites*, 30(9), 799–807.

[110] Chowdhury, E. U., Eedson, R., Bisby, L. A., Green, M. F., & Benichou, N. (2011). "**Mechanical Characterization of Fibre Reinforced Polymers Materials at High Temperature.**" *Fire Technology*, 47(4), 1063–1080.

[111] Wang, K., Young, B., & Smith, S. T. (2011). "**Mechanical Properties of Pultruded Carbon Fibre-Reinforced Polymer (CFRP) Plates at Elevated Temperatures.**" *Engineering Structures*, 33(7), 2154–2161.

[112] Yu, B. & Kodur, V. (2014). "**Effect of Temperature on Strength and Stiffness Properties of Near-Surface Mounted FRP Reinforcement.**" *Composites Part B: Engineering*, 58, 510–517.

[113] Hawileh, R. A., Abu-Obeidah, A., Abdalla, J. A., & Al-Tamimi, A. (2015). "**Temperature Effect on the Mechanical Properties of Carbon, Glass and Carbon–Glass FRP Laminates.**" *Construction and Building Materials*, 75, 342–348.

[114] Nguyen, P. L., Vu, X. H., & Ferrier, E. (2018). "**Experimental Study on the Thermo-Mechanical Behavior of Hand-Made Carbon Fiber Reinforced Polymer (H-CFRP)**

Simultaneously Subjected to Elevated Temperature and Mechanical Loading." *in Lecture Notes in Civil Engineering*, 8, 484–496.

[115] Nguyen, P. L., Vu, X. H., & Ferrier, E. (2018). "**Elevated Temperature Behaviour of Carbon Fibre-Reinforced Polymer Applied by Hand Lay-up (M-CFRP) under Simultaneous Thermal and Mechanical Loadings: Experimental and Analytical Investigation.**" *Fire Safety Journal*, 100, 103–117.

[116] Nguyen, P. L., Vu, X. H., & Ferrier, E. (2018). "**Characterization of Pultruded Carbon Fibre Reinforced Polymer (P-CFRP) under Two Elevated Temperature-Mechanical Load Cases: Residual and Thermo-Mechanical Regimes.**" *Construction and Building Materials*, 165, 395–412.

[117] Hamad, R. J. A., Megat Johari, M. A., & Haddad, R. H. (2017). "**Mechanical Properties and Bond Characteristics of Different Fiber Reinforced Polymer Rebars at Elevated Temperatures.**" *Construction and Building Materials*, 142, 521–535.

[118] Hajiloo, H., Green, M. F., & Gales, J. (2018). "**Mechanical Properties of GFRP Reinforcing Bars at High Temperatures.**" *Construction and Building Materials*, 162, 142–154.

[119] Saafi, M. (2002). "**Effect of Fire on FRP Reinforced Concrete Members.**" *Composite Structures*, 58(1), 11–20.

[120] Bisby, L. A., Green, M. F., & Kodur, V. K. R. R. (2005). "**Response to Fire of Concrete Structures That Incorporate FRP.**" *Progress in Structural Engineering and Materials*, 7(3), 136–149.

[121] Dai, J.-G., Gao, W.-Y., & Teng, J. G. (2015). "**Finite Element Modeling of Insulated FRP-Strengthened RC Beams Exposed to Fire.**" *Journal of Composites for Construction*, 19(2), 04014046.

[122] Chen, J. & Young, B. (2006). "**Stress–Strain Curves for Stainless Steel at Elevated Temperatures.**" *Engineering Structures*, 28(2), 229–239.

[123] Gibson, A. G., Wu, Y. S., Evans, J. T., & Mouritz, A. P. (2006). "**Laminate Theory Analysis of Composites under Load in Fire.**" *Journal of Composite Materials,* 40(7), 639–658.

[124] Klamer, E. L., Hordijk, D. A., & Janssen, H. J. M. (2005). "**The Influence of Temperature on the Debonding of Externally Bonded CFRP.**" *American Concrete Institute, ACI Special Publication*, SP-230, 1551–1570.

[125] Wu, Z., Iwashita, K., Yagashiro, S., Ishikawa, T., & Hamaguchi, Y. (2005). "**Temperature Effect on Bonding and Debonding Behavior between FRP Sheets and Concrete.**" *Zairyo/Journal of the Society of Materials Science, Japan*, 54(5), 474–480.

[126] Gamage, J. C. P. H., Al-Mahaidi, R., & Wong, M. B. (2006). "**Bond Characteristics of CFRP Plated Concrete Members under Elevated Temperatures.**" *Composite Structures*, 75(1–4), 199–205.

[127] Firmo, J. P., Correia, J. R., Pitta, D., Tiago, C., & Arruda, M. R. T. (2015). "**Experimental Characterization of the Bond between Externally Bonded Reinforcement (EBR) CFRP Strips and Concrete at Elevated Temperatures.**" *Cement and Concrete Composites*, 60, 44–54.

[128] Palmieri, A., Matthys, S., & Taerwe, L. (2011). "**Influence of High Temperature on Bond between NSM FRP Bars/Strips and Concrete.**" *in ACI Special Publication*, SP 275, 1–12.

[129] Yu, B. & Kodur, V. K. R. (2014). "**Effect of High Temperature on Bond Strength of Near-Surface Mounted FRP Reinforcement.**" *Composite Structures*, 110, 88–97.

[130] Firmo, J. P., Correia, J. R., Pitta, D., Tiago, C., & Arruda, M. R. T. (2015). "**Bond Behavior between Near-Surface-Mounted CFRP Strips and Concrete at High Temperatures.**" *Journal of Composites for Construction*, 19(4), 04014071.

[131] Ahmed, A. & Kodur, V. K. R. (2011). "**Effect of Bond Degradation on Fire Resistance of FRP-Strengthened Reinforced Concrete Beams.**" *Composites Part B: Engineering*, 42(2), 226–237.

[132] Yu, B. & Kodur, V. K. R. (2013). "**Factors Governing the Fire Response of Concrete Beams Reinforced with FRP Rebars.**" *Composite Structures*, 100, 257–269.

[133] Arruda, M. R. T., Firmo, J. P., Correia, J. R., & Tiago, C. (2016). "**Numerical Modelling of the Bond between Concrete and CFRP Laminates at Elevated Temperatures.**" *Engineering Structures*, 110, 233–243.

[134] Dai, J. G., Gao, W. Y., & Teng, J. G. (2013). "**Bond-Slip Model for FRP Laminates Externally Bonded to Concrete at Elevated Temperature.**" *Journal of Composites for Construction*, 17(2), 217–228.

[135] Bank, L. C. (1993). "**Properties of FRP Reinforcements for Concrete.**" *in Fiber-Reinforced-Plastic (FRP) Reinforcement for Concrete Structures, Ed., Nanni*, Elsevier: Oxford, 1st ed., 59–86.

[136] Nomura, S. & Ball, D. L. (1993). "**Micromechanical Formulation of Effective Thermal Expansion Coefficients of Unidirectional Fiber Composites.**" *Advanced Composite Materials*, 3(2), 143–151.

[137] Mallick, P. K. (2007). "**Fiber-Reinforced Composites: Materials, Manufacturing, and Design.**" 3rd ed.; CRC Press, Taylor & Francis Group: Boca Raton, FL, United States.

[138] Rahman, A., Taylor, D., & Kingsley, C. (1993). "**Evaluation of FRP as Reinforcement for Concrete Bridges.**" *American Concrete Institute Special Publication*, SP138(05), 71–86.

[139] Raghavan, J. & Meshii, M. (1998). "**Creep of Polymer Composites.**" *Composites Science and Technology*, 57(12), 1673–1688.

[140] Bai, Y., Keller, T., Correia, J. R., Branco, F. A., & Ferreira, J. G. (2010). "**Fire Protection Systems for Building Floors Made of Pultruded GFRP Profiles - Part 2: Modeling of Thermomechanical Responses.**" *Composites Part B: Engineering*, 41(8), 630–636.

[141] López, C., Firmo, J. P., Correia, J. R., & Tiago, C. (2013). "**Fire Protection Systems for Reinforced Concrete Slabs Strengthened with CFRP Laminates.**" *Construction and Building Materials*, 47, 324–333.

[142] Firmo, J. P., Arruda, M. R. T., & Correia, J. R. (2015). "**Numerical Simulation of the Fire Behaviour of Thermally Insulated Reinforced Concrete Beams Strengthened with EBR-CFRP Strips.**" *Composite Structures*, 126, 360–370.

[143] Kodur, V. K. R. K. R. & Shakya, A. M. M. (2013). "**Effect of Temperature on Thermal Properties of Spray Applied Fire Resistive Materials.**" *Fire Safety Journal*, 61, 314–323.

[144] Deuring, M. (1994). "**Brandversuche an Nachtraglich Verstarkten Tragern Aus Beton (Fire Tests on Strengthened Reinforced Concrete Beams).**" Dubendorf, Switzerland.

[145] Blontrock, H., Taerwe, L., & Vandevelde, P. (2000). "**Fire Tests on Concrete Beams Strengthened with Fiber Composite Laminates.**" *in Proceedings of the 3rd International PhD Symposium in Civil Engineering Volume II*, 151–161.

[146] Williams, B., Kodur, V., Green, M. F., & Bisby, L. (2008). "**Fire Endurance of Fiber-Reinforced Polymer Strengthened Concrete T-Beams.**" *ACI Structural Journal*, 105(1), 60–67.

[147] Ahmed, A. & Kodur, V. (2011). "**The Experimental Behavior of FRP-Strengthened RC Beams Subjected to Design Fire Exposure.**" *Engineering Structures*, 33(7), 2201–2211.

[148] Firmo, J. P., Correia, J. R., & França, P. (2012). "**Fire Behaviour of Reinforced Concrete Beams Strengthened with CFRP Laminates: Protection Systems with Insulation of the Anchorage Zones.**" *Composites Part B: Engineering*, 43(3), 1545–1556.

[149] Firmo, J. P. & Correia, J. R. (2015). "**Fire Behaviour of Thermally Insulated RC Beams Strengthened with EBR-CFRP Strips: Experimental Study.**" *Composite Structures*, 122, 144–154.

[150] Dong, K., Hu, K., & Gao, W. (2016). "**Fire Behavior of Full-Scale CFRP-Strengthened RC Beams Protected with Different Insulation Systems.**" *Journal of Asian Architecture and Building Engineering*, 15(3), 581–588.

[151] Gao, W. W.-Y., Hu, K., & Lu, Z. (2010). "**Fire Resistance Experiments of Insulated CFRP Strengthened Reinforced Concrete Beams.**" *China Civil Engineering Journal*, 43(3), 15–23.

[152] Blontrock, H., Taerwe, L., & Vandevelde, P. (2001). "**Fire Testing of Concrete Slabs Strengthened with Fibre Composite Laminates.**" *in Proceedings of the 5th International Conference on Fibre Reinforced Plastics for Reinforced Concrete Structures (FRPRCS-5)*, 547–556.

[153] Williams, B., Bisby, L., Kodur, V., Green, M., & Chowdhury, E. (2006). "**Fire Insulation Schemes for FRP-Strengthened Concrete Slabs.**" *Composites Part A: Applied Science and Manufacturing*, 37(8), 1151–1160.

[154] Adelzadeh, M., Green, M. F., & Bénichou, N. (2012). "**Behaviour of Fibre Reinforced Polymer-Strengthened T-Beams and Slabs in Fire.**" *Proceedings of the Institution of Civil Engineers - Structures and Buildings*, 165(7), 361–371.

[155] Stratford, T. J., Gillie, M., Chen, J. F., & Usmani, A. S. (2009). "**Bonded Fibre Reinforced Polymer Strengthening in a Real Fire.**" *Advances in Structural Engineering*, 12(6), 867–878.

[156] Hawileh, R. A., Naser, M., Zaidan, W., & Rasheed, H. A. (2009). "**Modeling of Insulated CFRP-Strengthened Reinforced Concrete T-Beam Exposed to Fire.**" *Engineering Structures*, 31(12), 3072–3079.

[157] Firmo, J. P., Arruda, M. R. T., Correia, J. R., & Rosa, I. C. (2018). "**Three-Dimensional Finite Element Modelling of the Fire Behaviour of Insulated RC Beams Strengthened with EBR and NSM CFRP Strips.**" *Composite Structures*, 183, 124–136.

[158] Kodur, V. (2010). "**Fire Resistance Requirements for FRP Structural Members.**"

[159] Gao, W.-Y., Dai, J.-G., & Teng, J. G. (2016). "**Fire Resistance Design of Un-Protected FRP-Strengthened RC Beams.**" *Materials and Structures*, 49(12), 5357–5371.

[160] ACI 318M-14. (2014). "**Building Code Requirements for Structural Concrete.**" *Ed., ACI Committee 318*, American Concrete Institute: Farmington Hills, MI, United States.

[161] Wang, Y. C. C. & Kodur, V. (2005). "**Variation of Strength and Stiffness of Fibre Reinforced Polymer Reinforcing Bars with Temperature.**" *Cement and Concrete Composites*, 27(9–10), 864–874.

[162] ASTM D3039/D3039M-17. (2017). "**Standard Test Method for Tensile Properties of Polymer Matrix Composite Materials.**" *Ed., ASTM Committee D30*, ASTM International: West Conshohocken, PA, United States.

[163] Firmo, J. P., Arruda, M. R. T., & Correia, J. R. (2014). "**Contribution to the Understanding of the Mechanical Behaviour of CFRP-Strengthened RC Beams**

Subjected to Fire: Experimental and Numerical Assessment." *Composites Part B: Engineering*, 66, 15–24.

[164] Zhang, C. & Usmani, A. (2015). "**Heat Transfer Principles in Thermal Calculation of Structures in Fire.**" *Fire Safety Journal*, 78, 85–95.

[165] Eurocode 1. (2002). "**EN 1991-1-2: Actions on Structures - Part 1-2: General Actions - Actions on Structures Exposed to Fire [Authority:**" *Ed., European Committee for Standardization*, CEN: Brussels, Belgium.

[166] Hutton, D. (2003). "**Fundamentals of Finite Element Analysis.**" 1st ed.; McGraw-Hill: New York, NY, United States.

[167] Harmathy, T. Z. (1983). "**Properties of Building Materials at Elevated Temperatures.**" Ottawa, ON, Canada.

[168] Campbell, T. I. & Kodur, V. K. R. (1990). "**Deformation Controlled Nonlinear Analysis of Prestressed Concrete Continuous Beams.**" *PCI Journal*, 35(5), 42–55.

[169] De Lorenzis, L. & Zavarise, G. (2009). "**Cohesive Zone Modeling of Interfacial Stresses in Plated Beams.**" *International Journal of Solids and Structures*, 46(24), 4181–4191.

[170] Lu, X. Z., Teng, J. G., Ye, L. P., & Jiang, J. J. (2005). "**Bond-Slip Models for FRP Sheets/Plates Bonded to Concrete.**" *Engineering Structures*, 27(6), 920–937.

[171] Dwaikat, M. B. & Kodur, V. K. R. R. (2008). "**A Numerical Approach for Modeling the Fire Induced Restraint Effects in Reinforced Concrete Beams.**" *Fire Safety Journal*, 43(4), 291–307.

[172] Benichou, N., Sultan, M., MacCallum, C., & Hum, J. (2001). "**Thermal Properties of Wood , Gypsum and Insulation at Elevated Temperatures IR-710.**" Ottawa, Ontario, Canada.

[173] Rafi, M. M., Nadjai, A., & Ali, F. (2007). "**Fire Resistance of Carbon FRP Reinforced-Concrete Beams.**" *Magazine of Concrete Research*, 59(4), 245–255.

[174] Bai, Y., Vallée, T., & Keller, T. (2008). "**Modeling of Thermal Responses for FRP Composites under Elevated and High Temperatures.**" *Composites Science and Technology*, 68(1), 47–56.

[175] Ahmad, A. (2010). "**Behavior of FRP-Strengthened Reinforced Concrete Beams under Fire Conditions.**" Michigan State University, East Lansing, MI, United States.

[176] Yu, B. (2013). "**Fire Response of Reinforced Concrete Beams Strengthened with Near-Surface Mounted FRP Reinforcement.**" Michigan State University, East Lansing, MI, United States.

[177] Adeli, H. (2001). "**Neural Networks in Civil Engineering: 1989-2000.**" *Computer-Aided Civil and Infrastructure Engineering*, 16(2), 126–142.

[178] Liao, T. W., Egbelu, P. J., Sarker, B. R., & Leu, S. S. (2011). "**Metaheuristics for Project and Construction Management – A State-of-the-Art Review.**" *Automation in Construction*, 20(5), 491–505.

[179] Amezquita-Sanchez, J. P., Valtierra-Rodriguez, M., Aldwaik, M., & Adeli, H. (2016). "**Neurocomputing in Civil Infrastructure.**" *Scientia Iranica*, 23(6), 2417–2428.

[180] Shahin, M. A. (2013). "**Artificial Intelligence in Geotechnical Engineering: Applications, Modeling Aspects, and Future Directions.**" *Metaheuristics in Water, Geotechnical and Transport Engineering*, 169–204.

[181] Salehi, H. & Burgueño, R. (2018). "**Emerging Artificial Intelligence Methods in Structural Engineering.**" *Engineering Structures*, 171, 170–189.

[182] Kicinger, R., Arciszewski, T., & De Jong, K. (2005). "**Evolutionary Computation and Structural Design: A Survey of the State-of-the-Art.**" *Computers and Structures*, 83(23–24), 1943–1978.

[183] Saka, M. P. & Geem, Z. W. (2013). "**Mathematical and Metaheuristic Applications in Design Optimization of Steel Frame Structures: An Extensive Review.**" *Mathematical Problems in Engineering*, 2013(271031), 1–33.

[184] Cabalar, A. F. & Cevik, A. (2009). "**Genetic Programming-Based Attenuation Relationship: An Application of Recent Earthquakes in Turkey.**" *Computers and Geosciences*, 35(9), 1884–1896.

[185] Tezcan, J. & Cheng, Q. (2012). "**Support Vector Regression for Estimating Earthquake Response Spectra.**" *Bulletin of Earthquake Engineering*, 10(4), 1205–1219.

[186] Dhanya, J. & Raghukanth, S. T. G. (2018). "**Ground Motion Prediction Model Using Artificial Neural Network.**" *Pure and Applied Geophysics*, 175(3), 1035–1064.

[187] Khosravikia, F., Clayton, P., & Nagy, Z. (2019). "**Artificial Neural Network-Based Framework for Developing Ground-Motion Models for Natural and Induced Earthquakes in Oklahoma, Kansas, and Texas.**" *Seismological Research Letters*, 90(2 A), 604–613.

[188] Xie, Y., Ebad Sichani, M., Padgett, J. E., & DesRoches, R. (2020). "**The Promise of Implementing Machine Learning in Earthquake Engineering: A State-of-the-Art Review.**" *Earthquake Spectra*, 36(4), 1769–1801.

[189] Joghataie, A. & Farrokh, M. (2008). "**Dynamic Analysis of Nonlinear Frames by Prandtl Neural Networks.**" *Journal of Engineering Mechanics*, 134(11), 961–969.

[190] Jeon, J. S., Shafieezadeh, A., & Desroches, R. (2014). "**Statistical Models for Shear Strength of RC Beam-Column Joints Using Machine-Learning Techniques.**" *Earthquake Engineering and Structural Dynamics*, 43(14), 2075–2095.

[191] Naderpour, H. & Mirrashid, M. (2019). "**Shear Failure Capacity Prediction of Concrete Beam–Column Joints in Terms of ANFIS and GMDH.**" *Practice Periodical on Structural Design and Construction*, 24(2), 04019006.

[192] Chou, J.-S., Chiu, C.-K., Farfoura, M., & Al-Taharwa, I. (2011). "**Optimizing the Prediction Accuracy of Concrete Compressive Strength Based on a Comparison of Data-Mining Techniques.**" *Journal of Computing in Civil Engineering*, 25(3), 242–253.

[193] Yan, K. & Shi, C. (2010). "**Prediction of Elastic Modulus of Normal and High Strength Concrete by Support Vector Machine.**" *Construction and Building Materials*, 24(8), 1479–1485.

[194] Tiryaki, S. & Aydin, A. (2014). "**An Artificial Neural Network Model for Predicting Compression Strength of Heat Treated Woods and Comparison with a Multiple Linear Regression Model.**" *Construction and Building Materials*, 62, 102–108.

[195] De Stefano, A., Sabia, D., & Sabia, L. (1999). "**Probabilistic Neural Networks for Seismic Damage Mechanisms Prediction.**" *Earthquake Engineering and Structural Dynamics*, 28(7–8), 807–821.

[196] German, S., Jeon, J.-S., Zhu, Z., Bearman, C., Brilakis, I., DesRoches, R., & Lowes, L. (2013). "**Machine Vision-Enhanced Postearthquake Inspection.**" *Journal of Computing in Civil Engineering*, 27(6), 622–634.

[197] Paal, S. G., Jeon, J.-S., Brilakis, I., & DesRoches, R. (2015). "**Automated Damage Index Estimation of Reinforced Concrete Columns for Post-Earthquake Evaluations.**" *Journal of Structural Engineering*, 141(9), 04014228.

[198] Mangalathu, S. & Burton, H. V. (2019). "**Deep Learning-Based Classification of Earthquake-Impacted Buildings Using Textual Damage Descriptions.**" *International Journal of Disaster Risk Reduction*, 36,

[199] Flood, I., Muszynski, L., & Nandy, S. (2001). "**Rapid Analysis of Externally Reinforced Concrete Beams Using Neural Networks.**" *Computers and Structures*, 79(17), 1553–1559.

[200] Mansour, M. Y., Dicleli, M., Lee, J. Y., & Zhang, J. (2004). "**Predicting the Shear Strength of Reinforced Concrete Beams Using Artificial Neural Networks.**" *Engineering Structures*, 26(6), 781–799.

[201] Sudarsana Rao, H. & Ramesh Babu, B. (2007). "**Hybrid Neural Network Model for the Design of Beam Subjected to Bending and Shear.**" *Sadhana - Academy Proceedings in Engineering Sciences*, 32(5), 577–586.

[202] Pannirselv, N., Raghunath, P. N., & Suguna, K. (2008). "**Neural Network for Performance of Glass Fibre Reinforced Polymer Plated RC Beams.**" *American Journal of Engineering and Applied Sciences*, 1(1), 82–88.

[203] Naser, M. Z. (2020). "**Machine Learning Assessment of Fiber-Reinforced Polymer-Strengthened and Reinforced Concrete Members.**" *ACI Structural Journal*, 117(6), 237–251.

[204] Inel, M. (2007). "**Modeling Ultimate Deformation Capacity of RC Columns Using Artificial Neural Networks.**" *Engineering Structures*, 29(3), 329–335.

[205] Rose-Pehrsson, S. L., Hart, S. J., Street, T. T., Williams, F. W., Hammond, M. H., Gottuk, D. T., Wright, M. T., & Wong, J. T. (2003). "**Early Warning Fire Detection System Using a Probabilistic Neural Network.**" *Fire Technology*, 39(2), 147–171.

[206] Hodges, J. L., Lattimer, B. Y., & Luxbacher, K. D. (2019). "**Compartment Fire Predictions Using Transpose Convolutional Neural Networks.**" *Fire Safety Journal*, 108, 102854.

[207] Hodges, J. L. & Lattimer, B. Y. (2019). "**Wildland Fire Spread Modeling Using Convolutional Neural Networks.**" *Fire Technology*, 55(6), 2115–2142.

[208] Chunyu, Y., Jun, F., Jinjun, W., & Yongming, Z. (2010). "**Video Fire Smoke Detection Using Motion and Color Features.**" *Fire Technology*, 46(3), 651–663.

[209] Mao, W., Wang, W., Dou, Z., & Li, Y. (2018). "**Fire Recognition Based On Multi-Channel Convolutional Neural Network.**" *Fire Technology*, 54(2), 531–554.

[210] Ramachandran, G. (2002). "**The Economics of Fire Protection.**" 1st ed.; Routledge: New York, NY, United States.

[211] Amatulli, G., Rodrigues, M. J., Trombetti, M., & Lovreglio, R. (2006). "**Assessing Long-Term Fire Risk at Local Scale by Means of Decision Tree Technique.**" *Journal of Geophysical Research: Biogeosciences*, 111(4), 1–15.

[212] Kim, O. & Kang, D.-J. (2013). "**Fire Detection System Using Random Forest Classification for Image Sequences of Complex Background.**" *Optical Engineering*, 52(6), 067202.

[213] Lei, C., Deng, J., Cao, K., Ma, L., Xiao, Y., & Ren, L. (2018). "**A Random Forest Approach for Predicting Coal Spontaneous Combustion.**" *Fuel*, 223, 63–73.

[214] Al-Khaleefi, A. M., Terro, M. J., Alex, A. P., & Wang, Y. (2002). "**Prediction of Fire Resistance of Concrete Filled Tubular Steel Columns Using Neural Networks.**" *Fire Safety Journal*, 37(4), 339–352.

[215] Lu, H., Zhao, X.-L., & Han, L. H. (2006). "**Fire Resistance of SCC Filled Square Hollow Structural Steel Sections.**" *in Tubular Structures XI-Proceedings of the 11th*

International Symposium on Tubular Structures-ISTS11 Quebéc, Canada, 1st ed., 403–409.

[216] Lazarevska, M. (2016). "**Neural-Network-Based Approach for Prediction of the Fire Resistance of Centrically Loaded Composite Columns.**" *Tehnicki Vjesnik - Technical Gazette*, 23(5), 1475–1480.

[217] Erdem, H. (2010). "**Prediction of the Moment Capacity of Reinforced Concrete Slabs in Fire Using Artificial Neural Networks.**" *Advances in Engineering Software*, 41(2), 270–276.

[218] McKinney, J. & Ali, F. (2014). "**Artificial Neural Networks for the Spalling Classification & Failure Prediction Times of High Strength Concrete Columns.**" *Journal of Structural Fire Engineering*, 5(3), 203–214.

[219] Chen, B. T., Chang, T. P., Shih, J. Y., & Wang, J. J. (2009). "**Estimation of Exposed Temperature for Fire-Damaged Concrete Using Support Vector Machine.**" *Computational Materials Science*, 44(3), 913–920.

[220] Wei, Y. Y., Zhang, J. Y., & Wang, J. (2018). "**Research on Building Fire Risk Fast Assessment Method Based on Fuzzy Comprehensive Evaluation and SVM.**" *in 8th International Conference on Fire Science and Fire Protection Engineering (ICFSFPE 2017), Eds., Pan, Wang,* & *Yao,* Elsevier Procedia: Nanjing, China, 211, 1141–1150.

[221] Naser, M. Z. (2019). "**Properties and Material Models for Modern Construction Materials at Elevated Temperatures.**" *Computational Materials Science*, 160, 16–29.

[222] Naser, M. Z. (2019). "**Heuristic Machine Cognition to Predict Fire-Induced Spalling and Fire Resistance of Concrete Structures.**" *Automation in Construction*, 106, 102916.

[223] Naser, M. Z. (2020). "**Autonomous Fire Resistance Evaluation.**" *Journal of Structural Engineering*, 146(6), 04020103.

[224] Vapnik, V. (1999). "**The Nature of Statistical Learning Theory.**" Springer Science \& Business Media.

[225] Smola, A. J. & Schölkopf, B. (2004). "**A Tutorial on Support Vector Regression.**" *Statistics and Computing*, 14(3), 199–222.

[226] Breiman, L. (2001). "**Random Forests.**" *Machine Learning*, 45(1), 5–32.

[227] Breiman, L. (1994). "**Bagging Predictors: Technical Report No. 421.**" *Journal of Time Series Analysis*, 17(421), 1–20.

[228] Liaw, A. & Wiener, M. (2002). "**Classification and Regression by RandomForest.**" *R News*, 2(3), 18–22.

[229] Svetnik, V., Liaw, A., Tong, C., Christopher Culberson, J., Sheridan, R. P., & Feuston, B. P. (2003). "**Random Forest: A Classification and Regression Tool for Compound Classification and QSAR Modeling.**" *Journal of Chemical Information and Computer Sciences*, 43(6), 1947–1958.

[230] Chen, X. & Ishwaran, H. (2012). "**Random Forests for Genomic Data Analysis.**" *Genomics*, 99(6), 323–329.

[231] Ibrahim, I. A. & Khatib, T. (2017). "**A Novel Hybrid Model for Hourly Global Solar Radiation Prediction Using Random Forests Technique and Firefly Algorithm.**" *Energy Conversion and Management*, 138, 413–425.

[232] Biau, G., Devroye, L., & Lugosi, G. (2008). "**Consistency of Random Forests and Other Averaging Classifiers.**" *Journal of Machine Learning Research*, 9, 2015–2033.

[233] Yang, Z. R. & Yang, Z. (2014). "**Artificial Neural Networks.**" 6; McGraw-Hill: New York, NY, United States.

[234] LeCun, Y., Bengio, Y., & Hinton, G. (2015). "**Deep Learning.**" *Nature*, 521(7553), 436–444.

[235] Hegazy, T., Fazio, P., & Moselhi, O. (1994). "**Developing Practical Neural Network Applications Using Back-Propagation.**" *Computer-Aided Civil and Infrastructure Engineering*, 9(2), 145–159.

[236] Zhang, G., Eddy Patuwo, B., & Y. Hu, M. (1998). "**Forecasting with Artificial Neural Networks: The State of the Art.**" *International Journal of Forecasting*, 14(1), 35–62.

[237] Pedregosa, F., Varoquaux, G., Gramfort, A., *et al.* (2011). "**Scikit-Learn: Machine Learning in Python.**" *Journal of Machine Learning Research*, 12, 2825–2830.

[238] Cholett, F. et al. (2015). "**Https://Github.Com/Keras-Team/Keras.**" *Keras*.

[239] Chou, J.-S., Tsai, C.-F., Pham, A.-D., & Lu, Y.-H. (2014). "**Machine Learning in Concrete Strength Simulations: Multi-Nation Data Analytics.**" *Construction and Building Materials*, 73, 771–780.

[240] Young, B. A., Hall, A., Pilon, L., Gupta, P., & Sant, G. (2019). "**Can the Compressive Strength of Concrete Be Estimated from Knowledge of the Mixture Proportions?: New Insights from Statistical Analysis and Machine Learning Methods.**" *Cement and Concrete Research*, 115, 379–388.

[241] Kohavi, R. (1995). "**A Study of Cross-Validation and Bootstrap for Accuracy Estimation and Model Selection.**" *in IJCAI'95: Proceedings of the 14th International Joint Conference on Artificial Intelligence*, 2, 1137–1143.

[242] Naser, M. . & Alavi, A. (2020). "**Insights into Performance Fitness and Error Metrics for Machine Learning.**" *CoRR-ArXiv*, 2006.00887, 1–25.

[243] Carlos, T. B., Rodrigues, J. P. C., de Lima, R. C. A., & Dhima, D. (2018). "**Experimental Analysis on Flexural Behaviour of RC Beams Strengthened with CFRP Laminates and under Fire Conditions.**" *Composite Structures*, 189, 516–528.

[244] Bhatt, P. P., Kodur, V. K. R., Shakya, A. M., & Alkhrdaji, T. (2021). "**Performance of Insulated FRP-Strengthened Concrete Flexural Members under Fire Conditions.**" *Frontiers of Structural and Civil Engineering*, 15(1), 177–193.